ABSTRACT

Title of dissertation: INSPIRAL-MERGER-RINGDOWN MODELS FOR SPINNING BLACK-HOLE BINARIES AT THE INTERFACE BETWEEN ANALYTICAL AND NUMERICAL RELATIVITY

Andrea Taracchini, Doctor of Philosophy, 2014

Dissertation directed by: Professor Alessandra Buonanno
Department of Physics

The long-sought direct detection of gravitational waves may only be a few years away, as a new generation of interferometric experiments of unprecedented sensitivity will start operating in 2015. These experiments will look for gravitational waves with frequencies from 10 to about 1000 Hz, thus targeting astrophysical sources such as coalescing binaries of compact objects, core collapse supernovae, and spinning neutron stars, among others. The search strategy for gravitational waves emitted by compact-object binaries consists in filtering the output of the detectors with template waveforms that describe plausible signals, as predicted by general relativity, in order to increase the signal-to-noise ratio.

In this work, we modeled these systems through the effective-one-body approach to the general-relativistic 2-body problem. This formalism rests on the idea that binary coalescence is universal across different mass ratios, from the test-particle limit to the equal-mass regime. It bridges the gap between post-Newtonian theory (valid in the slow-motion, weak-field limit) and black-hole perturbation the-

ory (valid in the small mass-ratio limit, but not limited to slow motion). The project unfolded along two main avenues of inquiry, with the goal of developing faithful inspiral-merger-ringdown waveforms for generic spinning, stellar-mass black-hole binaries. On the one hand, we studied the motion and gravitational radiation of test masses orbiting Kerr black holes in perturbation theory, with the goal of extracting strong-field information that can be incorporated into effective-one-body models. On the other hand, we worked at the interface between analytical and numerical relativity by calibrating effective-one-body models against numerical solutions of Einstein's equations, and testing their accuracy when extrapolated to different regions of the parameter space. In the course of this project, we also studied conservative effects of the 2-body dynamics, namely the periastron advance, and devised algorithms for generating realistic initial conditions for spinning, precessing black-hole binaries.

The waveform models developed in this project will be employed in data-analysis pipelines and gravitational-wave searches of advanced LIGO and Virgo. In the near future, natural extensions of this work will be the inclusion of tidal effects in the comparable-mass regime (relevant for neutron-star/black-hole binaries), and spin precession in the test-particle limit.

INSPIRAL-MERGER-RINGDOWN MODELS FOR SPINNING BLACK-HOLE BINARIES AT THE INTERFACE BETWEEN ANALYTICAL AND NUMERICAL RELATIVITY

by

Andrea Taracchini

Dissertation submitted to the Faculty of the Graduate School of the
University of Maryland, College Park in partial fulfillment
of the requirements for the degree of
Doctor of Philosophy
2014

Advisory Committee:
Professor Alessandra Buonanno, Chair/Advisor
Professor William D. Dorland
Professor Theodore A. Jacobson
Professor Michael C. Miller
Professor Peter Shawhan

Preface

The work presented in this thesis was supported by the United States National Science Foundation and by the Maryland Center for Fundamental Physics.

Acknowledgments

First and foremost, I would like to thank my advisor, Alessandra Buonanno. Over the course of these years, her passion for physics as well as her rigorous work ethic have been an inspiration and an example. Thanks to her precious guidance and encouragement I have been able to give my best, even through challenging times.

My deep gratitude goes to Yi Pan for his close collaboration on most of the research projects discussed in this thesis. I am especially thankful for his patience in teaching me many things about gravitational-wave physics and coding.

I would like to thank all of the co-authors on the papers which make up chapters of this thesis: Leor Barack, Enrico Barausse, Michael Boyle, Tony Chu, Daniel Hemberger, Tanja Hinderer, Scott Hughes, Gaurav Khanna, Lawrence Kidder, Alexandre Le Tiec, Geoffrey Lovelace, Abdul Mroué, Harald Pfeiffer, Norichika Sago, Mark Scheel, Béla Szilágyi, Nicholas Taylor, Anil Zenginoglu, and everyone in the NRAR collaboration. I would also like to thank Prayush Kumar at Syracuse University for collaborating with me on the LAL implementation of SEOBNRv3. I look forward to working with you again in the future.

I would like to thank all the wonderful and diverse people who have been part of the gravitational wave group at the University of Maryland during my PhD studies, for their help and for interesting discussions: Enrico Barausse, Collin Capano, Phil Graff, Tanja Hinderer, Alexandre Le Tiec, Tyson Littenberg, Sylvain Marsat, Evan Ochsner, Yi Pan, Craig Robinson.

I would like thank the Kavli Institute for Theoretical Physics in Santa Barbara

CA for its hospitality during the Summer of 2012.

I would like to thank the administrative staff of the Department of Physics at the University of Maryland for helping me jump through the hoops of bureaucracy.

I would like to thank my undergraduate advisor, Ennio Gozzi, for giving me the motivation to embark on this American adventure.

I would like to express my gratitude to Riccardo, Alberto and Claudio, for their unwavering friendship in spite of the many miles that divide us, and to Kanu and Rong, for sharing the ups and downs of graduate school. A thank you also to Rachael for listening to my early morning ramblings.

Lastly, a special thank you goes to my parents and sister, for always believing in me, and allowing me to pursue my dreams. Everything I am, I owe to them.

Table of Contents

List of Tables

List of Figures

List of Abbreviations

AR	Analytical Relativity
EMRI	Extreme Mass-Ratio Inspiral
EOB	Effective One Body
GW	Gravitational Wave
IMR	Inspiral-Merger-Ringdown
ISCO	Innermost Stable Circular Orbit
LR	Light Ring
NQC	Non-Quasicircular
NR	Numerical Relativity
NRAR	Numerical Relativity / Analytical Relativity
QNM	Quasinormal Mode
RD	Ringdown
SXS	Simulation of eXtreme Spacetimes
TPL	Test-Particle Limit

Chapter 1: **Preamble**

The theory of general relativity, formulated by Albert Einstein in the first decade of the 20th century [1, 2], describes the gravitational interaction between matter (and energy) distributions in terms of the geometry of a continuum, the spacetime. As opposed to the Newtonian approach to gravity, in general relativity space and time are no longer static and absolute quantities acting as a mere environment for the physical events, gravitation included. Instead, they are subject to dynamical deformations that are proportional to the matter and energy content of the Universe. A test body of mass m immersed in a background spacetime moves from point A to point B according to the following variational principle

$$\delta\left(-m\,c^2\int_A^B d\tau\right)=0\,, \tag{1.1}$$

where the proper time element $d\tau$ is specified by the components of the metric tensor $g_{\alpha\beta}$ through $c^2d\tau^2\equiv -g_{\alpha\beta}\,\mathrm{d}x^\alpha\mathrm{d}x^\beta$, once a coordinate system x^λ is chosen for the spacetime manifold; the paths $x^\lambda(\tau)$ that solve Eq. (1.1) are the (timelike) geodesics of the spacetime. Gravity is encoded in the geometry of the spacetime (or, equivalently, in the metric) via the field equations

$$R_{\alpha\beta}-\frac{1}{2}g_{\alpha\beta}R=\frac{8\pi G}{c^4}T_{\alpha\beta}\,, \tag{1.2}$$

where $R_{\alpha\beta}$ and R are the Ricci tensor and scalar, respectively, and $T_{\alpha\beta}$ is the energy-momentum tensor describing the mass-energy distribution in the physical system of interest. Therefore, in Einstein's theory, gravitational interactions are treated on a separate footing as compared to other fundamental forces, reflecting the fact that gravity obeys the Equivalence Principle, which expresses the local indistinguishability of inertial and gravitational mass.

General relativity has withstood a long and glorious series of experimental tests, ever since its formulation [3]. These tests have mostly probed the slow-motion and/or the weak-field regime, that is systems characterized by velocities that are small compared to the speed of light c, and/or by weak gravitational fields ($GM/c^2d \ll 1$ for a system of total mass M and size d). However, the opportunity of experimentally studying gravity in the relativistic, strong-field regime may be closer than ever, thanks to the effort of the LIGO [4], Virgo [5] and KAGRA [6] collaborations, which are upgrading/building a network of km-sized ground-based laser interferometers aimed at detecting gravitational waves with frequencies around $10 - 1000$ Hz. In the future, space-based laser interferometry (e.g., eLISA [7, 8]) will be able to probe gravitational waves at much lower frequencies, in the mHz range. Other detection experiments, operated by the NANOGrav [9], EPTA [10], and PPTA [11] collaborations, are measuring the period of several radio pulsars (also known as PTAs, pulsar timing arrays), and are looking for correlated changes in the times of arrival of the radio signals across the array caused by the passage of a gravitational wave.

The prediction of gravitational radiation is one key feature of general relativity

that Einstein himself discovered as early as 1916 [12, 13]. From a formal point of view, the linearization of the theory about a flat, Minkowskian background $\eta_{\alpha\beta}$ leads to perturbations $h_{\alpha\beta}$ (with $|h_{\alpha\beta}| \ll 1$) obeying a wave-like equation which, introducing the trace-reversed perturbation $\bar{h}_{\alpha\beta} \equiv h_{\alpha\beta} - \frac{1}{2}\eta_{\alpha\beta}h$ and the Lorenz gauge ($\partial^\beta \bar{h}_{\alpha\beta} = 0$), reads

$$\Box \bar{h}_{\alpha\beta} = -\frac{16\pi G}{c^4} T_{\alpha\beta}\,, \tag{1.3}$$

where $\Box$ is the flat D'Alambertian operator. In vacuum (i.e., $T_{\alpha\beta} = 0$), solutions to Eq. (1.3) can be expanded into transverse plane waves propagating at the speed of light. The number of independent degrees of freedom can be reduced from 10 (i.e., the number of independent components of a symmetric rank-2 tensor) down to 2 by exploiting gauge symmetries; historically, these are referred to as the $+$ and $\times$ polarization. The Lorenz gauge gives 4 conditions. Moreover, under the transformation $x^\alpha \to x^\alpha + \xi^\alpha(x)$, $\partial^\beta \bar{h}_{\alpha\beta}$ transforms into $\partial^\beta \bar{h}_{\alpha\beta} - \Box\xi_\alpha$, so in order to preserve the Lorenz gauge we have to require that $\Box\xi_\alpha = 0$. Defining $\xi_{\alpha\beta} \equiv \partial_\alpha\xi_\beta + \partial_\beta\xi_\alpha - \eta_{\alpha\beta}\partial_\gamma\xi^\gamma$, if $\Box\xi_\alpha = 0$, then also $\Box\xi_{\alpha\beta} = 0$, and we can choose the 4 functions ξ_α in such a way as to impose 4 conditions on $\bar{h}_{\alpha\beta}$.

If $\hat{\mathbf{N}}$ is the direction of propagation of the wave, one considers a basis $\{\hat{\mathbf{u}}, \hat{\mathbf{v}}\}$ in the plane orthogonal to $\hat{\mathbf{N}}$, and defines the polarization tensors

$$e^R_+(\hat{\mathbf{N}}) \equiv \hat{\mathbf{u}} \otimes \hat{\mathbf{u}} - \hat{\mathbf{v}} \otimes \hat{\mathbf{v}}\,, \tag{1.4}$$

$$e^R_\times(\hat{\mathbf{N}}) \equiv \hat{\mathbf{u}} \otimes \hat{\mathbf{v}} + \hat{\mathbf{v}} \otimes \hat{\mathbf{u}}\,, \tag{1.5}$$

where we made explicit the dependence on the direction of propagation of the radiation, and the superscript R stands for "radiation". Then the $+$ and $\times$ polarizations

are the projections of $h_{\alpha\beta}$ onto $(e^R_{+,\times})_{ij}$.

The effect of gravitational waves on matter amounts to a deviation of neighboring geodesics. The cleanest example is given by a circular ring of freely-falling test particles lying in a plane orthogonal to the direction of propagation of the waves, which will undergo stretching and squeezing (in + and ×-shaped patterns) caused by the passage of a wave.

Gravitational-wave signals are often described in terms of the (time-dependent) strain $h(t)$ (not to be confused with the trace of $h_{\alpha\beta}$), defined as the ratio between the change ΔL by the separation L between two freely-falling test masses caused by a wave: $h \equiv \Delta L/L$. The strain is related to the metric perturbation $h_{\alpha\beta}$ via convolution with geometrical factors which depend on the sky location of the source of gravitational waves as well as on the specific shape of the detector. Given the weak coupling of gravity to matter via Newton's constant G, typical strains on Earth produced by astrophysical sources in the experimentally accessible frequency range are $\sim 10^{-21}$. Therefore, the direct detection of gravitational waves requires an experimental apparatus capable of exquisite sensitivity. One class of direct-detection experiments, pioneered by the work of Joseph Weber in the 1960's, relies on bar detectors, which exploit resonance with the gravitational-wave frequency in order to magnify the mechanical deformations caused by the passing wave. The main disadvantages of such instruments are their narrow frequency band and limited sensitivity. Another, more sensitive category of detectors (to which LIGO, Virgo, and KAGRA belong) rely on accurate measurements of the positions of mirrors (acting as test masses) by means of lasers, with a setup akin to a Michelson interferometer.

At these facilities, the (design) sensitivity is going to be comparable to the indicative value of $\sim 10^{-24}$ for a fairly wide range of frequencies, $\sim 10 - 1000$ Hz. Laser interferometers rest on the idea of measuring the phase shift between the light circulating in the arms of the detectors, as their relative length changes under the effect of a gravitational wave. There are three main sources of noise that limit the strain sensitivity of such detectors: (i) the seismic noise, that dominates at low frequencies ($\lesssim 10$ Hz in advanced LIGO), caused by the coupling of the suspended mirrors to the ground; this kind of noise can be minimized by sophisticated mechanical isolation techniques; (ii) the thermal noise, that dominates the intermediate frequency range, and is due to thermal fluctuations of the surface of the mirrors and the suspension wires; this kind of noise can be reduced with cryogenics and a careful choice of the materials; (iii) the shot noise, of quantum origin, dominating at high frequencies, that consists of intensity fluctuations of the lasers, which can be suppressed with high-power devices and squeezed light configurations.

The chances of detecting gravitational waves with ground-based laser interferometers can be enhanced by an accurate knowledge of the signals that may realistically lie in the bandwidth of the detectors. First, let us consider the solution of Eq. (1.3) in the presence of a non-vanishing $T_{\alpha\beta}$. At leading-order, for weak-field and slowly moving sources, one finds that the gravitational perturbation far from the source in transverse and traceless (TT) gauge[1] ($h^{0\alpha} = 0$, $h^i{}_i = 0$, $\partial^j h_{ij} = 0$)

[1]One can obtain $h_{ij}^{\rm TT}$ from h_{kl} by application of the projection operator $\perp^k{}_i \perp^l{}_j - \frac{1}{2} \perp^{kl} \perp_{ij}$, where $\perp_{ab} \equiv \delta_{ab} - \hat{N}_a \hat{N}_b$.

reads [14]

$$h_{ij}^{\rm TT} = \frac{2G}{\mathcal{R}c^4}\ddot{Q}_{ij}^{\rm TT}\left(t - \frac{\mathcal{R}}{c}\right), \tag{1.6}$$

where i, j are spatial indices running over the 2 dimensions that are transverse to the direction of propagation, $\mathcal{R}$ is the distance to the source[2], and

$$Q_{ij} \equiv M_{ij} - \frac{1}{3}\delta_{ij}M_{kk}\,, \tag{1.7}$$

with $M^{ij} \equiv c^{-2}\int \mathrm{d}^3x\, x^i x^j T^{00}(t, \mathbf{x})$, is the mass quadrupole of the source, hence the name "quadrupole formula" for Eq. (1.6). At lowest order, T^{00}/c^2 is the mass density of the source.

While, in principle, any system with a time-varying mass quadrupole is expected to radiate gravitational waves, in practice, there is hope of detecting only emissions from events of astrophysical proportions, where the masses involved are $\mathcal{O}(M_\odot)$ (with $M_\odot \approx 1.99 \times 10^{30}$ kg), and the velocities are significant fractions of the speed of light. The clear disadvantage of such sources is their large distance from us, that suppresses the amplitude of the emitted gravitational waves. However, gravitational-wave detectors are sensitive to the amplitude of the metric perturbation itself (which decays only as $\mathcal{R}^{-1}$), and not to its carried energy (which, instead, decreases as $\mathcal{R}^{-2}$).

The rest of this thesis is organized as follows. In Chapter 2 we will give

[2]At leading order, Eq. (1.6) can be extended to the case of an expanding Universe by replacing $\mathcal{R}$ with the luminosity distance D_L, and introducing a time dilation factor $(1+z)$, where z is the redshift of the source.

an overview of the main motivations and results of work done by the author and collaborators concerning the analytical modeling of gravitational waveforms from spinning black-hole binaries within the effective-one-body approach. Chapter 3 will study the phenomenon of periastron advance in black-hole binaries as a way to test the conservative dynamics of the effective-one-body model. Chapter 4 will present results concerning the gravitational-wave emission from particles plunging into Kerr black holes. Chapter 5 will discuss an analytical model for the gravitational energy flux absorbed by the horizon of a Kerr black hole in the presence of a perturbing particle on a circular, equatorial orbit. Chapter 6 will develop an iterative algorithm to efficiently compute quasicircular initial conditions for numerical-relativity simulations of spinning, precessing black-hole binaries. Chapter 7 and 8 will present the calibration of an effective-one-body model for spinning, nonprecessing black-hole binaries to state-of-the-art numerical-relativity simulations. Chapter 9 will extrapolate the calibrated effective-one-body model presented in Chapter 7 outside its range of calibration, comparing it to simulations of the Numerical Relativity / Analytical Relativity Collaboration. Chapter 10 will compare the calibrated effective-one-body model presented in Chapter 7 to nonspinning numerical-relativity simulations of increasing length to test the stability of the nonspinning calibration. Chapter 11 will present an effective-one-body model for precessing black-hole binaries. Chapter 12 will present concluding remarks and future perspectives. The Appendices contain supplemental material from Chapters 4, 5, and 7.

Chapter 2: **Overview**

2.1 Compact-object binaries as sources for ground-based gravitational-wave detectors

We focus our attention on a specific class of astrophysical sources of gravitational waves, namely compact-object binaries, explaining why they are so interesting for gravitational-wave physics, and what are their likely formation scenarios.

2.1.1 Formation scenarios for binary systems of compact objects

One of the most studied potential sources of gravitational waves is a binary system of compact objects (such as black holes or neutron stars), also known as "compact binary". The specific interest in compact binaries (rather than ordinary stellar binaries) for gravitational-wave physics stems from the extremely short orbital periods that they can achieve; in fact, current and near-future ground-based detectors cannot detect gravitational waves with frequencies below $\mathcal{O}(10)$ Hz, which translates into orbital timescales for the source at most of order $\mathcal{O}(10^{-1})$ s. The gravitational-wave power radiated by compact binaries can approach $c^5/G = 3.6 \times 10^{52}$ W when they coalesce, a luminosity largely exceeding the electromagnetic luminosity of the

entire visible Universe [15].

The dissipative orbital dynamics of compact binaries is dictated mostly by gravitational radiation only after the relative separation of the objects goes below $\mathcal{O}(10^3)$ gravitational radii[1], and consists of three phases [16, 17]: (i) a long *inspiral* part, when the relative separation of the two objects shrinks at a rate that is much slower than the orbital frequency (*adiabatic* motion); (ii) a quick *plunge*, when the two objects reach the innermost stable circular orbit (ISCO) of the spacetime, develop inward radial motion (although the system is still quite adiabatic), and eventually *merge*, reaching the peak gravitational-wave luminosity; (iii) finally, a relaxation phase of the remnant to a stationary Kerr black hole (provided cosmic censorship holds), known as *ringdown*, characterized by decaying gravitational perturbations (the quasinormal modes, or QNMs [18]). By the time the binary reaches the ISCO, the system is relativistic. For black-hole binaries, the gravitational-wave emission displays a slow but steady growth of its amplitude and frequency. The amplitude then reaches a peak value close to the merger, and then quickly decays during the ringdown, while the frequency keeps growing until it plateaus in the late ringdown. Figure 2.1 summarizes the stages of black-hole binary evolution, along with the characteristic inspiral-merger-ringdown gravitational waveform and luminosity. In the case of neutron-star or neutron-star/black-hole binaries the merger-ringdown waveform displays a richer structure due to the presence of matter [19, 20].

Observations support the existence of binary neutron stars [21]. The first system of this kind ever discovered was the binary pulsar PSR B1913+16, that

[1]For a binary of total mass M, the gravitational radius is defined as $R_g \equiv 2GM/c^2$.

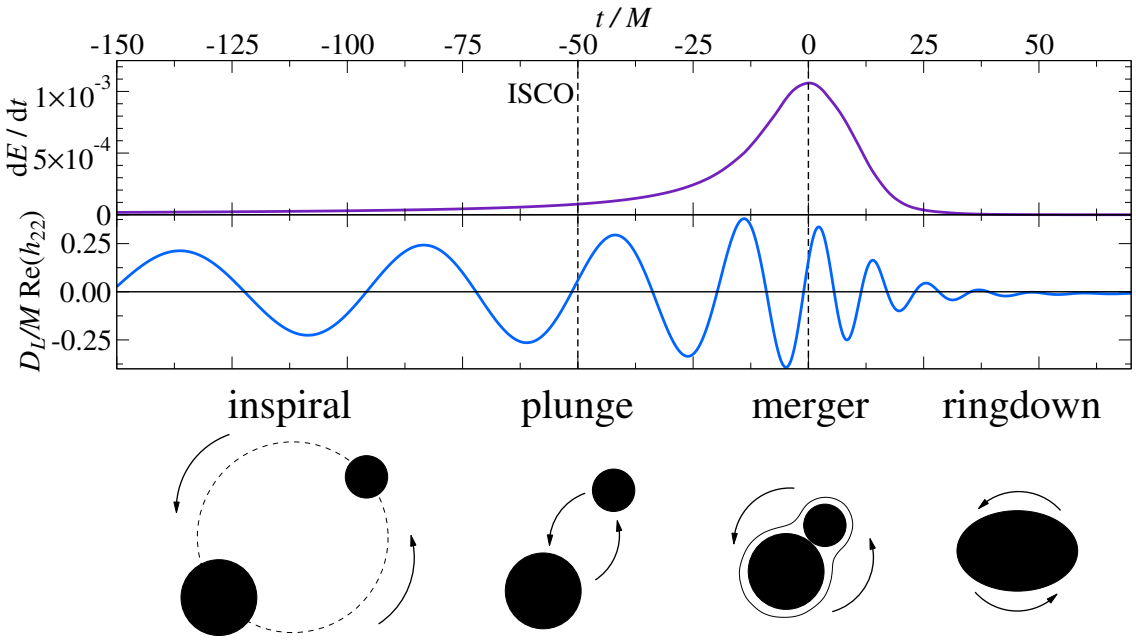

Figure 2.1: Diagram of black-hole binary coalescence (lower panel), the corresponding luminosity $\mathrm{d}E/\mathrm{d}t$ (upper panel), and the emitted gravitational waveform h_{22} (middle panel). Here we consider a binary with negligible eccentricity. During the *inspiral* the two black holes are far apart, and move on a slowly shrinking, quasicircular orbit; the waveform amplitude and frequency slowly increase over time during this phase. The *plunge* starts when the binary reaches the innermost stable circular orbit. The *merger* occurs when a common apparent horizon forms, and the gravitational-wave luminosity reaches its maximum value. Lastly, the *ringdown* is the relaxation of the remnant black hole to a stationary Kerr geometry via the emission of damped gravitational radiation. Here $G = c = 1$. The luminosity is computed at leading order from Eq. (2.35). D_L is the distance between the observer and the source, and M is the total mass of the compact binary. The $(\ell, m) = (2, 2)$ mode waveform h_{22} is defined by the multipolar decomposition in Eq. (2.15).

also allowed an indirect confirmation of the existence of gravitational radiation; in fact, measurements of the decay of its orbital period over the last four decades are in remarkable agreement with the general relativistic dissipation of energy into gravitational waves [22, 23], a discovery that earned Russell A. Hulse and Joseph H.

Taylor the 1993 Nobel prize in physics. The physical parameters of binary neutron stars are constrained by radio observations and formation models. Their component masses in observed systems are in the range $(1.35 \pm 0.04)M_\odot$, i.e., considerably more constrained than the full range $(1.25 - 2.01)M_\odot$ of well-measured neutron star masses [24]. The dimensionless spins[2] observed in binary neutron stars are ≤ 0.04 [25].

The existence of stellar-mass black-hole binaries is instead more speculative. Two are the main avenues that may lead to their formation: on the one hand, the evolution of stellar binaries, as studied by population synthesis models; on the other hand, dynamical capture events in dense stellar clusters [26–30]. X-ray observations indicate individual black-hole masses in the range from $5M_\odot$ to $20M_\odot$ [31], so that no black holes in the range $3-5M_\odot$ have been seen so far [32]. Recent theoretical models predict isolated black-hole masses up to $80M_\odot$ [33]. Masses as large as $100M_\odot$ can be achieved in particular astrophysical scenarios, like the evolution of massive stars in low metallicity environments [34], but there exist many uncertainties pertaining the mechanism involved. While mass ratios are not constrained by observations, modeling of field binaries (whose stars evolve into black holes in isolation from each other) suggests mass ratios from 1 to 4 as more likely [34]. The dimensionless spins of several black holes have been measured via X-ray observations, and have been found throughout the range compatible with general relativity (i.e., up to ~ 1) [35–37]. While correlations between the physical parameters of the black holes in the field

[2]For a compact object of mass M and angular momentum J, the dimensionless spin is defined as $\chi \equiv cJ/GM^2$.

binary scenario are plausible (such as partial alignment of the spins [38]), they are not expected for black-hole binaries formed through dynamical processes in dense environments.

There also exists indirect evidence for supermassive black-hole binaries, forming as a consequence of galaxy mergers [39]. The formation mechanism consists of different stages [40] : first, the black holes sink towards the center of the common gravitational potential due to friction with neighboring stars; second, a gaseous-disk driven phase causes a decay of the orbital period; finally, on a sub-parsec scale, the dissipation of energy of the binary is dominated by the gravitational-wave emission. However, because of the large masses of the component objects ($10^6 - 10^9 M_\odot$), merging supermassive black-hole binaries produce signals with frequencies in the mHz range[3], therefore they cannot be accessible to Earth-based interferometers, but they are instead one of the primary targets of space-based interferometers like eLISA [41] and of pulsar timing arrays (in the form of a stochastic background) [9–11].

There is also the possibility of compact binaries consisting of a neutron star and a stellar-mass black hole. Similarly to stellar-mass black-hole binaries, these sources may form through evolution of field binaries or through dynamical capture of a neutron star by a black hole [26, 42]. Neutron-star and neutron-star/black-hole binaries are promising candidates for powering short gamma-ray bursts [43] or

[3] A rough estimation of the merger frequency of a compact binary of total mass M is given by the frequency of the Schwarzschild innermost stable circular orbit (ISCO)

$$f_{\rm ISCO} \approx 4\,400 \left(\frac{M_\odot}{M}\right) {\rm Hz}\,. \tag{2.1}$$

producing an electromagnetic counterpart to the gravitational-wave emission that could be followed up [44].

In this thesis, we are going to focus mainly on stellar-mass black-hole binaries as sources of gravitational waves.

2.1.2 Detection rates

We now discuss how likely detections of gravitational waves from compact binaries are going to be in the advanced-detector era.

The rate R_D of detections of gravitational waves emitted by compact binaries that can coalesce within the Hubble time crucially depends on the abundance of such sources within the sensitive volume of the detectors [45]. In general, detection rates depend on the coalescence rate R of a specific type of binary in our Galaxy and on the number N_G of galaxies accessible to the detector: $R_D = R \times N_G$. In turn, the reach of a detector is expressed by the horizon distance $D_{\rm hor}$, defined as the distance at which an optimally oriented source can be detected with a signal-to-noise ratio (SNR) $\rho = 8$. The dependence on the specific detector enters the computation of the optimal SNR through the noise power spectral density[4] S_n via the following

[4]The noise spectral density of a detector characterized by stationary noise $n(t)$ is defined as

$$\langle \tilde{n}^*(f)\tilde{n}(f')\rangle = \delta(f-f')\frac{S_n(f)}{2}\,, \tag{2.2}$$

where $\langle\cdots\rangle$ indicates an average over different realizations of the noise, and $\tilde{n}(f)$ is the Fourier transform of $n(t)$.

equation

$$\rho^2 \equiv 4 \int_0^\infty \frac{|\tilde{h}(f)|^2}{S_n(f)} \mathrm{d}f \,, \tag{2.3}$$

where $\tilde{h}(f)$ is the Fourier transform of the strain $h(t)$. The amplitude $|\tilde{h}|$ is proportional to the inverse of the distance $\mathcal{R}$ to the source (see Eq. (1.6)). The specific source of interest (black-hole binary, neutron-star binary, or neutron-star/black-hole binary) determines the appropriate *waveform* $h(t)$ to use in the computation of $D_{\rm hor}$.

The number of accessible galaxies up to $\mathcal{R} = D_{\rm hor}$ is

$$N_G = \frac{4\pi}{3} \left(\frac{D_{\rm hor}}{\rm Mpc} \right)^3 (2.26)^{-3} (0.0116) \,, \tag{2.4}$$

where the factor $1/2.26$ is an average correction over all sky localizations and orientations, and 0.0116 Mpc^{-3} is the extrapolated density of Milky-Way-equivalent galaxies (MWEGs) in the local Universe [46].

The rates of coalescence R are affected by large uncertainties, since, with the sole exception of a handful of observed binary neutron stars, they can only be estimated from theoretical population synthesis models [47], that are typically only loosely constrained by observations, as already mentioned when discussing the formation mechanisms of compact binaries. For binary neutron stars one can alternatively extrapolate the few observations of binary pulsars [48,49]. Given d observations of binary pulsars within our Galaxy that would merge within the Hubble time, the coalescence rate of neutron-star binaries can be estimated as [50]

$$R = \sum_{i=1}^{d} \frac{V_G}{V_i^{\rm max} \tau_i} \,, \tag{2.5}$$

where V_G is the volume of the Milky Way, $V_i^{\rm max}$ is the volume that could be surveyed when discovering the i-th system, and τ_i is the total lifetime of the binary, estimated

as $\tau_i = P_i/(2\dot{P}_i) + \tau_{\rm merger}$, P_i being the observed pulsar period and $\tau_{\rm merger}$ being the time until merger (computed from the observed orbital parameters). This formula gets corrections due to the luminosity function (i.e., there may be fainter pulsars that could not be detected), and due to beaming (i.e., there may be systems where the radio beam of the pulsars never crosses our line of sight).

Realistic (i.e., mean) merger rates R are [45]: $1\,{\rm Mpc}^{-3}\,{\rm Myr}^{-1}$ for neutron-star binaries; $0.03\,{\rm Mpc}^{-3}\,{\rm Myr}^{-1}$ for neutron-star/black-hole binaries; $0.005\,{\rm Mpc}^{-3}\,{\rm Myr}^{-1}$ for black-hole binaries; error bars for these rates span a couple of orders of magnitude. Realistic (i.e., mean) detection rates R_D for advanced LIGO/Virgo for inspirals only[5] are [45]: $40\,{\rm yr}^{-1}$ for neutron-star binaries; $10\,{\rm yr}^{-1}$ for neutron-star/black-hole binaries; $20\,{\rm yr}^{-1}$ for black-hole binaries. Even if the value of R for black-hole binaries is low, gravitational-wave detectors have the largest reach for these sources, $\sim 2\,{\rm Gpc}$ for $(10+10)M_\odot$ systems, thanks to their large total mass, which puts the louder part of their signal (i.e., the plunging phase, close to coalescence) well within the sensitive band. Neutron-star binaries (i.e., $(1.4+1.4)M_\odot$ systems), instead, have an horizon distance of only $\sim 450\,{\rm Mpc}$, and neutron-star/black-hole binaries have an horizon distance of $\sim 900\,{\rm Mpc}$ for $(1.4+10)M_\odot$ systems.

2.2 Detection strategy for compact-object binaries

In an idealized detection experiment, a photodetector monitors the light output of a power-recycled Michelson interferometer with Fabry-Pérot cavities generat-

[5]This means that, when computing $D_{\rm hor}$, $h(t)$ does not include the plunge-merger-ringdown portion.

ing a time-dependent signal $s(t)$. In the presence of a gravitational-wave strain[6] $h(t)$, the output of the detector can be written as $s(t) = h(t) + n(t)$, where we introduced the noise $n(t)$. Typically, $|h| \ll |n|$. For simplicity, here we do not introduce the complication of dealing with the transfer function of the interferometer [14]. The standard strategy for detecting coalescing compact-object binaries is the *matched filtering* technique, which consists in filtering $s(t)$ with a prediction of the gravitational signal. More precisely, in the frequency domain, one can show [51] that $\tilde{h}(f)/S_n(f)$ is the optimal filter function (Wiener filter), i.e., the one maximizing the measured SNR ρ_m

$$\rho_m \equiv \frac{4\,\mathrm{Re}\int_0^\infty \frac{\tilde{h}^*(f)\tilde{s}(f)}{S_n(f)}\mathrm{d}f}{\left[4\int_0^\infty \frac{|\tilde{s}(f)|^2}{S_n(f)}\mathrm{d}f\right]^{1/2}}\,. \tag{2.6}$$

The observation time is always finite and the data are collected with a certain sampling rate: say one collects n samples in a time T. Let us consider the case of a monochromatic waveform $h(t) = h_0 e^{2\pi i f_0 t}$. The Fourier transform of $h(t)$ is a Dirac delta $\delta(f - f_0)$, that we can represent with

$$\delta(f - f_0) = \lim_{T\to\infty} \frac{\sin\left[(f - f_0)T\right]}{\pi(f - f_0)}\,. \tag{2.7}$$

Note that

$$\lim_{f\to f_0} \frac{\sin\left[(f - f_0)T\right]}{\pi(f - f_0)} = \frac{T}{\pi}\,, \tag{2.8}$$

so $|\tilde{h}(f)| \propto T$ for $f \approx f_0$. Also, for a finite time of observation T, we have [14] $\frac{1}{2}S_n(f) = \langle|\tilde{n}(f)|^2\rangle\Delta f$, where $\Delta f = 1/T$. In the simple case of white noise, S_n does not depend on f, hence $S_n(f) = (\text{const.}) \times \Delta f$. Thus, setting $f_k = k\,\Delta f$

[6] $h(t)$ is built by convolving the metric perturbation h_{ij} with the antenna pattern functions of the detector.

$(k = 1, \cdots, n)$, terms appearing in Eq. (2.6) can be approximated as

$$\int_0^\infty \frac{|\tilde{h}(f)|^2}{S_n(f)} \mathrm{d}f \approx \sum_k \frac{|\tilde{h}(f_k)|^2}{S_n(f_k)} \Delta f \propto T^2 \,, \tag{2.9}$$

$$\int_0^\infty \frac{\tilde{h}^*(f)\tilde{n}(f)}{S_n(f)} \mathrm{d}f \approx \sum_k \frac{\tilde{h}^*(f_k)\tilde{n}(f_k)}{S_n(f_k)} \Delta f \propto T^1 \,, \tag{2.10}$$

$$\int_0^\infty \frac{|\tilde{n}(f)|^2}{S_n(f)} \mathrm{d}f \approx \sum_k \frac{|\tilde{n}(f_k)|^2}{S_n(f_k)} \Delta f \propto T^0 \,. \tag{2.11}$$

Therefore, in the presence of pure noise (i.e., $s = n$) ρ_m grows with time as $\sqrt{T}$, while in the presence of a signal (i.e., $s = h + n$) it grows as T. Hence, the contribution to ρ_m from a real signal is enhanced with respect to the contribution from the noise by a factor proportional to $\sqrt{T}$. So one can dig into the floor of the noise provided the observation time is long enough. In the case of signals of duration smaller than the observation time, such as those from coalescing binaries, the enhancement depends on the number of gravitational-wave cycles in band.

The matched filtering technique requires the construction of accurate waveform templates that can track the "real" signal for many cycles. A discrete bank is built in such a way as to cover the physical parameter space with templates that have overlaps[7] greater or equal to 97% with their neighboring waveforms. One has to carefully choose a SNR threshold for detection by taking into account the probability that false alarms can be triggered by the noise of the detector. In general, the number

[7]The overlap integral of two model waveforms $h_1(t;\boldsymbol{\lambda}_1)$ and $h_2(t;\boldsymbol{\lambda}_2)$ (where $\boldsymbol{\lambda}_{1,2}$ denotes the collection of parameters of the model) is defined as $\mathcal{O}(h_1, h_2) \equiv \max_{\boldsymbol{\lambda}_1,\boldsymbol{\lambda}_2} \langle \hat{h}_1(\boldsymbol{\lambda}_1), \hat{h}_2(\boldsymbol{\lambda}_2) \rangle$, where we made use of the inner product in Fourier domain

$$\langle h_1, h_2 \rangle \equiv 4\,\mathrm{Re} \int_0^\infty \mathrm{d}f \frac{\tilde{h}_1(f;\boldsymbol{\lambda}_1)\tilde{h}_2^*(f;\boldsymbol{\lambda}_2)}{S_n(f)} \,, \tag{2.12}$$

and $\hat{h}_{1,2} \equiv h_{1,2}/\sqrt{\langle h_{1,2}, h_{1,2} \rangle}$.

of required templates increases with the dimensionality of the physical parameter space. However, a larger number of possible shapes means a greater chance of false detections, as a larger bank is more likely to match random noise fluctuations; in fact, the detector noise contains a number of non-Gaussian transients [52, 53]. One solution is to increase the detection threshold, but this comes at the expense of the detection rate R_D, because of the reduced horizon distance $D_{\rm hor}$. Therefore, there has to be a trade-off between a false-alarm probability and horizon distance. To enhance the rejection of false alarms, matched filtering is complemented by vetoing schemes [54], such as the χ^2 test [55]. To have a more quantitative idea, for advanced LIGO (considering the zero-detuned high-power configuration [4]) the bank for non-spinning black-hole binaries based on the EOBNRv2 model (which is the current nonspinning inspiral-merger-ringdown model used by LIGO that we shall discuss in Sec. 2.5) contains $\sim 20,000$ templates [56]. When moving to a spin-aligned search the number of templates is expected to grow to $\sim 630,000$ [57].

Besides the scientific target of detecting the gravitational-wave emission of compact-object binaries, another crucial task of gravitational-wave physics is the determination of the physical characteristics of the source (such as its masses, spins, sky localization, etc.), the so-called problem of "parameter estimation". In order to extract the source parameters with sufficient accuracy (i.e., with small biases with respect to their true values), one has to build waveform models whose dependence on the parameters is as close as possible to what general relativity predicts. Thus, models that can be employed in parameter-estimation studies must comply with more stringent quality requirements than models suitable for detection purposes

only. A more quantitative discussion can be found in Sec. 2.5.5

2.3 Computing waveforms for black-hole binaries in general relativity

We now discuss how one can predict the gravitational-wave emission (or waveform) for a black-hole binary, with the ultimate goal of using such prediction in matched filtering.

Different stages of a black-hole binary evolution require different methods to compute the waveforms. The long, adiabatic *inspiral* is well described by a post-Newtonian (PN) [58] expansion of the general relativistic equations for a pair of point particles, i.e., one solves the 2-body problem in the limit of weak self-gravity and slow orbital velocity. At leading order, the time-domain inspiral polarizations for a nonspinning black-hole binary with component masses $m_{1,2}$ are [14]

$$h_+(t) = \frac{1}{\mathcal{R}}\left(\frac{GM_c}{c^2}\right)^{5/4}\left(\frac{5}{c(t_c-t)}\right)^{1/4}\frac{1+\cos^2\iota}{2}\cos\left[\Phi(t_c-t)\right], \tag{2.13}$$

$$h_\times(t) = \frac{1}{\mathcal{R}}\left(\frac{GM_c}{c^2}\right)^{5/4}\left(\frac{5}{c(t_c-t)}\right)^{1/4}\cos\iota\,\sin\left[\Phi(t_c-t)\right], \tag{2.14}$$

where $\mathcal{R}$ is the distance to the source, M_c is the chirp mass, defined as $M_c \equiv (m_1 m_2)^{3/5}/(m_1+m_2)^{1/5}$, ι is the inclination of the orbital plane with respect to the line of sight, $\Phi(t_c-t) \equiv \Phi_c - 2\left(5GM_c/c^3\right)^{-5/8}(t_c-t)^{5/8}$ is the gravitational-wave phase (i.e., twice the orbital phase at this PN order), t_c is the time when the frequency $\omega \equiv \dot{\Phi}$ diverges, and Φ_c is the phase at time t_c. The gravitational-wave emission is not isotropic, as the $\times$ polarization has a vanishing amplitude along

the equator of the orbital plane. At leading order in the PN expansion, the only source parameters appearing in Eqs. (2.13)–(2.14) are the two black-hole masses $m_{1,2}$, which, however, enter only through the combination[8] M_c. Remarkably, the general relativistic computations of black-hole binary coalescences depend only on the mass ratio $q = m_1/m_2$, while the total mass of the binary $M = m_1 + m_2$ simply sets an overall scale. Finite-size effects can be relevant when at least one of the compact objects is a neutron star, because of the tidal deformations induced in the star by the companion; even then, tidal effects are formally 5PN order[9] in the waveform phasing, while, currently, nonspinning phasing effects are known only up to 4PN order.

To separate their angular and time dependence, it is convenient to decompose the polarizations in multipolar modes by projecting the complex combination $h_+ - ih_\times$ (referred to as the "complex strain", not to be confused with the strain measured by a detector, obtained by convolving $h_{+,\times}$ with the antenna pattern functions) onto the angular basis of -2-spin-weighted spherical harmonics [59]

$$h_+(t,\theta,\phi) - ih_\times(t,\theta,\phi) \equiv \sum_{\ell=2}^{\infty} \sum_{m=-\ell}^{\ell} {}_{-2}Y_{\ell m}(\theta,\phi) h_{\ell m}(t)\,, \tag{2.15}$$

where (θ,ϕ) are polar angles defined with respect to a convenient polar axis (for nonprecessing binaries, this is chosen to be in the direction of the orbital angular momentum). The $(\ell, m) = (2, 2)$ mode is the dominant one during the inspiral of

[8] This is just a simple instance of the more general problem of parameter degeneracies, which makes parameter estimation harder.

[9] nPN order means $\mathcal{O}\left(\frac{v^{2n}}{c^{2n}}\right)$, that, for a quasicircular binary of total mass M and orbital separation r, corresponds to $\mathcal{O}\left(\left(\frac{GM}{rc^2}\right)^n\right)$.

comparable-mass binaries, as suggested by PN theory. Other modes are suppressed by powers of v/c or by the mass asymmetry of the system $(m_1 - m_2)$.

From Eqs. (2.13)–(2.14), it is easy to show that $|h_{+,\times}(t)| \propto \omega^{2/3}$, where $\omega \equiv \dot{\Phi}$ is the instantaneous gravitational-wave frequency. Combining this with the formula for the number N_c of gravitational-wave cycles in band [14]

$$N_c = 1.6 \times 10^4 \left(\frac{10\,\mathrm{Hz}}{f_{\min}}\right)^{5/3} \left(\frac{1.2 M_\odot}{M_c}\right)^{5/3}, \tag{2.16}$$

where $f_{\min}$ is the lower frequency cutoff of the detector (for instance, 10 Hz for advanced LIGO), one finds that the SNR grows roughly like $\sqrt{N_c}$ [14] (see also the discussion following Eq. (2.6)), therefore the integrated SNR from matched filtering can exceed the instantaneous SNR (accumulated over one cycle, which is a more appropriate quantity to consider when discussing bursts) by more than one order of magnitude. The gain is dramatic for neutron-star binaries ($N_c \approx 1.6 \times 10^4$), and it is still significant for systems with large total mass (such as black-hole binaries), even though fewer cycles are in band ($N_c \approx 600$ for a $(10 + 10)M_\odot$ system).

Later stages of the binary evolution are best addressed using other techniques than the PN approximation. The *ringdown* phase, that is the relaxation of the remnant to a Kerr black hole, is best treated in black-hole perturbation theory [60]. The fully nonlinear regime of the *merger*, i.e., when the two black holes plunge and merge, was investigated analytically within the effective-one-body (EOB) approach [61, 62] (see Sec. 2.5), in an attempt to bridge the gap between the two perturbative regimes pertinent to PN and black-hole perturbation theory, respectively. The EOB model was based on the assumption of a fundamentally "smooth"

behavior of the coalescence process, even through merger, thanks to the gravitational potential of the newborn black hole (i.e., the remnant) shielding the outgoing radiation from complicated nonlinear imprints. Full numerical simulations of binary mergers later confirmed this assumption [63], and proved essential to settle the characterization of the highly relativistic part of the binary evolution, trying to make contact with analytical schemes in their domains of applicability.

Currently, numerical relativity is a well-established field [64, 65]. Hundreds of highly accurate black-hole binary simulations are now publicly available [66–68]. Up until 2012, most of the numerical-relativity simulations had explored nonspinning and spinning nonprecessing binaries, but recently the exploration of the large parameter space of precessing systems has started [66–68]. Numerical-relativity codes have gone through impressive improvements in the efficient generation of long and accurate gravitational waveforms from mergers in vacuum. However, the role of analytical models has not been diminished by the successes of numerical schemes. First, numerical-relativity simulations are still computationally expensive, requiring $\mathcal{O}(10^3)$ CPU hours to compute 1 ms of orbital evolution (near merger) at a reasonable resolution [65]. Second, advanced interferometers will require template banks with thousands of templates for detection and even more for parameter estimation studies [57]. Third, insights into the physics of the coalescence can be gained thanks to the analytics of the problem, rather than via a brute-force approach through numerics. Finally, even though astrophysical black holes are intrinsically simple objects (characterized only by their mass and spin), the dimensionality of the intrinsic physical parameter space for a generic black-hole binary (8D, for quasicircular sys-

tems[10]) represents a formidable challenge for numerical relativity. Therefore the cooperation between the numerical and analytical relativity communities has become urgent, more than ever before [71].

The problem of generating complete inspiral-merger-ringdown waveforms has been approached in several ways. As we shall discuss later, the effective-one-body model is a unified strategy that can describe the entire coalescence self-consistently in the time domain, and whose accuracy has been improved by calibrations to numerical-relativity simulations (see Sec. 2.10). In the frequency domain, phenomenological models [69, 72, 73] inspired by PN frequency expansions have been fitted to numerical simulations. One can also create hybrids by joining together numerical-relativity waveforms to PN approximants for the long, low frequency portion [74].

2.4 Motivations for going beyond post-Newtonian models

In this Section we discuss the main reasons why PN models of black-hole binaries are not adequate when the total binary mass is $> 3 - 12 M_{\odot}$, depending on the scientific goals (detection or parameter estimation).

One major drawback of PN models of black-hole binaries is the slow convergence of the PN approximation as one increases the PN order. This issue

[10]This number does not reflect the actual dimensionality of the waveform space. For instance, only a handful of numerical-relativity simulations were needed to inform and calibrate analytical models that can cover the entire nonprecessing parameter space [69,70]. A similar behavior is also expected for the fully precessing parameter space.

was discussed in the context of gravitational-wave physics already in the early 1990's in the test-particle limit, by comparing PN predictions to calculations done in perturbation theory [75, 76]. As an instructive example, consider the computation of the ISCO for a test particle in Schwarzschild spacetime. The fully relativistic result is $r_{\rm ISCO} = 6\,GM/c^2$ in Schwarzschild coordinates, derived by finding the extremum of the conserved energy (per unit mass) for circular orbits, $e(x) = c^2\,(1-2x)\,/\sqrt{1-3x}$, where $x \equiv \left(\frac{GM\Omega}{c^3}\right)^{2/3} = \frac{GM}{rc^2}$, Ω being the orbital frequency (i.e., $\mathrm{d}\phi/\mathrm{d}t$ in Schwarzschild coordinates), related to the radial separation r by Kepler's third law $r^3\Omega^2 = GM$. If we were to expand the energy in a PN series (using x as the expansion parameter), and compute the ISCO from the expanded $e(x)$, we would have to go up to 8PN order to have a 1% accurate ISCO (i.e., $\approx 5.94\,GM/c^2$).

Furthermore, the phase evolution of a black-hole binary can be computed using several PN approximants (such as TaylorT1, TaylorT2, TaylorT3, TaylorT4, TaylorEt), which give different results for the quasicircular evolution [77]. Two PN phase approximants, while being formally of the same PN order, differ in the way the differential equation for the orbital phase ϕ is manipulated, thus producing different results. In the adiabatic limit (i.e., for slow changes of the orbital frequency: $\Delta\Omega/\Omega \ll 1$ or, equivalently, $\dot{\Omega}/\Omega^2 \ll 1$) and for circular orbits, one can use the *balance equation*[11] $\dot{E} = -F$ (where E is the total relativistic energy of the binary

[11]The balance equation, although physically reasonable, is not derived from first principles in full general relativity. However, it has been shown to hold in PN theory up to the currently available PN order [58].

and F is the gravitational luminosity of the system) and the definition of the orbital velocity $v \equiv (GM\dot{\phi})^{1/3}$ (where $M \equiv m_1 + m_2$ is the total mass) to find that

$$\frac{\mathrm{d}E}{\mathrm{d}v}\frac{\mathrm{d}v}{\mathrm{d}t} = -F\,, \tag{2.17}$$

$$\frac{\mathrm{d}\phi}{\mathrm{d}t} = \frac{v^3}{GM}\,. \tag{2.18}$$

Hence

$$\frac{\mathrm{d}\phi}{\mathrm{d}v} = -\frac{v^3}{GM}\frac{E'(v)}{F(v)} \Rightarrow \phi(v) = \phi_{\rm ref} + \int_v^{v_{\rm ref}} \mathrm{d}v\, \frac{v^3}{GM}\frac{E'(v)}{F(v)}\,, \tag{2.19}$$

where $\phi_{\rm ref}$ and $v_{\rm ref}$ are integration constants, E is the binding energy for circular orbits, which, for nonspinning binaries, reads

$$E(v) = -\frac{1}{2}\nu M v^2\left[1 - \left(\frac{3}{4} + \frac{1}{12}\nu\right)\left(\frac{v}{c}\right)^2 + \cdots\right]\,, \tag{2.20}$$

where $\nu \equiv (m_1 m_2)/(m_1+m_2)^2$ is the symmetric mass ratio, and F is the gravitational energy flux, which, for nonspinning binaries, reads

$$F(v) = \frac{32}{5}\nu^2\frac{c^{15}}{G}\left(\frac{v}{c}\right)^{10}\left[1 - \left(\frac{1\,247}{336} + \frac{35}{12}\nu\right)\left(\frac{v}{c}\right)^2 + \cdots\right]\,. \tag{2.21}$$

The discrepancies between PN approximants arise from the arbitrariness in treating the ratio $E'(v)/F(v)$. For instance, one can perform the integral in Eq. (2.19) using the expressions for $E(v)$ and $F(v)$ in Eqs. (2.20) and (2.21) as they are. Alternatively, one can expand $E'(v)/F(v)$ in PN orders, making it a polynomial in v/c truncated at some order n. The two approaches then differ because of PN orders higher than n. Such higher PN orders become more and more important as the ISCO is approached.

In systems with low total mass (a few $M_\odot$'s), such as a neutron-star binaries, the signal has a small v whenever in band, and different PN approximants agree with

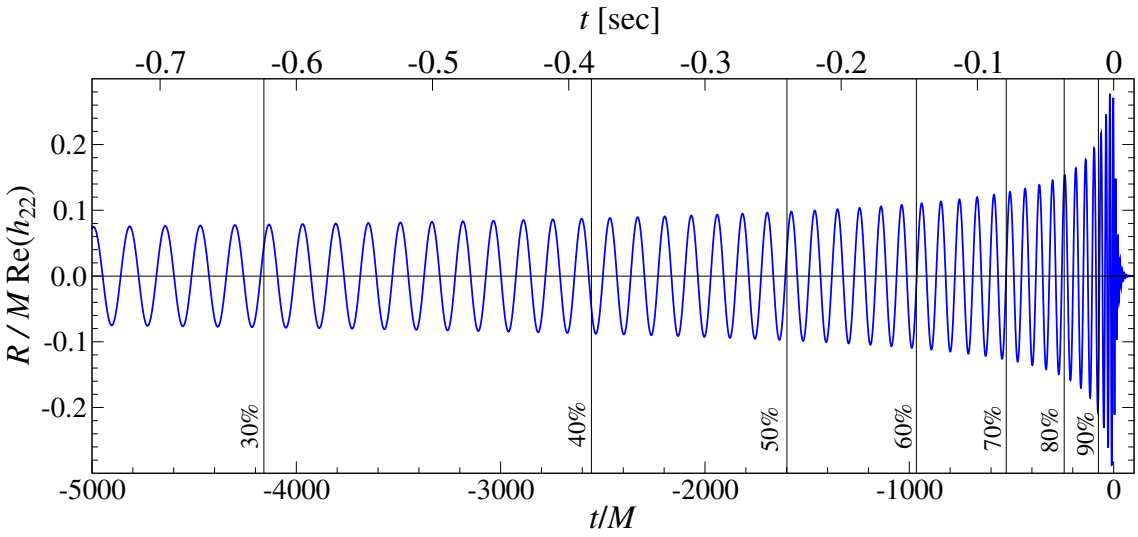

Figure 2.2: [From Ref. [66]] Dominant $(2,2)$ mode waveform of a black-hole binary with mass ratio $q = 3$, and dimensionless spins $\chi_1 = -0.6$, $\chi_2 = 0$. Shown is a time-domain EOB waveform model. For $M = 30M_\odot$, the vertical lines mark 10% intervals of accumulated SNR, and are labelled by the fraction of SNR accumulated before each line.

each other. Hence, PN waveforms are accurate enough for detecting the inspiral of these sources. But for black-hole and neutron-star/black-hole binaries with total mass larger than $12M_\odot$ [77] the ISCO moves in band, therefore several problems arise: (i) differences in the PN approximants become discernible, (ii) the balance equation ceases to be applicable since $E'(v)$ goes to 0 at the ISCO, and (iii) the adiabatic approximation does not hold after the ISCO since the system plunges. More precisely, the adiabatic approximation holds only if the orbital frequency Ω evolves on a timescale that is much longer than the orbital timescale: $\dot{\Omega}/\Omega^2 = \mathcal{O}\left(\frac{v^5}{c^5}\right) \ll 1$. This approximation breaks down close to the ISCO, and $\dot{\Omega}$ may even change sign before reaching it. Above $12M_\odot$ it is then crucial to model the nonadiabatic dynamics.

Moreover, for larger total masses ($M \gtrsim 30M_\odot$), the merger and ringdown portions of the waveform start to matter for the purpose of detection. In fact, during these stages of the compact-binary evolution, the gravitational-wave luminosity is the largest. Figure 2.2 shows (in blue) the dominant $(2,2)$ mode waveform emitted by a black-hole binary with mass ratio 3 and one of the bodies spinning with a spin of dimensionless magnitude 0.6, antialigned with the orbital angular momentum. For a total mass $M = 30M_\odot$, the figure illustrates how 60% of the SNR is accumulated in the last 30 cycles before merger and during the ringdown. For this binary, in fact, the merger occurs right in the middle of the best sensitivity band of the detector. To overcome the lack of merger and ringdown signals in purely PN models, over the years different resummation techniques have been developed, culminating with the proposal of the effective-one-body model (see Sec. 2.5), which is capable of generating a full inspiral-merger-ringdown signal for coalescing black-hole binaries.

2.5 Effective-one-body model of compact-object binaries

As we have seen, the PN adiabatic description of the motion and gravitational radiation of comparable-mass black-hole binaries severely limits the potential discovery of systems with total mass above $\sim 12M_\odot$. A successful approach to modeling these sources beyond PN theory was developed in the late 1990's by Alessandra Buonanno and Thibault Damour, under the name of effective-one-body (EOB) model [61, 62] (see Refs. [78, 79] for recent reviews). Before the numerical-relativity breakthroughs of the mid 2000's [80–82], this model made several predictions about

the final stages of the coalescence of black holes, such as (i) a smooth transition from inspiral to plunge, (ii) a sharp transition at merger to the ringdown signal, and (iii) the estimation of the radiated energy and the spin of the remnant black hole. The EOB model contains separate descriptions of the conservative and dissipative dynamics, which we are going to discuss in the following Sections.

2.5.1 The effective-one-body conservative dynamics

The treatment of the conservative dynamics in the EOB model was inspired by the quantum mechanical 2-body problem of electromagnetically interacting charged particles [83]. The basic assumption is that the general relativistic 2-body problem with arbitrary mass ratio is a smooth deformation of the test-particle limit. For the case of nonspinning bodies, the starting point in the construction of the EOB Hamiltonian is the nonspinning PN 2-body Hamiltonian $H_{\rm real}$ expressed in the center-of-mass frame in canonical relative coordinates $(\mathbf{r}, \mathbf{p})$, which reads as a series expansion in powers of $1/c^{2n}$ $(n = 0, 1, \cdots)$, currently known up to 4PN order [84–86]. The subscript "real" is a reminder of the fact that $H_{\rm real}$ describes, although approximately, the dynamics of the true physical system. The goal is to reduce the *real* 2-body problem to the problem of a test particle of mass μ moving in an *effective* background spacetime $g^{\rm eff}_{\alpha\beta}$ of mass M that is a deformation of Schwarzschild in the symmetric mass ratio $\nu \equiv \mu/M$. The symmetric mass ratio is a quantity varying between 0 (test-particle limit) and 1/4 (equal-mass binary). In the presence of spherical symmetry, the effective metric is then expressed in terms

of two potential functions A and D, and reads

$$ds^2_{\rm eff} = g^{\rm eff}_{\alpha\beta}\,{\rm d}X^\alpha_{\rm eff}{\rm d}X^\beta_{\rm eff} = -A(R)c^2{\rm d}t^2 + \frac{D(R)}{A(R)}{\rm d}R^2 + R^2{\rm d}\Omega^2\,, \tag{2.22}$$

where $X^\lambda_{\rm eff} \equiv (c\,t, \mathbf{R})$ are the EOB coordinates. The EOB potentials A and D are PN expansions in the dimensionless quantity (GM/Rc^2), where $M \equiv m_1 + m_2$ is the total mass of the real system, so that one can recover the Schwarzschild solution in an appropriate limit. Just like when one maps the Newtonian 2-body problem to the a one-body problem, the effective particle has a mass equal to the reduced mass of the real system: $\mu = m_1 m_2/(m_1 + m_2)$. Up to 2PN order, one assumes geodetic motion of the effective particle in the metric $g^{\rm eff}_{\alpha\beta}$. The Hamilton-Jacobi equation for geodesics reads

$$g^{\alpha\beta}_{\rm eff}\,\frac{\partial S_{\rm eff}}{\partial X^\alpha_{\rm eff}}\frac{\partial S_{\rm eff}}{\partial X^\beta_{\rm eff}} + \mu^2 c^2 = 0\,, \tag{2.23}$$

where $S_{\rm eff}$ is Hamilton's principal function, and is defined as the action evaluated along a solution of the equations of motion for the effective particle, that is

$$S_{\rm eff} \equiv -\mu\,c\int_A^B \sqrt{-g^{\rm eff}_{\alpha\beta}(X^\lambda_{\rm eff})\frac{{\rm d}X^\alpha_{\rm eff}}{{\rm d}\tau}\frac{{\rm d}X^\beta_{\rm eff}}{{\rm d}\tau}}\,{\rm d}\tau\,, \tag{2.24}$$

for a geodesic $X^\lambda_{\rm eff}(\tau)$ connecting A to B. After defining the canonical momenta as $P_\alpha \equiv \frac{\partial S_{\rm eff}}{\partial X^\alpha_{\rm eff}}$, and inverting Eq. (2.23) with respect to the conserved $P_0 \equiv H_{\rm eff}/c$, one obtains the effective Hamiltonian governing geodetic motion in the metric $g^{\rm eff}_{\alpha\beta}$

$$H_{\rm eff}(\mathbf{R},\mathbf{P}) = \mu c^2\sqrt{A(R)\left[1 + \frac{\mathbf{P}^2}{\mu^2c^2} + \frac{1}{\mu^2c^2}\left(\frac{A(R)}{D(R)} - 1\right)\left(\frac{\mathbf{R}\cdot\mathbf{P}}{R}\right)^2\right]}\,. \tag{2.25}$$

The EOB potentials are expressed as PN expansions in (GM/Rc^2) whose coefficients are determined by requiring that a certain mapping exists between the energies of

bound states in the real and in the effective problem. The identification is not between the energies themselves (as this would lead to inconsistencies when taking the nonrelativistic limit), but rather between variables that are easily identified within the Hamilton-Jacobi framework, and correspond to a radial action integral and the orbital angular momentum. In fact, the real nonspinning PN Hamiltonian is invariant under rotations, therefore its bound states can be labelled by the value of the orbital angular momentum and the radial action integral. Therefore, one assumes that generically the real and effective energies are related by $H_{\rm eff} = f(H_{\rm real})$. At Newtonian order, the nonrelativistic effective energy (i.e., $H_{\rm eff} - \mu c^2$) has to equal the real energy $H_{\rm real}$. At higher order we can write

$$\frac{H_{\rm eff} - \mu c^2}{\mu c^2} = \frac{H_{\rm real}}{\mu c^2} \left[1 + \alpha_1 \frac{H_{\rm real}}{\mu c^2} + \alpha_2 \left(\frac{H_{\rm real}}{\mu c^2} \right)^2 + \cdots \right] , \tag{2.26}$$

where one recognizes the nonrelativistic effective energy in the numerator of the LHS side. The coefficients α_i are fixed simultaneously with the coefficients entering the EOB potentials. At 2PN order one finds

$$\frac{H_{\rm eff}}{\mu c^2} = 1 + \frac{H_{\rm real}}{\mu c^2} \left(1 + \frac{\nu}{2} \frac{H_{\rm real}}{\mu c^2} \right) . \tag{2.27}$$

Equation (2.27) can be rewritten as

$$\frac{H_{\rm eff}}{\mu c^2} = \frac{(H_{\rm real} + Mc^2)^2 - m_1^2 c^4 - m_2^2 c^4}{2 m_1 m_2 c^4} = \frac{s c^2 - m_1^2 c^4 - m_2^2 c^4}{2 m_1 m_2 c^4} = - \frac{p_1 \cdot p_2}{m_1 m_2 c^2} , \tag{2.28}$$

where s is the Mandelstam variable $s = (H_{\rm real} + Mc^2)^2/c^2 = -(p_1 + p_2)^2 = m_1^2 c^2 + m_2^2 c^2 - 2(p_1 \cdot p_2)$, which clearly displays the symmetric character of the effective energy as opposed to the real energy $H_{\rm real}$. The resummed real Hamiltonian (also

referred to as the "EOB Hamiltonian" in what follows) is obtained from the inversion of Eq. (2.27) with respect to $H_{\rm real}$, and reads

$$H_{\rm EOB} \equiv Mc^2 \sqrt{1 + 2\nu \left(\frac{H_{\rm eff} - \mu c^2}{\mu c^2} \right)} - Mc^2 \,. \tag{2.29}$$

$H_{\rm EOB}$ generates the orbital dynamics via Hamilton's equations. When extending the EOB model up to 3PN nonspinning terms [87], in order to keep the same energy mapping of Eq. (2.29), the requirement of purely geodetic motion in the effective background $g^{\rm eff}_{\alpha\beta}$ had to be relaxed to include non-geodetic terms in the equations of motion. This is best seen using the Hamilton-Jacobi formalism, wherein the modified equation of motion becomes

$$g^{\alpha\beta}_{\rm eff} P_\alpha P_\beta + \mu^2 c^2 + Q_4 = 0 \,, \tag{2.30}$$

where Q_4 is a non-geodetic term of the form P_R^4/R^2, where $P_R \equiv (\mathbf{R}\cdot\mathbf{P})/R$. This has to be compared to Eq. (2.23). One could still insist on having a geodetic effective Hamiltonian, but the energy mapping would be more complicated (see Appendix A of Ref. [87]).

An alternative derivation of the nonspinning EOB model relies on the use of a canonical transformation that relates $H_{\rm eff}(\mathbf{R}, \mathbf{P})$ to $H_{\rm real}(\mathbf{r}, \mathbf{p})$ [61]. This approach was adopted in the development of the spinning EOB model as more convenient.

2.5.2 Validating the effective-one-body conservative dynamics

As a means of testing and validating the conservative part of the EOB dynamics, in Ref. [88] (see Chapter 3) we compared the EOB prediction for the periastron

advance in nonspinning black-hole binaries of varying mass ratios with what is measured in fully relativistic simulations [89]. Due to general relativistic effects, the orbit of a nonspinning binary with small but non-vanishing eccentricity precesses in a plane orthogonal to the angular momentum. The system is characterized by a radial frequency Ω_r (related to the coordinate time between consecutive periastron passages) and an average orbital frequency Ω_ϕ (defined as the coordinate-time average of the instantaneous orbital frequency over a radial period). The periastron advance is defined as the ratio $K \equiv \Omega_\phi/\Omega_r$. Note that K is a gauge invariant quantity. K goes to infinity as the eccentricity goes to 0, since on a circular orbit $\Omega_r = 0$. In the EOB formalism, by perturbing a circular orbit, one finds [90]

$$K = \sqrt{\frac{A'(u)D(u)}{\Delta(u)}}\,, \tag{2.31}$$

where $A(u)$ and $D(u)$ are the nonspinning EOB potentials in Eq. (2.22) expressed as functions of the dimensionless variable $u \equiv GM/Rc^2$, and $\Delta(u) \equiv A(u)A'(u) + 2u(A'(u))^2 - uA(u)A''(u)$ vanishes at the EOB ISCO.

Figure 2.3 compares the prediction for K coming from the nonspinning EOB model of Ref. [91] to numerical-relativity measurements (represented as cyan bands, due to the presence of numerical errors) for nonspinning black-hole binaries of mass ratio 1 and 8. The other curves are computed in PN theory and in the gravitational self-force formalism (GSFq and GSFν). A curve for Schwarzschild is added simply for reference, but it is not expected to track the numerical data at these mass ratios. The EOB prediction for the periastron advance K is in excellent agreement with numerical relativity, even without including information from numerical rela-

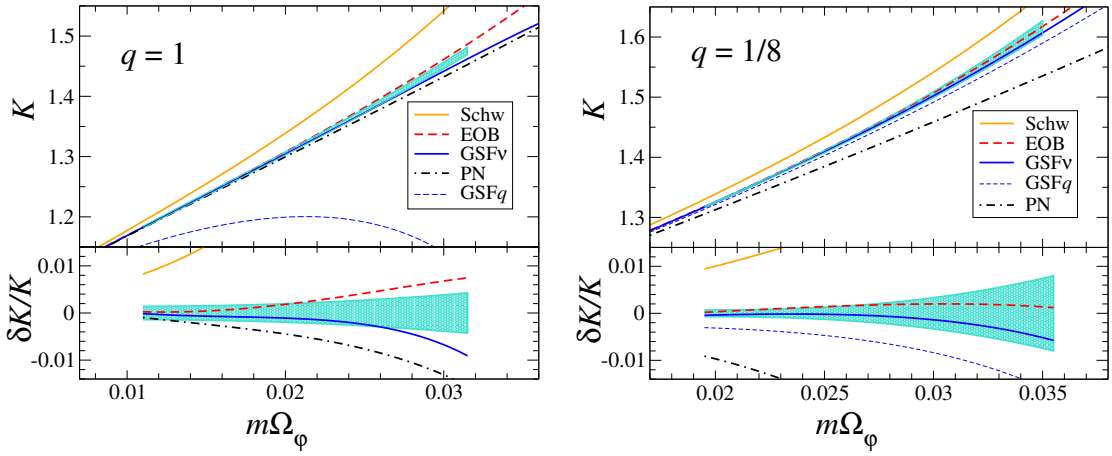

Figure 2.3: [From Ref. [88]] Periastron advance K in slightly eccentric nonspinning black-hole binaries (with mass ratios 1 and 8) as a function of the average orbital frequency. The plots compare full numerical-relativity measurements (cyan band) to analytical predictions from PN theory, gravitational self-force calculations (GSFq and GSFν), and the EOB formalism. In the lower panels, we show the relative errors on K. The Schwarzschild limit is included for reference. Here m denotes the total mass of the binary.

tivity, and simply relies on the resummation of the 3PN Hamiltonian. This has to be contrasted to the performance of the PN prediction, that lies well outside the numerical error bars. While this comparison mainly concerns the inspiral[12], it was not a priori obvious that an analytic model could achieve this degree of agreement with numerical simulations in full general relativity.

In Ref. [92], other authors extended these comparisons to spinning, nonprecessing black-hole binaries using the spinning EOB model we employed in Refs. [70, 93] (see Sec. 2.9), finding similar levels of agreement.

[12]For instance, for mass ratio 1 (shown in the left panel of Figure 2.3) the numerical data end about 10 gravitational-wave cycles before merger.

2.5.3 The effective-one-body dissipative dynamics

The other crucial ingredient of the EOB approach is the model for the radiation-reaction force $\boldsymbol{\mathscr{F}}$. The equations of motion are written as

$$\frac{\mathrm{d}\mathbf{R}}{\mathrm{d}t} = \frac{\partial H_{\mathrm{EOB}}}{\partial \mathbf{P}}\,, \tag{2.32}$$

$$\frac{\mathrm{d}\mathbf{P}}{\mathrm{d}t} = -\frac{\partial H_{\mathrm{EOB}}}{\partial \mathbf{R}} + \boldsymbol{\mathscr{F}}\,. \tag{2.33}$$

In the nonspinning case, we can work in planar polar coordinates (R, Φ, P_R, P_Φ). As shown in Ref. [62], for quasicircular orbits, only the azimuthal component of $\boldsymbol{\mathscr{F}}$ really matters, while its radial component is suppressed as $\dot{R}/(R\dot{\Phi})$. Therefore, within this approximation, radiation reaction is present only in the time variation of P_Φ, that is the orbital angular momentum,

$$\frac{\mathrm{d}P_\Phi}{\mathrm{d}t} = \mathscr{F}_\Phi\,, \tag{2.34}$$

where we exploited the Φ-independence of H_{EOB}. For quasicircular orbits, the angular momentum flux and the energy flux in gravitational waves are proportional to one another via the orbital frequency. Hence, from the balance equation, one can express $\mathscr{F}_\Phi$ in terms of the gravitational-wave energy flux F, available from PN theory in Taylor-expanded form [58]. One can study the convergence properties of the PN series in the test-particle limit [75,76], where the computation of the fully relativistic F can be performed via the Regge-Wheeler-Zerilli [94–96] (Teukolsky [97]) equation, which describes metric (curvature) perturbations on a Schwarzschild (Kerr) background in the presence of some stress-energy tensor (a point particle, typically), at leading order in the mass ratio. In the past, several resummation strategies were

devised in order to speed up the convergence of the PN expressions, the prominent ones being the Padé resummation [98] and the factorized resummation [99–101]. In the former approach, one replaces the PN series for F with a rational function whose Taylor expansion agrees with the PN series itself, with the goal of introducing a pole at the light ring. Of course, there are several possible choices of rational functions, and one ultimately has to check their performance against exact results. In the latter approach, the energy flux is written as a sum over multipolar waveforms $h_{\ell m}$

$$F = \frac{1}{8\pi}\left(\frac{c^5}{G}\right)\left(\frac{GM\Omega}{c^3}\right)^2 \sum_{\ell=2}^{\infty}\sum_{m=1}^{\ell} m^2 \left|\frac{\mathcal{R}c^2}{GM} h_{\ell m}\right|^2 , \tag{2.35}$$

where, of course, in practice the sum over ℓ is truncated at some $\ell_{\max}$ dictated by the available PN waveform calculations; each PN mode $h_{\ell m}$ is recast in factorized form as

$$\left(\frac{\mathcal{R}c^2}{GM}\right) h^{\rm F}_{\ell m} = h^{(N,\epsilon)}_{\ell m}\, \hat{S}^{(\epsilon)}_{\rm eff}\, T_{\ell m}\, (\rho_{\ell m})^{\ell}\, e^{i\delta_{\ell m}} , \tag{2.36}$$

where the definition of each term can be found in Appendix F. Note that all factors depend on the orbital frequency Ω, and $h^{(N,\epsilon)}_{\ell m}$ additionally depends on R. The term $h^{(N,\epsilon)}_{\ell m}$ is simply the restricted (or Newtonian) waveform, that is the leading-order waveform. $\hat{S}^{(\epsilon)}_{\rm eff}$ is an effective source term that in the circular-motion limit contains a pole at the EOB light ring (i.e., the unstable circular orbit of photons, determined by the massless limit of the EOB Hamiltonian). The factor $T_{\ell m}$ resums the leading-order logarithms of tail effects, due to the back-scattering of gravitational waves off the Schwarzschild background generated by the total mass monopole of the source; it is inspired by the structure of tail effects in the waveform modes as seen in PN calculations. The terms $\rho_{\ell m}$ and $\delta_{\ell m}$ are polynomial expressions in the orbital velocity

$v/c = (GM\Omega/c^3)^{1/3}$ such that $h^{\rm F}_{\ell m}$ agrees with the PN $h_{\ell m}$ upon Taylor expansion in v/c. The factorized resummation is inspired by the fully relativistic results obtained from the solution of the Regge-Wheeler-Zerilli and Teukolsky equations for test particles. In particular, one key feature is the divergence of the gravitational-wave flux emitted by particles in circular orbit close to the light ring, which the factorized model captures through $\hat{S}^{(\epsilon)}_{\rm eff}$. In fact, the energy-momentum tensor of a point particle in circular orbit around a black hole is proportional to its specific energy, which introduces a pole at the light ring. Even-parity ($\epsilon = 0$) modes are sourced by mass moments, which, at leading order, depend on the energy density, hence $\hat{S}^{(0)}_{\rm eff} \equiv H_{\rm eff}/\mu c^2$; odd-parity ($\epsilon = 1$) modes, instead, are sourced by current moments, which depend on the angular momentum density, hence $\hat{S}^{(1)}_{\rm eff} \equiv \sqrt{x} P_\Phi/(G\mu M)$, where P_Φ is the angular momentum and $x \equiv \left(\frac{GM\Omega}{c^3}\right)^{2/3}$. The radiation-reaction force (that is added to the evolution equation of the relative EOB momentum $\mathbf{P}$ (see Eq. (2.33)) is then given by [102]

$$\mathscr{F}_i \equiv \frac{F}{\Omega |\mathbf{R} \times \mathbf{P}|} P_i \,, \tag{2.37}$$

where $\Omega \equiv \hat{\mathbf{L}}_N \cdot (\mathbf{R} \times \dot{\mathbf{R}})/R^2$ (with $\hat{\mathbf{L}}_N$ the unit vector orthogonal to the orbital plane) is the orbital frequency.

The EOB orbital dynamics is computed by numerically solving the Hamilton's equations, supplemented with the radiation-reaction force in Eq. (2.37), that is Eqs. (2.32)–(2.33). The integration is carried out from some large initial separation down to the EOB event horizon. The binary is initialized on a quasicircular initial configuration [102], since it is expected [103] that black-hole binaries have

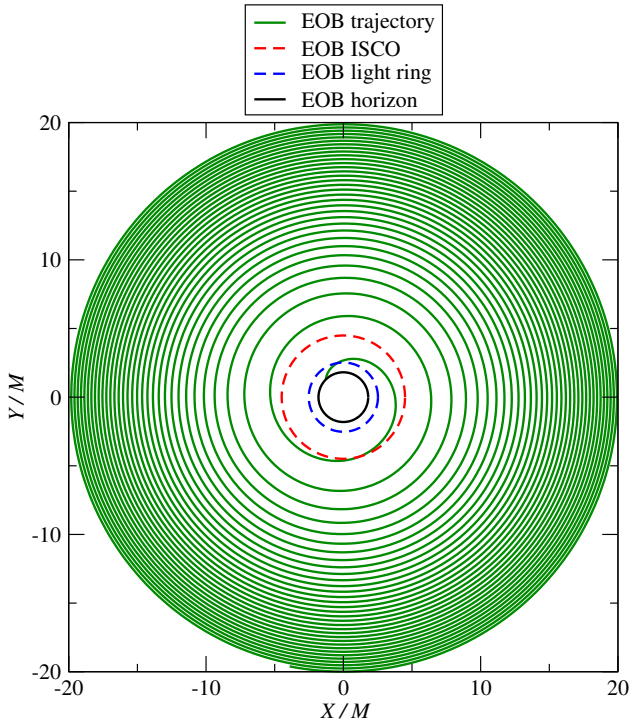

Figure 2.4: For an equal-mass, nonspinning black-hole binary, we plot the EOB trajectory in the orbital plane, starting from a separation of $20M$. The model is that of Ref. [70], based on a log-resummed radial potential, and calibrated to 38 numerical-relativity simulations. We also mark the position of the EOB ISCO, light ring, and event horizon. Here $G = c = 1$.

radiated all their orbital eccentricity by the time their gravitational-wave signal enters the frequency band of ground-based interferometers. In the EOB model it is straightforward to define the ISCO as well as the light ring. The inspiral motion of the binary consists of slowly shrinking circular orbits (spherical orbits in the case of precession). In Figure 2.4, as a representative example, we plot the EOB trajectory for an equal-mass, nonspinning black-hole binary, using the model that we shall discuss in more detail in Sec. 2.10. The plot highlights the very circular character of the inspiral (i.e., the portion down to the ISCO), as well as its long duration.

On the contrary, the plunge occurs over half an orbital cycle. The orbital frequency Ω grows monotonically until the light ring, where it peaks, and then decays to the horizon frequency, which is 0 in this case[13] (see also the lower panel of Figure 2.5).

2.5.4 Construction of the inspiral-merger-ringdown waveform

In this Section we discuss how to generate a complete inspiral-merger-ringdown waveform within the EOB approach.

The final ingredient of the EOB model is the gravitational waveform at null infinity, that is of direct interest for the experiments. For the inspiral-plunge stage, the waveform used in state-of-the-art EOB models is precisely the factorized expression of Eq. (2.36), computed along the orbital dynamics. For the late stage of the coalescence, i.e., the merger-ringdown, the waveform can be modeled as a linear superposition of quasinormal modes (QNMs), as suggested by black-hole perturbation theory [18]. In fact, a perturbed black hole radiates gravitational waves of characteristic frequencies and damping times, labeled by spheroidal-harmonic indices (ℓ, m). For each mode (ℓ, m), there exists an infinite tower of overtones, labeled by an integer n. The merger-ringdown model reads [62]

$$\left(\frac{\mathcal{R}c^2}{GM}\right) h^{\rm RD}(t) = \sum_{n=0}^{N-1} A_{\ell mn} e^{-i\,\omega_{\ell mn} t} e^{-t/\tau_{\ell mn}}\,, \tag{2.38}$$

where N is the number of overtones included in the model, $\omega_{\ell mn}$ is the QNM fre-

[13]Note that, in Kerr spacetime, when in Boyer-Lindquist coordinates, the geodetic of an equatorial particle approaching the horizon has divergent coordinate time t and azimuthal angle ϕ as functions of the proper time τ. However, close to the horizon, $\mathrm{d}\phi/\mathrm{d}t$ equals the horizon frequency $\Omega_{\rm H}$, which is defined through the helical Killing vector of the spacetime.

quency, and $\tau_{\ell mn}$ is the QNM damping time. The complex amplitudes $A_{\ell mn}$ are constants, and the time-dependence is solely due to the exponential functions. The QNM frequencies and damping times depend only on the final mass and spin of the remnant, which, in the earliest version of the model [62], were computed from the EOB binding energy and total angular momentum at the light ring. Finally, the full inspiral-merger-ringdown waveform is obtained from the smooth matching of the inspiral-plunge and merger-ringdown waveforms at a time close to the EOB light ring, which corresponds to a maximum in the orbital frequency Ω. Part of the appeal of the EOB model comes from the existence of a natural transition point (i.e., the light ring) between the inspiral-plunge description (based on the orbital dynamics) and the merger-ringdown (whose spectrum is prescribed by perturbation theory). Reference [104] showed that for an equal-mass, nonspinning system the EOB light-ring crossing occurs very close to the detection of a common apparent horizon in a numerical simulation. The matching procedure fixes the complex amplitudes $A_{\ell mn}$ in Eq. (2.38).

Figure 2.5 shows the EOB inspiral-merger-ringdown waveform for the equal-mass, nonspinning black-hole binary whose trajectory was plotted in Figure 2.4. We also plot the EOB gravitational-wave frequency ω_{22} and twice the orbital frequency of the effective particle. The ringdown attachment is done at the light ring, when Ω peaks. Different colors are used to distinguish the inspiral-plunge waveform (computed from the orbital trajectory using Eq. (2.36)) from the merger-ringdown waveform of Eq. (2.38). Up to the EOB light ring, the waveform consists of direct emission from the orbital motion; after that, the waveform is a signal filtering out

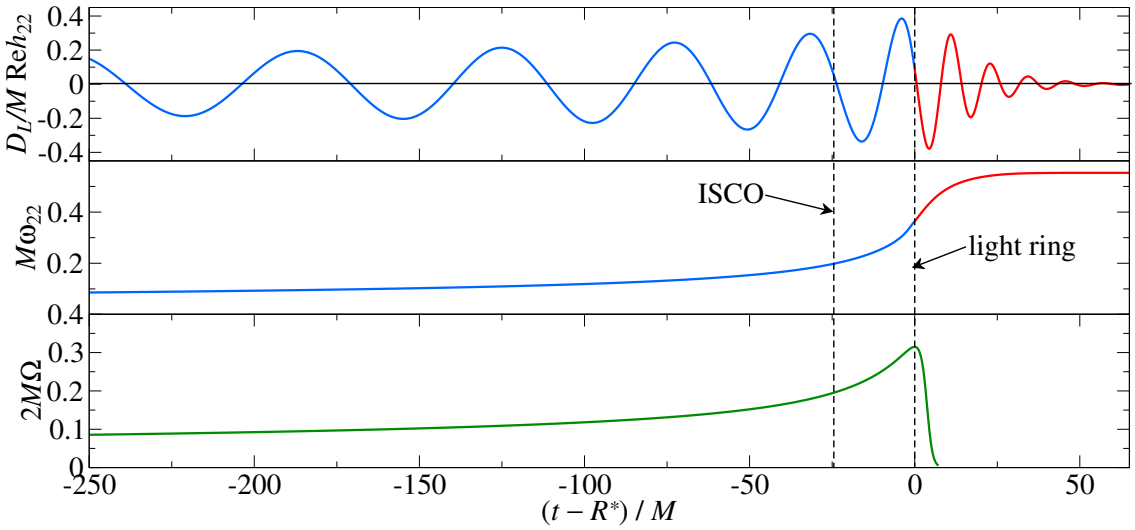

Figure 2.5: For an equal-mass, nonspinning black-hole binary, in the upper panel we plot the $(2, 2)$ mode EOB inspiral-merger-ringdown waveform versus retarded time. In the middle panel, we plot the EOB gravitational-wave frequency. In the lower panel, we plot twice the orbital frequency of the effective particle. Blue curves refer to the inspiral-plunge waveform, computed from the orbital trajectory via Eq. (2.36). Red curves refer to the merger-ringdown waveform of Eq. (2.38). The matching point between the two is at the light ring, where Ω peaks. Here R^* is the tortoise coordinate defined by $\mathrm{d}R^*/\mathrm{d}R \equiv \sqrt{D}/A$. D_L is the distance to the source. Also $G = c = 1$.

the potential barrier of the remnant black hole in the form of QNMs. The asymptotic value of ω_{22} at late times corresponds to the frequency ω_{220} of the least-damped QNM, i.e., the 0-th overtone of the $(2, 2)$ tower of QNMs. Because of their short decay times, higher overtones ($(2, 2, n)$, with $n > 0$) contribute only immediately after the matching time, and determine the slow rise of ω_{22} from its value at the matching point to its asymptotic value.

2.5.5 How to improve the effective-one-body model using numerical relativity

The EOB model, as presented above, is self-consistent, and relies only on computations done in PN and black-hole perturbation theory; it is capable of generating complete gravitational waveforms without external inputs about the strong-field regime from numerical relativity, and in fact it predated the first simulations of black-hole binaries. Ever since the numerical-relativity breakthroughs of the mid 2000's, the EOB model has been compared to numerical simulations.

The upper panel of Figure 2.6 shows how the EOB inspiral-merger-ringdown $(2,2)$ waveform for an equal-mass, nonspinning black-hole binary compares to the highly accurate numerical-relativity calculation produced by the Simulating eXtreme Spacetimes (SXS) Collaboration [105]. The numerical waveform is one of the longest publicly available, lasting about 65 gravitational-wave cycles. When comparing two waveforms in the time domain, given the freedom of choosing the phase and time of coalescence, one *aligns* them at low frequency by shifting the phase of one of them by Δt in time and $\Delta\Phi_{22}$ in phase, where Δt and $\Delta\Phi_{22}$ minimize the square of the phase difference integrated over a time window, i.e., the quantity

$$\int_{t_1}^{t_2} \left[\Phi_{22}^{(\mathrm{NR})}(t) - \Phi_{22}^{(\mathrm{AR})}(t+\Delta t) - \Delta\Phi_{22}\right]^2 \mathrm{d}t\,, \tag{2.39}$$

where $\Phi_{22}^{(\mathrm{AR,NR})}$ are the gravitational-wave phases of the two waveforms to align, and $[t_1, t_2]$ is a short interval (of about 10 cycles) that starts at the settling of any noise or artifacts in the numerical data (known as "junk radiation"). We see

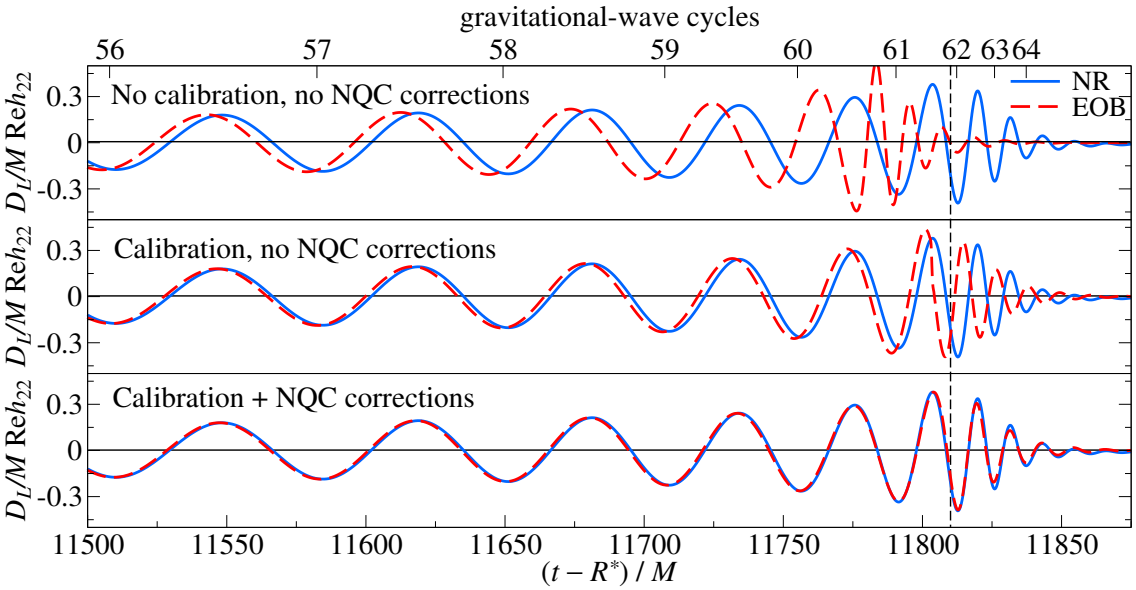

Figure 2.6: For an equal-mass, nonspinning black-hole binary, we compare the numerical-relativity $(2, 2)$ waveform to EOB inspiral-merger-ringdown waveforms (i) without inspiral calibration or non-quasicircular corrections (upper panel), (ii) with inspiral calibration, but without non-quasicircular corrections (middle panel), (iii) with both inspiral calibration and non-quasicircular corrections (lower panel). D_L is the distance to the source. Here $G = c = 1$. The waveforms are aligned in phase at low frequency. The vertical dashed line marks the position of the amplitude peak of the numerical-relativity waveform.

that the *uncalibrated* EOB model accumulates a visible dephasing by the time the waveform reaches its maximum amplitude (which is conventionally identified as the merger). It is worth noting that the uncalibrated model is off by only 2.5 out of 62 cycles at merger. This difference between model and simulation stems from a wrong time of merger in the uncalibrated model. The EOB model has an intrinsic flexibility to accommodate *tuning parameters* in the form of unknown high PN order terms. In the past, many studies, including part of this thesis, have been devoted to the calibration of a handful of such carefully chosen parameters with the goal

of building waveforms in better agreement with numerical relativity. The search for optimal values of the tuning parameters effectively amounts to incorporating nonperturbative information extracted from the numerical simulations. The second panel of Figure 2.6 shows the great improvement that a ν-dependent tuning of the EOB plunge can achieve. However, we can still notice an amplitude and frequency difference close to merger. The EOB plunge-merger waveform is then modified by the inclusion of phenomenological amplitude and phase *non-quasicircular* (NQC) corrections that are proportional to the radial momentum P_R. In fact, the factorized EOB waveforms of Eq. (2.36) do not account for NQC effects because they are based on quasicircular PN formulae. The NQC corrections are determined in such a way as to match the amplitude, the curvature, the frequency, and the slope of the frequency of the numerical-relativity waveform at the peak of the gravitational-wave emission. These quantities are collectively called "input values". The lower panel of Figure 2.6 shows the final result of tuning the inspiral and applying the NQC corrections. As part of the optimization of the EOB model, in particular of its ringdown, it is possible to introduce pseudo-QNMs that do not belong to the physical QNM spectrum (computed in linearized perturbation theory). We shall denote with the term *calibration* the optimization of the tuning parameters, the enforcement of NQC corrections, and the optimization of the ringdown.

Let us now formulate the accuracy requirements for EOB waveforms that can be used in data analysis for advanced LIGO and Virgo. Given two waveforms $h_1(t)$ and $h_2(t)$, one defines their inner product in the frequency domain as $\langle h_1, h_2\rangle \equiv 4\,\mathrm{Re}\int_0^\infty \mathrm{d}f \frac{\tilde{h}_1(f)\tilde{h}_2^*(f)}{S_n(f)}$, where $\tilde{h}_{1,2}(f)$ are the Fourier transforms of $h_{1,2}(t)$.

The *ineffectualness* (or *mismatch*) of an analytical model $h_{\rm AR}(t;\boldsymbol{\lambda})$ (where $\boldsymbol{\lambda}$ is the collection of parameters of the model) with respect to a numerical-relativity waveform $h_{\rm NR}(t)$ is defined as [98]

$$\bar{\mathcal{E}} \equiv 1 - \max_{t_c,\phi_c,\boldsymbol{\lambda}} \frac{\langle h_{\rm AR}, h_{\rm NR}\rangle}{\sqrt{\langle h_{\rm AR}, h_{\rm AR}\rangle}\sqrt{\langle h_{\rm NR}, h_{\rm NR}\rangle}}\,, \tag{2.40}$$

where t_c and ϕ_c are the time and phase of merger, respectively. For the sole purpose of detection, the real signal can trigger *any* template in the bank used for matched filtering, regardless of the true physical parameters of the source. In this case, one needs a waveform model that is *effectual*: the typical practice is to tolerate at most a $\sim 3\%$ ineffectualness due to modeling errors. This translates into a loss in event rate of about 10% [98, 106, 107]. To better understand this point, let us write the model waveform $h_{\rm AR}$ as the numerical waveform $h_{\rm NR}$ plus a small modeling error δh: $h_{\rm AR} = h_{\rm NR} + \delta h$. We also assume negligible errors on $h_{\rm NR}$. The optimal SNR is $\rho = \sqrt{\langle h_{\rm NR}, h_{\rm NR}\rangle}$. However, if we filter $h_{\rm NR}$ with $h_{\rm AR}$, we obtain a reduced SNR[14] [51] $\rho_m \equiv \langle h_{\rm NR}, h_{\rm AR}\rangle/\sqrt{\langle h_{\rm AR}, h_{\rm AR}\rangle} = (1-\bar{\mathcal{E}})\rho$. See also Eq. (2.6). In searches, one decides a maximum mismatch $\bar{\mathcal{E}}_{\rm max}$ compatible with the target detection efficiency. For sources uniformly distributed in space, since the horizon distance is $D_{\rm hor} \propto \rho_m$, and the detection rate is $R_D \propto N_G \propto D_{\rm hor}^3$, then the fractional reduction in detection rate due to a mismatch $\bar{\mathcal{E}}_{\rm max}$ is given by $1-(1-\bar{\mathcal{E}}_{\rm max})^3$, so that a 90% detection efficiency implies $\bar{\mathcal{E}}_{\rm max} \approx 3.5\%$. A sufficient condition on the modeling error to meet the $\bar{\mathcal{E}}_{\rm max}$ requirement is then [107]: $\langle \delta h, \delta h\rangle < 2\rho^2 \bar{\mathcal{E}}_{\rm max}$.

On the other hand, for the problem of parameter estimation, one would like

[14] Here optimization over time and phase of coalescence is understood.

systematic biases in the recovered source parameters which are smaller than the (hopefully small) statistical uncertainties. A model that can be reliably employed in parameter estimation pipelines has to be *faithful*, which means an *unfaithfulness* $\bar{\mathcal{F}}$ against numerical relativity within a few percent, where [98]

$$\bar{\mathcal{F}} \equiv 1 - \max_{t_c,\phi_c} \frac{\langle h_{\rm AR}, h_{\rm NR}\rangle}{\sqrt{\langle h_{\rm AR}, h_{\rm AR}\rangle}\sqrt{\langle h_{\rm NR}, h_{\rm NR}\rangle}} \,. \tag{2.41}$$

The definition of $\bar{\mathcal{F}}$ differs from the definition of $\bar{\mathcal{E}}$ in that there is no maximization over the parameters of the source $\boldsymbol{\lambda}$, hence it is a more stringent assessment of the quality of a model. The general criteria for observational indistinguishability of waveforms were studied by Refs. [107–111]. See also Ref. [112] for the first study of parameter biases using EOB nonspinning inspiral-merger-ringdown waveforms.

2.6 Black-hole binary coalescence in the test-particle limit

As discussed, the assumption underlying the EOB formalism is the universal character of black-hole coalescence across different mass ratios, or, equivalently, the absence of poles or branch cuts in the mass-ratio plane. It is then natural to look for insights into the physical process of merger in the test-particle limit, where black-hole perturbation theory is applicable. Perturbation theory [60] is an expansion of the general relativistic 2-body problem in the mass ratio, and it accounts for relativistic effects at all orders. The strong-field information that one extracts from the test-particle regime can directly inform analytical models for comparable-mass black-hole binaries. In the 1970's, pioneering studies investigated the gravitational-wave emission of a particle radially infalling into a Schwarzschild geometry [113].

For generic plunging orbits, the master equations of perturbation theory (Regge-Wheeler-Zerilli or Teukolsky equations) must be solved numerically, but they are significantly less expensive than evolving a black-hole binary in full numerical relativity.

2.6.1 Inspiral-merger-ringdown waveforms

In Ref. [114] (see Chapter 4) we studied the behavior of the inspiral-merger-ringdown signal of a plunging particle in the Kerr spacetime. These waveforms helped the extension of the comparable-mass EOB model for nonprecessing, spinning black-hole binaries of Ref. [70] to 10^3 mass ratios and large spins. In particular, a time delay was introduced between the orbital frequency peak and the matching point where the ringdown waveform is attached (see Sec. 2.5.4). The Teukolsky waveforms were also exploited to build fitting functions for the input values (i.e., amplitude, curvature, frequency, and slope of the frequency at merger), which are needed to impose non-quasicircular corrections to the merger EOB waveform.

The motion of a test mass around a compact object is influenced not only by gravitational radiation, but also by the perturbation that the particle itself imparts on the background spacetime. Since we were mostly interested in the merger-ringdown rather than in the accurate modeling of the inspiral phase, as is usually done for extreme mass-ratio inspirals (EMRIs), in Ref. [114] we employed a fixed Kerr background, and numerically solved the Teukolsky equation, thus retaining only the leading-order dissipative self-force correction to geodetic motion. The

Teukolsky equation is a partial differential equation expressed in Boyer-Lindquist coordinates r, θ, and t, whose axial dependence is trivially given by $e^{im\phi}$. It governs the evolution of curvature perturbations of spin weight s in a Kerr spacetime [97]. Let M and J be the mass and spin of the background. The equation for $s = -2$ describes the curvature perturbation ψ_4, a projection of the Weyl curvature tensor that represents outgoing radiation. Radiation at the hole's event horizon can be obtained with some manipulation [115]. The master equation for $s = -2$ separates by introducing the multipolar decomposition

$$\psi_4 = \frac{1}{(r - ia\cos\theta)^4} \int_{-\infty}^{\infty} \mathrm{d}\omega \sum_{\ell=2}^{\infty} \sum_{m=-\ell}^{\ell} R_{\ell m\omega}(r) S^{-}_{\ell m\omega}(\theta,\phi) e^{-i\omega t}\,, \tag{2.42}$$

where $a \equiv J/(Mc)$, and $S^{-}_{\ell m\omega}(\theta,\phi)$ is a spheroidal harmonic of spin weight -2, that reduces to the spin-weighted spherical harmonic ${}_{-2}Y_{\ell m}(\theta,\phi)$ when $\frac{a\omega}{c} = 0$. The radial dependence $R_{\ell m\omega}(r)$ is governed by the equation

$$\Delta^2 \frac{\mathrm{d}}{\mathrm{d}r}\left(\frac{1}{\Delta}\frac{\mathrm{d}R_{\ell m\omega}}{\mathrm{d}r}\right) - V(r) R_{\ell m\omega} = -\mathcal{T}_{\ell m\omega}(r)\,. \tag{2.43}$$

The quantity $\Delta \equiv r^2 - 2GMr/c^2 + a^2$ and the potential $V(r)$ can be found in Refs. [116, 117]. The source $\mathcal{T}_{\ell m\omega}(r)$ is built from certain projections of the energy-momentum tensor for a small body of mass $\mu \ll M$ orbiting the black hole. In turn, the energy-momentum tensor depends on the orbital motion. We solved the geodesic equation subject to a radiation-reaction force proportional to the (time averaged) gravitational energy flux (see Eq. (2.37)), and computed inspiraling and plunging trajectories for mass ratio 10^3 and dimensionless Kerr spins in the range $[-0.99, 0.99]$ (the general relativistic limit being ± 1). While, in principle, we could have used an analytical model for the energy flux, for instance the factorized resummed EOB flux

of Ref. [101] as in prior studies [118, 119], we instead employed the total Teukolsky flux (i.e., ingoing + outgoing) for circular, equatorial orbits (computed in Ref. [120]), since our main focus was on the Teukolsky waveforms rather than on the orbital dynamics, similarly to what had been done by Ref. [121]. Unlike the Teukolsky flux, the EOB flux contains relativistic effects only up to a finite PN order.

The Teukolsky equation was solved in the time domain using the code described in Ref. [119], with the addition of a hyperboloidal domain compactification that eliminates the error associated with the waveform extrapolation to null infinity. Moreover, the new code takes advantage of full parallelization on GPUs, allowing the fast computation of long waveforms at high resolution. In this context, by "resolution" we mean the spacing of the numerical grid covering the (tortoise) radial and azimuthal directions. The typical trajectories we computed were a few hundred orbits in length and the associated waveforms had discretization errors in the phase within a few $\times 10^{-3}$ radians for all the modes we considered. As the dimensionless spin of the Kerr black hole approaches 1, more and more multipolar modes of the radiation become important close to the merger, as compared to the dominant $(2, 2)$; we computed the dominant and leading subdominant modes: $(\ell, m) = (2, 2)$, $(2, 1)$, $(3, 3)$, $(3, 2)$, $(4, 4)$, and $(5, 5)$.

We found [114] that during the plunge, as the spin grows towards maximal, the amplitude of the modes tends to flatten out as a function of retarded time, displaying a great simplicity in spite of the highly relativistic regime. Figure 2.7 shows the case of the $(2, 2)$ mode for a dimensionless Kerr spin of 0.99. This should be contrasted with waveforms in the comparable-mass regime, whose peaks are

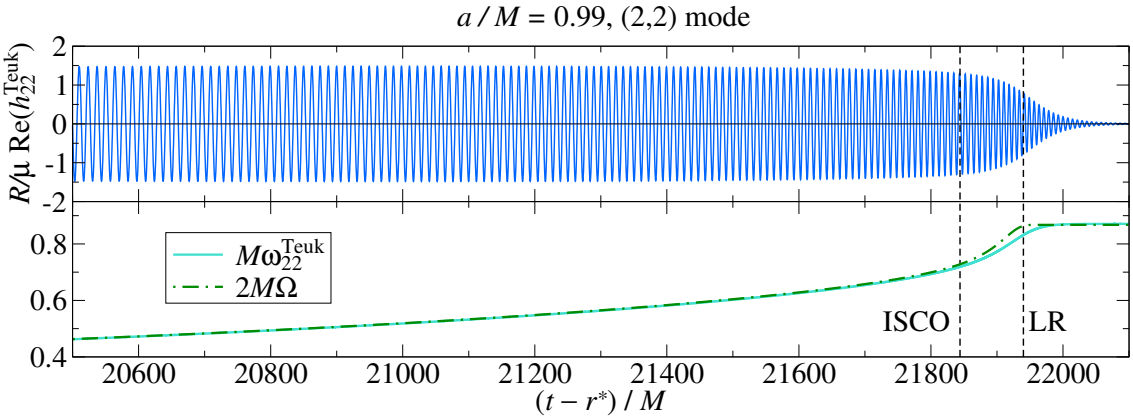

Figure 2.7: [From Ref. [114]] Late inspiral, plunge, merger and ringdown of the Teukolsky $(2,2)$ mode waveform $h_{22}^{\rm Teuk}$ (upper panel), its gravitational-wave frequency $\omega_{22}^{\rm Teuk}$, and orbital frequency Ω of the underlying dynamics (lower panel) for dimensionless Kerr spin 0.99. We note the simplicity of the amplitude during the last phase of the evolution. The plot spans a radial range from $r = 2.21M$ to the horizon, located at $r_+ = 1.14M$. Here, the ISCO is at $r_{\rm ISCO} = 1.45M$ and the light ring is at $r_{\rm LR} = 1.17M$. Vertical dashed lines mark the position of the ISCO and the light ring. R is the distance to the source. Here $G = c = 1$.

always rather sharp, even for almost extremal spins (see also Figure 2.16). We explained this phenomenon by observing that, as the spin grows larger, the ISCO moves to smaller separations and gets closer to the horizon, so that the plunging phase becomes shorter (in the radial coordinate), and moves to higher frequencies (see Figure 2.8). This is equivalent to saying that Kerr black holes with larger spins support longer quasicircular inspirals given the same initial orbital frequency. Furthermore, the radiation-reaction timescale becomes longer for larger spins, while the variation in the orbital frequency is less dramatic. As a result, the secular evolution is much slower for large spins, given the same initial separation. This can be accounted for by simple considerations at the leading order, combining the leading

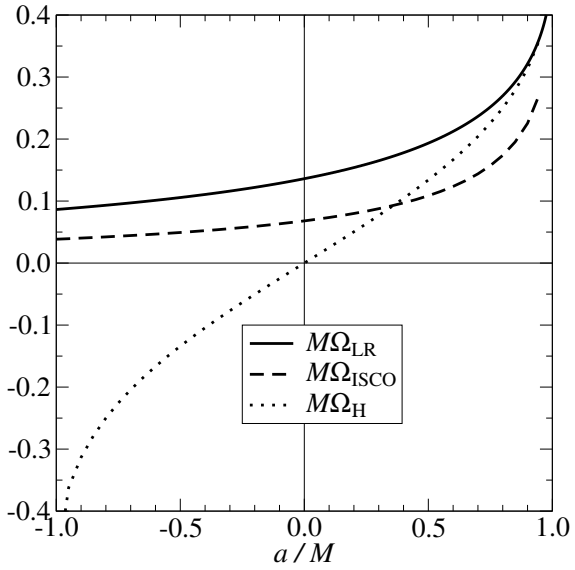

Figure 2.8: Frequencies of ISCO ($\Omega_{\rm ISCO}$), light ring ($\Omega_{\rm LR}$), and horizon ($\Omega_{\rm H}$) for a Kerr black hole, as functions of spin. Negative values of the horizon frequency correspond to retrograde systems. Here $G = c = 1$.

luminosity at infinity $F^{\infty,\,\rm N} = \frac{32}{5}\frac{c^5}{G}\left(\frac{\mu}{M}\right)^2\left(\frac{rc^2}{GM}\right)^4\left(\frac{GM\Omega}{c^3}\right)^6$ (here $\Omega = {\rm d}\phi/{\rm d}t$ is the orbital frequency) with the formula for the binding energy of circular orbits in Kerr $E_{\rm circ}$ [122]. In particular, the radiation-reaction timescale can be estimated from $T_{\rm rad} = -r/\dot{r} = -r({\rm d}E_{\rm circ}/{\rm d}r)/F^{\infty,\,\rm N}$, while the orbital timescale is readily estimated from the formula for the circular frequency in Kerr $\Omega_{\rm circ} = \left[r\sqrt{\frac{r}{GM}} + \frac{J}{Mc^2}\right]^{-1}$, as $T_{\rm orb} = 2\pi/\Omega_{\rm circ}$. During the inspiral and before the ISCO, we found [114] reasonable agreement between this estimation of the ratio $T_{\rm rad}/T_{\rm orb}$ and its numerical computation based on the numerical trajectories that solve the equations of motion. The conclusion is that $T_{\rm rad}/T_{\rm orb}$ increases with the spin at fixed radial separation. The total Teukolsky energy flux becomes very small close to and below the ISCO for almost extremal spins.

The phenomenology of the Teukolsky waveforms is very rich during the ringdown stage. As already found by previous numerical investigations [99,119,123–126], the dominant and leading subdominant ringdown Teukolsky modes can display complicated amplitude and frequency structures that hint at the interference of different quasinormal modes (QNMs) [18] of the Kerr black hole besides the overtones of the least-damped mode $(\ell, m, 0)$, a phenomenon known as *mode mixing*. In Ref. [114] we identified the two main sources of mode mixing in a change of angular basis to represent the waveforms and in the inversion of the orbital trajectory. The former effect arises from the use of a -2-spin-weighted spherical basis to decompose the complex strain $h_+ - ih_\times$ (that is the standard choice for analytical modeling in the PN approximation; see Eq. (2.15)) instead of the spheroidal basis in which the Teukolsky equation is separable; this entails that a spherical (ℓ, m) mode will be a sum over all spheroidal modes with the same m. The second source of mixing has to do with the motion of the orbiting particle: for retrograde systems[15], during the plunge the particle inverts its direction of motion until it gets locked to the rotating event horizon of the Kerr black hole, due to frame dragging; this in general enhances QNMs with opposite m.

We looked for both kinds of mixing by fitting the Teukolsky merger-ringdown

[15]Prograde (Retrograde) equatorial orbits have an angular momentum that is aligned (antialigned) with the Kerr spin. We indicate prograde (retrograde) systems with a positive (negative) sign of the Kerr spin.

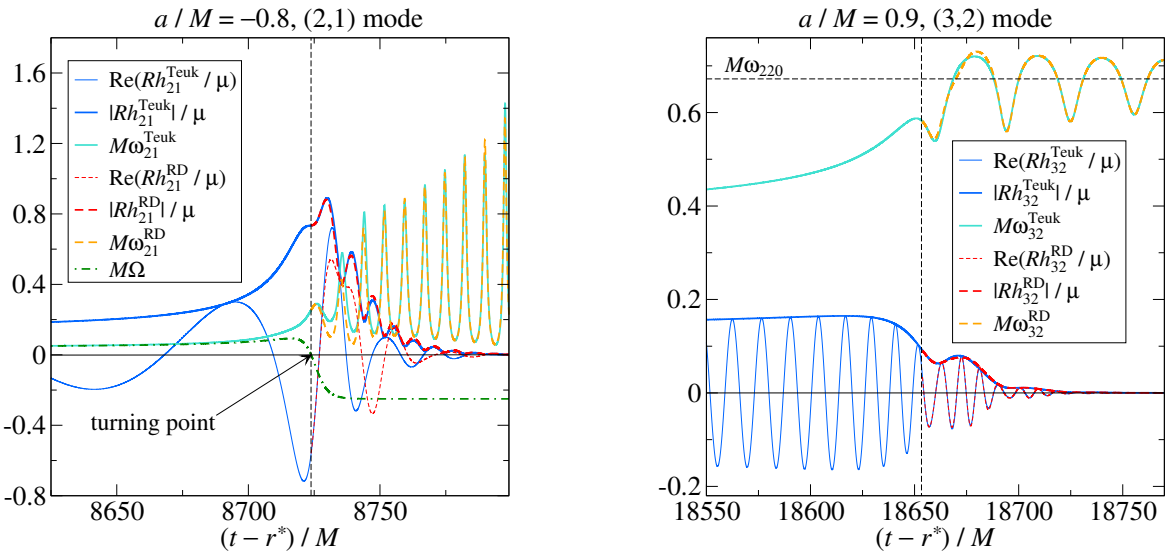

Figure 2.9: [From Ref. [114]] Teukolsky $(2,1)$ mode for spin -0.8 (left panel) and $(3,2)$ mode for spin 0.9 (right panel). The Teukolsky results are in blue, while the model of Eq. (2.44) is in red. For the -0.8 waveform, the modulations come from the interference of the $(2,1,0)$ and $(2,-1,0)$ QNMs; note how the amplitude peak is affected by the mixing, starting at a time where $\Omega = 0$, i.e., the turning point of the azimuthal motion. For the 0.9 waveform, instead, the ringdown contains the $(3,2,n)$'s and $(2,2,0)$ QNMs. R is the distance to the source. Here $G = c = 1$.

signal with a model of the form

$$\left(\frac{\mathcal{R}c^2}{GM}\right) h^{\rm RD}_{\ell m} = \sum_{n=0}^{N-1} A_{\ell m n} e^{-i\sigma_{\ell m n}(t-t^{\ell m}_{\rm match})} + \mathcal{S}(t)\left[A_{\ell' m 0} e^{-i\sigma_{\ell' m 0}(t-t^{\ell m}_{\rm match})} + A_{\ell -m 0} e^{i\sigma^*_{\ell -m 0}(t-t^{\ell m}_{\rm match})}\right], \tag{2.44}$$

where $t^{\ell m}_{\rm match}$ is the time of merger, N is the number of overtones included, the $A_{\ell m n}$'s are the (constant) coefficients of the overtones of the least-damped QNM $(\ell, m, 0)$, $\mathcal{S}(t)$ is a factor introduced to have a smooth switch-on of the interfering QNMs, and $A_{\ell' m 0}$ and $A_{\ell -m 0}$ are fitting parameters (ultimately related to the more fundamental

excitation coefficients of the perturbed black hole). $|A_{\ell' m0}/A_{\ell m0}|$ and $|A_{\ell -m0}/A_{\ell m0}|$ quantitatively describe the strength of the QNM mixing. Here $\sigma_{\ell mn} \equiv \omega_{\ell mn} - i/\tau_{\ell mn}$ is the complex frequency of the (ℓ, m, n) QNM [18,127]. Since overtones with $n > 0$ have short decay times with respect to those with $n = 0$, Eq. (2.44) is actually dominated by terms with $n = 0$ when $t \gg t^{\ell m}_{\rm match}$. Figure 2.9 shows two examples, with the Teukolsky waveform in blue, and the fitted model of Eq. (2.44) in red. The model captures fairly well the modulations, except during the early ringdown.

We found [114] that, for $\ell = m$ modes, the QNM mixing is present for negative spins (i.e., retrograde systems), and arises mainly due to modes with opposite m, whose excitation grows as the spin decreases. For $\ell \neq m$ modes, instead, we found QNM mixing across the entire spin range. For the $(2, 1)$ mode, the main source of mixing is the $(2, -1, 0)$ QNM. For the $(3, 2)$ mode, we recognized 3 different behaviors: when the Kerr spin exceeds 0.8, the ringdown is dominated by $(2, 2, 0)$ with contamination from $(3, 2, 0)$; when the spin is in the range $(0, 0.7]$, the ringdown is dominated by $(3, 2, 0)$ with contamination from $(2, 2, 0)$; when the spin is negative, the ringdown is dominated by $(3, 2, 0)$ with contamination from both $(3, -2, 0)$ and $(2, 2, 0)$.

In the near future, we plan to extend this work to precessing orbits, for which the orbital angular momentum is neither parallel nor antiparallel to the spin of the Kerr background.

2.6.2 Dissipative dynamics: the horizon-absorbed flux

Besides the individual multipolar waveforms, black-hole perturbation theory also provides valuable information about the orbital dynamics of a binary. In fact, the accurate knowledge of the total energy flux in gravitational waves can be used (via the energy balance equation) to compute the time evolution of a binary, as we did in Ref. [114]. In recent years, significant effort has been put into improving the analytical modeling of the gravitational-wave fluxes, both ingoing and at infinity, with respect to the numerical solution of the Teukolsky equation. In particular, Refs. [99, 100] proposed a factorization of the PN-expanded perturbation-theory formulae for the flux at infinity in the Schwarzschild case, improving the agreement with the numerical solution of the Regge-Wheeler-Zerilli equation. Reference [101] extended this approach to the spinning case. Reference [128] applied the same idea of factorizing the PN-expanded formulae to the flux absorbed by the horizon in the nonspinning limit, extending the model also to comparable-mass binaries. The ultimate goal is to develop improved analytical fluxes that can be extended to comparable-mass coalescences.

In Ref. [120] (see Chapter 5) we studied the gravitational energy flux that is absorbed by the event horizon of a Kerr black hole, and proposed a factorized model of it. In particular, we looked at the emission coming from particles in circular, equatorial orbit around a Kerr black hole. We considered a dimensionless Kerr spin $-0.99 \leq cJ/(GM^2) \leq 0.99$ and orbits down to the light ring. We solved the Teukolsky equation in the frequency domain using highly accurate numerical

schemes [116, 117, 129–132]. The energy-momentum tensor of the particle is

$$T_{\alpha\beta} = \frac{E}{\Sigma \sin\theta} \frac{\hat{p}_\alpha \hat{p}_\beta}{\hat{p}^t} \delta[r - r_{\rm o}(t)] \delta[\theta - \theta_{\rm o}(t)] \delta[\phi - \phi_{\rm o}(t)] \,, \tag{2.45}$$

where E is the energy of the particle, $\hat{p}^\alpha \equiv p^\alpha / E$ its normalized 4-momentum, $\Sigma \equiv r^2 + a^2 \cos^2\theta$, and the subscript "o" means "orbit" and labels the coordinates of the particle's worldline. One solves the radial Eq. (2.43) using the method of Green's functions, wherein the source $\mathcal{T}$ is integrated against homogeneous solutions of Eq. (2.43). The energy fluxes (at infinity and through the horizon) are expressed as sums over multipolar components labeled by (ℓ, m). As the light ring is approached, E diverges; this feature inspired the factorized resummation of the outgoing energy flux discussed in Sec. 2.5, first proposed by Ref. [99]. Furthermore, the ingoing energy flux displays another strong-field feature: each multipolar component vanishes whenever the orbital frequency Ω of the perturbing particle equals the frequency of the Kerr event horizon $\Omega_{\rm H} = \frac{c^2}{GM^2} \frac{J}{2r_+}$, with $r_+ = \frac{GM}{c^2} \left[1 + \sqrt{1 - (cJ/GM^2)^2}\right]$. This can happen only for prograde orbits, i.e., when the orbital angular momentum is parallel to the spin of the Kerr black hole. When $\Omega < \Omega_{\rm H}$, the ingoing flux has an opposite sign with respect to the outgoing flux, thus reducing the amount of orbital energy lost by the orbiting particle. This phenomenon goes under the name of "superradiance", and can be regarded as a Penrose-like process [133] of extraction of energy from the rotational motion of the Kerr black hole. Reference [134] formally suggested this interpretation for the first time for scalar perturbations of a Kerr black hole using the Teukolsky equation.

Furthermore, there exists an interesting parallel between the horizon-absorbed

flux in a black-hole binary and the phenomenon of tides. For a recent review, see Ref. [135]. In the early 1970's, Refs. [136,137] computed how a slowly rotating Kerr black hole responds to a stationary perturbing particle, finding that the black hole dissipates energy by spinning down. A similar behavior is found in the Newtonian interaction of a moon perturbing a planet that is covered by viscous oceans and is in slow rotation. This phenomenon is known as *tidal heating*. Both the black hole and the planet spin-down because of tidal interactions. Tidal effects induce a bulge on the black hole's event horizon, thus creating a torque on the orbit. Depending on the relative frequency of the orbit and the hole's rotation, this torque spins up or spins down the hole. Within the membrane paradigm [138], an effective viscosity can be associated to the black hole. In both cases, the geometry of the tidal bulge is determined by the viscosity (either of the fluid body or of the black hole).

Using black-hole perturbation theory, Ref. [139] computed in full analytical form the leading-order absorption flux for a particle in a circular orbit around a Schwarzschild black hole. These initial results indicated that the horizon flux is suppressed relative to the flux at infinity by a factor of $(v/c)^8$, where $v \equiv (GM\Omega)^{1/3}$ is the orbital speed. This result was generalized to the spinning case in Refs. [140,141], whose computation went up to 6.5PN order beyond the leading-order luminosity at infinity for circular orbits $F^{\infty,\mathrm{N}} \equiv \frac{32}{5}\frac{c^5}{G}\left(\frac{\mu}{M}\right)^2\left(\frac{v}{c}\right)^{10}$. The impact of the horizon flux significantly changes with spin: at leading order, the suppression factor becomes $\left[\left(\frac{v}{c}\right)^3 - \frac{cJ}{GM^2}\right]\left(\frac{v}{c}\right)^5$, instead of $(v/c)^8$. Numerical studies of strong-field radiation reaction showed that, for inspirals into rapidly spinning black holes, the neglect of the absorption flux introduces large errors [131].

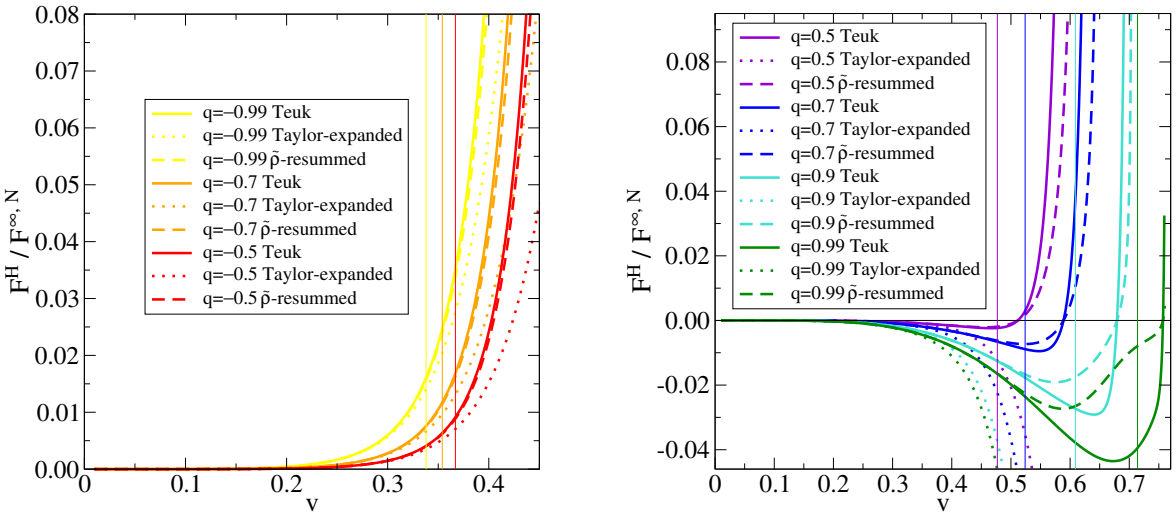

Figure 2.10: [From Ref. [120]] We compare the (numerically computed) Teukolsky-equation absorption flux (solid lines) to the Taylor-expanded PN model of Ref. [141] (dotted lines) and the factorized flux we proposed in Ref. [120] (dashed lines), as functions of v. All curves extend down to the light ring. Vertical lines mark the positions of the respective ISCOs. The fluxes are normalized to the leading-order flux at infinity $F^{\infty,\mathrm{N}}$. In the left panel we show cases with retrograde orbits, while in the right panel we show cases with prograde orbits. Here q is the dimensionless Kerr spin and $G = c = 1$.

We proposed [120] to resum each multipolar component of the absorption flux F^{H} as

$$F^{\mathrm{H}}_{\ell m} \equiv \left(1 - \frac{\Omega}{\Omega_{\mathrm{H}}}\right) F^{\mathrm{H,N}}_{\ell m} (\hat{S}^{(\epsilon)}_{\mathrm{eff}})^2 \left(\tilde{\rho}^{\mathrm{H}}_{\ell m}\right)^{2\ell} , \tag{2.46}$$

which has the advantage of enforcing the presence of the zero at a frequency equal to Ω_{H}. The leading term is defined as

$$F^{\mathrm{H,N}}_{\ell m} \equiv \frac{32}{5}\frac{c^5}{G}\left(\frac{\mu}{M}\right)^2 \left(\frac{v}{c}\right)^{7+4\ell+2\epsilon} n^{(\epsilon)}_{\ell m} c_{\ell m}(a) , \tag{2.47}$$

where ϵ is the parity of the mode, and $c_{\ell m}$ and $n^{(\epsilon)}_{\ell m}$ are mode-dependent constant factors. The source term $\hat{S}^{(\epsilon)}_{\mathrm{eff}}$ is the one entering the factorization of the flux at infinity in Eq. (2.36), divergent at the light ring. Finally, $\tilde{\rho}^{\mathrm{H}}_{\ell m}$ is a polynomial

in v/c such that the PN expansion of Eq. (2.46) agrees with the PN-expanded results of black-hole perturbation theory [140, 141] for the multipolar component of the ingoing energy flux. This model greatly improves the agreement with the numerically computed Teukolsky flux with respect to the PN-expanded model, as demonstrated in Figure 2.10.

In the near future we plan to extend the factorized model of the black-hole absorption flux to the case of spinning, comparable-mass binaries, so that it can be used in the EOB modeling when calibrating it to numerical-relativity simulations.

2.7 Motivations for including spin effects in gravitational waveforms

In this Section we explain why spins cannot be ignored when modeling black-hole binaries, and how their inclusion can help achieve important scientific goals in the advanced-detector era.

Astrophysical black holes (both stellar-mass and supermassive) are expected to carry spin, i.e., intrinsic angular momentum, and generically up to the maximal limit[16], as indicated by observational evidence [142–149]. Spins significantly affect the orbital evolution of black-hole binaries, as well as the radiated waveforms.

From the point of view of the theory, within the context of PN calculations for the inspiral, spins are formally counted with reference to maximally spinning black

[16]General relativity prescribes that a Kerr spacetime of mass M and spin $\mathbf{J}$ obeys the relation $cJ/(GM^2) \leq 1$.

holes. Spin-orbit (SO) effects were first studied by Refs. [150–153], and they first appear at 1.5PN order in the equations of motion and in the radiation field, and today are available up to 4PN order [154–156]. Spin-spin (SS) effects, instead, first appear at 2PN order [152, 153, 157–159], and are currently known up to 3PN order.

One remarkable example of spin effect is the dependence of the time to merger on the spins [160]: whenever the spins $\mathbf{S}_{1,2}$ of the two black holes in the binary are aligned with the orbital angular momentum $\mathbf{L}$ of the system, the binary performs more cycles before merger with respect to nonspinning or antialigned spinning binaries starting from the same initial orbital frequency. This can be understood from PN theory, since the leading order spin-orbit interaction potential increases the gravitational repulsion when $\mathbf{S}_{1,2} \cdot \mathbf{L} > 0$ [161]. Moreover, aligned-spin configurations have a large total angular momentum ($|\mathbf{J}| = |\mathbf{L}| + |\mathbf{S}_1| + |\mathbf{S}_2|$), so that a single black hole cannot be formed via coalescence of the binary until gravitational radiation has carried away enough angular momentum to comply with the Kerr limit (i.e., $c|\mathbf{J}_{\rm final}|/(GM^2_{\rm final}) \leq 1$). Also, the radiated energy in gravitational waves sensitively depends on the spin of the black holes: the larger the spin, the greater the energy loss; recent numerical-relativity simulations of equal-mass binaries with dimensionless spins as large as 0.97 showed that the system can radiate up to 11% of the initial total mass [162].

Another important spin-induced effect in black-hole binaries is the phenomenon of *precession*. When the spins are not aligned or antialigned with the orbital angular momentum $\mathbf{L}$, the system undergoes precession of the orbital plane, which results in complicated phase and amplitude modulations of the waveforms [163, 164]. At

1.5PN order [151, 165], the precession equations take on the form: $\dot{\mathbf{S}}_{1,2} \propto \hat{\mathbf{L}} \times \mathbf{S}_{1,2}$ (where $\hat{\mathbf{L}} \equiv \mathbf{L}/|\mathbf{L}|$), and $\dot{\mathbf{L}} \propto f\,\mathbf{S}_{1,2} \times \mathbf{L} + g\,\hat{\mathbf{L}}$ (where f and g are scalar functions of the masses, the spins, and the relative separation of the binary). Therefore, at this PN order, the spin magnitudes are conserved and, if $\mathbf{S}_{1,2}$ are parallel to $\mathbf{L}$, the vector $\hat{\mathbf{L}}$ stays constant, while $|\mathbf{L}|$ changes because of radiation reaction. Interestingly, the total angular momentum $\mathbf{J}$ changes only due to radiation reaction as

$$\dot{\mathbf{J}} = -\frac{32}{5}\frac{G\mu^2}{r}\left(\frac{GM}{rc^2}\right)^{5/2}\hat{\mathbf{L}}\,. \tag{2.48}$$

The precessional timescale is much longer than the orbital timescale, but it is also much shorter than the radiation-reaction timescale, at least during the adiabatic inspiral. One can distinguish two types of precessional motions: (i) *simple precession*, when $\hat{\mathbf{J}}$, $\hat{\mathbf{L}}$, and $\hat{\mathbf{S}} \equiv (\mathbf{S}_1+\mathbf{S}_2)/|\mathbf{S}_1+\mathbf{S}_2|$ precess on tight cones such that the opening angle of the $\hat{\mathbf{J}}$-cone is much smaller than the opening angle of the $\hat{\mathbf{L}}$-cone; $\hat{\mathbf{L}}$ precesses on a cone with growing opening angle; $\hat{\mathbf{L}}$ and $\hat{\mathbf{S}}$ precess around $\hat{\mathbf{J}}$; (ii) *transitional precession*, when $\mathbf{J} \approx 0$, i.e., when $\mathbf{L}$ and $\mathbf{S}$ are of similar magnitude and almost antiparallel: in this case, $\hat{\mathbf{L}}$ undergoes migration from simple precession about one direction to simple precession about a different direction. These two regimes were first discussed by Ref. [163] in the special case where SS terms could be neglected, but the study was later generalized by Ref. [166]. To analyze the waveforms, let us introduce the instantaneous angle $\phi(t)$ in the orbital plane between $-\hat{\mathbf{N}} \times \mathbf{L}$ (where $\hat{\mathbf{N}}$ is the direction of propagation of the wave) and the separation vector $\mathbf{r}$; in the

quadrupole approximation, the polarizations are given by [163]

$$h_+(t) = -\frac{1}{\mathcal{R}}\frac{4G\mu\Omega^2 r^2}{c^4}\frac{1+(\hat{\mathbf{L}}(t)\cdot\hat{\mathbf{N}})^2}{2}\cos 2\phi(t)\,, \tag{2.49}$$

$$h_\times(t) = \frac{1}{\mathcal{R}}\frac{4G\mu\Omega^2 r^2}{c^4}(\hat{\mathbf{L}}(t)\cdot\hat{\mathbf{N}})\sin 2\phi(t)\,. \tag{2.50}$$

These formulae are consistent with Eqs. (2.13)–(2.14) in the nonprecessing limit, using Kepler's third law for quasicircular orbits $r^3\Omega^2 = GM$, and plugging in the explicit time-evolution of the orbital variables. The strain is computed by convolution with the antenna pattern functions, which take into account the orientation of the detector relative to the binary. The amplitude modulations due to precession are apparent from the factors depending on $(\hat{\mathbf{L}}(t)\cdot\hat{\mathbf{N}})$. As to the phase, there are modulations of the strain polarization (i.e., changes in the relative phase between h_+ and $h_\times$), and there is a precessional correction to the carrier phase $\Phi_C(t) \equiv \int \Omega(t')\mathrm{d}t'$; while the corrections to the polarization depend on the orientation of the detector, the phase correction does not, as it depends only on $\hat{\mathbf{N}}$ and $\hat{\mathbf{L}}$.

Phenomena such as precession and the dependence of the time to merger on the spins suggest that the inclusion of spin effects is crucial, for both detection and parameter estimation. However, let us not forget that during detection searches the real signal can trigger *any* template in the bank, so that it is not a priori unconceivable that a nonspinning bank could be effective even for detecting spinning systems. More quantitatively, several papers studied the role of spin effects in black-hole binary searches [166–171], but were not able to conclusively prove that the inclusion of spins when building template banks increased the sensitivity of the search as compared to a purely nonspinning bank. However, Ref. [172] employed a spin-aligned

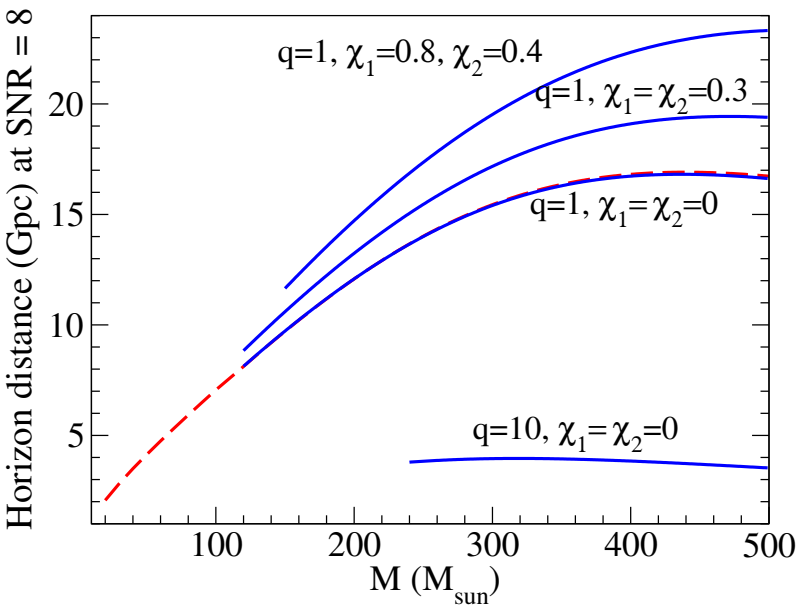

Figure 2.11: [From Ref. [66]] Horizon distance versus the total (redshifted) mass using some of the numerical-relativity inspiral-merger-ringdown waveforms produced by the NRAR collaboration [66]. For mass ratio $q = 1$ and no spin, we also show the numerical-relativity waveform of [175] (solid line) and the EOB waveform of [91] (dashed line). The numerical lines are shown only for those masses where the numerical waveform starts at frequency 10 Hz or below (i.e., where the advanced LIGO seismic wall is). $\chi_{1,2}$ are the dimensionless black-hole spins.

phenomenological inspiral-merger-ringdown model (IMRPhenomB [72]) and consistency tests to suppress false alarms, and could show that using aligned-spin templates can improve the detection efficiency up to 45%. Studies on neutron-star [173] and neutron-star/black-hole binaries [174] indicate gains in detection efficiency when using aligned-spin waveforms for generic binary black holes.

Furthermore, neglecting spin effects in the template waveforms can significantly reduce the horizon distance for spinning black-hole binaries, which directly translates into a reduction of the detection rate: $R_D \propto N_G \propto D^3_{\rm hor}$. Figure 2.11

shows the horizon distance for different spinning, nonprecessing binaries simulated in full numerical relativity (along with an EOB waveform); signals with larger spins produce louder gravitational-wave signals, that can be detected out to larger distances at fixed SNR threshold. Reference [72] shows how the inclusion of nonprecessing spin effects into phenomenological inspiral-merger-ringdown models can increase the detection rate by a factor of 5 for maximally spinning systems in initial LIGO. This can be compared to the case of binary neutron stars, where no significant loss in detection rate occurs when using nonspinning templates for advanced detectors as long as the neutron-star spins are < 0.05 [176].

Besides detection, the accurate modeling of spins is extremely important for the extraction of the physical parameters of the source [177]. An unbiased measurement of the component masses will provide information about the mass distribution of compact-object binaries, the maximum mass of neutron stars, the neutron-star equation of state [178], the minimum mass of stellar-mass black holes and the so-called mass gap [31, 32, 179]. Spin measurements of black-hole binaries originating from field binaries will help understand stellar binary evolution and supernova kicks. Sky localization [180, 181] may allow the identification of the host and searches of electromagnetic counterparts, opening the field of multimessenger astronomy [43, 182]. The correct determination of the luminosity distance will help cosmography at low redshifts.

2.8 Simulating spinning black-hole binaries in numerical relativity: initial conditions

After having made the case for the importance of spins in the construction of inspiral-merger-ringdown waveforms for black-hole binaries, in the next few Sections we are going to explain how to incorporate them in EOB models and how to calibrate them to numerical relativity. Before that, in this Section we discuss a project that can be regarded as a prerequisite for building faithful models, since it enabled the efficient computation of initial conditions for numerical-relativity simulations of spinning black holes moving along quasicircular orbits.

The computation of gravitational waveforms emitted by spinning black-hole binaries in full numerical relativity poses peculiar technical challenges, especially in the presence of precession. Stellar-mass black-hole binaries formed from binary stellar evolution [16] (instead of dynamical capture) are expected to have negligible orbital eccentricity [103] by the time they enter the frequency band of gravitational-wave detectors. Therefore, it is important to do numerical simulations for very low eccentricity binaries. In numerical relativity there are several reasons why building circularized initial conditions is challenging: (i) orbital parameters with negligible eccentricity are only known approximately thanks to PN theory [58]; (ii) differing coordinate systems and effects arising from solving the nonlinear Einstein's constraint equations [183] make it difficult to translate PN orbital parameters into a complete black-hole binary initial data set; (iii) finally, early in a numerical evolu-

tion each black hole relaxes toward a steady state, affecting the black-hole masses, spins [184–186], and orbital parameters. In Ref. [187] (see Chapter 6) we devised an iterative algorithm that removes spurious orbital eccentricity from numerical-relativity initial data. Our goal was to enable the generation of realistic numerical simulations of spinning binaries that could be used to validate and improve spinning EOB models (to be discussed in Sec. 2.9). This algorithm is now part of the standard codes of the SXS Collaboration, and is being used in all their simulations.

Residual orbital eccentricity manifests itself in the form of oscillations in the relative separation and orbital frequency of the binary, on top of the secular trend dictated by radiation reaction, as simple Newtonian considerations suggest; the characteristic frequency of these oscillations is somewhat larger than the average orbital frequency, because of periastron advance [89]. In the case of precessing systems, a PN analysis of the conservative dynamics at 2PN order in the spins demonstrates that SS effects give rise to radial and frequency oscillations as well; however, SS oscillations occur on a different timescale, that is half the orbital period. From the relative Newtonian 2-body Hamiltonian with the addition of 1.5PN SO terms and 2PN SS terms one gets the following differential equation for a perturbation δR of the radial separation R of a compact binary (in geometrized units $G = c = 1$)

$$\ddot{\delta R}(t) + \bar{\Omega}^2\, \delta R(t) = -\frac{3}{4M\bar{R}^4}\left[\left(\mathbf{S}_0(t)\cdot\hat{\boldsymbol{\lambda}}(t)\right)^2 - \left(\mathbf{S}_0(t)\cdot\hat{\mathbf{n}}(t)\right)^2\right], \tag{2.51}$$

where $\bar{R} \equiv \langle R(t)\rangle$, $\bar{\Omega} \equiv \langle \Omega(t)\rangle$ ($\langle\cdots\rangle$ being the time average over one orbital period, such that $\langle \delta R(t)\rangle = 0$), $\mathbf{S}_0(t) \equiv \left(1+\frac{m_2}{m_1}\right)\mathbf{S}_1(t) + \left(1+\frac{m_1}{m_2}\right)\mathbf{S}_2(t)$, $\hat{\mathbf{n}}$ is the unit vector along the relative separation, and $\hat{\boldsymbol{\lambda}}$ is the unit vector along the relative

velocity. Here there is no periastron advance because one does not include higher order nonspinning PN terms in the Hamiltonian. Note that $\hat{\mathbf{n}}$ and $\hat{\boldsymbol{\lambda}}$ lie in the instantaneous orbital plane, and they rotate about $\hat{\mathbf{L}}_N$ with angular velocity $\bar{\Omega}$, i.e., their time dependence is sinusoidal with frequency $\bar{\Omega}$. The precessional timescale is much longer than the orbital timescale $2\pi/\bar{\Omega}$, therefore the spin vector $\mathbf{S}_0$ can be treated as a constant for the purpose of studying the time evolution of δR. The homogeneous solution to Eq. (2.51) is a sinusoidal function oscillating at a frequency $\bar{\Omega}$; its initial amplitude and phase are fixed by the initial conditions of the binary; thus, it describes the effect of eccentricity if present in the initial conditions. On the other hand, a particular solution to Eq. (2.51) is a sinusoidal function oscillating at a frequency $2\bar{\Omega}$, because of the factors quadratic in $\hat{\mathbf{n}}$ and $\hat{\boldsymbol{\lambda}}$ in the RHS of the equation; it describes physical SS-induced oscillations, whose presence is not affected by the introduction of radiation reaction in the problem.

Radiation reaction suppresses the homogeneous solution, while it does not affect the particular solution. The two kinds of oscillations are neatly disentangled thanks to their different characteristic frequencies. Therefore, when constructing realistic, circularized initial conditions for precessing black-hole binaries, one should minimize any residual radial oscillation at a frequency $\bar{\Omega}$, while allowing for physical oscillations at a frequency $2\bar{\Omega}$.

Motivated by these considerations, in Ref. [187] we proposed an iterative algorithm that, at each step, extracts the eccentricity from the oscillations induced in $\Omega(t)$, and prescribes a small change in the orbital frequency of the initial data set. We showed that the contamination in the measurement of the eccentricity caused

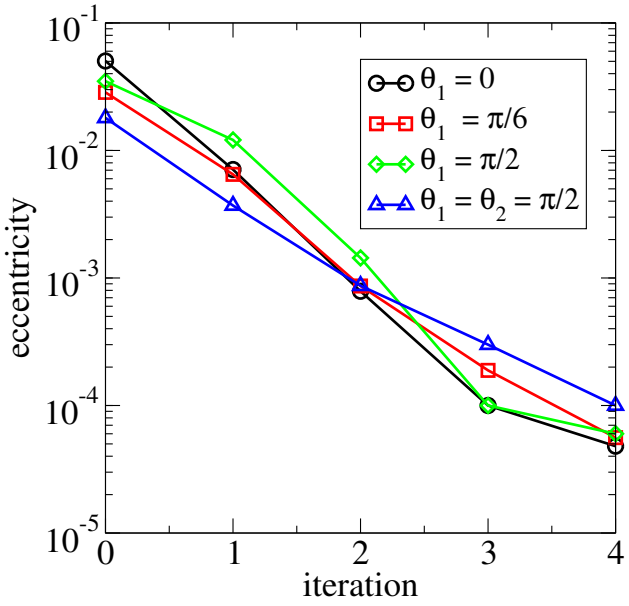

Figure 2.12: [From Ref. [187]] Reduction of the initial orbital eccentricity in black-hole binary simulations for different initial spin configurations by means of the iterative algorithm developed in Ref. [187]. Shown are three configurations with dimensionless spins $\chi_1 = 0.5, \chi_2 = 0$ and different spin directions θ_1 (i.e., the opening angle with respect to the initial orbital angular momentum), and one configuration with $\chi_1 = \chi_2 = 0.5$, with initially two orthogonal spins both tangent to the orbital plane. For all cases, the mass ratio is $m_1/m_2 = 1.5$.

by physical SS modulations is suppressed in the case of $\Omega(t)$, as compared to $R(t)$, thus resulting in a robust eccentricity removal algorithm. Typically, this method can reduce the initial eccentricity down to 10^{-4} at a separation of about $20\,GM/c^2$ within a few iterations, as shown in Figure 2.12 for four representative runs.

2.9 How to incorporate spin effects into the effective-one-body model

In this Section we come back to the EOB modeling of black-hole binaries, and turn our attention to the spin of the component objects.

Earlier attempts at modeling spinning black-hole binaries in the EOB formalism were carried out in Refs. [188,189], which considered the inclusion of the leading SO coupling. One maps the real PN 2-body dynamics (including the 1.5 PN SO terms) to the motion of an effective particle in a deformed Kerr background. Since spherical symmetry is broken by the presence of spins, the effective metric $g^{\rm eff}_{\alpha\beta}$ will in general contain off-diagonal components. One defines $\alpha \equiv (-g^{tt}_{\rm eff})^{-1/2}$, $\beta^i \equiv g^{it}_{\rm eff}/g^{tt}_{\rm eff}$, and $\gamma^{ij} \equiv g^{ij}_{\rm eff} - g^{it}_{\rm eff} g^{jt}_{\rm eff}/g^{tt}_{\rm eff}$, so that the Hamilton-Jacobi equation (2.30) can be rewritten as

$$H_{\rm eff} = \beta^i P_i + \alpha \sqrt{\mu^2 c^4 + \gamma^{ij} P_i P_j}\,. \tag{2.52}$$

One expresses the deformation in Boyer-Lindquist coordinates [190] through a modification of the Kerr potential $\Delta(R) \equiv R^2 + a^2 - 2GMR/c^2$, where $a \equiv |\mathbf{S}_{\rm Kerr}|/Mc$ is the Kerr spin for a geometry with total mass M and black-hole spin $\mathbf{S}_{\rm Kerr}$; the modification is different for the tt and RR components of the metric, and two distinct ν-deformed potentials are introduced, $\Delta_t(R)$ and $\Delta_R(R)$, that generalize the nonspinning EOB potentials $A(R)$ and $D(R)$ appearing in Eq. (2.22). The effective metric is then expressed in terms of Δ_t, Δ_R, and the effective spin $\mathbf{S}_{\rm Kerr}$ (see Eqs. (2.39)-(2.41) of Ref. [188]). After the usual energy mapping of Eq. (2.29) is

enforced, the mapping between the real spins $\mathbf{S}_{1,2}$ and the effective spin $\mathbf{S}_{\rm Kerr}$ is established by expanding $H_{\rm EOB}$ in PN orders and matching it with the real PN Hamiltonian: $\mathbf{S}_{\rm Kerr} = \left(1 + \frac{3m_2}{4m_1}\right)\mathbf{S}_1 + \left(1 + \frac{3m_1}{4m_2}\right)\mathbf{S}_2$, which is 1.5PN accurate in the spins.

Spin-spin effects were accommodated by allowing the effective particle to carry a spin $\mathbf{S}_*$. Spin-spin effects naturally arise: (i) from the coupling of the mass monopole of one black hole to the quadrupole of the other black hole (induced by its spin), hence these are terms of the form $m_1 S_2^2/m_2$ and $m_2 S_1^2/m_1$; (ii) from the one-graviton interaction between the two spins, hence these are terms of the form $S_1 S_2$.

References [191, 192] proposed an improved EOB spinning model that: (i) exactly reproduces the Hamiltonian of a spinning test particle in a Kerr spacetime[17] [193] in the extreme mass-ratio limit; (ii) guarantees the existence of an ISCO, a light ring, and a peak of the orbital frequency in the nonprecessing limit; (iii) includes SO and SS couplings up to 3.5PN and 2PN order, respectively. This represents a significant step forward with respect to the earlier spinning EOB model in that all the test-particle SO terms are resummed. In this model, the mapping between real ($\mathbf{S}_{1,2}$) and effective spins ($\mathbf{S}_{\rm Kerr}$ and $\mathbf{S}_*$) is of the form

$$\mathbf{S}_{\rm Kerr} = \mathbf{S}_1 + \mathbf{S}_2 \,, \tag{2.53}$$

$$\mathbf{S}_* = \frac{m_2}{m_1}\mathbf{S}_1 + \frac{m_1}{m_2}\mathbf{S}_2 + \mathbf{\Delta}^{(1)}_{\sigma^*} + \mathbf{\Delta}^{(2)}_{\sigma^*} \,, \tag{2.54}$$

[17] This computation was done at linear order in the spin of the particle, thus providing a Hamiltonian formulation of the Mathisson-Papapetrou-Piran equation.

where $\mathbf{\Delta}^{(1)}_{\sigma^*}$ and $\mathbf{\Delta}^{(2)}_{\sigma^*}$ are 2.5PN and 3.5PN order SO terms, respectively. The EOB radial potential that enters $g^{\rm eff}_{tt}$ is

$$\Delta_t(R) = R^2\,\bar{\Delta}_u(R)\left[1+\nu\Delta_0+\nu\log\left(1+\sum_{k=1}^{5}\Delta_k\left(\frac{GM}{Rc^2}\right)^k\right)\right], \tag{2.55}$$

where the Δ_k's ($k=0,5$) depend on ν and the spin a, and

$$\bar{\Delta}_u(R) \equiv \left(\frac{ac^2}{GM}\right)^2\left(\frac{1}{R}-\frac{1}{R^{\rm EOB}_+}\right)\left(\frac{1}{R}-\frac{1}{R^{\rm EOB}_-}\right), \tag{2.56}$$

where $R^{\rm EOB}_\pm \equiv GMc^{-2}\left[1+\sqrt{1-(ac^2/GM)^2}\right](1-\nu\kappa)$ are the EOB horizons, which deviate from the ones of Kerr (in Boyer-Lindquist coordinates) due to the presence of the tuning parameter κ. A log-resummation is applied to the potential entering $g^{\rm eff}_{RR}$ as well.

The dissipative part of the binary evolution is modeled via the factorized resummation of the multipolar modes (including spin effects) developed by Ref. [101] (see Eq. (2.36)). This accounts in a self-consistent way for the radiation-reaction force and the waveforms, via Eq. (2.35).

2.10 Calibration of a spinning, nonprecessing effective-one-body model to numerical relativity

In this Section we discuss how we improved the spinning EOB model presented before by exploiting state-of-the-art numerical-relativity simulations.

Having in mind the goal of building *faithful* waveforms for the coalescence of spinning, nonprecessing black-hole binaries, in Refs. [70, 93] we calibrated the spinning EOB model described in Sec. 2.9 to long and accurate numerical-relativity

simulations computed by the SXS Collaboration [105]. More details can be found in Chapters 7 and 8.

Dr Yi Pan and I developed a flexible C++ code that can accommodate several different versions of the EOB model, from the nonspinning, Padé-resummed version of Ref. [91] to the latest precessing version of Ref. [194]. In particular, each major ingredient of the model (conservative dynamics, gravitational-wave energy flux, waveforms, initial conditions, ordinary-differential-equation integrator) can be seamlessly modified. This coding structure allowed us to explore a large variety of possibilities when calibrating to numerical relativity. Any extension of the model via tuning parameters is guided by the principle of simplicity, hence it is fairly unconstrained, and several choices are possible. Among other things: (i) we implemented the automatic computation of non-quasicircular corrections via an iterative procedure that feeds them back into the orbital evolution; (ii) we implemented an automatic optimization of the inspiral tuning parameters given several numerical-relativity waveforms; (iii) for the precessing EOB model (see Sec. 2.12), we implemented routines to change the frame of reference; (iv) the code is compatible with the test-particle limit, where $\nu = 0$ everywhere in the model, except in the leading-term of the radiation-reaction force.

As explained in Sec. 2.5.5, in absence of any calibration the EOB waveforms, in general, are not faithful to the numerical simulations over the entire range of masses of physical interest $\mathcal{O}(10) \lesssim M/M_\odot \lesssim \mathcal{O}(100)$, even though they might be effectual. Different portions of the waveform are affected by different (known) limitations of the model: (i) because of the limited knowledge of PN corrections to

the 2-body motion, the inspiral will typically accumulate significant phase difference with respect to numerical relativity (see the upper panel of Figure 2.6); (ii) the factorized waveforms are a resummation of quasicircular PN formulae, therefore they cannot correctly describe the plunge, where radial motion is not negligible (see the middle panel of Figure 2.6); (iii) during the ringdown, we do not know a priori which QNMs are going to be excited and when their excitation exactly starts, nor we know if there is going to be a time-dependent excitation, so there is no guarantee that the simple model of Eq. (2.38) is going to work well for any black-hole binary configuration.

The two spinning, nonprecessing models we calibrated in Refs. [70, 93] differ in the scope of the catalog of numerical-relativity waveforms used to tune them. The first model was developed in 2011, when only 5 nonspinning and 2 equal-mass, moderately spinning numerical simulations of sufficient length and accuracy were available. The second model was developed in 2013, after advances in numerical-relativity codes had allowed the production of large catalogs of accurate waveforms, and used 8 nonspinning and 30 spinning simulations that spanned mass ratios from 1 to 8 and reached almost extremal spins in the equal-mass limit [67]. As a result, while in the former model we could extrapolate the calibration to any mass ratio but only up to spins of magnitude 0.6, in the latter model we could achieve full coverage of the 3-dimensional nonprecessing parameter space (i.e., any mass ratio and spin magnitude). Figure 2.13 shows the distribution in parameter space of the 38 numerical runs used in Ref. [70]: most of them lie along the equal-mass line $\nu = 1/4$, where their spins are as large as 0.98. These were the state-of-the-art in

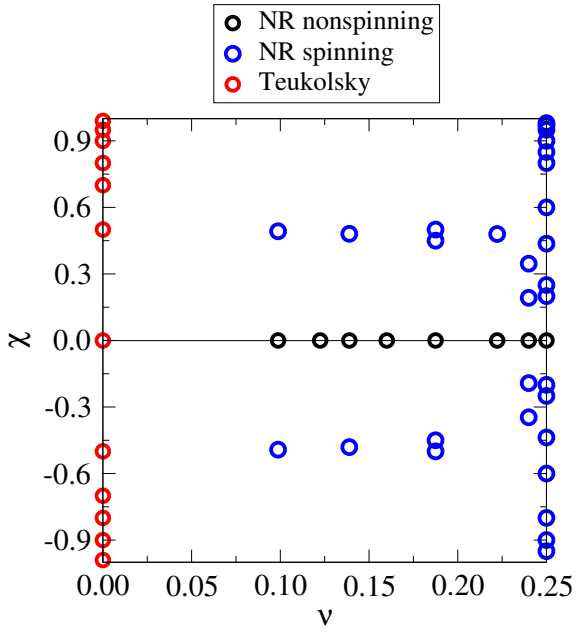

Figure 2.13: Physical parameters of state-of-the-art numerical-relativity runs used in the calibration of the spinning, nonprecessing EOB model of Ref. [70]. The runs are represented in the ν–χ space, where $\nu \equiv m_1 m_2/(m_1+m_2)^2$ is the symmetric mass ratio, and χ is an effective dimensionless spin defined as $\chi \equiv \chi_S + \chi_A \sqrt{1-4\nu}/(1-2\nu)$, with $\chi_{S,A} \equiv (\chi_1 \pm \chi_2)/2$. We also include the Teukolsky runs that we computed in Ref. [114]; these runs constrain the merger waveforms in the test-particle limit, for $\nu = 10^{-3}$.

numerical waveforms available at the time of developing our model, including the longest and most accurate simulations in the literature, as well as the largest spins ever simulated.

In order to achieve faithfulness, we addressed all the issues discussed above. To improve the inspiral, we introduced 4 carefully chosen tuning parameters, both nonspinning and spinning. In Figure 2.14, for an equal-mass, nonspinning black-hole binary, in the space of the 2 nonspinning tuning parameters $A^{(1)}$ and $A^{(2)}$ used in

Ref. [93], we show contours of global phase difference[18] $\Delta\Phi_{22}^{\rm global}$ between numerical relativity and the EOB model. A similar plot can be constructed for the relative amplitude difference $(\Delta A_{22}/A_{22})^{\rm global}$ between numerical relativity and the EOB model. Calibrating the tuning parameters of the EOB model amounts to minimizing the sum (in quadrature) of $\Delta\Phi_{22}^{\rm global}$ and $(\Delta A_{22}/A_{22})^{\rm global}$. The calibration point for the example in Figure 2.14 is indicated in green. When calibrating the model to several numerical simulations, we optimized all the waveforms together using a numerical simplex algorithm.

As to the merger, we fitted the main features of the numerical waveforms at their peak (i.e., amplitude, curvature, frequency, slope of the frequency, that is the input values in the model), and used this information to determine the phenomenological non-quasicircular corrections to the phase and amplitude of the EOB waveforms.

Finally, for the ringdown, we tuned a few QNMs in order to slow down the rising of the gravitational-wave frequency between the point of matching with the inspiral-plunge signal and its asympotic value (i.e., the frequency of the least-damped QNM). We also tuned the matching interval between the inspiral-plunge waveform and the merger-ringdown waveform.

When developing the models, we enforced constraints coming from the test-

[18]The global phase difference is defined as

$$\Delta\Phi_{22}^{\rm global} \equiv \max_t |\Phi_{22}^{\rm (NR)}(t) - \Phi_{22}^{\rm (AR)}(t+\Delta t) - \Delta\Phi_{22}|\,, \tag{2.57}$$

where $\Phi_{22}^{\rm (NR,AR)}$ are the numerical-relativity and EOB waveform phases, and Δt and $\Delta\Phi_{22}$ are determined by the low-frequency alignment (see Eq. (2.39) and the discussion below it).

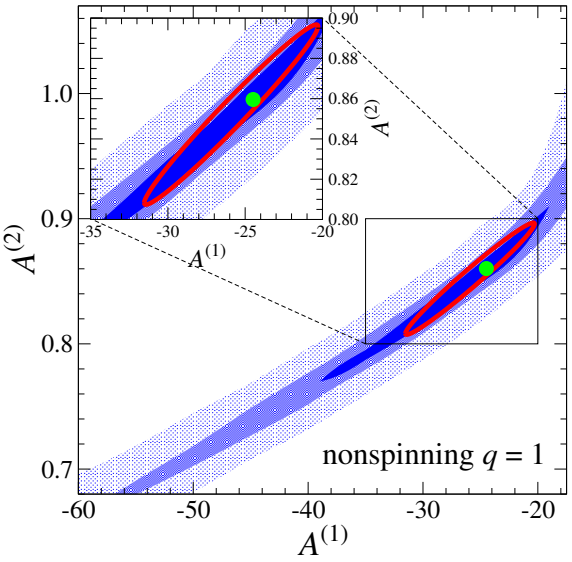

Figure 2.14: In the space of the 2 nonspinning calibration parameters used in Ref. [93], we show contours of phase difference between a numerical-relativity and an EOB waveform for an equal-mass, nonspinning black-hole binary. The shaded regions, from inside out, are 0.1, 0.2 and 0.5 radian contours. The point of minimum phase difference is the calibration point, and is marked in green. The numerical-relativity error box for the calibration point is shown by the red ellipse. The inset zooms in around the calibration point.

particle limit and the gravitational self-force. In particular, we fitted the input values for the non-quasicircular corrections in such a way as to recover the input values that were measured on the Teukolsky waveforms computed in Refs. [114,119], in order to guarantee a smooth connection to the limit $\nu \to 0$. In Figure 2.13 we plot the Teukolsky waveforms used to constrain the EOB model. We also imposed that one recovers the frequency shift of the ISCO as predicted by conservative self-force calculations at linear order in ν [195].

The main result of these calibrations is summarized in Figure 2.15, where we plot the unfaithfulness (see Eq. (2.41)) of the spinning model of Ref. [70] against the

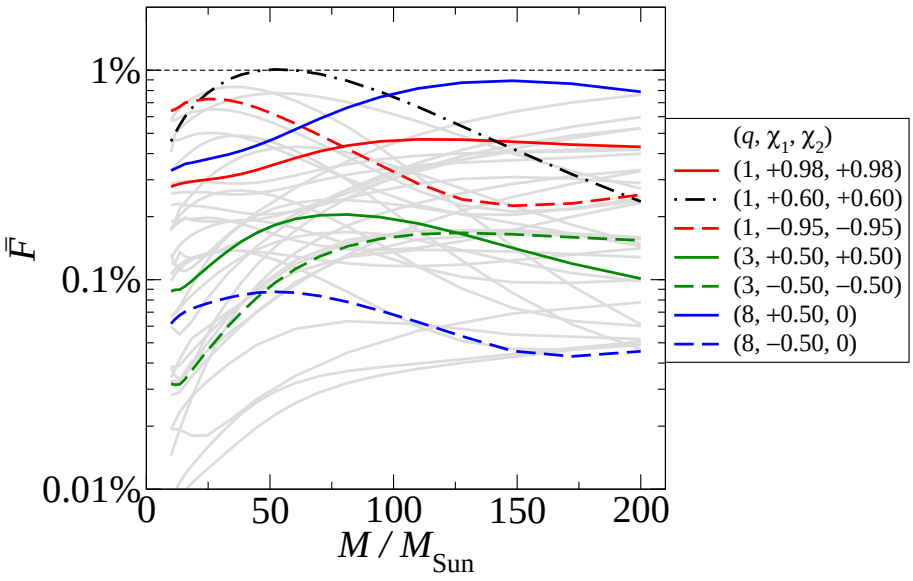

Figure 2.15: [From Ref. [70]] Unfaithfulness of (2,2) mode EOB waveforms [70] for *all* the 38 nonprecessing black-hole binaries in the SXS catalog [67]. Only a few selected cases are labeled in the legend. The zero-detuned high-power advanced LIGO noise curve was used.

38 numerical-relativity waveforms used to calibrate it. All cases have unfaithfulness below the 1% threshold. The ineffectualness (see Eq. (2.40)) is then well below 1%, typically a couple of orders of magnitude smaller than the unfaithfulness. This entails a negligible loss of detection rate due to modeling error, at least for black-hole binaries with large total masses ($\gtrsim 100 M_\odot$), such that the numerical-relativity waveforms can cover the advanced LIGO band[19] starting from $f_{\rm min} = 10$ Hz. In

[19]If a waveform starts at a dimensionless frequency $\hat{\omega}_{\rm NR} \equiv GM\omega_{\rm NR}/c^3$, then

$$f_{\rm NR} = \frac{c^3}{2\pi G M_\odot} \frac{\hat{\omega}_{\rm NR}}{M/M_\odot} = 32 \left(\frac{\hat{\omega}_{\rm NR}}{M/M_\odot} \right) {\rm kHz}\,. \tag{2.58}$$

For instance, one of the longest simulations to date (the nonspinning, equal-mass binary in the SXS catalog [67]) starts at $\hat{\omega}_{\rm NR} = 0.023$, so it can cover the advanced LIGO band from $f_{\rm min}$ if rescaled to a total mass $M = 75 M_\odot$.

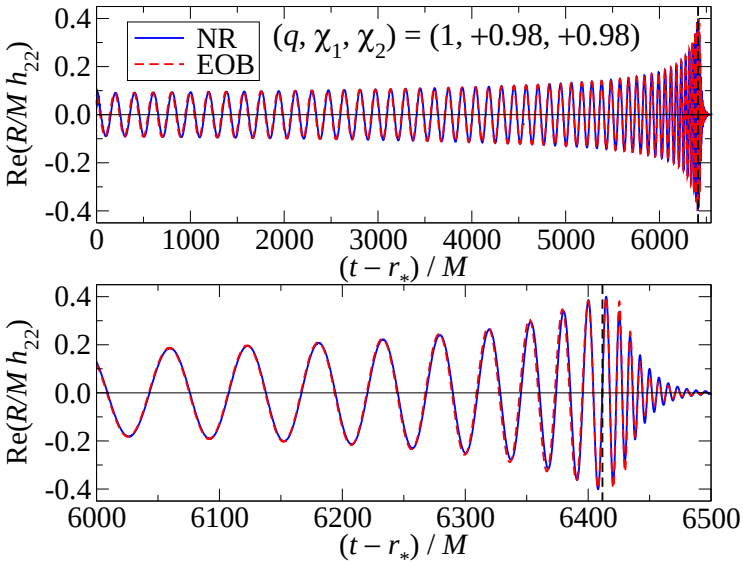

Figure 2.16: [From Ref. [70]] Comparison between the EOB model of Ref. [70] and numerical relativity for the (2,2) mode of an equal-mass binary with aligned spins of magnitude $\chi_{1,2} = 0.98$. The waveforms are aligned at their amplitude peak, indicated by the vertical dashed line. Here $G = c = 1$.

Figure 2.16 we also show the waveform comparison for one run in the SXS catalog, the equal-mass binary with dimensionless spins $\chi_{1,2} = 0.98$; at the time of writing, this is the numerical-relativity simulation of a coalescing black-hole binary with the largest spins available in the literature.

Together with members of the LIGO Scientific Collaboration (LSC), the author implemented the spinning EOB models discussed above into the LSC Algorithm Library (LAL), so that they could be available to experimenters. We performed stringent tests to ensure the robustness of the models across the physical parameter space. One of these models (SEOBNRv1 [93]) has already been used (i) for the study of neutron-star/black-hole mergers with PN approximants [176], (ii) in the study of

tidal effects in neutron-star/black-hole mergers [196], and (iii) for the construction of surrogate models [197]. At the time of writing, the complete spinning, nonprecessing model we developed in Ref. [70] has been chosen by the Compact Binary Coalescence Group of the LIGO Scientific Collaboration for searches of binary black holes with advanced LIGO during the first scientific run of Fall 2015 [57].

2.11 Validating the calibration of the spinning, nonprecessing effective-one-body model

The basic ingredients of the EOB model (conservative and dissipative dynamics, waveforms) are based on the physical idea of universality of the process of binary coalescence, from the comparable-mass regime to the test-particle limit. This gives us confidence that the model can be safely extended beyond the (limited) scope of its calibration. We confirmed this for the calibrated spinning, nonprecessing EOB model of Ref. [93] (discussed in Sec. 2.10), by testing its reliability: (i) outside the range of mass ratios and spin magnitudes used in its calibration, and (ii) when compared to longer numerical-relativity simulations.

2.11.1 Extrapolating the model outside its range of calibration

The spinning EOB model of Ref. [93] was calibrated to 5 nonspinning simulations with mass ratio $q = 1, 2, 3, 4, 6$, and 2 spinning, nonprecessing simulations with mass ratio 1 and spins $\chi_{1,2} = \pm 0.44$. It was also constrained by Teukolsky waveforms computed up to a Kerr spin of 0.9 [119]. This model can generate $(2, 2)$

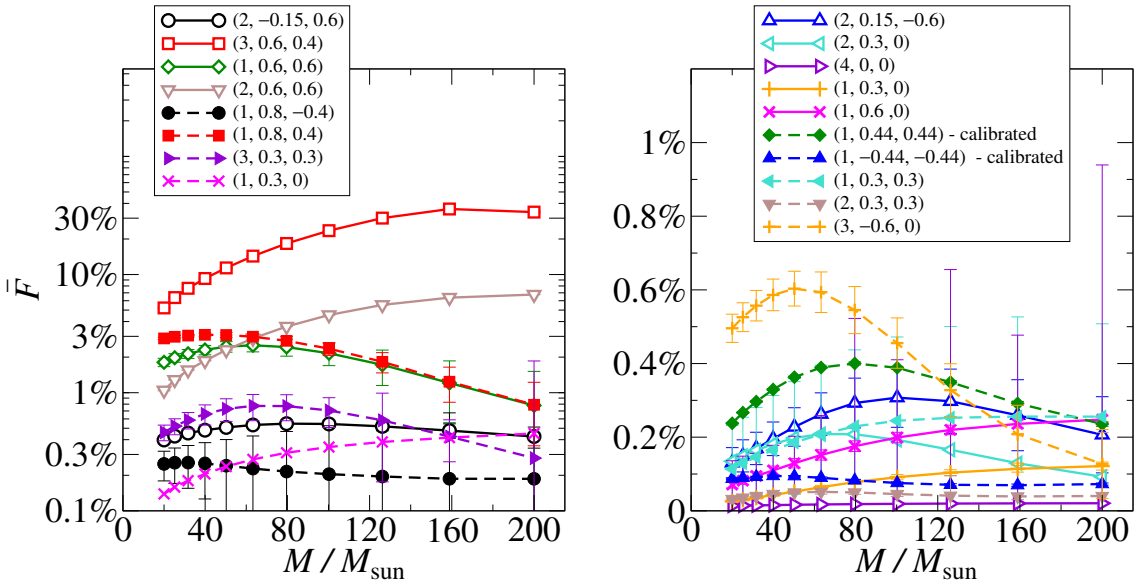

Figure 2.17: [Adapted from Ref. [66]] Unfaithfulness $\bar{\mathcal{F}}$ of the spinning EOB model of Ref. [93] compared to the spinning, nonprecessing NRAR numerical simulations. The horizontal axis shows the total mass, the vertical axis $\bar{\mathcal{F}}$ in percent. The waveforms are split between the two panels for readability. The legends indicate mass ratio and spin magnitudes. Note that for $M \lesssim 100 M_\odot$ the plot *disregards* the low-frequency portion of the waveform which is below the starting frequency of the numerical waveform in spite of substantial contribution to the SNR. Numerical-relativity error estimates on the computed unfaithfulness values are plotted as error bars. Note that the EOB model was calibrated to the equal-mass cases with spins ± 0.44, shown in the right panel.

mode inspiral-merger-ringdown waveforms for black-hole binaries of any mass ratio and with aligned/antialigned spins with magnitude ≤ 0.6. In spite of the limited set of calibration waveforms, the model turned out to give high faithfulness when compared to numerical-relativity waveforms outside its domain of calibration.

We carried out this comparison in Ref. [66] (see Chapter 9), within the Numerical Relativity / Analytical Relativity (NRAR) Collaboration. Note that this project predates the development of the spinning EOB model of Ref. [70]. The

NRAR Collaboration brought together 9 numerical-relativity groups and several researchers working in analytical modeling of compact binaries in an effort to coordinate a large scale production of numerical simulations that could be helpful to improving waveform models. As a result, 25 simulations were generated and analyzed by the Collaboration, mostly covering comparable-mass systems and moderate spins. Figure 2.17 shows the unfaithfulness (see Eq. (2.41)) of our EOB model against the 18 NRAR simulations that are spinning and nonprecessing. Note that only for $M \gtrsim 100M_{\odot}$ the numerical waveforms cover the entire bandwidth of the detector (in this case, advanced LIGO). Nonetheless, for smaller total masses, we did not hybridize the numerical waveforms with any analytical approximant, but instead we truncated the overlap integral: this means that for smaller total masses we cannot draw final conclusions about whether the model is sufficiently accurate for detection and/or measurement purposes. We found unfaithfulness within a few percent for all configurations except 2: for these 2 cases, the amplitudes and frequencies of the model have artificial oscillations around merger. However, we found that by minimizing only over the binary component masses the ineffectualness (see Eq. (2.40)) can already be reduced to below 2% for *all* 18 runs. A further reduction could be achieved when minimizing also over the black-hole spins. We concluded that for $M \gtrsim 100M_{\odot}$ the model is sufficiently accurate for detection purposes, i.e., the modeling error will cause a loss in detection rate smaller than 3%.

2.11.2 Extrapolating the model to longer inspirals

In Ref. [198] (see Chapter 10) we performed a study on the nonspinning sector of the EOB model of Ref. [93] that investigated the stability of the calibration when longer and longer numerical-relativity simulations are employed. As already discussed, numerical relativity is limited by computational costs, so that there exists a gap between the initial frequency $f_{\rm NR}$ where feasible numerical simulations can start and the frequency $f_{\rm PN}$ up to which different PN approximants are indistinguishable from one another (see also Sec. 2.4): $f_{\rm PN} \ll f_{\rm NR}$. Since the EOB model is the natural candidate to cover the interval $[f_{\rm PN}, f_{\rm NR}]$, one has to confirm whether the calibration quickly converges with the number of available numerical-relativity cycles and whether the calibrated EOB waveforms will be indistinguishable from numerical ones below $f_{\rm NR}$. For mass ratios $q = 1, 1.5, 5, 8$, we recalibrated the 2 nonspinning tuning parameters that determine the inspiral timescale (i.e., κ in the EOB horizon and a 4PN term in the amplitude of the $(2,2)$ mode) to varying lengths of numerical waveforms (up to 60 cycles for $q = 1$). We found that, when $q \leq 8$, EOB waveforms calibrated over the 30 cycles before merger are indistinguishable from those calibrated over 60 cycles up to an effective SNR[20] of 110. As discussed earlier, the criterion for indistinguishability of two waveforms $h_{1,2}$ was defined in Ref. [110] as $||h_1 - h_2||/||h_1|| < 1/\rho_{\rm eff}$, where $||h|| \equiv \sqrt{\langle h, h\rangle}$. The quantity $||h_1 - h_2||/||h_1||$ indicates the relative loss in SNR due to the difference of the waveforms. Under

[20] By "effective SNR" we mean $\rho_{\rm eff} \equiv \rho\sqrt{n_D}/\epsilon$, where ρ is the single detector SNR, n_D is the number of detectors in the network, and $1/\epsilon$ is a safe factor [199] of order unity.

rather conservative assumptions concerning the rate of growth of $||h_1 - h_2||/||h_1||$ as a function of the number of cycles, we concluded that the current calibration of the nonspinning EOB model is sufficiently accurate for advanced-LIGO parameter estimation when $\rho_{\rm eff} < 20$, $q < 5$ and $M \geq 20 M_\odot$. Moreover, EOB waveforms can completely replace PN + numerical-relativity hybrid waveforms [200–203].

2.12 Precessing black-hole binaries within the effective-one-body formalism

In this last Section, we discuss how we built an inspiral-merger-ringdown model for generic, precessing binaries starting from the nonprecessing EOB models that we calibrated in Ref. [70, 93], discussed in Sec. 2.10.

2.12.1 The precessing-frame convention

The gravitational-wave signal emitted by precessing black-hole binaries can be very complicated because of the amplitude and phase modulations imprinted by the motion of the orbital plane when looked at by an inertial observer. It is thus convenient to follow the *precessing convention* proposed by Ref. [166], and introduce a non-inertial reference frame that tracks the precession of the orbital plane: its unit

vectors obey the following equations of motion

$$\frac{\mathrm{d}\hat{\mathbf{e}}_1^P(t)}{\mathrm{d}t} = \mathbf{\Omega}_e(t) \times \hat{\mathbf{e}}_1^P(t)\,, \tag{2.59}$$

$$\frac{\mathrm{d}\hat{\mathbf{e}}_2^P(t)}{\mathrm{d}t} = \mathbf{\Omega}_e(t) \times \hat{\mathbf{e}}_2^P(t)\,, \tag{2.60}$$

$$\hat{\mathbf{e}}_3^P(t) = \hat{\mathbf{L}}_N(t)\,, \tag{2.61}$$

where $\hat{\mathbf{L}}_N$ is the direction of the Newtonian angular momentum $\mathbf{L}_N \equiv \mu M \mathbf{r} \times \dot{\mathbf{r}}$ (orthogonal to the plane of the orbit), and $\mathbf{\Omega}_e \equiv \hat{\mathbf{L}}_N \times \frac{\mathrm{d}\hat{\mathbf{L}}_N}{\mathrm{d}t}$. When computing the -2-spin-weighted spherical harmonic decomposition of the complex strain $h_+ - ih_\times$ in this precessing frame, one finds that, at leading PN order, the precessional effects in the waveforms are neatly disentangled from both amplitude and phase evolutions. Within the precessing convention, one expresses the precessing waveform as the product of a nonprecessing carrier waveform times a modulation term wherein all precessional effects are collected. The key point of the precessing convention is the removal of all precession-induced modulations from the accumulated orbital phase $\Psi(t)$, so that $\Psi(t)$ is simply given by the integral of the (monotonic) orbital frequency Ω, i.e. $\Psi(t) = \int \Omega(t')dt'$. In general, the unit vector $\hat{\mathbf{n}}$ along the relative separation between the compact objects can be expanded on any orbital-plane basis $\{\hat{\mathbf{e}}_1, \hat{\mathbf{e}}_2\}$ as $\hat{\mathbf{n}}(t) = \hat{\mathbf{e}}_1(t)\cos\Phi(t) + \hat{\mathbf{e}}_2(t)\sin\Phi(t)$. Similarly, the unit vector $\hat{\boldsymbol{\lambda}}$ along the relative velocity (orthogonal to $\hat{\mathbf{n}}$) can be written as $\hat{\boldsymbol{\lambda}}(t) = -\hat{\mathbf{e}}_1(t)\sin\Phi(t) + \hat{\mathbf{e}}_2(t)\cos\Phi(t)$. By construction, $\hat{\mathbf{n}} \times \hat{\boldsymbol{\lambda}} = \hat{\mathbf{L}}_N$. From the quadrupole formula (1.6)

$$h_{ij}(t) \propto \hat{n}_i(t)\hat{n}_j(t) - \hat{\lambda}_i(t)\hat{\lambda}_j(t) = (\hat{\mathbf{e}}_+)_{ij}\cos 2\Phi(t) + (\hat{\mathbf{e}}_\times)_{ij}\sin 2\Phi(t)\,, \tag{2.62}$$

where $\hat{\mathbf{e}}_+ \equiv \hat{\mathbf{e}}_1(t) \otimes \hat{\mathbf{e}}_1(t) - \hat{\mathbf{e}}_2(t) \otimes \hat{\mathbf{e}}_2(t)$ and $\hat{\mathbf{e}}_\times \equiv \hat{\mathbf{e}}_1(t) \otimes \hat{\mathbf{e}}_2(t) + \hat{\mathbf{e}}_2(t) \otimes \hat{\mathbf{e}}_1(t)$. The choice of $\hat{\mathbf{e}}_{1,2}(t) = \hat{\mathbf{e}}_{1,2}^P(t)$ made in the precessing convention implies that $\Phi(t) =$

$\Psi(t)$ + const. (see Appendix B in Ref. [166]), since the angular velocity of $\hat{\mathbf{e}}^P_{1,2}(t)$ (i.e., $\mathbf{\Omega}_e$) is orthogonal to $\hat{\mathbf{L}}_N$. The response of a detector lying along $\hat{\mathbf{N}}$ (i.e., the direction of propagation) will be

$$\begin{aligned} h(t) &= h_{ij}(t)\left[(\hat{\mathbf{e}}^R_+)^{ij}F_+ + (\hat{\mathbf{e}}^R_\times)^{ij}F_\times\right] , \\ &\propto \left[(\hat{\mathbf{e}}^P_+)_{ij}\cos 2\Psi(t) + (\hat{\mathbf{e}}^P_\times)_{ij}\sin 2\Psi(t)\right]\left[(\hat{\mathbf{e}}^R_+)^{ij}F_+ + (\hat{\mathbf{e}}^R_\times)^{ij}F_\times\right] , \end{aligned} \tag{2.63}$$

where the tensors $\hat{\mathbf{e}}^R_{+,\times}$ were defined in Eqs. (1.4) and (1.5), $F_{+,\times}$ are the antenna pattern functions, and the superscript P indicates that the precessing convention is applied. Thus, all precessional modulations are generated by the time-dependent tensors $\hat{\mathbf{e}}^P_{+,\times}$.

2.12.2 A precessing effective-one-body model

Following the same approach, in Ref. [194] we developed an EOB model for the inspiral-merger-ringdown of precessing binaries. See Chapter 11 for more details. Since waveforms in the precessing frame behave similarly to waveforms emitted by a nonprecessing system, there are several advantages with respect to working in an inertial frame: (i) the multipolar modes display a clean hierarchy; (ii) PN corrections to the waveforms are available to a much higher order; (iii) we can employ the calibrated nonprecessing EOB model, that already captures strong-field effects.

The EOB dynamics is completely general in that it can handle precession without any modification. In particular, the EOB spins are canonical variables [188], i.e., they obey the generalized Poisson bracket of angular momenta $\{S^a_1, S^b_1\} = \epsilon^{abc}S^c_1$

and $\{S_2^a, S_2^b\} = \epsilon^{abc} S_2^c$, therefore their time evolution is given by

$$\dot{\mathbf{S}}_i = \{\mathbf{S}_i, H_{\rm EOB}\} = \frac{\partial H_{\rm EOB}}{\partial \mathbf{S}_i} \times \mathbf{S}_i \,, \tag{2.64}$$

for $i = 1, 2$. Once the orbital dynamics is computed by solving Hamilton's equations (Eqs. (2.32), (2.33), and (2.64)), one builds the precessing frame $\{\hat{\mathbf{e}}_i^P\}$ $(i = 1, 3)$ using Eqs. (2.59)–(2.61); in this frame, one generates nonprecessing EOB waveforms using the nonprecessing model of Ref. [70], calibrated to numerical relativity. Finally, one rotates the waveforms from the precessing frame to any inertial frame of choice by using the rotation properties of rank-2 tensors

$$h_{\ell m}^{\rm (inertial)} = \sum_{m'=-\ell}^{\ell} D^{(\ell)\,*}_{m'm}(\alpha, \beta, \gamma) h_{\ell m'}^{\rm (precessing)} \,, \tag{2.65}$$

where $D^{(\ell)\,*}_{m'm}(\alpha, \beta, \gamma)$ is the complex conjugate of the Wigner D-matrix, and (α, β, γ) are the Euler angles parametrizing the rotation from the precessing frame to the inertial frame.

In Ref. [194] we compared this precessing EOB model to the two longest precessing simulations available [67], of 35 and 65 cycles, respectively. We found remarkable agreement on the $\ell = 2$ waveforms, as demonstrated in Figure 2.18. It is important to emphasize that this result was achieved *without* any calibration to the precessing runs, but solely relied on the nonprecessing calibration and on the precessing convention. The unfaithfulness is below 2% when maximizing only over time and phase of coalescence, and on the polarization angle. A further confirmation of the goodness of our model (specifically, of its orbital dynamics) came from the comparison of the time evolution of the spins, displayed in Figure 2.19; in the

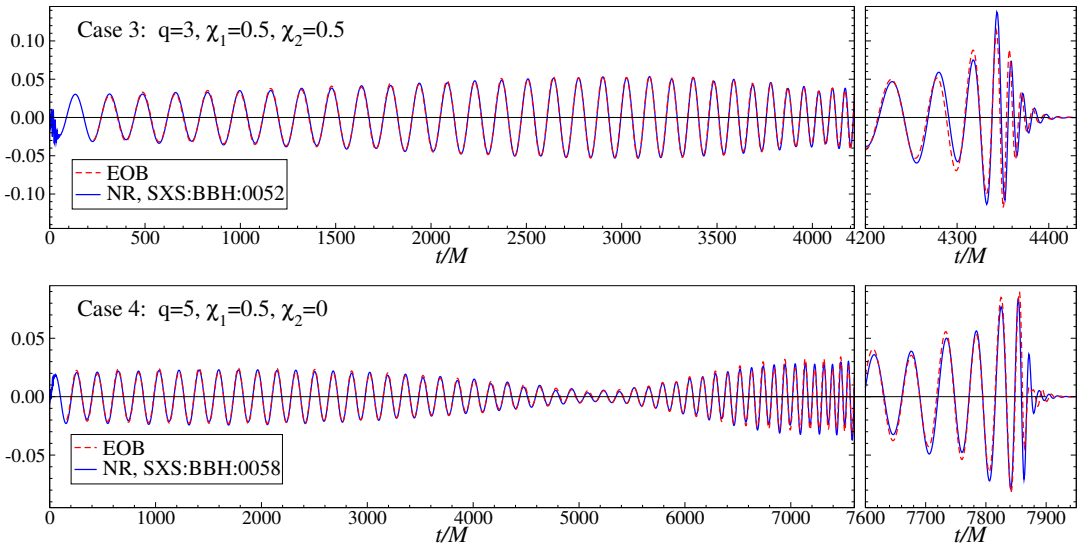

Figure 2.18: [From Ref. [194]] For cases 52 and 58 of the SXS catalog [67] (labeled "Case 3" and "Case 4", respectively), we show the numerical and EOB polarization h_+, containing contributions from $\ell = 2$ modes, for a specific direction of propagation $\hat{\mathbf{N}}$; the two runs have the spin of the largest black hole initially in the orbital plane. More details can be found in Ref. [194].

comparison we also included a PN approximant that is commonly used in the literature (SpinTaylorT4 [166]). The EOB dynamics correctly captures the precessional timescale, whereas the PN approximant overestimates it.

In the near future, we are going to compare this precessing EOB model to the entire SXS catalog (containing about 90 distinct precessing simulations), and improve its merger-ringdown signal.

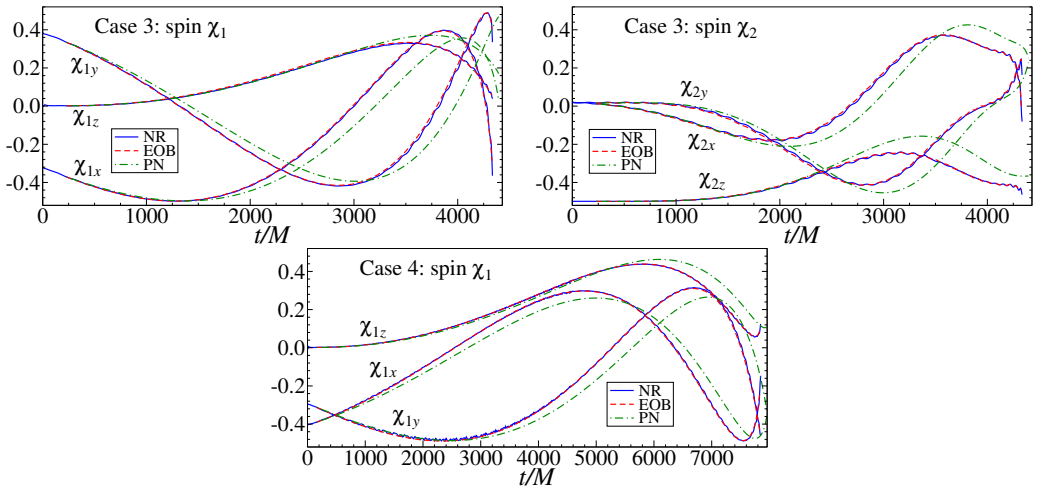

Figure 2.19: [From Ref. [194]] Evolutions of the dimensionless spin vectors $\boldsymbol{\chi}_1(t)$ and $\boldsymbol{\chi}_2(t)$ of the NR simulation and the EOB and PN models. Specifically, we show the projections of $\boldsymbol{\chi}_1$ and $\boldsymbol{\chi}_2$ on the basis vectors of an inertial source frame that is aligned with the initial orbital angular momentum. The top two panels show $\boldsymbol{\chi}_1$ and $\boldsymbol{\chi}_2$ for case 52 of the SXS catalog. The bottom panel shows $\boldsymbol{\chi}_1$ ($\boldsymbol{\chi}_2 = 0$) for case 58 of the SXS catalog. The numerical evolutions are compared to our EOB model and to the SpinTaylorT4 prediction.

Chapter 3: **Periastron advance in black-hole binaries**

Authors: *Alexandre Le Tiec, Abdul H. Mroué, Leor Barack, Alessandra Buonanno, Harald P. Pfeiffer, Norichika Sago, and Andrea Taracchini*[1]

Abstract: The general relativistic (Mercury-type) periastron advance is calculated here for the first time with exquisite precision in full general relativity. We use accurate numerical relativity simulations of spinless black hole binaries with mass ratios $1/8 \leqslant m_1/m_2 \leqslant 1$ and compare with the predictions of several analytic approximation schemes. We find the effective-one-body model to be remarkably accurate, and, surprisingly, so also the predictions of self-force theory [replacing $m_1/m_2 \to m_1 m_2/(m_1+m_2)^2$]. Our results can inform a universal analytic model of the two-body dynamics, crucial for ongoing and future gravitational-wave searches.

3.1 Introduction

The anomalous rate of Mercury's perihelion advance was originally recognized in 1859 by the astronomer Urbain Le Verrier. For the first time, Newton's law of universal gravitation could not be reconciled with observation. Treating Mercury as a test body in free fall in the gravitational field generated by the mass $M_\odot$ of

[1]Originally published as Phys. Rev. Lett. **107**, 141101 (2011)

the Sun, Einstein derived the lowest order (weak-field) general relativistic angular advance per orbit [204]

$$\Delta\Phi = \frac{6\pi G\, M_\odot}{c^2\, a\,(1-e^2)}\,, \tag{3.1}$$

where a and e are the semi-major axis and eccentricity of Mercury's orbit, respectively. Equation 3.1 perfectly accounted for the observed discrepancy of ~ 43" per century, thus providing the first successful test of general relativity. More recently, the same effect—but with a much larger amplitude, of order a few degrees per year—has been observed in the orbital motion of binary pulsars [205]. Today, the exciting prospects of observing gravitational waves from the inspiral and merger of compact binaries, using interferometric detectors like LIGO or Virgo, provide a modern context for the problem of relativistic periastron advance, and a motivation to go far beyond Einstein's weak-field test-particle approximation.

In this Letter we restrict our attention to binaries composed of two black holes. Their orbital dynamics can be analyzed using several approximation schemes in general relativity: post-Newtonian expansions [58], black hole perturbation theory [206], and the effective-one-body model [61]. It can also be studied using fully nonlinear numerical relativity (NR). While NR can now routinely perform accurate binary black hole simulations [207], approximation methods remain valuable given the high computational cost of these simulations, and their restricted utility when the mass ratio is too extreme. It is important to assess the predictions of the various approximations against the NR benchmark, since (i) it allows crucial cross-validation tests, (ii) it helps delineate the respective domains of validity of each method, and

(iii) it can inform the development of a universal semi-analytical model of the binary dynamics.

Neglecting radiation reaction, the motion of two non-spinning black holes on a generic eccentric orbit involves two frequencies: the radial frequency (or mean motion) Ω_r, and the averaged angular frequency Ω_φ, respectively defined by

$$\Omega_r = \frac{2\pi}{P}\,, \quad \Omega_\varphi = \frac{1}{P}\int_0^P \dot{\varphi}(t)\,\mathrm{d}t = K\,\Omega_r\,, \tag{3.2}$$

where P is the radial period, i.e. the time interval between two successive periastron passages, $\dot{\varphi} = \mathrm{d}\varphi/\mathrm{d}t$ is the time derivative of the orbital phase $\varphi(t)$, and $\Delta\Phi/(2\pi) = K - 1$ is the fractional advance of the periastron per radial period. In the circular orbit limit, the relation between $K = \Omega_\varphi/\Omega_r$ and Ω_φ is coordinate invariant (for a large class of physically reasonable coordinate systems), and therefore provides a natural reference for comparing between the predictions of the analytical and numerical methods currently available.

In this Letter we present new accurate NR simulations starting at lower orbital frequencies than in previous work [208–210]. We outline the respective computations of the invariant relation $K(\Omega_\varphi)$ in numerical relativity, post-Newtonian theory, the effective-one-body formalism, and black hole perturbation theory. We then perform an extensive comparison which, for the first time, (i) encompasses all of these methods, and (ii) focuses on the orbital dynamics of the binary, rather than the asymptotic gravitational waveform. We also discuss the implications for the modelling of coalescing compact binaries. (We henceforth set $G = c = 1$.)

3.2 Numerical relativity

The periastron advance of non-spinning black hole binaries was estimated for the first time in general relativistic numerical simulations in [89]. In the present work, we improve considerably on the accuracy of these calculations. Our results are based on new and longer simulations of the late stage of the inspiral of black hole binaries, using the Spectral Einstein Code `SpEC` [105, 211], with mass ratios $q \equiv m_1/m_2$ between 1:1 and 1:8, and eccentricities e in the range $[0.0015, 0.023]$. These runs are summarized in Table 3.1, and will be described in detail elsewhere [67, 210]. (Ref. [89] discusses the definition of e in these simulations.)

We compute Ω_φ and Ω_r using the orbital frequency $\Omega(t)$ extracted from the motion of the apparent-horizon centers (in harmonic coordinates): let $\mathbf{c}_i(t)$ be the coordinates of the center of each black hole, and define their relative separation $\mathbf{r} = \mathbf{c}_1 - \mathbf{c}_2$; then $\Omega = |\mathbf{r} \times \dot{\mathbf{r}}|/r^2$, where the Euclidean cross product and norm are used. The frequency $\Omega(t)$ can be written as the sum of a secular piece (given by the average frequency Ω_φ) and a small oscillatory remainder—both of which drift slowly in time due to radiation reaction. To compute $K_{\rm NR}$ at some coordinate time T, we choose a time interval of width $W \times 2\pi/\Omega(T)$, centered on T, and fit $\Omega(t)$ to the model $\Omega(t) = p_0(p_1 - t)^{p_2} + p_3 \cos\left[p_4 + p_5(t-T) + p_6(t-T)^2\right]$, where the p_i's are fitting parameters. We then write $\Omega_\varphi(T) = p_0(p_1 - T)^{p_2}$ and $\Omega_r(T) = p_5$, compute the ratio $K_{\rm NR}(T) = \Omega_\varphi(T)/\Omega_r(T)$, and hence obtain $K_{\rm NR}$ as a function of

q	d/m	e	$N_{\rm orb}$	a_0	a_1	a_2	$m\Omega_i$	$m\Omega_f$
1	19	0.021	34	0.9949	0.589	−79.1	0.0111	0.0312
2/3	18	0.023	27	0.9950	0.573	−75.9	0.0129	0.0316
1/3	14	0.002	29	0.9821	1.692	−87.1	0.0181	0.0313
1/5	14	0.008	23	0.9879	1.154	−62.8	0.0183	0.0361
1/6	13	0.015	20	0.9890	1.071	−57.0	0.0204	0.0333
1/8	13	0.0015	24	1.0028	−0.099	−26.8	0.0197	0.0355

Table 3.1: Simulation parameters. Here $q \equiv m_1/m_2$, $m \equiv m_1 + m_2$, d is the initial coordinate separation, e the initial eccentricity, and $N_{\rm orb}$ the total number of orbits in the simulation. The fitting parameters $\{a_0, a_1, a_2\}$ [cf. Eq. 3.3] are computed for the restricted frequency range $\Omega_i \leqslant \Omega_\varphi \leqslant \Omega_f$.

Ω_φ. Finally, we fit $K_{\rm NR}(\Omega_\varphi)$ to a smooth quadratic polynomial using

$$K_{\rm NR} = \left[a_0 + a_1(m\Omega_\varphi) + a_2(m\Omega_\varphi)^2\right] K_{\rm Schw}\,, \tag{3.3}$$

where $m = m_1 + m_2$ is the total mass of the binary. The results of the fits are given in Table 3.1. For convenience, the numerical periastron advance $K_{\rm NR}$ is normalized by the test-particle result $K_{\rm Schw}$, which is known in closed form as [130,212] $K_{\rm Schw} = (1-6x)^{-1/2}$, where $x = (m\Omega_\varphi)^{2/3}$ is the usual dimensionless coordinate invariant post-Newtonian parameter.

The variance in the numerical data for various window sizes W provides an estimate of the error in $K_{\rm NR}$. We point out that the finite (non-zero) eccentricity in the NR simulations introduces a small error, since we are interested in the $e \to 0$ limit. However, as the leading-order result 3.1 suggests, and calculations at higher post-Newtonian (PN) orders confirm, this error scales like e^2, which in our simulations is always $\lesssim 5 \times 10^{-4}$, and decreasing monotonically with time.

The numerical data form the basis for our comparisons. We will now discuss

the different approximation schemes in turn, summarizing the results in Figs. 3.1 and 3.2 (showing K as a function of frequency for two fixed mass ratios), and Fig. 3.3 (showing K as a function of mass ratio for a given frequency).

3.3 Post-Newtonian theory

Einstein's result 3.1 was generalized to arbitrary masses m_1 and m_2 by Robertson [213]. Following the discovery of binary pulsars in the 1970s, an improved modelling of the orbital dynamics of these compact binaries was required, leading to the extension of this 1PN result to 2PN order [212]. [As usual we refer to nPN as the order equivalent to terms $\mathcal{O}(c^{-2n})$ in the equations of motion beyond the Newtonian acceleration.] More recently, the need for extremely accurate gravitational-wave templates modelling the inspiralling phase of coalescing compact binaries motivated the computation of the equations of motion through 3PN order. These results allowed also the calculation of the periastron advance at the 3PN accuracy for eccentric orbits [214].

For quasi-circular orbits, combining Eqs. (5.8) and (5.25) of Ref. [214], we obtain the 3PN-accurate expression of K as

$$K_{\rm 3PN} = 1 + 3x + \left(\frac{27}{2} - 7\nu\right) x^2 + \left(\frac{135}{2} - \left[\frac{649}{4} - \frac{123}{32}\pi^2\right]\nu + 7\nu^2\right) x^3 + \mathcal{O}(x^4)\,. \quad (3.4)$$

The symmetric mass ratio $\nu \equiv m_1 m_2/m^2$ is such that $\nu = 1/4$ for an equal mass binary, and $\nu \to 0$ in the extreme mass ratio limit. The term $\propto \nu^2$ in Eq. 3.4, which is a 3PN effect, contributes less than 1% to $K_{\rm 3PN}$, for all mass ratios. This suggests that the exact K may be well approximated by a linear function of ν. Figures 3.1–

3.3 show a good agreement between the 3PN and NR results for $q = 1$, with $\lesssim 1\%$ relative difference even at the high-frequency end. However, the performance of the PN approximation deteriorates with decreasing q.

3.4 Effective-one-body

The EOB formalism [61] maps the conservative part of the PN dynamics of a compact binary system onto the dynamics of a test particle of reduced mass $\mu \equiv m\nu = m_1 m_2/m$ in a time-independent and spherically symmetric effective metric $\mathrm{d}s^2_{\rm eff} = -A(r;\nu)\,\mathrm{d}t^2 + B(r;\nu)\,\mathrm{d}r^2 + r^2(\mathrm{d}\theta^2 + \sin^2\theta\,\mathrm{d}\varphi^2)$, which reduces to the Schwarzschild metric of a black hole of mass m in the limit $\nu \to 0$. The expansions of the EOB potentials A and $\bar{D} \equiv (AB)^{-1}$ in terms of the Schwarzschild-like coordinate $u = m/r$ are known through 3PN order as [61, 87] $A = 1 - 2u + 2\nu\,u^3 + \left(\frac{94}{3} - \frac{41}{32}\pi^2\right)\nu\,u^4 + \mathcal{O}(u^5)$, and $\bar{D} = 1 + 6\nu\,u^2 + (52 - 6\nu)\,\nu\,u^3 + \mathcal{O}(u^4)$. To enforce the presence of an EOB innermost stable circular orbit (ISCO), Ref. [87] suggested replacing A by its Padé approximant of order $(1,3)$, $A_P = (1+au)/(1+bu+cu^2+du^3)$, whose Taylor series coincides with the known 3PN result.

From the recent analysis of slightly eccentric orbits in the EOB formalism [90], the effective-one-body prediction for the periastron advance in the limit of zero eccentricity is given by

$$K_{\rm EOB} = \sqrt{\frac{A'_P(u)}{\bar{D}(u)\Delta(u)}}\,, \tag{3.5}$$

where $A'_P = \mathrm{d}A_P/\mathrm{d}u$, and $\Delta = A_P A'_P + 2u(A'_P)^2 - uA_P A''_P$ vanishes at the EOB ISCO. To obtain the invariant relation $K_{\rm EOB}(x)$, one needs to compute u given x,

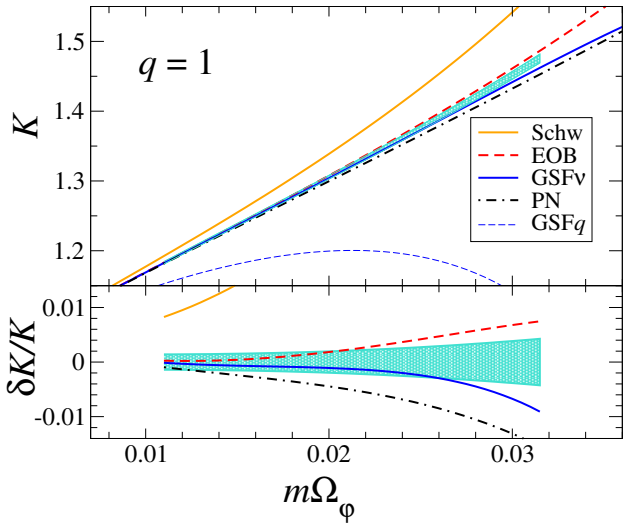

Figure 3.1: The periastron advance K of an equal mass black hole binary, in the limit of zero eccentricity, as a function of the orbital frequency Ω_φ of the circular motion. The NR results are indicated by the cyan-shaded region. The PN and EOB results are valid at 3PN order. The lower panel shows the relative difference $\delta K/K \equiv (K - K_{\rm NR})/K_{\rm NR}$.

which we do here numerically (for any given ν) from the expression of the EOB Hamiltonian restricted to circular orbits, and Hamilton's equations of motion [90]. The resulting curves are displayed in red in Figs. 3.1–3.3. For $q = 1$ and $2/3$, the EOB(3PN) prediction 3.5 is within the numerical error up to $m\Omega_\varphi \sim 0.022$. For all the other mass ratios, the EOB(3PN) result is within the numerical error at all frequencies. When using the EOB potential $A(u)$ with 4PN and 5PN terms calibrated to a set of highly accurate unequal mass non-spinning binary black hole simulations [91], the EOB prediction is within the numerical error at all frequencies and for all mass ratios considered. This remarkable agreement could be attributed in part to the "pole-like" structure at the EOB ISCO in Eq. 3.5, which is absent from the standard PN result 3.4.

3.5 Perturbation theory and the gravitational self-force

Extreme mass ratio inspirals (EMRIs) of compact objects into massive black holes, for which $m_2 \gg m_1$, are important sources of low-frequency gravitational radiation for future space-based detectors. Modelling the dynamics of these systems requires going beyond the geodesic approximation, by taking into account the back-reaction effect due to the interaction of the small object with its own gravitational perturbation. This "gravitational self-force" (GSF) effect has recently been computed for generic (bound) geodesic orbits around a Schwarzschild black hole [195, 215, 216]. In particular, the $\mathcal{O}(q)$ correction to the test-mass result $K_{\rm Schw}$ has been derived [217]. This calculation determined (numerically) the term $\rho(x)$ in the function $W \equiv 1/K^2 = 1 - 6x + q\,\rho(x) + \mathcal{O}(q^2)$. The results are well fitted (at the 10^{-5} level) by the rational function $\rho = 14x^2(1+\alpha x)/(1+\beta x+\gamma x^2)$, with $\alpha = 12.9906$, $\beta = 4.57724$, and $\gamma = -10.3124$. (This model improves upon the model of Ref. [217]; it is based on a much denser sample of GSF data points in the relevant frequency range.) In terms of the quantity K we have

$$K^q_{\rm GSF} = \frac{1}{\sqrt{1-6x}}\left[1 - \frac{q}{2}\frac{\rho(x)}{1-6x} + \mathcal{O}(q^2)\right]. \tag{3.6}$$

We used this expression, with the above analytic fit for $\rho(x)$, to produce the dashed blue curves in Figs. 3.1–3.3.

Since $\rho(x) > 0$ for all stable circular orbits, the $\mathcal{O}(q)$ GSF decreases the rate of precession. Note that the formal divergence of $K^q_{\rm GSF}$ at the ISCO limit ($x \to 1/6$) is simply a consequence of the fact that Ω_r vanishes there (by definition), while Ω_φ

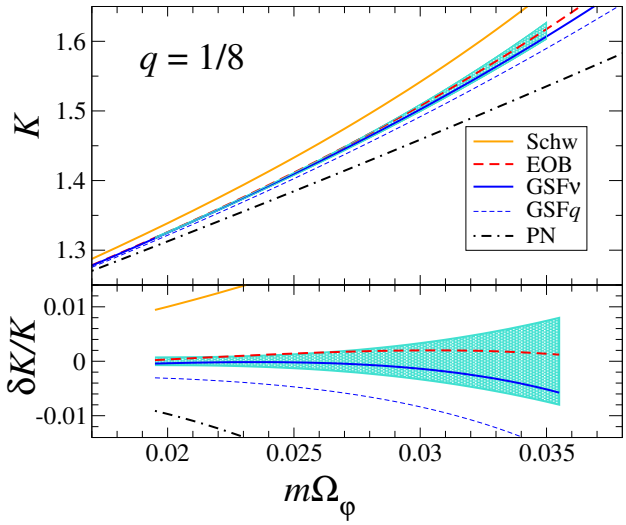

Figure 3.2: Same as in Fig. 3.1, but for a mass ratio $q = 1/8$. Note that for an orbital frequency $m\Omega_\varphi \sim 0.03$, corresponding to a separation $r \sim 10m$, the periastron advance reaches half an orbit per radial period.

remains finite. This divergence might explain why the convergence of the standard PN series seems to deteriorate with decreasing q [218], as also illustrated by our results (cf. Fig. 3.3). We remind the reader that Eq. 3.6 captures only the *conservative* effect of the GSF, and has a limited physical relevance near the ISCO, where the actual dynamics transitions from an adiabatic quasi-circular inspiral (driven by the dissipative piece of the GSF) to a direct plunge [62, 219].

We now turn to discuss one of the most striking findings of our study. Since q and $\nu = q/(1+q)^2$ coincide at leading order, namely $q = \nu + \mathcal{O}(\nu^2)$, we may recast Eq. 3.6 as

$$K^{\nu}_{\rm GSF} = \frac{1}{\sqrt{1-6x}}\left[1 - \frac{\nu}{2}\frac{\rho(x)}{1-6x} + \mathcal{O}(\nu^2)\right], \tag{3.7}$$

which, unlike $K^{q}_{\rm GSF}$, is symmetric under $m_1 \leftrightarrow m_2$. The solid blue curves in Figs. 3.1–3.3 show $K^{\nu}_{\rm GSF}$. Remarkably, while the agreement between $K^{q}_{\rm GSF}$ and $K_{\rm NR}$ becomes

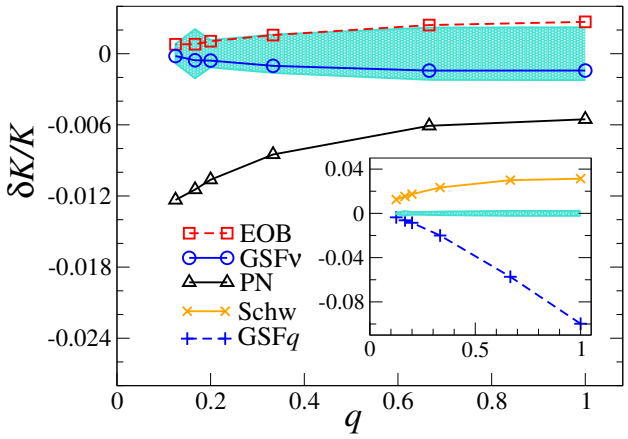

Figure 3.3: The relative difference $\delta K/K = (K - K_{\rm NR})/K_{\rm NR}$ as a function of the mass ratio q, for $m\Omega_\varphi = 0.022$. The PN and EOB results are valid at 3PN order. The shaded area marks the error margin of the NR data. The results are qualitatively identical and quantitatively similar for other values of Ω_φ.

manifest only at sufficiently small q (as expected), $K^\nu_{\rm GSF}$ appears to agree extremely well with $K_{\rm NR}$ at *all* mass ratios. This suggests that the substitution $q \to \nu$ amounts to an efficient "resummation" of the q-expansion, to the effect that much of the functional form $K(x)$ is captured by the $\mathcal{O}(\nu)$ term, even for large q.

A few heuristic explanations for this behavior may be suggested. (i) As mentioned earlier, quadratic corrections in ν enter the PN expression for K only at 3PN [recall Eq. 3.4], and account for less than 1% of K at this order. This implies that the linear-in-ν approximation must be very accurate, at least at small frequencies. (ii) The true function $K(x; m_1, m_2)$ must be invariant under exchange $m_1 \leftrightarrow m_2$. The expansion in ν, $K^\nu_{\rm GSF}$, satisfies this symmetry by definition of ν, whereas the expansion in q, $K^q_{\rm GSF}$, does not. (iii) Assuming the coefficients a_n in the formal expansion $K = \sum_n a_n(x)\nu^n$ do not increase with n (which, however, only a future calculation of higher-order GSF terms could confirm), this expansion will exhibit a

fast convergence since $0 < \nu \leqslant 1/4$; the same cannot be said of the q-expansion.

Comparison of the GSF curves in Figs. 3.1–3.3 with the NR benchmark leads us to yet another important observation. It is evident that the second-order GSF correction to K (i.e. the unknown term $\propto q^2$) has an *opposite* sign with respect to the first-order term; namely, the second-order GSF acts to increase the rate of periastron advance. This is a new result, which illustrates the potential merit of cross-cultural comparisons of the kind advocated in this work.

3.6 Conclusions

The advent of precision-NR technology allows us, for the first time, to extract accurate information about the *local* dynamics in binary black hole inspirals (previous studies focused primarily on asymptotic waveforms), and carry out meaningful comparisons with the results of analytic approaches to the problem. These comparisons and cross-check validations among analytic approximants and NR results are crucial for developing faithful analytic waveforms to be used in LIGO/Virgo searches.

Here we focused on a particular aspect of the dynamics, namely the relativistic periastron advance. We worked in a highly relativistic regime, where the periastron advance can reach values as high as half an orbit per radial period (far greater than the meagre ~ 43" per century advance of Mercury's perihelion!) We employed the invariant relation $K(\Omega_\varphi)$ as a reference for comparison, which is meaningful only in the adiabatic regime where the dissipative evolution is "slow". For the range of

inspiral orbits covered by our NR simulations, a measure of adiabaticity is provided by $0.3\% \lesssim \dot{\Omega}_\varphi/\Omega_\varphi^2 \lesssim 1.7\%$. This suggests that inclusion of dissipative effects in the PN/EOB/GSF results would not substantially affect our conclusions. The very good agreement between the analytical and NR results at low frequency, where the error in $K_{\rm NR}$ is smallest, also supports this expectation.

Our direct comparison between perturbative and full NR results is the first of its kind. The $\mathcal{O}(q)$ GSF prediction agrees with the NR data for small mass ratios (e.g. $q = 1/8$ or $1/6$) to within a relative difference of magnitude $\sim q^2$, as expected. This provides an extremely strong validity test for both NR and GSF calculations. Furthermore, the sign and magnitude of the difference $K_{\rm NR} - K^q_{\rm GSF}$ give us valuable, hitherto inaccessible information about the second-order GSF effect.

The above validation test is further reinforced by the 3PN result, which shows a good agreement with the NR data at small frequencies, or "large" separations (down to $r \sim 10m$), especially for comparable masses (e.g. for $q = 1$ or $2/3$). Our comparison also reaffirms the expectation that the PN approximation performs less well in the small mass-ratio regime.

We find that the EOB(3PN) prediction of the periastron advance is in very good agreement with the numerical one across the entire range of mass ratios and frequencies considered. This result supports the idea that the EOB formalism can describe the binary dynamics at *all* mass ratios.

Finally, we observe that the simple replacement $q \to \nu$ can extend the validity of the GSF approximation far beyond the EMRI regime. Indeed, our model $K^\nu_{\rm GSF}$ agrees very well with the NR data at all frequencies, and for all mass ratios con-

sidered, including the equal mass case. This surprising result suggests that GSF calculations may very well find application in a broader range of physical problems than originally envisaged, including the modelling of intermediate mass ratio inspirals, a plausible source of gravitational waves for Advanced LIGO/Virgo [220].

Chapter 4: **Small mass plunging into a Kerr black hole: anatomy of the inspiral-merger-ringdown waveforms**

Authors: *Andrea Taracchini, Alessandra Buonanno, Gaurav Khanna, and Scott A. Hughes*[1]

Abstract: We numerically solve the Teukolsky equation in the time domain to obtain the gravitational-wave emission of a small mass inspiraling and plunging into the equatorial plane of a Kerr black hole. We account for the dissipation of orbital energy using the Teukolsky frequency-domain gravitational-wave fluxes for circular, equatorial orbits, down to the light-ring. We consider Kerr spins $-0.99 \leq q \leq 0.99$, and compute the inspiral-merger-ringdown $(2,2)$, $(2,1)$, $(3,3)$, $(3,2)$, $(4,4)$, and $(5,5)$ modes. We study the large-spin regime, and find a great simplicity in the merger waveforms, thanks to the extremely circular character of the plunging orbits. We also quantitatively examine the mixing of quasinormal modes during the ringdown, which induces complicated amplitude and frequency modulations in the waveforms. Finally, we explain how the study of small mass-ratio black-hole binaries helps extending effective-one-body models for comparable-mass, spinning black-hole binaries to any mass ratio and spin magnitude.

[1]Accepted for publication in Phys. Rev. D

4.1 Introduction

Over the last few years, analytical and numerical studies have revealed interesting features of the dynamics and gravitational radiation of extreme mass-ratio black-hole binaries, especially during ringdown and when the spin of the central black hole is close to maximal, and the orbits approach the horizon. References [221–224] pointed out the possibility of describing analytically various processes of the dynamics and radiation in the near-horizon region of a nearly extremal black hole by exploiting an infinite-dimensional conformal symmetry that the Kerr metric satisfies in this particular limit. Applying the WKB method to the Teukolsky equation in the eikonal approximation, Ref. [225] found a geometric interpretation of the black-hole quasinormal modes (QNMs) through spherical light-ring orbits, extending to generic orbits what was previously derived for equatorial [226, 227] and polar orbits [228]. Moreover, an interesting bifurcation leading to a splitting of zero and non-zero damped QNMs was found as one approaches nearly-extremal spins [229,230]. Quite interestingly, Refs. [231, 232] found that damped modes different from the usual QNMs are present in the gravitational-radiation spectrum close to the black-hole horizon. It remains an open question whether those damped modes are excited as a test body plunges into the central black hole.

Furthermore, gravitational waveforms emitted during the inspiral, plunge and merger stages of a test body orbiting a Kerr black hole have been exploited to grasp unique, physical information on the merger phase and they have been employed to extend analytical models, notably the effective-one-body (EOB) model [61, 62],

from the comparable-mass to the test-particle limit case [93,99,119,120,125,126,233–236]. Solving the time-domain Regge-Wheeler or Teukolsky equations is significantly less expensive than evolving a black-hole binary in full numerical relativity. The possibility of using the test-particle limit to infer crucial information about the merger waveform of bodies of comparable masses follows from the universality of the merger process throughout the binary parameter space.

In Ref. [119], some of us investigated the inspiral-merger-ringdown waveforms produced by the time-domain Teukolsky equation where the source term is evaluated along the quasicircular plunging trajectory of a nonspinning test particle inspiraling in the equatorial plane. The trajectory was computed by solving Hamilton's equations in the Kerr spacetime, augmented by a suitable radiation-reaction force, notably the one constructed from the factorized energy flux of the EOB formalism [100, 101]. The Teukolsky waveforms were then used to improve spinning EOB waveforms during the transition from plunge-merger to ringdown. However, the study of Ref. [119] was limited to moderate spins of the Kerr black hole, i.e., $a/M \lesssim 0.8$. Here, we build on Ref. [119], and extend the analysis in a few directions. First, the analytical energy flux based on spinning, factorized multipolar waveforms [100,101] can differ from the Teukolsky flux; for instance, even for a moderate spin value of 0.7, the modeling error at the innermost stable circular orbit is as large as 10%. This error comes from a combination of insufficient knowledge of high-order post-Netwonian (PN) terms, and from the truncation at modes with $\ell = 8$. As the spin increases, the motion becomes more relativistic and a growing number of modes are excited. Therefore, to overcome this problem, in the equations of motion

for the orbital dynamics of the plunging particle, we employ the energy flux computed by a highly-accurate frequency-domain Teukolsky code [116,117]. Second, we consider spins in the range $-0.99 \leq a/M \leq 0.99$, but investigate in greater detail spins close to extremal, for prograde and retrograde orbits. In fact, those almost-extremal cases display peculiar features in the dynamics and waveforms. When the spin is close to 1, the merger waveforms are particularly simple, with a remarkably flat amplitude, as a consequence of the circular nature of the plunge. When the spin is close to -1, instead, the phenomenon of QNM mixing dominates the ringdown waveforms. Third, we use those findings to suggest a new procedure for modeling the transition from merger to ringdown in the EOB waveforms for spins larger than 0.8 and mass ratios smaller than $\sim 1/100$. Preliminary results of this paper were employed in Ref. [70] to build a spinning EOB model that is valid for any mass ratio and spin magnitude.

This paper is organized as follows. In Sec. 4.2 we describe how we build the orbital dynamics to compute the quasicircular plunging trajectory that is used in the source term of the Teukolsky equation. In Sec. 4.3 we review the time-domain Teukolsky code which computes the waveforms. In Sec. 4.4 we describe interesting features characterizing the dynamics and the merger waveforms for spins close to extremal. In Sec. 4.5 we carry out a detailed study to understand and model the mixing of QNMs for the dominant $(2,2)$, $(2,1)$, $(3,3)$, $(3,2)$, $(4,4)$, and $(5,5)$ waveforms. In Sec. 4.6 we explain how the information obtained from the Teukolsky waveforms has been used to design a new way of generating the EOB merger-ringdown waveform for spins larger than 0.8 and mass ratios smaller than $\sim 1/100$. In Sec. 4.7 we

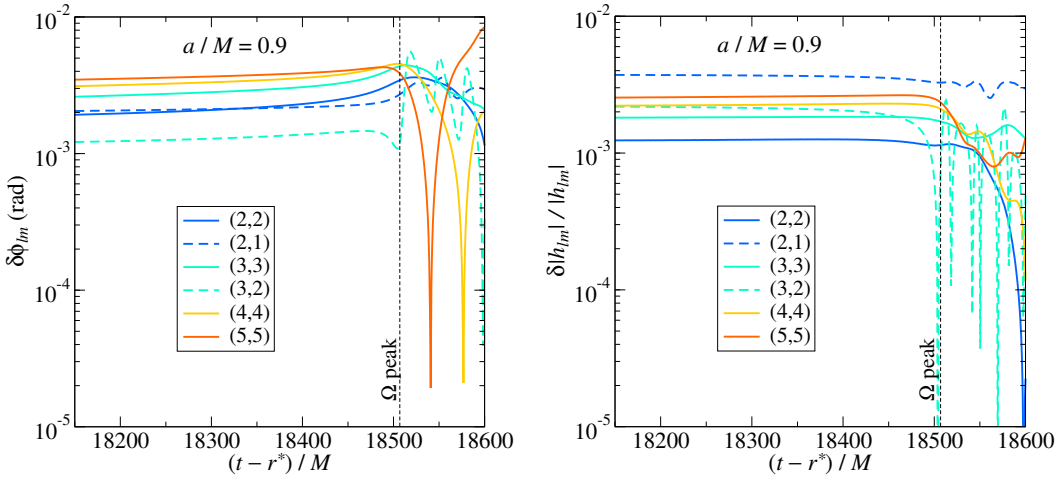

Figure 4.1: Numerical discretization errors in the phase (left panel) and amplitude (right panel) of the Teukolsky waveforms for the $(2,2)$, $(2,1)$, $(3,3)$, $(3,2)$, $(4,4)$, and $(5,5)$ modes. The plots are for spin $q = 0.9$. A vertical line marks the position of the peak of the orbital frequency, at time $t^{\Omega}_{\rm peak}$, which occurs close to merger.

compare spinning EOB waveforms developed in the comparable-mass regime [70] to the Teukolsky waveforms. Sec. 11.5 summarizes our main conclusions and discusses future directions. Appendix A provides numerical information about the Teukolsky merger waveforms that can be incorporated in generic spinning EOB models.

Henceforth, we use geometric units with $G = c = 1$.

4.2 Orbital dynamics to generate inspiral-merger-ringdown Teukolsky waveforms

In this section we review how the trajectory entering the source term of the Teukolsky equation is computed. We restrict our attention to systems where the smaller black hole (BH) is nonspinning, and the orbits are confined to the equatorial

plane of the larger, spinning BH. Let μ be the mass of the smaller object, and let M and $J \equiv aM \equiv qM^2$ (with [2] $-1 \leq q \leq 1$) be the mass and spin of the larger one. In this paper we consider systems with $\mu/M = 10^{-3}$. In the spirit of the EOB formalism, and as in Ref. [119], we model the orbital dynamics using the Hamiltonian of a nonspinning test particle of mass μ in the Kerr spacetime

$$H = \beta^i p_i + \alpha\sqrt{\mu^2 + \gamma^{ij} p_i p_j}\,, \tag{4.1}$$

where $\alpha \equiv (-g^{tt})^{-1/2}$, $\beta^i \equiv g^{it}/g^{tt}$ and $\gamma^{ij} \equiv g^{ij} - g^{it}g^{jt}/g^{tt}$, i, j are spatial indices, t is the time index, $g_{\mu\nu}$ is the Kerr metric in Boyer-Lindquist coordinates, and the p_i's are the conjugate momenta to the spatial coordinates. We numerically solve Hamilton's equations for H subject to a radiation-reaction force $\boldsymbol{\mathscr{F}}$ which describes the dissipation of energy into gravitational waves (GWs); the radiation-reaction force is proportional to the sum of the GW energy flux at infinity, F^{∞}, and through the horizon [3], $F^{\rm H}$. It reads [102]

$$\boldsymbol{\mathscr{F}} = \frac{F}{\Omega|\mathbf{r}\times\mathbf{p}|}\mathbf{p}\,, \tag{4.2}$$

where $F \equiv F^{\infty} + F^{\rm H}$, $\mathbf{r}$ is the separation vector, and $\Omega \equiv \hat{\mathbf{J}}\cdot(\mathbf{r}\times\dot{\mathbf{r}})/r^2$ is the orbital frequency, where $\hat{\mathbf{J}}$ is the unit vector along the spin of the Kerr BH. We indicate with an over-dot the derivative with respect to time t.

[2] Positive (negative) values of q indicate that the spin of the Kerr BH is aligned (anti-aligned) with the inspiral orbital angular momentum, i.e., the motion is prograde (retrograde) during the inspiral. At the end of the plunge, because of frame dragging, the trajectory always becomes prograde.

[3] The GW energy flux falling into the horizon is also referred to as "ingoing flux", "absorption flux", or "horizon flux".

Some of us, in Ref. [119], employed the outgoing factorized energy flux of Ref. [101] for the term F^{∞}, while setting $F^{\rm H}=0$; that choice was motivated partly by the focus on understanding the effect of the model flux, and partly by the availability of numerical Teukolsky energy fluxes only down to the innermost stable circular orbit (ISCO). Here, instead, we are mainly interested in the characterization of the Teukolsky waveforms, and we want to remove any modeling error from the orbital motion. Similarly to what is done in Ref. [121], we source our equations of motion with GW energy fluxes computed in perturbation theory; in particular, we use the Teukolsky fluxes of Ref. [120], where we numerically solved the Teukolsky equation in frequency domain [116,117] for circular, equatorial orbits all the way down to a radial separation of $r_{\rm min}=r_{\rm LR}+0.01M$, where $r_{\rm LR}/M\equiv 2+2\cos\left[\frac{2}{3}\arccos\left(-q\right)\right]$ is the position of the photon orbit, or light-ring (LR) [122]. The GW fluxes were computed for spins from $q=-0.9$ up to $+0.9$ in steps of 0.1, and also for $q=\pm 0.95,\pm 0.99$. Those computations assumed circular orbits, for which a precise relation between radius r and orbital frequency $\Omega_{\rm circ}$ holds, namely $M\Omega_{\rm circ}=[(r/M)^{3/2}+q]^{-1}$.

To accurately describe the transition from inspiral to plunge, we adopt here the same strategy used in the EOB models of comparable-mass BH binaries [237–239]. First, if we introduce the velocity parameter $v_{\Omega}\equiv(M\Omega)^{1/3}$, then the total GW flux for circular orbits can be written as $F=32\mu^2 v_{\Omega}^{10}\hat{F}(v_{\Omega})/(5M^2)$, where $\hat{F}(v_{\Omega})=1+\mathcal{O}(v_{\Omega}^2)$. Second, we replace v_{Ω} in the leading term of F with the non-Keplerian velocity for a circular orbit defined by $v_{\phi}\equiv\Omega r_{\Omega}$, where $r_{\Omega}/M\equiv(M\Omega_{\rm circ})^{-2/3}$ (see also Eq. (32) in Ref. [239]); note that since we work with nonadiabatic [4] orbital

[4]This means that the orbital motion includes not only tangential, but also radial velocities.

evolutions $\Omega \neq \Omega_{\rm circ}$. This replacement moderates the growth of the GW frequency close to merger [237], and allows a more accurate modeling of numerical-relativity waveforms in the comparable-mass regime, also when spins are present [239].

We need to integrate the equations of motion to the event horizon, $r_+/M \equiv 1+\sqrt{1-q^2}$. Teukolsky fluxes are only available, however, down to the radius $r_{\rm min} = r_{\rm LR} + 0.01$: Circular orbits do not exist at radii $r < r_{\rm LR}$, and the growing number of significant multipolar contributions force us to terminate our flux calculations slightly outside $r_{\rm LR}$ (see Sec. IIB of Ref. [120] for detailed discussion). Note that the radial distance between $r_{\rm min}$ and r_+ decreases from $3M$ when $q = -1$ down to $1M$ when $q = 0$, and vanishes for $q = 1$. Therefore, we have to provide a prescription for $\hat{F}$ in the interval $r_+ < r < r_{\rm min}$. Since these values of r are well within the plunge phase, where the conservative part of the dynamics is known to dominate, we decide to smoothly switch off the GW flux at $r_{\rm end} = r_{\rm min}$. Let $v_{\rm end}$ be the velocity of a circular orbit of radius $r_{\rm end}$. Explicitly, if $r < r_{\rm end}$ but $v_\Omega \leq v_{\rm end}$, then we suppress $\hat{F}(v_\Omega)$ by a factor $1/[1 + \exp[-(r - r_{\rm end})/\sigma]]$; if $r < r_{\rm end}$ and $v_\Omega > v_{\rm end}$, then we set $\hat{F}(v_\Omega) = \hat{F}(v_{\rm end})/[1 + \exp[-(r - r_{\rm end})/\sigma]]$. We find that, as long as $\sigma \lesssim 0.01M$, the trajectories are insensitive to the specific value of σ. We test the effect of the switch-off point by changing its position to $r_{\rm end} = r_{\rm LR}+b(r_{\rm ISCO}-r_{\rm LR})$, where $r_{\rm ISCO}$ is the position of the ISCO, and $b = 0.25, 0.5, 0.75$, for spins $q = 0.5, 0.9$; the difference in the orbital phase is always negligible, within 0.003 (0.006) rads for $q = 0.5$ (0.9) when $b = 0.75$ with respect to the fiducial case $r_{\rm end} = r_{\rm min}$ (i.e., $b \approx 0$), since the plunging motion is indeed geodetic to a good approximation, and is not affected by the details of the GW fluxes.

As in Ref. [119], we compute the trajectory from the equations of motion down to a point slightly outside the horizon (at $\sim 1.05 r_+$). Then, to model the locking of the plunging particle to the rotating horizon, we smoothly connect the trajectory obtained by solving Hamilton's equations to several orbital cycles at $r = r_+$ with frequency equal to that of the horizon $\Omega_{\rm H} \equiv q/(2r_+)$. As shown in Ref. [231], the trajectory asymptotes to r_+ and $\Omega_{\rm H}$ exponentially in time.

4.3 Numerical solution of the time-domain Teukolsky equation

In this section we review the numerical method used to solve the Teukolsky equation in the time domain. The approach we follow to solve this linear partial differential equation (PDE) is the same as presented in our earlier work (see Ref. [119] and references therein). The main points of this technique are as follows: (i) We first rewrite the Teukolsky equation using suitable coordinates — the tortoise radius r^* and Kerr azimuthal angle φ, defined precisely in [119]. (ii) Taking advantage of axisymmetry, we separate the dependence on azimuthal coordinate φ. We thus obtain a set of (2+1) dimensional equations. (iii) We recast these equations into a first-order, hyperbolic PDE form. (iv) Finally, we implement a two-step, second-order Lax-Wendroff, time-explicit, finite-difference numerical evolution scheme. The particle-source term on the right-hand-side of the Teukolsky equation requires some care for such a numerical implementation. All relevant details can be found in our earlier work [119] and the associated references.

Since Ref. [119] was published, two technical advances have been introduced into the solver code aimed at improving results for the present paper. First, a compactified hyperboloidal layer has been added to the outer portion of the computational domain [240]. This advancement allows us to map null infinity onto the computational grid and also completely solves the so-called "outer boundary problem" (i.e., it eliminates unphysical reflections from the artificial boundary of the domain). Therefore, differently from Ref. [119], we are now able to extract gravitational waveforms *directly* at null infinity, completely eliminating the "extraction error", as discussed in Ref. [119]. Secondly, we have taken advantage of advances made in parallel computing hardware, and we have developed a very high-performing OpenCL implementation of the Teukolsky code that takes full benefit of GPGPU-acceleration and cluster computing. Details on this parallel implementation and careful measurements of gains in overall performance can be found in Ref. [241].

These advances have helped improve the performance and accuracy of the time-domain Teukolsky code by several orders of magnitude over previous versions. In particular, Ref. [241] demonstrated that errors with the improved code are typically at the level of 0.01%, an order of magnitude better than earlier versions [119], while performing faster. For long evolutions, these improvements yield a several thousand-fold speedup [240]. Consider the impact of such improvements on modeling the evolution of a system for $20,000M$, a typical span for our studies. With our previous Cauchy-evolution-based Teukolsky code, we would need to place the outer boundary at $r \gtrsim 10,000M$ to avoid impact of boundary effects — outside the domain of causal influence for the location and duration of interest. Using hyperboloidal

slicing, the outer boundary can be placed as close as $50M$ [240]. This immediately gains two orders of magnitude in performance, while generating waveforms directly at null infinity as desired. In addition, the use of GPGPU compute hardware acceleration typically yields another order of magnitude gain in performance through many-core parallelism [241].

Since we now compute the waveforms exactly at null infinity (eliminating the extraction error entirely), the only remaining source of numerical error is the "discretization error" introduced by the finite-difference numerical scheme [119]. It is relatively straightforward to estimate this discretization error: We first compute the waveforms at multiple grid resolutions, in particular we choose $(\mathrm{d}r^*, \mathrm{d}\theta) = (M/80, \pi/128), (M/40, \pi/64)$ and $(M/20, \pi/32)$. Second, we derive the Richardson extrapolant using this data. Then, we simply use this extrapolant as a reference to estimate the discretization error in the original waveforms computed by our code. In other words, we take the relative difference between the highest resolution data and the Richardson extrapolant as a measure of the discretization error. As done typically in the literature, we decompose the waveforms in -2-spin-weighted spherical harmonic modes, labeled by (ℓ, m). In Fig. 4.1 we depict the discretization errors for the phase and the amplitude for one particular choice of the spin. These results should be considered representative of all the other cases that we present in this work. Figure 4.1 demonstrates that the numerical error in our waveform data is at a level of a few $\times$ 0.1%. As expected, the relative error is generally lower for the dominant modes such as h_{22} and h_{33}, and higher for the weaker ones. In addition, the error levels stay very uniform during the long inspiral phase of the

binary evolution and only begin to vary significantly during the plunge. This happens due to the fact that the numerical computation shifts from being dominated by the particle-source term during inspiral, to a nearly source-free evolution during and after the plunge phase. It should be noted that the numerical errors can be further reduced by an order of magnitude as demonstrated in Ref. [241], through an increase in grid resolution. However, given the large number and long duration of the evolutions presented in this work, reducing the numerical error further was neither very practical nor needed.

4.4 Simplicity of inspiral-plunge Teukolsky waveforms for large spins

In this section we characterize the salient features displayed by the Teukolsky waveforms during late inspiral and plunge. For spins $q = 0$, ± 0.5, ± 0.7, ± 0.8, ± 0.9, ± 0.95, and ± 0.99, we compute the Teukolsky $(2,2)$, $(2,1)$, $(3,3)$, $(3,2)$, $(4,4)$, and $(5,5)$ modes as explained in Secs. 4.2 and 4.3. In the test-particle limit, as the spin increases, more and more (ℓ, m) modes become important at merger (with respect to the $(2,2)$ mode); however, for the modeling of comparable-mass BH binaries, only the few modes above give significant contribution to the energy flux. Eventually, we are interested in exploiting the results of this paper in the comparable-mass limit, therefore we restrict the discussion to those modes.

In the large-spin regime, a prograde inspiraling particle reaches very relativistic speeds before getting to the horizon; for instance, when $q = 0.99$, the peak speed

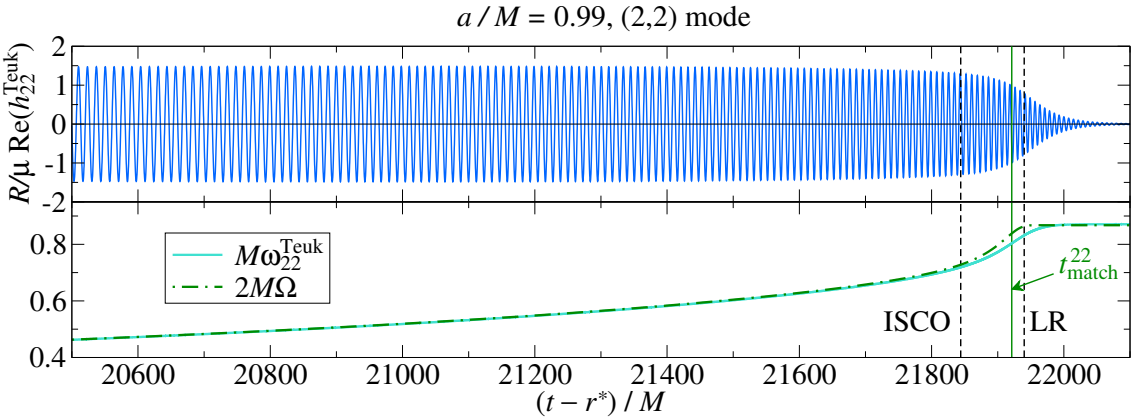

Figure 4.2: Late inspiral, plunge, merger and ringdown of the Teukolsky $h_{22}^{\rm Teuk}$ waveform (upper panel), its GW frequency $\omega_{22}^{\rm Teuk}$ and orbital frequency Ω of the underlying dynamics (lower panel) for spin $q = 0.99$. We note the simplicity of the amplitude during the last phase of the evolution. The plot spans a radial range from $r = 2.21M$ to the horizon,located at $r = 1.14M$; here, $r_{\rm ISCO} = 1.45M$ and $r_{\rm LR} = 1.17M$. Vertical dashed lines mark the position of the ISCO and the light-ring. A vertical green line marks the position $t^{22}_{\rm match} = t^{\Omega}_{\rm peak} + \Delta t^{22}_{\rm peak}$ of the ringdown matching as prescribed in the EOB model of Ref. [70] (see discussion in Sec. 4.6). R is the distance to the source.

(attained at the peak of the orbital frequency) is around 0.75. At such speeds, the PN expansion is inadequate for analytically describing such systems. However, the Teukolsky inspiral-merger waveforms turn out to be extremely simple. Consider, for example, the $(2, 2)$ mode emitted when $q = 0.99$, shown in Fig. 4.2. The prominent feature that we recognize is the extreme flatness of the amplitude versus time, across hundreds of M, well before the plunge starts at the ISCO. The GW frequency $\omega_{22}^{\rm Teuk}$, defined as $-\Im(\dot{h}_{22}^{\rm Teuk}/h_{22}^{\rm Teuk})$, does not display any particular characteristic, and we notice that it is well approximated by twice the orbital frequency even during ringdown, thanks to the fact that $2\Omega_{\rm H}$ is very close to the least-damped quasinormal mode. We find that the flattening of the amplitudes $|h_{\ell m}^{\rm Teuk}|$ around

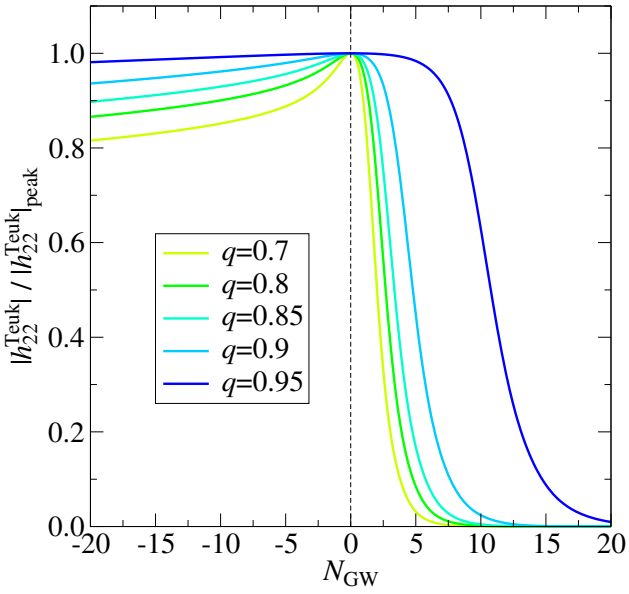

Figure 4.3: Flattening of the peak amplitude of the Teukolsky $(2,2)$ mode as the spin grows towards 1. The curves are normalized by the values of the amplitude at the peak. We align the waveforms in time at $t^{22}_{\rm peak}$, and plot them as functions of the number of GW cycles from the peak.

their respective peaks is more and more apparent as q approaches 1. This aspect of the numerical waveforms does not depend on minute details of the flux used to generate the underlying orbital dynamics. In Fig. 4.3 we show the amplitudes of the Teukolsky $(2,2)$ modes for $q = 0.7, 0.8, 0.85, 0.9, 0.95$ aligned at $t^{22}_{\rm peak}$, with $t^{\ell m}_{\rm peak}$ being the time when the (ℓ, m) mode reaches its maximum amplitude. The almost extremal case $q = 0.99$ was not included in Fig. 4.3 since its $(2,2)$ amplitude is so flat that it is quite difficult to localize $t^{22}_{\rm peak}$. In fact, across the $(2,2)$ peak, over a large time interval, its $\partial_t |h^{\rm Teuk}_{22}|$ is so small that it is dominated by numerical noise, making it difficult to clearly locate its zero. The curvature $(\partial_t^2 |h^{\rm Teuk}_{22}|)_{\rm peak}$ becomes vanishingly small as $q \to 1$; see also Fig. A.2. Although we have shown only $(2,2)$

mode waveforms, the same holds true for higher harmonics.

We can find a physical explanation for why this happens considering the underlying orbital dynamics. As the spin grows larger, the ISCO moves to smaller separations and gets closer to the horizon, so that the plunging phase becomes shorter (in the radial coordinate), and moves to higher frequencies. This is equivalent to saying that Kerr BHs with larger spins support longer quasicircular inspirals given the same initial frequency. For instance, let us consider spins 0.5 and 0.99. Their dimensionless horizon frequencies are 0.13 and 0.43 respectively. An initial orbital frequency of 0.1 corresponds to radial separations, $4.5M$ and $4.3M$, respectively, which are quite close to each other; while for spin 0.5 we are sitting just outside the ISCO ($r_{\rm ISCO}(q=0.5)=4.2M$), for spin 0.99 we are still far from it ($r_{\rm ISCO}(q=0.99)=1.5M$). Furthermore, for very large spins the orbital timescale $T_{\rm orb}$ is much shorter than the radiation-reaction timescale $T_{\rm rad}$. We can estimate these characteristic timescales for different values of q as $T_{\rm orb}=2\pi/\Omega$ and $T_{\rm rad}=-r/\dot{r}$. The orbital frequency grows during the inspiral, reaches a peak value $\Omega_{\rm peak}$ at time $t^{\Omega}_{\rm peak}$, and eventually converges to the horizon frequency $\Omega_{\rm H}$ at late times. One can show that, for all practical purposes, the peak of Ω occurs at a radius $r^{\Omega}_{\rm peak}$ which nearly coincides with $r_{\rm LR}$, the coincidence being exact for $q=0,1$. In Fig. 4.4 we plot the ratio $T_{\rm rad}/T_{\rm orb}$ as a function of the radial separation r. The solid lines are computed along nonadiabatic trajectories from the numerical integration of the equations of motion, up to the peak of the orbital frequency Ω. At fixed r, the orbital timescale $T_{\rm orb}$ does not vary much with q: for example, when $r=4M$, $T_{\rm orb}=53M$ for $q=0.5$, while $T_{\rm orb}=56M$ for $q=0.99$; but the ratio $T_{\rm rad}/T_{\rm orb}$ for

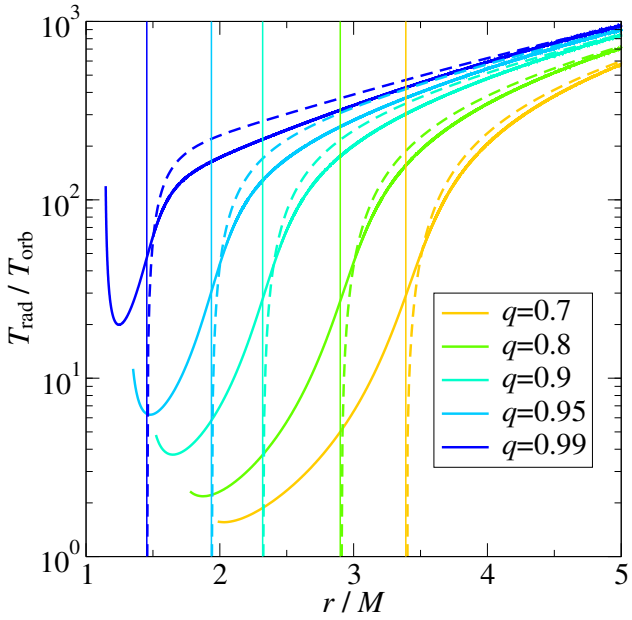

Figure 4.4: Ratio between the radiation-reaction timescale $T_{\rm rad}$ and the orbital period $T_{\rm orb}$ as a function of the radial separation for large positive spins. The curves extend up to the peak of the orbital frequency. The solid lines are computed from the numerical integration of the equations of motion. The dashed lines are the analytical predictions for the quasicircular regime, using only quadrupolar emission (Eq. (4.4)). Vertical lines mark the position of the respective ISCOs.

spin 0.99 is 55 times larger than for spin 0.5. Hence, the plot demonstrates that there is a clear hierarchy in the radiation-reaction timescales: the larger the spin, the larger $T_{\rm rad}$. As a result, the secular evolution is much slower for large spins, given the same initial separation. This hierarchy can be easily understood using analytical considerations at leading order. During the quasicircular inspiral we have $T_{\rm orb} \approx 2\pi/\Omega_{\rm circ}$ and the orbital energy E can be approximated by the energy of a circular orbit in Kerr spacetime [122]

$$\frac{E_{\rm circ}}{\mu} = \frac{1 - 2M/r + q(M/r)^{3/2}}{\sqrt{1 - 3M/r + 2q(M/r)^{3/2}}}\,. \tag{4.3}$$

Note that $E_{\rm circ}$ diverges at $r = r_{\rm LR}$. Moreover, assuming mainly leading quadrupolar energy loss [14] and circularity, we get $F = -\dot{E} \approx 32\mu^2 r^4 \Omega_{\rm circ}^6/5$; thus, we find that

$$T_{\rm rad} = -r\frac{{\rm d}E/{\rm d}r}{{\rm d}E/{\rm d}t} \approx \frac{{\rm d}E_{\rm circ}/{\rm d}r}{\frac{32}{5}\mu^2 r^3 \Omega_{\rm circ}^6}\,. \tag{4.4}$$

In Fig. 4.4 we plot the analytical estimate (4.4) with dashed lines, and find that it captures the numerical result (solid lines) fairly well at large r, and, most importantly, can account for the hierarchy of the curves due to the presence of spin. We can now understand why large-spin waveforms are so flat. For large q the radiation-reaction timescale is much larger than the orbital timescale, which means that the particle performs many orbits while sweeping very slowly through the frequency range up to the horizon, so that the secular evolution of the emitted GW signal is much slower as compared to systems with smaller q. This is consistent with the behavior of the frequency-domain Teukolsky fluxes that we employ in the equations of motion, whose $(2,2)$ component is plotted in Fig. 4.5 versus radius; at fixed r, the dissipation of energy is smaller for larger spins.

Notice that, only for this plot, we include spins as large as $q = \pm 0.9999$. Interestingly, as $q \to 1$ the fluxes become small even outside the ISCO and approach vanishingly small values beyond the ISCO, which accounts for the behavior of the ratio $T_{\rm rad}/T_{\rm orb}$ in the late inspiral and plunge. We notice that, starting from $q = 0.99$, F_{22} does not display the characteristic divergence at the light-ring as $(E_{\rm circ}/\mu)^2 \sim (r - r_{\rm LR})^{-1}$, which is well known [242–245]. Instead, F_{22} tends to decrease towards 0, and, remarkably, becomes linear in $(r - r_+)$ for $q = 0.9999$, when $r_{\rm LR} \sim r_+$. This is in agreement with analytical work on the gravitational radiation from a particle

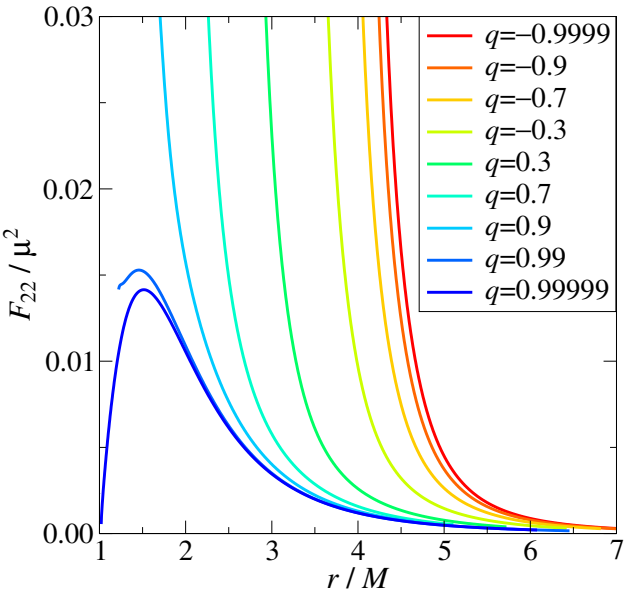

Figure 4.5: $(2,2)$ component of the ingoing + outgoing Teukolsky GW flux. The curves extend down to $r_{\rm min} = r_{\rm LR} + 0.01M$.

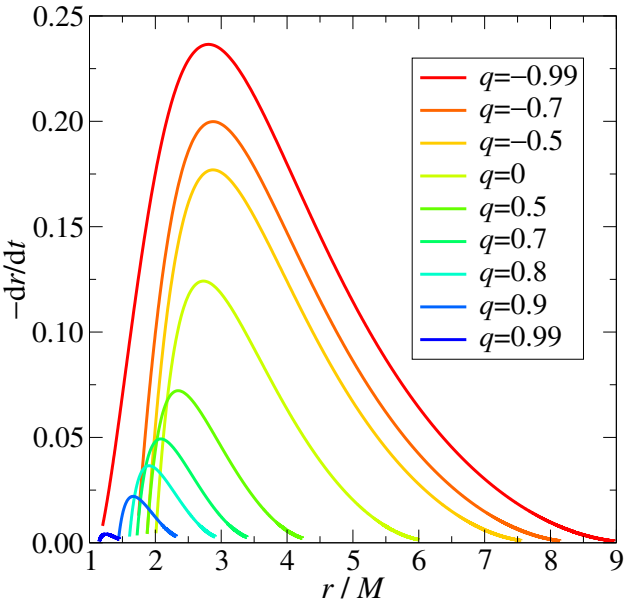

Figure 4.6: Radial velocity $\dot{r}$ during the plunge. The curves cover the range $r_+ < r < r_{\rm ISCO}$.

plunging into a nearly-extremal Kerr BHs in Ref. [223].

Furthermore, during the plunge (which is governed mostly by conservative effects), the radial velocity $\dot{r}$ reaches maximum values that decrease with q, meaning that for large spins even the plunge is not too far from being circular. Figure 4.6 plots the r–dependence of the radial velocity in the region inside the ISCO for several different spin configurations, using orbital evolutions obtained by solving Hamilton's equations. The peak radial velocity differs by more than one order of magnitude between $q = -0.99$ and $q = 0.99$.

4.5 Quasinormal-mode mixing in ringdown Teukolsky waveforms and its modeling

The merger of a BH binary (of any mass ratio) eventually leads to the formation of a remnant Kerr BH of mass M_f and dimensionless spin q_f. In this work, since we are dealing with an extreme mass-ratio system, we have $M_f = M$ and $q_f = q$. In the process of settling down to its final, stable state, the binary emits GWs. Those waves can be modeled as a linear superposition of quasinormal modes (QNMs) [18, 127] with complex frequencies $\sigma_{\ell mn}$, which depend only on M_f and q_f, and are labelled by the spheroidal-harmonic indices (ℓ, m) and by an overtone index $n = 0, 1, \cdots$. For future convenience, we define $\omega_{\ell mn} \equiv \Re(\sigma_{\ell mn})$ and $\tau_{\ell mn} \equiv -1/\Im(\sigma_{\ell mn})$. We adopt the convention that $\omega_{\ell mn} > 0$ and $\tau_{\ell mn} > 0$ for any choice of the indices (ℓ, m, n).

In general, the strain waveform h during the ringdown (RD) contains QNMs

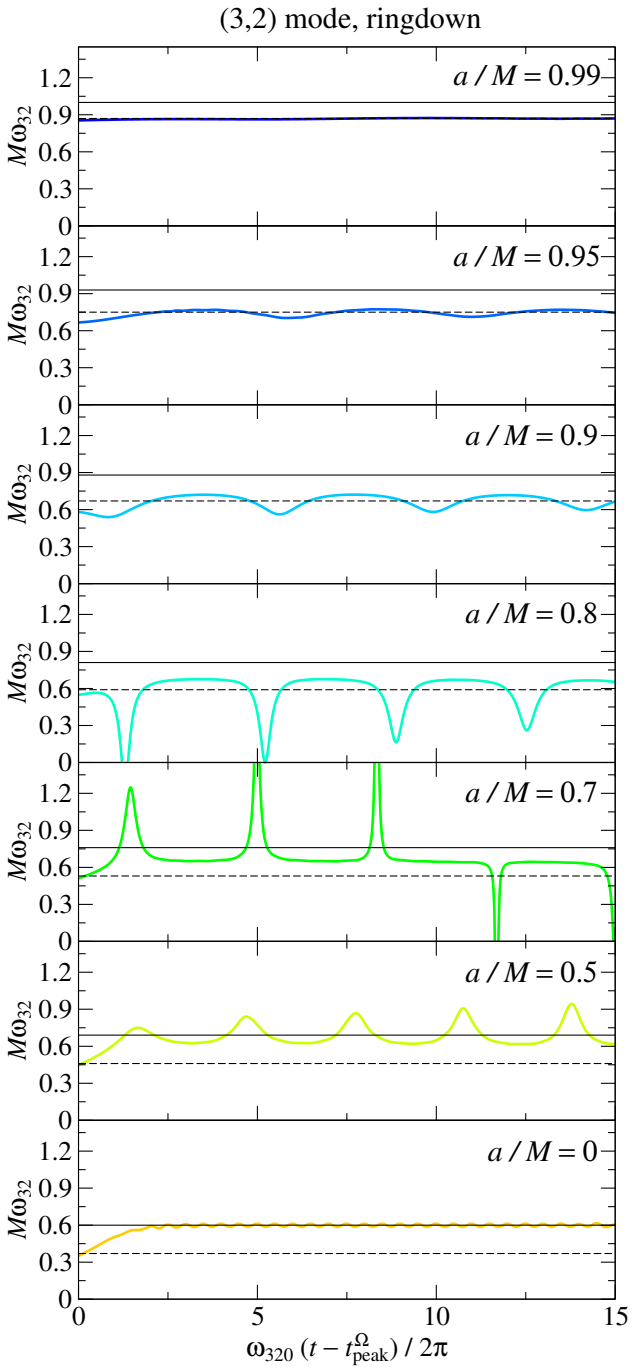

Figure 4.7: GW frequencies of Teukolsky $(3, 2)$ ringdown waveforms with positive spin. For the common x-axis, we use the time elapsed from the orbital frequency peak in units of $2\pi/\omega_{320}$. Solid horizontal lines indicate the value $M\omega_{320}$, while dashed horizontal lines indicate the value $M\omega_{220}$.

with all possible values of (ℓ, m, n). Additionally, given a spin q and indices (ℓ, m), the angular differential equation which stems from the separation of the Teukolsky equation in spheroidal coordinates admits a pair of solutions characterized by frequencies $\sigma_{\ell\pm mn}$. This implies that, whenever considering a specific component (ℓ, m) of h, even in principle, we get contributions from both positive- and negative-m modes. As argued by Ref. [18], restricting to only positive-m modes would enforce the assumption of circular polarization of the radiation. Of course, the actual importance of the modes depends on the details of how they are excited by the perturbing source, and by their decay times.

As already found by numerical investigations of the extreme and small mass-ratio limits [99, 119, 123–126], the dominant and leading subdominant ringdown Teukolsky modes can display a rich amplitude and frequency structure that hints at the interference of different QNMs besides the overtones of the least-damped mode, a phenomenon known as *mode mixing*. On the contrary, in the case of comparable-mass BH binaries, mode mixing seems less ubiquitous, and so far it has only been seen in the $(3, 2)$ mode [63, 91, 246–250]. For this reason, in the past, when modeling the ringdown of the (ℓ, m) mode in the EOB approach, one could simply use the (ℓ, m, n) QNMs. However, the lack of mode mixing during ringdown in the comparable-mass case is inferred by the analysis of nonspinning, nonprecessing or mildly precessing configurations. We do not know yet whether this conclusion will hold when strongly precessing systems with mass ratios $\geq 1/10$ will be considered.

QNM mixing manifests itself through striking features in the Teukolsky ringdown waveforms, which are modulated both in amplitude and frequency. To under-

stand the composition of the QNM spectrum of the Teukolsky data, we will study in particular the GW frequency of each mode, defined as $\omega_{\ell m}^{\rm Teuk} \equiv -\Im(\dot{h}_{\ell m}^{\rm Teuk}/h_{\ell m}^{\rm Teuk})$, since this quantity is directly related to the frequencies of the most excited QNMs, and is numerically well determined. As an example, Fig. 4.7 displays the ringdown $(3,2)$ mode frequencies for several positive spins, with a common time axis rescaled by $2\pi/\omega_{320}$. We observe that different spins have completely different ringdown frequencies; each case has distinct features (spikes, oscillations), occurring with specific periodicities. The averages of the oscillatory features are closer either to ω_{320} (as one would naively expect) or to ω_{220}, according to the value of q. Examples of amplitude modulations can be found in Figs. 4.8, 4.9, and 4.10, which show a few Teukolsky merger-ringdown waveforms (solid blue lines), chosen within the large set that we computed for this paper. Among them, the most modulated case is spin -0.99 (its $(2,2)$ mode is shown in the right panel of Fig. 4.8; a similar behavior is also present in its higher-order modes).

In extreme and small mass-ratio binaries, two instances may enhance the excitation and/or mixing of modes other than the (ℓ,m,n)'s in the ringdown of (ℓ,m). On the one hand, for modeling purposes, the strain waveform h is typically decomposed onto -2-spin-weighted spherical harmonics ${}_{-2}Y_{\ell m}$, while the Teukolsky equation is separated using -2-spin-weighted spheroidal harmonics ${}_{-2}S_{\ell m}^{q\omega}$, which depend on the Kerr spin q and the (possibly complex) frequency ω of the gravitational perturbation. The expansion of the ${}_{-2}S_{\ell m}^{q\omega}$'s in terms of the ${}_{-2}Y_{\ell m}$'s can be found (to order $(qM\omega)^2$) in Appendix F of Ref. [251]. Using this result, one can derive a formula relating the spherical to the spheroidal waveforms (see, e.g., Eq. (19)

of Ref. [101]) and one finds that the spherical mode $h_{\ell m}$ receives contributions from all spheroidal modes with the same m, but different ℓ (see also Eq. (38) in Ref. [63]). Another source of mixing is the orbital motion of the perturbing particle: whenever $q < 0$, the orbital frequency switches sign during the plunge, because of frame dragging exerted by the spinning BH; this results in a significant excitation of modes with opposite m, but with the same ℓ. Reference [250] investigated in detail the origin of the mixing in the $(3,2)$ mode of several comparable-mass, nonprecessing BH binaries, and attributed it mostly to angular-basis effects, using $\omega = q_f M_f \sigma_{320}$.

To understand quantitatively the QNM mixing in our Teukolsky waveforms, we model the ringdown as done in EOB models (i.e., as a linear superposition of overtones of the least-damped QNM), but with the addition of up to 2 further QNMs. While the least-damped mode and its overtones are going to account for the overall shape of the ringdown waveform, the additional QNMs are going to induce the modulations. More explicitly, (except for the $(3,2)$ mode of systems with $q = 0.99$) we model the (ℓ, m) mode of the ringdown waveforms as

$$\begin{aligned} h^{\rm RD}_{\ell m} = &\sum_{n=0}^{N-1} A_{\ell m n} e^{-i\sigma_{\ell m n}(t-t^{\ell m}_{\rm match})} \\ &+ \mathcal{S}(t)\left[A_{\ell' m 0} e^{-i\sigma_{\ell' m 0}(t-t^{\ell m}_{\rm match})} + A_{\ell -m 0} e^{i\sigma^*_{\ell -m 0}(t-t^{\ell m}_{\rm match})}\right] , \end{aligned} \tag{4.5}$$

where $t^{\ell m}_{\rm match}$ is the time of merger, N is the number of overtones included, the $A_{\ell m n}$'s are the (constant) coefficients of the overtones, $\mathcal{S}(t) \equiv [1 + \tanh[(t-t_{\rm s})/\tau_{\rm s}]]/2$ is a factor introduced to have a smooth switch-on of the interfering QNMs (with $t_{\rm s}$ and $\tau_{\rm s}$ optimized mode by mode), and $A_{\ell' m 0}$ and $A_{\ell -m 0}$ are constants computed from a fit (see below). $A_{\ell' m 0}$ and $A_{\ell -m 0}$ quantitatively describe the strength of the QNM

mixing. Note that $\sigma_{\ell -mn}(M_f, q_f) = \sigma_{\ell mn}(M_f, -q_f)$. Since overtones with $n > 0$ have short decay times with respect to those with $n = 0$, Eq. (4.5) is actually dominated by terms with $n = 0$ when $t \gg t^{\ell m}_{\rm match}$.

The coefficients $A_{\ell mn}$, $A_{\ell' m0}$, and $A_{\ell -m0}$ can be determined from the Teukolsky data as follows. Whenever mode mixing is resolved, $A_{\ell' m0}$ and $A_{\ell -m0}$ are obtained by fitting the GW frequency $\omega^{\rm RD}_{\ell m} = -\Im(\dot{h}^{\rm RD}_{\ell m}/h^{\rm RD}_{\ell m})$ to the ringdown Teukolsky GW frequency $\omega^{\rm Teuk}_{\ell m}$, while setting $A_{\ell mn} = 0$ for $n > 0$; we choose a fitting window as wide as possible, but still avoiding any numerical noise. Once $A_{\ell' m0}$ and $A_{\ell -m0}$ are fixed by the fit, the $A_{\ell mn}$'s are calculated via the hybrid matching procedure detailed in Ref. [91], which consists in a smooth stitching of the ringdown waveform $h^{\rm RD}_{\ell m}$ to the Teukoslky waveform $h^{\rm Teuk}_{\ell m}$ at a time $t^{\ell m}_{\rm match}$.

As in Ref. [119], we find that, in the test-particle limit, and when the spin is $q \lesssim 0$, some of the physical overtones included in Eq. (4.5) have frequencies smaller than $\omega^{\rm Teuk}_{\ell m}(t^{\ell m}_{\rm match})$, causing the slope of $\omega^{\rm RD}_{\ell m}$ to be too steep. Therefore, we introduce a pseudo-QNM (i.e., a mode not belonging to the physical QNM spectrum). In the past, pseudo-QNMs were exploited in comparable-mass EOB models [70,91,194,236] to reduce the slope of the GW frequency in the transition from plunge to ringdown.

To summarize, the matching procedure has the following tuning parameters: the matching point $t^{\ell m}_{\rm match}$; the size of the time interval over which one carries out the matching $\Delta t^{\ell m}_{\rm match}$; a pseudo-QNM mode with frequency and decay time $\omega^{\rm pQNM}_{\ell m}$ and $\tau^{\rm pQNM}_{\ell m}$; $t_{\rm s}$ and $\tau_{\rm s}$. These tuning parameters are chosen with the goal of minimizing the phase and relative amplitude difference between $h^{\rm RD}_{\ell m}$ and $h^{\rm Teuk}_{\ell m}$ when $t > t^{\ell m}_{\rm match}$.

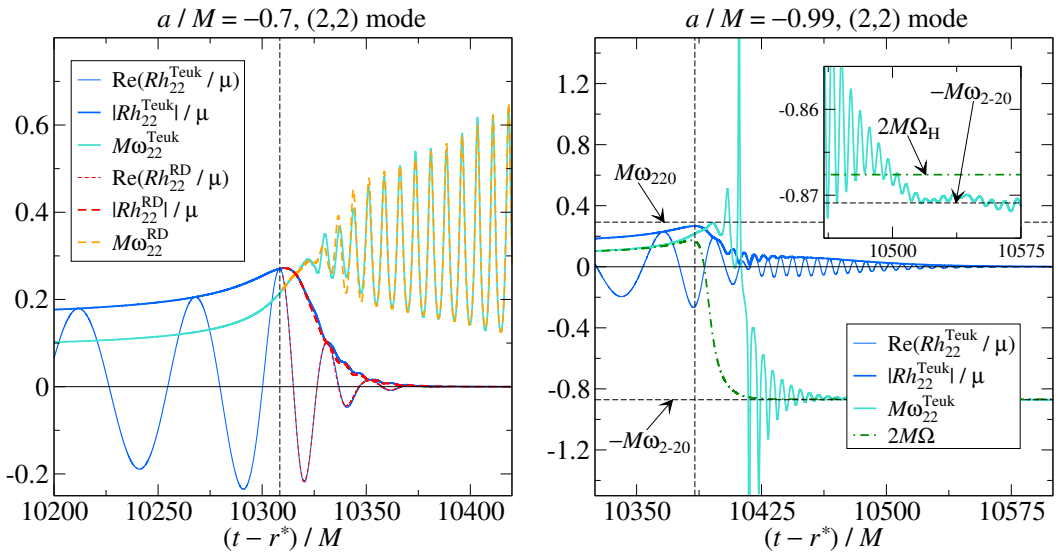

Figure 4.8: Teukolsky $(2,2)$ mode waveforms for spin $q = -0.7$ (left panel) and -0.99 (right panel), displaying mode mixing during the ringdown phase. For $q = -0.7$ we plot a ringdown waveform which contains the mode $(2,-2,0)$ besides the usual $(2,2,n)$ $(n = 0,1,\cdots)$. The vertical dashed lines mark $t = t^{22}_{\rm match}$. Note that the amplitudes have been rescaled by a factor of 5. R is the distance to the source.

Before modeling the entire ringdown waveforms, to better understand how the mixing works, let us consider the simple case of just 2 QNMs interfering: let $A_{\ell' m 0} = 0$ and $A_{\ell m n} = 0$ for $n > 0$ (i.e., a waveform dominated by the $(\ell, \pm m, 0)$ modes). This is similar to what was done in Refs. [119, 126], where the modulations in the ringdown frequency of the numerical modes were fitted with a simple analytical formula that accounted for the interference between the $(\ell, \pm m, 0)$ QNMs. The GW frequency is $\omega^{\rm RD}_{\ell m} = -\Im(\dot{h}^{\rm RD}_{\ell m}/h^{\rm RD}_{\ell m})$, thus we have (leaving out the factor $\mathcal{S}(t)$ for

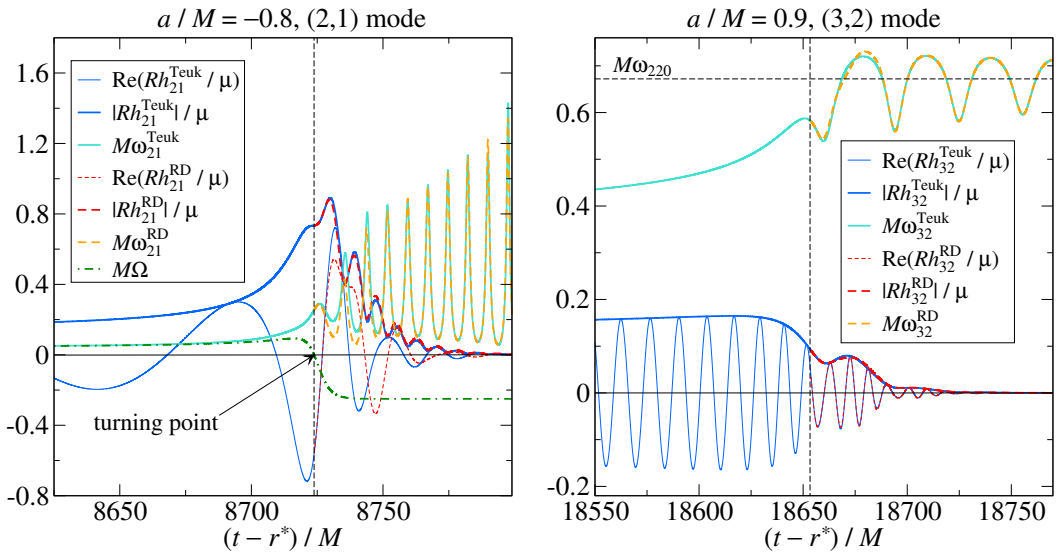

Figure 4.9: Teukolsky $(2,1)$ mode for spin $q=-0.8$ (left panel) and $(3,2)$ mode for spin $q=0.9$ (right panel). For the $q=-0.8$ waveform, the modulations come from the interference of $(2,1,0)$ and $(2,-1,0)$; note how the amplitude peak is affected by the mixing, starting at a time where $\Omega=0$, i.e., the turning point of the azimuthal motion. For the $q=0.9$ waveform, instead, the ringdown contains the modes $(3,2,n)$'s and $(2,2,0)$.The vertical dashed lines mark $t=t^{\ell m}_{\rm match}$. R is the distance to the source.

simplicity)

$$\omega^{\rm RD}_{\ell m} = \Big\{\omega_+ - \omega_- |\bar{A}|^2 e^{2(t-t^{\ell m}_{\rm match})\Delta\alpha} + |\bar{A}| e^{\alpha_+(t-t^{\ell m}_{\rm match})} \times \left[\Delta\omega \cos\left[\bar{\omega}(t-t^{\ell m}_{\rm match})+\bar{\theta}\right] - \Delta\alpha \sin\left[\bar{\omega}(t-t^{\ell m}_{\rm match})+\bar{\theta}\right]\right] \Big\} \times \Big\{1 + |\bar{A}|^2 e^{2(t-t^{\ell m}_{\rm match})\Delta\alpha} + 2|\bar{A}| \cos\left[\bar{\omega}(t-t^{\ell m}_{\rm match})+\bar{\theta}\right]\Big\}^{-1}, \tag{4.6}$$

where $\omega_\pm \equiv \omega_{\ell\pm m0}$, $\alpha_\pm \equiv 1/\tau_{\ell\pm m0}$, $\Delta\omega \equiv \omega_+ - \omega_-$, $\Delta\alpha \equiv \alpha_+ - \alpha_-$, $\bar{\omega} \equiv \omega_+ + \omega_-$, and $A_{\ell -m0}/A_{\ell m0} \equiv |\bar{A}| \exp(i\bar{\theta})$. Typically, $|\bar{A}| < 1$. Note that Eq. (19) in Ref. [126] is simpler than our Eq. (4.6) above since that paper considered the Schwarzschild case, for which $\sigma_{\ell mn} = \sigma_{\ell -mn}$. Equation (4.6) describes a function with exponentially

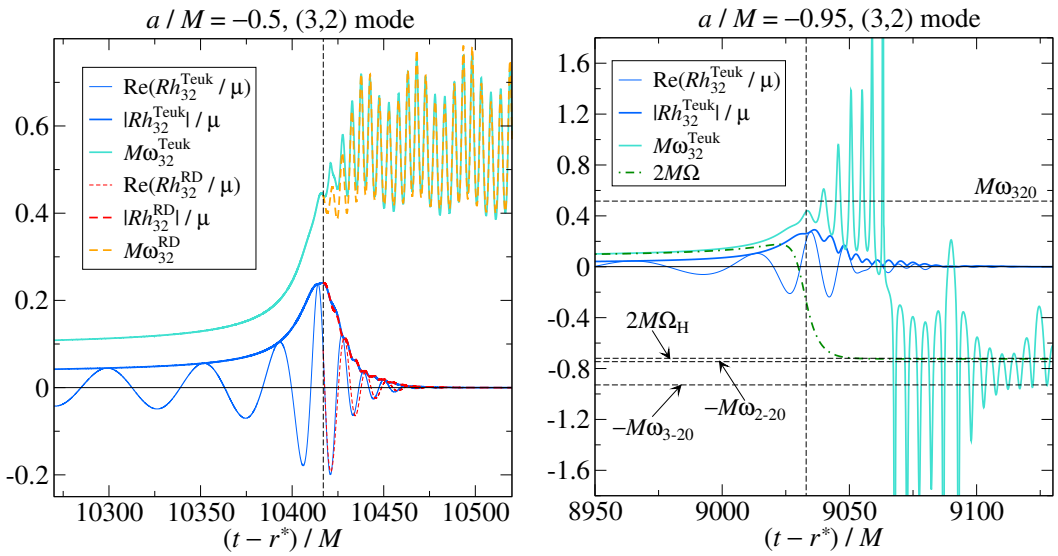

Figure 4.10: Teukolsky $(3,2)$ waveforms for spin $q=-0.5$ (left panel) and -0.95 (right panel). For $q=-0.5$, the ringdown waveform contains the modes $(3,-2,0)$ and $(2,2,0)$ besides the usual $(3,2,n)$'s. For the $q=-0.95$ waveform, the GW frequency modulations in the late ringdown are not centered neither about $-\omega_{3-20}$ nor about $-\omega_{2-20}$, and we cannot apply the simple model of Eq. (4.5). The vertical dashed lines mark $t=t^{32}_{\rm match}$. R is the distance to the source.

growing oscillations about ω_+ when $t^{\ell m}_{\rm match} < t < t^{\ell m}_{\rm match} - \log|\bar{A}|/\Delta\alpha \equiv t_{\rm p}$, and with exponentially decreasing oscillations about $-\omega_-$ when $t > t_{\rm p}$; the frequency of the oscillations is $\bar{\omega}$. The point $t_{\rm p}$ marks the transition from oscillations about ω_+ to oscillations about $-\omega_-$; note that if $t_{\rm p} - t^{\ell m}_{\rm match} \gg 1/\alpha_+$ then the transition occurs in a region where the amplitude is absolutely negligible. Given the size of the numerical errors discussed in Sec. 4.3, we consider that the ringdown has ended whenever the amplitude drops below $10^{-4}\mu/R$, where R is the distance to the source.

	(2, 2) mode		(3, 3) mode	
a/M	$\lvert A_{2-20}/A_{220}\rvert$	$\arg\left(A_{2-20}/A_{220}\right)$	$\lvert A_{3-30}/A_{330}\rvert$	$\arg\left(A_{3-30}/A_{330}\right)$
0	0.0036	−5.70	0.0029	−4.07
−0.5	0.052	−0.24	0.049	−1.26
−0.7	0.12	−0.26	0.22	4.31
−0.8	0.10	−0.41	0.22	3.03
−0.9	0.28	−1.31	0.27	1.41

	(4, 4) mode		(5, 5) mode	
a/M	$\lvert A_{4-40}/A_{440}\rvert$	$\arg\left(A_{4-40}/A_{440}\right)$	$\lvert A_{5-50}/A_{550}\rvert$	$\arg\left(A_{5-50}/A_{550}\right)$
0	0.0035	−5.80	0.0047	−7.58
−0.5	0.056	3.82	0.073	2.82
−0.7	0.29	2.86	0.39	1.60
−0.8	0.31	1.02	0.38	−0.81
−0.9	0.32	−1.76	0.46	−4.55

Table 4.1: Relative amplitude and phase of the QNMs responsible for mixing in modes with $\ell = m$. No QNM mixing is present when the spins are positive. Spins $q = -0.95, -0.99$ cannot be modeled with Eq. (4.6) due to the presence of additional interfering QNMs that we are unable to extract, which results in a GW frequency drift at late times (see, for instance, the inset in the right panel of Fig. 4.8).

	(2,1) mode		(3,2) mode			
a/M	$\lvert A_{2-10}/A_{210}\rvert$	$\arg(A_{2-10}/A_{210})$	$\lvert A_{220}/A_{320}\rvert$	$\arg(A_{220}/A_{320})$	$\lvert A_{3-20}/A_{320}\rvert$	$\arg(A_{3-20}/A_{320})$
0.99	0.038	13.7	only $(2,2,n)$ overtones			
0.95	0.030	9.82	2.91	6.44		
0.9	0.0025	5.61	2.11	5.99		
0.8	0.0024	4.24	1.13	2.86		
0.7	0.0051	3.73	0.71	−2.10		
0.5	0.010	−0.16	0.34	−7.02		
0	0.069	−3.46			0.010	−1.08
−0.5	0.21	−5.64	0.13	−2.46	0.093	5.26
−0.7	0.26	−6.58	0.15	3.47	0.22	10.6
−0.8	0.30	−7.37	0.16	3.91	0.23	12.4
−0.9	0.32	−8.50	-	-	-	-

Table 4.2: Relative amplitude and phase of the QNMs responsible for mixing in modes with $\ell \neq m$. A blank entry means that that QNM is not excited. A dash indicates that the mode, while present, cannot be reliably fitted. Spins $q = -0.95, -0.99$ and the $(3,2)$ mode of spin $q = -0.9$ cannot be modeled due to the presence of additional interfering QNMs we are unable to extract with the simple model of Eq. (4.5). The $(3,2)$ mode of spin 0.99 is modeled using only $(2,2,0)$ and its overtones.

a/M	$\Delta t^{\ell\ell}_{\rm match}/M$	$\Delta t^{21}_{\rm match}/M$	$\Delta t^{32}_{\rm match}/M$
0.99	15 (20)	15	20
0.95	13	13	13
0.9	11	11	11
0.8	9	9	9
0.7	7	7	7
0.5	5	5	5
0	5	5	5
-0.5	5	3	15
-0.7	5	3	15
-0.8	5	3	20
-0.9	5	3	-

Table 4.3: Intervals for ringdown hybrid matching. When $q = 0.99$, $\Delta t^{22}_{\rm match} = \Delta t^{33}_{\rm match} = 15M$ and $\Delta t^{44}_{\rm match} = \Delta t^{55}_{\rm match} = 20M$. The table does not include those spins that we are not able to model.

In the next two sections we shall discuss how we apply Eq. (4.5) to model the $\ell = m$ and $\ell \neq m$ numerical modes, respectively. The main conclusions can be summarized as follows. We are able to model the $\ell = m$ modes for any spin $q \geq -0.9$. The reason why we cannot model spins smaller than -0.9 is the conjectured presence of one or more QNMs that we are unable to recognize, which manifest themselves in a drift of the Teukolsky GW frequency at late times (see discussion in Sec. 4.5.1). We can model the $(2,1)$ mode for any spin except $q = -0.95, -0.99$ because of large inaccuracies in capturing modulations in the early ringdown. Finally, we can model the $(3,2)$ mode for any spin except $q = -0.9, -0.95, -0.99$ because for these very negative spins the oscillations in the amplitude and GW frequency become very dramatic, preventing us from reliably fitting the amplitude and phase of all the modes (see the right panel of Fig. 4.10).

Note that we use a unique tuning for the pseudo-QNM, namely $\omega_{\ell m}^{\rm pQNM} = [\omega_{\ell m 0} + \omega_{\ell m}^{\rm Teuk}(t_{\rm match}^{\ell m})]/2$ and $\tau_{\ell m}^{\rm pQNM} = 0.2\tau_{\ell m 0}$. When no mode mixing is present, the pseudo-QNM replaces the 8-th physical overtone $(\ell, m, 7)$, otherwise it is added to the rest of the mode spectrum. For all the spins that we have been able to model, the matching intervals $\Delta t_{\rm match}^{\ell m}$ are listed in Table 4.3.

4.5.1 $\ell = m$ modes

For all modes with $\ell = m$, we choose $t_{\rm match}^{\ell m} = t_{\rm peak}^{\Omega}$, which is the time when the orbital frequency Ω peaks, very close to the light-ring; this choice has the advantage of avoiding the ambiguity of locating the amplitude peak when $q \sim 1$ (see Sec. 4.4). For the $(2,2)$ and $(3,3)$ modes we choose $t_{\rm s} = t_{\rm match}^{\ell m} + 20M$ and $\tau_{\rm s} = 7.5M$; when $(\ell, m) = (4,4), (5,5)$ we choose instead $t_{\rm s} = t_{\rm match}^{\ell m} + 25M$ and $\tau_{\rm s} = 4.5M$.

Let us first consider the dominant $(2,2)$ mode. For spins $q \gtrsim 0.5$, we find that the ringdown is quite standard, as no appreciable mode mixing is present, and $h_{22}^{\rm Teuk}$ is well described by a linear superposition of overtones of the least-damped mode (i.e., Eq. (4.5) with $A_{\ell' 20}$, $A_{2-20} = 0$). The matching interval $\Delta t_{\rm match}^{22}$ varies with q as prescribed in Table 4.3. We find that $\Delta t_{\rm match}^{22}$ tends to grow towards large, positive spins since the light-ring (i.e., the matching point) occurs progressively later, during the ringdown, well past the amplitude peak, in a region where the waveform is rapidly decaying. For spins $q \leq 0$, we find it necessary to include the $(2, -2, 0)$ mode in the QNM spectrum (i.e., Eq. (4.5) with $A_{\ell' 20} = 0$); this mode has an amplitude $|A_{2-20}|$ that grows (relative to $|A_{220}|$) as the spin decreases, which

can be understood based on the fact that the portion of orbit with $\Omega < 0$ (due to frame dragging during the plunge) becomes progressively longer. In Table 4.1 we provide magnitude and phase of A_{2-20}/A_{220}, i.e., the ratio of $(2, -2, 0)$ relative to the least-damped QNM. The numbers in the table are obtained from a fit of $\omega_{22}^{\rm Teuk}$ using Eq. (4.6).

The typical performance of the model is illustrated in the left panel of Fig. 4.8, which shows the case with spin -0.7. The Teukolsky amplitude (frequency) is plotted in blue (cyan), while the model amplitude (frequency) is plotted in red (orange). We clearly recognize the growing oscillations of the GW frequency about $M\omega_{220} \approx 0.31$; by fitting, we find that $|A_{2-20}|/|A_{220}| \approx 0.12$, so that $t_{\rm p} \approx t_{\rm match}^{\ell m} + 270M$ (i.e., in a region where $|Rh_{22}^{\rm Teuk}|/\mu \ll 10^{-4}$). The waveform $h_{22}^{\rm RD}$ does a good job at capturing the modulations everywhere, except in the early ringdown ($t_{\rm match}^{\ell m} < t \lesssim t_{\rm s}$), where the oscillations in $\omega_{22}^{\rm Teuk}$ occur at a frequency $\bar{\omega} \neq \omega_{220} + \omega_{2-20}$, and with an amplitude growth whose timescale does not clearly relate to either τ_{220} or τ_{2-20}, as one would expect from Eq. (4.6). One limitation inherent to our approach is the specific form $\mathcal{S}(t)$ of the time dependence of the coefficients $A_{\ell' m 0}$ and $A_{\ell -m 0}$, which may not correctly model the process of excitation (in spite of the two adjustable parameters $t_{\rm s}$ and $\tau_{\rm s}$). Note that in comparable-mass EOB models the coefficients in front of the QNMs in $h_{\ell m}^{\rm RD}$ have no time dependence.

For spins $q < -0.8$, the point $t_{\rm p}$ moves closer to $t_{\rm match}^{\ell m}$, and the performance of the model in the early ringdown (i.e., $t_{\rm match}^{\ell m} < t < t_{\rm p}$) becomes worse; however, Eq. (4.5) with $A_{\ell' 20} = 0$ can still describe the region $t > t_{\rm p}$ quite accurately.

We find that the most difficult ringdown waveforms to model are the ones

with spin -0.95 and-0.99; the case $q = -0.99$ is shown in the right panel of Fig. 4.8. These are the cases with the longest inversion of the trajectory due to frame dragging. We have verified that the numerical errors during the ringdown are not responsible for creating any of the modulations. Note that for such extreme (negative) spins we have $2\Omega_{\rm H} \sim -\omega_{2-20}$. We suspect that the reason why we cannot model spins smaller than -0.9 is the interference of other QNMs besides those included in Eq. (4.5), which we are unable to identify; their presence is hinted by the (physical) drift in the GW frequency at late times. This is exemplified in the right panel of Fig. 4.8, which refers to the $(2,2)$ mode of spin -0.99. The inset therein zooms into the late ringdown, past the point where $\omega_{22}^{\rm Teuk}$ transitions to oscillations about a negative frequency. One can see that the average of the oscillations is not $-\omega_{2-20}$, but instead it slowly asymptotes to that value from above.

As to the other modes with $\ell = m$, they behave similarly to the $(2,2)$ mode, namely for spins $q > 0$ no significant mode mixing is present, while for $q \leq 0$ the mode $(\ell, -m, 0)$ is excited. In Table 4.1 we list the extracted coefficients (relative to the coefficient of the dominant QNM) of those QNMs that cause amplitude and frequency modulations. Again, the simple ringdown model of Eq. (4.5) with $A_{\ell' m 0} = 0$ fails to accurately describe the early ringdown for spins $q < -0.8$, so that we cannot model $q = -0.95, -0.99$.

We have also tried to look for contributions from the horizon modes suggested by Refs. [231, 232], whose frequency is $m\Omega_{\rm H}$, but their decay time $r_+/(2\sqrt{1-q^2})$ is not compatible with any of the timescales present in the Teukolsky data, and we did not observe their presence in the numerical waveforms.

4.5.2 $\ell \neq m$ modes

We find that the $(2,1)$ mode shows mode mixing all across the physical spin range: the $(2,-1,0)$ component can be excited also for $q > 0$, although to a limited extent. Explicitly, we model its ringdown via Eq. (4.5), setting $A_{\ell' 10} = 0$. If $q > 0$ we can choose $t^{\ell m}_{\rm match} = t^{\Omega}_{\rm peak}$, $t_{\rm s} = t^{21}_{\rm match} + 15M$, $\tau_{\rm s} = 7.5M$. For positive spins, the amplitude of $(2,-1,0)$ (shown in Table 4.2) turns out to be rather small ($|A_{2-10}/A_{210}| \sim 10^{-3}$–$10^{-2}$). The model performs very well in this region.

Starting from the nonspinning case, and for smaller spins, $t^{\Omega}_{\rm peak}$ occurs quite early with respect to the beginning of the $(2,1)$ ringdown, therefore we find it necessary to modify our matching prescriptions. The option of choosing $t^{21}_{\rm peak}$ is certainly viable for $q = 0$. However, when $q < 0$, the onset of mode mixing is quite prompt, so that even the amplitude peak itself is affected by it. To illustrate this point, in the left panel of Fig. 4.9 we plot the $(2,1)$ merger-ringdown waveform for spin -0.8; the left half of the amplitude peak is standard, whereas the right half is modulated by the QNM mixing (featuring several bumps). We observe that the amplitude oscillations begin at the turning point of the particle's azimuthal motion (i.e., when Ω vanishes); thus, we choose this as our $t^{\ell m}_{\rm match}$ for negative spins. We also choose $t_{\rm s} = t^{\ell m}_{\rm match} + 10M$ and $\tau_s = 7.5M$. The correct modeling of the amplitude modulations critically depends on the prescriptions used for the matching, in particular $\Delta t^{21}_{\rm match}$, which can be found in Table 4.3. The model performs quite well for spins as small as -0.9, except for the first couple of oscillations induced by QNM mixing, as can be seen in the left panel Fig. 4.9, mainly due to $\mathcal{S}(t)$. In spite of

the different ringdown prescriptions used in the positive versus negative spin regime, we can see from Table 4.2 that $|A_{2-10}/A_{210}|$ and $\arg(A_{2-10}/A_{210})$ are well-behaved functions of spin. Spins -0.95 and -0.99 cannot be modeled accurately, the issue being the early ringdown (i.e., $t^{21}_{\rm match} < t < t_{\rm p}$), whose modulations become rather extreme, and are not captured by $\mathcal{S}(t)$. The late ringdown (i.e., $t > t_{\rm p}$) follows instead well our model.

The more challenging mode to model is the $(3,2)$. For $q > 0$ we use $t^{\ell m}_{\rm match} = t^{\Omega}_{\rm peak}$, $t_{\rm s} = t^{32}_{\rm match} + 2.5M$, and $\tau_{\rm s} = 10M$. As already seen in Fig. 4.7, when $q \gtrsim 0.7$ the QNM mixing induces a transition of the average (final) ringdown frequency from the expected least-damped mode frequency ω_{320} to ω_{220}. Note how the case $q = 0.7$ (fifth panel of Fig. 4.7) sits at the transition between the two regimes, featuring wide frequency oscillations around both ω_{320} and ω_{220}. The case $q = 0.99$ stands out, since its ringdown can be described by the $(2,2)$-mode spectrum (i.e., $h^{\rm RD}_{32} = \sum_n A_{22n} \exp\left[-i\sigma_{22n}(t - t^{\ell m}_{\rm match})\right]$ is a good model for $h^{\rm Teuk}_{32}$). This happens because there are no significant mode-mixing modulations (see the first panel of Fig. 4.7) and the asymptotic GW frequency is $\omega^{\rm Teuk}_{32}(t \to \infty) = \omega_{220}$. In the range $0 < q \leq 0.95$, instead, we model the ringdown via Eq. (4.5), setting $A_{3-20} = 0$ and $\ell' = 2$, i.e., the QNM spectrum is that of the $(3,2)$ mode with interference from $(2,2,0)$. When $0.8 \lesssim q \lesssim 0.95$, the ringdown displays large features, with a GW frequency oscillating about ω_{220} (see second to fourth panel of Fig. 4.7); this means that $(2,2,0)$ is more excited than the least-damped mode $(3,2,0)$, which is confirmed by our fits, as $|A_{220}/A_{320}| > 1$ (see Table 4.2). The right panel of Fig. 4.9 shows the good agreement of the model to the Teukolsky data for $q = 0.9$. Notice

how the matching point lies in a region where the amplitude has already started to drop, quite a bit later than the peak. As already discussed, the case with $q = 0.7$ represents a sort of threshold, in that its GW frequency oscillates about ω_{320} in the early ringdown and then about ω_{220} in the late ringdown (see the fifth panel of Fig. 4.7).

Similarly to the $(2, 1)$ mode, when $q \leq 0$, $t^{\Omega}_{\rm peak}$ occurs quite early; when $q < 0$, the $(3, 2)$ amplitude peak is modulated by the mode mixing, but now the turning point of the particle happens somewhat earlier relative to it. Therefore, when $q \leq 0$, we choose the matching point in the "middle" of the amplitude peak, where $\partial_t^3 |h^{\rm Teuk}_{32}| = 0$; we also choose $t_s = t^{32}_{\rm match} + 10M$ and $\tau_s = 7.5M$. In terms of QNM spectrum, as happens for all the modes we studied, for $q \leq 0$ the mode with opposite m is excited (i.e., $(3, -2, 0)$). However, the $(2, 2, 0)$ mode can still be extracted from the $(3, 2)$ waveforms for spins as small as $-0.8 \leq q < 0$. Here we use Eq. (4.5) with A_{3-20}, $A_{220} \neq 0$. The function that we fit to the Teukolsky data is simply the generalization of Eq. (4.6) to three interfering QNMs. The extracted coefficients are found in Table 4.2. An example of this regime is shown in the left panel of Fig. 4.10, for spin -0.7; one can notice two effects in $\omega^{\rm Teuk}_{32}$, the high-frequency modulations due to the interference of $(3, -2, 0)$, and the low-frequency ones due to the interference of $(2, 2, 0)$. It is also possible to appreciate how well the model (red and orange lines) can capture all these features. For spins $q \leq -0.9$, the waveforms asymptote to a frequency lying between $-\omega_{2-20}$ and $-\omega_{3-20}$, and we cannot extract the coefficients because $\omega^{\rm Teuk}_{32}$ has a very irregular behavior and we find it hard to determine the appropriate fitting window. This problematic regime is depicted in

the right panel of Fig. 4.10, where we plot the $(3,2)$ mode of spin -0.95.

4.6 Considerations on the modeling of comparable-mass binary systems

In this section we explain how the findings of Secs. 4.4 and 4.5 can help EOB waveform modeling.

The EOB approach employs factorized analytical (multipolar) waveforms that resum the circular PN formulae, while incorporating strong-field and non-circular effects [99–101, 120, 128] [5]. An example of strong-field feature is the divergence of the factorized modes at the light-ring for circular orbits through the "source" term proportional to the binding energy (angular momentum) for $\ell = m$ ($\ell \neq m$) modes. Deviations from circularity are modeled in the EOB waveforms through a phenomenological non-quasicircular (NQC) factor that reshapes the EOB factorized waveforms during plunge and around merger in order to better match the numerical waveforms (computed either with numerical-relativity or Teukolsky-equation codes). The NQC factor is determined once the numerical "input values" (i.e., the amplitude $|h^{\rm num}_{\ell m}|$, the slope $\partial_t |h^{\rm num}_{\ell m}|$, the curvature $\partial^2_t |h^{\rm num}_{\ell m}|$, the frequency $\omega^{\rm num}_{\ell m}$, the slope of the frequency $\partial_t \omega^{\rm num}_{\ell m}$) are prescribed. Typically, the input values are read off at the peak of the numerical waveforms, and, on the EOB side, they are enforced at a

[5] Reference [120] (see Appendices C and D) computed mode-by-mode amplitude fits of the Teukolsky modes generated by a frequency-domain code, which assumed circular orbits in Kerr. High, unknown PN terms in the factorized waveforms were fitted up to the ISCO, for both ingoing and outgoing radiation.

specific time relative to the peak of the orbital frequency (which occurs at $t = t^{\Omega}_{\rm peak}$). That same time is used as the attachment point for the ringdown waveform (for more details, see Sec. IV of Ref. [119]).

As discussed in Sec. 4.4, the very circular character of the Teukolsky waveforms when $q \to 1$ is very appealing from the point of view of the modeling, since the EOB factorized modes (without NQC corrections) are built under the assumption of quasicircular adiabatic motion. However, highly spinning systems are also very relativistic, and current PN waveforms (on which the factorized ones are based) are not accurate enough for such regimes already hundreds of cycles before merger. As already pointed out in Refs. [101, 119] by comparisons with frequency-domain Teukolsky waveforms, due to the lack of enough PN knowledge in the test-particle limit, the amplitude of the factorized waveforms performs poorly even before the ISCO for large spins, implying also inaccurate multipolar fluxes. While we were finalizing this paper, Ref. [252] was posted; the author computed the energy fluxes for a particle in circular, equatorial orbit in Kerr spacetime up to 20PN order. In spite of the high PN order of the calculation, the relative accuracy of the analytical flux (when compared to numerical Teukolsky data) is within 10^{-3} only down to $2.97 r_{\rm ISCO}$ for spin 0.9, i.e., for an orbital speed around 0.37 (to be compared with $v_{\rm ISCO} \approx 0.61$). As we shall see in Sec. 4.7, even modeling errors as small as 10^{-3} at the ISCO may result in large dephasings once the analytical fluxes are employed in time evolutions.

Moreover, as originally found in Ref. [119], the larger the spin, the earlier the $(2, 2)$ mode peaks with respect to $t^{\Omega}_{\rm peak}$: when $q \geq 0.9$, the peak occurs before the

ISCO, during the inspiral phase, where the radial motion is absolutely negligible, as we discussed in Sec. 4.4. As a consequence, when calculated at the amplitude peak, the NQC functions are heavily suppressed for large and positive spins, because they are proportional to $p_{r^*} \propto \dot{r}$ (see Fig. 4.6), and cannot help correcting the waveform. One could see what can be gained by applying the factorized resummation procedure to the PN-expanded fluxes of Ref. [252], or keep the current factorized flux while including the fits of Ref. [120], and obtain EOB amplitudes in greater agreement with the numerical ones without any need for NQC corrections. Note that the fits of Ref. [120] were computed up to the ISCO. Hence, after the peak, when the amplitude is falling off, the EOB waveform with fits can still differ from the Teukolsky one. However, applying an NQC correction at that late stage could be a viable option.

Furthermore, if we followed the standard EOB prescription of attaching the ringdown waveform at $t^{\ell m}_{\rm peak}$, we would not be able to successfully model the Teukolsky waveform, because its ringdown sets in at times which are rather close to the peak of the orbital frequency at time $t^{\Omega}_{\rm peak}$, while $t^{\ell m}_{\rm peak} \ll t^{\Omega}_{\rm peak}$. As we shall see below, to overcome this issue, we suggest a new prescription for the matching point of the ringdown in the EOB approach for small mass-ratios and large spins.

These findings for large spins were effectively exploited in the construction of the EOB model of Ref. [70], which extended the model of Ref. [93] to generic mass ratios and spins; only the dominant $(2, 2)$ mode was considered. The model was calibrated to 38 numerical-relativity nonprecessing waveforms produced by the SXS Collaboration [67,162,253,254], spanning mass ratios from 1 to 8, spin magnitudes up to 0.98, and with 40 to 60 GW cycles. By construction, any EOB model incorporates

the test-particle limit, since the whole formalism is based on a deformation of the Kerr spacetime [6]. As explained above, the merger waveform critically depends on the information from numerical-relativity waveforms, in the form of input values. Since numerical-relativity simulations are still unable to explore the small mass-ratio limit [7], the Teukolsky waveforms are extremely valuable in bridging the gap between mass ratio $\sim 1/10$ and $\sim 1/1000$.

The prototype nonprecessing, spinning EOB model of Ref. [93] (which could cover spins only up to 0.6) introduced, for the first time, a spin-dependent (negative) time delay $\Delta t^{22}_{\rm peak}$ between $t^{\Omega}_{\rm peak}$ and the peak of $|h_{22}|$, which was inspired by the time delay seen in the Teukolsky data of Ref. [119]. Such time delay had already been found in Ref. [233] for the (2,2) mode in nonspinning binaries with small mass ratio, but because the time delay in the nonspinning case is quite small, it was not needed when modeling the (2,2) mode of nonspinning, comparable-mass systems [91]. Furthermore, Ref. [93] fixed the small mass-ratio limit of $\omega^{\rm num}_{22}$ and $\partial_t \omega^{\rm num}_{22}$ based on the Teukolsky waveforms of Ref. [119]. In the same spirit of Ref. [93], some of us used the additional information on the test-particle limit provided in this paper (in particular, the behavior of the Teukolsky waveforms beyond spin 0.8) to extend the nonprecessing EOB model to any spin and mass ratio [70].

First, we built a time-delay function $\Delta t^{22}_{\rm peak}$ that, in the small mass-ratio limit,

[6] The deformation parameter is the symmetric mass ratio $m_1 m_2/(m_1+m_2)^2$, m_1 and m_2 being the BH masses.

[7] A roadmap for future, challenging numerical-relativity simulations is outlined in the first paper of the NRAR Collaboration [66].

decreases with spin beyond 0.8; this guarantees that the ringdown starts close to $t^{\Omega}_{\rm peak}$ and that the NQC equations are always enforced in a region with significant radial motion (at time $t^{\Omega}_{\rm peak} + \Delta t^{22}_{\rm peak}$), as opposed to the extremely circular region around the amplitude peak (at time $t^{22}_{\rm peak}$). As an example, in Fig. 4.2 we indicate with a vertical green line where the point $t^{\Omega}_{\rm peak} + \Delta t^{22}_{\rm peak}$ occurs for such time-delay function when the mass ratio is 1/1000 and the spin is 0.99: the point safely lies well after the ISCO, close to the light-ring. Remember that the analysis of Sec. 4.5.1 has shown that for $(2, 2)$ modes and large spin one can reliably attach the ringdown waveform at the light-ring.

Second, we built piecewise continuous fitting functions for the input values along the spin dimension [8] such that, beyond spin 0.8 and for mass ratio smaller than $\sim 1/100$, they approach $|h_{22}|$, $\partial_t |h_{22}|$, $\partial^2_t |h_{22}|$, ω_{22}, $\partial_t \omega_{22}$ of the EOB factorized waveform itself (without any spinning NQC correction), evaluated at time $t^{\Omega}_{\rm peak} + \Delta t^{22}_{\rm peak}$. This entails that, beyond spin 0.8 and for mass ratio 1/1000, the EOB model will not agree too well with the Teukolsky waveforms produced with the numerical flux, as in this paper. This is mainly a consequence of the limitation of the current factorized waveforms that we discussed above (especially as far as the amplitude is concerned). Imposing the exact Teukolsky input values beyond spin 0.8 at mass ratio 1/1000 would result in unwanted features (such as bumps in the inspiral amplitude), because the NQC corrections act only over short time intervals, while the factorized waveforms are discrepant over much longer spans for this corner

[8] Note that, in both EOB models of Refs. [93] and [70], the input values are functions of only two parameters: the symmetric mass ratio and an effective spin (see definition in Eq. (32) of Ref. [93]).

of the parameter space. This limitation will be overcome once the current factorized waveforms are improved.

Third, in the model of Ref. [70], the Teukolsky waveforms were also exploited to establish robust ringdown prescriptions in the small mass-ratio limit, especially for binaries with large spins. Indeed, we found it necessary to introduce mass-ratio and spin dependence in the ringdown tuning parameters (i.e., the size of the matching interval, frequency and decay time of the pseudo-QNMs).

Finally, in Appendix A we provide input values measured from the Teukolsky waveforms of this paper, as well as the measured time delay $\Delta t^{\ell m}_{\rm peak}$, as functions of the spin. This data can be used for future, improved versions of the EOB model.

4.7 The comparable-mass EOB model in the test-particle limit

In this section we compare the comparable-mass EOB model of Ref. [93] to the numerical waveforms computed via the Teukolsky formalism in the test-particle limit. Before discussing the waveforms, we have to point out that the orbital dynamics generated by the EOB model in this section is quite different from that generated following the prescriptions of Sec. 4.2. In fact, as already discussed, the EOB energy flux used in Ref. [93], which was based on Refs. [100, 101] and used all the PN corrections available at the time of publication, has several shortcomings in the test-particle limit.

First, the EOB energy flux used in Ref. [93] does not account for the ingoing

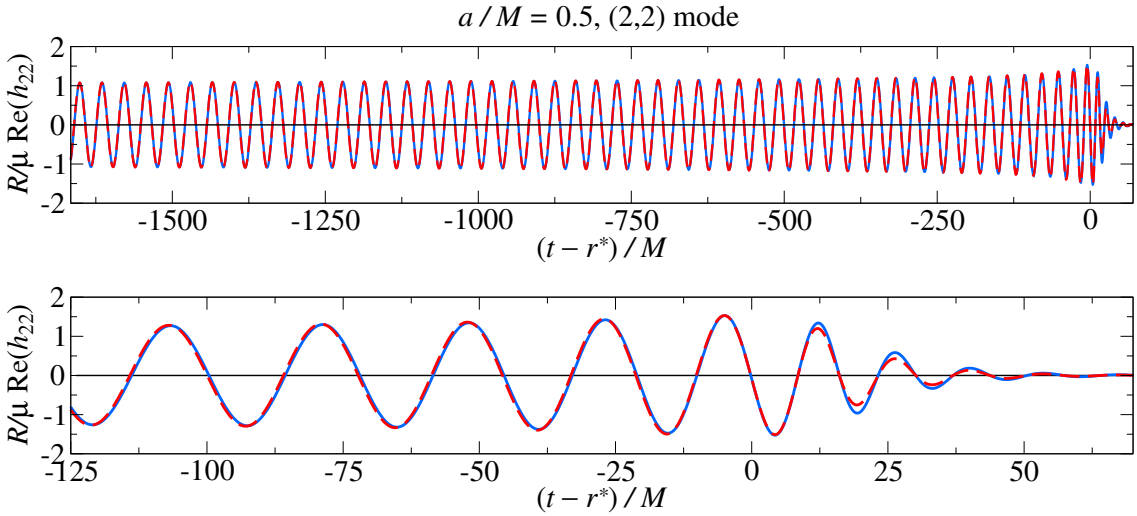

Figure 4.11: For spin 0.5, comparison between Teukolsky $(2,2)$ mode waveform (solid blue lines) and the EOB model of Ref. [93] evaluated in the test-particle limit (dashed red lines). The Teukolsky waveform is evaluated along the EOB trajectory. The waveforms are aligned at their amplitude peak, which corresponds to 0 retarded time; 50 GW cycles before the peak are shown. R is the distance to the source.

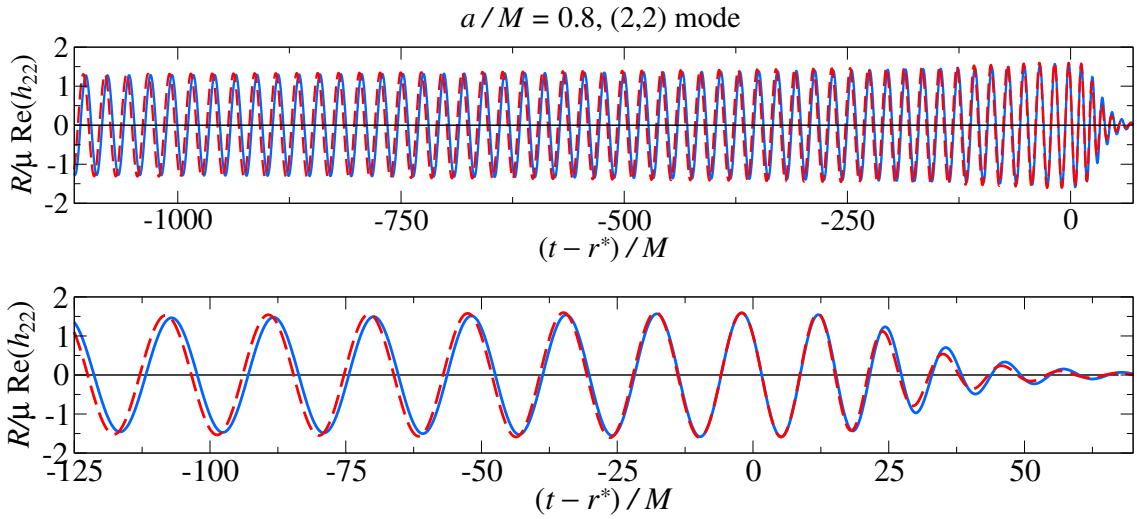

Figure 4.12: Same as Figure 4.11, but for spin 0.8.

portion of the GW flux. Horizon absorption has the largest effect for nearly extremal positive spins, thanks to the slower rate of energy loss, due to superradiance. Note that the relative sign between ingoing and outgoing fluxes changes when the orbital frequency crosses the horizon frequency. When $\Omega \leq \Omega_{\rm H}$ and $q > 0$, the ingoing fraction subtracts from the outgoing flux; otherwise, the absorption flux adds to the outgoing flux. For instance, when the spin is 0 (0.99), the absorption flux increases (decreases) dissipation by $\sim 0.3\%$ ($\sim 9\%$) for a particle orbiting at the ISCO (see Fig. 1 of Ref. [120]). References [116, 255] found that in the nearly extremal case $q = 0.998$ the inspiral up to the ISCO can be longer by $\sim 5\%$ at low inclinations, depending on whether the ingoing flux is included or not. A study extending up to merger was done in the Schwarzschild case by Ref. [235], which considered an EOB evolution including the model absorption flux of Ref. [128]; when the symmetric mass ratio is 10^{-3}, they found a dephasing of 1.6 rads for the (2,2) mode waveform at merger over an entire evolution of about 41 orbital cycles. As to the spinning case, Ref. [118] included the spinning horizon flux in an EOB model, using the Taylor-expanded expressions of Refs. [140, 141]; the inclusion of absorption turned out to be important to obtain good agreement with the full Teukolsky flux, at least up to the ISCO. When modeling spinning binaries, one should bear in mind that the spin changes the PN order (with respect to the leading order flux at infinity) at which absorption enters in the energy flux: while this effect enters at 4PN order for Schwarzschild BHs, it enters at 2.5PN order for nonzero spin.

To confirm the impact of neglecting the ingoing flux, we evolve trajectories with either the total or only the outgoing Teukolsky flux, relying again on the data

of Ref. [120]. We consider $(2,2)$ waveforms that begin 100 GW cycles before the ISCO. For comparison, we align their phases both at low frequency (over the first 10 GW cycles) and at high frequency [9] (over the 10 GW cycles following the ISCO), and then measure the phase difference either during ringdown (for the low frequency alignment) or at the beginning of the waveform (for the high frequency alignment), using the case with the total flux as fiducial. After the low frequency alignment, we find that for spin 0 (0.99) the horizon absorption induces a dephasing of about -2 ($+23$) rads. After the high frequency alignment, we find that for spin 0 (0.99) the horizon absorption induces a dephasing of about -0.1 ($+8$) rads. The different sign in the dephasings for spin 0 and 0.99 reflects the fact that for $q \leq 0$ the ingoing flux increases the rate of dissipation (thus hastening the coalescence), while for $q > 0$ superradiance extracts energy from the rotation of the massive BH and transfers it into the orbital motion (thus delaying the coalescence). These effects can play a major role for space-based GW detectors, whose integration time will have to be of the order of 10^6 GW cycles (or more) to achieve detection [256], hence requiring very long and accurate GW templates.

In principle, horizon absorption may also alter the merger waveform, which constitutes a numerical input for the EOB model via the NQC procedure outlined in Sec. 4.6. For $q = 0$ we compute the $(2,2)$ mode input values $|h_{22}^{\rm Teuk}|$, $\partial_t^2|h_{22}^{\rm Teuk}|$, $\omega_{22}^{\rm Teuk}$, $\partial_t\omega_{22}^{\rm Teuk}$ at $t_{\rm peak}^{22}$ (here, of course, $\partial_t|h_{22}^{\rm Teuk}| = 0$), while for $q = 0.99$, due to the flatness of the amplitude and the lack of an orbital frequency peak, we compute

[9] Note that aligning the waveforms at the amplitude peak is not an option, given their extreme flatness when $q = 0.99$.

them at the ISCO [10]. For spin 0 (0.99), the relative difference induced by horizon absorption on the four input values is respectively: 0.0014% (0.17%), 0.50% (5.8%), 0.082% (0.29%), and 0.091% (5.2%). Similar results apply to higher-order modes. The larger discrepancies can be seen on the curvature and on the slope of the GW frequency, but the NQC procedure is only mildly sensitive to these two quantities, as the most important features to reproduce are the amplitude and the GW frequency, which means that the horizon absorption does not impact the merger waveform significantly.

Second, as compared to the total outgoing Teukolsky flux, the current EOB energy flux does not account for modes with $\ell > 8$. We can quantitatively assess this truncation error in the frequency domain by using the multipolar components of the Teukolsky fluxes computed in Ref. [120]. We find that, for a particle orbiting at the ISCO, the fractional contribution to the total outgoing flux coming from modes beyond $\ell = 8$ varies between 10^{-5} for $q = -0.99$ and 3×10^{-3} for $q = 0.99$. The growing relevance of higher modes with spin is consistent with the trend that one sees when studying the amplitude hierarchy between the dominant $(2, 2)$ mode and higher modes [119]. For spins $q = 0, 0.99$, we compute the Teukolsky waveforms along trajectories sourced by Teukolsky flux modes only up to $\ell = 8$, and compare them to the waveforms generated using the total outgoing flux (taken as fiducial). We measure the dephasings with the same approach discussed above when studying the effect of horizon absorption. After the low frequency alignment, we find that

[10] For $q = 0.99$, the ISCO is only $0.3M$ away from the horizon in the radial coordinate. See also Fig. 4.2 for a more precise idea in the case of the $(2, 2)$ mode.

for spin 0 (0.99) the higher-ℓ modes induce a dephasing of about -0.3 (-7.5) rads. After the high frequency alignment, we find that for spin 0 (0.99) the higher-ℓ modes induce a dephasing of about -0.015 (-3) rads. The negative signs indicate that, obviously, whenever we neglect $\ell > 8$ modes the rate of dissipation is lower, hence the coalescence occurs later. These phase differences are less dramatic than those seen when neglecting the ingoing flux. Nonetheless, they are relevant for the purpose of generating templates for extreme and small mass-ratio inspirals.

Third, as discussed in Sec. 4.6, the modeling error on the amplitude of the individual factorized modes with $\ell \leq 8$ can be significant even before the ISCO for large spins: a more quantitative assessment of the disagreement with numerical amplitudes can be found in Ref. [101]. The origin of the poor performance lies in the limited PN knowledge, since for large spins the ISCO moves to a more relativistic regime: $v_{\rm ISCO} \approx 0.41$ when $q = 0$, while $v_{\rm ISCO} \approx 0.79$ when $q = 1$. Again, one could include the amplitude fits of Ref. [120] or apply the factorized resummation to the analytical energy flux of Ref. [252], and recalibrate the comparable-mass model to numerical-relativity simulations.

We now move on to discuss the waveforms. We evaluate the comparable-mass EOB model of Ref. [93] in the test-particle limit by setting the symmetric mass-ratio μ/M to zero everywhere in the model, except in the leading term of the GW flux, where we set it to 10^{-3}; this choice is consistent with the prescriptions of Sec. 4.2 for building orbital evolutions with the Teukolsky fluxes. The GW flux of the model is a sum of time derivatives of multipolar modes up to $\ell = 8$, according to Eq. (13) of Ref. [93]. All the modes are the ρ-resummed factorized ones of Ref. [101],

except those with $\ell \leq 4$ and odd m, which instead follow the prescription given in appendix A of Ref. [93]; test-particle limit nonspinning effects are included up to 5.5PN order (beyond the leading order), while spinning effects are included up to 4PN order (beyond the leading order). Here we are not interested in testing the EOB orbital dynamics, but we rather want to focus on the waveforms, therefore the Teukolsky waveforms are calculated along the EOB trajectories. The same approach was adopted in Ref. [119] for the case with spin 0. For spins as large as $q \sim 0.5$, the EOB waveforms are in good agreement with the numerical waveforms. In Fig. 4.11, for $q = 0.5$, we align EOB and Teukolsky $(2, 2)$ mode waveforms at the amplitude peak; we find a dephasing within 0.1 rads and a relative amplitude error which is negligible everywhere except during ringdown (where it is around 30%). For larger spins, however, a large discrepancy in the amplitude shows up well before merger. In Fig. 4.12, for $q = 0.8$, we find an amplitude error around 5% during the late inspiral; the dephasing is quite large too, reaching about 0.8 rads 50 GW cycles before merger, and growing as one moves to lower frequencies.

4.8 Conclusions

Using the Teukolsky equation in the time domain, we have computed inspiral-merger-ringdown waveforms produced by the inspiraling motion of a nonspinning test particle in the equatorial plane of a Kerr BH with dimensionless spin $-0.99 \leq q \leq 0.99$, thus extending work done in Ref. [119]. The trajectory of the particle has been obtained from the geodesic equation, subject to a radiation-reaction force that

is proportional to the total energy flux in GWs. We have used the GW fluxes computed for circular orbits down to the light-ring with a frequency-domain Teukolsky code [120]. We have computed the dominant and leading subdominant modes of the radiation: $(2,2)$, $(2,1)$, $(3,3)$, $(3,2)$, $(4,4)$, and $(5,5)$.

In Sec. 4.4, we have pointed out the simplicity of the waveforms emitted by systems with large, positive spins, in spite of the highly relativistic regime probed by the inspiraling orbital trajectories. The main feature of the mode amplitudes is their flattening towards the ISCO and during the plunge as the spin grows (see Fig. 4.3). We have given an explanation of this phenomenon in terms of the ratio between the orbital and the radiation-reaction timescales. On the one hand, as $q \to 1$ the total (i.e., ingoing + outgoing) GW flux tends to decrease, partly thanks to the extraction of energy from the rotation of the Kerr BH via superradiance. On the other hand, as $q \to 1$ the horizon (i.e., the final point of the orbital evolution) moves to smaller radii, which implies higher orbital frequencies accessible to the inspiraling particle. This results in a significant increase in the number of orbits per unit frequency as $q \to 1$; the orbital motion becomes extremely circular, and highly relativistic.

In Sec. 4.5, we have systematically studied the ringdown stage, whose waveforms display complicated amplitude and frequency modulations due to the interference of QNMs. In the comparable-mass range, with the notable exception of the $(3,2)$ mode, the (ℓ, m) modes of nonprecessing BH binaries can be successfully modeled by the linear superposition of overtones of the least-damped QNM, i.e., (ℓ, m, n), with $n = 0, 1, \cdots$ [62, 63, 91, 246–250]. However, in the extreme and small mass-ratio regime, other QNMs can be excited [99, 119, 123–126]. We have found

that, for $\ell = m$ modes, the QNM mixing is present when $q \leq 0$ (see Fig. 4.8), and arises mainly due to modes with opposite m, whose excitation grows as the spin decreases; for negative spins, the orbit changes direction during plunge (since the particle eventually locks to the rotating BH horizon), thus exciting $(\ell, -m, 0)$ modes. For $\ell \neq m$ modes, instead, we have found QNM mixing across the entire spin range. For the $(2, 1)$ mode, the main source of mixing is the $(2, -1, 0)$ QNM. For the $(3, 2)$ mode (see Fig. 4.7), we have recognized 3 different behaviors: when $q \gtrsim 0.8$ the ringdown is dominated by $(2, 2, 0)$ with contamination from $(3, 2, 0)$; when $0 < q \lesssim 0.7$, the ringdown is dominated by $(3, 2, 0)$ with contamination from $(2, 2, 0)$; when $q \leq 0$, the ringdown is dominated by $(3, 2, 0)$ with contamination from both $(3, -2, 0)$ and $(2, 2, 0)$. The excitation of QNMs with the same m, but with different ℓ, is understood as a basis effect, since the QNMs are computed in a -2-spin-weighted spheroidal-harmonic separation of the Teukolsky equation, while the waveforms used in modeling are decomposed in -2-spin-weighted spherical-harmonic modes. We have fitted the relative amplitude between the main QNMs that are interfering for each mode (see Tables 4.1 and 4.2), and have been able to model the ringdown Teukolsky waveforms using Eq. (4.5) for all spins except $q = -0.95, -0.99$ for all modes, and also $q = -0.9$ for the (3,2) mode.

In Sec. 4.6, we have discussed how the inspiral-merger-ringdown Teukolsky waveforms helped the extension of the comparable-mass EOB model for nonprecessing, spinning BH binaries of Ref. [70] to small mass ratios and large spins. In particular, a time delay $\Delta t^{22}_{\rm peak}$ was introduced between the orbital frequency peak $t^{\Omega}_{\rm peak}$ and the point $t^{\Omega}_{\rm peak} + \Delta t^{22}_{\rm peak}$ where non-quasicircular corrections are applied

to the merger waveform. The specific dependence of the time-delay function on the spin takes into account the extreme circularity of the orbits encountered in the test-particle limit for large spins, and guarantees that $t^{\Omega}_{\rm peak} + \Delta t^{22}_{\rm peak}$ always lies in a region with significant radial motion. Older EOB models took $t^{\Omega}_{\rm peak} + \Delta t^{22}_{\rm peak}$ to coincide with the peak of the amplitude; however, in this paper, we have shown that such prescription is not adequate in the test-particle limit and, more generally when the mass ratio is smaller than $\sim 1/100$ if $q > 0.8$, since the peak occurs much before the ISCO and light-ring. The Teukolsky waveforms were also exploited to build fitting functions for the input values (i.e., $|h_{22}|$, $\partial_t^2|h_{22}|$, ω_{22}, $\partial_t\omega_{22}$ at a point in time during merger) which are needed to impose non-quasicircular corrections to the merger EOB waveform.

Finally, in Sec. 4.7, we have evaluated the comparable-mass EOB model of Ref. [70] in the test-particle limit, and compared it to Teukolsky waveforms computed along the same EOB trajectory. We have found that, up to a spin $\sim$ 0.5, the EOB waveforms (based on the factorized resummation of PN formulae in Refs. [100, 101]) perform well, with phase differences within 0.1 rads and amplitude errors which are negligible up to merger (see Fig. 4.11). For larger spins, instead, while the EOB model can produce a reasonable $(2, 2)$ mode waveform (see Fig. 4.12), still it disagrees with the Teukolsky data, due to the poor performance of the current factorized waveforms in such highly relativistic regimes — for example for $q = 0.8$, we find an amplitude error around 5% during the late inspiral and a dephasing of about 0.8 rads 50 GW cycles before merger, and growing as one moves to lower frequencies. We have also discussed the limitations of the current factorized

EOB energy flux, namely the lack of horizon-absorption terms and the truncation at $\ell = 8$ modes.

The natural extension of this project will consider inclined orbits in Kerr spacetime. Even at the level of geodetic motion, there exist orbits with constant separation and inclination (with respect to the direction of the Kerr spin), which display precession of the orbital plane. Thus, these orbits will radiate waveforms which carry amplitude and phase modulations due to the precession. On the analytical side, we have shown in this paper several limitations of the current EOB factorized flux [100, 101] for large spins. Thus, it will be crucial to improve this flux in the future either by designing a new resummation scheme, or by incorporating higher-order PN terms that have been recently computed [252]. Moreover, the current EOB flux was developed for nonprecessing BH binaries only; we plan to test different prescriptions that could extend its validity to the precessing case. Such work can help the more challenging EOB modeling of precessing, comparable-mass BH binaries, which has first been tackled in Ref. [194].

Chapter 5: **Modeling the horizon-absorbed gravitational flux for equatorial circular orbits in Kerr spacetime**

Authors: *Andrea Taracchini, Alessandra Buonanno, Scott A. Hughes, and Gaurav Khanna*[1]

Abstract: We propose an improved analytical model for the horizon-absorbed gravitational-wave energy flux of a small body in circular orbit in the equatorial plane of a Kerr black hole. Post-Newtonian (PN) theory provides an analytical description of the multipolar components of the absorption flux through Taylor expansions in the orbital frequency. Building on previous work, we construct a mode-by-mode factorization of the absorbed flux whose Taylor expansion agrees with current PN results. This factorized form significantly improves the agreement with numerical results obtained with a frequency-domain Teukolsky code, which evolves through a sequence of circular orbits up to the photon orbit. We perform the comparison between model and numerical data for dimensionless Kerr spins $-0.99 \leq q \leq 0.99$ and for frequencies up to the light ring of the Kerr black hole. Our proposed model enforces the presence of a zero in the flux at an orbital frequency equal to the frequency of the horizon, as predicted by perturbation theory. It also

[1]Originally published as Phys. Rev. D **88**, 044001 (2013)

reproduces the expected divergence of the flux close to the light ring. Neither of these features are captured by the Taylor-expanded PN flux. Our proposed absorption flux can also help improve models for the inspiral, merger, ringdown of small mass-ratio binary systems.

5.1 Introduction

Extreme-mass-ratio inspirals (EMRIs) are among the most interesting candidate sources for future space-based gravitational wave (GW) detectors. In these systems a particle/small body, like a star or a black hole (BH), orbits a supermassive BH and spirals in due to energy losses in GWs. Computational modeling of EMRIs is uniquely challenging due to the long duration and the high level of accuracy required in the waveforms for the purposes of detection [256]. This implies that the orbital dynamics needs to be computed over long time intervals with sufficient accuracy. To lowest order in the mass ratio, EMRIs can be described using black hole perturbation theory to compute how the "self force" produced by the small body interacts with its own spacetime deformation (see, e.g., Refs. [257, 258] for recent reviews). If the system evolves slowly enough, the impact of *dissipative* self-forces can be described using the Teukolsky equation [97] to compute the slowly changing evolution of the integrals of Kerr geodesic orbits (i.e., an orbit's energy, angular momentum, and Carter constant). The inspiral is then well described by a slowly evolving sequence of geodesic orbits. In Refs. [116, 117, 129–132], this approach has been pursued through purely numerical schemes.

Purely analytical approaches and modeling are also viable. Since the motion of the particle eventually becomes significantly relativistic, a post-Newtonian (PN) treatment [60, 259, 260] of this problem (taking the limit of small mass ratio) is bound to fail toward the end of the inspiral. In fact, PN theory used for long-time integration of EMRIs leads to significant discrepancies in the number of orbital cycles. These accumulate rather uniformly during the inspiral, even before reaching the innermost stable circular orbit (ISCO) [261]. More suitable approaches are BH perturbation theory and the self-force formalism [97, 258], which include all relativistic effects but expand in the small mass-ratio parameter.

In this work we focus on a specific aspect of the problem, namely the GW energy flux absorbed by the BH horizon. The particle orbiting the central Kerr BH radiates GWs, which partly leave the binary toward null infinity (and constitute the so-called flux at infinity) and partly fall into the event horizon (and constitute the so-called absorption flux). Interest in the absorption flux was shown as early as the 1970s, when Ref. [262] investigated its possible impact on the dynamics of bodies in the vicinity of the supermassive BH at the center of our galaxy.

For some orbits and black-hole spins, the absorption of GWs by the event horizon can be described as a Penrose-like process [133], i.e., as the extraction of rotational energy of the Kerr BH by means of negative-energy GWs. The "absorbed" flux in these cases is actually negative. Reference [134] formally suggested this Penrose-like interpretation for scalar (instead of gravitational) perturbations of a Kerr BH using the Teukolsky equation. The authors also looked for orbits that would have a perfect balance between the energy losses in scalar waves to infinity and

the aforementioned energy extraction. Such orbits would have a constant radius and were named "floating orbits."[2] Subsequently, Ref. [115] extended the calculation of the ingoing energy flux to gravitational perturbations of a Kerr BH [see in particular Eq. (4.44) therein], and computed it numerically for different values of the spin of the central object [see Fig. 2 in Ref. [115]]. Reference [264] later definitively ruled out the existence of floating orbits in the case of gravitational perturbations. More recent work [265] suggests that floating orbits can only exist around central bodies with an extremely unusual multipolar structure. In the context of alternative theories of gravity, it was shown [266] that floating is possible when massive scalar fields coupled to matter are present.

Further insight into the horizon-absorbed flux in a BH binary system can be gained from a parallel with the phenomenon of tides. For a recent review, see Ref. [135]. In the early 1970s, Refs. [136, 137] computed how a stationary particle tidally perturbs a slowly rotating Kerr BH, finding that the BH dissipates energy by spinning down. The same phenomenon happens in a Newtonian binary system, such as when a moon perturbs a slowly rotating planet (treated as a fluid body with viscosity). This phenomenon is known as "tidal heating." Somewhat remarkably, there is a close analogy between the spin-down of a black hole and the spin-down of a fluid body due to the tidal interaction: The tidal interaction raises a bulge on the black hole's event horizon, and one can regard that bulge as exerting a torque on the orbit. This torque spins up or spins down the hole, depending on the relative

[2]Similar behavior was noted by Hod in the context of massive-scalar fields, so-called "stationary clouds" [263].

frequency of the orbit and the hole's rotation. Using the membrane paradigm [138], one can even associate an effective viscosity to the black hole. The hole's viscosity relates the rate at which the horizon's generators are sheared to the rate at which the hole's area (or entropy) is increased. The black hole's viscosity plays an important role in determining the geometry of the hole's bulge, much as the viscosity of a fluid body in part determines the geometry of its tidal bulge.

A renewed interest in the BH-absorption flux was rekindled in the 1990s, when, using BH perturbation theory, Ref. [139] computed in full analytical form the leading-order absorption flux for a particle in a circular orbit around a Schwarzschild BH. These initial results indicated that the horizon flux is suppressed relative to the flux to infinity by a factor of v^8, where v is the orbital speed. This result was then generalized to the spinning case in Refs. [140, 141], where the ingoing flux was computed up to 6.5PN order beyond the leading order luminosity at infinity. Spin dramatically changes the leading impact of the horizon flux: The suppression factor becomes $(v^3 - q)v^5$ (where $q \equiv a/M$ is the Kerr parameter per unit mass). Numerical studies of strong field radiation reaction showed that neglect of the horizon flux would introduce large errors into Kerr inspiral models — many thousands of radians for inspiral into rapidly rotating black holes [131].

The extension to comparable-mass BH binaries was first attempted in Ref. [267], which computed the changes in mass and angular momentum of the holes up to 4PN order beyond the leading order luminosity at infinity. Reference [268] constructed a general approach to this problem, deriving formulas for the flow of energy and angular momentum into a BH as functions of the generic tidal fields perturbing

it. This formalism was applied in Ref. [269] to the specific tidal environment of a comparable-mass binary in the slow-motion approximation, allowing the computation of the spinning absorption fluxes to higher PN order than Ref. [267]. Recently Ref. [270] pushed the calculation of Ref. [269] to an even higher PN order. Recent numerical work [271] found horizon absorption to be crucial in the ultrarelativistic grazing collision of comparable-mass BHs, in that it puts a limit on the maximum radiation that can be produced in such events.

In recent years, significant effort has been put into improving the analytical modeling of the GW fluxes, both ingoing and at infinity, with respect to the exact, numerical solution of the Teukolsky equation. In particular, Refs. [99, 100] proposed a factorization of the Taylor-expanded PN formulas for the flux at infinity in the Schwarzschild case, improving the agreement with the numerical data. Reference [101] extended this approach to the spinning case. Later on Ref. [128] applied the same idea of factorizing the Taylor-expanded PN predictions to the absorption flux in the nonspinning limit, extending the model also to comparable-mass binaries. Our work has the primary goal of studying the factorization of the BH-absorption flux for the Kerr case. The orbits we consider are circular and lie in the equatorial plane of the central, rotating BH. The PN-expanded formulas for the spinning absorption flux can be found in Refs. [140, 141].

An improved analytical modeling of the GW fluxes in the test-particle limit is crucial because of the practical need for fast generation of reliable time-domain waveforms for these systems. Several papers [118, 119, 126, 233–235] have already incorporated analytical fluxes into effective-one-body (EOB) models for EMRIs. One

solves the Hamilton equations for the Kerr Hamiltonian with dissipation effects introduced through a radiation-reaction force that is proportional to the GW flux. As far as the ingoing flux is concerned, Ref. [118] worked with spinning EMRIs, including the BH-absorption terms in Taylor-expanded PN form [140, 141]. The authors of Ref. [235] focused on the nonspinning case, and used the factorized nonspinning absorption flux of Ref. [128]. Our work can be regarded as a step beyond Ref. [118] toward building a high-quality EOB model for EMRIs with spinning black holes. Besides the specific problem of the long inspiral in EMRIs, the EOB model has proven effective in describing the whole process of inspiral, merger and ringdown — for example Ref. [114] has used the results of this work to model merger waveforms from small mass-ratio binary systems for any BH spin.

This paper is organized as follows. In Sec. 5.2 we discuss the numerical computation of energy fluxes at infinity and into the BH horizon using the frequency-domain Teukolsky equation. We investigate the behavior of these fluxes close to the photon orbit, discussing their main features. In Sec. 5.3 we review the factorization of the analytical GW fluxes computed in PN theory and apply it to the spinning BH-absorption flux. In Sec. 5.4 we show comparisons of the factorized and Taylor-expanded PN fluxes to the numerical fluxes. In Sec. 5.5 we conclude and discuss future research. Appendix B discusses in more depth aspects of the near-light-ring fluxes, in particular how these fluxes diverge at the photon orbit, and how this divergence can be analytically factored from the fluxes. Appendix C contains the explicit formulas for a particular choice of the factorization model of the BH-absorption flux. Last, in Appendices D and E we provide fits to the Teukolsky-equation fluxes that

can be employed for accurate evolution of EMRIs or inspiral, merger, and ringdown waveforms for small mass-ratio binary systems.

Throughout this paper, we use geometrized units with $G = c = 1$. We use μ to label the mass of the small body; M and $q \equiv a/M$ are the mass and dimensionless spin of the Kerr black hole, respectively. The spin parameter q ranges from -1 to $+1$, with positive values describing prograde orbits, and negative values retrograde ones. With this convention, the orbital angular momentum L_z and orbital frequency Ω are always positive. When we discuss radiation and fluxes, we will often decompose it into modes. Through most of the paper, we decompose the radiation using spheroidal harmonics $S_{\ell m\omega}(\theta, \phi)$, discussed in more detail in Sec. 5.2. In Sec. 5.3, we will find it useful to use an alternative decomposition into spherical harmonics, $Y_{lm}(\theta, \phi)$. We will strictly use the harmonic indices (ℓ, m) for spheroidal harmonics and (l, m) for spherical harmonics.

5.2 Numerical computation of the gravitational-wave fluxes

In this section we first outline how we numerically compute GW fluxes (both ingoing and at infinity) by solving the frequency-domain Teukolsky equation. Much of this has been described in detail in other papers, in particular, Refs. [116, 117], so our discussion just highlights aspects that are crucial to this paper. Then, we discuss the main characteristics of those fluxes, their strength as a function of the spin and their behavior close to the photon orbit.

5.2.1 Synopsis of numerical method

The Teukolsky "master" equation is a partial differential equation in Boyer-Lindquist coordinates r, θ, and t (the axial dependence is trivially separated as $e^{im\phi}$). It describes the evolution of perturbing fields of spin weight s to a Kerr black hole [97]. The equation for $s = -2$ describes the curvature perturbation ψ_4, a projection of the Weyl curvature tensor that represents outgoing radiation. With some manipulation, solutions for $s = -2$ give radiation at the hole's event horizon as well [115].

The master equation for $s = -2$ separates by introducing the multipolar decomposition

$$\psi_4 = \frac{1}{(r - iMq\cos\theta)^4} \int_{-\infty}^{\infty} d\omega \sum_{\ell m} R_{\ell m\omega}(r) S^{-}_{\ell m\omega}(\theta,\phi) e^{-i\omega t} \, . \tag{5.1}$$

Here and elsewhere in this paper, any sum over ℓ and m is taken to run over $2 \leq \ell < \infty$ and $-\ell \leq m \leq \ell$, unless explicitly indicated otherwise. The function $S^{-}_{\ell m\omega}(\theta,\phi)$ is a spheroidal harmonic of spin weight -2; the minus superscript is a reminder of this spin weight. It reduces to the spin-weighted spherical harmonic when $qM\omega = 0$: $S^{-}_{\ell m\omega}(\theta,\phi) = Y^{-}_{\ell m}(\theta,\phi)$ in this limit. The radial dependence $R_{\ell m\omega}(r)$ is governed by the equation

$$\Delta^2 \frac{d}{dr}\left(\frac{1}{\Delta}\frac{dR_{\ell m\omega}}{dr}\right) - V(r) R_{\ell m\omega} = -\mathcal{T}_{\ell m\omega}(r) \, . \tag{5.2}$$

The quantity $\Delta = r^2 - 2Mr + M^2q^2$ and the potential $V(r)$ can be found in Refs. [116, 117]. Note that in Eqs. (5.1), (5.2), (5.3), and (5.4), the variable r labels the coordinate of an arbitrary field point. This is true only in these specific equations;

elsewhere in this paper, r gives the radius of a circular orbit.

Equation (5.2) is often called the frequency-domain Teukolsky equation, or just the Teukolsky equation. The source $\mathcal{T}_{\ell m\omega}(r)$ is built from certain projections of the stress-energy tensor for a small body orbiting the black hole:

$$T_{\alpha\beta} = \frac{\mu u_\alpha u_\beta}{\Sigma \sin\theta (dt/d\tau)} \delta[r - r_{\rm o}(t)]\delta[\theta - \theta_{\rm o}(t)]\delta[\phi - \phi_{\rm o}(t)] \, . \tag{5.3}$$

The subscript "o" means "orbit" and labels the coordinates of an orbiting body's worldline. We focus on circular equatorial orbits, so $\theta_{\rm o}(t) = \pi/2$, and $r_{\rm o}(t) = r_{\rm orb} =$ constant. Notice the factor $(dt/d\tau)^{-1}$ that appears here. As the light ring (LR) is approached, $dt/d\tau \to 0$, and this factor introduces a pole into the energy fluxes. We discuss the importance of this pole in more detail below, and describe how it can be analytically factored from the fluxes in Appendix B.

We consider orbits from $r_{\rm orb}$ near the light ring out to a very large radius ($r_{\rm orb} \simeq 10^4 M$). Previous work has typically only considered orbits down to the ISCO. However, our code can solve Eq. (5.2) for any bound orbit, including unstable ones.[3] No modifications are needed to broaden our study to these extremely strong-field cases, though there are some important considerations regarding convergence, which we discuss below.

We solve Eq. (5.2) by building a Green's function from solutions to the homogeneous equation (i.e., with $\mathcal{T}_{\ell m\omega} = 0$) and then integrating over the source; see

[3] In Ref. [118], we stated that our code did not work inside the ISCO because there are no stable orbits there. It is true that we cannot relate the fluxes to quantities like the rate of change of orbital radius, inside the ISCO, but the code can compute fluxes from unstable orbits perfectly well in this regime.

Refs. [116, 117] for details. The resulting solutions have the form

$$R_{\ell m\omega}(r) = \begin{cases} Z^{\rm H}_{\ell m\omega} R^{\infty}_{\ell m\omega}(r) & r \to \infty, \\ Z^{\infty}_{\ell m\omega} R^{\rm H}_{\ell m\omega}(r) & r \to r_+, \end{cases} \tag{5.4}$$

where

$$Z^{\rm H}_{\ell m\omega} = C^{\rm H} \int_{r_+}^{r_{\rm orb}} dr' \frac{R^{\rm H}_{\ell m\omega}(r') \mathcal{T}_{\ell m\omega}(r')}{\Delta(r')^2} , \tag{5.5}$$

$$Z^{\infty}_{\ell m\omega} = C^{\infty} \int_{r_{\rm orb}}^{\infty} dr' \frac{R^{\infty}_{\ell m\omega}(r') \mathcal{T}_{\ell m\omega}(r')}{\Delta(r')^2} , \tag{5.6}$$

and where $R^{\star}_{\ell m\omega}(r)$ are the homogeneous solutions from which we build the Green's function ($\star$ means ∞ or H, as appropriate). The symbol $C^{\star}$ is shorthand for a collection of constants whose detailed form is not needed here (see Sec. III of Ref. [117] for further discussion).

The code we use to compute these quantities is described in Refs. [116, 117], updated to use the methods introduced by Fujita and Tagoshi [272, 273] (see also Ref. [60]). This method expands the homogeneous Teukolsky solutions as a series of hypergeometric functions, with the coefficients of these series determined by a three term recurrence relation, Eq. (123) of Ref. [60]. Successfully finding these coefficients requires that we first compute a number ν that determines the root of a continued fraction equation, Eq. (2.16) of Ref. [272]. Provided we can find ν, we generally find very accurate[4] solutions for $R^{\star}_{\ell m\omega}$. However, there are some cases, very close to the light ring and for $\ell \gtrsim 60$, in which our code fails to find a solution

[4]We estimate our solutions to have a fractional error $\sim 10^{-14}$ in these cases. Fujita has provided numerical data computed with an independent Teukolsky solver. We find 15 or more digits of agreement in our computed amplitudes in all cases.

for ν. In these cases, the root of the continued fraction lies so close to a pole of this equation that our root finder cannot distinguish root from pole. (Figures 4 and 5 of Ref. [272] show examples of the pole and root structure of this equation for less problematic cases.) We discuss where this limitation impacts our analysis below.

For periodic orbits, the coefficients $Z^{\star}_{\ell m\omega}$ have a discrete spectrum,

$$Z^{\star}_{\ell m\omega} = Z^{\star}_{\ell m}\delta(\omega - \omega_m) \,, \tag{5.7}$$

where $\omega_m = m\Omega$, with Ω the orbital frequency of the small body. The amplitudes $Z^{\star}_{\ell m}$ then completely determine the fluxes of energy and angular momentum:

$$\dot{E}^{\infty} = \sum_{\ell m} \frac{|Z^{\rm H}_{\ell m}|^2}{4\pi\omega_m^2} \equiv \sum_{\ell m} F^{\infty}_{\ell m,{\rm Teuk}} = F^{\infty}_{\rm Teuk} \,, \tag{5.8}$$

$$\dot{E}^{\rm H} = \sum_{\ell m} \frac{\alpha_{\ell m}|Z^{\infty}_{\ell m}|^2}{4\pi\omega_m^2} \equiv \sum_{\ell m} F^{\rm H}_{\ell m,{\rm Teuk}} = F^{\rm H}_{\rm Teuk} \,. \tag{5.9}$$

For circular and equatorial orbits, fluxes of angular momentum are simply related to energy fluxes: $\dot{E}^{\star} = \Omega\dot{L}^{\star}$.

The factor $\alpha_{\ell m}$ that appears in fluxes on the horizon arises from converting the curvature scalar ψ_4 to ψ_0 in order to determine, via the area theorem, the rate at which the black hole's mass and spin change due to tidal coupling with the orbiting body (see Ref. [115] for discussion). The fluxes carried by radiation are then determined by imposing global conservation of energy and angular momentum.[5] This factor is given by

$$\alpha_{\ell m} = \frac{256(2Mr_+)^5 p_m(p_m^2+4\epsilon^2)(p_m^2+16\epsilon^2)\omega_m^3}{|c_{\ell m}|^2} \,, \tag{5.10}$$

[5]Our ability to use these conservation laws follows from the fact that the Kerr spacetime admits timelike and axial Killing vectors.

where $r_+/M = 1 + \sqrt{1-q^2}$ and $M\Omega_{\rm H} = q/(2r_+)$ are the radial position and frequency of the event horizon, $p_m = \omega_m - m\Omega_{\rm H}$, $\epsilon = \sqrt{1-q^2}/(4r_+)$, and

$$\begin{aligned} |c_{\ell m}|^2 &= \left[(\lambda+2)^2 + 4mqM\omega_m - 4q^2M^2\omega_m^2\right](\lambda^2 + 36mqM\omega_m - 36q^2M^2\omega_m^2) \\ &+ (2\lambda+3)(96q^2M^2\omega_m^2 - 48mqM\omega_m) + 144M^2\omega_m^2(1-q^2)\ . \end{aligned} \tag{5.11}$$

In this quantity,

$$\lambda = \mathcal{E}_{\ell m} - 2qMm\omega_m + q^2M^2\omega_m^2 - 2\ . \tag{5.12}$$

(Note that the subscript was incorrectly left off of ω_m when λ was defined in Ref. [118].) The number $\mathcal{E}_{\ell m}$ is the eigenvalue of the spheroidal harmonic; in the Schwarzschild limit, it reduces to $\ell(\ell+1)$. Notice that $\alpha_{\ell m} \propto p_m \propto (\Omega - \Omega_H)$. This means that the horizon flux is negative when $\Omega < \Omega_H$, consistent with the leading order result, Eq. (5.21).

All the data computed with these methods will be referred to as "numerical data" in the rest of the paper.

5.2.2 Discretization of orbits and convergence of the flux sums

We compute these fluxes on a pair of grids evenly spaced in the velocity variable

$$v \equiv (M\Omega)^{1/3} = \left[(r/M)^{3/2} + q\right]^{-1/3}\ . \tag{5.13}$$

(In this section and beyond, there is no longer an ambiguity between labels for field point or orbital radius. In the remainder of the paper, r will label the radius of a circular orbit.) Our "outer" grid consists of 10^4 points spaced from $v = 0.01$

($r \simeq 10^4 M$) to the ISCO radius [122],

$$\begin{aligned}
\frac{r_{\rm ISCO}}{M} &= 3 + Z_2 \mp \sqrt{(3-Z_1)(3+Z_1+2Z_2)}\,, \\
Z_1 &= 1 + (1-q^2)^{1/3}\left[(1+q)^{1/3} + (1-q)^{1/3}\right]\,, \\
Z_2 &= (3q^2 + Z_1^2)^{1/2}\,. \qquad (5.14)
\end{aligned}$$

[The upper sign in Eq. (5.14) is for prograde orbits, $q > 0$, and the lower for retrograde, $q < 0$.] Our "inner" grid consists of 100 points spaced from the ISCO to just outside the light ring: $r_{\rm min} = r_{\rm LR} + 0.01M$, where [122]

$$\frac{r_{\rm LR}}{M} = 2\left[1 + \cos\left(\frac{2}{3}\arccos(-q)\right)\right]\,. \qquad (5.15)$$

In some cases, we put $r_{\rm min} = r_{\rm LR} + 0.009M$. This is to avoid the problem mentioned in the text following Eq. (5.6): For very strong-field (large Ω) orbits, when $\ell \gtrsim 60$, we sometimes find a value of $m\Omega$ for which we cannot find the number ν, and hence cannot solve the Teukolsky equation. The cause of this difficulty, as mentioned above, is that we compute ν by finding a root of a particular continued fraction equation, Eq. (2.16) of Ref. [272]. This equation also has several poles. When $m\Omega$ and ℓ are large, the roots and poles can be so close to one another that they cannot be distinguished at double precision, and this method fails for that multipole. This (rather annoying) behavior will be discussed in more detail in a forthcoming paper [274]. For our purposes, it suffices to note that we find empirically that modifying the grid slightly to avoid those problematic frequencies fixes this problem.

For circular, equatorial orbits, the largest contributions to the sums for $F^\star$ tend to come at small ℓ (usually $\ell = 2$), and then fall off as explained in Eq. (5.18) as we go

to higher values of ℓ. We consider a sum to have "converged" when we reach a value $\ell \equiv \ell_{\rm max}$ such that the fractional change in the sum due to all terms with $\ell = \ell_{\rm max}$ is smaller than 10^{-14} for three consecutive values of ℓ. This criterion was also used in Ref. [118]. For all orbits up to and including the ISCO, we were able to achieve this convergence for every spin that we examined. However, the $\ell_{\rm max}$ needed varies considerably with spin, mostly because the location of the ISCO varies strongly with spin: The deeper into the strong field we must go, the more multipoles are needed for convergence. For Schwarzschild, convergence required going to $\ell_{\rm max} = 30$ at the ISCO. For prograde $q = 0.99$, the same level of convergence took us to $\ell_{\rm max} = 66$ at the ISCO.

We were unable to achieve this convergence criterion for all orbits inside the ISCO. As we approach the light ring, the falloff of contributions to the flux sums becomes shallow, and the number of multipoles needed to converge becomes extremely large. At our innermost grid point $r_{\rm min}$, for $\ell \sim 70$ we find

$$\frac{F^\star_\ell}{F^\star_{\ell-1}} \simeq 1 - \epsilon \,, \tag{5.16}$$

where $F^\star_\ell \equiv \sum_m F^\star_{\ell m}$, $\epsilon \approx$ a few $\times\, 0.01$. This is consistent with past analytical work on geodesic synchrotron radiation [242–245], which showed that a similar flux quantity (defined by summing over all allowed values of ℓ for a fixed m) is proportional to $(m_{\rm c}/m)\exp(-2m/m_{\rm c})$, where

$$m_{\rm c} \equiv \frac{2\sqrt{3}}{\pi}\frac{r_{\rm LR}/M + 3}{\sqrt{r_{\rm LR}/M}}\left(\frac{E}{\mu}\right)^2 \,, \tag{5.17}$$

and E is the binding energy for circular orbits given in Eq. (5.29), which diverges at the light ring as $(r - r_{\rm LR})^{-1/2}$. The sums are dominated by the $\ell = |m|$ contribu-

tions, so either limiting form — $(m_{\rm c}/m)\exp(-2m/m_{\rm c})$ or $(\ell_{\rm c}/\ell)\exp(-2\ell/\ell_{\rm c})$ — is accurate. In our case, we find

$$F_\ell^\infty \propto \frac{(E/\mu)^2}{\ell}\exp\left[-2\ell\left(\frac{r}{r_{\rm LR}}-1\right)\right], \tag{5.18}$$

where E is the energy of the circular orbit at radius r, given by Eq. (5.29) below. It was shown that the same result holds also for the absorption flux for orbits close to the photon orbit. When $r = r_{\rm min}$ the exponential factor is ≈ 1 up to $\ell \sim \mathcal{O}((r_{\rm min}-r_{\rm LR})^{-1}) \gtrsim 100$, which is consistent with the behavior described by Eq. (5.16). These flux sums would converge eventually if we computed enough multipolar contributions. However, at very large values of ℓ and m, the methods we use to solve for the homogeneous Teukolsky solutions $R^\star_{\ell m\omega}(r)$ fail to find a solution. For all prograde orbits, we terminate the flux sums at $\ell = 70$ if the convergence criterion has not been met at this point. Large q retrograde orbits are more of a challenge; we have difficulty computing these modes (for the reasons discussed in Sec. 5.2.1 above) for somewhat smaller values of ℓ for large, negative q. We terminate our sums when we cannot reliably compute $R^\star_{\ell m\omega}(r)$. The value of ℓ we reach is shown in Table 5.1 and varies from 70 for $q = -0.5$ to 43 for $q = -0.99$.

To understand how much error we incur by terminating these sums, we examine how the flux behaves at the innermost grid point at $\ell_{\rm max}$ and $\ell_{\rm max}-1$. The fractional error due to the multipoles that have been neglected in our sum is

$$\varepsilon^\star_{\rm negl} \equiv \frac{1}{F^\star}\sum_{\ell=\ell_{\rm max}+1}^{\infty} F^\star_\ell\ . \tag{5.19}$$

If we assume that $F^\star_\ell$ falls off as suggested by Eq. (5.18) for $\ell \gtrsim \ell_{\rm max}$, this error can

q	$\ell_{\rm max}$	$F^{\infty}_{\ell=\ell_{\rm max}}/F^{\infty}$	$F^{\rm H}_{\ell=\ell_{\rm max}}/F^{\rm H}$	$\varepsilon^{\infty}_{\rm negl}$	$\varepsilon^{\rm H}_{\rm negl}$
0.99	70	7.06×10^{-5}	6.78×10^{-9}	0.0398%	3.82×10^{-6}%
0.9	70	6.93×10^{-4}	2.28×10^{-4}	1.10%	0.36%
0.7	70	1.38×10^{-3}	1.17×10^{-3}	3.54%	3.00%
0.5	70	1.49×10^{-3}	1.44×10^{-3}	4.80%	4.64%
0.0	70	1.82×10^{-3}	2.04×10^{-3}	8.07%	9.05%
-0.5	70	2.03×10^{-3}	2.36×10^{-3}	10.9%	12.7%
-0.7	66	2.31×10^{-3}	2.71×10^{-3}	13.1%	15.4%
-0.9	56	3.10×10^{-3}	3.68×10^{-3}	18.1%	21.5%
-0.99	43	4.75×10^{-3}	5.66×10^{-3}	23.5%	28.1%

Table 5.1: Diagnostics of convergence at our innermost grid point, $r_{\rm min} = r_{\rm LR} + 0.01M$, where the convergence is poorest. The second column lists the $\ell_{\rm max}$ where we end the sums for the total fluxes $F^{\star}$. The third column shows the flux to infinity in all $\ell = \ell_{\rm max}$ modes, normalized to the total flux (all modes up to and including $\ell = \ell_{\rm max}$). The third column is the same data for the horizon flux. The fourth and fifth columns give the error measure $\varepsilon^{\star}_{\rm negl}$, defined by Eq. (5.20). Convergence rapidly improves as we move away from this radius, with errors falling to 10^{-14} at radii a few $\times\, 0.1M$ from the light ring.

be estimated to be

$$\begin{aligned}
\varepsilon^{\star}_{\rm negl} &= \frac{F^{\star}_{\ell_{\rm max}}}{F^{\star}}\left[\frac{F^{\star}_{\ell_{\rm max}+1}}{F^{\star}_{\ell_{\rm max}}} + \frac{F^{\star}_{\ell_{\rm max}+2}}{F^{\star}_{\ell_{\rm max}}} + \cdots\right] \\
&\le \frac{F^{\star}_{\ell_{\rm max}}}{F^{\star}}\sum_{\ell=\ell_{\rm max}+1}^{\infty}\left(\frac{F^{\star}_{\ell}}{F^{\star}_{\ell-1}}\right)^{\ell-\ell_{\rm max}} \\
&= \frac{F^{\star}_{\ell_{\rm max}}}{F^{\star}}\sum_{\ell=\ell_{\rm max}+1}^{\infty}\left(\frac{\ell-1}{\ell}e^{-2/\ell_{\rm c}}\right)^{\ell-\ell_{\rm max}} .
\end{aligned} \tag{5.20}$$

Equation (5.20) is quite simple to compute and is accurate enough for our purposes.

Table 5.1 summarizes how the fluxes behave at our innermost data point for all the spins we have examined. We see that $\varepsilon_{\rm negl}$ varies from less than a percent to about 20%–30% at the innermost grid point in our study. The largest errors are for the high spin retrograde cases, where we are forced to terminate the sum relatively

early.

These errors improve very rapidly as we move away from the light ring. For the case of $q = -0.99$ (the case with the largest errors due to neglected modes in our study), the contribution at $r \simeq r_{\rm LR} + 0.05M$ has $F^{\infty}_{\ell_{\rm max}}/F^{\infty} \simeq 1.16 \times 10^{-3}$, and $F^{\infty}_{\ell_{\rm max}}/F^{\infty}_{\ell_{\rm max}-1} \simeq 0.930$; similar values describe the horizon flux at this location. Our rough estimate of the error falls to about 1.5%, an order of magnitude smaller than at our innermost grid point. We typically find that neglected terms in the sum contribute less than 10^{-14} to the total by the time we are a few $\times\, 0.1M$ out from the light ring.

As was mentioned in the text following Eq. (5.3), the factor of $(dt/d\tau)^{-1}$ in the point-particle stress energy tensor introduces a pole in the fluxes, leading to strong divergence as a power of $1/(v - v_{\rm LR})$ as we approach the light ring. We have confirmed this behavior on a mode-by-mode basis and have studied it using a modified version of our code in which this behavior is analytically factored from the fluxes (see Appendix B). Our numerical data up to $r_{\rm min}$ are consistent with a divergence of the total fluxes of the form $\sim (E/\mu)^2$.

It is worth emphasizing that if we use the WKB approximation [242–245] and normalize the fluxes (at infinity or through the BH horizon) to the specific energy and compute them exactly at the LR, we have $\left[F^{\star}_{\ell}/(E/\mu)^2\right]_{r_{\rm LR}} \sim 1/\ell$. Thus, in the WKB approximation the total normalized fluxes diverge logarithmically when computed at the LR. A similar divergence was also found by Ref. [275] in the case of plunging orbits in Schwarzschild spacetime with an impact parameter fine-tuned next to the LR (see in particular Fig. 12 therein); for ultrarelativistic infalls the

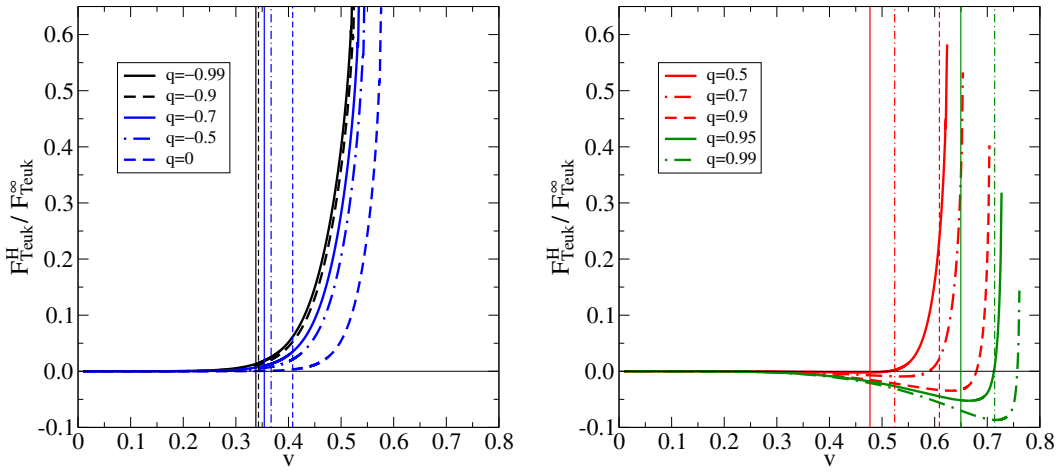

Figure 5.1: We show the ratio between the energy flux absorbed by the horizon $F^{\rm H}$ and the energy flux radiated to infinity F^{∞} for different possible values of the spin q, as a function of $v \equiv (M\Omega)^{1/3}$. The data come from the numerical solution of the Teukolsky equation in the adiabatic approximation. All plots extend up to $r = r_{\rm LR} + 0.01M$. Vertical lines mark the positions of the respective ISCOs.

authors also saw a scaling of the radiated energy with E^2.

5.2.3 Features of numerical fluxes

We now analyze the numerical fluxes and describe their main features to gain insight for the analytical modeling.

In Boyer-Lindquist coordinates, at leading order in the PN expansion or Newtonian order, the ingoing GW flux reads [see, e.g., Eq. (11) in Ref. [267]]

$$F^{\rm H,\,N} = \frac{32}{5}\frac{\mu^2 M^6}{r^6}\Omega\left(\Omega - \Omega_{\rm H}\right) , \tag{5.21}$$

where r is the radial separation and Ω is the orbital frequency of the particle. This

can be compared to the leading-order luminosity at infinity in GWs [260]

$$F^{\infty,\,\mathrm{N}} = \frac{32}{5}\mu^2 r^4 \Omega^6 \,. \tag{5.22}$$

For quasicircular inspiral, Eqs. (5.21) and (5.22) tell us that $F^{\mathrm{H},\,\mathrm{N}}/F^{\infty,\,\mathrm{N}} \sim (M\Omega)^{5/3}$ for $q \neq 0$, so the horizon flux is 2.5PN orders beyond the flux to infinity. In the nonspinning limit, $F^{\mathrm{H},\,\mathrm{N}}/F^{\infty,\,\mathrm{N}} \sim (M\Omega)^{8/3}$ — 4PN order in this case. Note that to obtain these ratios we used Eq. (5.13).

Thus, at leading order the absorption flux is suppressed with respect to the flux at infinity by $\mathcal{O}((M\Omega)^{5/3})$ for $q \neq 0$ or by $\mathcal{O}((M\Omega)^{8/3})$ for $q = 0$. To have a more accurate assessment of the relative importance of F^{H} and F^{∞}, in Fig. 5.1 we plot the ratio between the numerical fluxes at infinity and into the horizon $F^{\mathrm{H}}/F^{\infty}$ versus orbital velocity[6] for different values of the spin q. All curves in this figure extend up to a point just outside their respective equatorial LRs; the decreasing trend of $F^{\mathrm{H}}/F^{\infty}$ as a function of q is primarily due to how the factor $\Omega(\Omega - \Omega_{\mathrm{H}})$ behaves at the LR. We indicate the position of the respective ISCOs with vertical lines. For convenience, we list in Table 5.2 the position of the ISCOs and LRs expressed in terms of v for the spin cases considered in this paper.

In Ref. [118] [see Fig. 2 therein] the authors considered the total numerical flux $F^{\infty}_{\mathrm{Teuk}} + F^{\mathrm{H}}_{\mathrm{Teuk}}$ computed with the Teukolsky equation up to the ISCO for different spins, and compared it to a flux model where F^{∞} is the factorized flux of Ref. [101] and F^{H} is the Taylor-expanded PN flux of Refs. [140, 141]. They found that the

[6] Our $v \equiv (M\Omega)^{1/3}$ should not be confused with $v = (M/r)^{1/2}$ used in Ref. [141]. These definitions only agree when $q = 0$.

q	-0.99	-0.9	-0.7	-0.5	0	0.5	0.7	0.9	0.99
$v_{\rm ISCO}$	0.338	0.343	0.354	0.367	0.408	0.477	0.524	0.609	0.714
$v_{\rm LR}$	0.523	0.527	0.536	0.546	0.577	0.625	0.655	0.706	0.763

Table 5.2: We show the orbital velocities corresponding to the positions of ISCO and LR for different values of the spin.

inclusion of the analytical ingoing flux is crucial for improving the agreement with the Teukolsky solution during the very long inspiral, implying that $F^{\rm H}$ is a significant fraction of F^{∞}. Our numerical data extend the analysis of Ref. [118] to more extreme spins (up to 0.99) and higher frequencies (up to the LRs). Figure 5.1 shows that $F^{\rm H}$ is typically a few percent of F^{∞} at the ISCO for $q \leq 0.7$, increasing to 8.7% when $q = 0.99$.

Another important feature that Fig. 5.1 shows is that $F^{\rm H}$ changes sign for $q > 0$ ($F^{\infty} > 0$ in all cases). Orbits for which $F^{\rm H}/F^{\infty} < 0$ are called "superradiant." They can be interpreted as due to a Penrose-like mechanism [133] in which the rotational energy of the BH is extracted. The change of sign of $F^{\rm H}$ for $q > 0$ can be understood by noticing that the sign of each mode $F^{\rm H}_{\ell m}$ is fixed by its specific structure in BH perturbation theory [see Eq. (5.10)]

$$F^{\rm H}_{\ell m} = m^2 \Omega \left(\Omega - \Omega_{\rm H}\right) \tilde{F}^{\rm H}_{\ell m} \,, \tag{5.23}$$

where $\tilde{F}^{\rm H}_{\ell m} > 0$. If $q > 0$, $\Omega_{\rm H} > 0$ as well, so when $0 < \Omega < \Omega_{\rm H}$, we have $F^{\rm H}_{\ell m} < 0$. This means that the particle gains energy through the GW modes with that specific value of m. Zeros in $F^{\rm H}$ for $q > 0$ in Fig. 5.1 coincide with the horizon velocities: $v_{\rm H} \equiv (M\Omega_{\rm H})^{1/3}$. We notice that for $q > 0$, an inspiraling test particle will always

go through the zero of $F^{\rm H}$. In fact, the test particle's velocity reaches its maximum value, which is always larger than $v_{\rm H}$, during the plunge. Afterwards, the test particle's velocity decreases and gets locked to that of the horizon [114].

As discussed in the Introduction and as can be seen in Fig. 5.1, we always have $|F^{\rm H}|/F^{\infty} < 1$, meaning that we find no so-called "floating orbits." Although superradiance of the down-horizon modes does not allow for floating orbits, these modes nonetheless have a strong impact on inspiral. Comparing an inspiral that includes both $F^{\rm H}$ and F^{∞} with one that is driven only by F^{∞}, one finds that these modes make inspiral last longer, radiating additional cycles before the final plunge [118]. A more quantitative assessment of this delayed merger can be found for instance in the nonspinning limit in Ref. [235]. In that work, the authors considered EOB orbital evolutions that include the horizon flux model developed in Ref. [128]. For $\mu/M = 10^{-3}$, they found that neglecting the horizon flux induces a dephasing of 1.6 rads for the (2,2) mode waveform h_{22} at merger over an evolution of about 41 orbital cycles. They also studied what happens for larger mass ratios, since their flux model worked even in the comparable-mass limit. However, in this regime the effects are much smaller, with a (2,2) mode dephasing of only 5×10^{-3} rads at merger cumulated over 15 orbits. This result is consistent with the estimations of Ref. [267], which considered an equal-mass spinning case under a leading-order PN evolution.

In the case of spinning binaries with extreme mass ratio, Refs. [116, 255] found that in the nearly extremal case $q = 0.998$ the last few hundred days of inspiral at mass ratio 10^{-6} are augmented by $\sim 5\%$ at low inclinations, depending on whether

the ingoing flux is included or not. Using the exact Teukolsky-equation fluxes of this paper in the EOB equations of motion, Ref. [114] computed how the number of orbital cycles within a fixed radial range before the LR is affected by the addition of ingoing flux. Several different values of the spin were considered. For prograde orbits, the ingoing flux can increase the number of cycles by as much as $\sim 7\%$ for $q = 0.99$, which corresponds to about 45 rads of GW dephasing in the (2,2) mode over 100 GW cycles. On the other hand, for retrograde orbits or nonspinning black holes, the horizon flux tends to make inspiral faster, decreasing the number of cycles before the plunge thanks to the additional loss of energy absorbed by the horizon in these cases. The horizon flux changes the duration of inspiral by at most $\sim 1\%$ when $q = -0.99$, a somewhat less significant effect.

Since we are going to model the multipolar modes $F^{\rm H}_{\ell m}$ rather than the total ingoing GW flux $F^{\rm H}$, it is useful to understand their relative importance. In Figs. 5.2 and 5.3 we show the ratio between the first few subdominant modes and the dominant (2,2) mode $F^{\rm H}_{22}$ as a function of the orbital velocity for the two extremal spin cases $q = \pm 0.99$. For $q = -0.99$ we note that at the ISCO the most important subdominant modes are the (3,3) and the (2,1), and they are both only a few percent of the dominant (2,2) mode. For $q = 0.99$, at the ISCO the subdominant modes that are at least 1% of the (2,2) mode are many more: (3,3), (4,4), (2,1), (5,5), (3,2), and (6,6). This is a general result: As the spin of the Kerr BH grows to large positive values, more and more multipolar modes become important relative to the dominant (2,2) mode, even before the plunging phase, which starts after the crossing of the ISCO. Close to the LR all modes with $\ell = |m|$ become

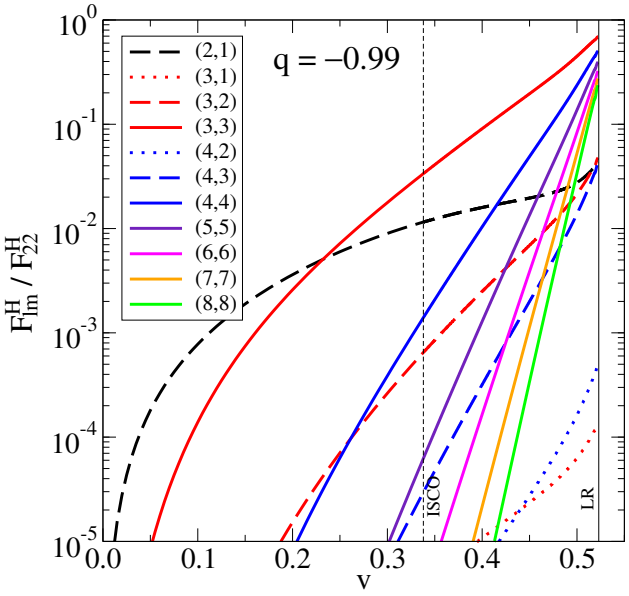

Figure 5.2: We compare the Teukolsky-equation ingoing multipolar fluxes, normalized by the dominant mode $F^{\rm H}_{22}$, for spin $q = -0.99$. Vertical lines mark the position of the ISCO and the LR. The graphs extend up to $r = r_{\rm LR} + 0.01M$.

comparable to the (2,2) mode for both spins. This is similar to what happens for the multipolar decomposition of F^{∞} (see, e.g., Ref. [276]). Reference [119] already pointed out a similar behavior while discussing the spherical modes at infinity h_{lm}, which directly relate to the -2 spin-weighted spherical harmonic decomposition of F^{∞} [see Eq. (5.26) below].

A compact representation of the ratio $F^{\rm H}_{\ell m}/F^{\rm H}_{22}$ across the entire range of physical spins is given in Fig. 5.4. Choosing to evaluate the ratio at the same orbital frequency for different values of q would not be meaningful, since the position of the horizon changes with q, so we choose instead as the common physical point the ISCO for all the spins. We see that at the ISCO the only modes that are consis-

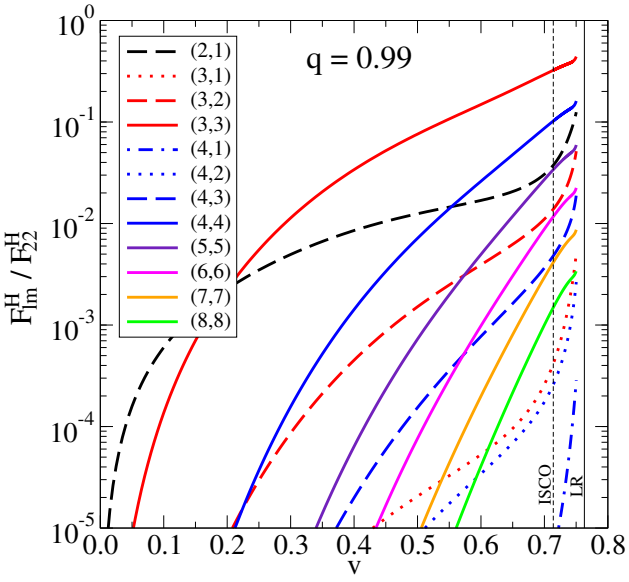

Figure 5.3: We compare the Teukolsky-equation ingoing multipolar fluxes, normalized by the dominant mode $F^{\rm H}_{22}$, for spin $q = 0.99$. Vertical lines mark the position of the ISCO and the LR. The graphs extend up to $v \approx (M\Omega_{\rm H})^{1/3}$.

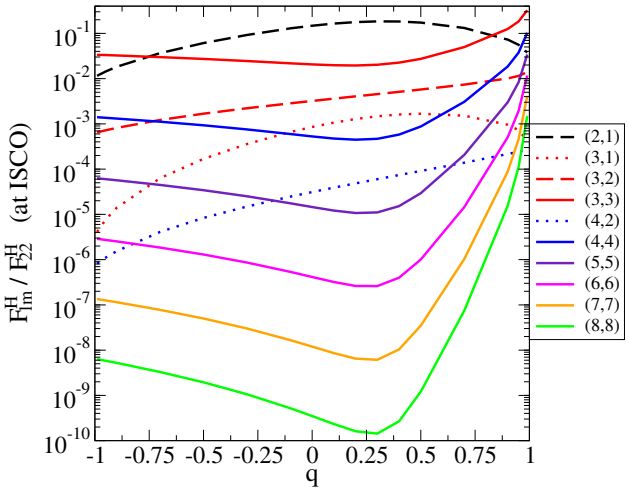

Figure 5.4: We compare the Teukolsky-equation ingoing multipolar fluxes, normalized by the dominant mode $F^{\rm H}_{22}$, evaluated at the respective ISCOs.

tently at least 1% of $F^{\rm H}_{22}$ are the (2,1) and (3,3) modes; only when $q \gtrsim 0.95$ are the (4,4), (5,5), (6,6), and (3,2) modes above 1% of the (2,2). Modes with $\ell = |m|$ appear to be evenly spaced on the logarithmic scale used for all spins. In other words, $F^{\rm H}_{\ell\ell}/F^{\rm H}_{22} \propto 10^{c(q)\ell}$, where $c(q)$ is a spin-dependent constant.[7] We therefore do not see crossings among these modes as q varies between -1 and 1. On the other hand, we do see crossings between the largest subdominant modes, (2,1) and (3,3): When $-0.75 \lesssim q \lesssim 0.8$ we have $F^{\rm H}_{21} \geq F^{\rm H}_{33}$, otherwise (for almost extremal spins) $F^{\rm H}_{21} \leq F^{\rm H}_{33}$. The nature of these crossings seems to depend mostly on $|q|$, as it is also indirectly confirmed in Figs. 5.2 and 5.3, where the crossing of (2,1) and (3,3) (now considered in plots versus v at fixed q) occurs at a similar velocity $v \approx 0.2$ for both $q = -0.99$ and $q = 0.99$. A simple explanation of what we just discussed is the fact that, as q grows, the ISCO moves deeper into the strong field and the ISCO orbital velocity increases. In this circumstance, higher multipoles can become comparable in size to the (2,2) mode in spite of their higher PN order.

From Figs. 5.2–5.4 we also observe that, among modes with the same value of ℓ, the dominant ones are those with $\ell = |m|$, independently of the frequency. For the case of scalar perturbations of a Schwarzschild BH, Ref. [277] provided an analytical argument to account for this peculiar hierarchy. Within the WKB approximation (valid for $\ell \gg 1$) and for an orbit at $r \gg r_{\rm LR}$, it was shown that $F^{\infty}_{\ell m}/F^{\infty}_{\ell\ell} \propto \exp\left[-2C\left(\ell - |m|\right)\right]$, where C is a positive numerical constant that depends on r. As a consequence, nearly all of the power at infinity at a frequency $m\Omega$ is emitted in the $\ell = |m|$ modes. Similar arguments apply to the case of gravita-

[7] This behavior is consistent with Eq. (5.16).

tional perturbations [243] and, more generally, to perturbations of a Kerr BH [244]. Explicitly, one finds that

$$F^{\infty}_{\ell m} \propto \exp\left[-2\int_{r^*_{\rm orb}}^{\bar{r}^*}\sqrt{V(r'^*)-m^2\Omega^2}\,{\rm d}r'^*\right]. \tag{5.24}$$

Here, V is the radial potential seen by the perturbation, and r^* is the tortoise coordinate,

$$r^* = r + \frac{2Mr_+}{r_+-r_-}\ln\left(\frac{r-r_+}{2M}\right) - \frac{2Mr_-}{r_+-r_-}\ln\left(\frac{r-r_-}{2M}\right), \tag{5.25}$$

where $r_\pm/M = 1\pm\sqrt{1-q^2}$. The integral's upper limit $\bar{r}^*$ is the larger of the two solutions to the equation $V(\bar{r}^*) = m^2\Omega^2$. Recall that Ω depends on r through Eq. (5.13). Note that $r^*_{\rm orb}$ is always smaller than $\bar{r}^*$. For a nonspinning BH and $\ell \gg 1$ the radial potential is the same regardless of the spin of the perturbing field [277], and reads $V(r) = \ell(\ell+1)(1-2M/r)/r^2$. Therefore the lower the value of m, the larger the value of $\bar{r}^*$, the larger the magnitude of the argument inside the exponential, and hence the larger the suppression. An analogous explanation applies to the absorption flux.

Finally, as we discussed in Sec. 5.2.2, the existence of a cutoff value $\ell_{\rm c}$ for sums over the flux modes reduces in practice the number of modes that contribute to the total flux. For orbits very close to the LR, $\ell_{\rm c}$ is a decreasing function of the spin. When $q \approx 1$ very few modes contribute, and the total flux is basically given by the (2,2) mode. This is consistent with Fig. 5.3, where in the strong-field region only the (3,3), (4,4) and (2,1) modes are at least 10% of the (2,2) mode. On the other hand, in Fig. 5.2 we can see that the (3,3), (4,4), (5,5), (6,6), (7,7) and (8,8) modes

are all larger than 10% of the (2,2) mode at $r_{\rm min}$, and indeed the estimated $\ell_{\rm c}$ at that radial separation is ~ 200.

5.3 Factorization of the energy fluxes

The analytical representation of the ingoing flux in PN-expanded form provided in Ref. [141] turns out to be monotonic in the orbital frequency for all possible values of the spin, so that the sign flip discussed above is not present. Moreover comparisons with the numerical fluxes (see Fig. 5.7) show that these PN formulas start performing poorly even before the ISCO, especially for large positive values of q. This is to be expected, since the ISCO moves to smaller radii (i.e. larger orbital frequencies) as q increases, that is outside the range of validity of the PN expansion; Ref. [278] attempted to determine the region of validity of the PN absorption flux more quantitatively. For instance, when $q = 0.9$, the Taylor-expanded PN model for $F^{\rm H}$ differs from the numerical data by more than 100% around an orbital velocity $v \approx 0.4$, while $v_{\rm ISCO} \approx 0.61$. An improved analytical model for $F^{\rm H}$ is therefore needed. In this section we will propose a factorization of the absorbed flux similar to what was done for the flux at infinity [99–101, 128].

5.3.1 Factorization of the energy flux at infinity

For a particle spiraling in along an adiabatic sequence of circular orbits, the GW flux at infinity can be expressed as a sum over the waveform modes at infinity

h_{lm}, as

$$F^{\infty} = \frac{M^2\Omega^2}{8\pi} \sum_{l=2}^{\infty} \sum_{m=1}^{l} m^2 \left| \frac{\mathcal{R}}{M} h_{lm} \right|^2 , \tag{5.26}$$

where $\mathcal{R}$ is the distance to the source. The mode decomposition here is done using the -2 spin-weighted spherical harmonics, rather than the spheroidal harmonics considered in the previous section; as discussed at the end of the Introduction, the indices are labeled (l, m) rather than (ℓ, m) to flag this change of basis. In Ref. [99] a novel approach to improve the analytical modeling of the GW flux at infinity for a test particle in Schwarzschild was introduced. This approach was then generalized to spinning BHs in Ref. [101]. The idea is to start from the PN knowledge of h_{lm}, and recast the formulas, mode by mode, in a factorized form

$$h_{lm} \equiv h_{lm}^{(\mathrm{N},\epsilon)} T_{lm} \hat{S}_{\mathrm{eff}}^{(\epsilon)} f_{lm} e^{i\delta_{lm}} , \tag{5.27}$$

where ϵ is either 0 if $l+m$ is even or 1 if $l+m$ is odd, $h_{lm}^{(\mathrm{N},\epsilon)}$ is the leading order term, T_{lm} resums an infinite number of leading logarithms entering the tail effects, $\hat{S}_{\mathrm{eff}}^{(\epsilon)}$ is an effective source term that is divergent for circular motion at the LR, f_{lm} and δ_{lm} are polynomials in the variable v [see, e.g., Ref. [101] for more details]. The term f_{lm} is fixed by requiring that Eq. (5.27), when expanded in powers of v, agrees with the PN-expanded formulas. When computing the f_{lm}'s, one assumes quasicircular orbits, and this is reflected by the choice of the source term,

$$\hat{S}_{\mathrm{eff}}^{(\epsilon)} = \begin{cases} \dfrac{E}{\mu}, & \text{if} \quad \epsilon = 0 \ , \\ \dfrac{L_z}{\mu M/v}, & \text{if} \quad \epsilon = 1 \, , \end{cases} \tag{5.28}$$

where E and L_z are the energy and angular momentum of a circular equatorial orbit in Kerr [122]

$$\frac{E}{\mu} = \frac{1-2M/r+q(M/r)^{3/2}}{\sqrt{1-3M/r+2q(M/r)^{3/2}}}\,, \tag{5.29}$$

$$\frac{L_z}{\mu M} = \sqrt{\frac{r}{M}}\frac{1-2q(M/r)^{3/2}+q^2(M/r)^2}{\sqrt{1-3M/r+2q(M/r)^{3/2}}}\,, \tag{5.30}$$

and $\mu M/v$ in the denominator of Eq. (5.28) is the Newtonian angular momentum for circular orbits. Note that this specific choice of the effective source term is not the only one possible. References [100, 101] also explored the possibility of using $\hat{S}^{(0)}_{\rm eff} = \hat{S}^{(1)}_{\rm eff} = E/\mu$ and labeled the resulting factorized odd-parity modes with the "H" superscript (meaning "Hamiltonian"), as opposed to the factorization done with the prescription in Eq. (5.28), whose odd-parity modes were labeled with the "L" superscript (meaning "angular momentum"). In the rest of the paper we are going to consider only the effective source of Eq. (5.28), and we will omit the "L" superscript.

Reference [100] found that the 1PN coefficient of the f_{lm} polynomials grows linearly with l, and therefore proposed a better-behaved factorization, namely

$$h_{lm} \equiv h^{(\mathrm{N},\epsilon)}_{lm} T_{lm} \hat{S}^{(\epsilon)}_{\rm eff} (\rho_{lm})^l e^{i\delta_{lm}}\,, \tag{5.31}$$

where the f_{lm} factor is replaced by $(\rho_{lm})^l$. Both factorized representations of F^∞ show an improved agreement with the numerical data with respect to PN approximants, as pointed out in Refs. [99, 100] for the nonspinning case and in Ref. [101] for the spinning case. Moreover, the ρ_{lm} factorization turns out to perform better than the f_{lm} factorization when compared with the Teukolsky-equation fluxes; this is discussed in more detail in Appendix D.

5.3.2 Factorization of the BH-absorption energy flux

Let us now consider the BH-absorption flux. For the special case of nonrotating BHs, Refs. [139] and [269] computed the lowest PN terms of $F^{\rm H}$, in the test-particle and comparable-mass limits, respectively. The spinning case was considered in Refs. [140, 141] in the test-particle limit and in Ref. [267] in the comparable-mass limit. In particular, Ref. [141] computed the PN expanded BH-absorption flux into a Kerr BH up to 6.5PN order beyond the leading order luminosity at infinity for circular orbits in the equatorial plane. The idea behind that calculation is to solve the Teukolsky equation in two different limits, for separations $r \to \infty$ and for separations approaching the horizon, and then to match the two solutions in an intermediate region where both approximations are valid. These Taylor-expanded PN expressions are then decomposed into spheroidal[8] multipolar modes $F^{\rm H}_{\ell m}$, so that

$$F^{\rm H} = 2 \sum_{\ell=2}^{\infty} \sum_{m=1}^{\ell} F^{\rm H}_{\ell m} \,, \tag{5.32}$$

where we used $F^{\rm H}_{\ell 0} = 0$ and $F^{\rm H}_{\ell m} \equiv F^{\rm H}_{\ell |m|}$. Note that this decomposition stems from the separation of variables of the Teukolsky equation in oblate spheroidal coordinates [115, 279].

Here, we count the PN orders with respect to the leading order luminosity at infinity of Eq. (5.22), which can be rewritten

$$F^{\infty,\,{\rm N}} = \frac{32}{5} \left(\frac{\mu}{M}\right)^2 v^{10} \,, \tag{5.33}$$

for circular orbits. Thus, as discussed above, for a nonspinning binary the leading

[8] In this case, the modes are of spin weight +2.

order term in the BH-absorbed GW flux is 4PN [$\mathcal{O}(v^8)$ beyond the leading order luminosity at infinity], whereas for a Kerr BH it is 2.5PN [$\mathcal{O}(v^5)$ beyond the leading order luminosity at infinity].

Reference [128] considered the case of a nonspinning BH binary and applied a factorization to the multipolar ingoing GW flux, recasting it in the following form

$$F^{\rm H}_{\ell m} \equiv F^{\rm H,\,N}_{\ell m} (\hat{S}^{(\epsilon)}_{\rm eff})^2 \left(\rho^{\rm H}_{\ell m}\right)^{2\ell} , \tag{5.34}$$

where $F^{\rm H,\,N}_{\ell m}$ is the nonspinning leading term, and $\rho^{\rm H}_{\ell m}$ is a polynomial in v determined by requiring that Eq. (5.34) agrees with the PN-expanded formulas from Refs. [139, 269] when expanded in powers of v. Here the "H" superscript refers to "horizon." Note that Ref. [128] defined the multipolar modes differently: their (ℓ, m) mode is the sum of our (ℓ, m) and $(\ell, -m)$ modes, so there is an overall factor 1/2. Reference [128] computed $\rho^{\rm H}_{22}$ up to 1PN order beyond $F^{\rm H,N}_{22}$ (i.e., 5PN order in our convention) in the Schwarzschild case and also in the comparable-mass case. However, in the Schwarzschild case, the total ingoing GW flux is actually known through 6PN order [141]

$$F^{\rm H}(q=0) = F^{\infty,\,\rm N} v^8 \left[1 + 4v^2 + \frac{172}{7} v^4 + \mathcal{O}(v^5)\right] , \tag{5.35}$$

and specifically the individual mode $F^{\rm H}_{22}$ is known to the same PN order as $F^{\rm H}$, so that the factorization in Ref. [128] can be extended from 5PN to 6PN order (beyond the leading order luminosity at infinity).

Let us now consider the spinning case. As pointed out before, the Taylor-expanded PN form of the ingoing GW flux does not preserve the zero $(\Omega - \Omega_{\rm H})$, which is instead present in the exact expression of the $F^{\rm H}_{\ell m}$'s from BH perturbation

theory. This means that, if we were to use a factorization like the one in Eq. (5.34) also for the Kerr case, our factorized flux would inherit this unwanted feature, since the factorization only tries to match the Taylor-expanded PN flux. Therefore, we propose the factorized form

$$F^{\rm H}_{\ell m} \equiv \left(1-\frac{\Omega}{\Omega_{\rm H}}\right) F^{\rm H,\,N}_{\ell m} (\hat{S}^{(\epsilon)}_{\rm eff})^2 (\tilde{f}^{\rm H}_{\ell m})^2 \,, \tag{5.36}$$

which has the advantage of enforcing the presence of the zero at a frequency equal to $\Omega_{\rm H}$. The leading term is defined as

$$F^{\rm H,\,N}_{\ell m} \equiv \frac{32}{5}\left(\frac{\mu}{M}\right)^2 v^{7+4\ell+2\epsilon} n^{(\epsilon)}_{\ell m} c_{\ell m}(q) \,, \tag{5.37}$$

where

$$n^{(0)}_{\ell m} \equiv -\frac{5}{32}\frac{(\ell+1)(\ell+2)}{\ell(\ell-1)}\frac{2\ell+1}{[(2\ell+1)!!]^2}\frac{(\ell-m)!}{[(\ell-m)!!]^2}\frac{(\ell+m)!}{[(\ell+m)!!]^2} \,, \tag{5.38}$$

$$n^{(1)}_{\ell m} \equiv -\frac{5}{8\ell^2}\frac{(\ell+1)(\ell+2)}{\ell(\ell-1)}\frac{2\ell+1}{[(2\ell+1)!!]^2}\frac{[(\ell-m)!!]^2}{(\ell-m)!}\frac{[(\ell+m)!!]^2}{(\ell+m)!} \,, \tag{5.39}$$

and

$$\begin{aligned} c_{\ell m}(q) \;&\equiv\; \frac{1}{q}\prod_{k=0}^{\ell}\left[k^2+\left(m^2-k^2\right)q^2\right] = qm^2\left(1-q^2\right)^{\ell}\times \\ &\times\; \left(1-\frac{imq}{\sqrt{1-q^2}}\right)_{\ell}\left(1+\frac{imq}{\sqrt{1-q^2}}\right)_{\ell} \,, \end{aligned} \tag{5.40}$$

where $(z)_n \equiv z(z-1)\cdots(z-n+1)$ is the Pochhammer symbol. The factors $n^{(\epsilon)}_{\ell m}$ and $c_{\ell m}(q)$ allow the $\tilde{f}^{\rm H}_{\ell m}$'s to start with either 1 or 0. The definition of the factor $c_{\ell m}(q)$ is inspired by the derivation of the $\ell = 2$ modes in the slow-motion approximation in Ref. [268] [see Eq. (9.31) therein]. The definition of $n^{(\epsilon)}_{\ell m}$ is derived from Eqs. (5.17) and (5.18) in Ref. [139] (which considered the Schwarzschild case),

but a few additional factors were included. These new factors are a prefactor of $1/(m\ell!)^2$ generated by our definition of $c_{\ell m}(q)$, a numerical factor of $-1/4$ due to the presence of $(1-\Omega/\Omega_{\rm H})$ in Eq. (5.36), and a factor of $1/2$ due to the definitions used in Ref. [139]. We also consider the factorization

$$F^{\rm H}_{\ell m} \equiv \left(1-\frac{\Omega}{\Omega_{\rm H}}\right) F^{\rm H,N}_{\ell m}(\hat{S}^{(\epsilon)}_{\rm eff})^2 \left(\tilde{\rho}^{\rm H}_{\ell m}\right)^{2\ell} , \tag{5.41}$$

where the factor $\tilde{f}^{\rm H}_{\ell m}$ in Eq. (5.36) is replaced by $\left(\tilde{\rho}^{\rm H}_{\ell m}\right)^{\ell}$, just as was done by Ref. [100] for F^{∞}. [Note that our $\tilde{\rho}_{\ell m}$'s are different from the $\rho_{\ell m}$'s in Ref. [128].]

Appendix I of Ref. [141] lists the Taylor-expanded modes $F^{\rm H}_{\ell m}$ that are needed to compute the BH-absorption Taylor-expanded flux through 6.5PN order. Since the $F^{\rm H}_{\ell m}$'s in Ref. [141] are expressed in terms of the velocity parameter $(M/r)^{1/2}$, we use Eq. (5.13) to replace r with v. A straightforward but tedious calculation gives us the following expressions for the $\tilde{\rho}^{\rm H}_{\ell m}$ functions:

$$
\begin{aligned}
\tilde{\rho}_{22}^{\mathrm{H}} = 1 + v^2 &- \left\{ 2B_2 + \frac{q}{1+3q^2}\left[4 + \kappa\left(5+3q^2\right)\right] \right\} v^3 + \left(\frac{335}{84} - \frac{2}{21}q^2 \right) v^4 \\
&- \left\{ 2B_2 + \frac{q}{1+3q^2}\left[\frac{47}{18} - \frac{25}{6}q^2 + \kappa\left(5+3q^2\right) \right] \right\} v^5 \\
&+ \left\{ \frac{293\,243}{14\,700} - \frac{2}{3}\pi^2 - \frac{6\,889}{1\,134}q^2 + \frac{3}{2}q^4 + 2B_2^2 + 4C_2\left(1+\frac{2}{\kappa}\right) \right. \\
&- \frac{428}{105}\left(A_2 + \gamma_E + \log 2 + \log\kappa + 2\log v\right) - \frac{1}{1+3q^2}\left[\frac{124}{9} - 8qB_2 - 2q\kappa B_2\left(5+3q^2\right) \right] \\
&\left. + \frac{1}{\left(1+3q^2\right)^2}\left[\frac{56}{3} + 2\kappa\left(5 - 6q^2 + 3q^4 - 18q^6\right) \right] \right\} v^6 \\
&- \frac{1}{42}\left\{ B_2\left(335 - 8q^2\right) + \frac{q}{1+3q^2}\left[\frac{1\,670}{3} - \frac{3\,131}{9}q^2 + \frac{73}{3}q^4 + \frac{\kappa}{2}\left(5+3q^2\right)\left(335-8q^2\right) \right] \right\} v^7 \\
&+ \left\{ \frac{6\,260\,459}{151\,200} - \frac{2}{3}\pi^2 - \frac{25\,234}{5\,292}q^2 + \frac{8\,439}{5\,292}q^4 - \frac{148}{7}\gamma_E - \frac{428}{105}A_2 + 2B_2^2 \right. \\
&+ 4C_2\left(1+\frac{2}{\kappa}\right) - \frac{25}{9}qB_2 + \frac{1}{1+3q^2}\left[-\frac{322}{27} + 8qB_2 + 2\kappa qB_2\left(5+3q^2\right) \right] \\
&+ \frac{1}{\left(1+3q^2\right)^2}\left[\frac{56}{3} + \kappa\left(10 - \frac{341}{18}q^2 - 19q^4 - \frac{97}{2}q^6 \right) \right] \\
&\left. - \frac{4\,012}{105}\log 2 - \frac{428}{105}\log\kappa - \frac{2\,648}{105}\log v \right\} v^8 + \mathcal{O}(v^9)\,, \qquad (5.42)
\end{aligned}
$$

$$\tilde{\rho}_{21}^{\mathrm{H}} = 1 - \frac{q}{3}v + \left(\frac{7}{12} - \frac{q^2}{18}\right)v^2 - \left\{B_1 + \frac{1}{18}q\left(\frac{1}{3}q^2 - \frac{31}{2}\right) + \frac{q}{4-3q^2}\left[1 + \kappa\left(5 - 3q^2\right)\right]\right\}v^3$$
$$+ \left\{\frac{521}{672} + \frac{1}{3}qB_1 - q^2\left(\frac{1\,847}{1\,512} + \frac{5}{648}q^2\right) + \frac{1}{4-3q^2}\left[\frac{4}{9} + q^2\kappa\left(\frac{5}{3} - q^2\right)\right]\right\}v^4$$
$$+ \left[-\frac{B_1}{36}\left(21 - 2q^2\right) - \frac{1}{4-3q^2}\left(-\frac{347}{72}q\right.\right.$$
$$\left.\left. + \frac{3\,053}{864}q^3 + \frac{703}{1\,944}q^5 - \frac{7}{648}q^7 + \frac{1}{36}\kappa q\left(21 - 2q^2\right)\left(5 - 3q^2\right)\right)\right]v^5$$
$$+ \left\{\frac{267\,092\,969}{38\,102\,400} - \frac{32\,125}{12\,096}q^2 + \frac{81\,167}{54\,432}q^4 - \frac{7}{3\,888}q^6\right.$$
$$- \frac{107}{105}\left(A_1 + \gamma_E + \log 2 + \log\kappa + 2\log v\right) + \frac{1}{2}B_1^2 + C_1\left(1 + \frac{2}{\kappa}\right) - \frac{\pi^2}{6}$$
$$- \frac{1}{4-3q^2}\left[\frac{298}{243} + qB_1\left(\frac{22}{9} - \frac{287}{108}q^2 + \frac{1}{18}q^4 - \kappa\left(5 - 3q^2\right)\right)\right]$$
$$\left. + \frac{1}{(4-3q^2)^2}\left[-\frac{4}{3} + \kappa\left(40 - \frac{1\,208}{9}q^2 + \frac{14\,539}{108}q^4 - \frac{177}{4}q^6 + \frac{1}{6}q^8\right)\right]\right\}v^6 + \mathcal{O}(v^7)\,, \tag{5.43}$$

$$\tilde{\rho}_{33}^{\mathrm{H}} = 1 + \frac{7}{6}v^2 - \left\{2B_3 + \frac{2q}{(1+8q^2)(4+5q^2)}\left[\frac{131}{9} + \frac{314}{9}q^2 - \frac{40}{9}q^4 + 3\kappa\left(5 + 13q^2\right)\right]\right\}v^3$$
$$+ \left(\frac{353}{120} - \frac{5}{18}q^2\right)v^4 + \mathcal{O}(v^5)\,, \tag{5.44}$$

$$\tilde{\rho}_{32}^{\mathrm{H}} = 1 - \frac{1}{4}qv + \left(\frac{5}{6} - \frac{1}{16}q^2\right)v^2 + \mathcal{O}(v^3)\,, \tag{5.45}$$

$$\tilde{\rho}_{31}^{\mathrm{H}} = 1 + \frac{29}{18}v^2 - \frac{2}{3}\left\{B_1 + \frac{q}{4-3q^2}\left[\kappa\left(5 - 3q^2\right) + \frac{1}{9-8q^2}\left(65 - \frac{866}{9}q^2 + \frac{104}{3}q^4\right)\right]\right\}v^3$$
$$+ \left(\frac{1\,903}{648} + \frac{1}{6}q^2\right)v^4 + \mathcal{O}(v^5)\,, \tag{5.46}$$

$$\tilde{\rho}_{44}^{\mathrm{H}} = 1 + \mathcal{O}(v)\,, \tag{5.47}$$

$$\tilde{\rho}_{43}^{\mathrm{H}} = \mathcal{O}(v)\,, \tag{5.48}$$

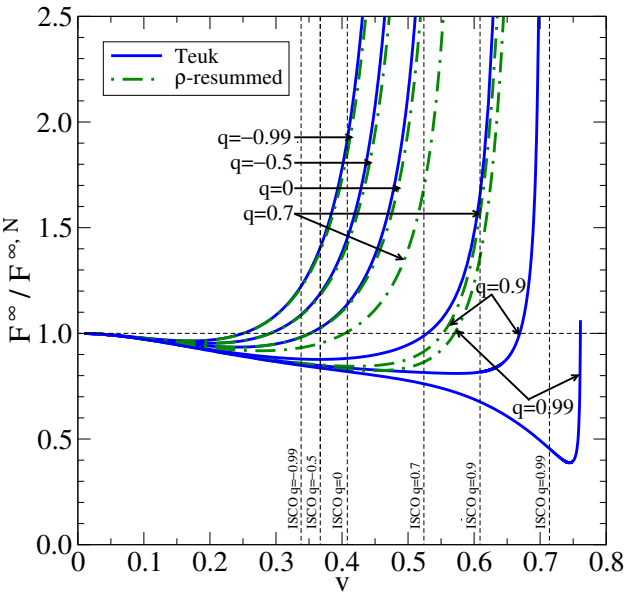

Figure 5.5: We compare the Teukolsky-equation flux at infinity with the factorized flux of Ref. [101]. The computation is done up to the $r_{\rm LR} + 0.01M$.

$$\tilde{\rho}^{\rm H}_{42} = 1 + \mathcal{O}(v)\,, \tag{5.49}$$

$$\tilde{\rho}^{\rm H}_{41} = \mathcal{O}(v)\,. \tag{5.50}$$

In these equations, $\gamma_E \approx 0.57721\ldots$ is the Euler-Mascheroni constant, $\kappa \equiv \sqrt{1-q^2}$, and

$$A_n \equiv \frac{1}{2}\left[\psi^{(0)}\left(3+\frac{inq}{\kappa}\right)+\psi^{(0)}\left(3-\frac{inq}{\kappa}\right)\right], \tag{5.51}$$

$$B_n \equiv \frac{1}{2i}\left[\psi^{(0)}\left(3+\frac{inq}{\kappa}\right)-\psi^{(0)}\left(3-\frac{inq}{\kappa}\right)\right], \tag{5.52}$$

$$C_n \equiv \frac{1}{2}\left[\psi^{(1)}\left(3+\frac{inq}{\kappa}\right)+\psi^{(1)}\left(3-\frac{inq}{\kappa}\right)\right]; \tag{5.53}$$

$\psi^{(n)}$ is the polygamma function.

The explicit expressions of the $\tilde{f}^{\rm H}_{\ell m}$ functions can be found in Appendix C. Given the limited number of available modes in Taylor-expanded PN form, we are

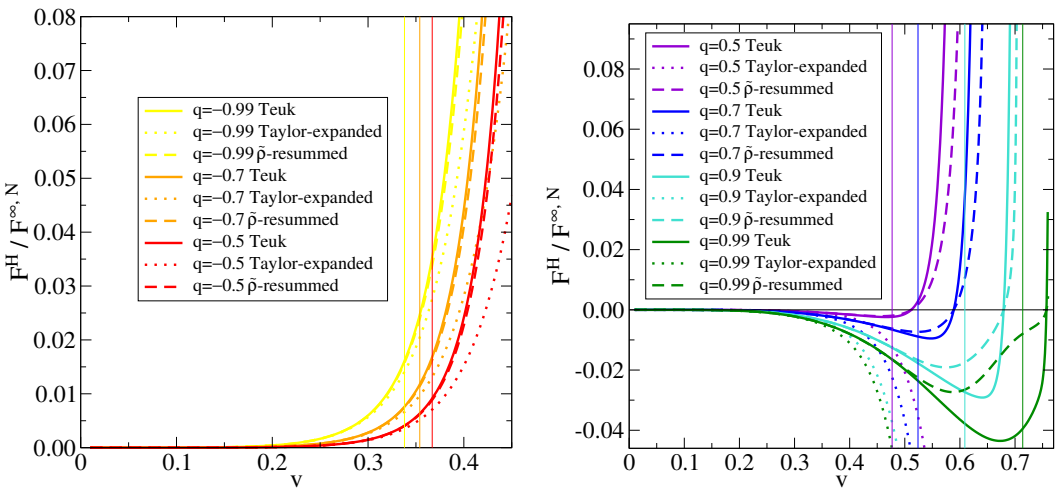

Figure 5.6: We compare the Teukolsky-equation BH-absorption flux (solid lines) to the Taylor-expanded PN model of Ref. [141] (dotted lines) and the factorized flux proposed in this work (dashed lines), as functions of v. All curves extend up to $r = r_{\rm LR} + 0.01M$. Vertical lines mark the positions of the respective ISCOs. The fluxes are normalized to the leading order flux at infinity $F^{\infty,\rm N}$. In the left panel we show cases with $q < 0$, while in the right panel we show cases with $q > 0$.

not able to convincingly argue that the $\tilde{\rho}^{\rm H}_{\ell m}$ factorization is preferable to the $\tilde{f}^{\rm H}_{\ell m}$ factorization on the basis of the growth with ℓ of the 1PN coefficient in the $\tilde{f}^{\rm H}_{\ell m}$'s, as done in Refs. [100, 101] for F^{∞}. We prefer the $\tilde{\rho}^{\rm H}_{\ell m}$ factorization over the $\tilde{f}^{\rm H}_{\ell m}$ factorization because we find that it compares better to the numerical data.

5.4 Comparison with numerical results

In this section we compare the Teukolsky-equation fluxes (both at infinity and ingoing) to the analytical models discussed in Sec. 5.3.

5.4.1 Comparison with the numerical flux at infinity

In Fig. 5.5 we show the Teukolsky-equation flux at infinity for several different spin values up to the LR and compare it to the factorized flux reviewed in Sec. 5.3.1 and developed in Ref. [101]. We note that the factorized flux is fairly close to the numerical data until the LR for retrograde and nonspinning cases. For large spin prograde cases, the modeling error instead becomes large already at the ISCO.[9] Following the approach of Ref. [118], in Appendix D we have improved the factorized flux at infinity by fitting the $\rho_{\ell m}$'s to the Teukolsky-equation data. These fits can be useful for very accurate numerical evolution of PN or EOB equations of motions for EMRIs, and also for the merger modeling of small mass-ratio binary systems [114].

5.4.2 Comparison with the numerical flux through the black-hole horizon

In Fig. 5.6 we compare the BH-absorption Taylor-expanded PN flux from Ref. [141] and our factorized flux to the numerical flux produced with the frequency-domain Teukolsky equation, normalized to the leading order luminosity at infinity. In Fig. 5.7 we plot the fractional difference between numerical and factorized fluxes. The factorized model is quite effective in reproducing the numerical data, not only because we have factorized the zero $(1 - \Omega/\Omega_H)$ in Eq. (5.36), but also because

[9] Besides the $\rho_{\ell m}$–factorization discussed in Sec. 5.3.1, Ref. [101] also proposed an improved resummation of the $\rho_{\ell m}$ polynomials, which consists in factoring out their 0.5PN, 1PN and 1.5PN order terms, with a significant improvement in the modeling error.

we have factorized the pole at the LR through the source term $\hat{S}_{\rm eff}^{(\epsilon)}$ in Eq. (5.36). As we see in Fig. 5.6, the factorized flux is quite close to the numerical flux up to $q \leq 0.5$, but starts performing not very well soon after the ISCO when $q \geq 0.7$, systematically underestimating $|F^{\rm H}|$ in the range $v_{\rm ISCO} < v < v_{\rm H}$ for large positive spins. As we see in Fig. 5.7, for spins $-1 \leq q \leq 0.5$ the agreement of the factorized model to the numerical data is better than 1% up to the ISCO, with a remarkable improvement over the Taylor-expanded PN model. For instance, for $q = 0.5$, the ISCO is located at $v_{\rm ISCO} \approx 0.48$. Up to the ISCO the agreement is below 1%, while in the last part of the frequency range (up to the LR) we see that the performance becomes worse. For larger spins the factorized model starts to visibly depart from the numerical data even before the ISCO, but the error is still within 50% at the ISCO for $q = 0.9$. By contrast, the Taylor-expanded PN model is completely off. For positive spins we see that the relative error of the factorized model goes to zero at $v = (M\Omega_{\rm H})^{1/3} \equiv v_{\rm H}$, which is where our model by construction agrees with the Teukolsky-equation data thanks to the factor $(1 - \Omega/\Omega_{\rm H})$. On the other hand, the Taylor-expanded PN model has the wrong sign at high frequencies when $q > 0$.

The large modeling error of the factorized flux for $q \geq 0.7$ after the ISCO should not be a reason for significant concern. Physical inspirals will not include circular motion beyond the ISCO; the main purpose of modeling fluxes from these orbits is to properly include the influence of this pole near the light ring. The physical motion will in fact transition to a rapid plunge near the ISCO, generating negligible flux. In Ref. [114], we evolved EOB equations of motions incorporating the absorption flux into the radiation reaction force. We found that using the

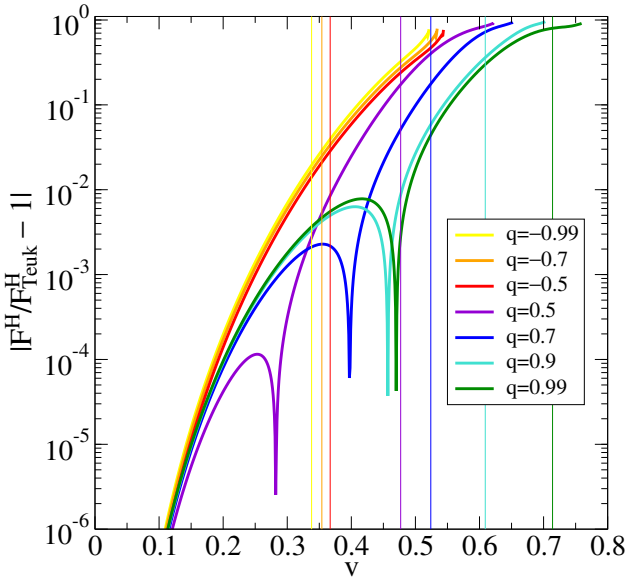

Figure 5.7: We show the fractional difference between the total factorized and Teukolsky-equation fluxes. All curves extend up to the respective LRs. Vertical lines mark the positions of the respective ISCOs.

exact Teukolsky-equation flux or the factorized model flux of this paper makes very little difference in terms of the duration of the inspiral. For the large spin cases (i.e., those with the largest modeling error even before the ISCO) the length of the inspiral varies by at most $\sim 0.5\%$. In any case, if higher modeling accuracy on $F^{\rm H}$ is needed, one can of course resort to a similar approach to what Refs. [118,128] did for F^{∞}, namely fitting the numerical data. We pursue this task in Appendix E.

Let us now focus on the multipolar modes of the BH-absorption flux, rather than the total flux. In Figs. 5.8 and 5.9 we compare the dominant (2,2) mode and leading subdominant (2,1) mode. We only show the results for the $\tilde{\rho}^{\rm H}$ factorization, but comment also about the performance of the Taylor flux below. For the $\ell = 2$ modes, the relative error of our factorized model is at least 1 order of magnitude

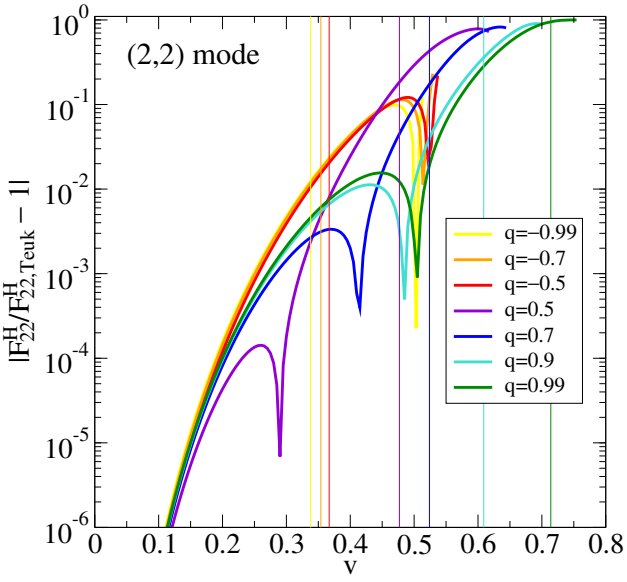

Figure 5.8: We show the fractional error of our model with respect to the (2,2) mode of the Teukolsky-equation BH-absorption flux. All curves extend up to the respective LRs. Vertical lines mark the positions of the respective ISCOs.

smaller than the Taylor-expanded PN model across the entire frequency range up to the LR. We also find that for the (3,3) mode the improvement of the factorized model over the Taylor-expanded PN model is more modest, especially at higher frequencies. For positive spins the Taylor-expanded PN (3,3) mode has actually a comparable performance to the factorized flux. This can be explained from the fact that the analytical knowledge for $\ell = 3, 4$ modes is pretty limited [see Eqs. (I2)-(I7) in Ref. [141]], so that the two models cannot differ drastically.

As we have discussed, in the factorized approach, the main ingredient of modeling the absorption flux is the polynomial factor $\tilde{\rho}^{\rm H}_{\ell m}$. Future progress in the PN knowledge of the analytical fluxes will directly translate into new, higher-order terms in the $\tilde{\rho}^{\rm H}_{\ell m}$ polynomials. Therefore it is useful to explicitly compute the Teukolsky-

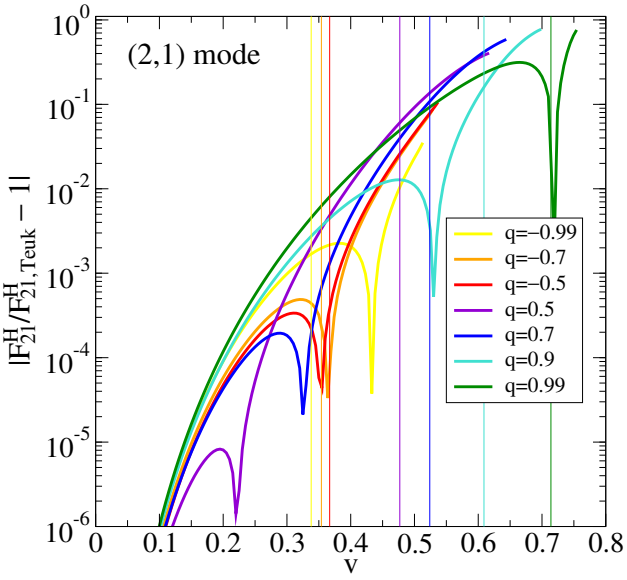

Figure 5.9: We show the fractional error of our model with respect to the (2,1) mode of the Teukolsky-equation BH-absorption flux. All curves extend up to the respective LRs. Vertical lines mark the positions of the respective ISCOs.

equation $\tilde{\rho}^{\rm H}_{\ell m,{\rm Teuk}}$'s. We simply divide $F^{\rm H}_{\ell m,{\rm Teuk}}$ by the leading and source terms, and take the 2ℓth root. The result is shown in Fig. 5.10, only for the $\ell = 2$ modes. A peculiar feature (generically seen in all modes with $\ell = m$) is the peak in $\tilde{\rho}^{\rm H}_{22,{\rm Teuk}}$ in the strong-field regime, inside the ISCO and close to the LR. Such feature is completely missed by the polynomial model of Eq. (F.11). Reference [128] noticed a similar shape in the nonspinning limit, using their $\rho^{\rm H}_{22}$ mode [defined through Eq. (5.34)], and proposed to fit it through a rational function. The $\tilde{\rho}^{\rm H}_{21,{\rm Teuk}}$'s do not display any relevant feature at high frequencies; this is the case also for all the other $\ell \neq |m|$ modes that we checked. In Appendix E we provide a more accurate analytical representation of the absorption flux by fitting the Teukolsky-equation flux $F^{\rm H}$. These fits can be useful for very accurate numerical evolution of PN or EOB equations

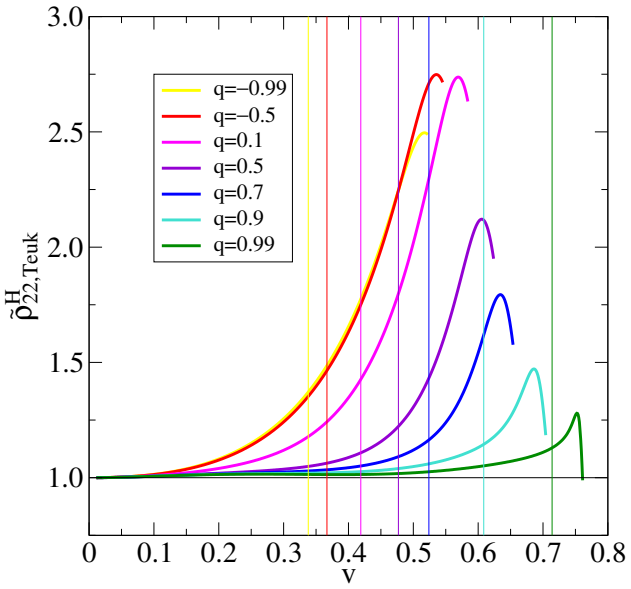

Figure 5.10: We show the Teukolsky-equation $\tilde{\rho}^{\rm H}_{22}$ as functions of v. All curves extend up to $r = r_{\rm LR} + 0.01M$. As in the nonspinning case [128], also in the spinning case the Teukolsky-equation $\tilde{\rho}^{\rm H}_{22}$ behaves nonmonotonically in the strong-field region close to the LR. This peculiar behavior cannot be easily captured by a polynomial model. This holds true also for other modes with $\ell = m$. On the other hand, the Teukolsky-equation $\tilde{\rho}^{\rm H}_{\ell m}$'s for $\ell \neq |m|$ [e.g., the (2,1) mode] have monotonic dependence on v up to the LR. Vertical lines mark the positions of the respective ISCOs.

of motion for EMRIs, and also for the merger modeling of small mass-ratio binary systems [114].

5.4.3 Comparing black-hole absorption fluxes in the nonspinning case

Before ending this section we want to compare our nonspinning results to the numerical data and to the results of Ref. [128]. As discussed above, the BH-absorption Taylor-expanded PN flux is known through 6PN order beyond $F^{\infty,\rm N}$ [see Eq. (5.35)]. However, in Ref. [128], where the Schwarzschild case was considered,

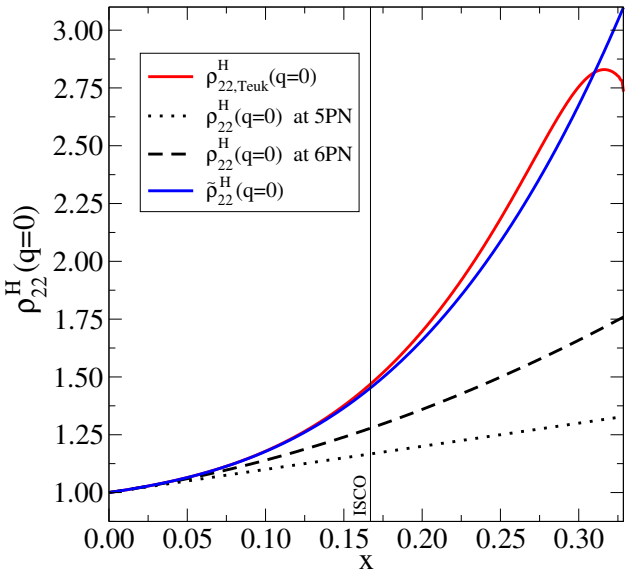

Figure 5.11: We compare the nonspinning $\rho^{\rm H}_{22}$ computed from the Teukolsky-equation data of $F^{\rm H}_{22}$ with the nonspinning factorized flux derived in Ref. [128] up to 5PN order and in this paper up to 6PN order. We also include the nonspinning limit of the factorized flux $\tilde{\rho}^{\rm H}_{22}$ proposed in this paper. The curves are plotted against $x \equiv (M\Omega)^{2/3} = v^2$ and extend up to the LR in $x_{\rm LR} = 1/3$. A vertical line marks the ISCO in $x_{\rm ISCO} = 1/6$.

the authors used the Taylor-expanded PN flux only through 5PN order and, as a consequence, using Eq. (5.34) they computed the BH-absorption factorized flux only up to 5PN order. Using the full information contained in Refs. [140, 141] for the Taylor-expanded PN flux we obtain $\rho^{\rm H}_{22}$ through 6PN order, that is,

$$\rho^{\rm H}_{22}(q=0) = 1 + v^2 + \frac{335}{84} v^4 + \mathcal{O}(v^6)\,. \tag{5.54}$$

In Fig. 5.11 we show for $q = 0$ the $\rho^{\rm H}_{22}$ extracted from the numerical data as

$$\rho^{\rm H}_{22,\,\rm Teuk}(q=0) \equiv \left[\frac{2F^{\rm H}_{22,\,\rm Teuk}(q=0)}{\frac{32}{5}\left(\frac{\mu}{M}\right)^2 v^{18} (\hat{S}^{(0)}_{\rm eff})^2}\right]^{1/4}, \tag{5.55}$$

the $\rho^{\rm H}_{22}$ at 5PN and 6PN order from Eq. (5.54), and the nonspinning limit of the $\tilde{\rho}^{\rm H}_{22}$ proposed in this paper.

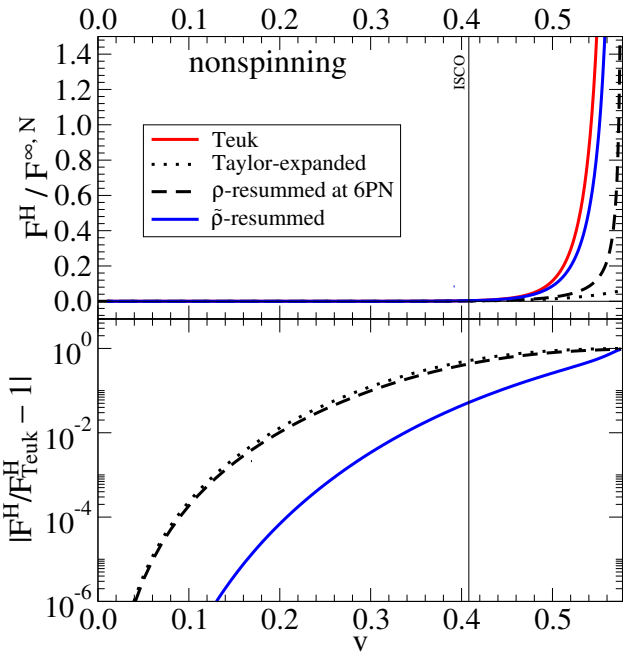

Figure 5.12: We compare the nonspinning BH-absorption Teukolsky-equation flux to the nonspinning Taylor-expanded PN model of Ref. [141] [see Eq. (5.35)], the $\rho^{\rm H}_{\ell m}$-factorized model [see Eq. (5.34)], and the nonspinning limit of the $\tilde{\rho}^{\rm H}_{\ell m}$-factorized model of this paper. A vertical line marks the ISCO. The curves extend up to the LR.

It is interesting to observe that our $\tilde{\rho}^{\rm H}_{22}$ is much closer to the numerical data than the $\rho^{\rm H}_{22}$. We emphasize that in the nonspinning limit $\tilde{\rho}^{\rm H}_{22}$ contains higher-order PN terms produced by the factorization procedure, which singles out the zero $(1-\Omega/\Omega_H)$.

For the sake of completeness, we list the rest of the $\rho^{\rm H}_{\ell m}$'s defined in Eq. (5.34) for $q=0$, which are computed starting from the nonspinning limit of the Taylor-

expanded modes:

$$\rho^{\rm H}_{21}(q=0) = 1+\frac{19}{12}v^2+\mathcal{O}(v^4)\,, \tag{5.56}$$

$$\rho^{\rm H}_{33}(q=0) = \rho^{\rm H}_{31}(q=0)=1+\mathcal{O}(v^2)\,, \tag{5.57}$$

$$\rho^{\rm H}_{32}(q=0) = \rho^{\rm H}_{4m}(q=0)=\mathcal{O}(v)\,. \tag{5.58}$$

Last, in Fig. 5.12 we consider the nonspinning limit and compare the BH-absorption total numerical flux to the nonspinning (i) Taylor-expanded PN flux [141], (ii) the $\rho^{\rm H}_{\ell m}$ factorized flux from Eq. (5.35) and (iii) the $\tilde{\rho}^{\rm H}_{\ell m}$ factorized flux proposed in this paper and given in Eq. (5.41).

5.5 Conclusions

Building on Refs. [100, 101, 128], we have proposed a new analytical model for the BH-absorption energy flux of a test particle on a circular orbit in the equatorial plane of a Kerr BH. We recast the Taylor-expanded PN flux in a factorized form that allowed us to enforce two key features present in BH perturbation theory: the presence of a zero at a frequency equal to the frequency of the horizon, and the divergence at the LR. The latter was also adopted for the energy flux at infinity in Refs. [100, 101, 128]. These features are not captured by the Taylor-expanded PN flux. We compared our model to the absorption flux computed from the numerical solution of the Teukolsky equation in the frequency domain [116, 117, 131]. In particular, we computed the gravitational-wave fluxes both at infinity and through the horizon for a Kerr spin $-0.99 \leq q \leq 0.99$, and for the first time down to a radial separation $r = r_{\rm LR} + 0.01M$. This extended previous work [118] to unstable circular

orbits below the ISCO.

We investigated the hierarchy of the multipolar flux modes. As the spin grows to large positive values, more and more modes become comparable to the dominant (2,2) mode, even before the ISCO. Among modes with the same value of ℓ, the dominant ones are those with $\ell = |m|$. Close to the LR all modes with $\ell = |m|$ become comparable to the (2,2) mode. We also studied how the mode hierarchy changes at the ISCO frequency when we vary the spin. We found that only the $(2, 1)$ and $(3, 3)$ modes are always larger than 1% of the $(2, 2)$ mode (see Fig. 5.4); only when $q \gtrsim 0.95$ are the (4,4), (5,5), (6,6), and (3,2) modes above the 1% threshold at the ISCO. One can understand these facts analytically within the WKB approximation, as already pointed out by old studies on geodesic synchrotron radiation [242–245]. One can rewrite the radial Teukolsky equation in a Schrödinger-like form, so that the flux modes turn out to be proportional to a barrier-penetration factor that exponentially suppresses modes with $\ell \neq |m|$.

We compared the numerical fluxes at infinity and through the horizon with the factorized fluxes for several spin values $-0.99 \leq q \leq 0.99$. For the energy flux at infinity, we found that the factorized model developed in Ref. [101] is reliable for retrograde orbits and in the nonspinning case almost up to the LR, but performs rather poorly for large spin prograde orbits close to the LR. For the BH-absorption energy flux we found that the agreement of the factorized flux to the numerical flux is always better than the one of the Taylor-expanded PN flux. The fractional difference between the numerical and factorized flux is less than 1% up to the ISCO for $-1 \leq q \leq 0.5$. For spins $q > 0.7$ the factorized flux starts performing worse, even

before the ISCO, but it always performs better than the Taylor-expanded PN flux. We expect that the large modeling error after the ISCO for $q > 0.7$ will not affect much the inspiral, merger, and ringdown waveforms produced with the time-domain Teukolsky equation evolved with the factorized flux. In fact, the energy flux does not have much effect beyond the ISCO, since the system's dynamics at that point are well described by a plunging geodesic. In Ref. [114] we show that evolving an EOB dynamics with the factorized model instead of the numerical flux introduces a difference in the time of coalescence smaller than half of a percent across the whole spin range.

Finally, in Appendices D and E we computed fits to the numerical fluxes at infinity and through the horizon that could be used for highly accurate numerical evolution of EMRIs using PN or EOB equations of motion, and also for modeling the merger waveforms of small mass-ratio binary systems [114].

Future work may address the issue of why the total energy fluxes normalized to the specific energy diverge when computed exactly at the photon orbit. In fact, as we discussed, in this case the WKB treatment suggests a nonconvergent sum over the multipolar modes [see Eq. (5.18)], since the cutoff mode index ℓ_c would go to $+\infty$. This issue is of broader interest, since it is also present in the context of ultrarelativistic BH encounters [275].

In the near future we plan to extend the factorized model of the BH-absorption flux to the case of spinning comparable-mass BHs, so that it can be used in the EOB model when calibrating it to numerical-relativity simulations.

Chapter 6: **Reducing orbital eccentricity of precessing black-hole binaries**

Authors: *Alessandra Buonanno, Lawrence E. Kidder, Abdul H. Mroué, Harald P. Pfeiffer, and Andrea Taracchini*[1]

Abstract: Building initial conditions for generic binary black-hole evolutions which are not affected by initial spurious eccentricity remains a challenge for numerical-relativity simulations. This problem can be overcome by applying an eccentricity-removal procedure which consists of evolving the binary black hole for a couple of orbits, estimating the resulting eccentricity, and then restarting the simulation with corrected initial conditions. The presence of spins can complicate this procedure. As predicted by post-Newtonian theory, spin-spin interactions and precession prevent the binary from moving along an adiabatic sequence of spherical orbits, inducing oscillations in the radial separation and in the orbital frequency. For single-spin binary black holes these oscillations are a direct consequence of monopole-quadrupole interactions. However, spin-induced oscillations occur at approximately twice the orbital frequency, and therefore can be distinguished and disentangled from the initial spurious eccentricity which occurs at approximately the orbital frequency.

[1]Originally published as Phys. Rev. D **83**, 104034 (2011)

Taking this into account, we develop a new eccentricity-removal procedure based on the derivative of the orbital frequency and find that it is rather successful in reducing the eccentricity measured in the orbital frequency to values less than 10^{-4} when moderate spins are present. We test this new procedure using numerical-relativity simulations of binary black holes with mass ratios 1.5 and 3, spin magnitude 0.5, and various spin orientations. The numerical simulations exhibit spin-induced oscillations in the dynamics at approximately twice the orbital frequency. Oscillations of similar frequency are also visible in the gravitational-wave phase and frequency of the dominant $l = 2$, $m = 2$ mode.

6.1 Introduction

Over the last few years, numerical simulations of binary black holes have improved tremendously (see e.g., the recent reviews [280–282]). These simulations are now used to aid data analysts for gravitational-wave detectors in the construction of analytical templates [72, 239, 283–286], and in testing the efficiency of detector pipelines by injecting numerical waveforms [287].

During the gravitational-radiation driven inspiral of a binary black hole, the orbital eccentricity decreases very quickly [103, 288]. For binary black holes formed from binary stellar evolution [289] (instead of dynamical capture [290, 291]), the orbital eccentricity is expected to be essentially zero by the time the binary enters the frequency band of ground-based gravitational-wave detectors. Therefore, it is important that numerical simulations can be done for very low eccentricity binaries.

Performing black-hole simulations with very small orbital eccentricity is not easy for several reasons. Orbital parameters that result in vanishing eccentricity are only known approximately through post-Newtonian (PN) theory [292]. The translation of orbital parameters from PN theory into a complete binary black-hole initial-data set is ambiguous, because of differing coordinate systems and effects arising from solving the non-linear Einstein constraint equations [183]. And finally, early in a numerical evolution each black hole relaxes toward a steady state, affecting the black-hole masses, spins [184–186], and orbital parameters.

The complete evolution of a binary black hole is determined by its initial data. Therefore, control of orbital eccentricity has to be addressed in the construction of the initial data. The first approaches to construct low-eccentricity initial data were based on the assumption of *circular* orbits with the orbital frequency determined by the effective potential method [293–295] and the "Komar mass" ansatz [296–300]. Both methods were shown to give similar results [300]. Reference [301] presented techniques to measure eccentricity based on initial data alone. When binary black-hole evolutions became possible [80–82], it was realized that initial data constructed using the assumption of circular orbits resulted in a *spurious* orbital eccentricity of order one percent [**?**, **?**, 304], primarily due to neglecting the radial inspiral velocity, and due to the initial relaxation of the black holes.

Two techniques are in use to achieve an orbital eccentricity smaller than what can be achieved with quasi-circular initial data. One approach [302] evolves PN equations for the trajectories of the centers of the black holes. This subsidiary evolution of ordinary differential equations is started at large initial separation, so that

any spurious eccentricity due to the initial conditions dies out and the binary settles down to an inspiraling orbit with non-zero radial velocity. At the desired separation, the subsidiary evolution is stopped, the positions and velocities of the particles are read off, and are used as initial data parameters for the construction of the initial data set for the subsequent numerical evolution. This approach reduces eccentricity to about 0.002 for equal-mass, non-spinning binaries, but is less successful for unequal masses or high spins [303].

The second approach, proposed in Ref. [304] and refined in Ref. [305], performs an iterative procedure (see also Ref. [306]). One begins with initial data with reasonably low eccentricity, e.g., quasi-equilibrium initial data or initial data utilizing PN information. One evolves this initial data for about two to three orbits, analyzes the orbit, and computes an improved initial data set with (hopefully) lower eccentricity. This procedure can be repeated until the desired degree of eccentricity is obtained.

In past applications, eccentricity removal was based on the behavior of the proper separation s between the black hole apparent horizons. For non-spinning black hole binaries [210] or binaries with spins parallel to the orbital angular momentum [186, 307], this works very well, and the eccentricity drops by about an order of magnitude with each iteration. However, when one applies this eccentricity removal procedure to *precessing* binaries, one encounters the difficulties illustrated in Fig. 6.1. At high eccentricity $e \gtrsim 0.01$, $\dot{s}$ (where we indicate with a dot the derivative with respect to time) shows the expected oscillations with a period some-

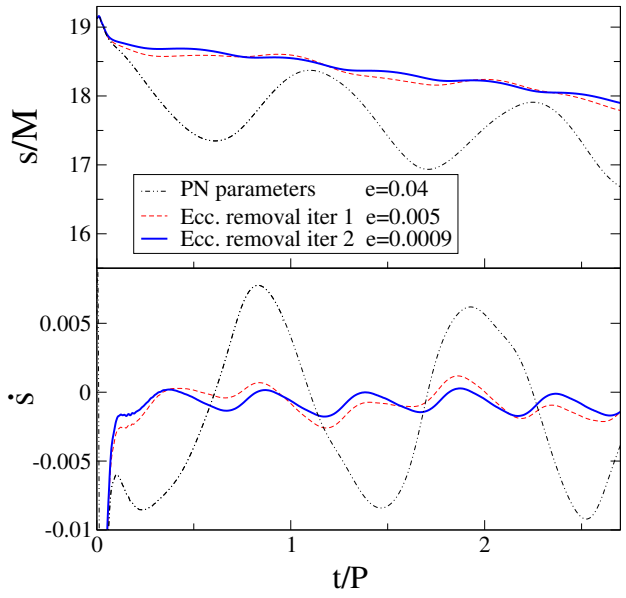

Figure 6.1: Eccentricity removal based on **proper separation** applied to a *precessing* binary black hole: The horizontal axis represents time in units of the initial orbital period $P = 442M$. For eccentricity $e \gtrsim 0.01$, oscillations due to orbital eccentricity with period $\sim P$ dominate, and eccentricity removal is effective. For $e \sim 0.01$ oscillations at *one-half* the orbital period become apparent, spoiling further eccentricity removal based on $\dot{s}$. In this example, the mass-ratio is $m_1/m_2 = 1.5$, the larger black hole carries spin $S_1 = 0.5m_1^2$ with initial direction tangent to the orbital plane, and the smaller black hole has zero spin.

what longer than the orbital period.[2] At sufficiently small eccentricity, however, the proper separation s and the radial velocity $\dot{s}$ exhibit oscillations at *twice* the orbital frequency (or one-half the orbital period). This frequency is distinct from the frequency of oscillations caused by orbital eccentricity, and its presence makes it very hard to further reduce eccentricity based on an analysis of the proper separation s.

In this paper, we investigate these oscillations at twice the orbital frequency, and develop techniques for eccentricity removal for precessing binaries that mitigate

[2]The period of radial oscillations exceeds the orbital period because of periastron advance [308].

the issues illustrated in Fig. 6.1. We can understand these oscillations based on PN calculations. In fact, as it was shown in Refs. [153,309,310], spin-spin interactions in the dynamics and spin precession, can introduce oscillations in the orbital separation and orbital frequency that prevent the binary from moving along a sequence of spherical orbits. Moreover, for single-spin binary black holes, the presence of spin-induced oscillations in the dynamics is a direct consequence of monopole-quadrupole interactions, that is of interactions of the form $m_1 S_2^2/m_2$ and $m_2 S_1^2/m_1$. It turns out that the amplitude of the *spin-induced oscillations* in the orbital frequency is half the amplitude of the oscillations in the coordinate separation. Therefore, we propose to base the iterative eccentricity removal on the orbital frequency and its time-derivative. We develop the relevant updating formulae for iterative eccentricity removal based on the (time-derivative) of the orbital frequency, and demonstrate with fully numerical simulations that iterative eccentricity removal can proceed to much smaller eccentricities $e \lesssim 10^{-4}$ that are measured in the orbital frequency.

We also find that PN theory predicts spin-induced oscillations in the separation with much smaller amplitude than those visible in Fig. 6.1. Figure 6.1 utilizes the *proper separation* s between the apparent horizons along a line element joining their centers. We find that use of the *coordinate separation* between the centers of the apparent horizons instead results in much smaller oscillations. Finally, we find that the spin-induced oscillations are also present in the gravitational-wave frequency and phase, and are qualitatively reproduced by the simple PN model used here.

This paper is organized as follows. In Sec. 6.2, we work out the spin-induced oscillations in the radial separation and orbital frequency for a PN model utiliz-

ing the Taylor-expanded PN Hamiltonian with only the lowest order PN terms responsible for the spin-induced oscillations. We also compare the obtained analytic formulae with numerical solutions of the ordinary differential equations describing a PN binary. In Sec. 6.3, we present the new method to reduce orbital eccentricity in presence of spins. In Sec. 6.4, we apply our improved eccentricity-removal procedure to fully general-relativistic simulations of single and double spin binary black holes, and compare the results with the earlier eccentricity-removal procedure based on the proper horizon separation. We also investigate the presence of spin-induced oscillations in the gauge-invariant gravitational-wave phase and frequency of a single-spin binary black hole. Finally, in Sec. 11.5 we summarize our main conclusions.

6.2 Eccentricity and spin-induced oscillations

As mentioned in the introduction, spin-spin effects and precession can induce oscillations in the orbital radial separation and frequency preventing the binary black holes from moving along an adiabatic sequence of spherical orbits. This result can be obtained in a straightforward manner in PN theory [153, 309, 310]. Here we re-analyse it in some detail using the PN Hamiltonian formalism.

As we shall see, when spins are not aligned with the initial direction of the orbital angular momentum, the spin-induced oscillations are unavoidable and their importance increases at smaller distances, since at leading order spin-spin interactions scale as $1/r^3$, where r is the binary separation. Thus, if we were to start the binary black-hole evolution at large separation with some initial orbital eccentricity,

we expect that, by the time the binary reaches smaller separations, only spin-induced oscillations would be left. However, numerical-relativity simulations start the evolution at a separation where the initial orbital eccentricity is not negligible. As we shall discuss, there exists an efficient way to distinguish and disentangle the initial orbital eccentricity from the spin-induced oscillations, namely the typical frequency at which these two effects occur.

Henceforth we use natural units $G = c = 1$.

6.2.1 Eccentricity in Newtonian dynamics

Here we briefly review some useful formulae of Newtonian dynamics of eccentric orbits that we shall use below.

In the center-of-mass frame, the two-body problem reduces to a one-body problem for a particle of reduced mass $\mu = m_1\, m_2/M$, subject to the acceleration $\ddot{\mathbf{r}} = -M/r^3\, \mathbf{r}$, where $M = m_1 + m_2$ is the total mass of the binary. In the Keplerian parametrization, a Newtonian orbit of eccentricity e can be described in terms of the eccentric anomaly u (see, e.g., Ref. [14])

$$u(t) - e \sin u(t) = \bar{\Omega}\, t, \tag{6.1}$$

where $\bar{\Omega} = \sqrt{M/a^3}$, a being the semi-major axis, so that

$$r(t) = \frac{\bar{r}}{1 - e^2}\, \left[1 - e\, \cos u(t)\right], \tag{6.2}$$

where $\bar{r} = a\,(1 - e^2)$. In the limit of small e we can approximate $r(t)$ using only the first harmonic, that is

$$r(t) = \bar{r}\, \left[1 - e\, \cos\left(\bar{\Omega} t\right)\right] + \mathcal{O}(e^2). \tag{6.3}$$

In fact, although the frequency spectrum of $r(t)$ contains all harmonics in $\bar{\Omega}$, a Fourier analysis of $r(t)$ shows that harmonics beyond the first one are quite suppressed in presence of a small eccentricity (see, e.g., Ref. [14]). In the Keplerian parametrization the orbital frequency reads

$$\Omega(t) = \frac{\bar{\Omega}\sqrt{1-e^2}}{\left[1 - e\,\cos u(t)\right]^2}\,, \tag{6.4}$$

and in the limit of small e we find

$$\Omega(t) = \bar{\Omega}\left[1 + 2e\,\cos\left(\bar{\Omega}t\right)\right] + \mathcal{O}(e^2). \tag{6.5}$$

So, in Newtonian dynamics, whenever we have an eccentricity in $r(t)$, we expect oscillations of amplitude $2e\,\bar{\Omega}$ at the frequency $\bar{\Omega}$ in $\Omega(t)$.

6.2.2 Two-body dynamics for spinning black holes in PN theory

We consider a binary composed of two black holes with masses m_1 and m_2 and spins $\mathbf{S}_1$ and $\mathbf{S}_2$. The binary dynamics can be described using the spinning Taylor-expanded PN Hamiltonian. In the center-of-mass frame, the Hamiltonian depends on the canonical variables $(\mathbf{r}, \mathbf{p})$ which describe the motion of a particle of reduced mass μ, and on the spins $\mathbf{S}_1$ and $\mathbf{S}_2$.

For the purposes of our analysis, it is sufficient to restrict the discussion to the Newtonian Hamiltonian, $H_{\rm Newt}$, and include only the leading 1.5PN spin-orbit (SO) interaction [311], $H_{\rm SO}$, and the leading 2PN spin-spin (SS) interaction [150], $H_{\rm SS}$, where the SS interaction includes spin-induced monopole-quadrupole terms [188]. The Hamiltonian reads

$$H = H(\mathbf{r}, \mathbf{p}; \mathbf{S}_1, \mathbf{S}_2) = H_{\rm Newt} + H_{\rm SO} + H_{\rm SS}, \tag{6.6}$$

where

$$H_{\rm Newt} = \frac{\mathbf{p}^2}{2\mu} - \frac{\mu M}{r}, \tag{6.7}$$

$$H_{\rm SO} = \frac{2}{r^3}\mathbf{S}_{\rm eff}\cdot\mathbf{L}, \tag{6.8}$$

$$H_{\rm SS} = \frac{\mu}{2Mr^3}\left[3\left(\mathbf{S}_0\cdot\hat{\mathbf{n}}\right)^2 - \mathbf{S}_0^2\right], \tag{6.9}$$

with $\mathbf{L} = \mathbf{r}\times\mathbf{p}$, $\hat{\mathbf{n}} = \mathbf{r}/|\mathbf{r}|$ and

$$\mathbf{S}_{\rm eff} = \left(1+\frac{3m_2}{4m_1}\right)\mathbf{S}_1 + \left(1+\frac{3m_1}{4m_2}\right)\mathbf{S}_2, \tag{6.10}$$

$$\mathbf{S}_0 = \left(1+\frac{m_2}{m_1}\right)\mathbf{S}_1 + \left(1+\frac{m_1}{m_2}\right)\mathbf{S}_2. \tag{6.11}$$

For reference, we point out that $\mathbf{S}_0$ can be rewritten in dimensionless form as

$$\frac{\mathbf{S}_0}{M^2} = \frac{m_1}{M}\,\frac{\mathbf{S}_1}{m_1^2} + \frac{m_2}{M}\,\frac{\mathbf{S}_2}{m_2^2}. \tag{6.12}$$

The Hamilton equations of motion are given by

$$\dot{r}^i = \{r^i, H\} = \frac{\partial H}{\partial p_i}, \tag{6.13}$$

$$\dot{p}_i = \{p_i, H\} + F_i = -\frac{\partial H}{\partial r^i} + F_i, \tag{6.14}$$

where F_i is the radiation-reaction force. Here we follow Ref. [102] and express F_i in terms of the Newtonian energy flux $\mathcal{F}_{\rm N} = 32\mu^2/(5M^2)\,v^{10}$ [see Eqs. (3.15), (3.27) in Ref. [102])] where for quasi-circular orbits $v = (M\,\Omega)^{1/3}$. Equations (6.13), (6.14) must be supplemented with the spin precession equations

$$\dot{S}_1^i = \{S_1^i, H\} = \varepsilon^{ijk}\,\frac{\partial H}{\partial S_1^j}\,S_{1k}, \tag{6.15}$$

$$\dot{S}_2^i = \{S_2^i, H\} = \varepsilon^{ijk}\,\frac{\partial H}{\partial S_2^j}\,S_{2k}, \tag{6.16}$$

where ε^{ijk} is the Levi-Civita symbol in flat spacetime. The non-spinning conservative part of the dynamics together with the lowest-order SO interactions allows the existence of spherical orbits [$r(t)$=const.] [188]. In fact, if we consider $H = H_{\rm Newt} + H_{\rm SO}$, it is straightforward to show that the Hamiltonian is a spherically symmetric function that depends *only* on the radial separation and its conjugated momentum, i.e., $H = H(r, p_r)$. This happens because the other degrees of freedom are constrained by the constants of motion: $\mathbf{L}^2$ and $\mathbf{S}_{\rm eff} \cdot \mathbf{L}$. More explicitly

$$H(r, p_r) = \frac{1}{2\mu}\left(p_r^2 + \frac{\mathbf{L}^2}{r^2}\right) - \frac{\mu M}{r} + \frac{2}{r^3}\mathbf{S}_{\rm eff} \cdot \mathbf{L}. \tag{6.17}$$

Imposing that at $t = 0$, $r = r_0 = $ const., we have

$$[\dot{r}]_0 = \left[\frac{\partial H}{\partial p_r}\right]_0 = \left[\frac{p_r}{\mu}\right]_0 = 0 \tag{6.18}$$

and to have a stable spherical orbit we have to require also that $[\dot{p}_r]_0 = 0$, hence

$$\begin{aligned} [\dot{p}_r]_0 &= \left[-\frac{\partial H}{\partial r}(r, p_r = 0)\right]_0 \\ &= \left[\frac{\mathbf{L}^2}{\mu\, r^3} - \frac{\mu\, M}{r^2} + \frac{6}{r^4}\mathbf{S}_{\rm eff} \cdot \mathbf{L}\right]_0 = 0. \end{aligned} \tag{6.19}$$

Choosing properly $\mathbf{L}^2$ and $\mathbf{S}_{\rm eff} \cdot \mathbf{L}$ to satisfy Eq. (6.19), we obtain spherical orbits. However, once SS interactions are included, this is no longer true, since $\mathbf{L}^2$ and $\mathbf{S}_{\rm eff} \cdot \mathbf{L}$ are no longer constants of motion. Therefore, we must expect oscillations induced by SS terms in the radial separation and orbital frequency about their average values.

6.2.3 Oscillations induced by leading SS interactions: conservative dynamics

In this section, we investigate the behavior of the radial separation r and of the orbital frequency Ω at 2PN order for the conservative non-spinning dynamics. While doing so, we will also assume a negligible precession of the spins and of the orbital plane, since it takes place on a longer timescale than the effects we are interested in. Henceforth, we follow the method outlined in Appendix B of Ref. [310].

As a first step, we restrict ourselves to the case in which radiation-reaction is not present (i.e., $F_i = 0$). As discussed earlier, the presence of SS terms prevents r and Ω from being constant. Thus, we write [310]

$$r(t) = \bar{r} + \delta r(t), \quad \Omega(t) = \bar{\Omega} + \delta\Omega(t), \tag{6.20}$$

where the bar stands for time-average $\langle \dots \rangle$ over one orbital period; hence, by definition, $\langle \delta r(t) \rangle = \langle \delta\Omega(t) \rangle = 0$. Our goal is to determine the equations that the oscillations $\delta r(t)$ and $\delta\Omega(t)$ must obey at 2PN order. For convenience, we decompose vectors with respect to the triad defined by

$$\hat{\mathbf{n}} = \frac{\mathbf{r}}{r}, \quad \hat{\mathbf{L}}_{\rm N} = \frac{\mathbf{r} \times \dot{\mathbf{r}}}{|\mathbf{r} \times \dot{\mathbf{r}}|}, \quad \hat{\boldsymbol{\lambda}} = \hat{\mathbf{L}}_{\rm N} \times \hat{\mathbf{n}}. \tag{6.21}$$

This triad is such that $\hat{\mathbf{n}}$ and $\hat{\boldsymbol{\lambda}}$ are in the instantaneous orbital plane, while $\hat{\mathbf{L}}_{\rm N}$ is orthogonal to it. In the instantaneous orbital plane, we have the velocity

$$\mathbf{v} = \dot{\mathbf{r}} = \dot{r}\, \hat{\mathbf{n}} + \Omega\, r\, \hat{\boldsymbol{\lambda}}\,, \tag{6.22}$$

and the acceleration

$$\mathbf{a} = a_{\rm rad}\, \hat{\mathbf{n}} + a_{\rm tan}\, \hat{\boldsymbol{\lambda}} + a_{\perp} \hat{\mathbf{L}}_{\rm N}, \tag{6.23}$$

with

$$a_{\rm rad} = \hat{\mathbf{n}} \cdot \ddot{\mathbf{r}} = \ddot{r} - r\,\Omega^2, \tag{6.24}$$

$$a_{\rm tan} = \hat{\boldsymbol{\lambda}} \cdot \ddot{\mathbf{r}} = \frac{1}{r}\frac{d}{dt}\left(r^2\,\Omega\right), \tag{6.25}$$

and

$$a_{\perp} = \hat{\mathbf{L}}_{\rm N} \cdot \ddot{\mathbf{r}} = r\,\Omega\left(\hat{\boldsymbol{\lambda}} \cdot \frac{d\hat{\mathbf{L}}_{\rm N}}{dt}\right). \tag{6.26}$$

For future reference, we define the projection of $\mathbf{S}_0$ on the instantaneous orbital plane

$$\mathbf{S}_{0\perp} = \mathbf{S}_0 - \mathbf{S}_0 \cdot \hat{\mathbf{L}}_{\rm N}. \tag{6.27}$$

Note that Eq. (6.22) implicitly defines Ω. We have $\Omega = (\dot{\mathbf{r}} \cdot \hat{\boldsymbol{\lambda}})/r$. We need the acceleration $\ddot{\mathbf{r}}$ so we take a time derivative of Eq. (6.13) and substitute Eq. (6.14) into that. We note that the Newtonian orbital angular momentum can be written as

$$\mathbf{L}_{\rm N} = \mu\,\Omega\,r^2\,\hat{\mathbf{L}}_{\rm N}, \tag{6.28}$$

while the orbital angular momentum $\mathbf{L} = \mathbf{r} \times \mathbf{p}$ can be obtained from the Hamilton equation (6.13), that is to say

$$\dot{\mathbf{r}} = \frac{\mathbf{p}}{\mu} + \frac{2}{r^3}\left(\mathbf{S}_{\rm eff} \times \mathbf{r}\right), \tag{6.29}$$

so that

$$\mathbf{L} = \mathbf{L}_{\rm N} - \frac{2\mu}{r}\left[\mathbf{S}_{\rm eff} - \hat{\mathbf{n}}\left(\mathbf{S}_{\rm eff} \cdot \hat{\mathbf{n}}\right)\right]. \tag{6.30}$$

Since we want to work consistently at 2PN order, we replace $\mathbf{L}$ with Eq. (6.30) whenever it shows up in our calculations and drop higher PN terms. It is then

straightforward to compute the radial component of the acceleration

$$a_{\rm rad} = -\frac{M}{r^2}\left\{1 - \frac{2}{\mu M r^2}(\mathbf{S}_{\rm eff}\cdot\hat{\mathbf{L}}_{\rm N}) - \frac{3}{2M^2r^2}\,\left[3\,(\mathbf{S}_0\cdot\hat{\mathbf{n}})^2 - \mathbf{S}_0^2\right]\right\} \tag{6.31}$$

Since the leading-order spin acceleration is of 1.5PN order, we assume that the radial oscillations scale at least as $\dot{r} = \mathcal{O}(3)$.[3] Hence, when computing the tangential component of the acceleration, at 2PN accuracy, we set $\dot{r} = 0$ ($\mathbf{v} = r\,\Omega\,\hat{\boldsymbol{\lambda}}$) and $p_r = 0$ in every term coming from SO or SS interactions. Moreover, we also neglect any term depending on the time derivative of the spin in $a_{\rm tan}$, since it is of higher PN order. This means that we are implicitly assuming that the spins are constant. At 2PN order, we are left with

$$a_{\rm tan} = -\frac{3}{M\,r^4}\,(\mathbf{S}_0\cdot\hat{\mathbf{n}})\,(\mathbf{S}_0\cdot\hat{\boldsymbol{\lambda}}). \tag{6.32}$$

Combining Eq. (6.25) with Eq. (6.32), we solve for $r^2\,\Omega$ by integrating Eq. (6.32). In doing that, we assume that r and Ω in the right-hand side of Eq. (6.32) are constants, as their time derivatives are at least $\mathcal{O}(3)$, and also the spins are constants, that is they do not precess. Thus, under those assumptions, the time evolution of the triad $\{\hat{\mathbf{n}},\ \hat{\boldsymbol{\lambda}},\ \hat{\mathbf{L}}_{\rm N}\}$ is such that $\hat{\mathbf{n}}$ and $\hat{\boldsymbol{\lambda}}$ swipe the orbital plane at a frequency $\bar{\Omega}$ while $\hat{\mathbf{L}}_{\rm N}$ stays fixed:

$$\hat{\mathbf{n}}(t) = \cos(\bar{\Omega}t)\,\hat{\mathbf{n}}_0 + \sin(\bar{\Omega}t)\,\hat{\boldsymbol{\lambda}}_0, \tag{6.33}$$

$$\hat{\boldsymbol{\lambda}}(t) = -\sin(\bar{\Omega}t)\,\hat{\mathbf{n}}_0 + \cos(\bar{\Omega}t)\,\hat{\boldsymbol{\lambda}}_0, \tag{6.34}$$

$$\hat{\mathbf{L}}_{\rm N}(t) = \hat{\mathbf{L}}_{\rm N\,0}, \tag{6.35}$$

[3] We denote the nPN order as $\mathcal{O}(2n)$

where $\hat{\mathbf{n}}_0 = \hat{\mathbf{n}}(0)$, $\hat{\boldsymbol{\lambda}}_0 = \hat{\boldsymbol{\lambda}}(0)$ and $\hat{\mathbf{L}}_{\rm N\,0} = \hat{\mathbf{L}}_{\rm N}(0)$, and also

$$\dot{\hat{\mathbf{n}}} = \bar{\Omega}\,\hat{\boldsymbol{\lambda}} \qquad\qquad \dot{\hat{\boldsymbol{\lambda}}} = -\bar{\Omega}\,\hat{\mathbf{n}}. \tag{6.36}$$

Moreover, since we assume that the spins remain constant, we formally set $\mathbf{S}_1(t) = \mathbf{S}_1(0)$ and $\mathbf{S}_2(t) = \mathbf{S}_2(0)$, so in what follows $\mathbf{S}_0 = \mathbf{S}_0(0)$ and $\mathbf{S}_{\rm eff} = \mathbf{S}_{\rm eff}(0)$. By inserting Eqs. (6.20) into Eqs. (6.31) and (6.32), one obtains a pair of coupled differential equations:

$$\begin{aligned}\delta\ddot{r} - \bar{r}\,\bar{\Omega}^2 - \bar{\Omega}^2\,\delta r - 2\bar{r}\,\bar{\Omega}\,\delta\Omega = -\frac{M}{\bar{r}^2}\ \times \\ \times\left\{1 - \frac{2\bar{\Omega}}{M}(\mathbf{S}_{\rm eff}\cdot\hat{\mathbf{L}}_{\rm N}) - \frac{3}{2M^2\,\bar{r}^2}\left[3\,(\mathbf{S}_0\cdot\hat{\mathbf{n}})^2 - \mathbf{S}_0^2\right]\right\} + 2\frac{M}{\bar{r}^3}\delta r\end{aligned} \tag{6.37}$$

and

$$2\bar{\Omega}\,\bar{r}\,\delta r + \bar{r}^2\,\delta\Omega = k - \frac{3}{2M\,\bar{\Omega}\,\bar{r}^3}(\mathbf{S}_0\cdot\hat{\mathbf{n}})^2. \tag{6.38}$$

Here, k is an integration constant and, again, in the right-hand-side of the above equations we keep only terms through 2PN order. To fix k we time-average the above equations. We have

$$\begin{aligned}\left\langle(\mathbf{S}_0\cdot\hat{\mathbf{n}}(t))^2\right\rangle = S_{0i}\,S_{0j}\,\langle n^i(t)\,n^j(t)\rangle = \\ = S_{0i}\,S_{0j}\frac{1}{2}\left(\delta^{ij} - \hat{L}^i_{N0}\,\hat{L}^j_{N0}\right) = \frac{1}{2}\left[\mathbf{S}_0^2 - (\mathbf{S}_0\cdot\hat{\mathbf{L}}_{\rm N\,0})^2\right],\end{aligned} \tag{6.39}$$

obtaining

$$k = \frac{3}{4M\,\bar{\Omega}\,\bar{r}^3}\,\left[\mathbf{S}_0^2 - (\mathbf{S}_0\cdot\hat{\mathbf{L}}_{\rm N\,0})^2\right]. \tag{6.40}$$

Taking the time average of Eq. (6.37), we derive the following modified version of Kepler's law relating $\bar{r}$ and $\bar{\Omega}$

$$\bar{\Omega}^2 = \frac{M}{\bar{r}^3} - \frac{2\bar{\Omega}}{\bar{r}^3}\mathbf{S}_{\rm eff}\cdot\hat{\mathbf{L}}_{\rm N\,0} + \frac{3}{4M\bar{r}^5}\left[3(\mathbf{S}_0\cdot\hat{\mathbf{L}}_{\rm N\,0})^2 - \mathbf{S}_0^2\right]. \tag{6.41}$$

We decouple Eq. (6.37) from Eq. (6.38), then we use Eq. (6.41). Since we expect that $\delta r = \mathcal{O}(4)$, we find that at 2PN order

$$\delta\ddot{r} + \bar{\Omega}^2\,\delta r = -\frac{3}{4M\,\bar{r}^4}\left[(\mathbf{S}_0\cdot\hat{\boldsymbol{\lambda}})^2 - (\mathbf{S}_0\cdot\hat{\mathbf{n}})^2\right], \tag{6.42}$$

in agreement with Eq. (B13) of Ref. [310]. The solution of the homogeneous equation is simply

$$\delta r(t)_{\rm hom} = A_r\cos\left(\bar{\Omega}t + \varphi_r\right), \tag{6.43}$$

where A_r and φ_r are fixed by the initial conditions. Equation (6.43) describes possible oscillations due to the initial eccentricity of the orbit. This eccentricity occurs at the average orbital frequency and in principle can be removed as long as quasi-circular initial conditions are enforced. Note that Eq. (6.43) is also consistent with the Newtonian result of Eq. (6.3).[4] It is worth noting that Eq. (6.3) was derived as an expansion for a small eccentricity e, while in this section we never explicitly referred to e at all. As a matter of fact, we are dealing with quasi-circular orbits here, so that consistency between Eqs. (6.3) and (6.43) should be expected.

On the other hand, the spin-induced oscillations are described by the particular solution of Eq. (6.42) which reads

$$\delta r_{\rm part}(t) = \frac{1}{4M^2\,\bar{r}}\left[(\mathbf{S}_0\cdot\hat{\boldsymbol{\lambda}}(t))^2 - (\mathbf{S}_0\cdot\hat{\mathbf{n}}(t))^2\right]. \tag{6.44}$$

These oscillations are a signature of SS interactions since they depend on $\mathbf{S}_0$, which enters $H_{\rm SS}$. Once we know $\delta r = \delta r_{\rm hom} + \delta r_{\rm part}$, we solve Eq. (6.38) for $\delta\Omega$. Similarly to

[4]Note that Eq. (6.3) does not depend on φ because in Eq. (6.2) the radial separation at $t = 0$ is picked to be equal to the semi-major axis.

what we found above, the homogeneous solution accounts for the initial conditions, while the particular solution accounts for the oscillations induced by SS effects.

$$\delta\Omega_{\rm part}(t) = \frac{\bar{\Omega}}{4M^2\,\bar{r}^2}\left[(\mathbf{S}_0\cdot\hat{\boldsymbol{\lambda}}(t))^2 - (\mathbf{S}_0\cdot\hat{\mathbf{n}}(t))^2\right]. \tag{6.45}$$

The above equation is also consistent with the Newtonian result of Eq. (6.5).

So far, we have assumed the nonspinning dynamics to be Newtonian. If we included nonspinning PN corrections through 3PN order in the Hamiltonian, we would still find the particular solutions (6.44) and (6.45), but in this case the oscillations would occur at a frequency which will differ from Eq. (6.41) because of nonspinning PN corrections.

Using the previous results, it is straightforward to compute the time derivatives of the oscillations $\delta\dot{r}$, Eq. (6.44), and $\delta\dot{\Omega}$, Eq. (6.45). They read

$$\delta\dot{r}(t) = B_r\,\sin(\bar{\Omega}t+\varphi_r) - \frac{\bar{\Omega}}{M^2\,\bar{r}}\,(\mathbf{S}_0\cdot\hat{\mathbf{n}}(t))\,(\mathbf{S}_0\cdot\hat{\boldsymbol{\lambda}}(t)), \tag{6.46}$$

$$\delta\dot{\Omega}(t) = B_\Omega\,\sin(\bar{\Omega}t+\varphi_\Omega) - \frac{\bar{\Omega}^2}{M^2\,\bar{r}^2}\,(\mathbf{S}_0\cdot\hat{\mathbf{n}}(t))\,(\mathbf{S}_0\cdot\hat{\boldsymbol{\lambda}}(t)). \tag{6.47}$$

We note that when the spins are initially aligned or antialigned to $\hat{\mathbf{L}}_{\rm N\,0}$, the SS oscillations disappear, since in this situation $\mathbf{S}_0$ remains perpendicular to $\hat{\mathbf{n}}$ and $\hat{\boldsymbol{\lambda}}$ throughout the evolution. We see that for both quantities the time dependence of the SS term is

$$(\mathbf{S}_0\cdot\hat{\mathbf{n}}(t))\,(\mathbf{S}_0\cdot\hat{\boldsymbol{\lambda}}(t)) = C\,\sin(2\bar{\Omega}\,t+\gamma), \tag{6.48}$$

where

$$C = \frac{(\mathbf{S}_0\cdot\hat{\mathbf{n}}_0)^2 + (\mathbf{S}_0\cdot\hat{\boldsymbol{\lambda}}_0)^2}{2} \tag{6.49}$$

and γ satisfies

$$\sin\gamma = \frac{1}{2}\sin(2\alpha),$$
$$\cos\gamma = -\frac{1}{2}\cos(2\alpha), \tag{6.50}$$

with $\cos\alpha = \hat{\mathbf{S}}_{0\perp}\cdot\hat{\mathbf{n}}_0$. Thus, the spin-induced oscillations occur at *twice* the average orbital frequency, and they can be neatly disentangled from the eccentricity induced by initial conditions which occurs at the average orbital frequency.

Moreover, the amplitude of spin-induced oscillations is quite small. To place their amplitude into perspective, consider a binary with orbital eccentricity e. Taking a time-derivative of Eqs. (6.2) and (6.5), and comparing to Eqs. (6.46) and (6.47) we find $B_r = \bar{r}\bar{\Omega}\,e$ and $B_\Omega = 2\bar{\Omega}^2\,e$. Equating the amplitudes of the spin-induced oscillations with the amplitude of the eccentricity-induced term, we see that spin-induced oscillations dominate only for eccentricities

$$e < \begin{cases} \frac{1}{2}\frac{S_{0\perp}^2}{M^4}\left(\frac{\bar{r}}{M}\right)^{-2} & \text{for } \delta\dot{r}, \\ \frac{1}{4}\frac{S_{0\perp}^2}{M^4}\left(\frac{\bar{r}}{M}\right)^{-2} & \text{for } \delta\dot{\Omega}. \end{cases} \tag{6.51}$$

Numerical binary black-hole simulations typically start at a separation $\bar{r}/M \approx 15$, and in that case, spin-induced oscillations will dominate $\delta\dot{r}$ and $\delta\dot{\Omega}$ only for $e < 0.002 S_{0\perp}^2/M^4$ and for $e < 0.001 S_{0\perp}^2/M^4$, respectively. For maximally spinning black holes with least-favorable spin orientations, $S_{0\perp}/M^2 = 1$, so that even in this case spin-induced oscillations become relevant only at eccentricities of $\lesssim 0.001$. For smaller spins, their effect is still smaller. We note that spin-induced oscillations do affect $\delta\dot{\Omega}$ somewhat less than $\delta\dot{r}$, indicating that eccentricity-removal based on the orbital frequency will be preferable.

Let us notice that were we including the precession of the spins, the characteristic frequency at which the spin-induced oscillations occur would change. This can easily be seen if we assume that the precession is mainly due to SO effects, with $\mathbf{S}_1$ and $\mathbf{S}_2$ precessing about $\hat{\mathbf{L}}_{\rm N}$ at frequencies Ω_1 and Ω_2. In this case, using Eqs. (6.15), (6.16), we derive

$$\Omega_1 = \frac{2\mu\,\bar{\Omega}}{\bar{r}}\left(1+\frac{3\,m_2}{4\,m_1}\right), \tag{6.52}$$

$$\Omega_2 = \frac{2\mu\,\bar{\Omega}}{\bar{r}}\left(1+\frac{3\,m_1}{4\,m_2}\right). \tag{6.53}$$

If in Eqs. (6.48) (6.49) and (6.50), we let $\mathbf{S}_0$ precess, we obtain that oscillations occur at frequencies given by linear combinations of $\bar{\Omega}$, Ω_1 and Ω_2, namely $2\bar{\Omega}-\Omega_1-\Omega_2$, $2(\bar{\Omega}-\Omega_1)$ and $2(\bar{\Omega}-\Omega_2)$. For the binary black-hole evolutions considered in this paper, $\Omega_{1,2} \ll \bar{\Omega}$, so the spin-induced oscillations occur at the frequency $2\bar{\Omega}$.

Lastly, the results of this section could be extended to higher PN orders by including next-to-leading SO terms (2.5PN order [312–315]) and SS terms (3PN order [316–321]).

6.2.4 Oscillations induced by leading SS terms: inspiraling dynamics

In this section we compare the approximate analytical predictions for $\delta\dot{r}$ and $\delta\dot{\Omega}$ with the results obtained by numerically integrating the Hamilton equations (6.13) and (6.14), including the radiation reaction force F_i. Since we actually want to extract the spin-induced oscillations, we need to remove the homogeneous part which is due to the eccentricity introduced by the initial conditions. In fact, in the presence of radiation-reaction the initial radial velocity has to be carefully chosen

to guarantee that the binary moves along a quasi-adiabatic sequence of spherical orbits, progressively shrinking. Those initial conditions have been worked out in the analytical PN dynamics at post-circular [62] and post-post-circular [322] orders. However, those initial conditions become more and more approximate if we start the evolution of the Hamilton equations at smaller and smaller separations. Moreover, from the study of the conservative dynamics in Sec. 6.2.3, we understood that because of SS interactions it is impossible to have spherical orbits. To remove the oscillations at a frequency $\bar{\Omega}$ (the homogeneous part), we perform a fit of the data with a function

$$f_{\rm oscill}(t; B_{\rm fit}, \omega_{\rm fit}, \varphi_{\rm fit}) = B_{\rm fit} \sin(\omega_{\rm fit} t + \varphi_{\rm fit}); \tag{6.54}$$

where $\omega_{\rm fit}$ is close to $\bar{\Omega}$. We subtract the fitted function $f_{\rm oscill}$ from the raw data sample, obtaining a residual that oscillates at a frequency $2\bar{\Omega}$, superimposed to the smooth numerical inspiral. The reason why we need to fit also the frequency $\omega_{\rm fit}$ is that there is an ambiguity as to what value we use for $\bar{\Omega}$. In principle, this value should be the average orbital frequency, but a priori we can only use the initial value $\Omega_0 = \Omega(0)$ because we do not have an analytic prediction for $\bar{\Omega}$. This is also true for the value of $\bar{r}$, which we replace with $r_0 = r(0)$ throughout. We want to compare these residuals with analytical predictions based on Eqs. (6.46) and (6.47). We use the expression of the Newtonian flux to derive the effect of the radiation reaction (RR) on the two quantities $\dot{r}$ and $\dot{\Omega}$. Within the context of Newtonian dynamics, we have

$$\dot{r}_{\rm RR}(t) = -\frac{64}{5}\,\mu\,M^2 \left(r_0^4 - \frac{256}{5}\mu\,M^2\,t\right)^{-3/4}, \tag{6.55}$$

where $r_0 = r(0)$ and

$$r_{\rm RR}(t) = \left(r_0^4 - \frac{256}{5} \mu \, M^2 \, t \right)^{1/4} . \tag{6.56}$$

A similar expression can be found also for $\dot{\Omega}_{\rm RR}$. Considering that in a quasi-circular inspiral

$$\frac{\dot{r}_{\rm RR}}{r_{\rm RR}} = -\frac{2}{3} \frac{\dot{\Omega}_{\rm RR}}{\Omega_{\rm RR}} \tag{6.57}$$

and $r_{\rm RR}^3 \Omega_{\rm RR}^2 = M$, we find

$$\dot{\Omega}_{\rm RR}(t) = -\frac{3}{2} M^{1/2} \frac{\dot{r}_{\rm RR}(t)}{r_{\rm RR}^{5/2}(t)}. \tag{6.58}$$

Therefore our analytical predictions will be given by

$$\dot{r}_{\rm pred}(t) = \dot{r}_{\rm RR}(t) + \delta \dot{r}_{\rm part}(t) \tag{6.59}$$

$$\dot{\Omega}_{\rm pred}(t) = \dot{\Omega}_{\rm RR}(t) + \delta \dot{\Omega}_{\rm part}(t), \tag{6.60}$$

where $\delta \dot{r}_{\rm part}(t)$ and $\delta \dot{\Omega}_{\rm part}$ are given by the second term in the RHS of Eqs. (6.46) and (6.47).

Figure 6.2 shows the results for a particular black-hole binary with mass ratio $q = m_2/m_1 = 2$ and maximal spin magnitudes $|\mathbf{S}_1|/m_1^2 = |\mathbf{S}_2|/m_2^2 = 1$. In these plots the initial orbital frequency is $\Omega_0 M = 0.015$ which corresponds to a period $P = 418M$. As can be seen, the raw data (dotted lines) are dominated by the eccentricity at the orbital frequency, while the residuals (solid lines) oscillate at twice the orbital frequency, as expected. As far as the amplitude of the residual oscillations is concerned, we see that it is compatible with that of the predictions computed using Eqs. (6.59), (6.60), even though the agreement is not striking (red dashed lines, called non-precessing). In fact, we find that the effectiveness of the

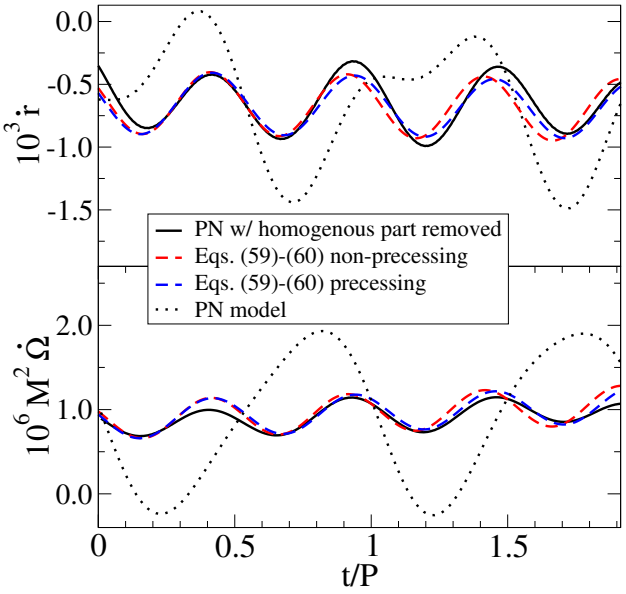

Figure 6.2: **Spin induced oscillations in PN model.** We compare two PN calculations of spin-induced oscillations. The dashed lines are the predictions from Eqs. (6.59) and (6.60), with the two lines differing by whether $\hat{\mathbf{L}}_{\rm N}$ is held constant ("non-precessing") or evolving ("precessing"). The solid line represents a solution of the full PN equations of motions, with the homogenous oscillations fitted and subtracted. (Here, mass-ratio $q = 2$, with maximal spins of initial orientations $(\theta_1 = \pi/3, \phi_1 = 0)$ and $(\theta_2 = 2\pi/3, \phi_2 = \pi/3)$ at the initial orbital frequency $M\Omega_0 = 0.015$, that is an average initial orbital period $P = 418M$, and the dotted curve represents the solutions of the PN model including inspiral motion).

removal procedure of the homogeneous part is deeply affected by the value of $\omega_{\rm fit}$. Numerical studies have shown that differences of a few percent on $\omega_{\rm fit}$ can completely alter the residuals. Tweaking by hand the value of $\omega_{\rm fit}$ instead of using the best fit value can lead to a much better agreement on the amplitudes, at least for the first cycle. Note that in Fig. 6.2 no such ad hoc tweaking is used. Also, the fact that the predictions quickly get out of phase with respect to the residuals is mainly due to the assumption made in Sec. 6.2.3 of keeping the spins constant or non-precessing,

that is using the evolution of the triad $\{\hat{\mathbf{n}}, \hat{\boldsymbol{\lambda}}, \hat{\mathbf{L}}_{\rm N}\}$ specified by Eqs. (6.33)–(6.35). By contrast better phase agreement can be obtained numerically if we use the time-evolution of the spins and of the reference triad (blue dashed lines, called precessing) or analytically if we had considered a reference triad in which the precession of the orbital plane and spins were taken into account.

Another interesting feature is the relative importance of the spin-induced oscillations with respect to the eccentricity induced by the initial conditions. Both types of oscillations are showing up in the raw data of $\dot{r}$, while in the case of $\dot{\Omega}$ we only see the oscillations due to the initial conditions. This can be explained by our analytical predictions. Using Eqs. (6.2), (6.5), we write for the eccentricity

$$e_r^{\rm NS} = \frac{|B_r|}{\bar{r}\,\bar{\Omega}} \quad \text{or} \quad e_\Omega^{\rm NS} = \frac{|B_\Omega|}{2\bar{\Omega}^2}, \tag{6.61}$$

where B_r and B_Ω are the amplitudes of the oscillations of the homogeneous solutions. We want to keep distinct notations for $\dot{r}$ and $\dot{\Omega}$, even though at Newtonian level $e_r^{\rm NS} = e_\Omega^{\rm NS} = e$ and therefore $|B_r| = \bar{r}|B_\Omega|/2\bar{\Omega}$. If we now call C_r and C_Ω the SS amplitudes, namely

$$C_r = -\frac{\bar{\Omega}\,C}{M^2\,\bar{r}}\,, \qquad C_\Omega = -\frac{\bar{\Omega}^2\,C}{M^2\,\bar{r}^2}, \tag{6.62}$$

we parametrize the spin-induced oscillations in terms of a spin-induced "eccentricity",

$$e_r^{\rm SS} = \frac{|C_r|}{\bar{r}\,\bar{\Omega}} = \frac{|C|}{M^2\,\bar{r}^2}\,, \qquad e_\Omega^{\rm SS} = \frac{|C_\Omega|}{2\bar{\Omega}^2} = \frac{|C|}{2M^2\,\bar{r}^2}. \tag{6.63}$$

We have that the relative ratio is

$$\frac{e_\Omega^{\rm SS}}{e_r^{\rm SS}} = \frac{1}{2}, \tag{6.64}$$

so it is expected that the significance of the spin-induced oscillations is smaller for $\dot{\Omega}$.

6.3 Iterative eccentricity removal in presence of spins

In the preceding sections, we showed that the PN Hamiltonian with leading SS terms predicts oscillations with two distinct periods: the orbital period, with amplitude and phase depending on initial conditions that can genuinely be associated with orbital eccentricity; and half the orbital period, independent of the initial conditions and caused by spin-spin couplings. We furthermore showed that these spin-induced oscillations are suppressed in $\dot{\Omega}$ as compared to $\dot{r}$ [see, e.g., Eq. (6.64)].

Our task is to find initial conditions that remove or at least minimize the oscillations caused by eccentricity. As in earlier work, we shall begin with some trial initial conditions, evolve the binary for about two orbits, analyze the motion of the black holes, and then correct the initial conditions. To exploit this suppression of spin-induced oscillations in $\dot{\Omega}$, we will derive updating formulae based on $\dot{\Omega}$.

6.3.1 Updating formulae

The basis for the updating formulae are the Newtonian expressions for distance r and orbital frequency Ω (Eqs. (6.3) and (6.5))

$$r_N(t) = \bar{r}\,[1 - e\,\sin\phi(t)]\,, \tag{6.65}$$

$$\Omega_N(t) = \bar{\Omega}\,[1 + 2e\,\sin\phi(t)]\,, \tag{6.66}$$

where $\phi(t)$ is the phase of the radial oscillations. General relativistic periastron advance will cause $\phi(t)$ to deviate from the orbital phase. Taking a time-derivative, we find

$$\dot{r}_N = -\bar{r}\, e\, \omega\, \cos(\omega t + \phi_0), \tag{6.67}$$

$$\dot{\Omega}_N = 2\bar{\Omega}\, e\, \omega\, \cos(\omega t + \phi_0), \tag{6.68}$$

with $\omega = (d\phi/dt)(0)$, $\phi_0 = \phi(0)$.

Let us now consider a compact binary inspiral starting at $t = 0$ at initial separation r_0, with orbital frequency Ω_0 and radial velocity $\dot{r}_0$. We take $\dot{r}(t)$ or $\dot{\Omega}(t)$ from a general relativistic inspiral, and fit it with functional forms

$$\dot{r}_{\rm NR}(t) = S_r(t) + B_r\, \cos(\omega_r t + \phi_r), \tag{6.69}$$

$$\dot{\Omega}_{\rm NR}(t) = S_\Omega(t) + B_\Omega\, \cos(\omega_\Omega t + \phi_\Omega). \tag{6.70}$$

The subscripts r and Ω indicate whether the fit was performed on $\dot{r}_{\rm NR}$ or $\dot{\Omega}_{\rm NR}$, and we will use a bullet $\bullet$ in the subscript to represent either r or Ω. The first part of each fit, $S_\bullet$, is a non-oscillatory function that captures the radiation-reaction driven inspiral, whereas the oscillatory piece captures the orbital eccentricity. We neglect spin-induced oscillations. The precise functional form of $S_\bullet$ is important, and sometimes it is advisable to include a quadratic term Ct^2 within the argument of the cosine. We comment on these considerations below in Sec. 6.3.2

Equation (6.69) shows that at $t = 0$, orbital eccentricity contributes $\dot{r}_{\rm ecc,0} = B_r \cos\phi_r$ and $\ddot{r}_{\rm ecc,0} = -B_r\omega_r \sin\phi_r$ to the radial velocity and acceleration. Our goal is to now modify the initial data parameters $\dot{r}_0$ and Ω_0 such that $\dot{r}_{\rm ecc,0}$ and $\ddot{r}_{\rm ecc,0}$

vanish. The radial velocity is a free parameter of the initial data, so $\dot{r}_{0,\rm new} = \dot{r}_0 + \Delta\dot{r}$, where

$$\Delta\dot{r} = -\dot{r}_{\rm ecc,0} = -B_r \cos\phi_r. \tag{6.71}$$

To utilize our information about the radial acceleration $\ddot{r}_{\rm ecc,0}$ we recall that for the Newtonian Hamiltonian we have

$$\ddot{r} = \frac{\dot{p}_r}{\mu} = -\frac{1}{\mu}\frac{\partial H_{\rm N}}{\partial r} = \frac{\mathbf{L}^2}{\mu^2 r^3} - \frac{M}{r^2} = r\,\Omega^2 - \frac{M}{r^2}\,. \tag{6.72}$$

A small change $\Omega_0 \to \Omega_{0,new} = \Omega_0 + \Delta\Omega$ therefore changes the radial acceleration by $\Delta\ddot{r} = 2r_0\Omega_0\Delta\Omega$. This change cancels $\ddot{r}_{\rm ecc,0}$ when

$$\Delta\Omega = \frac{B_r\omega_r \sin\phi_r}{2r_0\Omega_0}. \tag{6.73}$$

Equations (6.71) and (6.73) are one version of the updating formulae for the eccentricity removal based on the separation coordinate. A sometimes more effective formula is presented below in Eq. (6.77) which in earlier numerical work [185,186,305] was applied to the *proper separation* between the horizons of the black holes.

A convenient way to derive updating formulae based on $\dot{\Omega}(t)$ begins by noting that the ratio of the amplitudes of oscillations in Eqs. (6.67) and (6.68) is $-\bar{r}/(2\bar{\Omega})$. Therefore, we obtain the desired updating formulas by replacing B_r with $-\bar{r}B_\Omega/(2\bar{\Omega})$:

$$\Delta\dot{r} = \frac{r_0 B_\Omega}{2\Omega_0}\cos\phi_\Omega, \tag{6.74}$$

$$\Delta\Omega = -\frac{B_\Omega\omega_\Omega}{4\Omega_0^2}\sin\phi_r. \tag{6.75}$$

[A sometimes more effective replacement for Eq. (6.75) is presented below in Eq. (6.78).]

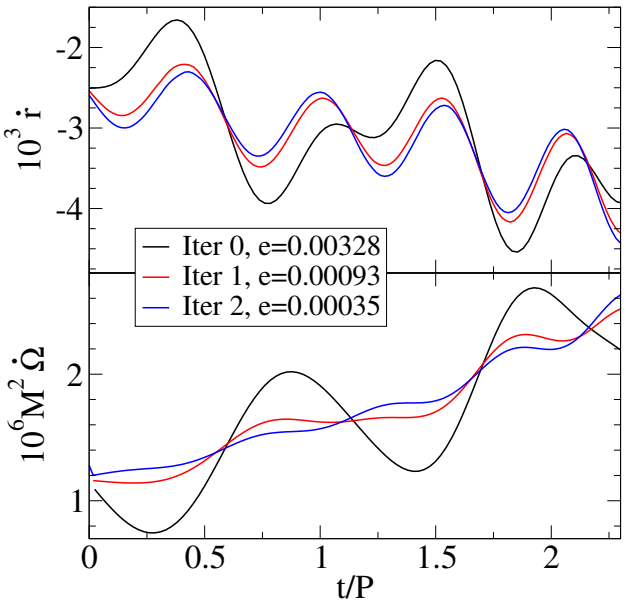

Figure 6.3: Eccentricity removal based on $\dot{\Omega}$ applied to a **PN model**. Shown is the initial orbital evolution, and two iterations of eccentricity removal. Parameters of the black-hole binary: mass-ratio $q = 1$, spins of magnitude $\chi_1 = \chi_2 = 0.8$ with initial orientations $(\theta_1 = 0, \phi_1 = 0)$ and $(\theta_2 = \pi/3, \phi_2 = 0)$ with respect to $\hat{\mathbf{L}}_{\mathrm{N}\,0}$ and initial $M\Omega_0 = 0.0315$, that is an initial orbital period $P = 200M$.

In Fig. 6.3, we present three steps of this eccentricity removal procedure. We use the PN-expanded Hamiltonian with non-spinning terms up to 3PN order [87, 102], and spinning terms up to 2PN order [102, 188]. The radiation-reaction effects are included through 2PN order as in Ref. [102].

We indicate in the legends the value of the eccentricity estimated from the fitted amplitude of the oscillations, once the smooth inspiral has been removed. Note that the initial orbital period is about $200M$. At the 0^{th} step the plots are showing the evolution of the binary system with initial conditions determined according to the procedure outlined in Ref. [62], leading to the presence of an initial eccen-

tricity. From the plots, we clearly see that we go from a situation dominated by the homogeneous oscillations occurring at the average orbital frequency (step 0) to the situation in which only spin-induced oscillations occurring at twice the average orbital frequency are visible (step 2).

The configuration considered in Fig. 6.3 is close to merger, where the rapid evolution of the orbit makes it more difficult to apply eccentricity removal. In the next section we discuss how to improve the convergence of the iterative procedure.

6.3.2 Practical considerations

Unfortunately, iterative eccentricity removal is sensitive to a variety of effects which are not immediately obvious. Without sufficient care, iterative eccentricity removal converges slowly, or not at all. In this section, we describe important details for the effective and practical application of the eccentricity removal, as well as diagnostics that allow users to evaluate whether the eccentricity removal proceeds optimally.

The fits in Eqs. (6.69) and (6.70) are used to compute the values of the oscillating part $B_\bullet \cos(\omega_\bullet t + \phi_\bullet)$ at $t = 0$. Therefore it is crucial that the function $S_\bullet$ that is intended to fit the inspiral portion does *not* fit this oscillatory piece. Initially, we used a polynomial for $S_\bullet$, but sometimes, especially for shorter fitting intervals, such a polynomial picks up a contribution of the oscillatory piece and results in an unusable fit. Therefore we have constructed more robust fitting functions that

cannot capture oscillations. Our current preferred choice is

$$S_{\Omega}^{(k)} = \sum_{n=0}^{k-1} A_k (T_c - t)^{-11/8-n/4}, \tag{6.76}$$

with free parameters A_k and T_c. The functional form and the exponents are motivated by PN inspirals, and we keep either $k = 1$ or $k = 2$ terms of this expansion (for $k = 2$, we use the same T_c in both terms).

Another crucial ingredient for a reliable fit is a suitably chosen fitting interval. This interval needs to cover enough oscillations to break degeneracies among the fitting parameters. However, if it becomes too long, the evolution in the inspiral part will be harder to capture with $S_\bullet$ and the quality of the fit will deteriorate.

Finally, the fit is used to compute $\dot{r}_{\rm ecc,0}$ and $\ddot{r}_{\rm ecc,0}$, which are quantities at $t = 0$. It is desirable that the fitting interval starts as close to $t = 0$ as possible to minimize extrapolation from the fitting interval to $t = 0$. However, a numerical evolution relaxes in its early stages due a quasi steady-state, and features during this relaxation need to be excluded from the fitting interval.

A good means to ensure a satisfactory fit is to perform several fits, and ensure that the results are consistent. We perform four distinct fits to $\dot{\Omega}$, where we change the order $k = 1, 2$ of the inspiral component, Eq. (6.76), and where we change the order of the polynomial within the cosine in Eq. (6.70) between $l = 1$ as shown in Eq. (6.70) and $l = 2$ (i.e. adding a quadratic term $C_\bullet t^2$). In addition, we vary the location and length of the fitting interval and check that the updates $\delta\dot{r}$ and $\Delta\Omega$ are unaffected.

Figure 6.4 demonstrates a useful way to visualize and assess the effectiveness

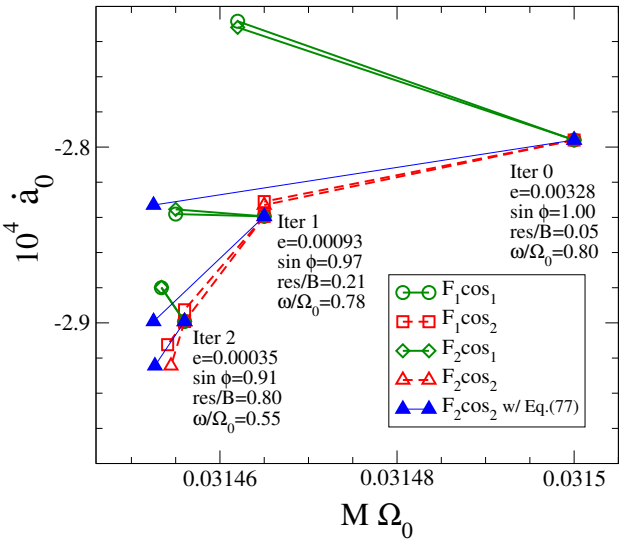

Figure 6.4: Visualization of the eccentricity removal performed in Fig. 6.3 in the Ω_0–$\dot{a}_0$ plane. This plot summarizes a large amount of diagnostic information which can be utilized to ensure reliability of the eccentricity removal procedure (see main text). The symbols B, ϕ and ω have a subscript Ω suppressed for clarity.

of iterative eccentricity removal. This plot shows the plane of the initial-data parameters $\Omega_0, \dot{a}_0$, with $\dot{a}_0 = \dot{r}_0/r_0$. The solid symbols correspond to the three PN evolutions shown in Fig. 6.3. The lines emanating from each of the symbols denote different fits based on this particular evolution. The different fits are denoted $F_k \cos_l$, where $k = 1, 2$ denotes the fitting order in $S_\bullet$ and l denotes the order of the polynomial inside the cosine. Each of these lines ends at the predicted improved parameters $\Omega_{0,\mathrm{new}}, \dot{a}_{0,\mathrm{new}}$. Clustering of these lines, and convergence of the symbols indicates that eccentricity removal is proceeding well. As can be seen by comparing the solid dark green and dashed red curves, the order k of the fitting function for the smooth part S_Ω has almost no impact on the updated parameters $\Omega_{0,\mathrm{new}}, \dot{a}_{0,\mathrm{new}}$ in this case. However, using a quadratic polynomial inside the cosine

($l = 2$) significantly improves the quality of the $\dot{\Omega}_0$–update.

Figure 6.4 can also be used to assess the potential quality for different updating formulae. While we have kept the orbital frequency Ω_0 separate from the eccentricity oscillation frequency ω_Ω, for Newtonian orbits both frequencies agree. Therefore, our Newtonian motivation does not provide a means to choose whether to include extra powers of Ω_0/ω_Ω. Specifically, we could replace Eqs. (6.73) and (6.75) by either

$$\Delta\Omega = -\frac{B_r}{2r_0}\,\sin\phi_r, \tag{6.77}$$

or

$$\Delta\Omega = -\frac{B_\Omega}{4\Omega_0}\,\sin\phi_\Omega, \tag{6.78}$$

for updates based on $\dot{r}(t)$ and $\dot{\Omega}(t)$, respectively. The predictions of the updating formula Eq. (6.77) are shown in Fig. 6.4 as filled blue triangles. It is obvious that Eq. (6.77) predicts an updated Ω_0 significantly closer to the final best value for Ω_0, even when applied to Iter 0. Therefore, to summarize the discussion in the preceding paragraphs, for most effective eccentricity removal we recommend the fit of the form $F_2\cos_2$ combined with Eq. (6.77).

Finally, we discuss several diagnostics that can help to assess the quality of eccentricity removal, and which are included next to each symbol in Fig. 6.4. The first diagnostic is the estimated eccentricity e, which should be monotonically decaying. The second diagnostic is $\sin\phi_\Omega$. As can be seen from Eqs. (6.74) and (6.75), the angle ϕ_Ω parametrizes the relative importance of the Ω_0 and $\dot{a}_0$ updates. For $\sin\phi_\Omega \approx 1$, the whole weight is carried by the Ω_0 update. This is the case here,

and indicates that the starting value for $\dot{a}_0$ was already very good, and that the apparent inconsistent predictions for $\dot{a}_{0,\mathrm{new}}$ will not have an adverse impact on the eccentricity fitting procedure (note that all fits predict consistent values for $\Omega_{0,\mathrm{new}}$). The third diagnostic is the ratio of the root-mean-square residual of the fit, res, to the amplitude of the oscillatory part, B_Ω. When $\mathrm{res}/B \ll 1$, then $\dot{\Omega}$ has indeed the assumed form Eq. (6.70), a prerequisite for eccentricity removal. When $\mathrm{res}/B \sim 1$, we can no longer isolate the oscillatory piece, and eccentricity removal ceases to be effective. The final diagnostic is the ratio of frequencies of radial oscillations ω_Ω to orbital frequency Ω_0. For a good fit, ω_Ω/Ω_0 should be somewhat less than unity, where the deviation from unity is caused by periastron advance. For moderately small eccentricities, this ratio should furthermore be independent of the precise value of eccentricity. This is indeed the case for "Iter 0" and "Iter 1", but "Iter 2" results in a questionably small ratio, which furthermore differs from the values for iterations 0 and 1. Again, an indication that we cannot further proceed with eccentricity removal.

6.4 Application to fully numerical binary black-hole simulations

We now apply the method outlined in Sec. 6.3 to reduce the initial eccentricity of single-spin and double-spin precessing binary black-hole simulations. We compare the periodicity in the oscillations of the orbital frequency and the proper horizon separation to the PN predictions described in Sec. 6.2 and also to the periastron-

advance results of Ref. [308]. Finally, for one binary configuration, we also extract the $l = 2$, $m = 2$ mode of the gravitational waveform and investigate the presence of spin-induced oscillations in its phase and frequency.

6.4.1 Numerical methods

Binary black hole initial data is constructed using the conformal thin sandwich formalism [323,324] and quasi-equilibrium boundary conditions [300,325,326], incorporating radial velocity as described in Ref. [304]. The resulting set of five nonlinear coupled elliptic equations is solved with multi-domain pseudo-spectral techniques described in Ref. [327]. As in earlier work, we choose conformal flatness and maximal slicing. To obtain desired masses and spins, we utilize a root-finding procedure to adjust freely specifiable parameters in the initial data [210].

Thus, a binary black-hole initial data set is determined by the mass-ratio, the spins of both black holes, and coordinate separation d between the coordinate centers of the black holes, orbital frequency Ω_0, and radial velocity $\dot{r}_0 = \dot{a}_0 d$, where $\dot{a}_0$ is the dimensionless expansion factor. For fixed d, eccentricity removal consists of finding values for Ω_0 and $\dot{a}_0$ that result in sufficiently small eccentricity.

The constructed initial data are evolved with the Spectral Einstein Code `SpEC` [105]. This code evolves a first-order representation [328] of the generalized harmonic system [329–331] and includes terms that damp away small constraint violations [328,331,332]. The computational domain extends from excision boundaries located just inside each apparent horizon to some large radius. No boundary

conditions are needed or imposed at the excision boundaries, because all characteristic fields of the system are outgoing (into the black hole) there. The boundary conditions on the outer boundary [328, 333, 334] are designed to prevent the influx of unphysical constraint violations [335–341] and undesired incoming gravitational radiation [342,343], while allowing the outgoing gravitational radiation to pass freely through the boundary. Interdomain boundary conditions are enforced with a penalty method [344, 345].

6.4.2 Eccentricity removal based on orbital frequency: single-spin binary black hole

In this section we re-visit eccentricity removal for the configuration considered in the introduction and Fig. 6.1. The binary has a mass-ratio of $m_1/m_2 = 1.5$, and only the larger black hole carries spin, namely $\chi_1 = 0.5$ with initial spin direction in the orbital plane pointing exactly away from the smaller black hole. Note that spins in the orbital plane maximize spin-induced oscillations [see, e.g., Eqs. (6.44) and (6.45)]. The initial coordinate separation between the holes is $d=16M$, orbital frequency $M\Omega_0 = 0.0142$, and $\dot{a}_0 = -5 \times 10^{-5}$. These parameters were determined from the so-called TaylorT3 PN approximant for non-spinning binaries [292].

Orbital frequency, both in the initial data and in the subsequent evolution, is defined by the coordinate motion of the center of the apparent horizons. Let $\mathbf{c}_i(t)$ be the coordinates of the center of each black hole, and define their relative separation

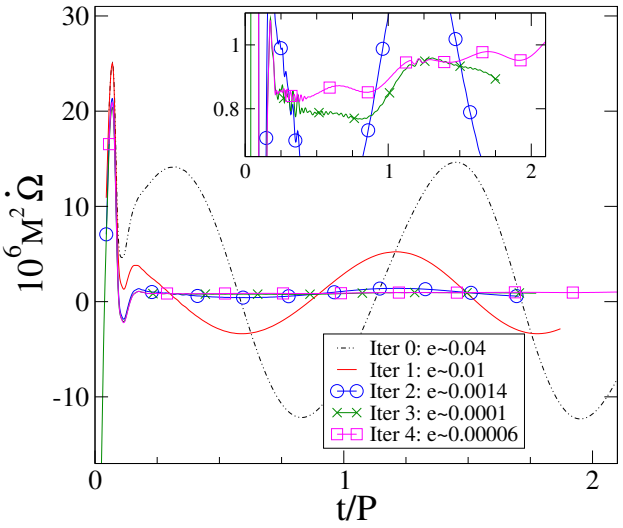

Figure 6.5: **Eccentricity removal based on time derivative of the orbital frequency** $d\Omega/dt$, applied to a single-spin *precessing* binary black hole with the same initial parameters as in Fig. 6.1. Shown is $\dot{\Omega}$ vs. time in units of initial orbital period $P = 442M$ for the initial run (based on PN parameters) and four eccentricity-removal iterations. The amplitude of spin-induced oscillations is several orders of magnitude smaller than in Fig. 6.1, and becomes only visible in Iter 4.

$\mathbf{r}(t) = \mathbf{c}_1(t) - \mathbf{c}_2(t)$. The instantaneous orbital frequency is then computed as

$$\mathbf{\Omega} = \frac{\mathbf{r} \times \dot{\mathbf{r}}}{r^2}, \tag{6.79}$$

and Ω is defined as the magnitude of $\mathbf{\Omega}$. All these calculations are performed using standard Euclidean vector calculus.

We start the first run using PN initial conditions for the orbital frequency and radial velocity and evolve the binary black hole for about two orbits. From the orbital frequency we measure an eccentricity $e \sim 0.04$, and Eqs. (6.74) and (6.75) give improved values for Ω_0 and $\dot{a}_0$. Evolution of the initial data computed from these improved values is labeled "Iter 1" in Fig. 6.5, and reduces the eccentricity to

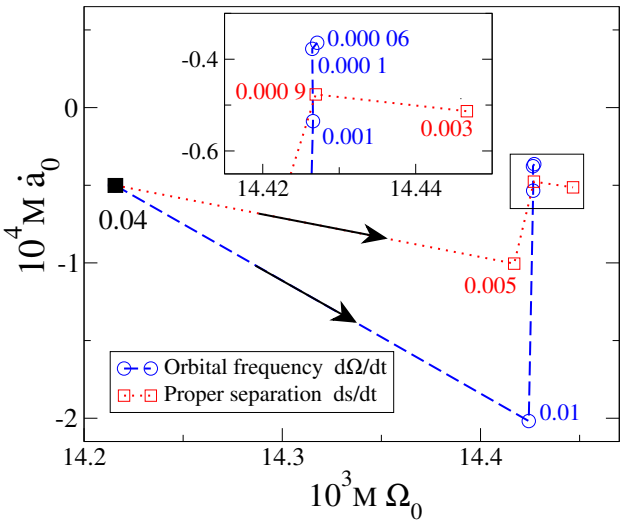

Figure 6.6: **Convergence of the eccentricity-removal procedures in the $(\Omega_0, \dot{a}_0)$ plane.** Blue circles: eccentricity removal sequence of Fig. 6.5. Red squares: eccentricity removal sequence shown in Fig. 6.1. The number next to each symbol gives the eccentricity of the respective evolution. The inset shows an enlargement of the boxed area. The eccentricity-removal procedure based on the orbital frequency keeps converging until the fourth iteration, while the one based on the proper separation fails to converge any further beyond the second iteration.

about 0.01. The same procedure is then repeated three more times. For Iter 0 to Iter 2, we exclude $t \lesssim 100M$ from the fit. For Iter 3 the variations in $\dot{\Omega}$ are so small that numerical noise is dominant for about half an orbital period, and we exclude $t \lesssim 250M$ from the fit. The final eccentricity in the orbital frequency is $e \sim 6 \times 10^{-5}$.

In Fig. 6.6, we show how the initial orbital frequency Ω_0 and the radial expansion factor $\dot{a}_0$ converge to the final values (minimal eccentricity). The blue circles indicate the successive iterations for the successful eccentricity removal based on $\dot{\Omega}$ (see Fig. 6.5). Note that the parameters $(\Omega_0, \dot{a}_0)$ converge well for all iterations. In contrast, the red squares denote the unsuccessful eccentricity removal based on

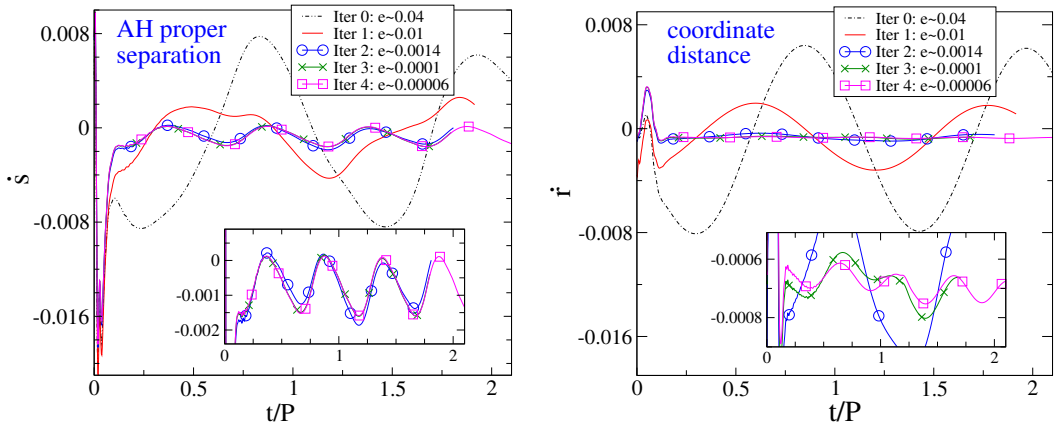

Figure 6.7: **Radial velocity** between the black holes for the same series of evolutions shown in Fig. 6.5. **Left:** Derivative of proper separation between the apparent horizons $\dot{s}$. **Right:** Derivative of coordinate distance between centers of the apparent horizons $\dot{r}$. The time-axis is given in units of the initial orbital period $P = 442M$. Proper separation $\dot{s}$ exhibits large spin-induced oscillations, whereas $\dot{r}$ shows spin-induced oscillations of similarly small amplitude as in Fig. 6.5. Note that the inset in the right panel is ten times more magnified than in the left panel.

proper separation $\dot{s}$ (see Fig. 6.1). Starting with the third iteration, the updated values of the orbital frequency and expansion radial coefficient move away from the line of minimum eccentricity, with an increase of eccentricity from 0.001 to 0.003. All eccentricity estimates shown in this figure are computed from $\dot{\Omega}$, even when eccentricity removal is based on $\dot{s}$. This allows us to measure eccentricities $e < 0.01$, which would not be possible from $\dot{s}$, because the latter is dominated by large spin-induced oscillations.

The absence of spin-induced oscillations in Fig. 6.5 is striking, especially when compared to Fig. 6.1. Spin-induced oscillations are visible in Fig. 6.5 only at $e < 10^{-4}$. For the runs with larger eccentricity (Iter 0–3), eccentricity–induced

oscillations dominate with a period somewhat larger than P (somewhat larger because of periastron–advance [308]).

We shall now investigate spin-induced oscillations in the numerical-relativity simulations in more detail. First, by comparing the time-derivatives of orbital frequency $\dot{\Omega}$, proper separation between horizons $\dot{s}$, and coordinate separation between centers of apparent horizons $\dot{r}$. Subsequently, by comparing their amplitude and frequency with PN predictions from Sec. 6.2.

Figure 6.7 shows time-derivatives of proper separation $\dot{s}$ and coordinate separation $\dot{r}$ for the evolutions shown in Fig. 6.5. Spin-induced oscillations are already noticeable in $\dot{s}$ for Iter 1 with $e = 0.01$. These oscillations dominate for Iter 2–4, i.e. $e \leq 0.0014$. In contrast, the coordinate distance $\dot{r}$ is less susceptible to spin-induced oscillations. In the right plot of Fig. 6.7, spin-induced oscillations become apparent only for eccentricities of $\sim 10^{-4}$ or smaller. The spin-induced oscillations in $\dot{r}$ are smaller by a factor of almost 20 than those in $\dot{s}$.

When comparing Iter 3 and Iter 4 between Fig. 6.5 and the right panel of Fig. 6.7, one notices that $\dot{\Omega}$ shows slightly less pronounced spin-induced oscillations. That is consistent with the PN calculations, where Eq. (6.64) predicted that spin-induced oscillations in $\dot{\Omega}$ should be suppressed by a factor of 2 relative to those in $\dot{r}$. When comparing Iter 4 between Fig. 6.5 and the right plot of Fig. 6.7, we find that the spin-induced oscillations in $\dot{\Omega}$ and $\dot{r}$ are *in phase*. This is again consistent with the PN prediction, where the last terms of Eqs. (6.46) and (6.47) have the same sign. The phase of spin-induced oscillations in $\dot{\Omega}$ and $\dot{r}$ differs from the effect of orbital eccentricity: for an eccentric orbit, the orbital frequency is maximal when

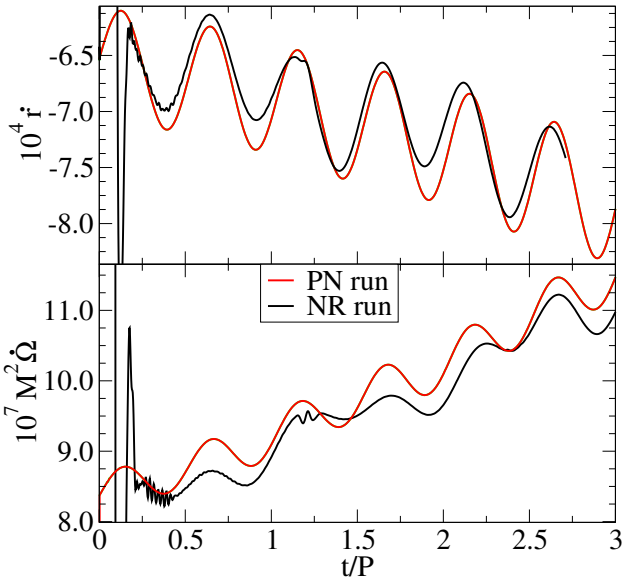

Figure 6.8: Spin-induced oscillations of the lowest-eccentricity numerical simulation (Iter 4 of Fig. 6.5) in comparison with the PN calculations of Sec. 6.2.3.

the separation is minimal, and therefore $\dot{\Omega}$ and $\dot{r}$ are out of phase (see Iter 0 and Iter 1 of Figs. 6.5 and 6.7).

We have shown in Sec. 6.2.3 that the PN Hamiltonian predicts spin-induced oscillations: Equations (6.46)–(6.49) contain an oscillatory component at twice the orbital frequency with amplitudes

$$A_{\delta\dot{r}} = \frac{\bar{\Omega}\,\mathbf{S}_{0\perp}^2}{2M^2\,\bar{r}}, \tag{6.80}$$

$$A_{\delta\dot{\Omega}} = \frac{\bar{\Omega}^2\,\mathbf{S}_{0\perp}^2}{2M^2\,\bar{r}^2}. \tag{6.81}$$

Figure 6.8 shows numerical data for the lowest-eccentricity numerical simulation (Iter 4 from Fig. 6.5). These numerical data are compared with the prediction of the PN equations. The PN calculation reproduces very accurately the amplitude of spin-induced oscillations in the numerical-relativity simulation for $\dot{\Omega}$ and $\dot{r}$. By

contrast, the spin-induced oscillations in $\dot{s}$ are larger by a factor ~ 20 than those in $\dot{r}$. This can be due to deformations of the apparent horizons due to spin effects. Finally, we notice that a small amplitude oscillation of the numerical data on the orbital time-scale is also visible, corresponding to the small, but non-zero eccentricity $e = 6 \times 10^{-5}$ of the numerical simulation.

6.4.3 Oscillations in the (2,2) mode of the gravitational wave

In Sec. 6.4.2 we found spin-induced oscillations in the coordinate distance of the black holes and the orbital frequency, consistent with PN predictions. We now investigate the gravitational radiation emitted by this binary. Specifically, we extract the $l = 2, m = 2$ mode of the gravitational waveform in the inertial frame where the binaries are *initially* placed along the x-axis and the initial angular momentum is parallel to the z-axis. We compute phase and frequency for the waveforms extracted at extraction radii $R = 130M$ and $R = 220M$.

Spin-induced oscillations represent a physical effect independent of orbital eccentricity. Nevertheless, the concept of eccentricity estimators [308] will be very useful when discussing spin-induced oscillations, because it removes overall secular trends (especially in the gravitational-wave phase), and because it makes it easy to relate the amplitude of oscillations to an "equivalent eccentricity." As Ref. [308], we define $e_{\phi_{\rm GW}}(t)$

$$e_{\phi_{\rm GW}}(t) = \frac{\phi_{\rm NR}(t) - \phi_{\rm fit}(t)}{4}\,, \tag{6.82}$$

where $\phi_{\rm NR}(t)$ is the gravitational-wave phase of the (2,2) mode and $\phi_{\rm fit}(t)$ is the

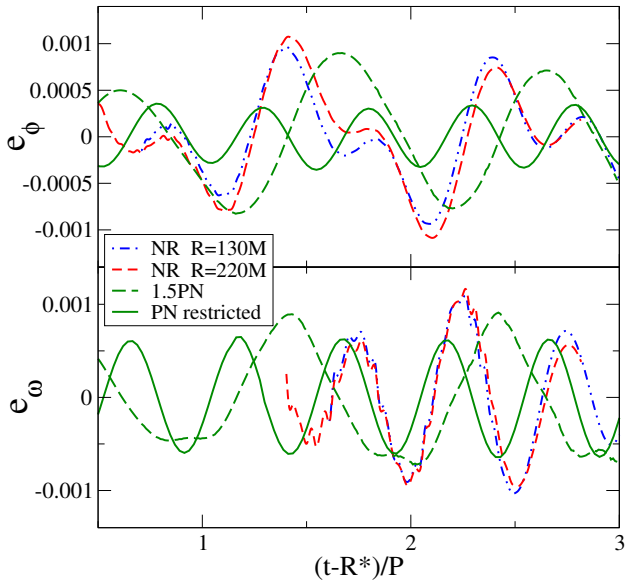

Figure 6.9: **Eccentricity estimator for the gravitational-wave phase and frequency** for the final eccentricity-removal iteration of Fig. 6.5. The upper panel shows the gravitational-wave–phase eccentricity estimator for two extraction radii versus the retarded time, the lower panel the eccentricity estimator computed from the gravitational wave frequency. In both panels we clearly see oscillations at twice the orbital frequency. We also show the PN result for the restricted waveform.

quasi-circular polynomial fit of the gravitational-wave phase [see Ref. [308] for more details]. Similarly, using the gravitational-wave frequency of the (2,2) mode and its quasi-circular polynomial fit as in Ref. [308], we define the eccentricity estimator $e_{\omega_{\rm GW}}(t)$

$$e_{\omega_{\rm GW}}(t) = \frac{\omega_{\rm NR}(t) - \omega_{\rm fit}(t)}{2\omega_{\rm fit}(t)} \,. \tag{6.83}$$

In Fig. 6.9, we plot the eccentricity estimators $e_{\phi_{\rm GW}}(t)$ (upper panel) and $e_{\omega_{\rm GW}}(t)$ (lower panel) for the two extraction radii $R = 130M$ and $R = 220M$ versus the retarded time $t - R^*$, where R^* is the tortoise-coordinate radius defined as

$$R^* \equiv R + 2M \, \ln\left(\frac{R}{2M} - 1\right) \,, \tag{6.84}$$

where $M = 1$ is the total mass of the initial data. Quite interestingly, the plots show oscillations happening at twice the orbital frequency. The magnitude of the oscillations in $e_{\phi_{\rm GW}}(t)$ or $e_{\omega_{\rm GW}}(t)$ is $\sim 10^{-3}$, although the eccentricity in the orbital frequency has been reduced to $\sim 6\times10^{-5}$ (see Fig. 6.5). We note that the amplitude of the oscillations at twice the orbital frequency does not depend on the extraction radius, suggesting that they are gauge invariant.

We also compare these numerical result with what is predicted by the PN model. For the orbital evolution we use the model Hamiltonian (6.6), where SO and SS interactions are included through 2PN order, nonspinning effects through 3PN order, and radiation-reaction effects through 2PN order. As to the analytical model, we employ the waveform derived in Ref. [346], where the precession of the orbital plane and the spins of the black holes are taken into account through 1.5PN order. In particular, we compute the estimators $e_{\phi_{\rm GW}}$ and $e_{\omega_{\rm GW}}$ using Eqs. (4.15), (4.16a) in Ref. [346] for the h_{22} mode with the amplitude computed at lowest order in v/c (restricted waveform)[5]. This means that the precession of the orbital plane is considered only in the gravitational-wave phase, but not in the amplitude.

Before computing the PN eccentricity estimators, we perform an alignment between the phase of the PN h_{22} and the phase of the numerical-relativity Ψ_4. To do that, we follow the procedure outlined in Sec. IIIA of Ref. [239]. This alignment is obtained over a time window of $1000M$ (in the range $500M < t < 1500M$), and it

[5]Since the numerical-relativity (2,2) mode is computed using as z-axis the direction perpendicular to the orbital plane, we apply the Wigner rotation to the restricted h_{22} of Ref. [346] and keep only the lowest-order term in v/c.

amounts to a time-shift and a global offset in the PN phase. The result is shown as green curves in Fig. 6.9. We see a qualitative agreement between numerical-relativity results and the restricted PN model for the oscillations at twice the orbital frequency in $e_{\omega_{\rm GW}}$ and $e_{\phi_{\rm GW}}$. However, the numerical-relativity $e_{\phi_{\rm GW}}$ also shows oscillations at the orbital frequency which are absent in the restricted PN waveform. We find that oscillations at the orbital frequency can be generated in the PN model of Ref. [346] if we included higher order PN corrections in the amplitude of the (2,2) mode [see Eq. (4.16a) in Ref. [346]]. Such oscillations cannot be iterated away by our procedure, even in principle, since the removal algorithm concerns the orbital dynamics and they rather appear as a physical effect of the waveform. The upper panel of Fig. 6.9 shows comparatively large oscillations at period $\sim P$; because the PN model predicts modes at this frequency, these oscillations cannot be used to compute orbital eccentricity. A further analysis of the inclusion of higher-order PN corrections is warranted. We prefer to postpone such an analysis to be able to test against a larger sample of numerical–relativity waveforms.

6.4.4 Eccentricity-removal for generic binary black holes

In the previous sections we studied our new eccentricity-removal procedure in detail for one test-case: a binary with only one non-zero spin, and with mass-ratio $m_1/m_2 = 1.5$. We now test the procedure for other binary configurations with the same mass ratio. We consider two further configurations where only the large black hole carries spin, parametrized by the angle θ_1 between the orbital angular momen-

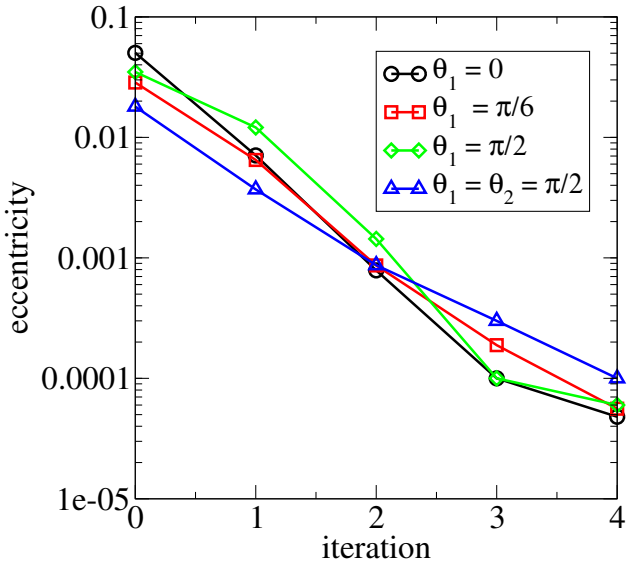

Figure 6.10: **Eccentricity removal for different spin–configurations.** We illustrate of how the eccentricity is reduced to very low values when the iterations are applied to the orbital frequency. Shown are three configurations with $S_1/M_1^2 = 0.5, S_2 = 0$ and different spin directions θ_1, and one configuration with $S_1/M_1^2 = S_2/M_2^2 = 0.5$, with initially two orthogonal spins both tangent to the orbital plane. For all cases, the mass-ratio is $m_1/m_2 = 1.5$. The run shown in green triangles was discussed in detail in Figs. 6.5 to 6.9.

tum and the spin axis of the first black hole. In the previous sections, we considered $\theta_1 = \pi/2$, and now we extend to $\theta_1 = 0, \pi/6$, and $\phi_1 = 0$. The first of these new cases is non-precessing and verifies that eccentricity removal based on $\dot{\Omega}$ works effectively for non-precessing systems. We also consider a binary where both black holes carry spin, with initial spin-direction in the orbital plane ($\theta_1 = \theta_2 = \pi/2$), $\mathbf{S}_1$ parallel to the initial separation vector between the black holes, and $\mathbf{S}_2$ normal to the separation vector. (All spinning black holes have dimensionless spin-magnitude of 0.5.) Figure 6.10 demonstrates the effectiveness of the eccentricity removal procedure based on $\dot{\Omega}$ and Eqs. (6.74) and (6.75). In all cases, the eccentricity is reduced

to less than 10^{-4} in four iterations.

The number of required eccentricity removal iterations depends on the quality of the guess for Ω_0 and $\dot{a}_0$ for the first iteration. Once eccentricity removal has been performed for several different configurations, we expect to be able to interpolate between configurations, to improve the initial guess substantially.

6.5 Conclusions

The removal of the initial spurious orbital eccentricity in binary black-hole simulations is quite challenging, and it becomes more complicated in the presence of spins. As predicted by PN theory, and worked out in Sec. 6.2, spin-spin interactions (notably $S_1\,S_1$, $S_2\,S_2$ and $S_1\,S_2$ terms) and precession induce oscillations in the binary radial separation and orbital frequency. These *spin-induced oscillations* are also present in the gravitational radiation emitted by the binary, and their frequency is close to twice the average orbital frequency. In Sec. 6.4 we confirm the presence of spin-induced oscillations in fully numerical simulations of black hole binaries. The agreement between the numerical simulations and PN calculations is as good as can be expected given the low order of the PN calculations, and the differing coordinate gauges.

Spin-induced oscillations can be distinguished from oscillations caused by orbital eccentricity by their characteristic frequencies. Moreover, the amplitude of spin-induced oscillations is quite small, so that it becomes visible only at small eccentricities, as can be seen from Eq. (6.51): At separations relevant for numerical sim-

ulations, spin-induced oscillations dominate orbital eccentricity only for $e \lesssim 0.001$, even for maximal spins in the least favorable orientation (parallel spins in the orbital plane). The amplitude of spin-induced oscillations is proportional to $S_{0,\perp}^2$, so that for spin $S/M^2 \sim 0.5$ as considered here, spin-induced oscillations become visible at orbital eccentricity $e \sim 10^{-4}$.

Spin-induced oscillations affect the orbital frequency derivative $\dot{\Omega}$ less than the radial velocity $\dot{r}$. Therefore, we develop in Sec. 6.3 a new eccentricity-removal procedure based on the derivative of the orbital frequency, and apply it to PN inspirals. Subsequently, we successfully apply the eccentricity removal procedure to fully numerical binary black hole evolutions to achieve eccentricities smaller than 10^{-4}. At this residual eccentricity, spin-induced oscillations begin to dominate over orbital eccentricity oscillations, as expected from our PN calculations. In Sec. 6.4.4, we tested the new eccentricity-removal procedure on fully numerical binary black hole simulations for several different spin configurations.

The computational cost for eccentricity reduction depends on the number of eccentricity removal iterations. Great care is necessary when performing the fitting, in order to achieve a large reduction in eccentricity per iteration. Section 6.3.2 gives guidance to improve these fits. With a good initial guess of $\Omega_0, \dot{a}_0$ for the 0-th iteration, one can start eccentricity removal from an already small initial eccentricity. As the number of data-points increases, we expect to be able to compute a better initial guess by interpolating between already computed low-eccentricity binary black-hole configurations.

Perhaps surprising, our present study indicates that eccentricity removal should

not be based on the proper separation between the apparent horizons. These new findings supersede the practice of earlier papers [185, 186, 305] to base eccentricity removal on proper separation rather than coordinate separation to take advantage of reduced numerical noise. As apparent in Figs. 6.7 and 6.8, spin-induced oscillations in $\dot{s}$ are about 15 times larger than in $\dot{r}$. Therefore, eccentricity-removal based on $\dot{s}$ will fail at ~ 15 times larger eccentricity than using $\dot{r}$, and at ~ 30 times larger eccentricity than for $\dot{\Omega}$. A likely cause for the unsatisfactory behavior of $\dot{s}$ lies in the deformation of the apparent horizons due to spin. For spins with a component in the orbital plane, the "bulge" of the apparent horizon rotates through the line connecting the two black holes as the black holes orbit each other. Earlier work [185, 186, 305] considered spins aligned with the orbital angular momentum, where this effect is absent; in those cases use of $\dot{s}$ was in order — but for precessing binaries, use of $\dot{s}$ is not advisable.

Even when the orbital frequency indicates $e < 10^{-4}$ for a fully numerical binary black-hole simulation, the extracted (2,2) mode of the gravitational radiation still shows oscillations at the orbital frequency in the wave phase with amplitude $\sim 10^{-3}$. While future work is necessary for a detailed understanding, the PN model predicts oscillations in the GW at the orbital frequency, and therefore, one cannot use the gravitational waveforms to estimate orbital eccentricity for precessing binaries. The wave phase and frequency of the NR simulation also shows oscillations at twice the orbital frequency with amplitude $\sim 3 \times 10^{-4}$ which are qualitatively reproduced by the restricted PN model of Ref. [346]. We postpone the study of the details of these features in the gravitational waveform to future work. Quite interestingly, it

proves, for this particular binary configuration in which only one hole spins, that those spin-induced oscillations are a direct consequence of monopole-quadrupole interactions [188, 309, 310, 347, 348].

All fully relativistic simulations presented here were performed using generalized harmonic coordinates. It would be very interesting to perform a similar study within the moving-puncture BSSN approach to investigate whether our conclusions are applicable in other gauges.

Chapter 7: **Prototype effective-one-body model for nonprecessing spinning inspiral-merger-ringdown waveforms**

Authors: *Andrea Taracchini, Yi Pan, Alessandra Buonanno, Enrico Barausse, Michael Boyle, Tony Chu, Geoffrey Lovelace, Harald P. Pfeiffer, and Mark A. Scheel*[1]

Abstract: We present a tunable effective-one-body (EOB) model for black-hole (BH) binaries of arbitrary mass ratio and aligned spins. This new EOB model incorporates recent results of small-mass-ratio simulations based on Teukolsky's perturbative formalism. The free parameters of the model are calibrated to numerical-relativity simulations of nonspinning BH-BH systems of five different mass ratios and to equal-mass non-precessing BH-BH systems with dimensionless BH spins $\chi_i \simeq \pm 0.44$. The present analysis focuses on the orbital dynamics of the resulting EOB model, and on the dominant $(\ell,m)=(2,2)$ gravitational-wave mode. The calibrated EOB model can generate inspiral-merger-ringdown waveforms for non-precessing, spinning BH binaries with any mass ratio and with individual BH spins $-1 \leq \chi_i \lesssim 0.7$. Extremizing only over time and phase shifts, the calibrated EOB model has overlaps larger than 0.997 with each of the seven numerical-relativity

[1]Originally published as Phys. Rev. D **86**, 024011 (2012)

waveforms for total masses between $20M_\odot$ and $200M_\odot$, using the Advanced LIGO noise curve. We compare the calibrated EOB model with two additional equal-mass highly spinning ($\chi_i \simeq -0.95, +0.97$) numerical-relativity waveforms, which were not used during calibration. We find that the calibrated model has overlap larger than 0.995 with the simulation with nearly extremal *anti-aligned* spins. Extension of this model to black holes with *aligned* spins $\chi_i \gtrsim 0.7$ requires improvements of our modeling of the plunge dynamics and inclusion of higher-order PN spin terms in the gravitational-wave modes and radiation-reaction force.

7.1 Introduction

Coalescing compact-object binary systems (binaries, for short) are among the most promising sources of gravitational waves (GWs) for detectors like the U.S. Laser Interferometer Gravitational-Wave Observatory (LIGO), the British-German GEO, and the French-Italian Virgo [349–351]. LIGO and Virgo are undergoing upgrades to Advanced configurations [4], which will improve sensitivity by about a factor of 10. A detailed and accurate understanding of the GWs radiated as the bodies in a binary spiral towards each other is crucial not only for the initial detection of such sources, but also for maximizing the information that can be obtained from the GW signals once they are observed.

The matched-filtering technique is the primary data-analysis tool used to extract the GW signals from the detectors' noise. It requires accurate waveform models of the expected GW signals. Analytical templates based on the post-Newtonian

(PN) approximation [60, 157, 259, 292] of the Einstein field equations developed over the past thirty years accurately describe the inspiraling stage of the binary evolution. In 1999 a new approach to the two-body dynamics of compact objects, the so-called effective-one-body (EOB) approach, was proposed with the goal of extending the analytical templates throughout the last stages of inspiral, plunge, merger, and ringdown. The EOB approach uses the results of PN theory, black-hole perturbation theory, and, more recently, the gravitational self-force formalism. It does not, however, use the PN results in their original Taylor-expanded form (i.e., as polynomials in v/c), but in a resummed form.

The EOB formalism was first proposed in Refs. [61, 62] and subsequently improved in Refs. [87, 102, 188]. Using physical intuition and results from black-hole perturbation theory and the close-limit approximation, Refs. [62, 102] computed preliminary plunge, merger, and ringdown signals of nonspinning and spinning black-hole binaries. After breakthroughs in numerical relativity (NR) [80–82], the EOB inspiral-merger-ringdown waveforms were improved by calibrating the model to progressively more accurate NR simulations, spanning larger regions of the parameter space [**?**, **?**, **?**, 91, 238, 239, 283, 285, 286, 322, 395]. More recently, an EOB model for the dominant $(2, 2)$ mode and four subdominant modes was built for nonspinning binaries of comparable masses [91] and the small-mass-ratio limit [119]. These results, at the interface between numerical and analytical relativity, have already had an impact in LIGO and Virgo searches. The first searches of high-mass and intermediate-mass black-hole binaries in LIGO/Virgo data [352, 353] used the inspiral-merger-ringdown templates generated by the EOB model calibrated in Ref. [283], as well as the phe-

nomenological templates proposed in Ref. [354].

Stellar-mass black holes are expected to carry spins, which significantly increases the dimension of the binary parameter space. The first EOB Hamiltonian with leading-order (1.5PN) spin-orbit and (2PN) spin-spin couplings was developed in Ref. [188]. Then, Ref. [102] worked out the radiation-reaction force in the EOB equations of motion in the presence of spins and computed inspiral-merger-ringdown waveforms for generic spinning binaries, capturing their main features, including the so-called "hang up". Later, Ref. [189] incorporated the next-to-leading-order (2.5PN) spin-orbit couplings in the EOB Hamiltonian. By construction, in the test-particle limit the Hamiltonian of Ref. [189] does not reduce to the Hamiltonian of a spinning test particle in the Kerr spacetime. Moreover, the Hamiltonian of Ref. [189] rewrites the EOB radial potential using Padé summation, causing spurious poles in some regions of parameter space. Nevertheless, the Hamiltonian of Ref. [189] was adopted in Ref. [239] to demonstrate the possibility of calibrating the EOB model for spinning binaries.

Since then, substantial progress has been made towards improving the spin EOB Hamiltonian. Ref. [193] worked out the Hamiltonian for a spinning test-particle in a generic spacetime, which was used in Ref. [191] to derive a spin EOB Hamiltonian having the correct test-particle limit. Furthermore, Ref. [191] rewrote the EOB radial potential in a way that guarantees the absence of poles without employing the Padé summation. As a consequence, the EOB Hamiltonian of Ref. [191] has desirable strong-field circular-orbit features, such as the existence of an innermost-stable circular orbit (ISCO), a photon circular orbit (or light-ring), and a maximum in

the orbital frequency during the plunge. Still preserving these properties, the spin EOB Hamiltonian of Ref. [191] was recently extended to include the next-to-next-to-leading-order (3.5PN) spin-orbit couplings in Ref. [192]. The EOB Hamiltonian of Ref. [189] was also recently extended through 3.5PN order in the spin-orbit sector in Ref. [355].

In the non-conservative sector of the EOB model, the radiation-reaction force in the EOB equations of motion is built from the GW energy flux, which, in turn, is computed from a decomposition of the waveform into spherical harmonic (ℓ, m) modes. These modes, instead of being used in their Taylor-expanded form, are resummed (or factorized). This factorization was originally proposed in Refs. [99, 100] for nonspinning black-hole binaries, and was then extended to include spin effects in Ref. [101] and higher-order PN spinless terms in Refs. [356, 357]. In the test-particle limit, the factorized waveforms are known at very high PN order—for example their sum generates the GW energy flux for nonspinning binaries through 14PN [357] order and to 4PN order in terms involving the black-hole spins. However, in the comparable-mass case the GW modes are known only at a much lower PN order. Despite the fact that the GW energy flux in the comparable-mass case is known through 3.5PN [358, 359] and 3PN [360] order in the nonspinning and spin-orbit sectors, and 2PN order in the spin-spin sector, the GW modes have been computed only through 1.5PN order for spin-orbit couplings and 2PN order for spin-spin couplings [101, 361]. Currently, this lack of information in the GW modes is the main limitation of our spin EOB model, and, as we will see, it affects the performance of the model for prograde orbits and large spin values.

In this paper, we build upon the past success in analytically modeling inspiral-merger-ringdown waveforms through the EOB formalism, and develop a prototype EOB model for non-precessing spinning black-hole binaries that covers a large region of the parameter space and can be used for detection purposes and future calibrations. More specifically, we adopt the EOB Hamiltonian derived in Refs. [191, 192], the GW energy flux and factorized waveforms derived in Refs. [100, 101], and calibrate the EOB (2,2) dominant mode to seven NR waveforms: five nonspinning waveforms with mass ratios $1, 1/2, 1/3, 1/4$ and $1/6$ [91] and two equal-mass non-precessing spinning waveforms of spin magnitudes 0.44 [186]. We combine the above results with recent small-mass-ratio results produced by the Teukolsky equation [119] to build a prototype EOB model for inspiral-merger-ringdown waveforms for non-precessing spinning black-hole binaries with any mass ratio and individual black-hole spins $-1 \leq \chi_i \lesssim 0.7$. For $\chi_i \gtrsim 0.7$, although the EOB dynamics can be evolved until the end of the plunge, the EOB (2,2) mode peaks too early in the evolution, where the motion is still quasicircular. As a consequence, we cannot correct the EOB (2,2) mode to agree with the NR (2,2) mode peak using non-quasicircular amplitude coefficients. This limitation, which also affects the small-mass-ratio limit results [119], is caused by the poor knowledge of PN spin effects in the GW modes and makes the prototype EOB waveforms unreliable for $\chi_i \gtrsim 0.7$. Two NR waveforms with nearly extremal spin magnitudes [307, 362] became available to us when we were finishing calibration of the spin EOB model. We use them to examine the limitations of the spin prototype EOB model, and extract from them useful information for future work.

The paper is organized as follows. In Sec. 7.2, we describe the spin EOB model used in this work, its dynamics, waveforms, and adjustable parameters. Section 7.3.1 discusses the alignment procedure used to compare EOB and NR waveforms at low frequency, and the statistics used to quantify the differences between the waveforms. We then calibrate the EOB model to the NR waveforms in Sec. 7.3.2. In Sec. 7.4, we combine the results of Sec. 7.3.1 with those of Ref. [119] to build a prototype EOB model that interpolates between the calibrated EOB waveforms and extends them to a larger region of the parameter space. We also investigate how this prototype EOB model performs with respect to two NR waveforms with nearly extremal spin, which were not used in the calibration. Finally, Sec. 7.5 summarizes our main conclusions. In Appendix F we explicitly write the factorized waveforms used in this work, including spin effects.

7.2 Effective-one-body dynamics and waveforms in the presence of spin effects

In this section, we define the spin EOB model that we will later calibrate using NR waveforms. Henceforth, we use geometric units $G = c = 1$.

In the spin EOB model [188,189,191,192,355] the dynamics of two black holes of masses m_1 and m_2 and spins $\boldsymbol{S}_1$ and $\boldsymbol{S}_2$ is mapped into the dynamics of an effective particle of mass $\mu = m_1\, m_2/(m_1 + m_2)$ and spin $\boldsymbol{S}_*$ moving in a deformed Kerr metric with mass $M = m_1 + m_2$ and spin $\boldsymbol{S}_{\rm Kerr}$. The position and momentum vectors of the effective particle are described by $\boldsymbol{R}$ and $\boldsymbol{P}$, respectively. Here, for

convenience, we use the reduced variables

$$\boldsymbol{r} \equiv \frac{\boldsymbol{R}}{M}\,, \qquad\qquad \boldsymbol{p} \equiv \frac{\boldsymbol{P}}{\mu}\,. \tag{7.1}$$

Since we will restrict the discussion to spins aligned or anti-aligned with the orbital angular momentum, we define the (dimensionless) spin variables χ_i as $\boldsymbol{S}_i \equiv \chi_i\, m_i^2\, \hat{\mathbf{L}}$, where $\hat{\mathbf{L}}$ is the unit vector along the direction of the orbital angular momentum. We also write $\boldsymbol{S}_{\rm Kerr} \equiv \chi_{\rm Kerr} M^2 \hat{\mathbf{L}}$.

7.2.1 The effective-one-body dynamics

In this paper we adopt the spin EOB Hamiltonian proposed in Refs. [191–193]. The real (or EOB) Hamiltonian is related to the effective Hamiltonian $H_{\rm eff}$ through the relation

$$H_{\rm real} \equiv \mu \hat{H}_{\rm real} = M\sqrt{1 + 2\nu\left(\frac{H_{\rm eff}}{\mu} - 1\right)} - M\,, \tag{7.2}$$

where $H_{\rm eff}$ describes the conservative dynamics of an effective spinning particle of mass μ and spin $\boldsymbol{S}^*$ moving in a deformed Kerr spacetime of mass M and spin $\boldsymbol{S}_{\rm Kerr}$. The symmetric mass ratio $\nu = \mu/M$ acts as the deformation parameter. Through 3.5PN order in the spin-orbit coupling, the mapping between the effective and real spin variables reads [191, 192]

$$\boldsymbol{S}_{\rm Kerr} = \boldsymbol{S}_1 + \boldsymbol{S}_2\,, \tag{7.3}$$

$$\boldsymbol{S}^* = \frac{m_2}{m_1}\,\boldsymbol{S}_1 + \frac{m_1}{m_2}\,\boldsymbol{S}_2 + \boldsymbol{\Delta}^{(1)}_{\sigma^*} + \boldsymbol{\Delta}^{(2)}_{\sigma^*}\,, \tag{7.4}$$

where $\boldsymbol{\Delta}^{(1)}_{\sigma^*}$ and $\boldsymbol{\Delta}^{(2)}_{\sigma^*}$ are the 2.5PN and 3.5PN spin-orbit terms given explicitly in Eqs. (51) and (52) of Ref. [192]. They depend on the dynamical variables $\boldsymbol{r}$ and

$\boldsymbol{p}$, the spin variables $\boldsymbol{S}_i$, and on several gauge parameters. These parameters are present because of the large class of canonical transformations that can map between the real and effective descriptions. Their physical effects would cancel out if the PN dynamics were known at arbitrarily high orders; since this is clearly not the case, the gauge parameters can have a noticeable effect [192] and may in principle be used as spin EOB adjustable parameters. In this paper however, we set all gauge parameters to zero and introduce a spin EOB adjustable parameter at 4.5PN order in the spin-orbit sector by adding the following term to Eq. (7.4)

$$\boldsymbol{\Delta}^{(3)}_{\sigma^*} = \frac{d_{\rm SO}\,\nu}{r^3}\left(\frac{m_2}{m_1}\,\boldsymbol{S}_1 + \frac{m_1}{m_2}\,\boldsymbol{S}_2\right) . \tag{7.5}$$

Here $d_{\rm SO}$ is the spin-orbit EOB adjustable parameter. The effective Hamiltonian reads [191]

$$\begin{aligned}\frac{H_{\rm eff}}{\mu} = \beta^i p_i + \alpha\sqrt{1+\gamma^{ij}p_i p_j + \mathcal{Q}_4(\boldsymbol{p})} + \frac{H_{\rm SO}}{\mu} + \frac{H_{\rm SS}}{\mu} \\ - \frac{1}{2Mr^5}(r^2\delta^{ij} - 3r^i r^j)S^*_i S^*_j\,,\end{aligned} \tag{7.6}$$

where the first two terms are the Hamiltonian of a nonspinning test particle in the deformed Kerr spacetime, α, β^i and γ^{ij} are the lapse, shift and 3-dimensional metric of the effective geometry and $\mathcal{Q}_4(\boldsymbol{p})$ is a non-geodesic term quartic in the linear momentum introduced in Ref. [363]. The quantities $H_{\rm SO}$ and $H_{\rm SS}$ in Eq. (7.6) contain respectively spin-orbit and spin-spin couplings that are *linear* in the effective particle's spin $\boldsymbol{S}^*$, while the term $-1/(2Mr^5)(r^2\delta^{ij} - 3r^i r^j)S^*_i S^*_j$ is the leading-order coupling of the particle's spin to itself, with δ^{ij} being the Kronecker delta. More explicitly, using Ref. [191] we can obtain $H_{\rm SO}$ and $H_{\rm SS}$ by inserting Eqs. (5.31), (5.32), Eqs. (5.47a)–(5.47h), and Eqs. (5.48)–(5.52) into Eqs. (4.18) and (4.19);

α, β^i and γ^{ij} are given by inserting Eqs. (5.36a)–(5.36e), Eqs. (5.38)–(5.40) and Eqs. (5.71)–(5.76) into Eqs. (5.44)–(5.46). We will elucidate our choice of the quartic term $\mathcal{Q}_4(\boldsymbol{p})$ at the end of this section, when introducing the tortoise variables.

Following Ref. [239], we introduce another spin EOB adjustable parameter in the spin-spin sector. Thus, we add to Eq. (7.6) the following 3PN term

$$\frac{d_{\rm SS}\,\nu}{r^4}\left(\frac{m_2}{m_1}\,\boldsymbol{S}_1+\frac{m_1}{m_2}\,\boldsymbol{S}_2\right)\cdot(\boldsymbol{S}_1+\boldsymbol{S}_2)\,, \tag{7.7}$$

with $d_{\rm SS}$ the spin-spin EOB adjustable parameter. For what concerns the nonspinning EOB sector, we adopt the following choice for the EOB potentials Δ_t and Δ_r entering α, β_i and γ_{ij} (see Eq. (5.36) in Ref. [191]). The potential Δ_t is given through 3PN order by

$$\Delta_t(u)=\frac{1}{u^2}\,\Delta_u(u)\,, \tag{7.8}$$

$$\Delta_u(u)=A(u)+\chi^2_{\rm Kerr}\,u^2\,, \tag{7.9}$$

$$A(u)=1-2u+2\nu\,u^3+\nu\left(\frac{94}{3}-\frac{41}{32}\pi^2\right)u^4\,, \tag{7.10}$$

where $u\equiv 1/r$. Reference [191] suggested rewriting the quantity $\Delta_u(u)$ as

$$\Delta_u(u)=\bar{\Delta}_u(u)\,\left[1+\nu\,\Delta_0+\nu\,\log\left(1+\Delta_1\,u+\Delta_2\,u^2\;\;+\Delta_3\,u^3+\Delta_4\,u^4\right)\right]\,,$$

where Δ_i with $i=1,2,3,4$ are explicitly given in Eqs. (5.77)–(5.81) of Ref. [191], and

$$\bar{\Delta}_u(u)=\,\chi^2_{\rm Kerr}\left(u-\frac{1}{r^{\rm EOB}_+}\right)\left(u-\frac{1}{r^{\rm EOB}_-}\right)\,, \tag{7.11}$$

$$r^{\rm EOB}_\pm=\,\left(1\pm\sqrt{1-\chi^2_{\rm Kerr}}\right)\,(1-K\,\nu)\,. \tag{7.12}$$

Here, $r_{\pm}^{\rm EOB}$ are radii reducing to those of the Kerr event and Cauchy horizons when the EOB adjustable parameter K goes to zero. The logarithm in Eq. (7.11) was introduced in Ref. [191] to quench the divergence of the powers of u at small radii. Its presence also allows the existence of an ISCO, a photon circular orbit (or light-ring), and a maximum in the orbital frequency during the plunge. The reason for modeling $\Delta_u(u)$ with Eq. (7.11) instead of using the Padé summation of $\Delta_u(u)$, as proposed in Ref. [189], is threefold. First, we did not want to use the Padé summation of $\Delta_u(u)$ because Ref. [239] found that for certain regions of the parameter space spurious poles can appear. Second, although we could have applied the Padé summation only to $A(u)$ and used the Padé potential $A(u)$ calibrated to nonspinning waveforms in Ref. [91], we want to take advantage of the good properties of the potential (7.11) during the late inspiral, as found in Ref. [191]. Third, we find it useful to develop a variant of the EOB potential so that in the future we can test how two different EOB potentials (both calibrated to NR waveforms at high frequency) compare at low frequency.

Furthermore, for the potential Δ_r at 3PN order entering the EOB metric components (5.36) in Ref. [191], we choose

$$\Delta_r(u) = \Delta_t(u)\, D^{-1}(u)\,, \tag{7.13}$$

$$D^{-1}(u) = 1 + \log[1 + 6\nu\, u^2 + 2(26 - 3\nu)\,\nu\, u^3]\,. \tag{7.14}$$

Once expanded in PN orders, the EOB Hamiltonian (8.1) with the effective Hamiltonian defined in Eq. (7.6) and the spin mapping defined in Eqs. (7.3) and (7.4), reproduces all known PN orders—at 3PN, 3.5PN and 2PN order in the nonspinning, spin-

orbit and spin-spin sectors, respectively—except for the spin-spin terms at 3PN and 4PN order, which have been recently computed in Refs. [158,313,320,321,364–367]. Furthermore, in the test-particle limit the real Hamiltonian contains the correct spin-orbit couplings linear in the test-particle spin, at *all* PN orders [191,193].

Let $\hat{t} \equiv t/M$. In terms of the reduced Hamiltonian $\hat{H}_{\rm real}$, the EOB Hamilton equations are given in dimensionless form by [239]

$$\frac{d\boldsymbol{r}}{d\hat{t}} = \{\boldsymbol{r}, \hat{H}_{\rm real}\} = \frac{\partial \hat{H}_{\rm real}}{\partial \boldsymbol{p}}\,, \tag{7.15}$$

$$\frac{d\boldsymbol{p}}{d\hat{t}} = \{\boldsymbol{p}, \hat{H}_{\rm real}\} + \hat{\boldsymbol{\mathscr{F}}} = -\frac{\partial \hat{H}_{\rm real}}{\partial \boldsymbol{r}} + \hat{\boldsymbol{\mathscr{F}}}\,, \tag{7.16}$$

where $\hat{\boldsymbol{\mathscr{F}}}$ denotes the non-conservative force that accounts for radiation-reaction effects. Following Ref. [102], we use [2]

$$\hat{\boldsymbol{\mathscr{F}}} = \frac{1}{\nu \hat{\Omega} |\boldsymbol{r} \times \boldsymbol{p}|} \frac{dE}{dt} \boldsymbol{p}\,, \tag{7.17}$$

where $\hat{\Omega} \equiv M|\boldsymbol{r} \times \dot{\boldsymbol{r}}|/r^2$ is the dimensionless orbital frequency and dE/dt is the GW energy flux for quasicircular orbits obtained by summing over the modes (ℓ, m) as

$$\frac{dE}{dt} = \frac{\hat{\Omega}^2}{8\pi} \sum_{\ell=2}^{8} \sum_{m=0}^{\ell} m^2 \left| \frac{\mathcal{R}}{M} h_{\ell m} \right|^2 . \tag{7.18}$$

Here $\mathcal{R}$ is the distance to the source, and simply eliminates the dominant behavior of $h_{\ell m}$. We sum over positive m modes only since $|h_{\ell,m}| = |h_{\ell,-m}|$. Expressions for the modes $h_{\ell m}$ are given in the next section. In this paper, we restrict the calibration to non-precessing binaries, and thus we omit the Hamilton equations of the spin variables.

[2] The over-dot stands for d/dt.

It was demonstrated in previous work [99, 368] that by replacing the radial component of the linear momentum $p_r \equiv (\boldsymbol{p}\cdot\boldsymbol{r})/r$ with p_{r^*}, which is the conjugate momentum of the EOB tortoise radial coordinate r^*, one can improve the numerical stability of the EOB equations of motion. This happens because p_r diverges when approaching $r_+^{\rm EOB}$ while p_{r^*} does not. In this paper we follow the definition of the EOB tortoise radial coordinate in Appendix A of Ref. [239].[3] However, when applying the tortoise coordinate transformation to the quartic term in Eq. (7.6), we get [239]

$$\mathcal{Q}_4(\boldsymbol{p}) \propto \frac{p_{r^*}^4}{r^2}\frac{D^2}{\Delta_t^4}(r^2+\chi_{\rm Kerr}^2)^4\,, \tag{7.19}$$

which clearly diverges at $r = r_+^{\rm EOB}$. As in the nonspinning case [91, 99, 368], we neglect contributions higher than 3PN order and rewrite Eq. (7.19) as

$$\mathcal{Q}_4(\boldsymbol{p}) \propto \frac{p_{r^*}^4}{r^2}(r^2+\chi_{\rm Kerr}^2)^4\,, \tag{7.20}$$

which is well behaved throughout the EOB orbital evolution.

Lastly, we integrate the EOB Hamilton equations. In order to get rid of any residual eccentricity when the EOB orbital frequency is close to the initial frequency of the NR run, we start the EOB evolution at large separation, say $50M$, and use the quasispherical initial conditions developed in Ref. [102]. We stop the integration when the orbital frequency Ω reaches a maximum.

[3]Note that all the formulas in Appendix A of Ref. [239] are written in physical dynamical variables, namely $\boldsymbol{R}$ and $\boldsymbol{P}$, while here we use reduced variables $\boldsymbol{r}$ and $\boldsymbol{p}$.

7.2.2 The effective-one-body waveforms

Following Refs. [91, 99, 239, 285, 286] we write the inspiral-plunge modes as

$$h_{\ell m}^{\text{insp-plunge}} = h_{\ell m}^{\text{F}} N_{\ell m}, \tag{7.21}$$

where the $h_{\ell m}^{\text{F}}$ are the factorized modes developed in Refs. [99–101], and the $N_{\ell m}$ are non-quasicircular (NQC) corrections that model deviations from quasicircular motion, which is assumed when deriving the $h_{\ell m}^{\text{F}}$. The factorized modes read

$$h_{\ell m}^{\text{F}} = h_{\ell m}^{(N,\epsilon)} \hat{S}_{\text{eff}}^{(\epsilon)} T_{\ell m} e^{i\delta_{\ell m}} \left(\rho_{\ell m}\right)^{\ell} , \tag{7.22}$$

where ϵ is the parity of the waveform. All the factors entering the $h_{\ell m}^{\text{F}}$ can be explicitly found in Appendix F. We emphasize here again that despite the fact that the GW energy flux in the comparable-mass case is known through 3PN order in the spin-orbit sector [360], the spin-orbit couplings in the factorized (or PN-expanded) modes have been computed only through 1.5PN order [101, 361]. This limitation will degrade the performances of our spin EOB model for prograde orbits and large spin values, as already observed in the test-particle limit in Refs. [101, 119]. To improve the knowledge of spin effects in the GW modes, Refs. [101, 239] added spin couplings in the test-particle limit through 4PN order in the factorized waveforms. However, since the mapping between the Kerr spin parameter in the test-particle limit and the black-hole spins in the comparable-mass case is not yet unambiguously determined [191, 192], and since we do not have many NR spinning waveforms at our disposal to test the mapping, we decide not to include here the spinning test-particle-limit couplings in the factorized waveforms computed in Ref. [101]. We

have checked before performing any calibration that EOB models with or without test-particle spin effects (with Kerr spin parameter $\chi_{\rm Kerr}$) give similar performances.

In all the calibrations of the nonspinning EOB model, two EOB adjustable parameters were needed to calibrate the EOB Hamilton equations—for example Refs. [91, 285] used the 4PN and 5PN order coefficients in the EOB potential $A(r)$. As discussed in the previous section, for the EOB model adopted in this paper, the EOB nonspinning conservative dynamics depend so far only on the adjustable parameter K. We introduce a second EOB adjustable parameter in the non-conservative non-spinning EOB sector by adding a 4PN order non-spinning term in ρ_{22} and denote the coefficient of this unknown PN term by $\rho_{22}^{(4)}$ [see Eq. (F.11)]. This adjustable parameter enters the EOB Hamilton equations through the energy flux defined in Eq. (11.9).

As shown in Ref. [91], the NQC corrections of modes with $(\ell, m) \neq (2, 2)$ have marginal effects on the dynamics. Also, our goal in this work is to calibrate only the $(2, 2)$ mode, so in the following we set $N_{\ell m} = 1$ for $(\ell, m) \neq (2, 2)$. We have[4]

$$\begin{aligned} N_{22} = &\left[1 + \left(\frac{p_{r^*}}{r\,\hat{\Omega}}\right)^2 \left(a_1^{h22} + \frac{a_2^{h22}}{r} + \frac{a_3^{h22}}{r^{3/2}} + \frac{a_4^{h22}}{r^2} + \frac{a_5^{h22}}{r^{5/2}}\right)\right] \\ &\times \exp\left[i \frac{p_{r^*}}{r\,\hat{\Omega}} \left(b_1^{h22} + p_{r^*}^2 b_2^{h22} + \frac{p_{r^*}^2}{r^{1/2}} b_3^{h22} + \frac{p_{r^*}^2}{r} b_4^{h22}\right)\right], \end{aligned} \tag{7.23}$$

where a_i^{h22} (with $i = 1...5$) are the (real) NQC amplitude coefficients and b_i^{h22} (with $i = 1...4$) are the (real) NQC phase coefficients. We will explain in detail how these coefficients are determined at the end of this section.

[4]Note that in Ref. [119] the $N_{\ell m}$ were written in terms of physical dynamical variables, rather than the reduced variables used here.

The EOB merger-ringdown waveform is built as a linear superposition of the quasinormal modes (QNMs) of the final Kerr black hole [**?**,62,283,286,322,369,395], as

$$h_{22}^{\text{merger-RD}}(t) = \sum_{n=0}^{N-1} A_{22n}\, e^{-i\sigma_{22n}(t-t^{22}_{\text{match}})}\,, \tag{7.24}$$

where N is the number of overtones, A_{22n} is the complex amplitude of the n-th overtone, and $\sigma_{22n} = \omega_{22n} - i/\tau_{22n}$ is the complex frequency of this overtone with positive (real) frequency ω_{22n} and decay time τ_{22n}. The complex QNM frequencies are known functions of the mass and spin of the final Kerr black hole. Their numerical values can be found in Ref. [370]. The mass and spin of the final black hole, M_f and a_f, can be computed through analytical phenomenological formulas reproducing the NR predictions. Here, we adopt the formulas given in Eq. (8) of Ref. [371] and in Eqs. (1) and (3) of Ref. [372]. We notice that the formula for the final mass in Ref. [371] was obtained using numerical simulations of small-spin black-hole binaries with mildly unequal masses. As a consequence, the formula is not very accurate for the large-spin, unequal-mass binaries considered in this paper. However, other formulas available in the literature are either very accurate but only valid for equal-mass binaries [373], or have not been yet extensively tested against NR simulations [208,374]. Thus, for the time being we stick with Eq. (8) of Ref. [371], but we plan to construct a better formula in the future using all recent data in the literature.

Furthermore, we follow the hybrid matching procedure of Ref. [91] to fix the N complex amplitude coefficients A_{22n} in Eq. (11.22). We set up N complex linear

equations by imposing that the inspiral-plunge and merger-ringdown waveforms $h_{22}^{\text{inspiral-plunge}}$ and $h_{22}^{\text{merger-RD}}$ coincide on $N-2$ points (evenly sampled over a range $[t^{22}_{\text{match}} - \Delta t^{22}_{\text{match}}, t^{22}_{\text{match}}]$) and that their time derivatives $\dot{h}_{22}^{\text{inspiral-plunge}}$ and $\dot{h}_{22}^{\text{merger-RD}}$ coincide at $t^{22}_{\text{match}} - \Delta t^{22}_{\text{match}}$ and t^{22}_{match}. As in previous works, we introduce the EOB adjustable parameter $\Delta t^{22}_{\text{match}}$ which describes the size of the comb over which we impose continuous and smooth matching in order to determine the ringdown waveform.

In Refs. [91, 119, 286], pseudo QNMs (pQNMs) were proposed and applied to moderate the rise of the EOB GW frequency during the merger-ringdown transition—for example Sec. IIC of Ref. [91] discussed in some detail the advantage of using pQNMs for higher-order GW modes. In this paper, we find it useful to introduce a pQNM for the $(2,2)$ mode. Therefore, we choose $N=8$ in Eq. (11.22) and replace the highest overtone in the summation with this pQNM.

Finally, we build the full inspiral-plunge-merger-ringdown EOB waveform by joining the inspiral-plunge waveform $h_{22}^{\text{inspiral-plunge}}(t)$ and the merger-ringdown waveform $h_{22}^{\text{merger-RD}}(t)$ at the matching time t^{22}_{match} as

$$h_{22}^{\text{EOB}}(t) = h_{22}^{\text{inspiral-plunge}}(t)\,\theta(t^{22}_{\text{match}} - t) + h_{22}^{\text{merger-RD}}(t)\,\theta(t - t^{22}_{\text{match}})\,. \tag{7.25}$$

In Fig. 7.1, we summarize how the inspiral-plunge–merger-ringdown EOB waveform is constructed. Beyond the ISCO, the quasi-circular inspiral waveform is followed by a short plunge waveform [5] where the radial motion is no longer negligible and NQC corrections quickly become important. The plunge ends roughly when the

[5] The number of gravitational-wave cycles during the plunge scales roughly as $\nu^{-1/5}$ [62].

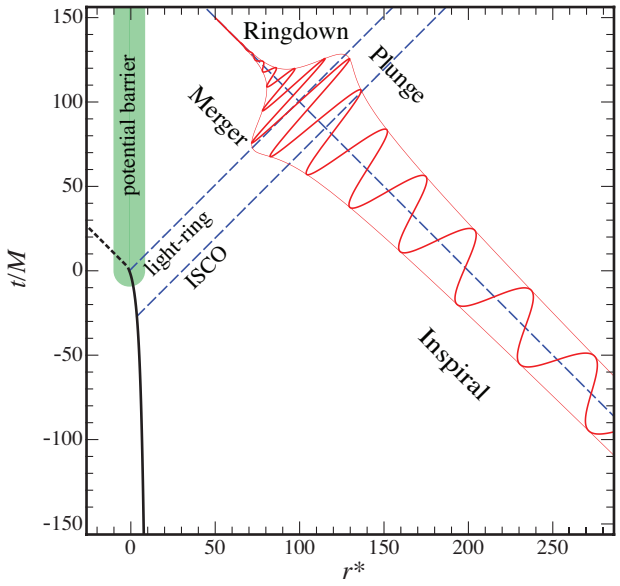

Figure 7.1: We show in the spacetime diagram $(\hat{t}, r^*)$ the trajectory of the effective particle in the EOB description (black solid line in the left part of the diagram) and the EOB (2,2) gravitational mode (red solid oscillating line) for an equal-mass nonspinning black-hole binary. Although we only need to evolve the EOB trajectory until the orbital frequency reaches its maximum ("light ring"), the model's dynamics allows the trajectory to continue to negative r^* (short-dashed black line in the left part of the diagram). The blue dashed lines represent $\hat{t} \pm r^* =$ const. surfaces and ingoing/outgoing null rays. The EOB (2,2) mode is a function of the retarded time $\hat{t} - r^*$, plotted here orthogonal to $\hat{t} - r^* =$ const. surfaces, at a finite $\hat{t} + r^*$ distance. The two outgoing null rays are drawn at the $\hat{t} - r^*$ retarded times when the EOB particle crosses the EOB ISCO and light-ring radii, respectively. The shaded green area is a rough sketch of the potential barrier around the newborn black hole.

effective particle in the EOB description crosses the light-ring, which, in the nonspinning case, coincides approximately with the peak of EOB orbital frequency $\hat{\Omega}$ and waveform amplitude $|h_{22}|$. Until this moment, the GW radiation in the EOB description is obtained directly from the motion of the effective particle. After this moment that we identify as the merger, the direct emission of GWs from the ef-

fective particle is strongly attenuated and filtered by the potential barrier formed around the newborn black hole. Thus, in the EOB description the merger-ringdown waveform is no longer obtained from the motion of the effective particle, but it is built through a superposition of QNMs. This procedure of constructing the full EOB waveform, in particular replacing the direct emission with a superposition of QNMs beyond the light ring, was first proposed in Refs. [62, 102] for nonspinning and spinning comparable-mass black-hole binaries. It was inspired by the close limit approximation [375] and results in Refs. [376, 377] where it was observed that once the radially infalling particle is inside the potential barrier which peaks around the light ring, the direct gravitational radiation from the particle is strongly filtered by the potential barrier. Part of the energy produced in the strong merger-burst remains stored in the resonant cavity of the geometry, i.e., inside the potential barrier, and what is released outside is just the ringdown signal. The non-linear scattering of GW radiation (tails) against the curvature potential of the newborn black hole also contributes to the merger-ringdown waveform. Currently, in the EOB description the merger-ringdown waveform is effectively the tail of a δ-function impulse at merger. When spin effects are present, the overall picture depicted in Fig. 7.1 survives, but with some differences due to the fact that the EOB light-ring position, peak of the orbital frequency $\hat{\Omega}$ and waveform amplitude $|h_{22}|$ can be displaced in time [119]. We notice that the physical picture of the merger-ringdown that emerged from the studies in Refs. [375–377] and was incorporated in the EOB description in Refs. [62, 102], has also recently motivated the hybrid approach of Refs. [378, 379].

We now continue our detailed review of how the EOB waveform is built and

q	1	1/2	1/3	1/4	1/6	1	1
$\chi_1 = \chi_2$	0	0	0	0	0	+0.43655	−0.43757
$\lvert h^{\rm NR}_{22,\rm peak}\rvert$	0.3940	0.3446	0.2855	0.2403	0.1810	0.3942	0.3935
$10^4 M^2 \partial_t^2 \lvert h^{\rm NR}_{22,\rm peak}\rvert$	−10.3	−8.8	−6.9	−5.5	−3.9	−7.7	−12.4
$M\omega^{\rm NR}_{22,\rm peak}$	0.3593	0.3467	0.3324	0.3218	0.3084	0.3989	0.3342
$10^3 M^2 \dot{\omega}^{\rm NR}_{22,\rm peak}$	11.3	10.5	9.6	8.9	8.1	11.2	10.7

Table 7.1: Exact NR-input values used in the right-hand side of Eqs. (7.26)–(7.30) to calibrate the EOB inspiral-plunge waveforms.

discuss how we fix the NQC coefficients in Eq. (11.18). Since we do not expect spin effects in the NQC correction until 1.5PN order in either amplitude or phase, the coefficients $a_i^{h_{22}}$ with $i = 1, 2$ and $b_i^{h_{22}}$ with $i = 1, 2$ only depend on ν, while $a_i^{h_{22}}$ with $i = 4, 5$ and $b_i^{h_{22}}$ with $i = 3, 4$ are functions of ν linearly proportional to the spins $\chi_{1,2}$. The coefficient $a_3^{h_{22}}$ is given by the sum of a nonspinning term (dependent only on ν) and a spinning term (proportional to the spins $\chi_{1,2}$). In Sec. 7.3 we first calibrate the nonspinning waveforms, and then the spinning ones. Thus, we determine the ten coefficients in Eq. (11.18) in two steps. First, we set $\chi_1 = \chi_2 = 0$, thus $a_i^{h_{22}} = 0$ (with $i = 4, 5$) and $b_i^{h_{22}} = 0$ (with $i = 3, 4$) and calculate the values of the five NQC coefficients $a_i^{h_{22}}$ (with $i = 1, 2, 3$) and $b_i^{h_{22}}$ (with $i = 1, 2$) by imposing the following five conditions [91, 119]:

1. Let $t^{\Omega}_{\rm peak}$ be the time at which the EOB orbital frequency reaches its peak. Then, the peak of the EOB $(2, 2)$ mode must happen at the matching time $t^{22}_{\rm match} = t^{\Omega}_{\rm peak} + \Delta t^{22}_{\rm peak}$, that is

$$\left.\frac{d|h^{\rm EOB}_{22}|}{dt}\right|_{t^{\Omega}_{\rm peak}+\Delta t^{22}_{\rm peak}} = 0\,, \tag{7.26}$$

where $\Delta t^{22}_{\rm peak}$ is an EOB adjustable parameter, which will be specified in Sec. 7.3. We note that in Ref. [119] the quantity $\Delta t^{22}_{\rm peak}$ was computed by comparing the times at which the Teukolsky (2,2) mode and the EOB orbital frequency reach their peaks. This was possible because the EOB trajectory was used in the Teukolsky equation to evolve the dynamics. However, in the NR simulation, we do not know what $\Delta t^{22}_{\rm peak}$ is, because the EOB dynamics does not determine the NR dynamics.

2. The amplitudes of the NR and EOB $(2,2)$ modes are the same,

$$|h^{\rm EOB}_{22}(t^{\Omega}_{\rm peak}+\Delta t^{22}_{\rm peak})| = |h^{\rm NR}_{22}(t^{\rm NR}_{\rm peak})|\,. \tag{7.27}$$

3. The curvatures of the amplitudes of the NR and EOB $(2,2)$ modes are the same,

$$\left.\frac{d^2|h^{\rm EOB}_{22}|}{dt^2}\right|_{t^{\Omega}_{\rm peak}+\Delta t^{22}_{\rm peak}} = \left.\frac{d^2|h^{\rm NR}_{22}|}{dt^2}\right|_{t^{\rm NR}_{\rm peak}}\,. \tag{7.28}$$

4. The GW frequencies of the NR and EOB $(2,2)$ modes are the same,

$$\omega^{\rm EOB}_{22}(t^{\Omega}_{\rm peak}+\Delta t^{22}_{\rm peak}) = \omega^{\rm NR}_{22}(t^{\rm NR}_{\rm peak})\,. \tag{7.29}$$

5. The time derivatives of the GW frequency of the NR and EOB $(2,2)$ modes are the same,

$$\left.\frac{d\omega^{\rm EOB}_{22}}{dt}\right|_{t^{\Omega}_{\rm peak}+\Delta t^{22}_{\rm peak}} = \left.\frac{d\omega^{\rm NR}_{22}}{dt}\right|_{t^{\rm NR}_{\rm peak}}\,. \tag{7.30}$$

We summarize in Table 7.1 all the NR-input values that we use in the right-hand side of Eqs. (7.27)–(7.30). After the five nonspinning NQC coefficients have been computed, we plug them back into the EOB dynamics through the energy flux,

start a new EOB evolution, generate a new EOB $(2,2)$ mode, and calculate new NQC coefficients. We repeat this procedure until the values of the NQC coefficients converge. Then, when calibrating spinning waveforms, we set a_i^{h22} and b_i^{h22} (with $i = 1, 2$), as well as the nonspinning part of a_3^{h22}, to the values just calculated for $\chi_1 = \chi_2 = 0$, and apply the five conditions above in an iterative way, obtaining the final coefficients a_i^{h22} (with $i = 3, 4, 5$) and b_i^{h22} (with $i = 3, 4$). Note that in order to generate GW templates, this procedure can be computationally expensive, since to generate one EOB $(2,2)$ mode one has to evolve the dynamics a few times. The current computational cost of generating an EOB waveform long enough for the LIGO bandwidth varies between a fraction of a second to a few seconds,[6] depending on the masses. The iterative procedure can increase this cost by a factor of a few.

In order for the NQC coefficients to be effective in correcting the EOB mode peak, the latter has to occur in a region where the radial motion is comparable to or at least $\sim 30\%$ of the tangential motion. Such a condition is in principle not a necessary requirement for the EOB model to work. In fact, the radial motion *is* expected to be strongly suppressed for almost extremal black holes, at least in the test-particle limit, since the ISCO coincides with the horizon for $\chi = 1$ [380]. However, if the factorized (2,2) mode, given by Eq. (11.4), differs substantially from the NR (2,2) mode because of the lack of high-order spin-orbit terms, the inability of the NQC coefficient to change the waveform during the plunge at high spins may prevent the EOB model to work properly. This is because the NQC coefficients cannot artificially compensate the missing higher-order spin orbit terms

[6]The time is measured by running a code that is not optimized in speed on a single CPU.

in the waveforms, as they partially do at low spins. In fact, we will see that this problem arises for $\chi_i \gtrsim 0.7$, making the EOB prototype waveforms unreliable for large positive spins.

We list in Table 7.2 all the EOB adjustable parameters that we exploit in this work to calibrate the EOB model to NR simulations.

7.3 Effective-one-body calibration

In this section, we calibrate the EOB model using seven NR waveforms, namely five nonspinning waveforms of mass ratios $q \equiv m_2/m_1 = 1, 1/2, 1/3, 1/4$ and $1/6$ and two equal-mass spinning waveforms with $\chi_1 = \chi_2 = +0.43655$ and $\chi_1 = \chi_2 = -0.43757$. The calibration is achieved by minimizing the amplitude and phase differences between the NR and EOB $(2,2)$ modes over the six EOB adjustable parameters: K, $d_{\rm SO}$ and $d_{\rm SS}$ in the EOB conservative dynamics, and $\rho_{22}^{(4)}$, $\Delta t_{\rm peak}^{22}$, $\Delta t_{\rm match}^{22}$, $\omega_{22}^{\rm pQNM}$ and $\tau_{22}^{\rm pQNM}$ in the EOB waveforms (see Table 7.2).

7.3.1 Alignment of EOB and NR waveforms

When calibrating NR and EOB waveforms, we first align the waveforms at low frequency following the procedure of Refs. [91, 239, 286]. This procedure consists of minimizing the square of the difference between the NR and EOB $(2,2)$-mode phases $\phi_{22}^{\rm NR}$ and $\phi_{22}^{\rm EOB}$, integrated over the time window (t_1, t_2),

$$\int_{t_1}^{t_2} \left[\phi_{22}^{\rm EOB}(t+t_0) + \phi_0 - \phi_{22}^{\rm NR}(t)\right]^2 dt\,, \tag{7.31}$$

with respect to the time shift t_0 and phase shift ϕ_0, where it is understood that $\phi_{22}^{\rm EOB}$ is computed for a chosen set of adjustable parameters. The time window (t_1, t_2) should: (i) begin as early as possible, where the NR and EOB GW-phase evolutions agree best, (ii) begin late enough to avoid the junk radiation present in the numerical simulation, (iii) be long enough to average over numerical noise, and (iv) extend from peak to peak (or trough to trough) over an integer number of oscillations in the GW frequency, which are caused by the residual eccentricity in the numerical initial conditions. In Table 7.3, we list our choices of (t_1, t_2) for the seven numerical waveforms at our disposal. Each time window extends through 10 eccentricity oscillation cycles in the numerical frequency evolution.

Let $\bar{\phi}_0$ and $\bar{t}_0$ be the alignment parameters. Then, we define the phase and relative amplitude differences between the EOB and NR (2,2) modes as follows:

$$\Delta\phi(t) = \phi_{22}^{\rm EOB}(t + \bar{t}_0) + \bar{\phi}_0 - \phi_{22}^{\rm NR}(t)\,, \tag{7.32}$$

and

$$\left(\frac{\Delta A}{A}\right)(t) = \frac{|h_{22}^{\rm EOB}|(t + \bar{t}_0)}{|h_{22}^{\rm NR}|(t)} - 1\,. \tag{7.33}$$

We then define the global phase and relative amplitude differences over a time window (t_1, t_3) with

$$\Delta\phi_{\rm global} = \max_{t\in(t_1,t_3)} |\Delta\phi(t)|\,, \tag{7.34}$$

and

$$\left(\frac{\Delta A}{A}\right)_{\rm global} = \max_{t\in(t_1,t_3)} \left|\left(\frac{\Delta A}{A}\right)(t)\right|\,. \tag{7.35}$$

In the following, when measuring the difference between NR and EOB inspiral-plunge waveforms we set $t_3 = t_{\rm match}^{22}$, while when we measure the difference between

EOB dynamics adjustable parameters	EOB waveform adjustable parameters
K	$\rho_{22}^{(4)}$
$d_{\rm SO}, d_{\rm SS}$	$\Delta t_{\rm match}^{22}, \Delta t_{\rm peak}^{22}$
	$\omega_{22}^{\rm pQNM}, \tau_{22}^{\rm pQNM}$

Table 7.2: Summary of adjustable parameters of the spin EOB model considered in this paper. The values of the EOB adjustable parameters used in this paper are given in Eqs. (7.38), (7.39), (7.40), (7.42), (7.43), and (7.49). In addition, the NQC parameters $a_i^{h_{22}}$ and $b_i^{h_{22}}$ are fixed from NR-input values through Eqs. (7.26)–(7.30).

full inspiral-merger-ringdown waveforms we use $t_3 = t_{\rm end}$, where $t_{\rm end}$ is chosen as late as possible into the ringdown stage, but before numerical errors due to gauge effects become noticeable [286]. We list the values of $t_{\rm match}^{22}$ and $t_{\rm end}$ for the seven NR waveforms in Table 7.3.

7.3.2 Procedure to calibrate the EOB adjustable parameters

Recently, Ref. [119] computed the waveforms in the small-mass-ratio limit by evolving a time-domain Teukolsky equation in which the source term is evaluated using an EOB trajectory. It was found that there exists a time difference between the Teukolsky $(2,2)$-mode amplitude peak and the EOB orbital-frequency peak. This difference is parametrized by the quantity $\Delta t_{\rm peak}^{22}$ introduced in Eq. (7.26). Table III in Ref. [119] lists this difference as a function of the Kerr spin parameter: for nonspinning and retrograde cases $-3M \leq \Delta t_{\rm peak}^{22} \leq 1.6M$, while for prograde cases $\Delta t_{\rm peak}^{22}$ decreases quickly as function of the spin. Let us consider $\chi_{\rm Kerr}$, which

explicitly reads

$$\chi_{\rm Kerr} = (1-2\nu)\,\chi_{\rm S} + \sqrt{1-4\nu}\,\chi_{\rm A}\,, \tag{7.36}$$

and also define

$$\chi \equiv \chi_{\rm S} + \chi_{\rm A}\,\frac{\sqrt{1-4\nu}}{1-2\nu}\,, \tag{7.37}$$

where $\chi_{\rm S,A} \equiv (\chi_1 \pm \chi_2)/2$. For an equal-mass, equal-spin binary ($\nu = 1/4, \chi_1 = \chi, \chi_2 = \chi$) we have $\chi_{\rm Kerr} = \chi/2$, while in the test-particle limit we have $\chi_{\rm Kerr} = \chi$ (that is the spin parameter of the background spacetime). Therefore, inspired by the results in the test-particle limit, we assume here that for an equal-mass, equal-spin binary $\Delta t^{22}_{\rm peak}$ depends on the black-hole spins through χ. Explicitly we choose

$$\Delta t^{22}_{\rm peak} = \begin{cases} -2.5M & \text{if } \chi \leq 0\,, \\ -2.5M - 1.77M\left(\frac{\chi}{0.437}\right)^4 & \text{if } \chi > 0\,, \end{cases} \tag{7.38}$$

which models qualitatively Table III in Ref. [119]. Following Refs. [91, 239, 286], we calibrate the EOB adjustable parameters in two steps. These steps are performed for each of our seven calibration NR waveforms separately, resulting in seven sets of calibration parameters. First, for each of the NR waveform at our disposal, we use $\Delta t^{22}_{\rm peak}$ in Eq. (7.38), insert the NR-input values from Table 7.1 into Eqs. (7.26)–(7.30), solve them iteratively for the NQC coefficients, and calibrate K, $\rho^{(4)}_{22}$ (or $d_{\rm SO}$ and $d_{\rm SS}$ if spins are present) by minimizing Eq. (7.34) with $t_3 = t^{22}_{\rm match}$. This process provides us with the EOB inspiral-plunge waveform. Second, to obtain the EOB merger-ringdown waveform, we calibrate the size of the comb $\Delta t^{22}_{\rm match}$ and the pQNM (complex) frequency by applying Eq. (7.34) with $t_3 = t_{\rm end}$. As in Ref. [91],

q	1	1/2	1/3	1/4	1/6	1	1
$\chi_1 = \chi_2$	0	0	0	0	0	+0.43655	−0.43757
t_1/M	820	770	570	670	870	800	610
t_2/M	2250	2255	1985	1985	2310	2150	1850
$t^{22}_{\rm match}/M$	3943	3729	3515	3326	4892	3367	2402
$t_{\rm end}/M$	3990	3770	3560	3370	4940	3410	2430

Table 7.3: We list the parameters t_1, t_2 entering the alignment procedure defined in Eq. (7.31), and the parameter t_3 (both $t^{22}_{\rm match}$ and $t_{\rm end}$) entering the computation of waveforms' differences in Eqs. (7.34) and (7.35).

we find that a constant value for the comb size, notably

$$\Delta t^{22}_{\rm match} = 7.5M\,, \tag{7.39}$$

gives a very good performance for all the different mass ratios and spins. A detailed study of the pQNM (complex) frequency has revealed that the best result is obtained when $\omega_{22}^{\rm pQNM}$ lies between the GW frequency $\omega_{22}^{\rm EOB}M/M_f$ at $t^{22}_{\rm match}$ and the frequency of the least-damped QNM ω_{220}, and when $\tau_{22}^{\rm pQNM}$ is (not much) shorter than τ_{220}. Specifically, we use the simple choice

$$\omega_{22}^{\rm pQNM} = \frac{1}{2}\left[\omega_{22}^{\rm EOB}(t^{22}_{\rm match})\frac{M}{M_f} + \omega_{220}\right]\,, \tag{7.40}$$

$$\tau_{22}^{\rm pQNM} = \frac{3}{10}\tau_{220}\,, \tag{7.41}$$

for all different mass ratios and spins. Before ending this section, we discuss in more detail how we carry out the calibration of the parameters K, $\rho^{(4)}_{22}$, for the nonspinning sector, and the parameters $d_{\rm SO}$, $d_{\rm SS}$, for the spinning sector.

7.3.2.1 Calibrating nonspinning waveforms

In general, the adjustable parameters K and $\rho_{22}^{(4)}$ depend on the mass ratio and we assume that they are polynomial functions of ν. In principle, we should determine $K(\nu)$ and $\rho_{22}^{(4)}(\nu)$ by a global minimization of $\Delta\phi_{\rm global}$ and $(\Delta A/A)_{\rm global}$ [as defined in Eqs. (7.34) and (7.35) using $t_3 = t^{22}_{\rm match}$] with respect to the unknown coefficients entering the $K(\nu)$ and $\rho_{22}^{(4)}(\nu)$ polynomials. However, as in previous studies [91,285], we find a strong degeneracy among the EOB adjustable parameters, when calibrating each mass ratio separately. The degeneracy is partially broken when we combine all the available mass ratios together, but it is not completely lifted. In particular, different choices of $K(\nu)$ and $\rho_{22}^{(4)}(\nu)$ lead to EOB models that can match equally well with NR waveforms. We are thus relieved from a rigorous yet expensive global search and follow a simplified procedure to find satisfactory $K(\nu)$ and $\rho_{22}^{(4)}(\nu)$. First, we locate two points $(0.8154, -35)$ and $(1.188, -20)$ in the K–$\rho_{22}^{(4)}$ plane where $\Delta\phi_{\rm global} < 0.1$ rad and $(\Delta A/A)_{\rm global} < 0.1$ for $q = 1$ and $q = 1/6$ ($\nu = 0.25$ and $\nu = 0.1224$), respectively. We then determine a linear function $\rho_{22}^{(4)}(\nu)$ by imposing that $\rho_{22}^{(4)}(0.25) = -35$ and $\rho_{22}^{(4)}(0.1224) = -20$, leading to

$$\rho_{22}^{(4)}(\nu) = -5.6 - 117.6\,\nu\,. \tag{7.42}$$

At $q = 1/2, 1/3$ and $1/4$, we choose $\rho_{22}^{(4)}$ according to Eq. (7.42) and determine the value of K that minimizes $\Delta\phi_{\rm global}$ and a range of K values that satisfy $\Delta\phi_{\rm global} < 0.1$ rad.

We now have a complete set of calibration parameters for each of our non-

spinning NR waveforms. In order to obtain calibration parameters that interpolate between the NR waveforms, we build a least-squares fit quadratic in ν against these K values. By construction, we fix two of the three free parameters in the fit by requiring that in the test-particle limit $K(\nu)$ reproduces the ISCO shift of Refs. [191, 215, 381] and that the optimal equal-mass value $K(0.25)$ is recovered exactly. Even with these two constraints and just one free parameter to fit, the residuals are within 1% (see Fig. 7.2). We find

$$K(\nu) = 1.447 - 1.715\,\nu - 3.246\,\nu^2\,. \tag{7.43}$$

Finally, since the iterative procedure to compute the NQC coefficients through

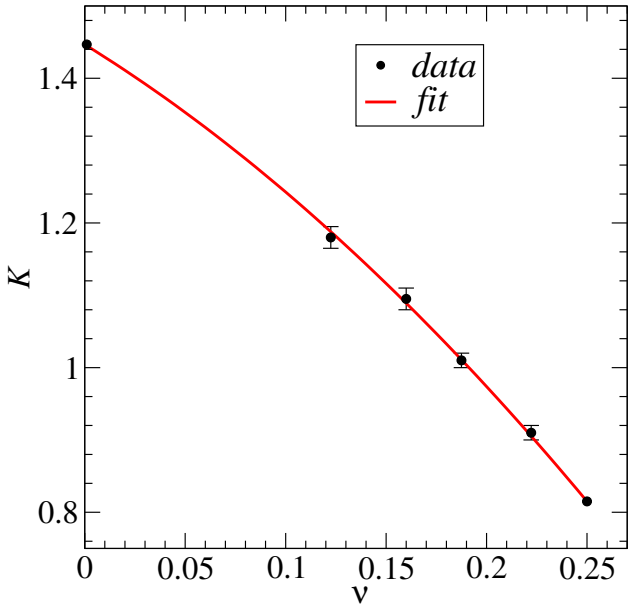

Figure 7.2: We show the quadratic fit in ν for the adjustable parameter K. This parameter is calibrated using the five nonspinning NR waveforms, assuming $\rho^{(4)}_{22}(\nu)$ in Eq. (7.42). The error bars are determined by the intersection of the contours of $\Delta\phi_{\rm global} = 0.1$ rads with $\rho^{(4)}_{22}(\nu)$ for each mass ratio considered.

Eqs. (7.26)–(7.30) can be expensive, we have parametrized them through quadratic fits, finding rather small residuals. Explicitly, we obtain

$$a_1^{h_{22}} = -12.68 + 75.42\,\nu - 106.6\,\nu^2, \tag{7.44}$$

$$a_2^{h_{22}} = 101.5 - 757.3\,\nu + 1473\,\nu^2, \tag{7.45}$$

$$a_3^{h_{22}} = -107.7 + 857.6\,\nu - 1776\,\nu^2, \tag{7.46}$$

$$b_1^{h_{22}} = -1.464 + 12.82\,\nu - 60.10\,\nu^2, \tag{7.47}$$

$$b_2^{h_{22}} = 7.477 - 85.26\,\nu + 353.3\,\nu^2. \tag{7.48}$$

7.3.2.2 Calibrating spinning waveforms

When calibrating the EOB inspiral-plunge waveforms to the two NR equal-mass, equal-spin waveforms at our disposal ($\chi_1 = \chi_2 = +0.43655$ and $\chi_1 = \chi_2 = -0.43757$), we use the nonspinning EOB adjustable parameters K and $\rho_{22}^{(4)}$ in Eqs. (7.43)-(7.42), and calibrate the spinning EOB adjustable parameters $d_{\rm SO}$ and $d_{\rm SS}$. We reach this goal by building contour plots in the plane $d_{\rm SO}$–$d_{\rm SS}$ for $\Delta\phi_{\rm global}$ in Eq. (7.34) with $t_3 = t^{22}_{\rm match}$. We find that the contours of $\Delta\phi_{\rm global} = 0.2$ rads associated with the two NR spinning waveforms intersect each other for the following choice of the adjustable parameters

$$d_{\rm SO} = -69.5\,, \qquad d_{\rm SS} = 2.75\,. \tag{7.49}$$

Note that when computing the spinning NQC coefficients, we use the NQC coefficients parametrized in Eq. (7.44), and solve iteratively the five conditions (7.26)–

$f^{\rm NR}$	Curve	Fit
$\lvert h^{\rm NR}_{22,\rm peak}\rvert$	$(\nu=0,\chi)$	0
	$(\nu=1/4,\chi)$	0.3961
$M^2\partial_t^2\lvert h^{\rm NR}_{22,\rm peak}\rvert$	$(\nu=0,\chi)$	0
	$(\nu=1/4,\chi)$	$10^{-3}\times(-1.007+0.5415\chi)$
$M\omega^{\rm NR}_{22,\rm peak}$	$(\nu=0,\chi)$	$0.2758-0.08898\log(1-\chi)$
	$(\nu=1/4,\chi)$	$0.3604+0.08242\chi+0.02794\chi^2$
$M^2\dot{\omega}^{\rm NR}_{22,\rm peak}$	$(\nu=0,\chi)$	$10^{-3}\times[5.953+(0.7199+1.210\chi)\log(1-\chi)]$
	$(\nu=1/4,\chi)$	0.01113

Table 7.4: Fits of the NR-input values $f^{\rm NR}$ that are used to build the global fits in Eq. (7.52) for the test-particle and equal-mass limits.

(7.30) for $a_i^{h_{22}}$ $(i=3,4,5)$ and $b_i^{h_{22}}$ $(i=3,4)$.[7]

7.4 A prototype effective-one-body model for non-precessing spinning waveforms

We now build on the results of Sec. 7.3, and also on recent outcomes of small-mass-ratio simulations produced by the Teukolsky equation [119], to construct a self-contained set of prescriptions to generate EOB inspiral-merger-ringdown waveforms in a larger region of the parameter space (ν,χ_1,χ_2) of the binary.

[7]Note that the NQC coefficient $a_3^{h_{22}}$ is solved for twice, first in the nonspinning calibration and then in the spinning one.

7.4.1 Interpolating the EOB model outside the domain of calibration

Since we only have seven NR waveforms at our disposal (and just two of them with spins), when extending the EOB model to regions of the parameter space without NR waveforms, we are forced to make assumptions on the behavior of the adjustable parameter $\Delta t^{22}_{\rm peak}$ and the NR-input values in Table 7.1. In this work we assume that the 3 dimensional space (ν, χ_1, χ_2) can be treated as the 2 dimensional space (ν, χ). [Note that $\nu \in [0, 1/4]$ and $\chi \in [-1, 1]$.] More specifically, given a binary described by the parameters (ν, χ_1, χ_2) having in general $\chi_1 \neq \chi_2$, we consider an auxiliary equal-spin binary with parameters (ν, χ, χ), where χ is defined as in Eq. (7.37). With this choice, the auxiliary binary has the same value of $\chi_{\rm Kerr}$ as the original binary. We stress that the auxiliary binary is used only to extend the EOB adjustable parameters and the NR-input values to regions of the parameter space in which we do not have NR results. Of course the EOB dynamics and waveforms are computed for the original binary, not the auxiliary one.

Thus, in the prototype EOB model, the EOB adjustable parameter $\Delta t^{22}_{\rm peak}$ in Eq. (7.38) is evaluated using for χ the value from Eq. (7.37). To compute the spinning NQC coefficients in the prototype model, we need to prescribe the input values in the right-hand side of Eqs. (7.27)–(7.30) using the parameters of the auxiliary binary. We proceed as follows. We only have knowledge of the NR-input values at merger for a few regions of the (ν, χ) parameter space. We can obtain the NR-input values along the curve $(\nu = 0, \chi)$ from the Teukolsky waveforms of Ref. [119]. In particular, both $|h^{\rm NR}_{22,\rm peak}|$ and $\partial^2_t |h^{\rm NR}_{22,\rm peak}|$ are set to 0 (since they are proportional

to ν), while for $\omega^{\rm NR}_{22,\rm peak}$ and $\dot{\omega}^{\rm NR}_{22,\rm peak}$ we use the data in Table V of Ref. [119]. We can extract the peak information along the curve $(\nu = 1/4, \chi)$ from the three equal-mass waveforms used in the calibration of this paper, together with the two nearly extremal spin cases $\chi_1 = \chi_2 = -0.94905$ and $\chi_1 = \chi_2 = +0.9695$ (not used for the calibration of the adjustable parameters $d_{\rm SO}$ and $d_{\rm SS}$), which we will discuss in Sec. 7.4.4. Along the curve $(\nu, \chi = 0)$ we can use the NR-input values of the nonspinning waveforms from Refs. [91, 119]. In Table 7.4 we list the fits for each NR-input value $f^{\rm NR} \in \{|h^{\rm NR}_{22,\rm peak}|, \partial_t^2 |h^{\rm NR}_{22,\rm peak}|, \omega^{\rm NR}_{22,\rm peak}, \dot{\omega}^{\rm NR}_{22,\rm peak}\}$ in the test-particle and equal mass limits. Along the nonspinning profile, fits quadratic in ν give a good description of the exact NR-input values, hence we assume that the dependence of $f^{\rm NR}$ on ν is quadratic as well and has the simple form

$$f^{\rm NR}(\nu, \chi) = c_2(\chi)\, \nu^2 + c_1(\chi)\, \nu + c_0(\chi)\,. \tag{7.50}$$

We can fix two of the coefficients c_i by imposing that the test-particle limit and equal-mass cases are exactly recovered when $\nu = 0$ and $\nu = 1/4$, respectively. We can fit the third coefficient to the exact NR-input values along the nonspinning direction. This means that the fits along the nonspinning profile are not exactly recovered by the global fits $f^{\rm NR}(\nu, \chi)$, but we find that the residuals are negligible. Explicitly, we fit c_1 in the following expression

$$f^{\rm NR}(\nu, 0; c_1) = \{16[f^{\rm NR}(1/4, 0) - f^{\rm NR}(0, 0)] - 4c_1\}\, \nu^2 + c_1 \nu + f^{\rm NR}(0, 0)\,, \tag{7.51}$$

and denote the fitted value with $\bar{c}_1$. Finally, we extend the result outside the nonspinning profile assuming that the global fit reads

$$f^{\rm NR}(\nu, \chi) = \{16[f^{\rm NR}(1/4, \chi) - f^{\rm NR}(0, \chi)] - 4\bar{c}_1\}\, \nu^2 + \bar{c}_1 \nu + f^{\rm NR}(0, \chi)\,. \tag{7.52}$$

	$\lvert h^{\rm NR}_{22,\rm peak}\rvert$	$M^2\partial_t^2\lvert h^{\rm NR}_{22,\rm peak}\rvert$	$M\omega^{\rm NR}_{22,\rm peak}$	$M^2\dot{\omega}^{\rm NR}_{22,\rm peak}$
$\bar{c}_1$	1.355	-2.5×10^{-3}	0.1935	0.01204

Table 7.5: Fitted values of $\bar{c}_1$ for the four NR-input values as defined in Eq. (7.52).

In Table 7.5 we list the values of $\bar{c}_1$ for the four NR-input values that are needed to compute the right-hand sides in Eqs. (7.27)–(7.30).

Having in hand $\Delta t^{22}_{\rm peak}$ and the NR-input values, we complete the construction of the prototype EOB model by fixing the EOB adjustable parameters K, $\rho^{(4)}_{22}$, and $d_{\rm SO}$, $d_{\rm SS}$ to the values in Eqs. (7.43)-(7.42) and (7.49), respectively, employing the pQNM (complex) frequency in Eq. (7.40), the comb size in Eq. (7.39), and the NQC coefficients in Eqs. (7.44).

To test the robustness of the construction of the quantity $f^{\rm NR}(\nu,\chi)$, we study how the spinning NQC coefficients change across the plane (ν,χ). We focus on binaries with $\chi_1=\chi_2=\chi$. We compute iteratively the NQC amplitude coefficients $a_i^{h_{22}}$ (with $i=3,4,5$) for different mass ratios in the range $1/100\leq q\leq 1$ and for different spins in the range $-1\leq\chi_i\lesssim 0.7$ $(i=1,2)$. Typically, we get convergence of the NQC coefficients within five iterations. Unfortunately, we cannot span larger, positive values of χ_i since the NQC corrections tend to diverge as the spin magnitude grows in the prograde case. The reason is that they become less effective in reshaping the EOB (2,2) peak as prescribed by the fits $f^{\rm NR}(\nu,\chi)$. This happens because the peak of the EOB (2,2) mode occurs too early in the evolution when the orbital motion is still quasicircular. Hence the NQC coefficients must be very large to

compensate for the small values of $p_{r^*}/(r\hat{\Omega})$ and be able to reshape the EOB (2,2) amplitude around the peak in a satisfactory way. As discussed earlier, this would not be a problem in principle if higher-order spin-orbit terms were known in the factorized waveforms, but, as a result of the lack of knowledge of those, our EOB prototype waveforms are reliable only up to $\chi_i \lesssim 0.7$.

7.4.2 Performance for nonspinning waveforms

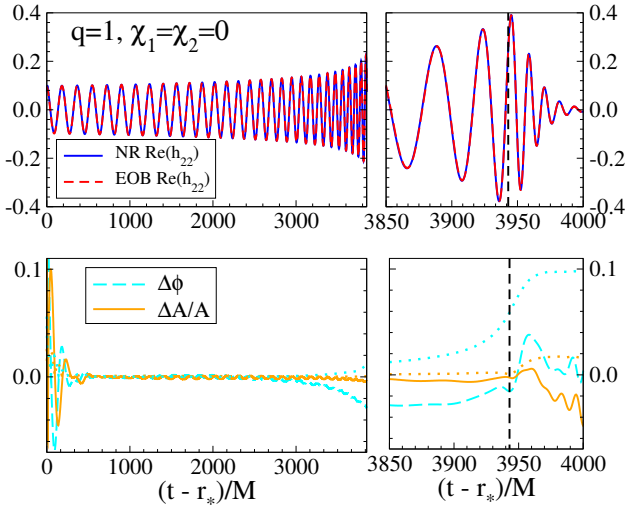

Figure 7.3: Comparison of the NR and EOB (2, 2) mode for $q = 1$, $\chi_1 = \chi_2 = 0$. In the upper panels we show the comparison between the real part of the two waveforms, zooming into the merger region in the upper right plot. In the lower panels we show the dephasing and relative amplitude difference over the same time ranges as the upper panels. A vertical dashed line marks the position of the NR amplitude peak. The dotted curves are the NR errors.

In Figs. 7.3 and 7.4 we show how the inspiral-merger-ringdown EOB waveforms computed according to the prescriptions of Sec. 7.4.1 compare with the NR waveforms for two representative mass ratios $q = 1, 1/6$. In general, for all the non-

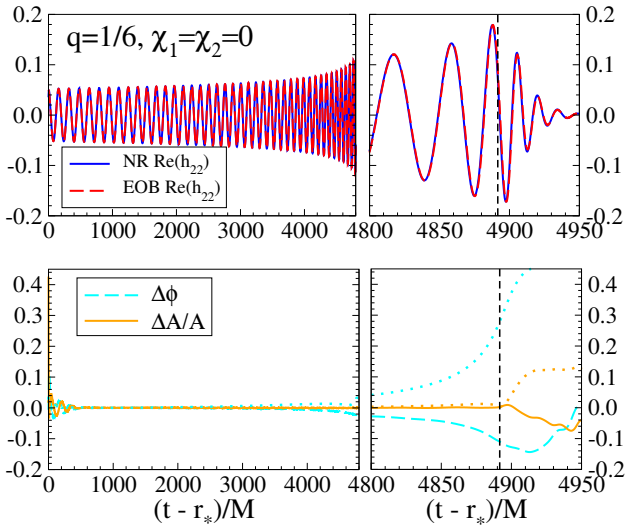

Figure 7.4: Same as in Fig. 7.3 but for $q = 1/6$, $\chi_1 = \chi_2 = 0$.

spinning waveforms we find that the dephasing is typically within 0.1 rads up until $t^{22}_{\rm match}$ (merger time) and always within 0.2 rads when including the ringdown stage. The figures also show in dotted lines the NR phase and amplitude errors obtained by combining the extrapolation and resolution errors in quadrature. We notice that the EOB and NR amplitudes' agreement is remarkably good up to the merger time, while during the ringdown the relative amplitude difference may grow up to about 15%, approaching the estimated NR error.

In Ref. [91] the authors calibrated a different version of the nonspinning EOB model to the same set of nonspinning NR waveforms used in this paper, the main difference between the two EOB models being the choice of the EOB potential $A(r)$, as we discussed in Sec. 11.3.1. We find that the difference between the EOB inspiral-merger-ringdown waveforms and the NR waveforms in Ref. [91] is comparable to and for some mass ratios marginally worse than what we have achieved in this work

using the prototype EOB model. The only noticeable qualitative difference is that the phase error of the prototype EOB model accumulates more slowly during the merger-ringdown transition because of the introduction of the pQNM in the $(2,2)$ mode. We point out that the inclusion of the pQNM (complex) frequency in the EOB merger-ringdown waveform is not strictly needed for the nonspinning case, but we use it even in this case for uniformity with the spinning sector, where the pQNM frequency is instead crucial.

We can quantify the differences between NR and EOB waveforms by computing the mismatch ($\mathcal{M}$), as defined in Eq. (43) of Ref. [91], which is one minus the overlap between two waveforms, weighted by the noise spectral density of the detector and maximized over the initial time, phase and binary parameters. If we use an Advanced LIGO noise curve, named `ZERO_DET_HIGH_P` in Ref. [4], we obtain that the $\mathcal{M}$, maximizing only over the initial phase and time, is always smaller than 0.001 when the binary total mass varies between $20M_{\odot}$ and $200M_{\odot}$. For these total masses, the NR waveforms start in band. We taper them using the Planck-taper window function [382] to reduce numerical artifacts. The width of the window function is set to the length of NR waveforms, ranging from $0.35(M/20M_{\odot})$ to $0.65(M/20M_{\odot})$ seconds. The window function smoothly rises from 0 to 1 in the first 0.0625 seconds and falls from 1 to 0 in the last 0.0125 seconds. We restrict the $\mathcal{M}$ integration to the frequency band for which NR waveform is available.

7.4.3 Performance for spinning waveforms

In Figs. 7.5 and 7.6 we present the results of the prototype EOB model for the two moderately spinning waveforms at our disposal. We observe that the choice (7.49) gives a larger dephasing for $\chi_1 = \chi_2 = +0.43655$ than for $\chi_1 = \chi_2 = -0.43757$ or the nonspinning runs. In fact at the merger time the dephasing for the $\chi_1 = \chi_2 = +0.43655$ waveform grows beyond the NR error. For the amplitude, we instead get a similar performance, on the same level as the other runs. The worse performance of the $\chi_1 = \chi_2 = +0.43655$ waveform can be explained by the more relativistic nature of this run. In fact, in this case the EOB ISCO moves to smaller radial separations as the spin parameter χ increases towards positive values (aligned runs). On the other hand, for negative values of χ (anti-aligned runs) the EOB ISCO moves outwards to a less relativistic regime and one expects a better behavior of the EOB model. This expectation is confirmed by the calibration of the $\chi_1 = \chi_2 = -0.43757$ run, for which we find that very good performances can be achieved in large regions of the EOB adjustable parameter space. Fig. 7.5 shows that in this case the dephasing is well within the NR error at the merger time. For these spinning waveforms, we obtain that the $\mathcal{M}$, maximizing only over the initial phase and time, is always smaller than 0.003 when the binary total mass varies between $20M_\odot$ and $200M_\odot$.

7.4.4 Performance for nearly extremal spin waveforms

Here we compare the EOB waveforms of the prototype model developed in Sec. 7.4.1, against two equal-mass NR waveforms with nearly extremal spins: $\chi_1 =$

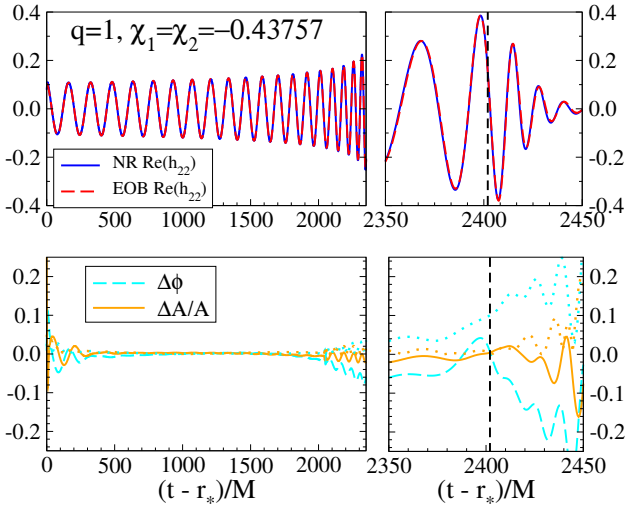

Figure 7.5: Same as in Fig. 7.3 but for $q = 1$, $\chi_1 = \chi_2 = -0.43655$.

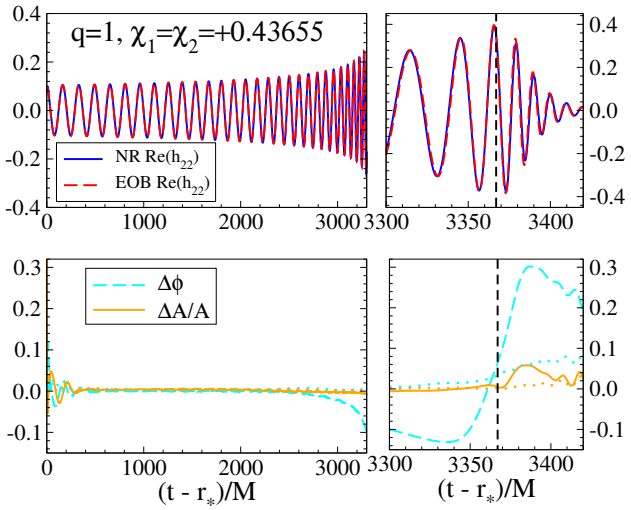

Figure 7.6: Same as in Fig. 7.3 but for $q = 1$, $\chi_1 = \chi_2 = +0.43756$.

$\chi_2 = -0.94905$ and $\chi_1 = \chi_2 = +0.9695$ [307, 362]. We stress that these NR waveforms were not used when calibrating the spin EOB adjustable parameters $d_{\rm SO}$ and $d_{\rm SS}$ in Eq. (7.49). The only information that we used from these two nearly extremal spin waveforms was their NR-input values when building the fits $f^{\rm NR}(\nu, \chi)$.

As already discussed, when the spins are anti-aligned, the EOB ISCO moves towards larger radial separations, so that the binary is less relativistic throughout its orbital evolution as compared to the aligned configurations. Therefore, we expect that in this case the EOB model is more effective. The results in Fig. 7.7 for the case $\chi_1 = \chi_2 = -0.94905$ confirm this expectation. The dephasing grows up to about 2 rads during the ringdown, while the relative amplitude difference grows up to about 40%. Despite the large phase difference at merger, we find that, even without maximizing over the binary parameters but only the initial phase and time, the $\mathcal{M}$ is always smaller than 0.005 for systems with total mass between $20M_\odot$ and $200M_\odot$.

For the case $\chi_1 = \chi_2 = +0.9695$, which is outside the domain of validity of our prototype EOB model, we cannot successfully run the NQC iterations, since the NQC corrections are so large that they cause a divergent sequence of NQC coefficients. Nonetheless, we deem it interesting to generate the EOB inspiral-plunge waveform where only the nonspinning NQC coefficients $a_i^{h_{22}}$ $(i = 1, 2, 3)$ and $b_i^{h_{22}}$ $(i = 1, 2)$ are used and compare it to the NR waveform. In Fig. 7.8 we show how our waveform performs. We notice that the NR waveform is very long, almost 50 GW cycles. The phase difference between the EOB and NR waveforms is smaller than 0.04 rads over the first 20 GW cycles, and then grows up to 0.18 rads during the subsequent 10 GW cycles and it becomes 0.9 rads when 10 GW cycles are left before merger. The fractional amplitude difference is only 3% when 10 GW cycles are left before merger.

It is worth emphasizing that although our prototype model is not yet able

to generate merger-ringdown waveforms for spins larger than +0.7, nevertheless, as the comparison with the nearly extremal case $\chi_1 = \chi_2 = +0.9695$ has proven, the Hamiltonian of Refs. [191, 192] and the resummed flux of Refs. [100, 101] can evolve the EOB dynamics in this highly relativistic case beyond the orbital-frequency's peak, until $r \approx 1.9M$, without encountering unphysical features. This suggests that relevant strong-field effects are well grasped by the EOB dynamics and waveforms [100, 101, 191, 192], at least as far as the NR runs used in this paper are concerned. Moreover, the large amplitude difference causing the NQC iteration to break down for large, positive spins was already observed in Refs. [101, 119] where it was pointed out that it is important to improve the modeling of spin effects in the EOB waveform amplitude. Finally, as observed above, the breaking down of the NQC procedure in this highly relativistic case, although not a problem in principle if higher-order spin-orbit terms were known in the factorized waveforms, is due to the fact that the peak of the EOB (2,2) mode occurs too early in the orbital evolution where non-quasicircular orbit effects are still negligible.

7.5 Conclusions

Using the EOB spin Hamiltonian in Refs. [191, 192], the factorized waveforms in Refs. [100, 101], and the adjustable parameters in Table 7.2, we have developed a prototype EOB model for non-precessing spinning black-hole binaries that can be used for detection purposes in LIGO and Virgo searches and employed for future calibrations [383]. The prototype model is built by first calibrating the

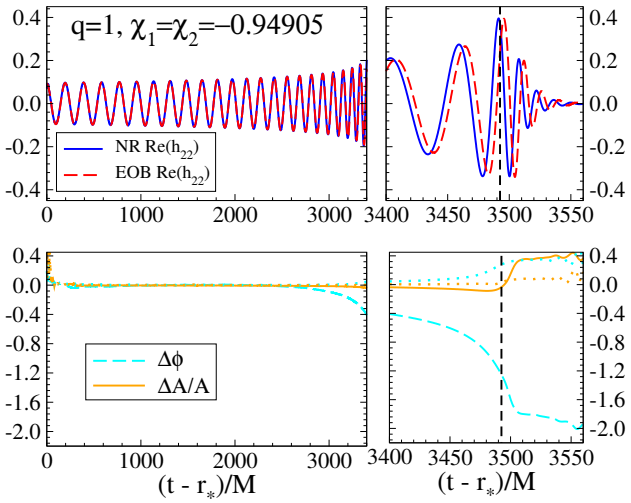

Figure 7.7: Same as in Fig. 7.3 but for $q = 1$, $\chi_1 = \chi_2 = -0.94905$. This NR waveform was *not* used to calibrate the adjustable parameters $d_{\rm SO}$ and $d_{\rm SS}$. Alignment between the NR and EOB waveforms was performed using Eq. (7.31), with $t_1 = 860\,M$ and $t_2 = 2470\,M$.

EOB adjustable parameters against five nonspinning waveforms with mass ratios $q = 1, 1/2, 1/3, 1/4, 1/6$ and two equal-mass, equal-spin NR waveforms with moderate spins. Then, those results, at the interface with NR, are combined with recent results at the interface with black-hole perturbation theory [119]. The resulting prototype EOB model interpolates between calibrated points in the binary parameter space, and generates inspiral-merger-ringdown waveforms with any mass ratio and individual spin magnitudes $-1 \leq \chi_i \lesssim 0.7$. This EOB model has been implemented in the freely available LIGO Algorithm Library (LAL) [384] with the model name "SEOBNRv1".[8]

We found that the EOB waveforms generated with the prototype model agree

[8]Two nonspinning EOB models are also available in LAL, "EOBNRv1" and "EOBNRv2", which were calibrated to NR waveforms in Refs. [91, 283].

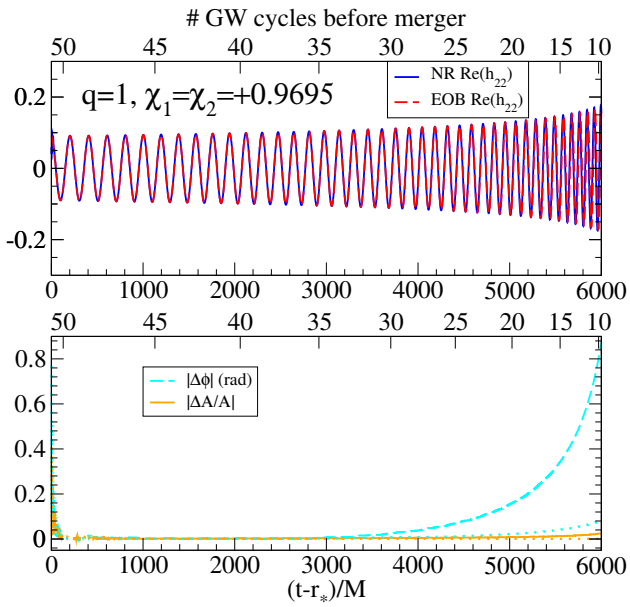

Figure 7.8: Same as in Fig. 7.3 but for $q = 1$, $\chi_1 = \chi_2 = +0.9695$ and only the inspiral portion. This NR waveform was *not* used to calibrate the adjustable parameters $d_{\rm SO}$ and $d_{\rm SS}$. Also, in the aligned case our prototype EOB model only covers $\chi_{1,2} \lesssim 0.7$. Note that in this plot we do not include spinning NQC corrections in our EOB waveform. Alignment between the NR and EOB waveforms was performed using Eq. (7.31), with $t_1 = 1170\,M$ and $t_2 = 2790\,M$.

with the NR waveforms used to calibrate them within ~ 0.1 rads at merger for the nonspinning sector, and within ~ 0.15 rads at merger for the spinning sector. In terms of amplitude differences at merger, both nonspinning and spinning runs agree to within 5%. The $\mathcal{M}$s for Advanced LIGO computed by maximizing only with respect to the initial phase and time are always smaller than 0.003 for binaries with total masses between $20M_\odot$ and $200M_\odot$.

We also compared the prototype EOB model to two equal-mass, equal-spin NR waveforms of black holes with nearly extremal spins, notably $\chi_i = -0.94905, +0.9695$. Those NR waveforms were not part of the original set of waveforms used to cali-

brate the EOB model. We found that for the anti-aligned case the prototype EOB model performs quite well for detection purposes, with $\mathcal{M}$s smaller than 0.003 without maximizing over the binary parameters, but only on initial phase and time. In the aligned case, which is highly relativistic due to a spin as large as +0.9695 (outside the range of validity of our prototype model), we compared the inspiral-plunge waveform for 40 GW cycles and found a dephasing of ~ 0.8 rad. During the last 10 GW cycles before merger the dephasing grows up to several radians. This non-satisfactory performance during plunge and merger for large, positive spins is not surprising. In our prototype spin EOB model the factorized modes [101] used in the radiation-reaction force generate spin couplings in the GW energy flux at a PN order much lower than what is known today. In fact, the GW energy flux is currently known through 3PN order in the spin-orbit sector[9] [360] and 2PN order in the spin-spin sector. However, the -2 spin-weighted spherical harmonics that are used to build the factorized waveforms employed in this paper are known only through 1.5PN order in the spin-orbit sector [361]. Moreover, the performance we found for large spin values and prograde orbits confirms what was already found in Ref. [119], where EOB waveforms in the test-particle limit could be calibrated to Teukolsky-type waveforms only up to a Kerr spin value of $\sim +0.7$. For larger spin values, the factorized waveforms start deviating from the exact ones even before reaching the ISCO [101, 119].

The prototype spin EOB model can be improved in the future in different

[9]Reference [362] found that the tail spin-orbit terms in the energy flux at 3PN order dominate all the other spin-orbit contributions and improve the agreement with NR waveforms.

directions. First, the choice of the spin EOB adjustable parameters done in Sec. 7.2 was rather arbitrary and assumed that all gauge parameters that enter the spin EOB conservative dynamics are zero. Of course, it would have been difficult to carry out a more sophisticated study in this work considering that we had at our disposal only two equal-mass, equal-spin NR waveforms. When several more spin NR waveforms will be available, the spin EOB parameters (together with the nonspinning ones) should be explored and calibrated simultaneously against all the available NR waveforms. Second, it is urgent to compute higher-order PN spin-orbit terms in the -2 spin weighted spherical harmonics and in the factorized modes, thus making the EOB spin model reliable also for large, positive spins, i.e., for $\chi_i > 0.7$. Third, the spin EOB Hamiltonian at 3.5PN order used in this paper predicts for large, positive spins that the position of the peak of the EOB orbital-frequency varies non-monotonically as function of the spin and lies in a region which is not very relativistic. It would be important to correct this behavior calibrating the gauge parameters present in the spin EOB Hamiltonian. Fourth, recent results in Refs. [90, 217, 381, 385] at the interface between PN theory and the self-force formalism, have allowed Ref. [386] to compute the nonspinning EOB potentials at all orders in PN theory, but linear in the symmetric mass ratio ν. These new results will be incorporated in the future to improve the nonspinning conservative dynamics of the prototype EOB model, and will be extended to include spin effects.

Chapter 8: **Effective-one-body model for black-hole binaries with generic mass ratios and spins**

Authors: *Andrea Taracchini, Alessandra Buonanno, Yi Pan, Tanja Hinderer, Michael Boyle, Daniel A. Hemberger, Lawrence E. Kidder, Geoffrey Lovelace, Abdul H. Mroué, Harald P. Pfeiffer, Mark A. Scheel, Béla Szilágyi, Nicholas W. Taylor, and Anil Zenginoglu*[1]

Abstract: Gravitational waves emitted by black-hole binary systems have the highest signal-to-noise ratio in LIGO and Virgo detectors when black-hole spins are aligned with the orbital angular momentum and extremal. For such systems, we extend the effective-one-body inspiral-merger-ringdown waveforms to generic mass ratios and spins calibrating them to 38 numerical-relativity nonprecessing waveforms produced by the SXS Collaboration. The numerical-relativity simulations span mass ratios from 1 to 8, spin magnitudes up to 98% of extremality, and last for 40 to 60 gravitational-wave cycles. When the total mass of the binary is between $20M_{\odot}$ and $200M_{\odot}$, the effective-one-body nonprecessing (dominant mode) waveforms have overlap above 99% (using the advanced-LIGO design noise spectral density) with all of the 38 nonprecessing numerical waveforms, when maximizing only on initial phase

[1]Originally published as Phys. Rev. D **89**, 061502 (R) (2014)

and time. This implies a negligible loss in event rate due to modeling. We also show that – without further calibration – the precessing effective-one-body (dominant mode) waveforms have overlap above 97% with two very long, strongly precessing numerical-relativity waveforms, when maximizing only on the initial phase and time.

8.1 Introduction

In the next few years, second-generation ground-based interferometers, such as advanced LIGO [4], advanced Virgo [5] and KAGRA [6], will start to collect data with unprecedented sensitivity, making the long-sought detection of gravitational waves (GWs) a realistic prospect. Coalescing binaries of compact objects are among the most promising astrophysical sources in the accessible frequency band of such experiments. The search for GWs from these sources exploits the matched-filtering technique, in which the noisy output of the interferometer is correlated with a bank of template waveforms describing all expected signals. An accurate knowledge of the gravitational radiation is thus crucial for maximizing the chances of detection. However, matched-filtering not only requires templates that are accurate, but their generation must also be sufficiently cheap that they cover the entire physical parameter space. While in principle the most precise waveforms are obtained by solving Einstein's equations in numerical relativity (NR), their considerable computational cost makes it necessary to resort to analytical models that meet both criteria of accuracy and computational efficiency.

A unified analytical description of the entire compact binary coalescence, from

the quasicircular inspiral, through the merger, and to the ringdown of the remnant, is achieved by the effective-one-body (EOB) model [61, 62]. In the EOB approach, one replaces the *real* problem of two compact objects of mass m_i, spin $\boldsymbol{S}_i$ $(i = 1, 2)$ and mass ratio q orbiting each other with the *effective* problem of an extreme mass-ratio binary, where the more massive object is a deformed-Kerr black hole (BH) and the small object is an effective spinning particle. The deformation parameter of the Kerr metric is the symmetric mass ratio $\nu \equiv q/(1+q)^2$. The EOB model incorporates results from post-Newtonian (PN) theory (in resummed form), BH perturbation theory, and more recently also from the gravitational self-force formalism. A mapping between the physical parameters of the two problems is established by requiring that the effective dynamics is equivalent (when PN-expanded in powers of $1/c^2$) to the original, PN-expanded dynamics. Thus, solving exactly the effective problem of a spinning particle in the deformed-Kerr geometry amounts to introducing a particular *non-perturbative* method for resumming the PN-expanded equations of motion.

The accuracy of the EOB waveforms has recently been improved by including in the EOB dynamics higher-order (yet unknown) PN terms and calibrating them to NR simulations, which have progressively grown in number, length and accuracy. State-of-the-art calibrations of these *adjustable* parameters in the nonspinning sector (including also higher harmonics) can be found in Refs. [91, 93, 236]. An EOB model for spinning, nonprecessing BH binaries was calibrated to 5 nonspinning and only 2 spinning, nonprecessing NR simulations in Ref. [93][2]; it can generate dominant (2,2)

[2]The EOB models of Refs. [91, 93, 283] have been implemented in the LIGO Algorithm Li-

mode waveforms for any mass ratio, but only for BH spin magnitudes up to 0.6. Moreover, the EOB model in Ref. [93] was compared and validated against a large set of new NR simulations of nonprecessing BHs produced by several groups within the numerical-relativity and analytical-relativity (NRAR) Collaboration [66]. Recently, Ref. [194] provided a general procedure to generate EOB waveforms for spinning, precessing BH binaries starting from a generic spinning, nonprecessing EOB model; when using the EOB model in Ref. [93] as the underlying nonprecessing model, the authors found remarkable agreement with two precessing NR simulations. Finally, the conservative dynamics of the EOB model has also been tested and validated through the study of the periastron advance in BH binaries [88, 92].

In this work, we calibrate the nonprecessing sector of a generic spinning EOB model to the (2,2) mode of a catalog of highly-accurate NR simulations produced by the SXS Collaboration [67, 162, 253, 254]. They include 8 nonspinning and 30 spinning, nonprecessing BH binaries with spins up to 98% of extremality, they cover mass ratios up to 8, and have orbital eccentricities in the range of a few percent down to 10^{-5}. The simulations follow more orbits on average (up to 35.5), allowing a more reliable calibration of analytical waveforms.

8.2 Effective-one-body model

In what follows we set $G = c = 1$. Let $\hat{\boldsymbol{L}}$ be the direction perpendicular to the binary's instantaneous orbital plane, and let us define the dimensionless

brary under the names `EOBNRv1`, `EOBNRv2` and `SEOBNRv1`, respectively, and have been used in GW searches [387].

projections of the spins along $\hat{\boldsymbol{L}}$ as $\chi_i \equiv (\boldsymbol{S}_i \cdot \hat{\boldsymbol{L}})/m_i^2$. We assume $m_1 \geq m_2$, hence $q \equiv m_1/m_2 \geq 1$. In the spinning EOB formalism of Ref. [192], the effective Hamiltonian $H_{\rm eff}$ is that of a particle of mass $\mu \equiv m_1 m_2/(m_1+m_2)$ and effective spin $\boldsymbol{S}^* \equiv \boldsymbol{S}^*(\boldsymbol{S}_1, \boldsymbol{S}_2)$ moving in a deformed-Kerr geometry of mass $M \equiv m_1 + m_2$ and spin $\boldsymbol{S}_{\rm Kerr} \equiv \boldsymbol{S}_1 + \boldsymbol{S}_2$; the conservative orbital dynamics is then derived via Hamilton's equations using the real EOB-resummed Hamiltonian

$$H_{\rm real} = M \sqrt{1 + 2\nu \left(\frac{H_{\rm eff}}{\mu} - 1 \right)} - M \,. \tag{8.1}$$

We use here the same EOB Hamiltonian as in Ref. [93], but augment the deformed-Kerr metric potential Δ_u with 4PN nonspinning terms to obtain [192]

$$\Delta_u(u) \;\; = \;\; \bar{\Delta}_u(u) \left[1 + \nu\, \Delta_0 + \nu \, \log\left(1 + \sum_{i=1}^{5} \Delta_i u^i \right) \right] , \tag{8.2}$$

where $u \equiv 1/r$ and r is the EOB radial coordinate in units of M. Here,

$$\bar{\Delta}_u(u) = \chi^2_{\rm Kerr} \left(u - \frac{1}{r_+^{\rm EOB}} \right) \left(u - \frac{1}{r_-^{\rm EOB}} \right) , \tag{8.3}$$

$$r_\pm^{\rm EOB} = \left[1 \pm \left(1 - \chi^2_{\rm Kerr} \right)^{1/2} \right] \left(1 - K\, \nu \right) , \tag{8.4}$$

with $\chi_{\rm Kerr} \equiv (\boldsymbol{S}_{\rm Kerr} \cdot \hat{\boldsymbol{L}})/M^2$; the coefficients $\Delta_0, \ldots, \Delta_5$ are determined by requiring that Δ_u agrees with the Taylor-expanded EOB potential $A(r)$ [386, 388] up to 4PN order. By construction, $r_\pm^{\rm EOB}$ reproduce the Kerr horizons when $\nu = 0$. Similarly to what was done in Ref. [93], we exploit K as an adjustable parameter, i.e., a parameter that we calibrate to NR waveforms. For the identification between the effective particle's spin $\boldsymbol{S}^*$ and the spins $\boldsymbol{S}_i$ we use the 3.5PN-accurate spin mapping of Ref. [192], with all the arbitrary gauge parameters set to zero and with the

addition of a 4.5PN spin-orbit term of the form $(d_{\rm SO}\nu \boldsymbol{S}_{\rm Kerr})/r^3$, where $d_{\rm SO}$ is an adjustable parameter. The EOB description of conservative spin effects is completed by adding a 3PN spin-spin term of the form $d_{\rm SS}\nu(\boldsymbol{S}_1^2+\boldsymbol{S}_2^2)/r^4$ to $H_{\rm eff}/\mu$, where $d_{\rm SS}$ is another adjustable parameter.

The adjustable parameters are chosen to be polynomials in ν whose coefficients are determined by minimizing the phase and relative amplitude difference between EOB and NR waveforms (defined as in Eqs. (29)-(30) of Ref. [93]) via the numerical simplex method for each mass ratio. First, we calibrate the nonspinning sector and find $K = 1.712 - 1.804\nu - 39.77\nu^2 + 103.2\nu^3$, where the ν-independent term is consistent with the frequency shift of the innermost stable circular orbit (ISCO) due to conservative self-force effects in the small-mass-ratio limit [195]. Next, we calibrate the spin parameters and obtain $d_{\rm SO} = -74.71 - 156.0\nu + 627.5\nu^2$ and $d_{\rm SS} = 8.127 - 154.2\nu + 830.8\nu^2$.

Dissipative effects are modeled by supplementing Hamilton's equations with a radiation-reaction force which is a sum over (time derivatives of) the -2-spin-weighted spherical modes at infinity. In our model, these modes are written as a factorized resummation of the PN waveforms [100, 101]

$$h^{\rm F}_{\ell m} = h^{(N,\epsilon)}_{\ell m}\, \hat{S}^{(\epsilon)}_{\rm eff}\, T_{\ell m}\, e^{i\delta_{\ell m}}\, (\rho_{\ell m})^{\ell} \tag{8.5}$$

(see Ref. [93] for the definition of the individual factors). In particular, here we also include comparable-mass spin-orbit and spin-spin effects up to 2PN order, using the most recent PN-waveform calculations in Ref. [159]. We use the $\rho_{\ell m}$-factorization in Eq. (11.4) for all modes except those with $\ell \leq 4$ and odd m, which instead

follow the prescription of Ref. [93] (see the discussion above Eq. (A8a) therein). In addition, we also include all the known spin effects from the test-particle limit given in Ref. [101], by replacing the Kerr spin parameter a/M with $\chi_{\rm Kerr}$; this helps the modeling of unequal-mass, spinning systems. As such, the mode amplitudes contain no adjustable parameters. In fact, the improved knowledge of the nonspinning sector (i.e., the addition of 4PN terms in Δ_u) allowed us to remove the nonspinning adjustable parameter $\rho_{22}^{(4)}$ which had been introduced in Ref. [93], thus simplifying the nonspinning model. The resulting residuals on the amplitude of the (2,2) mode are within a few percent at merger for $\chi_{1,2} \sim 1$ even without adding non-quasicircular corrections. However, we need to introduce an adjustable parameter in the spin terms of the phase δ_{22} to enhance the EOB GW frequency close to merger with respect to its leading-order value (twice the orbital frequency Ω), which tends to underestimate the NR value for $\partial_t \phi_{22}$ when spins are close to 1. For $\chi_{1,2} = 0.98$, we find that the ISCO is crossed only $10M$ before the light ring crossing, thus greatly reducing the region in which the non-quasicircular corrections (see below) can be effective. Explicitly, if $\chi \geq 0$, we add the 3PN term $540\,\nu\chi(M\Omega)^2$ to δ_{22}, where $\chi \equiv \chi_{\rm S} + \chi_{\rm A}\sqrt{1-4\nu}/(1-2\nu)$, with $\chi_{\rm S,A} \equiv (\chi_1 \pm \chi_2)/2$.

Non-quasicircular (NQC) effects that become important near the merger are included in $h_{22}^{\rm F}$ through a factor N_{22} (see Eq. (18) of Ref. [93]). The NQC coefficients are fixed by requiring that the EOB (2,2) mode agrees with the NR input values for $|h_{22}|$, $\partial_t |h_{22}|$, $\partial_t^2 |h_{22}|$, $\partial_t \phi_{22}$ and $\partial_t^2 \phi_{22}$, evaluated at the peak of $|h_{22}|$. Using the 38 NR nonprecessing waveforms in the SXS catalog and Teukolsky waveforms computed in the small-mass-ratio limit [114], we updated the fitting formulas for the NR input

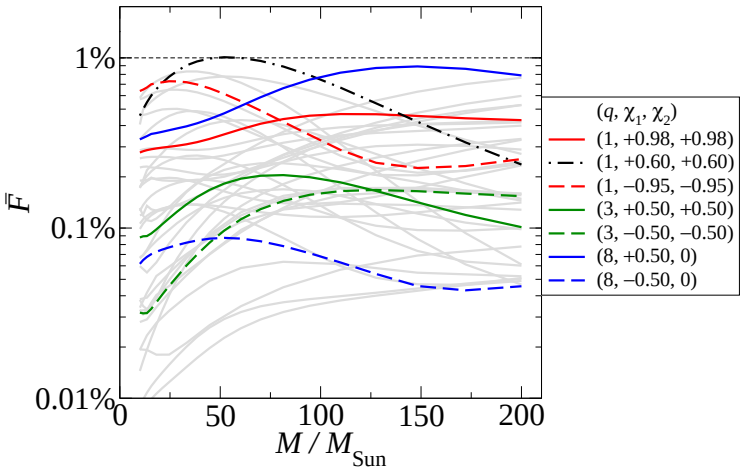

Figure 8.1: Unfaithfulness of (2,2) EOB waveforms for *all* the 38 non-precessing BH binaries in the SXS catalog. Only a few selected cases are labeled in the legend.

values given in Table IV of Ref. [93]. We use these to iteratively compute the NQC coefficients as described in Sect. IIB of Ref. [93]. While previous nonspinning EOB models [283] were calibrated without enforcing any time delay between the peak in the (2,2) amplitude and in the orbital frequency, here, as in Refs. [91,93], we require a lag $\Delta t^{22}_{\rm peak}$ which varies with the physical parameters of the binary. The idea of introducing $\Delta t^{22}_{\rm peak}$ into the model was inspired by studies in the small-mass-ratio limit, where such time delay was first seen with EOB trajectories sourcing Teukolsky waveforms [119] and accurately quantified in Ref. [114]. Finally, the inspiral-plunge waveform is simply defined as $h^{\rm insp-plunge}_{22} \equiv N_{22} h^{\rm F}_{22}$, and $h^{\rm insp-plunge}_{\ell m} \equiv h^{\rm F}_{\ell m}$ when $(\ell, m) \neq (2, 2)$.

As usual, the EOB merger-ringdown (RD) waveform is built as a linear com-

bination of quasi normal-modes (QNMs) of the remnant BH [62]

$$h_{\ell m}^{\rm merger-RD}(t) = \sum_{n=0}^{N-1} A_{\ell mn}\, e^{-i\sigma_{\ell mn}(t-t^{\ell m}_{\rm match})}\,, \tag{8.6}$$

where N is the number of overtones, $t^{\ell m}_{\rm match}$ is the time when $|h_{\ell m}^{\rm insp-plunge}|$ peaks, $A_{\ell mn}$ is the complex amplitude of the n-th overtone of the (ℓ, m) mode, and $\sigma_{\ell mn} = \omega_{\ell mn} - i/\tau_{\ell mn}$ is its complex frequency, having positive (real) frequency $\omega_{\ell mn}$ and decay time $\tau_{\ell mn}$. The frequencies $\sigma_{\ell mn}$ depend on the mass M_f and spin a_f of the final Kerr BH, and are tabulated in Ref. [18]. To predict M_f we use the phenomenological formula proposed by Ref. [389], but we replace its equal-mass limit [Eq. (11) therein] with the highly accurate fit given in Eq. (9) of Ref. [162]. To compute a_f, we start from the formula of Ref. [372] (which also predicts the direction of the final spin for precessing binaries), and use the simulations in the SXS calatog to refit its nonprecessing limit; the main change we introduce are 4 new fitting coefficients designed to improve the equal-mass, high-spin corner of the parameter space, where the prediction of Ref. [372] has residuals exceeding 5%. We improve the stability of the ringdown modeling across the entire parameter space by (i) assuming a monotonic behavior of a_f with decreasing ν for extremal spins, and (ii) replacing some of the higher physical overtones with pseudo-QNMs that depend on the merger frequency, on σ_{220} and on ν, and moderate the rise of the ringdown GW frequency [91, 93].

Finally, the complete inspiral-merger-ringdown waveform is built as the smooth matching of $h_{\ell m}^{\rm insp-plunge}$ to $h_{\ell m}^{\rm merger-RD}$ at $t^{\ell m}_{\rm match}$, over an interval $\Delta t^{\ell m}_{\rm match}$, following the hybrid matching procedure of Ref. [91] to fix the coefficients $A_{\ell mn}$ in Eq. (11.22).

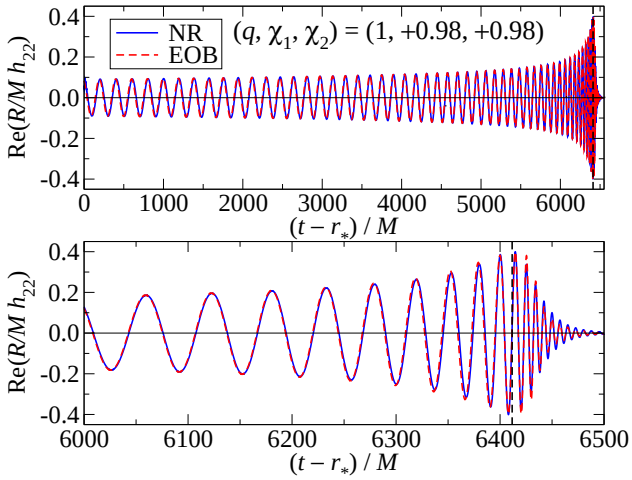

Figure 8.2: NR and EOB (2,2) waveforms of the BH binary with $q = 1$ and $\chi_1 = \chi_2 = 0.98$. The two waveforms are aligned at their amplitude peak (marked by a vertical dashed line). R is the distance to the source and r_* is the tortoise coordinate.

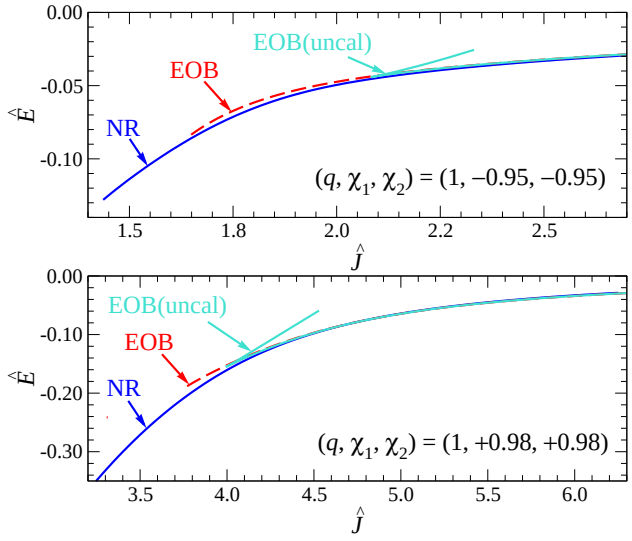

Figure 8.3: The specific binding energy $\hat{E} = E/\mu$ as a function of the dimensionless total angular momentum $\hat{J} = J/(\mu M)$ of the BH binaries with $q = 1$ and $\chi_1 = \chi_2 = -0.95$, 0.98 computed in NR, conservative uncalibrated EOB model and the calibrated EOB model of this paper.

8.3 Results and discussion

The SXS catalog includes 8 nonspinning BH binaries with $q = 1$, 1.5, 2, 3, 4, 5, 6, 8, and 30 spinning, nonprecessing BH binaries with: $q = 1$ and $\chi_1 = \chi_2 = 0.98$, 0.97, ± 0.95, ± 0.9, 0.85, ± 0.8, ± 0.6, ± 0.44, ± 0.2; $q = 1$, 1.5, 3, 5, 8, $\chi_1 = \pm 0.5$ and $\chi_2 = 0$; $q = 1.5$ and $\chi_1 = -\chi_2 = \pm 0.5$; $q = 2$, $\chi_1 = 0.6$ and $\chi_2 = 0$; $q = 3$ and $\chi_1 = \chi_2 = \pm 0.5$. We find that to accurately match all 38 nonprecessing waveforms, it is sufficient to calibrate the EOB model to a much smaller subset of them. However, since our goal is an accurate model for the entire parameter space, most of which is not covered by the NR waveforms, we prefer to exploit all available non-degenerate NR information in the calibration. In Fig. 8.1 we compare the EOB waveforms to *all* the 38 nonprecessing NR waveforms by computing their unfaithfulness

$$\bar{F} \equiv 1 - \max_{t_0,\phi_0} \frac{\langle h_{22}^{\rm EOB}, h_{22}^{\rm NR} \rangle}{||h_{22}^{\rm EOB}||\,||h_{22}^{\rm NR}||}\,, \tag{8.7}$$

where t_0 and ϕ_0 are the initial time and phase, $||h|| \equiv \sqrt{\langle h, h\rangle}$, and the inner product between two waveforms is defined as $\langle h_1, h_2\rangle \equiv 4{\rm Re}\int_{f_{\rm min}}^{\infty} \tilde{h}_1(f)\tilde{h}_2^*(f)/S_n(f)\,df$, where $S_n(f)$ is the zero-detuned, high-power noise spectral density of advanced LIGO [4] and $f_{\rm min}$ is the starting frequency of the NR waveform (after junk radiation has settled). The normalized inner product of two waveforms is their overlap. We do not hybridize the NR waveforms at low frequency ($f < f_{\rm min}$) with any analytic approximant but instead taper the EOB waveforms. When $M \leq 100 M_\odot$ the NR waveforms do not cover the entire frequency bandwidth of the detector, but we expect that the unfaithfulness $\bar{F}$ would not change much when longer NR waveforms

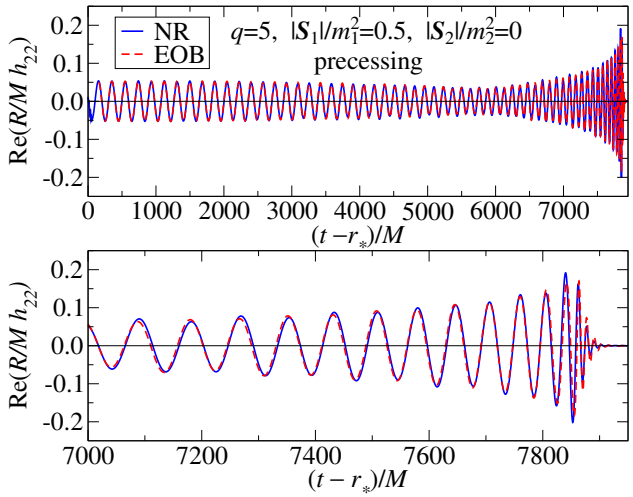

Figure 8.4: NR and EOB (2,2) precessing waveforms of the BH binary with $q = 5$ and initial spins $|\boldsymbol{S}_1|/m_1^2 = 0.5$ in the orbital plane and $|\boldsymbol{S}_2|/m_2^2 = 0$. The two waveforms are aligned at low frequency. R is the distance to the source and r_* is the tortoise coordinate.

will be employed because the EOB calibration has been shown to be quite stable with respect to the number of GW cycles used for the calibration [198]. The unfaithfulness is always below 1% for total masses from $20M_\odot$ to $200M_\odot$, implying a negligible loss in event rate due to the modeling error alone.

To estimate the NR error for each binary configuration, we choose the NR simulation with the largest number of cycles, with the highest resolution, and extrapolated to infinity with extrapolation order $N = 3$ as the fiducial waveform. We then compute the model's unfaithfulness against NR waveforms: i) with a different extrapolation order but the same resolution; ii) with a different resolution but the same extrapolation order; and obtain a conservative error bound on $\bar{F}$ from the difference between the fiducial and the most discrepant waveform. For the binary with $q = 1$ and $\chi_1 = \chi_2 = 0.98$, which we take as a representative case for the rest

of the catalog, the errors on $\bar{F}$ are within 0.005%.

Figure 8.2 shows the agreement between EOB and NR waveforms for the nearly extremal BH binary with $q = 1$ and $\chi_1 = \chi_2 = 0.98$, when aligning them at their amplitude peak; the phase difference is always within 0.6 rads. The coordinate invariant relation $\hat{E}(\hat{J})$ between the specific energy $\hat{E}$ and the total angular mometum $\hat{J}$ is a useful tool for evaluating analytical descriptions of the binary dynamics [381, 390]. In Fig. 8.3, for the cases with $q = 1$ and $\chi_1 = \chi_2 = -0.95$, 0.98, we compare $\hat{E}(\hat{J})$ from NR (using Cauchy-characteristics-extracted waveforms), the conservative uncalibrated EOB model, and the EOB model calibrated in this paper. The numerical errors of $\hat{E}(\hat{J})$ increase from 10^{-5} at low frequency to 10^{-4} at high frequency. We find that when the spins are close to extremal, there is a difference of 10^{-3} between NR and analytical (EOB or even PN) $\hat{E}(\hat{J})$ at low frequency that is not explained by numerical errors. By contrast the difference is within numerical errors when the spin magnitudes are less than ~ 0.6. We plan to further investigate those results in the future. The cusps in the conservative EOB curves indicate the presence of an ISCO; this point lies $60M$ ($10M$) in time before merger for spin -0.95 (0.98). The calibrated EOB curves instead extend up to the light ring, which is very close to the merger. The good agreement between EOB and NR results validate the calibration procedure in yielding an accurate description of the binary evolution up to merger. The improved model for the nonprecessing limit developed here (as compared to Ref. [93]) is also the foundation for precessing binaries, via the procedure of transforming from the precessing frame to an inertial frame described in Ref. [194]. Without further calibration, we tested our model against the 2 long

precessing waveforms that were used in Ref. [194], one with $q = 3$ and initial spins (both of magnitude 0.5) respectively in the orbital plane and antialigned with $\hat{\boldsymbol{L}}$, and the other with $q = 5$ and initial spins (of magnitude 0.5 and 0, respectively) in the orbital plane, and found that $\bar{F} < 3\%$ for both cases. We show EOB and NR precessing waveforms of the $q = 5$ case in Fig. 8.4.

8.4 Conclusions

Using 38 NR (2,2) mode waveforms for spinning, nonprecessing BH binaries produced by the SXS Collaboration, we have calibrated the nonprecessing sector of the EOB model of Refs. [192, 194], which is valid for any mass ratio and spins. Throughout the entire parameter space covered by the NR simulations, the EOB model of this paper achieves an unfaithfulness within 1%, implying a negligible loss in event rate due to the modeling error alone. By extending the EOB model to nearly extremal spins, we have increased the distance reach of advanced detectors. Furthermore, the EOB model can be used to generate precessing waveforms using the prescriptions in Ref. [194]. The EOB model developed here will be implemented in the LIGO Algorithm Library, so that it can be employed by advanced LIGO and Virgo to detect gravitational-waves from spinning binary BHs and to extract physical information once the waves are observed. EOB models are computationally expensive to generate (although far faster than doing NR simulations) and work is underway to speed them up. Future work will continue to improve the EOB radiation-reaction sector and the calibration of the EOB conservative dynamics,

extend the modeling to higher-order modes, investigate the performance of the model against the precessing configurations in the SXS catalog, and check its stability against much longer NR simulations, thus extending the studies recently carried out in Ref. [198] for nonspinning BHs.

Chapter 9: **Error-analysis and comparison to analytical models of numerical waveforms produced by the NRAR Collaboration**

[For reasons of space, the content of this Chapter can be found in Class. Quant. Grav. **31**, 025012 (2014)]

Authors: *Ian Hinder, Alessandra Buonanno, Michael Boyle, Zachariah B. Etienne, James Healy, Nathan K. Johnson-McDaniel, Alessandro Nagar, Hiroyuki Nakano, Yi Pan, Harald P. Pfeiffer, Michael Pürrer, Christian Reisswig, Mark A. Scheel, Erik Schnetter, Ulrich Sperhake, Bela Szilágyi, Wolfgang Tichy, Barry Wardell, Anil Zenginoğlu, Daniela Alic, Sebastiano Bernuzzi, Tanja Bode, Bernd Brügmann, Luisa T. Buchman, Manuela Campanelli, Tony Chu, Thibault Damour, Jason D. Grigsby , Mark Hannam, Roland Haas, Daniel A. Hemberger, Sascha Husa, Lawrence E. Kidder, Pablo Laguna, Lionel London, Geoffrey Lovelace, Carlos O. Lousto, Pedro Marronetti, Richard A. Matzner, Philipp Mösta, Abdul Mroué, Doreen Müller, Bruno C. Mundim, Andrea Nerozzi, Vasileios Paschalidis, Denis Pollney, George Reifenberger, Luciano Rezzolla, Stuart L. Shapiro, Deirdre Shoemaker, Andrea Taracchini, Nicholas W. Taylor, Saul A. Teukolsky, Marcus Thier-*

felder, Helvi Witek, and Yosef Zlochower[1]

Abstract: The Numerical-Relativity–Analytical-Relativity (NRAR) collaboration is a joint effort between members of the numerical relativity, analytical relativity and gravitational-wave data analysis communities. The goal of the NRAR collaboration is to produce numerical-relativity simulations of compact binaries and use them to develop accurate analytical templates for the LIGO/Virgo Collaboration to use in detecting gravitational-wave signals and extracting astrophysical information from them. We describe the results of the first stage of the NRAR project, which focused on producing an initial set of numerical waveforms from binary black holes with moderate mass ratios and spins, as well as one non-spinning binary configuration which has a mass ratio of 10. All of the numerical waveforms are analysed in a uniform and consistent manner, with numerical errors evaluated using an analysis code created by members of the NRAR collaboration. We compare previously-calibrated, non-precessing analytical waveforms, notably the effective-one-body (EOB) and phenomenological template families, to the newly-produced numerical waveforms. We find that when the binary's total mass is ~ 100–$200 M_{\odot}$, current EOB and phenomenological models of spinning, non-precessing binary waveforms have overlaps above 99% (for advanced LIGO) with all of the non-precessing-binary numerical waveforms with mass ratios ≤ 4, when maximizing over binary parameters. This implies that the loss of event rate due to modelling error is below 3%. Moreover, the non-spinning EOB waveforms previously calibrated to five non-spinning waveforms with mass ratio smaller than 6 have overlaps above 99.7% with

[1]Originally published as Class. Quant. Grav. **31**, 025012 (2014)

the numerical waveform with a mass ratio of 10, without even maximizing on the binary parameters.

Chapter 10: **Stability of nonspinning effective-one-body model in approximating two-body dynamics and gravitational-wave emission**

Authors: *Yi Pan, Alessandra Buonanno, Andrea Taracchini, Michael Boyle, Lawrence E. Kidder, Abdul H. Mroué, Harald P. Pfeiffer, Mark A. Scheel, Béla Szilágyi, and Anil Zenginoglu*[1]

Abstract: The detection of gravitational waves and the extraction of physical information from them requires the prediction of accurate waveforms to be used in template banks. For that purpose, the accuracy of effective-one-body (EOB) waveforms has been improved over the last years by calibrating them to numerical-relativity (NR) waveforms. So far, the calibration has employed a handful of NR waveforms with a total length of ~ 30 cycles, the length being limited by the computational cost of NR simulations. Here we address the outstanding problem of the stability of the EOB calibration with respect to the length of NR waveforms. Performing calibration studies against NR waveforms of nonspinning black-hole binaries with mass ratios 1, 1.5, 5, and 8, and with a total length of ~ 60 cycles, we find that EOB waveforms calibrated against either 30 or 60 cycles will be indistin-

[1]Originally published as Phys. Rev. D **89**, 061501 (R) (2014)

guishable by the advanced detectors LIGO and Virgo when the signal-to-noise ratio (SNR) is below 110. When extrapolating to a very large number of cycles, using very conservative assumptions, we can conclude that state-of-the-art nonspinning EOB waveforms of *any* length are sufficiently accurate for parameter estimation with advanced detectors when the SNR is below 20, the mass ratio is below 5 and total mass is above $20M_{\odot}$. The results are not conclusive for the entire parameter space because of current NR errors.

10.1 Introduction

Coalescing compact-object binaries are among the most promising gravitational-wave (GW) sources for ground-based interferometric detectors such as LIGO, Virgo and KAGRA [4–6]. Accurate waveform models are crucial for detecting the signals and measuring the physical parameters of the sources. By solving the Einstein equations numerically [207], it is possible to produce accurate waveforms for the very late inspiral, merger and ringdown stages of the coalescence process. However, the length of numerical-relativity (NR) simulations is limited by their high computational cost, and today it is unrealistic to generate sufficiently many NR waveforms long enough to be used directly in GW searches. The post-Newtonian (PN) formalism [292] is a slow-motion, weak field approximation to the Einstein field equations that provides reliable low-frequency inspiral waveforms. However, the PN approach becomes increasingly inaccurate close to merger [77]. Several studies [199–203] showed that there is a substantial gap between the frequency $f_{\rm PN}$ where PN waveforms cease

being accurate and the frequency $f_{\rm NR}$ where NR simulations start being available. The width of the frequency gap $f_{\rm NR}$–$f_{\rm PN}$ depends on source parameters and it is generally believed to increase rapidly with increasing mass ratio and spin magnitudes. Much longer NR simulations can reduce $f_{\rm NR}$ while knowledge of higher-order PN terms in the two-body dynamics and radiation-reaction force can increase $f_{\rm PN}$ [203], but it is extremely challenging to achieve those goals. An accurate description of the waveform in the frequency gap is thus an outstanding and pressing problem of GW source modeling, especially because advanced detectors will be operational in a few years.

The effective-one-body formalism [61, 62] (EOB) is a successful approach that provides a complete description of the coalescence of compact-object binaries. It uses the PN-expanded results in a resummed form and incorporates results of black-hole perturbation theory to produce waveforms for the inspiral, merger and ringdown stages. By construction, the EOB model reduces to the PN approximation at low frequency, while in the strong-field regime it models the merger and ringdown signals using physically motivated guesses and insights from perturbation theory. Following the breakthrough in merger simulations in NR [80, 82, 391], the EOB model has been improved by calibrating it to progressively more accurate and longer NR simulations, spanning also larger regions of the parameter space [66, 91, 93, 194, 236]. Considering the success in calibrating NR waveforms, we expect that the EOB model will be able to interpolate/extrapolate NR waveforms over the entire source parameter space. However, it is not yet clear whether the EOB calibration is stable under variation of the length of the NR waveforms that are used to calibrate the model, and whether

EOB waveforms of length larger than the one used for calibration can safely be used to detect GW signals and extract physical parameters with advanced detectors.

In this paper, we focus on the low-frequency, inspiral performance of the EOB model and assume, based on previous calibrations, that calibrated EOB merger and ringdown waveforms can be made indistinguishable from the NR ones [112]. The EOB adjustable parameters that are used to calibrate the model not only improve EOB waveforms at high frequency, so that they match NR waveforms very accurately above $f_{\rm NR}$, but they also introduce deviations from known PN results in the frequency gap $f_{\rm PN}$–$f_{\rm NR}$. Below $f_{\rm PN}$ all PN-waveform families and the EOB waveforms agree with each other. The goal of this paper is to understand the accuracy of the EOB waveforms in the frequency gap, addressing the following questions: Is the EOB calibration stable with respect to the length of NR waveforms (i.e., with respect to varying $f_{\rm NR}$)? If the calibration is stable when using the current length of NR simulations, for which we still have $f_{\rm NR} \gg f_{\rm PN}$, can we conclude that the calibrated EOB waveforms will be indistinguishable from the exact ones for all frequencies below $f_{\rm NR}$?

10.2 Calibrating the effective-one-body model

We calibrate the EOB model against four nonspinning binary black-hole waveforms with mass ratios $q = 1$, 1.5, 5 and 8. The $q = 1$ simulation was first presented in [203], and all four simulations are presented in [67]. Table 10.1 lists the total number of GW cycles of the NR waveforms up to merger and including the junk

q	1	1.5	5	8
$N_{\rm sim}$	65	66	58	52
$N_{\rm max}$	60	60	55	50

Table 10.1: Total number of GW cycles $N_{\rm sim}$ of NR simulations (including junk radiation) up to merger and maximum number of cycles $N_{\rm max}$ used for EOB-model calibration, i.e., without junk radiation.

radiation, and the maximum number of cycles $N_{\rm max}$ that we use when calibrating the EOB model (i.e., after removing the junk radiation). We decompose the EOB waveforms in -2-spin-weighted spherical-harmonic modes (ℓ, m). Previous studies [91] have shown that during the inspiral stage the frequency of all modes is well approximated by the m multiple of the orbital frequency. Therefore, here for simplicity, we consider only the dominant $(\ell = 2, m = 2)$ mode. We expect that the results of our study hold to a considerable extent for the other modes since phase evolution of every mode is synchronized with the orbital phase. However, since higher-order modes give smaller contributions and have larger NR errors, it will be more challenging to extend the current study to these other modes.

The EOB inspiral-plunge dynamics for quasi-circular orbits is described by a set of Hamilton equations that include a dissipative force proportional to the rate of loss of the orbital energy. One then introduces adjustable parameters, i.e., unknown, higher-order PN terms, to improve both conservative and dissipative parts of the dynamics. To match EOB to NR waveforms within the NR error, only a few adjustable parameters are needed and their choice is not unique. In the nonspinning limit, the EOB model depends only on two (or even one [114]) adjustable parameters

$A^{(i)}$, $i = 1, 2$. We follow the parametrization of Ref. [93], where two adjustable parameters were used in the nonspinning sector. The EOB inspiral waveform of mass ratio q is therefore determined by the pair $\{A^{(1)}, A^{(2)}\}$, where these coefficients depend on the mass ratio q. We calibrate the EOB model by mapping the phase difference between EOB and NR waveforms in the $A^{(1)}$–$A^{(2)}$ parameter space, taking into account NR errors in the simulations.

In our calibration procedure, we measure the phase difference at the end of inspiral, after aligning the EOB and NR waveforms at low frequency by shifting the EOB waveform in time and phase. We determine the time and phase shifts $\bar{t}_0$ and $\bar{\phi}_0$ by minimizing the square of the difference between the GW phases of the NR and EOB waveforms

$$\int_{t_1}^{t_2} \left[\phi_{22}^{\rm EOB}(t + t_0) + \phi_0 - \phi_{22}^{\rm NR}(t)\right]^2 dt \,, \tag{10.1}$$

with respect to t_0 and ϕ_0. The phase difference at a given time is given by

$$\Delta\phi(t) = \phi_{22}^{\rm EOB}(t + \bar{t}_0) + \bar{\phi}_0 - \phi_{22}^{\rm NR}(t) \,, \tag{10.2}$$

where $\bar{t}_0$ and $\bar{\phi}_0$ are the alignment parameters that minimize Eq. (10.1). The global phase difference over a time window (t_1, t_3) is defined as

$$\Delta\phi_g = \max_{t\in(t_1,t_3)} |\Delta\phi(t)| \,. \tag{10.3}$$

We set t_3 to the time of merger, i.e., to the time at which $|h_{22}^{\rm EOB}|$ reaches its maximum. Here, we are interested in the inspiral performance of the EOB model, thus we ignore the phase difference beyond the time of merger, which is affected by the procedure of building the merger-ringdown waveform. Because of NR errors in $\phi_{22}^{\rm NR}$, the time shift

t_0 and the global phase difference $\Delta\phi_g$ are rather sensitive to the choice of the time window (t_1, t_2). To alleviate the effect of NR errors, we choose (t_1, t_2) following the prescription of Ref. [93]. We also repeat the alignment using four different choices of (t_1, t_2) to estimate the uncertainty of $\Delta\phi_g$ due to NR errors. To calibrate the EOB model, we find those parameters $\{\bar{A}_N^{(1)}(q), \bar{A}_N^{(2)}(q)\}$ that minimize $\Delta\phi_g$. The subscript N indicates that calibration was performed using the last N GW cycles, i.e. t_1 corresponds to a time N cycles before merger, and t_3 is at merger. When building a calibrated EOB model [93], we fit the calibrated points $\{\bar{A}_N^{(1)}(q), \bar{A}_N^{(2)}(q)\}$ to a smooth function in q. However, since the fits' residuals are typically smaller than the NR errors, we use here the calibrated points instead of the fitted functions. We then increase N from 30 to $N_{\max}$ with a step size of 5 and determine how the point $\{\bar{A}_N^{(1)}(q), \bar{A}_N^{(2)}(q)\}$ moves in the parameter space. Besides systematic errors in the EOB model, the calibration point can change also because of the NR errors.

The NR errors affect $\{\bar{A}_N^{(1)}(q), \bar{A}_N^{(2)}(q)\}$ in two ways. The oscillatory phase errors at low frequency (due to residual eccentricity) introduce uncertainties in the alignment procedure, while the secular phase errors introduce uncertainties directly in the global phase difference $\Delta\phi_g$. To estimate the impact of those NR errors on $\{\bar{A}_N^{(1)}(q), \bar{A}_N^{(2)}(q)\}$, we calculate those calibrated points using four different choices of the alignment time window (t_1, t_2) and three numerical waveforms: (i) the high resolution, extrapolated to infinity with polynomial degree 3, (ii) the high resolution, extrapolated to infinity with polynomial degree 4, and (iii) the medium resolution, extrapolated to infinity with polynomial degree 3. The differences between these numerical waveforms represent the typical truncation and extrapolation

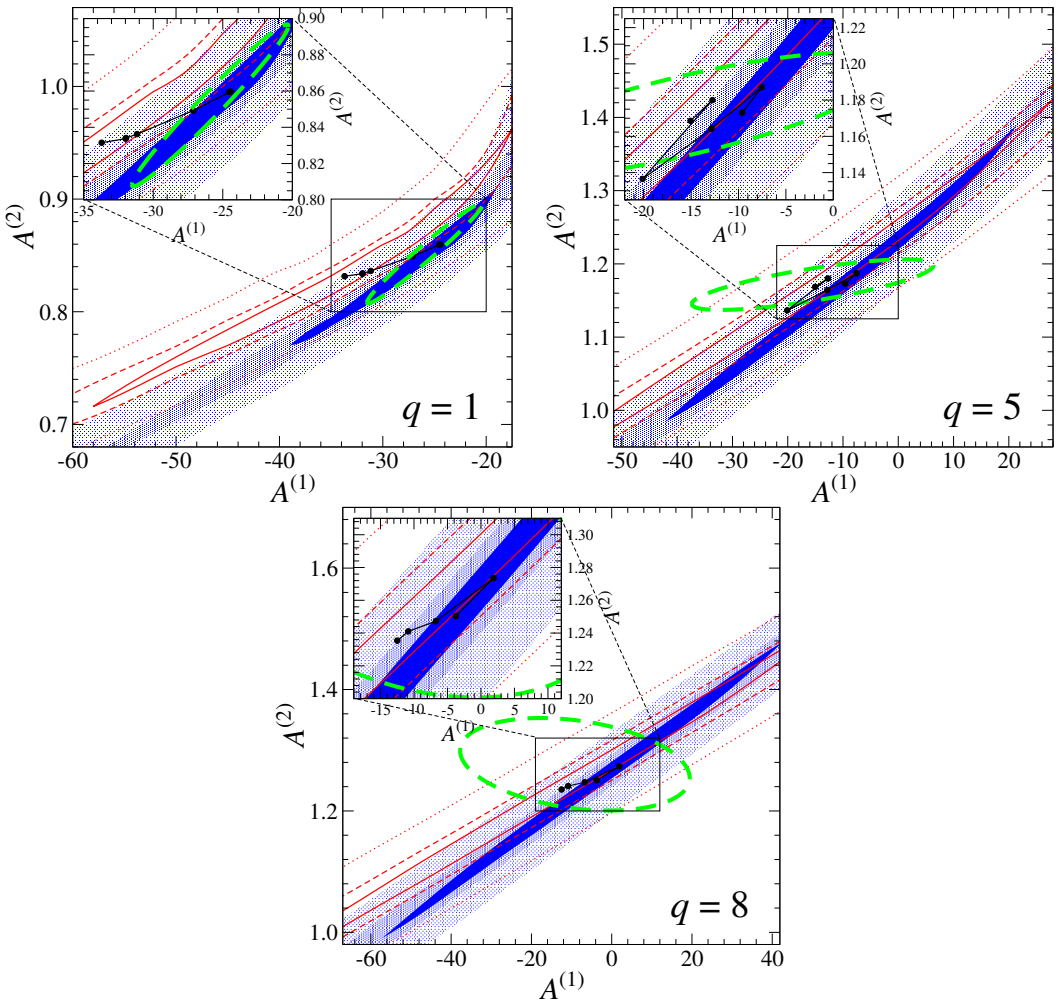

Figure 10.1: Contours of global phase difference $\Delta\phi_g$ between nonspinning NR waveforms of N GW cycles and EOB waveforms with adjustable parameters $\{A^{(1)}, A^{(2)}\}$. The three panels show results for mass ratios $q = 1$, 5 and 8 (from left to right). The shaded regions, from inside out, are 0.1, 0.2 and 0.5 radian contours for comparisons with $N_{\rm max}$ cycles of NR waveforms. The solid, dashed and dotted lines are the same contours for comparisons with 30 cycles of NR waveforms. The connected black dots are the calibrated points $\{\bar{A}^{(1)}_N(q), \bar{A}^{(2)}_N(q)\}$ for N values changing from 30 to $N_{\rm max}$. The inset zooms around these points. The NR error box of the calibrated point $\{\bar{A}^{(1)}_{N_{\rm max}}(q), \bar{A}^{(2)}_{N_{\rm max}}(q)\}$ is show with the dashed ellipse.

errors. Since we are only interested in the position (mean) and spread (variance) of $\{\bar{A}_N^{(1)}(q), \bar{A}_N^{(2)}(q)\}$, we do not investigate higher central moments and assume for simplicity a bivariate normal distribution of $\{\bar{A}_N^{(1)}(q), \bar{A}_N^{(2)}(q)\}$. We use the 12 data points to calculate the maximum likelihood estimators of their mean and variance.

We summarize our results in Fig. 10.1 for $q = 1, 5, 8$ and omit the $q = 1.5$ case because it is very similar to the $q = 1$ case. When N increases from 30 to $N_{\max}$, the volume enclosed by the $\Delta\phi_g$ contours decreases gradually, reflecting tighter constraints from the calibration against longer NR simulations. Somewhat unexpectedly, the contours also shift and rotate smoothly, indicating a possible systematic change of the calibrated EOB model. For clarity, we show in Fig. 10.1 only the contours of $N = 30$ and $N_{\max}$ calibrations. In the inset of each panel, we zoom in around the calibrated points $\{\bar{A}_N^{(1)}(q), \bar{A}_N^{(2)}(q)\}$ to show their path when N changes from 30 to $N_{\max}$. We show also the NR error box of $\{\bar{A}_{N_{\max}}^{(1)}(q), \bar{A}_{N_{\max}}^{(2)}(q)\}$, which is the symmetric 95% quantile of the estimated bivariate normal distributions. In the $q = 1$ case, the systematic drift of $\{\bar{A}_N^{(1)}(1), \bar{A}_N^{(2)}(1)\}$ with increasing N is not fully accounted for by the NR errors. Of course, it is in principle possible to improve the accuracy of the EOB model by calibrating it to the $N_{\max}$-cycle numerical waveforms. However, since the systematic differences between $\{\bar{A}_N^{(1)}(1), \bar{A}_N^{(2)}(1)\}$ are not much larger than the NR error boxes, the NR waveforms have to be as accurate as the $q = 1$ waveforms employed in this paper to bring new information to the EOB calibration. For instance, the calibrated point $\{\bar{A}_{30}^{(1)}(1), \bar{A}_{30}^{(2)}(1)\}$ sits on the 0.5-radian contour of $\Delta\phi_g$ obtained from the $N = 60$ calibration. That is to say, aligning a $q = 1$, 60-cycle NR waveform with a 60-cycle EOB waveform generated by

a model calibrated to a 30-cycle NR waveform, such as the EOB model in Ref. [93], their accumulated phase difference at merger is only ~ 0.5 radians. Any NR phase error at merger larger than that, accumulated over 60 cycles, would not improve the low-frequency accuracy of the EOB model. In fact, the $q = 5$ and $q = 8$ NR waveforms, despite being rather long and accurate, do not provide new information to the EOB calibration. Truncation errors of these simulations dominate over other numerical errors and EOB modeling errors. More accurate NR simulations of large q are therefore needed to further improve the low-frequency accuracy of the EOB model.

10.3 Stability of the EOB calibration

Although the differences among $\{\bar{A}_N^{(1)}(1), \bar{A}_N^{(2)}(1)\}$ waveforms can be distinguished by the global phase difference $\Delta\phi_g$, which is a highly sensitive quantity, it is not clear whether they can be distinguished by interferometric advanced detectors, such as LIGO. Using the zero-detuned high-power advanced LIGO noise curve [4] and a total mass for the black-hole binary of $20M_\odot$, we quantify the data-analysis consequence of the differences between $\{\bar{A}_N^{(1)}(q), \bar{A}_N^{(2)}(q)\}$. Our study follows the procedure of Ref. [203] and our results can be compared directly with those of Ref. [203].

First, we employ the quantity $||dh||/||h||$ [110] to measure the difference between waveforms h_1 and h_2, where $dh \equiv h_1 - h_2$, $h = h_1$. The norm is defined through the inner-product $\langle h_1, h_2\rangle \equiv 4\mathrm{Re}\int_0^\infty (\tilde{h}_1(f)\tilde{h}_2^*(f))/S_n(f)\, df$ where $S_n(f)$ is

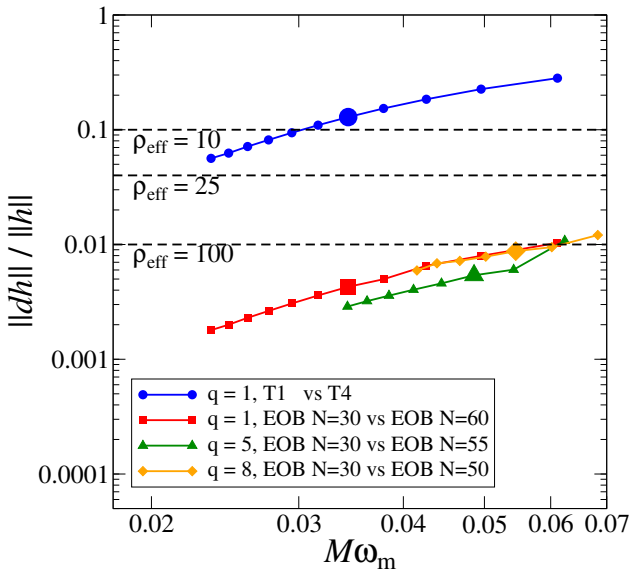

Figure 10.2: We show $||dh||/||h||$ minimized over time and phase of coalescence as a function of the hybrid matching frequency ω_m for EOB+NR hybrids where EOB waveforms are generated with the calibrated points $\{\bar{A}^{(1)}_{30}(q), \bar{A}^{(2)}_{30}(q)\}$ and $\{\bar{A}^{(1)}_{N_{\rm max}}(q), \bar{A}^{(2)}_{N_{\rm max}}(q)\}$. We also show the same quantity for PN+NR hybrids using TaylorT1 and TaylorT4 approximants. The bigger symbol in each data set marks the matching frequency where the hybrid is built using 30 cycles of NR waveforms. The horizontal lines mark the effective SNR 10, 25 and 100, below which the difference between waveforms can not be distinguished by advanced LIGO detectors.

the noise spectral density.

When we minimize over time and phase of coalescence, as well as physical parameters, $||dh||/||h||$ measures the relative loss of signal-to-noise ratio (SNR). When we minimize over only the time and phase of coalescence, $||dh||/||h||$ measures the bias in measuring source parameters, due to modeling errors. The bias is less than statistical errors when $||dh||/||h|| < 1/\rho_{\rm eff}$, where the effective SNR $\rho_{\rm eff} = 1/\epsilon\sqrt{n_D}\rho$ is proportional to the single-detector SNR ρ with a coefficient given by the number of detectors n_D and a safe factor $1/\epsilon$ [199] of order unity. Satisfying this condition

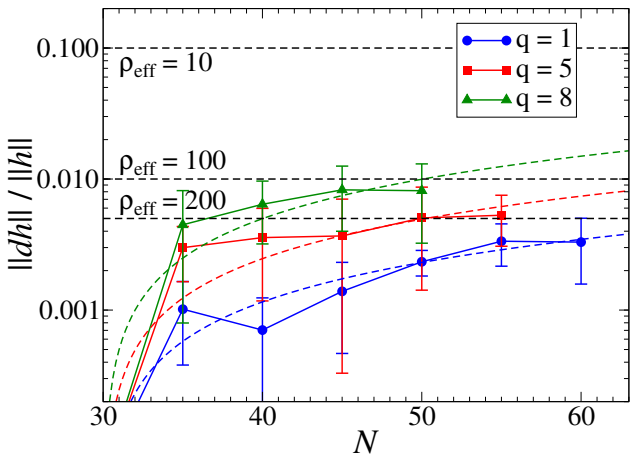

Figure 10.3: We show $||dh||/||h||$ between EOB waveforms generated with the calibrated points $\{\bar{A}^{(1)}_{30}(q), \bar{A}^{(2)}_{30}(q)\}$ and $\{\bar{A}^{(1)}_{N}(q), \bar{A}^{(2)}_{N}(q)\}$ as a function of the number of NR cycles N. We minimize $||dh||/||h||$ over time and phase of coalescence and use 30 cycles of NR waveforms in the EOB+NR hybrids. The horizontal lines mark the effective SNR 100 and 200, below which the difference between waveforms can not be distinguished by advanced LIGO detectors.

means that the detector cannot distinguish h_1 and h_2. Either is an accurate enough template to measure the source parameters of the other. [We emphasize that the criterion of indistinguishability proposed in Ref. [110], i.e., $||dh|| < 1$, is a sufficient, but not necessary criterion, and it has been shown to be highly restrictive [112].]

In order to calculate $||dh||/||h||$, we need to complete the EOB inspiral waveforms $\{\bar{A}^{(1)}_{N_{\rm max}}(q), \bar{A}^{(2)}_{N_{\rm max}}(q)\}$ with merger and ringdown waveforms. Previous studies demonstrated that it is always possible to calibrate the EOB merger and ringdown waveforms to sufficient accuracy once the inspiral waveforms are accurately calibrated [91, 112]. So, here, we do not include the EOB merger and ringdown waveforms, but simply attach the NR late-inspiral, merger and ringdown waveforms to the EOB inspiral waveforms, starting at the matching frequency ω_m, i.e., we con-

struct EOB+NR hybrid waveforms. This allows us to directly compare our results with the ones of Ref. [203]. In fact, for this reason, when building EOB + NR waveforms, we also follow the prescription of Ref. [203] on the matching frequency, the time window for alignment and the choice of blending function.

In Fig. 10.2, we show $||dh||/||h||$ between $\{\bar{A}^{(1)}_{30}(q), \bar{A}^{(2)}_{30}(q)\}$ and $\{\bar{A}^{(1)}_{N_{\rm max}}(q), \bar{A}^{(1)}_{N_{\rm max}}(q)\}$ waveforms as a function of the matching frequency. We include also a comparison between PN+NR hybrid waveforms constructed using the TaylorT1 and TaylorT4 approximants [392] as a validation of our code and to compare with Ref. [203]. The difference between $\{\bar{A}^{(1)}_{30}(q), \bar{A}^{(2)}_{30}(q)\}$ and $\{\bar{A}^{(1)}_{N_{\rm max}}(q), \bar{A}^{(2)}_{N_{\rm max}}(q)\}$ EOB waveforms is more than an order of magnitude smaller than the one obtained using the Taylor-PN approximants. Specifically, when attaching a 30-cycle NR waveform at the end of the EOB inspiral waveform, the difference cannot be distinguished as long as $\rho_{\rm eff} < 110$, which is an unlikely high SNR for advanced detectors [202]. This implies that nonspinning EOB waveforms calibrated to 30 or to $N_{\rm max}$ cycles of NR waveforms are equivalent when searching for GWs and extracting binary parameters with advanced LIGO detectors. For the EOB model calibrated to 30-cycle NR waveforms, we emphasize that the implication of these results is not just the agreement of its waveform with $N_{\rm max}$-cycle NR waveforms, but its agreement with the EOB model calibrated to 60-cycle NR simulations, i.e., the stability and convergence of the calibrated EOB model up to 60 cycles. Moreover, this result also demonstrates that calibrated higher-order PN terms (i.e., adjustable parameters) do not have a large effect at low frequency.

Can we extend this conclusion to $N > N_{\rm max}$? In Fig. 10.3, we show $||dh||/||h||$

between EOB waveforms computed at the calibrated points $\{\bar{A}^{(1)}_{30}(q), \bar{A}^{(2)}_{30}(q)\}$ and $\{\bar{A}^{(1)}_{N}(q), \bar{A}^{(2)}_{N}(q)\}$ as function of N. We see that when N increases from 30 to $N_{\rm max}$, $||dh||/||h||$ increases moderately from zero to $< 1\%$ and the increase seems to be slowing down or becoming negative as we approach $N_{\rm max}$. The oscillations in $||dh||/||h||$ are consistent with the NR error bars indicated in the plot and estimated using the 12 different $\{\bar{A}^{(1)}_{N}(q), \bar{A}^{(2)}_{N}(q)\}$ points. If we assume that the very mild increase of $||dh||/||h||$ is largely explained by NR errors, we might be tempted to conclude that the EOB model has converged beyond $N_{\rm max}$. However, we must be cautious in extrapolating the results. Nevertheless, it is reasonable to expect that the variation of $||dh||/||h||$ per unit increase of N eventually becomes a decreasing function of N when N is large enough, and consequently $||dh||/||h||$ becomes a concave function of N. We therefore obtain a conservative estimate of $||dh||/||h||$ by applying a linear extrapolation of $||dh||/||h||$ that goes through 0 at $N = 30$ and best fit the data points. We find that $||dh||/||h|| < 0.05$ until $N = 370$, 235 and 120 for mass ratios $q = 1$, 5 and 8, respectively. That is to say, when $\rho_{\rm eff} \leq 20$, EOB waveforms calibrated to those numbers of NR cycles cannot be distinguished from EOB waveforms calibrated to 30-cycle NR waveforms. One may hence generate 30-cycle NR simulations to calibrate the EOB model, and use the calibrated model to produce EOB waveforms that are, for data analysis purposes, identical to NR waveforms of hundreds of cycles.

Finally, we compare these results to the length requirements of NR waveforms set by previous works [199–203] to guarantee the accuracy of PN+NR hybrid waveforms for parameter estimation. Basically, when NR simulations are sufficiently long,

their starting frequency $f_{\rm NR}$ can be reduced to $f_{\rm PN}$, below which all PN waveform families and PN-based EOB model are consistent. Direct estimates of the number of NR cycles before merger required for accurate hybrid waveforms were made in Ref. [199] (see the table in Fig. 4 of Ref. [199]). When $\rho_{\rm eff} \leq 20$, for advanced LIGO detectors, the number of GW cycles required for $q = 1$, 4 and 10 nonspinning NR simulations is 12, 190 and 1268, respectively. Combining those results with ours we conclude that when $\rho_{\rm eff} \leq 20$ and $q \leq 5$ the nonspinning EOB waveforms of *any* length are sufficiently accurate for parameter estimation with advanced LIGO detectors. Note again that these EOB waveforms are generated by the EOB model calibrated to *only* 30-cycle NR simulations.

10.4 Conclusions

We found that the EOB-model calibration against NR simulations is stable with respect to the length of NR simulations. In the nonspinning limit with mass ratio $q \leq 8$, the difference between EOB waveforms calibrated against 30-cycle and $\sim$ 60-cycle NR simulations can not be distinguished by advanced LIGO detectors when $\rho_{\rm eff} < 110$. Extrapolating our results to a larger number of cycles, making rather conservative assumptions, which use the overstrict criterion from Ref. [110], we estimated that the nonspinning EOB model calibrated to existing NR simulations is sufficiently accurate for advanced-LIGO parameter estimation when $\rho_{\rm eff} < 20$, $q < 5$ and $M \geq 20 M_{\odot}$. Moreover, since EOB waveforms overcome the frequency gap, they can completely replace PN + NR hybrid waveforms [200–203]. Extending this

conclusion to larger $\rho_{\rm eff}$ or q requires longer and more accurate NR simulations. We plan in the near future to extend this kind of study to the spinning EOB model [114]. We expect that in the presence of spins, we might need longer and more accurate NR simulations, especially in the extremal-spin limit, but the length can be much less than those suggested by previous studies that aimed at reducing $f_{\rm NR}$ to $f_{\rm PN}$.

Chapter 11: **Inspiral-merger-ringdown waveforms of spinning, precessing black-hole binaries in the effective-one-body formalism**

Authors: *Yi Pan, Alessandra Buonanno, Andrea Taracchini, Lawrence E. Kidder, Abdul H. Mroué, Harald P. Pfeiffer, Mark A. Scheel, and Béla Szilágyi*[1]

Abstract: We describe a general procedure to generate spinning, precessing waveforms that include inspiral, merger and ringdown stages in the effective-one-body (EOB) approach. The procedure uses a precessing frame in which precession-induced amplitude and phase modulations are minimized, and an inertial frame, aligned with the spin of the final black hole, in which we carry out the matching of the inspiral-plunge to merger-ringdown waveforms. As a first application, we build spinning, precessing EOB waveforms for the gravitational modes $\ell = 2$ such that in the nonprecessing limit those waveforms agree with the EOB waveforms recently calibrated to numerical-relativity waveforms. Without recalibrating the EOB model, we then compare EOB and post-Newtonian precessing waveforms to two numerical-relativity waveforms produced by the Caltech-Cornell-CITA collaboration. The numerical waveforms are strongly precessing and have 35 and 65 gravitational-wave

[1]Originally published as Phys. Rev. D **89**, 084006 (2014)

cycles. We find a remarkable agreement between EOB and numerical-relativity precessing waveforms and spins' evolutions. The phase difference is ~ 0.2 rad at merger, while the mismatches, computed using the advanced-LIGO noise spectral density, are below 2% when maximizing only on the time and phase at coalescence and on the polarization angle.

11.1 Introduction

An international network of gravitational-wave (GW) detectors operating in the frequency band 10–10^3 Hz exists today. It is composed of the LIGO detectors in Hanford, WA and Livingston, LA, in the United States, the French-Italian Virgo detector [393], and the British-German GEO600 detector [350]. Those detectors have collected and analysed data for several years. Since 2010 they have been shut down to be upgraded to the advanced LIGO and Virgo configurations [4]. The design sensitivity for advanced detectors, which is planned to be achieved by 2019 [181], will be a factor of ten better than the one of the initial detectors. This improvement implies an increase in the event rates of coalescing binary systems of (roughly) one thousand, thus making very likely the first detection of gravitational waves [181] with the advanced detector network. Furthermore, efforts to build a gravitational-wave detector in space are underway [394].

Binary systems composed of compact objects, such as black holes and neutron stars (compact binaries for short) are the most promising sources for groundbased GW detectors. The signal detection and interpretation is based on a matched-

filtering technique, where the noisy detector output is cross-correlated with a bank of theoretical templates.

Fueled by numerical relativity (NR) simulations, there has been substantial progress in building and validating accurate templates for the inspiral, merger and ringdown stages of nonprecessing [2] black-hole (BH) binaries [69, 72, 91, 93, 236, 239, 283, 285, 286, 322, 354, 354, 395] (see also Ref. [66] where several analytical templates have been compared to simulations produced by the numerical-relativity and analytical-relativity (NRAR) collaboration). Despite this progress, template modeling for generic, spinning BH binaries is far from being complete. In this paper we focus on BH binary systems moving on quasi-spherical orbits, i.e., generic precessing orbits that are circularized and shrunk by radiation reaction.

During the last several years, the post-Newtonian (PN) formalism, which expands the Einstein equations in powers of v/c (v being the characteristic velocity of the binary and c the speed of light), has extended the knowledge of the dynamics and gravitational waveform for quasi-spherical orbits through 3.5PN [156, 360] and 2PN [159] order, respectively. Precession-induced modulations in the phase and amplitude of gravitational waveforms become stronger as the opening angle between the orbital angular momentum and the total angular momentum of the binary increases. Compact binaries with large mass ratios can have larger opening angles than those with comparable masses.

Pioneering studies aimed at understanding and modeling precession effects

[2] Here, nonprecessing means that the BH spins are either zero or aligned/antialigned with the orbital angular momentum.

in inspiraling compact binaries were carried out in the mid 90s [164, 396]. As GW detectors came online in early 2000, it became more urgent to develop template families for spinning, precessing binaries in which precession-induced modulations were incorporated in an efficient way, reducing also the dimensionality of the parameter space. In 2003, Buonanno, Chen and Vallisneri [166] introduced the *precessing convention* and proposed a template family for precessing binaries in which precessional effects are neatly disentangled from nonprecessing effects in both the amplitude and phase evolutions. They also showed that the (restricted) waveform in the frame that precesses following the precessing convention takes the simple nonprecessing form, and that strong correlations exists between the nonprecessing phase evolution and spin parameters, notably the opening angle between the spin and orbital angular momentum (see Fig. 15 in Ref. [166]). This correlation was further studied and modeled in Ref. [397]. More recently, Ref. [398] explicitly demonstrated the agreement between nearly nonprecessing waveforms in the precessing frame and exact nonprecessing waveforms generated by neglecting the spin components on the orbital plane. The precessing convention was initially introduced to model phenomenological or detection template families [166], and then it was extended to physical templates of single-spin binary systems in Refs. [167, 397]. In the past few years, geometric methods have been developed to construct preferred precessing reference frames [399–402] for numerical or analytical waveforms, achieving a similar disentanglement of precessional effects. Waveforms decomposed in such frames exhibit relatively smooth amplitude and phase evolutions and are well approximated by nonprecessing waveforms [68, 398].

Here, we use the effective-one-body (EOB) formalism [61,62,87,188] to model precessing inspiral, merger and ringdown waveforms. The basic idea of the EOB approach is to map by a canonical transformation the conservative dynamics of two compact objects of masses m_1 and m_2 and spins $\boldsymbol{S}_1$ and $\boldsymbol{S}_2$ into the dynamics of an effective particle of mass $\mu = m_1\, m_2/(m_1 + m_2)$ and spin $\boldsymbol{S}_*$ moving in a deformed Kerr metric with mass $M = m_1 + m_2$ and spin $\boldsymbol{S}_{\rm Kerr}$, the deformation parameter being the symmetric mass ratio $\nu = \mu/M$. In the mid 2000s, Buonanno, Chen and Damour [102] modeled EOB inspiral, merger and ringdown waveforms including for the first time spinning, precessing effects.

In this paper we build on Refs. [102,166], and also on the most recent analytical work [191–193] and the work at the interface between numerical and analytical relativity [93,239], and develop a general procedure to generate spinning, precessing waveforms in the EOB approach. The procedure employs the precessing convention of Ref. [166] and an inertial frame aligned with the spin of the final BH. As a first application, we construct spinning, precessing waveforms that contain only the $\ell = 2$ gravitational mode and reduce to the nonprecessing waveforms calibrated to numerical-relativity (NR) waveforms [186, 210, 305, 403] in Ref. [93]. We compare these EOB precessing waveforms to Taylor-expanded PN waveforms and to two NR waveforms recently produced by the Caltech-Cornell-CITA collaboration [67].

The paper is organized as follows. In Sec. 11.2 we discuss the main coordinate frames that are used to describe precessing waveforms and their physical characteristics. We also review different proposals that have been suggested in the analytical and numerical-relativity communities for the precessing source frame, in

which precession-induced modulations in the waveform's phase and amplitude are minimized. We also study how spin components parallel to the orbital plane affect the energy flux and multipolar waveforms. In Sec. 11.3 we build EOB precessing waveforms using a precessing source frame aligned with the Newtonian orbital angular momentum and an inertial frame aligned with the direction of the final BH spin. In Sec. 11.4 we compare EOB precessing waveforms computed in different precessing source frames and carry out comparisons between EOB, Taylor-expanded PN and NR precessing waveforms. Section 11.5 summarizes our main conclusions and future work.

11.2 Modeling precessing waveforms

11.2.1 Conventions and inertial frames

Throughout the paper, we adopt geometric units $G = c = 1$ and the Einstein summation convention, unless otherwise specified. The masses of the BHs are m_1 and m_2 and we choose $m_1 \geq m_2$. The total mass, mass ratio and symmetric mass ratio are $M = m_1 + m_2$, $q = m_1/m_2$ and $\nu = m_1 m_2/M^2$, respectively. The position, linear momentum and spin vectors of the BHs are $\boldsymbol{r}_i(t)$, $\boldsymbol{p}_i(t)$ and $\boldsymbol{S}_i(t) = \chi_i m_i^2 \hat{\boldsymbol{S}}_i$, where $i = 1, 2$ and χ_i is the dimensionless spin magnitude. In the EOB framework, we solve the time evolution of the relative (rescaled) position vector $\boldsymbol{r}(t) \equiv (\boldsymbol{r}_1(t) - \boldsymbol{r}_2(t))/M$, the center-of-mass–frame (rescaled) momentum vector $\boldsymbol{p}(t) \equiv \boldsymbol{p}_1(t)/\mu = -\boldsymbol{p}_2(t)/\mu$, and the spins variables $\boldsymbol{S}_1(t)$ and $\boldsymbol{S}_2(t)$.

We start with an arbitrary orthonormal basis $\{\boldsymbol{e}_x, \boldsymbol{e}_y, \boldsymbol{e}_z\}$. Without loss of

generality, we align the initial relative position vector $\boldsymbol{r}_0$ with $\boldsymbol{e}_x$ and the initial orbital orientation $[\hat{\boldsymbol{L}}_N]_0 \equiv \hat{\boldsymbol{L}}_N(0) \equiv \boldsymbol{r}_0 \times \dot{\boldsymbol{r}}_0/|\boldsymbol{r}_0 \times \dot{\boldsymbol{r}}_0|$ with $\boldsymbol{e}_z$, where we indicate with an over-dot the time derivative and $\dot{\boldsymbol{r}}_0 = \dot{\boldsymbol{r}}(0)$ is the initial relative velocity. The initial spin directions are specified by the spherical coordinates θ_1^S, ϕ_1^S, θ_2^S and ϕ_2^S associated with this basis.

In the nonprecessing case, $\hat{\boldsymbol{L}}_N$ is a constant and it is natural to choose a *source frame* described by the (unit) basis vectors $\{\boldsymbol{e}_1^S, \boldsymbol{e}_2^S, \boldsymbol{e}_3^S\}$ whose $\boldsymbol{e}_3^S$ is aligned with $\hat{\boldsymbol{L}}_N$. In the precessing case, we choose to align the source frame $\{\boldsymbol{e}_1^S, \boldsymbol{e}_2^S, \boldsymbol{e}_3^S\}$ with $\{\boldsymbol{e}_x, \boldsymbol{e}_y, \boldsymbol{e}_z\}$. The basis vector $\boldsymbol{e}_3^S$ is aligned with the initial orbital orientation $\hat{\boldsymbol{L}}_N(0)$ but not with $\hat{\boldsymbol{L}}_N(t)$ at later times.

The GW polarizations h_+ and $h_\times$ can be obtained by projecting the strain tensor h_{ij} onto the *radiation frame* described by the (unit) basis vectors $\{\boldsymbol{e}_1^R, \boldsymbol{e}_2^R, \boldsymbol{e}_3^R \equiv \hat{\boldsymbol{N}}\}$, the basis vector $\hat{\boldsymbol{N}}$ being along the direction of propagation of the wave (see Fig. 11.1). That is

$$h_+ = \frac{1}{2}\left[\boldsymbol{e}_1^R \otimes \boldsymbol{e}_1^R - \boldsymbol{e}_2^R \otimes \boldsymbol{e}_2^R\right]^{ij} h_{ij}\,, \tag{11.1a}$$

$$h_\times = \frac{1}{2}\left[\boldsymbol{e}_1^R \otimes \boldsymbol{e}_2^R + \boldsymbol{e}_2^R \otimes \boldsymbol{e}_1^R\right]^{ij} h_{ij}\,, \tag{11.1b}$$

where the basis vectors $\boldsymbol{e}_1^R$ and $\boldsymbol{e}_2^R$ are defined by (see Fig. 11.1)

$$\boldsymbol{e}_1^R \equiv \frac{\boldsymbol{e}_z \times \hat{\boldsymbol{N}}}{|\boldsymbol{e}_z \times \hat{\boldsymbol{N}}|}\,, \tag{11.2a}$$

$$\boldsymbol{e}_2^R \equiv \hat{\boldsymbol{N}} \times \boldsymbol{e}_1^R\,. \tag{11.2b}$$

In the source frame $\{\boldsymbol{e}_1^S, \boldsymbol{e}_2^S, \boldsymbol{e}_3^S\}$, we can decompose the polarizations h_+ and $h_\times$ in

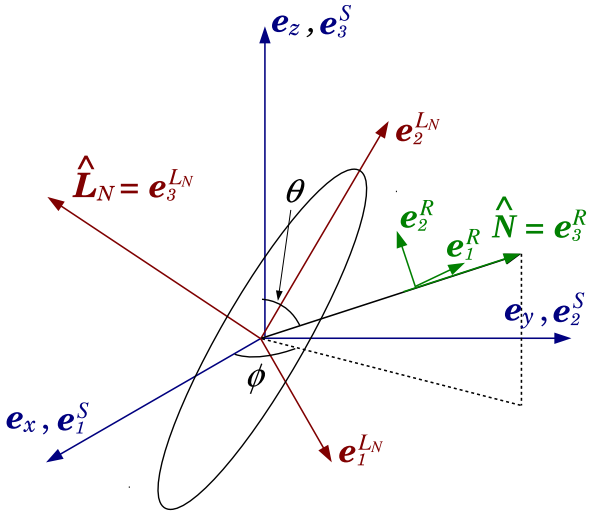

Figure 11.1: We show the *radiation frame* $\{\boldsymbol{e}_1^R, \boldsymbol{e}_2^R, \boldsymbol{e}_3^R\}$, the inertial *source frame* $\{\boldsymbol{e}_1^S, \boldsymbol{e}_2^S, \boldsymbol{e}_3^S\}$ and the *precessing source frame* $\{\boldsymbol{e}_1^{L_N}, \boldsymbol{e}_2^{L_N}, \boldsymbol{e}_3^{L_N}\}$ employed to describe a precessing BH binary and its GW radiation.

-2 spin-weighted spherical harmonics ${}_{-2}Y_{\ell m}(\theta, \phi)$ as

$$h_+(\theta,\phi) - i h_\times(\theta,\phi) = \sum_{\ell=2}^{\infty} \sum_{m=-\ell}^{\ell} {}_{-2}Y_{\ell m}(\theta,\phi) h_{\ell m} \,. \tag{11.3}$$

The modes $h_{\ell m}$ can be calculated by applying the orthogonality condition valid for the ${}_{-2}Y_{\ell m}(\theta, \phi)$'s. Thus

$$h_{\ell m} = \int \left[h_+(\theta,\phi) - i h_\times(\theta,\phi)\right] {}_{-2}Y^*_{\ell m}(\theta,\phi)\, d\Omega \,, \tag{11.4}$$

where θ and ϕ are the inclination and azimuthal angles of the unit vector $\hat{\boldsymbol{N}}$ as measured in the source frame. Note that in the above expressions, we omit the dependence of the GW polarizations on time and binary parameters.

11.2.2 Precessing source frames in analytical-relativity waveforms

In the nonprecessing case, the orbital orientation is constant and coincides with the directions of the orbital angular momentum $\boldsymbol{L} \equiv \mu M \boldsymbol{r} \times \boldsymbol{p}$, the Newtonian angular momentum $\boldsymbol{L}_N \equiv \mu M \boldsymbol{r} \times \dot{\boldsymbol{r}}$, and the total angular momentum $\boldsymbol{J} \equiv \boldsymbol{L} + \boldsymbol{S}_1 + \boldsymbol{S}_2$. If the source frame is aligned with the orbital orientation, the gravitational polarizations are quite simple and are described mainly by the $(2, 2)$ mode and a few subdominant modes [91, 93]. In this case, the wave's amplitude and frequency increase monotonically during the inspiral and plunge stages, and the amplitudes of the GW modes display a clean hierarchy. By contrast, precessing waveforms decomposed in an inertial source frame show strong amplitude and phase modulations. In this case the amplitudes of the GW modes do not necessarily follow a clean hierarchy [346]. Ideally we would like to conduct comparisons and calibrations between analytical and numerical waveforms in a time dependent source frame that minimizes precession-induced modulations. Fortunately, this is possible if we choose a source frame that precesses with the binary orbital plane [166, 397, 399–401].

Buonanno, Chen and Vallisneri [166] proposed the *precessing convention* that neatly disentangles precessional effects from both amplitude and phase evolutions in restricted (i.e., leading-order) PN waveforms. In the precessing convention, the precessing waveform is written as the product of a nonprecessing carrier waveform and a modulation term that collects all precessional effects. In Refs. [166, 397] the authors chose the precessing source frame aligned with the Newtonian orbital angular momentum $\boldsymbol{L}_N$. In this case, the basis vectors of the precessing source

frame, $\{\boldsymbol{e}_1^{L_N}(t), \boldsymbol{e}_2^{L_N}(t), \boldsymbol{e}_3^{L_N}(t)\}$ in Fig. 11.1, read [166]

$$\boldsymbol{e}_3^{L_N}(t) = \hat{\boldsymbol{L}}_N(t)\,, \tag{11.5a}$$

$$\dot{\boldsymbol{e}}_1^{L_N}(t) = \boldsymbol{\Omega}_e(t) \times \boldsymbol{e}_1^{L_N}(t)\,, \tag{11.5b}$$

$$\dot{\boldsymbol{e}}_2^{L_N}(t) = \boldsymbol{\Omega}_e(t) \times \boldsymbol{e}_2^{L_N}(t)\,, \tag{11.5c}$$

where

$$\boldsymbol{\Omega}_e(t) \equiv \boldsymbol{\Omega}_L(t) - \left[\boldsymbol{\Omega}_L(t) \cdot \hat{\boldsymbol{L}}_N(t)\right] \hat{\boldsymbol{L}}_N(t) = \hat{\boldsymbol{L}}_N(t) \times \dot{\hat{\boldsymbol{L}}}_N(t)\,, \tag{11.6}$$

and $\boldsymbol{\Omega}_L(t)$ is the angular velocity of the precession of $\hat{\boldsymbol{L}}_N(t)$ and satisfies $\dot{\hat{\boldsymbol{L}}}_N(t) = \boldsymbol{\Omega}_L(t) \times \hat{\boldsymbol{L}}_N(t)$. Aligning the precessing source frame with $\hat{\boldsymbol{L}}_N(t)$ in Eq. (11.5a) removes the precession-induced amplitude modulations. Intuitively, Eqs. (11.5b)–(11.6) impose that $\boldsymbol{e}_1^{L_N}(t)$ and $\boldsymbol{e}_2^{L_N}(t)$ follow the precession of $\boldsymbol{e}_3^{L_N}(t) = \hat{\boldsymbol{L}}_N(t)$, but do not precess around it. The key point of the precessing convention is the removal of all precession-induced modulations from the orbital phase $\Phi(t)$, so that $\Phi(t)$ is simply given by the integral of the (monotonic) orbital frequency Ω, i.e. $\Phi(t) = \int \Omega(t')dt'$ (see for details Sec. IVA in Ref. [166]). The freedom of choosing the constant of integration, or the initial phase, is degenerate with the only degree of freedom left in defining the precessing source frame, namely a constant rotation of $\boldsymbol{e}_1^{L_N}$ and $\boldsymbol{e}_2^{L_N}$ around $\boldsymbol{e}_3^{L_N}$.

We want to test now the precessing convention on inspiraling PN waveforms computed beyond the restricted approximation, i.e., beyond leading order. We employ the waveforms of Ref. [346] that have spin-amplitude corrections through 1.5PN order. We decompose the $h_{\ell m}$'s in two source frames: (i) the inertial source frame aligned with the initial total angular momentum $\boldsymbol{J}_0$ [346] and (ii) the precessing

source frame $\{\boldsymbol{e}_1^{L_N}(t), \boldsymbol{e}_2^{L_N}(t), \boldsymbol{e}_3^{L_N}(t)\}$ defined by Eqs. (11.5a)–(11.6). The waveforms decomposed in the $\boldsymbol{J}_0$-frame are given explicitly in Appendix B of Ref. [346]. We calculate the waveforms decomposed in the precessing $\boldsymbol{L}_N(t)$-frame from the waveforms decomposed in the $\boldsymbol{J}_0$-frame by properly rotating the $h_{\ell m}$ modes.

In general, given a set of spin-weighted spherical harmonics $h^{(o)}_{\ell m}$ decomposed in an original frame and the Euler angles (α, β, γ) that define the rotation from the original frame to a new frame, the modes $h^{(n)}_{\ell m}$ decomposed in the new frame are given by [346, 404]

$$h^{(n)}_{\ell m} = \sum_{m'=-\ell}^{\ell} D^{\ell\,*}_{m'm}(\alpha, \beta, \gamma) h^{(o)}_{\ell m'} \,, \tag{11.7}$$

where $D^{\ell\,*}_{m'm}(\alpha, \beta, \gamma)$ is the complex conjugate of the Wigner D-matrix

$$D^{\ell}_{m'm}(\alpha, \beta, \gamma) = (-1)^{m'} \sqrt{\frac{4\pi}{2\ell+1}}\, {}_{-m'}Y_{\ell m}(\beta, \alpha) e^{im'\gamma} \,, \tag{11.8}$$

where ${}_{-m'}Y_{\ell m}$ is the spherical harmonic of spin-weight $-m'$. The transformation is closed among modes with the same index ℓ. In this paper, we focus on the $\ell = 2$ modes both for simplicity and because even when precession is present the $\ell = 2$ modes still dominate. Nevertheless, the $\ell > 2$ modes are not negligible and we plan to extend the precessing EOB model to those modes in the future, following the same approach we propose and demonstrate here with the $\ell = 2$ modes.

In Fig. 11.2, we compare the $\boldsymbol{J}_0$-frame and $\boldsymbol{L}_N(t)$-frame h_{2m} inspiraling waveforms emitted by a BH binary with mass ratio $q = 6$ and spin magnitudes $\chi_1 = \chi_2 = 0.8$. We choose spin orientations that give strong precession-induced modulations. As we can see, there is a clear hierarchy among the h_{2m}'s amplitudes when decomposed in the $\boldsymbol{L}_N(t)$-frame, but not when the decomposition is done in the $\boldsymbol{J}_0$-frame.

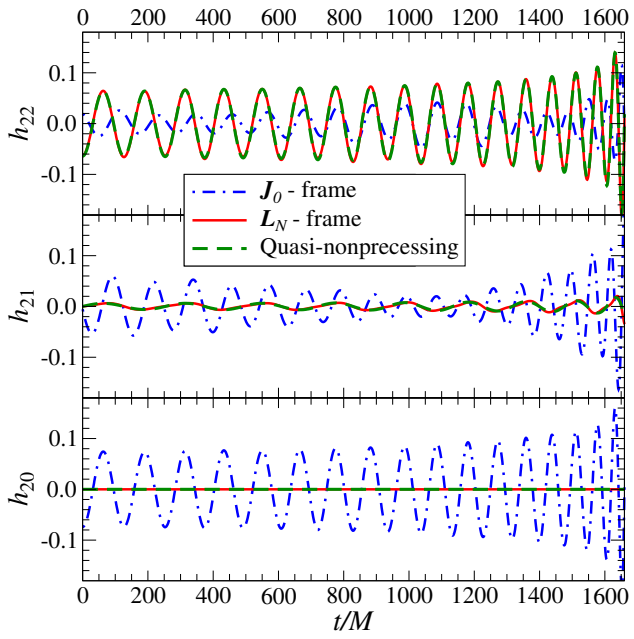

Figure 11.2: We show inspiraling, precessing PN waveforms decomposed in the inertial source frame aligned with the initial total angular momentum $\boldsymbol{J}_0$ and in the precessing source frame aligned with the Newtonian orbital angular momentum $\boldsymbol{L}_N(t)$. For comparison, we show also the quasi-nonprecessing PN waveforms defined in Sec. 11.2.2. They lie on top of the $\boldsymbol{L}_N(t)$-frame waveforms. The three panels use the same scale on the y-axis so that the amplitudes of the modes h_{22}, h_{21} and h_{20} can be easily compared.

In fact, in the $\boldsymbol{J}_0$-frame, the $(2,1)$ and $(2,0)$ modes have even larger amplitudes than the $(2,2)$ mode. We notice that the strong amplitude and phase modulations of the modes in the $\boldsymbol{J}_0$-frame almost completely disappear when the $\boldsymbol{L}_N(t)$-frame is used.

Furthermore, we find it interesting to compare the modes of the precessing waveforms to the ones of a "nonprecessing" binary system having the same mass ratio and $\chi_i(t) \equiv \chi_i \hat{\boldsymbol{S}}_i(t) \cdot \hat{\boldsymbol{L}}_N(t)\,,\ (i = 1,2)$. That is to say, we keep only the components of the spin vectors along the direction of the Newtonian angular mo-

mentum $\boldsymbol{L}_N(t)$, and set all the other components to zero. For convenience, we refer to such "nonprecessing" waveforms as the *quasi-nonprecessing* waveforms. We use the adjective "quasi" because, differently from the nonprecessing waveforms, where the spins are aligned or antialigned with the orbital angular momentum and remain constant throughout the evolution, in the quasi-nonprecessing waveforms the spins evolve (according to Eqs. (11.11c)–(11.11d) given below) and over time change their projections onto $\boldsymbol{L}_N$. As can be seen in Fig. 11.2, the near-perfect agreement between $\boldsymbol{L}_N(t)$-frame and quasi-nonprecessing waveforms indicates that the spin components along $\boldsymbol{L}_N(t)$ dominate the spin effects. This conjecture is reinforced by the observation that, because of parity symmetry, the spin-orbit couplings contribute to the GW energy flux to infinity (known through 3.5PN order) only through terms of the form $\boldsymbol{S}_i(t)\cdot\hat{\boldsymbol{L}}_N(t)\,,\ (i=1,2)$ [153, 156, 360, 405]. The energy flux is a frame independent quantity. It is given, in the adiabatic assumption, by [3]

$$\frac{dE}{dt}=\frac{(M\Omega)^2}{8\pi}\sum_{\ell=2}^{\infty}\sum_{m=-\ell}^{\ell}m^2\left|\frac{\mathcal{R}}{M}h_{\ell m}\right|^2\,, \tag{11.9}$$

where $\mathcal{R}$ is the distance to the source (and simply cancels the dependence on $\mathcal{R}$ hidden in the $h_{\ell m}$'s). The fact that the spin-orbit effects in dE/dt depend on spins only through $\boldsymbol{S}_i(t)\cdot\hat{\boldsymbol{L}}_N(t)\,,\ (i=1,2)$ suggests that the dependence of the modes on spin's components parallel to the orbital plane disappears when all the modes are summed up to make the total energy flux.

Therefore, beyond the leading-order results of Ref. [166], we find that PN pre-

[3] Following the nonprecessing EOB model of Ref. [93], we include in dE/dt the spin-orbit terms through 1.5PN order [101], even if some of us have recently computed the spin-orbit and spin-spin terms in the factorized flux through 2PN order using results in Ref. [159].

cessing waveforms [346] reduce to nearly nonprecessing waveforms when decomposed to spin-weighted spherical harmonics in the source frame $\{\boldsymbol{e}_1^{L_N}(t), \boldsymbol{e}_2^{L_N}(t), \boldsymbol{e}_3^{L_N}(t)\}$ of the precessing convention [166]. In addition, the PN quasi-nonprecessing waveforms are a good first approximations to the $h_{\ell m}$'s modes in the precessing frame.

11.2.3 Precessing source frames in numerical-relativity waveforms

The possibility of demodulating precessing waveforms using precessing source frames was recently verified with and generalized to NR waveforms in Refs. [398–400]. In particular, Schmidt *et al.* [398,399] and O'Shaughnessy *et al.* [400] identified the preferred *radiation axis* at infinity and showed that if a precessing frame aligned with the radiation axis is chosen, then the amplitude and phase modulations of numerical waveforms are removed and a clean hierarchy among the modes is restored.

In particular, Schmidt *et al.* proposed the so-called quadrupole-preferred frame in which the power of the $(\ell, \pm m) = (2, 2)$ mode is maximized. O'Shaughnessy *et al.* proposed a more general and geometrical choice of the precessing frame in which the z component of the radiated angular momentum is maximized. The latter proposal reduces to the choice of Schmidt *et al.* when the radiated angular momentum is calculated using only the $(\ell, \pm m) = (2, 2)$ modes. Boyle *et al.* [401] then proposed the *minimal rotation* condition to remove the remaining arbitrariness in the azimuthal rotation of the precessing frame and in the phase modulations of the waveform. Given an inertial frame $\{\boldsymbol{e}_x, \boldsymbol{e}_y, \boldsymbol{e}_z\}$ and the first two Euler angles $\alpha(t)$ and $\beta(t)$ that align $\boldsymbol{e}_z$ with the radiation axis, the minimal rotation condition

on the third Euler angle $\gamma(t)$ is given by

$$\dot{\gamma}(t) = -\dot{\alpha}(t)\cos\beta(t)\,. \tag{11.10}$$

This condition is equivalent to Eqs. (11.5b)–(11.6) above on the evolution of $\boldsymbol{e}_1^{L_N}(t)$ and $\boldsymbol{e}_2^{L_N}(t)$. If $\alpha(t)$ and $\beta(t)$ are the first two Euler angles that align $\boldsymbol{e}_z$ with $\hat{\boldsymbol{L}}_N$, then $\gamma(t) - \gamma(t_0)$ is the angle by which $\boldsymbol{e}_1^{L_N}(t)$ and $\boldsymbol{e}_2^{L_N}(t)$ shall rotate in the instantaneous orbital plane, relative to their positions at a reference time t_0, to satisfy the precession convention. Recently, Boyle [402] proposed a geometric definition of the angular-velocity vector of a waveform, to determine a frame in which the modes' amplitudes become very simple and the phases are nearly constant.

Schmidt *et al.* [398] showed that precessing PN inspiral waveforms computed in the precessing source frame aligned with the preferred radiation axis are well approximated by nonprecessing PN waveforms. Furthermore, they proposed that precessing waveforms can be generated with good accuracy by transforming nonprecessing waveforms from precessing source frames to inertial source frames. In a recent study, Pekowsky *et al.* [68] studied the mapping of precessing waveforms to nonprecessing ones using a large number of (short) numerical simulations and the analytical `IMRPhenomB` [72] waveforms. They found that precessional degrees of freedom that cannot be reproduced by nonprecessing models (such as spin's components perpendicular to $\hat{\boldsymbol{L}}_N$) give rise to corrections to the nonprecessing waveforms that are very small during inspiral, but they can become significant during merger and ringdown.

11.2.4 Strategy to build precessing effective-one-body waveforms

Motivated by the results discussed in Secs. 11.2.2 and 11.2.3 of a nearly complete separation of precession-induced modulations in precessing waveforms when using appropriate precessing source frames, we propose the following approach to generate generic EOB waveforms.

First, we evolve the EOB dynamics and solve Eqs. (11.5a)–(11.6) for the precessing source frame $\{\boldsymbol{e}_1^{L_N}(t), \boldsymbol{e}_2^{L_N}(t), \boldsymbol{e}_3^{L_N}(t) = \hat{\boldsymbol{L}}_N(t)\}$. Since the difference between $\boldsymbol{L}_N$ and $\boldsymbol{L}$ starts at 1PN order, the leading-order conclusions achieved by the precessing $\boldsymbol{L}_N$-frame hold if we replace $\boldsymbol{L}_N$ with $\boldsymbol{L}$ in Eqs. (11.5a)–(11.6). We have verified that precessing waveforms decomposed in the $\boldsymbol{L}$-frame agree equally well with the quasi-nonprecessing waveforms generated by keeping only spin's components along $\boldsymbol{L}$. Furthermore, in Sec. 11.4 we compare precessing EOB waveforms (generated either in the $\boldsymbol{L}_N$-frame or in the $\boldsymbol{L}$-frame) to NR waveforms, and find that their mutual difference is marginal. Without a more accurate calibration and comprehensive comparisons with NR waveforms, we do not know *a priori* whether the $\boldsymbol{L}_N$-frame or the $\boldsymbol{L}$-frame is more preferable, nor can we say which of them captures the precession effects more faithfully. Thus, at the current stage, we simply adopt the $\boldsymbol{L}_N$-frame as the default precessing source frame in the EOB model.

Second, because of the simple features of the inspiral-plunge modes in the precessing source frame — little modulation and clean hierarchy — we choose to model the precessing inspiral-plunge EOB modes in this frame, and generate modes in any arbitrary source frame through Eq. (11.7). Since factorized EOB modes for

precessing spins are not available yet and EOB modes have been calibrated only to nonspinning and spinning, nonprecessing NR modes [91, 93], we choose to work in the precessing source frame and use quasi-nonprecessing modes as good approximations to precessing modes (as discussed in Secs. 11.2.2 and 11.2.3). In particular, we employ the quasi-nonprecessing inspiral-plunge modes based on the latest spinning, nonprecessing EOB model that was calibrated to NR modes in Ref. [93]. Note that we are not obliged to use in the future quasi-nonprecessing waveforms in the precessing source frame. In fact, using the same EOB dynamics for the comparable-mass binary configurations considered in this paper, we find that the Taylor expanded precessing 2.5PN modes [346] generated in the inertial frame are practically indistinguishable from the EOB modes generated through the frame-rotation procedures described above. However, unlike the factorized resummed modes, Taylor expanded PN modes agree much worse with Teukolsky waveforms in the test-particle limit [101], especially for large spins [119]. We thus expect the precessing model based on factorized-resummed quasi-nonprecessing waveforms to be more reliable when extrapolated beyond the comparable-mass configurations. As soon as factorized EOB modes for precessing spins become available, we shall relax the assumption of using quasi-nonprecessing inspiral-plunge modes [4]. The strategy that we present in this paper is generic and can easily be applied to future calibrations and analytical improvements of the EOB model.

[4]It remains to be investigated, though, whether it is necessary to include precessing effects in the EOB modes decomposed in the precessing source frame to meet more stringent accuracy requirements for advanced LIGO and Virgo searches.

Third, we rotate the quasi-nonprecessing modes from the precessing source frame to the inertial frame whose z-axis coincides with the direction of the total angular momentum $\boldsymbol{J}$ at a time very close to merger when the direction of $\boldsymbol{J}$ is a good approximation to the direction of the spin of the final BH. In this inertial frame we match the inspiral-plunge to merger-ringdown modes following the usual prescription in the EOB approach [93]. After generating inspiral-merger-ringdown modes in this frame, it is straightforward to calculate EOB modes $h_{\ell m}$ in any source frame or EOB polarizations $h_{+,\times}$ in any radiation frame.

11.3 **Precessing effective-one-body model**

In this section we construct a generic, precessing EOB model following the general strategy outlined above — it employs the precessing source frame introduced in Ref. [166] and the quasi-nonprecessing waveforms based on the nonprecessing EOB model developed in Ref. [93].

11.3.1 Effective-one-body dynamics

Since we employ exactly the same EOB dynamics calibrated against NR simulations in Ref. [93], we review only the key ingredients of the dynamics and refer the readers to Ref. [93] for further details.

The EOB dynamics of spinning BH binary systems is obtained solving the

following Hamilton equations

$$\frac{d\boldsymbol{r}}{d\hat{t}} = \{\boldsymbol{r}, \hat{H}_{\rm real}\} = \frac{\partial \hat{H}_{\rm real}}{\partial \boldsymbol{p}}\,, \tag{11.11a}$$

$$\frac{d\boldsymbol{p}}{d\hat{t}} = \{\boldsymbol{p}, \hat{H}_{\rm real}\} + \hat{\boldsymbol{\mathscr{F}}} = -\frac{\partial \hat{H}_{\rm real}}{\partial \boldsymbol{r}} + \hat{\boldsymbol{\mathscr{F}}}\,, \tag{11.11b}$$

$$\frac{d\boldsymbol{S}_1}{dt} = \{\boldsymbol{S}_1, \mu\hat{H}_{\rm real}\} = \mu\frac{\partial \hat{H}_{\rm real}}{\partial \boldsymbol{S}_1} \times \boldsymbol{S}_1\,, \tag{11.11c}$$

$$\frac{d\boldsymbol{S}_2}{dt} = \{\boldsymbol{S}_2, \mu\hat{H}_{\rm real}\} = \mu\frac{\partial \hat{H}_{\rm real}}{\partial \boldsymbol{S}_2} \times \boldsymbol{S}_2\,, \tag{11.11d}$$

where $\hat{t} \equiv t/M$ is the dimensionless time variable, $\hat{H}_{\rm real}$ is the reduced EOB Hamiltonian derived in Refs. [191–193] and reviewed in Sec. IIA of Ref. [93], and $\hat{\boldsymbol{\mathscr{F}}}$ is the reduced radiation reaction force. Following Ref. [102], we use

$$\hat{\boldsymbol{\mathscr{F}}} = \frac{1}{\nu\hat{\Omega}|\boldsymbol{r}\times\boldsymbol{p}|}\frac{dE}{dt}\boldsymbol{p}\,, \tag{11.12}$$

where $\hat{\Omega} \equiv M|\boldsymbol{r}\times\dot{\boldsymbol{r}}|/r^2$ is the dimensionless orbital frequency and dE/dt is the energy flux for quasi-spherical orbits. We use Eq. (11.9) with $\ell \leq 8$, namely

$$\frac{dE}{dt} = \frac{\hat{\Omega}^2}{8\pi}\sum_{\ell=2}^{8}\sum_{m=-\ell}^{\ell} m^2 \left|\frac{\mathcal{R}}{M}h_{\ell m}\right|^2\,. \tag{11.13}$$

Because under a change of frame the $h_{\ell m}$ modes for a given ℓ transform into modes with the same ℓ, Eq. (11.13) is still frame-independent. We insert the quasi-nonprecessing modes $h_{\ell m}$, i.e., the modes decomposed in the precessing source frame aligned with $\boldsymbol{L}_N(t)$, into Eq. (11.13). The quasi-nonprecessing modes can be calculated directly in the inertial frame $\{\boldsymbol{e}_x, \boldsymbol{e}_y, \boldsymbol{e}_z\}$ in which we solve the EOB dynamics. The only difference from the procedure of Ref. [93] is to replace the constant χ_1 and χ_2 with $\chi_1\hat{\boldsymbol{S}}_1(t)\cdot\hat{\boldsymbol{L}}_N(t)$ and $\chi_2\hat{\boldsymbol{S}}_2(t)\cdot\hat{\boldsymbol{L}}_N(t)$.

11.3.2 Initial conditions

For applications in data analysis and comparisons with numerical or analytical waveforms, we need initial conditions that start the orbital evolution with sufficiently small eccentricity at a given orbital separation (or GW frequency) and spins orientation. The analytical quasi-spherical initial conditions proposed in Ref. [102] is a good first approximation.

In the nonprecessing case [91, 93, 239], the residual eccentricity can be further reduced by starting the evolution at a larger separation (smaller GW frequency) and waiting for the orbits to be better circularized by radiation reaction. In the precessing case, however, we can not easily reduce the eccentricity in this way because we need specific spin directions at the initial separation. In order to reduce eccentricity by starting the evolution at a larger separation, we need to figure out what are the spin directions at this larger separation to ensure the desired spin directions at a given (smaller) initial separation. To reach this goal and reduce the eccentricity for quasi-spherical initial conditions we employ the method developed in Ref. [187], which is based on [304, 305] [5]. Thus, we first evolve the binary for a few orbits and estimate the eccentricity through oscillations in orbital frequency Ω and separation r. We then apply corrections to the initial conditions following Eqs. (74) and (75) in Ref. [187]. We repeat these steps until the eccentricity is sufficiently small.

[5] This method has been employed to reduce eccentricity in NR simulations of BH binary systems [186, 210, 253, 307, 406, 407].

11.3.3 Nonprecessing effective-one-body waveforms

The EOB nonprecessing inspiral-plunge modes $h_{\ell m}^{\rm NP,\ insp\text{-}plunge}$ developed in Ref. [93] are given by

$$h_{\ell m}^{\rm NP,\ insp\text{-}plunge} = h_{\ell m}^{\rm F}\, N_{\ell m}\,, \tag{11.14}$$

where $h_{\ell m}^{\rm F}$ are the factorized modes derived in Refs. [99–101], and $N_{\ell m}$ are nonquasicircular (NQC) corrections that model deviations from the quasicircular motion, that is assumed when deriving $h_{\ell m}^{\rm F}$. The factorized modes read

$$h_{\ell m}^{\rm F} = h_{\ell m}^{(N,\epsilon)}\, \hat{S}_{\rm eff}^{(\epsilon)}\, T_{\ell m}\, e^{i\delta_{\ell m}}\, (\rho_{\ell m})^{\ell}\ , \tag{11.15}$$

where ϵ is the parity of the mode. All the factors entering $h_{\ell m}^{\rm F}$ can be explicitly found in the Appendix of Ref. [93]. As discussed above, when using these expressions to generate quasi-nonprecessing modes, the only minor modification we have to take into account is to replace the constant spin magnitudes χ_1 and χ_2 by their time dependent counterparts. More specifically, in the nonprecessing case, the leading order spin-orbit effects in $\rho_{\ell m}$ are parametrized by two linear combinations of the constant dimensionless spin parameters

$$\chi_S \equiv \frac{\chi_1 + \chi_2}{2}\,, \tag{11.16a}$$

$$\chi_A \equiv \frac{\chi_1 - \chi_2}{2}\,. \tag{11.16b}$$

In the precessing case, both χ_S and χ_A become linear combinations of the time varying spin vectors projected along $\hat{\boldsymbol{L}}_N(t)$,

$$\chi_S(t) \equiv \frac{1}{2}\left(\frac{\boldsymbol{S}_1(t)}{m_1^2} + \frac{\boldsymbol{S}_2(t)}{m_2^2}\right)\cdot\hat{\boldsymbol{L}}_N(t)\,, \tag{11.17a}$$

$$\chi_A(t) \equiv \frac{1}{2}\left(\frac{\boldsymbol{S}_1(t)}{m_1^2} - \frac{\boldsymbol{S}_2(t)}{m_2^2}\right)\cdot\hat{\boldsymbol{L}}_N(t)\,. \tag{11.17b}$$

In Ref. [93], the inspiral-merger-ringdown mode $(2,2)$ was calibrated against NR simulations. Studies in the test-particle nonspinning [100] and spinning, nonprecessing [101] cases suggest that the factorized modes $h^{\rm F}_{\ell m}$ are good approximations of the inspiral-plunge modes even without any NQC correction or calibration. Thus, we model the inspiral-plunge $(2,1)$ mode with $h^{\rm F}_{21}$. The $(2,0)$ mode has been computed in PN theory at leading order and its amplitude is $5/14\sqrt{6} \simeq 0.15$ times the amplitude of the leading order $(2,2)$ mode [358]. However, this prediction does not agree with NR results. In fact, we find [408] that for the nonspinning NR simulations of mass ratios $q = 1, 6$ [91], the amplitude of the $(2,0)$ mode during the inspiral is smaller than the one of the $(2,2)$ mode by a factor $\sim 10^3$. Since we do not yet understand the origin of this discrepancy we have decided that in this first investigation we neglect the nonprecessing EOB $(2,0)$ mode.

The NQC correction to the $(2,2)$ mode, N_{22}, is given by

$$\begin{aligned} N_{22} = &\left[1 + \left(\frac{p_{r^*}}{r\,\hat{\Omega}}\right)^2\left(a_1^{h_{22}} + \frac{a_2^{h_{22}}}{r} + \frac{a_3^{h_{22}}}{r^{3/2}} + \frac{a_4^{h_{22}}}{r^2} + \frac{a_5^{h_{22}}}{r^{5/2}}\right)\right] \\ &\times \exp\left[i\frac{p_{r^*}}{r\,\hat{\Omega}}\left(b_1^{h_{22}} + p_{r^*}^2 b_2^{h_{22}} + \frac{p_{r^*}^2}{r^{1/2}} b_3^{h_{22}} + \frac{p_{r^*}^2}{r} b_4^{h_{22}}\right)\right], \end{aligned} \tag{11.18}$$

where the amplitude coefficients $a_i^{h_{22}}$ (with $i = 1...5$) and the phase coefficients $b_i^{h_{22}}$ (with $i = 1...4$) are obtained through the iterative procedure described in Sec. IIB

of Ref. [93]. Since only equal-mass, equal-spin, nonprecessing NR simulations were used to calibrate the EOB model of Ref. [93], we have to map the N_{22} from generic spin configurations to equal-spin, nonprecessing configurations. Without further calibrations, we first adopt a mapping from precessing to nonprecessing configurations that equates the $\chi_S(0)$ and $\chi_A(0)$ of a precessing configuration (defined in Eqs. (11.17a) and (11.17b)) to the constant χ_S and χ_A of a nonprecessing configuration. Then, we apply the mapping from a generic nonprecessing configuration to an equal-spin, nonprecessing configurations as defined in Sec. IVA of Ref. [93].

11.3.4 Precessing source frame

Let $\boldsymbol{e}_3^{L_N}(t) = \hat{\boldsymbol{L}}_N(t)$ be the third (unit) basis vector of the precessing source frame. We solve the other two (unit) basis vectors $\boldsymbol{e}_1^{L_N}(t)$ and $\boldsymbol{e}_2^{L_N}(t)$ by applying the minimal rotation condition. We do it because the latter involves only one differential equation, namely Eq. (11.10), instead of Eqs. (11.5b) and (11.5c) for the precessing convention. Specifically, with the help of the inertial source frame $\{\boldsymbol{e}_x^S, \boldsymbol{e}_y^S, \boldsymbol{e}_z^S\}$, we define

$$\alpha(t) = \arctan\left[\frac{\boldsymbol{e}_3^{L_N}(t)\cdot\boldsymbol{e}_y^S}{\boldsymbol{e}_3^{L_N}(t)\cdot\boldsymbol{e}_x^S}\right], \tag{11.19a}$$

$$\beta(t) = \arccos\left[\boldsymbol{e}_3^{L_N}(t)\cdot\boldsymbol{e}_z^S\right], \tag{11.19b}$$

and solve [6]

$$\dot{\gamma}(t) = -\dot{\alpha}(t)\cos\beta(t)\,. \tag{11.20}$$

Those Euler angles $\alpha(t)$, $\beta(t)$ and $\gamma(t)$ describe the time-dependent rotation from the inertial source frame $\{\boldsymbol{e}_x^S, \boldsymbol{e}_y^S, \boldsymbol{e}_z^S\}$ to the precessing source frame $\{\boldsymbol{e}_1^{L_N}(t), \boldsymbol{e}_2^{L_N}(t), \boldsymbol{e}_3^{L_N}(t)\}$ with the latter satisfying the minimal rotation condition. The only freedom in the definition of the precessing source frame is a constant shift in $\gamma(t)$ that is degenerate with the initial orbital phase.

11.3.5 Precessing effective-one-body waveforms

We build the complete inspiral-plunge-merger-ringdown waveforms in an inertial frame following the usual procedure in the EOB approach [**?**, 61, 62, 91, 93, 236, 239, 283, 285, 286, 322, 395]. More specifically, we join the inspiral-plunge waveform $h_{\ell m}^{\text{insp-plunge}}$ and the merger-ringdown waveform $h_{\ell m}^{\text{merger-RD}}$ at a matching time $t_{\text{match}}^{\ell m}$ as

$$h_{\ell m}^{\text{EOB}}(t) = h_{\ell m}^{\text{inspiral-plunge}}(t)\,\theta(t_{\text{match}}^{\ell m} - t) + h_{\ell m}^{\text{merger-RD}}(t)\,\theta(t - t_{\text{match}}^{\ell m})\,. \tag{11.21}$$

Given the quasi-nonprecessing inspiral-plunge modes $h_{\ell m}^{\text{NP, insp-plunge}}$ decomposed in the precessing source frame and the Euler angles (not necessarily those in Eqs. (11.19a)–(11.20), which are specific to $\{\boldsymbol{e}_x^S, \boldsymbol{e}_y^S, \boldsymbol{e}_z^S\}$) defining the rotation from the precessing

[6] Following Boyle *et al.* [401], we integrate $\gamma(t)$ by parts and implement $\gamma(t) = -\alpha(t)\cos\beta(t) - \int \alpha(t)\dot{\beta}(t)\sin\beta(t)\,dt$ to avoid differentiating $\alpha(t)$, which can be noisy near the coordinate singularities at $\beta(t) = 0$ and $\beta(t) = \pi$. We note that Boyle [402] recently proposed a much more accurate and robust method to integrate $\gamma(t)$ using quaternions.

source frame to any inertial frame, the inspiral-plunge modes in the inertial frame are given by Eqs. (11.7). To study the h_{2m} modes, we need all $\ell = 2$ modes in the precessing source frame. As discussed in Sec. 11.3.3, we employ the calibrated $(2, 2)$ mode of Ref. [93], $h^{\rm F}_{21}$ for the $(2, 1)$ mode, and zero for the $(2, 0)$ mode. In the precessing source frame, since we use quasi-nonprecessing inspiral-plunge modes to approximate precessing modes, we further assume reflection symmetry, which, combined with parity invariance, gives modes with $m < 0$ through $h^{\rm NP,\ insp\text{-}plunge}_{2,-m}(t) = h^{\rm NP,\ insp\text{-}plunge\,*}_{2m}(t)$. Pekowsky *et al.* [68] discussed how this symmetry is broken by precessional effects, giving rise to a contribution to the $(2, 2)$ mode which is odd under reflection. In the only example investigated in Ref. [68], the ratio between the component of the $(2, 2)$ mode of the Weyl scalar $\Psi_{4,22}$ that is odd under reflection and the one that is even under reflection is ~ 0.01, while the ratio between the former and the $(2, 1)$ mode of the Weyl scalar $\Psi_{4,21}$ is ~ 1. Since the Weyl scalar and the metric perturbation are related by $\Psi_{4,\ell m} = \ddot{h}_{\ell m} \simeq m^2\hat{\Omega}^2 h_{\ell m}$ during the inspiral, the odd component of the h_{22}'s amplitude is about a fourth of the h_{21}'s. The odd component of the h_{22}'s amplitude becomes substantial only during the merger and ringdown. Thus, in this first study, we ignore the component of the $(2, 2)$ mode that is odd under reflection when describing the inspiraling waveform in the precessing frame, but we include the odd component when building the merger-ringdown waveform.

It is convenient to choose an inertial frame in which the merger-ringdown waveforms take simple forms. A natural choice is the frame aligned with the spin of the final BH, in which the merger-ringdown waveforms are expressed as linear combinations of the quasinormal modes (QNMs) [**?**, 61, 62, 91, 93, 236, 239, 283, 285,

286, 322, 395]. Barausse *et al.* [372] found strong evidence that the spin of the final BH is aligned with the initial total angular momentum of the binary. Using this assumption they derived accurate formulas for the final spin of a BH formed by merger. The success of their model verifies the PN-motivated assumption that the radiated angular momentum averaged over precessional cycles is almost aligned with the total angular momentum. Thus, the direction of the latter is preserved with high accuracy during the inspiral [396]. Here we employ the formulas in Ref. [372] to predict the magnitude of the spin of the final BH, and we align the final-spin direction with $\boldsymbol{J}(t^{\rm EOB}_{\Omega{\rm peak}})$, which is the total angular momentum at the time the EOB orbital frequency reaches its peak ($t^{\rm EOB}_{\Omega{\rm peak}}$). The time $t^{\rm EOB}_{\Omega{\rm peak}}$ has been adopted in most previous EOB models as the reference time of merger [91, 93, 236, 239, 285, 286]. Without further information from NR simulations of precessing, spinning BHs, we consider $\boldsymbol{J}(t^{\rm EOB}_{\Omega{\rm peak}})$ our best prediction of the final-spin direction. We expect that not a lot of angular momentum is radiated during the swift transition from merger to ringdown [**?**] and the small amount being radiated is likely to be nearly aligned with $\boldsymbol{J}(t^{\rm EOB}_{\Omega{\rm peak}})$. Besides, in the rare case of transitional precession, the assumption of Ref. [372] does not hold anymore, while our choice of $\boldsymbol{J}(t^{\rm EOB}_{\Omega{\rm peak}})$ is still valid.

The inspiral-plunge waveform $h^{\rm insp\text{-}plunge}_{\ell m}$ in the inertial frame aligned with $\boldsymbol{J}(t^{\rm EOB}_{\Omega{\rm peak}})$ contains NQC corrections from the nonprecessing $(2,2)$ mode $h^{\rm NP,\ insp\text{-}plunge}_{\ell m}$. Those corrections are derived based on the assumption that the inspiral-plunge waveforms in the precessing frame are the calibrated nonprecessing waveforms generated with the specific mapping of spin parameters defined in Sec. 11.3.3. Although we expect that such assumption introduces systematic errors in $h^{\rm insp\text{-}plunge}_{\ell m}$, we are not

able to quantify them before comparing $h_{\ell m}^{\text{insp-plunge}}$ with precessing NR waveforms. Therefore, we do not apply any further correction to the inspiral-plunge waveform in this model. This choice also guarantees that $h_{\ell m}^{\text{insp-plunge}}$ modes reduce to the calibrated modes of Ref. [93] in the nonprecessing limit.

The merger-ringdown waveform is built following almost exactly the approach described in Ref. [93]. We first give a brief review of this approach and then describe the differences. The merger-ringdown waveform is modeled by a linear superposition of the QNMs of the final Kerr BH as

$$h_{\ell m}^{\text{merger-RD}}(t) = \sum_{n=0}^{N-1} A_{\ell m n}\, e^{-i\sigma_{\ell m n}(t - t^{\ell m}_{\text{match}})}\,, \tag{11.22}$$

where N is the number of overtones, $A_{\ell mn}$ is the complex amplitude of the n-th overtone of the (ℓ, m) mode, and $\sigma_{\ell mn}$ is the complex frequency of the n-th overtone. The complex frequencies are known function of the mass and spin of the final BH [370]. The mass of the final BH is given in Eq. (8) of Ref. [371]. The spin magnitude of the final BH, as discussed earlier, is given in Eqs. (6), (8) and (10) of Ref. [372]. Following Ref. [93], we replace the highest physical overtone (the 7-th) of the $(2, 2)$ mode with a pseudo QNM whose calibrated complex frequency is given in Eqs. (35a) and (35b) of Ref. [93]. Finally, we fix the complex amplitudes $A_{\ell mn}$ though a matching procedure [91] that imposes a C^1-smooth connection over a time interval $\Delta t^{\ell m}_{\text{match}}$ between the merger-ringdown waveform and the inspiral-plunge waveform, in the inertial frame aligned with $\boldsymbol{J}(t^{\text{EOB}}_{\Omega\text{peak}})$.

In Ref. [93], the matching time $t^{\ell m}_{\text{match}}$ and the time interval $\Delta t^{\ell m}_{\text{match}}$ were calibrated only for the $(2, 2)$ mode. Here we need to specify those quantities also

for the remaining $\ell = 2$ modes. We find that in order to keep the matching procedure stable when the binary is strongly precessing around merger, we have to introduce in $t^{\ell m}_{\rm match}$ and $\Delta t^{\ell m}_{\rm match}$ a dependence on how much the orbital and total angular momentum are misaligned at merger, i.e. on the quantity $\hat{\boldsymbol{L}}(t^{\rm EOB}_{\Omega{\rm peak}}) \cdot \hat{\boldsymbol{J}}(t^{\rm EOB}_{\Omega{\rm peak}})$. More specifically, in strongly precessing cases, the directions of $\boldsymbol{L}(t)$ and $\boldsymbol{J}(t)$ can be very different close to merger. As a consequence, the inspiral-plunge modes in the inertial $\boldsymbol{J}(t^{\rm EOB}_{\Omega{\rm peak}})$-frame can present strong amplitude and frequency oscillations around merger. [Technically those strong oscillations are generated by drastic time-dependent rotations from well-behaved quasi-nonprecessing inspiral-plunge modes as the merger is approached.] Thus, to keep the matching procedure stable in strongly precessing situations we set the matching time $t^{\ell m}_{\rm match}$ earlier and make the matching interval $\Delta t^{\ell m}_{\rm match}$ longer. We choose

$$t^{\ell m}_{\rm match} = t^{22,{\rm Cal}}_{\rm match} - 10M \left(1 - |\kappa_{LJ}(t^{\rm EOB}_{\Omega{\rm peak}})|\right) , \tag{11.23}$$

$$\Delta t^{\ell m}_{\rm match} = \Delta t^{22,{\rm Cal}}_{\rm match} \left(10 - 9|\kappa_{LJ}(t^{\rm EOB}_{\Omega{\rm peak}})|\right) , \tag{11.24}$$

where

$$\begin{aligned} t^{22,{\rm Cal}}_{\rm match} &= t^{\rm EOB}_{\Omega{\rm peak}} - \begin{cases} 2.5M & \chi \leq 0 \\ 2.5M + 1.77M \left(\dfrac{\chi}{0.437}\right)^4 & \chi > 0 \end{cases} , \\ \Delta t^{22,{\rm Cal}}_{\rm match} &= 7.5M \end{aligned} \tag{11.25}$$

are the calibrated values of the $(2,2)$ mode in Ref. [93],

$$\chi = \chi_S + \chi_A \frac{\sqrt{1-4\nu}}{1-2\nu} \tag{11.26}$$

Case	q	χ_1	χ_2	θ_1^S	θ_2^S	ϕ_1^S	ϕ_2^S	$M\Omega_0$	$N_{\rm cyc}$
1	2	0.6	0.6	$\pi/3$	$\pi/3$	0	$\pi/2$	0.0112	77
2	6	0.8 [8]	0.6	$\pi/2$	$2\pi/3$	$\pi/2$	$\pi/2$	0.0112	128
3	3	0.5	0.5	0.5π	0.99π	0.77π	0.31π	0.0177	35
4	5	0.5	0	0.5π	0	-0.79π	0	0.0158	65

Table 11.1: We list the binary parameters and number of GW cycles $N_{\rm cyc}$ of the four precessing EOB waveforms that we consider in Sec. 11.4. Case 3 corresponds to the NR simulation SXS:BBH:0052 of Ref. [67], and case 4 corresponds to SXS:BBH:0058.

is a linear combination of initial spin projections on $\boldsymbol{L}_N$, and

$$\kappa_{LJ}(t^{\rm EOB}_{\Omega{\rm peak}}) = \hat{\boldsymbol{L}}(t^{\rm EOB}_{\Omega{\rm peak}}) \cdot \hat{\boldsymbol{J}}(t^{\rm EOB}_{\Omega{\rm peak}}) \tag{11.27}$$

is the cosine of the opening angle between the orbital and total angular momenta at the reference time of merger $t^{\rm EOB}_{\Omega{\rm peak}}$. When $\kappa_{LJ}(t^{\rm EOB}_{\Omega{\rm peak}}) = 0$, the matching time $t^{\ell m}_{\rm match}$ is $10M$ earlier than that of the aligned case, and the time interval $\Delta t^{\ell m}_{\rm match}$ is 10 times that of the aligned case. The choice of $10M$ and the factor of 10 made in this paper are rather arbitrary. They are based on the only requirement of producing qualitatively sound merger-ringdown waveforms. We verify in Sec. 11.4 and especially in the comparison with NR waveforms in Sec. 11.4.2 that these choices indeed achieve our goal. Further improvements of the matching procedure, which likely go beyond a simple tuning of these parameters [7], will be carried out when more accurate and strongly precessing NR waveforms become available.

[7] The post-merger precession of QNMs observed through NR waveforms in Ref. [409] should be considered, for instance.

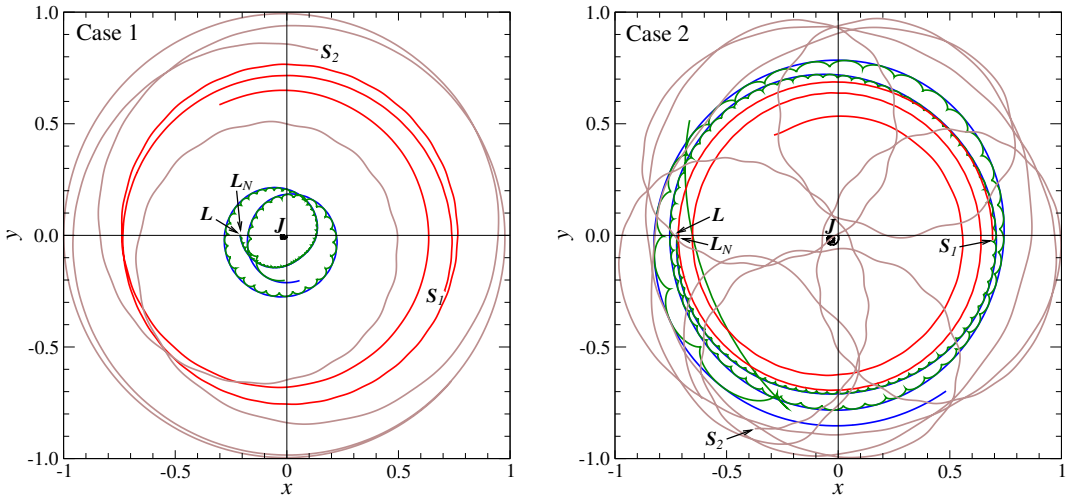

Figure 11.3: We show the projections of $\hat{\boldsymbol{J}}(t)$, $\hat{\boldsymbol{L}}(t)$, $\hat{\boldsymbol{L}}_N(t)$, $\hat{\boldsymbol{S}}_1(t)$, and $\hat{\boldsymbol{S}}_2(t)$ on the x-y plane of the inertial frame whose z-axis is aligned with $\boldsymbol{J}(t^{\rm EOB}_{\Omega{\rm peak}})$. In the top and bottom panels we show trajectories of these unit vectors for cases 1 and 2 of Table 11.1, respectively. The initial point of each trajectory is marked by its name. The trajectory of $\hat{\boldsymbol{J}}(t)$ ends at the origin, by definition. The trajectory of $\hat{\boldsymbol{L}}_N(t)$ follows that of $\hat{\boldsymbol{L}}(t)$ with oscillations due to nutation.

11.4 Comparison between precessing waveforms

We generate four examples of EOB precessing waveforms using the model defined in Sec. 11.3. The first two examples are a $q = 2$ BH binary system exhibiting moderate precession-induced modulations and a $q = 6$ binary system exhibiting strong modulations. The other two examples are chosen among the 171 NR simulations reported in Ref. [67] with the criterion of long and accurate waveforms exhibiting strong modulations. In these cases we compare NR, PN and EOB precessing waveforms. The physical parameters of the four binary configurations are listed in Table 11.1.

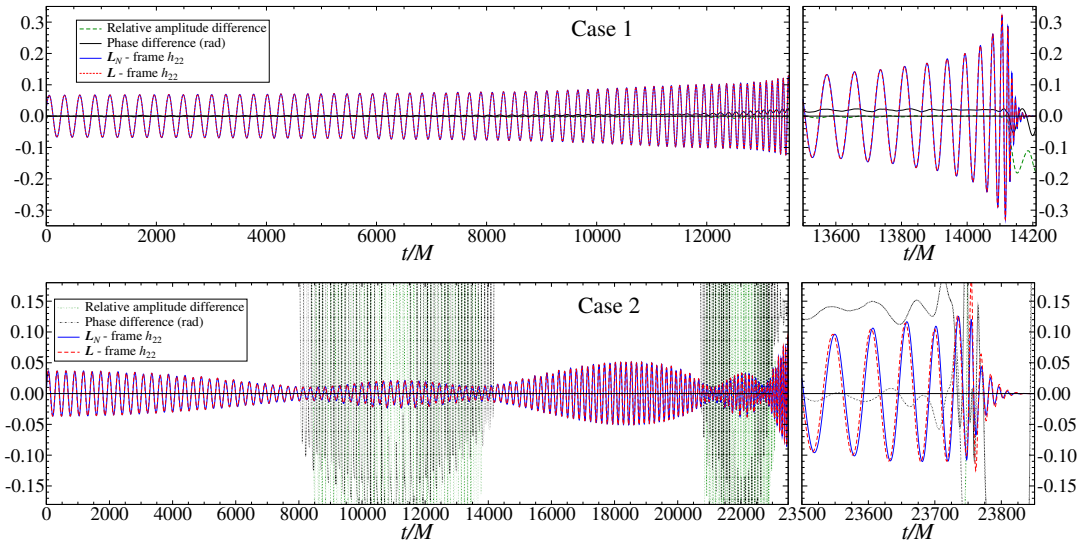

Figure 11.4: We show the $\hat{\boldsymbol{L}}_N(t)$-frame and the $\hat{\boldsymbol{L}}(t)$-frame precessing waveforms, as well as their relative amplitude and phase differences. The top and bottom panels are waveforms for cases 1 and 2 of Table 11.1. The left and right panels show the inspiral and the plunge-merger-ringdown stages of the waveforms, respectively.

11.4.1 Precessing and radiation-axis frames

In Sec. 11.3.4, we have proposed $\hat{\boldsymbol{L}}_N(t)$ and $\hat{\boldsymbol{L}}(t)$ as possible basis vectors for the precessing source frame. In this section, we compare their trajectories and the corresponding precessing waveforms generated through their respective precessing source frames. For convenience, we refer to waveforms generated in these precessing source frames as the $\hat{\boldsymbol{L}}_N(t)$-frame and $\hat{\boldsymbol{L}}(t)$-frame waveforms, respectively. Furthermore, we extract the quadrupole-preferred radiation axis [399] from the precessing waveforms and compare their trajectories with either $\hat{\boldsymbol{L}}_N(t)$ or $\hat{\boldsymbol{L}}(t)$.

Figure 11.3 shows for cases 1 and 2 of Table 11.1 the trajectories of the unit vectors $\hat{\boldsymbol{J}}$, $\hat{\boldsymbol{L}}$, $\hat{\boldsymbol{L}}_N$, $\hat{\boldsymbol{S}}_1$, and $\hat{\boldsymbol{S}}_2$ in the plane perpendicular to $\boldsymbol{J}(t^{\rm EOB}_{\Omega{\rm peak}})$. In both cases,

the BHs complete more than two cycles of precession and the directions of $\boldsymbol{J}(t)$ are well conserved during the entire inspiral phase. All other vectors precess around $\boldsymbol{J}(t)$. These are expected features of the well-known simple-precession picture of spinning binaries in PN theory [396]. Another common feature in both cases is the difference between the trajectories of $\boldsymbol{L}_N(t)$ and $\boldsymbol{L}(t)$. The trajectory of $\boldsymbol{L}_N(t)$ shows nutation at twice the orbital frequency and its average follows the smooth precession trajectory of $\boldsymbol{L}(t)$. From PN theory [153]

$$\boldsymbol{L} = \boldsymbol{L}_N + \boldsymbol{L}_{\rm PN} + \boldsymbol{L}_{\rm SO} + \mathcal{O}(c^{-4})\,, \tag{11.28}$$

where

$$\boldsymbol{L}_{\rm PN} \equiv \boldsymbol{L}_N \left[\frac{1}{2}v^2(1-3\nu) + (3+\nu)\frac{M}{r}\right]\,, \tag{11.29}$$

$$\boldsymbol{L}_{\rm SO} \equiv -\frac{2\mu}{r}\left[(\boldsymbol{S}_{\rm eff}\cdot\hat{\boldsymbol{L}}_N)\hat{\boldsymbol{L}}_N + (\boldsymbol{S}_{\rm eff}\cdot\hat{\boldsymbol{\lambda}})\hat{\boldsymbol{\lambda}}\right]\,, \tag{11.30}$$

with $v \equiv \hat{\Omega}^{1/3}$, $\hat{\boldsymbol{\lambda}} \equiv (\hat{\boldsymbol{L}}_N \times \boldsymbol{r})/r$ and

$$\boldsymbol{S}_{\rm eff} \equiv \left(1+\frac{3m_2}{4m_1}\right)\boldsymbol{S}_1 + \left(1+\frac{3m_1}{4m_2}\right)\boldsymbol{S}_2\,. \tag{11.31}$$

Note that the unit vector $\hat{\boldsymbol{\lambda}}$ instantaneously rotates about $\hat{\boldsymbol{L}}_N$ at the orbital frequency Ω. In addition, $\boldsymbol{L}$ obeys a simple precession equation about $\boldsymbol{J}$, i.e. $\dot{\boldsymbol{L}} \propto \boldsymbol{J}\times\boldsymbol{L}$ (see Eq. (2.13) of Ref. [153]). This, together with Eq. (11.28), implies that $\boldsymbol{L}_N$ cannot simply precess about $\boldsymbol{J}$. When computing $\dot{\boldsymbol{L}}_N$, the spin-orbit term $\boldsymbol{L}_{\rm SO}$ generates contributions of the form

$$(\boldsymbol{S}_{\rm eff}\cdot\dot{\hat{\boldsymbol{\lambda}}})\hat{\boldsymbol{\lambda}} \quad \text{and} \quad (\boldsymbol{S}_{\rm eff}\cdot\hat{\boldsymbol{\lambda}})\dot{\hat{\boldsymbol{\lambda}}}\,, \tag{11.32}$$

which indeed oscillate at twice the orbital frequency, accounting for the nutations seen in Fig. 11.3. Note that this behavior is consistent with the observation of

Ref. [399] while it does not agree with Ref. [410], where the authors used orbit-averaged formula to describe the precession of $\boldsymbol{L}_N(t)$.

The main difference between the two cases is the size of the opening angle between $\boldsymbol{J}(t)$ and $\boldsymbol{L}(t)$ and correspondingly the strength of the orbital precession. In the comparable-mass $q = 2$ case, $\boldsymbol{L}(t)$ always dominates over the BH spins during inspiral and the angle between $\boldsymbol{J}(t)$ and $\boldsymbol{L}(t)$ remains small. The orbital precession is therefore mild. In the $q = 6$ case, on the contrary, the contribution of $\boldsymbol{S}_1(t)$ to $\boldsymbol{J}(t)$ is comparable to that of $\boldsymbol{L}(t)$ initially and becomes more and more dominant. Because of the large opening angle between $\boldsymbol{J}(t)$ and $\boldsymbol{L}(t)$, the direction of $\boldsymbol{L}(t)$ changes more than $\pi/2$ during precession and an initially face-on binary becomes edge-on a few times during the inspiral.

In Fig. 11.4, we compare precessing waveforms generated in the $\hat{\boldsymbol{L}}_N(t)$ and $\hat{\boldsymbol{L}}(t)$ precessing source frames. Considering the oscillatory difference between the trajectories of $\hat{\boldsymbol{L}}_N(t)$ and $\hat{\boldsymbol{L}}(t)$ shown in Fig. 11.3, it is somewhat unexpected that the precessing waveforms agree quite well. In case 1, the waveforms are visually indistinguishable during inspiral — with relative amplitude difference below 1% and phase difference below 0.02 radians. Even in the $q = 6$ case 2, where precession is strong, the waveforms agree reasonably well. Although the relative amplitude and phase differences oscillate strongly when the amplitudes of the waveforms are small, their averages differ only by $< 5\%$ and < 0.15 radians over the $\sim 24\,000M$ long inspiral. The oscillations are due to the precession-induced modulation and are expected to be strong when the orbital plane goes through a nearly edge-on phase, corresponding to small waveform amplitudes.

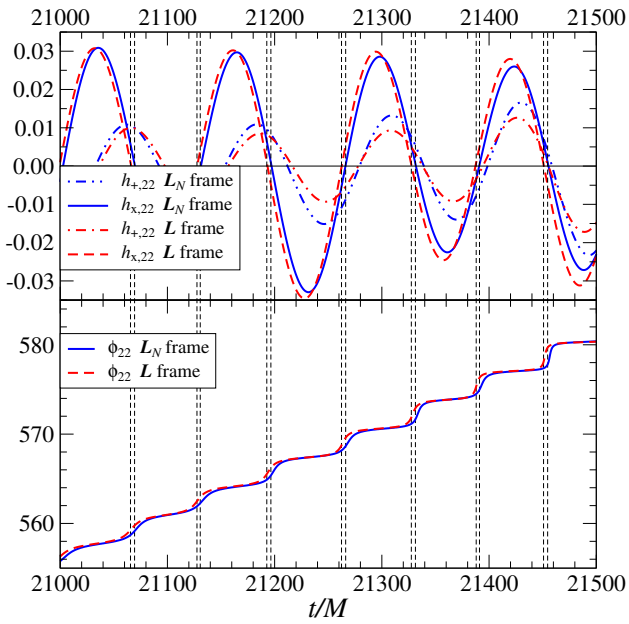

Figure 11.5: For case 2 of Table 11.1, we show the $\hat{\boldsymbol{L}}_N(t)$-frame and $\hat{\boldsymbol{L}}(t)$-frame waveforms in the top panel and their phase evolutions in the bottom panel, over a short time period from $t = 21\,000M$ to $21\,500M$. The vertical lines mark the time when the dominant quadrature (the imaginary part for this specific instance) of any waveform becomes zero. It coincides with the time when the corresponding phase evolution in the bottom panel experiences a rapid growth. The absolute phase values are not relevant.

In Fig. 11.5, we examine closely the waveforms as well as their phase evolutions over a time period of $500M$. The real and imaginary parts of h_{22}, i.e. its $+$ and $\times$ polarizations in the radiation frame, show substantial amplitude difference, implying a deviation from circular polarization due to the orbital plane inclination. The phase evolves most rapidly when the dominant quadrature (the imaginary part in this example) goes through zero. Even a small difference in the times when this happens for the two waveforms leads to a burst of phase difference. Such phase differences can be partly removed by time-shifting the two waveforms, but not

through a phase shift. In spite of these bursts of amplitude and phase difference, the overall agreement of the waveforms is good. The overlaps between the $\hat{\boldsymbol{L}}_N(t)$-frame and $\hat{\boldsymbol{L}}(t)$-frame waveforms, optimized over time and phase of coalescence, are above 0.999 in case 1 and above 0.985 in case 2 [9]. The lower overlaps in case 2 are due to the larger difference between $\hat{\boldsymbol{L}}_N(t)$-frame and $\hat{\boldsymbol{L}}(t)$-frame waveforms during merger and ringdown.

Finally, we examine the preferred radiation axis determined by the waveforms extracted at infinity. Since we developed only the $\ell = 2$ modes in the current EOB model, we calculate the quadrupole-preferred radiation axis [399] with a small modification. In Ref. [399], the quadrupole-preferred axis is determined by maximizing the power in the $(2, 2)$ and $(2, -2)$ modes of the Weyl scalar $\Psi_4(t)$. We determine the quadrupole-preferred axis by maximizing the power in the strain modes $h_{22}(t)$ and $h_{2,-2}(t)$. Specifically, given the $h^{(o)}_{2m}(t)$ modes in an arbitrary original frame, the $h^{(n)}_{2m}(t)$ modes in a new frame are given by Eq. (11.7); so we compute the Euler angles $\alpha(t)$, $\beta(t)$ and $\gamma(t)$ (defining the rotation from the original to the new frame) that maximize the quantity $|h^{(n)}_{22}(t)|^2 + |h^{(n)}_{2,-2}(t)|^2$. The quadrupole-preferred axis is then given by the z-axis of the new frame defined by these Euler angles. We find that the quadrupole-preferred axis computed from $\hat{\boldsymbol{L}}_N(t)$-frame or $\hat{\boldsymbol{L}}(t)$-frame waveforms agrees with $\hat{\boldsymbol{L}}_N(t)$ or $\hat{\boldsymbol{L}}(t)$ to within 0.3° during inspiral. That is to say, the preferred radiation axis determined by EOB waveforms coincides with the reference axis ($\hat{\boldsymbol{L}}_N(t)$ or $\hat{\boldsymbol{L}}(t)$) of the precessing frame determined by the EOB dy-

[9] The overlaps are calculated using the zero-detuned high-power Advanced LIGO noise curve [4] for the range of binary total masses from 20 to $200M_\odot$.

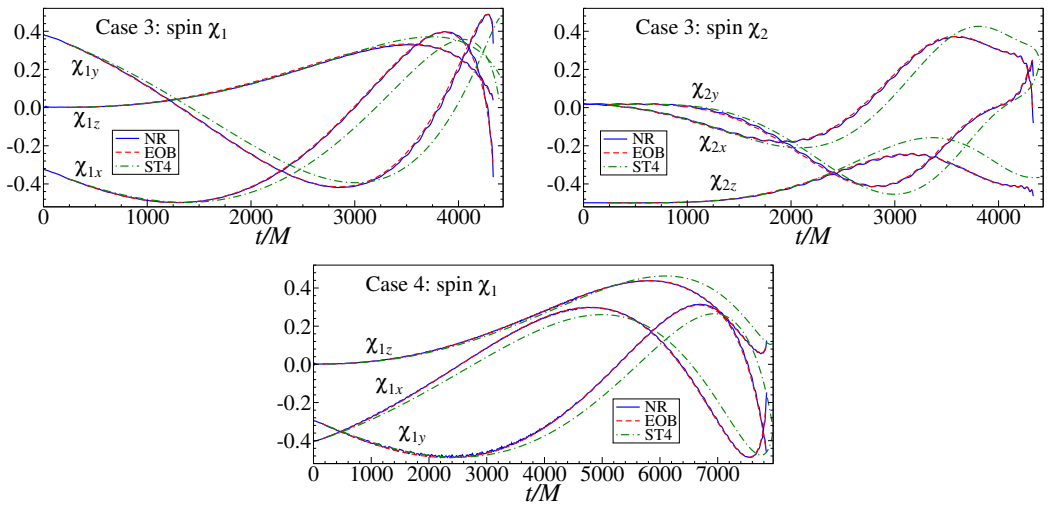

Figure 11.6: We show evolutions of the dimensionless spin vectors $\boldsymbol{\chi}_1 = \boldsymbol{S}_1(t)/m_1^2$ and $\boldsymbol{\chi}_2 = \boldsymbol{S}_2(t)/m_2^2$ of the NR simulation and the EOB and ST4 models. Specifically, we show the projections of $\boldsymbol{\chi}_1$ and $\boldsymbol{\chi}_2$ on the basis vectors of the inertial source frame $\{\boldsymbol{e}_1^S, \boldsymbol{e}_2^S, \boldsymbol{e}_3^S\}$ that is aligned with the initial orbital orientation $[\hat{\boldsymbol{L}}_N]_0$ (see Fig. 11.1). The top two panels show $\boldsymbol{\chi}_1$ and $\boldsymbol{\chi}_2$ for case 3 of Table 11.1. The bottom panel shows $\boldsymbol{\chi}_1$ ($\boldsymbol{\chi}_2 = 0$) for case 4 of Table 11.1. The EOB and ST4 data start at the after-junk-radiation time in the NR simulations, which are $t = 230M$ and $t = 160M$ for cases 3 and 4, respectively.

namics. Therefore, comparisons of preferred radiation axes determined by NR and EOB precessing waveforms will provide direct information for calibrating the precession dynamics, in particular the dynamics of $\hat{\boldsymbol{L}}_N(t)$ and $\hat{\boldsymbol{L}}(t)$, of the EOB model.

11.4.2 Comparison with numerical-relativity waveforms

The precessing EOB model defined in Sec. 11.3 is not calibrated to any precessing numerical simulations. The only nonperturbative information extracted from NR simulations and employed in this precessing EOB model is contained in the spin-

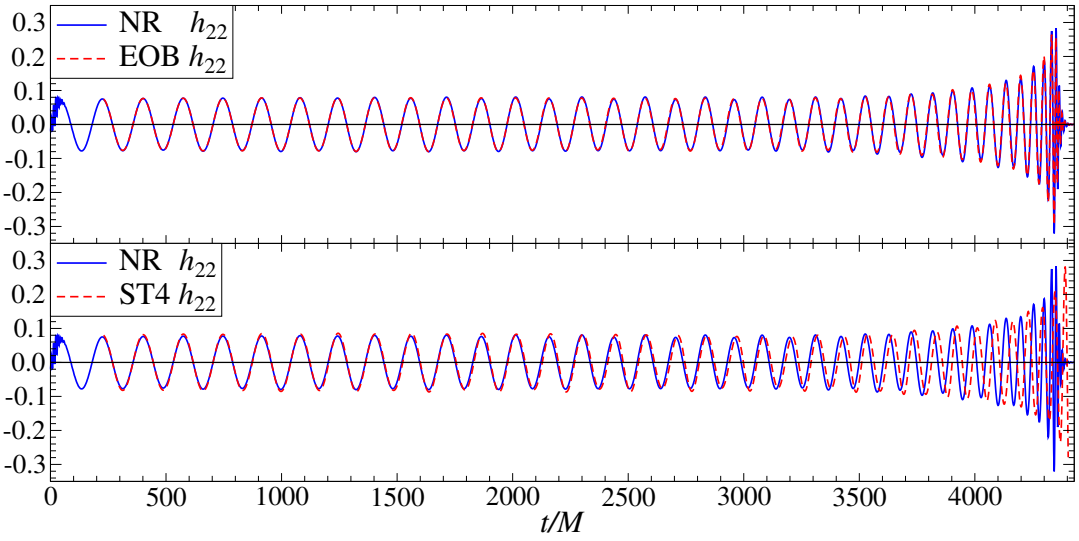

Figure 11.7: We show for case 3 of Table 11.1 the h_{22} mode decomposed in the inertial source frame $\{\boldsymbol{e}_1^S, \boldsymbol{e}_2^S, \boldsymbol{e}_3^S\}$ that is aligned with the initial orbital orientation $[\hat{\boldsymbol{L}}_N]_0$ (see Fig. 11.1). For clarity, we show the NR and EOB h_{22} in the top panel and the NR and ST4 h_{22} in the bottom panel. The EOB and ST4 data start at the after-junk-radiation time of $t = 230M$.

ning, nonprecessing sector, which was calibrated to *only* two equal-mass, spinning, nonprecessing numerical simulations [186] and five nonspinning ones [210, 403] in Ref. [93]. It is therefore highly interesting to compare the EOB precessing waveforms to NR waveforms.

The Caltech-Cornell-CITA collaboration has recently produced a large number of long and accurate waveforms [67]. We choose among them two precessing waveforms that are sufficiently long (~ 35 and ~ 65 GW cycles) and display strong precessional modulations. The physical parameters of these two waveforms are given in the last two rows of Table 11.1. We compare those numerical waveforms also with the PN SpinTaylorT4 (ST4) inspiraling waveforms [166], which are commonly used

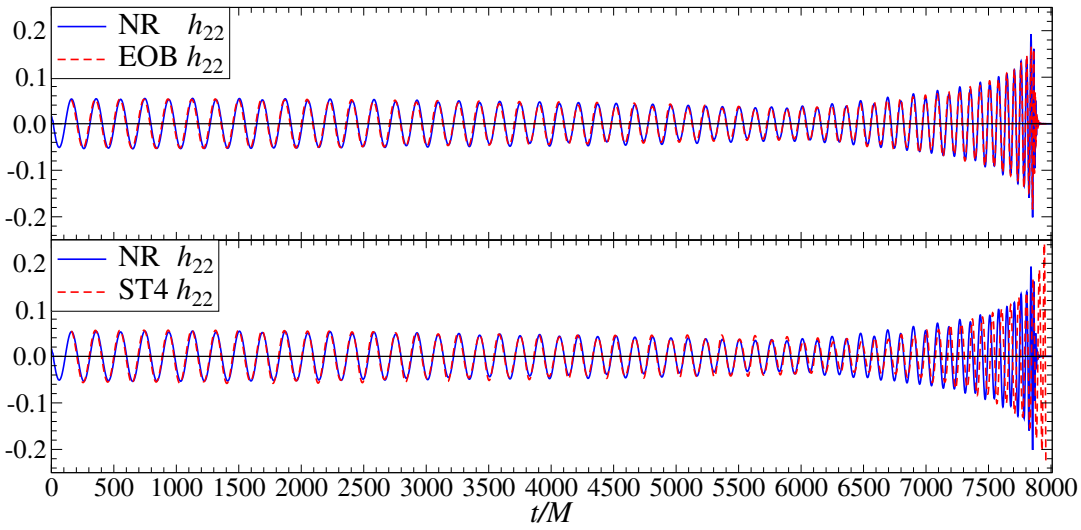

Figure 11.8: We show for case 4 of Table 11.1 the h_{22} mode decomposed in the inertial source frame $\{\boldsymbol{e}_1^S, \boldsymbol{e}_2^S, \boldsymbol{e}_3^S\}$ that is aligned with the initial orbital orientation $[\hat{\boldsymbol{L}}_N]_0$ (see Fig. 11.1). For clarity, we show the NR and EOB h_{22} in the top panel and the NR and ST4 h_{22} in the bottom panel. The EOB and ST4 data start at the after-junk-radiation time of $t = 160M$.

in the literature and in LIGO and Virgo software. We generate the ST4 waveforms at the highest PN order available today, namely spin-amplitude corrections through 1.5PN order [346] [10] and phase corrections through 3.5PN order [156] using the LIGO Algorithm Library [384].

We extract the initial values of $\boldsymbol{S}_1$, $\boldsymbol{S}_2$ and GW frequency from the NR data soon after the junk radiation, which typically carries away unphysical radiation present in the initial data. We then set EOB and ST4 initial conditions using these values and start their evolutions after the junk-radiation time, which is $t = 230M$

[10]The 2PN spin-amplitude corrections have been derived in Ref. [159]. Since they are not yet implemented in any ready-to-use software package and are not crucial for the purpose of our comparisons, we do not include them here.

for case 3 of Table 11.1 and $t = 160M$ for case 4 of Table 11.1. We align the orbital orientation $\hat{\boldsymbol{L}}_N$ at these after-junk-radiation times with the inertial source frame $\{\boldsymbol{e}_1^S, \boldsymbol{e}_2^S, \boldsymbol{e}_3^S\}$ (see Fig. 11.1) and use it as the default frame for our comparisons. Unlike the case of nonprecessing dynamics and waveforms, we must impose specific $\boldsymbol{S}_1$ and $\boldsymbol{S}_2$ directions relative to the initial binary separation vector $\boldsymbol{r}_0$ at a specific after-junk-radiation time. Thus, we *do not* apply any time or phase shifts when comparing numerical and analytical waveforms.

In Fig. 11.6 we compare the evolutions of the dimensionless spin vectors $\boldsymbol{\chi}_1(t) = \boldsymbol{S}_1(t)/m_1^2$ and $\boldsymbol{\chi}_2(t) = \boldsymbol{S}_2(t)/m_2^2$ ($\boldsymbol{\chi}_2 = 0$ for case 4) for the NR, EOB and ST4 dynamics. Quite remarkably, the EOB spins follow the NR ones rather accurately all the way through the inspiral-plunge stage, while the ST4 spins, although capturing the qualitative precessional behavior of the NR ones, show quantitative differences in both the inspiral and precessional time scales.

In Figs. 11.7 and 11.8, we compare NR, EOB and ST4 h_{22} modes decomposed in the inertial source frame $\{\boldsymbol{e}_1^S, \boldsymbol{e}_2^S, \boldsymbol{e}_3^S\}$. Since the source frame is aligned with the initial orbital orientation $[\hat{\boldsymbol{L}}_N]_0$ and the binary orbit precesses only moderately in case 3, there are only moderate modulations on h_{22} in this case. The modulations in case 4 are strong, though. In both cases, the agreement between NR and EOB h_{22} modes is remarkable. Their amplitudes agree quite well and their phases, aligned at the initial time, differ by only ~ 0.2 rad at merger, i.e., at the peak of the NR (2,2) mode. The agreement between NR and ST4 h_{22} modes, although not comparable with the agreement between NR and EOB, is also very good. Even though the amplitudes differ by $\sim 10\%$ during the inspiral, because amplitude corrections are

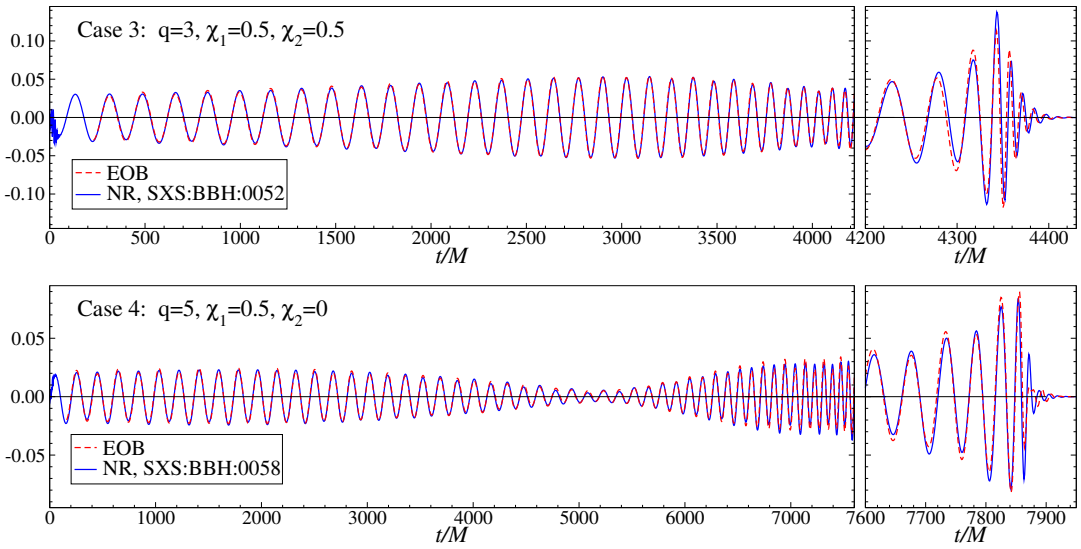

Figure 11.9: We show for cases 3 and 4 of Table 11.1 the GW polarization h_+, containing contributions from $\ell = 2$ modes, that propagates along a direction $\hat{\boldsymbol{N}}$ specified by spherical coordinates $\theta = \pi/3$ and $\phi = \pi/2$ associated with the inertial source frame $\{\boldsymbol{e}_1^S, \boldsymbol{e}_2^S, \boldsymbol{e}_3^S\}$. The EOB waveforms start at the after-junk-radiation times of $t = 230M$ and $t = 160M$, respectively.

known only through 1.5PN order in the spinning case [346], their phases agree quite well for tens of cycles but start departing from each other 10 GW cycles before merger. Quite interestingly, we have found that using the newly available 3.5PN spin-orbit effects [156] in the phasing of ST4 improves the agreement with the NR waveforms. If we were using the 2.5PN phasing, the end of the inspiral would occur $\sim 460M$ $(960M)$ instead of $\sim 60M$ $(140M)$ after the merger of the NR waveform, for case 3 (4). Moreover, we find for cases 3 and 4 that when we align the 3.5PN and NR phasing at the after–junk- radiation time, they accumulate a difference of 1 GW cycle only 1 cycle before merger. By contrast the 2.5PN phasing differs from the NR phasing by 1 GW after 28 (37) GW cycles [or 6 (16) GW cycles before merger]

for case 3 (4).

The agreement between NR and EOB modes $(2,1)$ and $(2,0)$ modes are also very good. Rather than the modes, we show in Fig. 11.9 the NR and EOB polarizations $h_+(t)$ given by Eq. (11.3). Since only the $\ell = 2$ modes are available in the current precessing EOB model, we limit the summation over ℓ to only $\ell = 2$. To include substantial contributions from all $\ell = 2$ modes, we choose $\theta = \pi/3$ and $\phi = \pi/2$ for the direction of GW propagation $\boldsymbol{N}$ (see Fig. 11.1). As expected from the very good agreement of the individual modes, the NR and EOB polarizations also agree remarkably.

Finally, we measure the difference between EOB and NR polarizations with the *unfaithfulness* [411], defined as

$$\bar{\mathcal{F}} = 1 - \max_{t_c,\phi_c,\psi} \frac{\langle h_{\rm NR}|h_{\rm EOB}\rangle}{\sqrt{\langle h_{\rm NR}|h_{\rm NR}\rangle\langle h_{\rm EOB}|h_{\rm EOB}\rangle}}\,, \tag{11.33}$$

where the EOB waveform of the detector response is

$$h_{\rm EOB}(t;t_c,\phi_c,\psi,\boldsymbol{\lambda}) \propto \cos\psi h_{\rm EOB,+}(t;t_c,\phi_c,\boldsymbol{\lambda}) + \sin\psi h_{\rm EOB,\times}(t;t_c,\phi_c,\boldsymbol{\lambda})\,, \tag{11.34}$$

and the maximization is over the time and phase of coalescence t_c and ϕ_c, as well as the polarization angle ψ that combines the $+$ and $\times$ polarizations in the radiation frame. We do not optimize over the physical binary parameters $\boldsymbol{\lambda}$, i.e.,we use the same $\boldsymbol{\lambda}$ in $h_{\rm NR}$ and $h_{\rm EOB}$. Note that since we include modes with different m, ϕ_c and ψ are no longer degenerate and both of them have to be maximized over. We define the inner product between two waveforms through the following integral in

the frequency domain

$$\langle h_1, h_2 \rangle \equiv 4\mathrm{Re} \int_0^\infty \frac{\tilde{h}_1(f)\tilde{h}_2^*(f)}{S_h(f)} df \,, \tag{11.35}$$

where $\tilde{h}_1(f)$ and $\tilde{h}_2(f)$ are frequency domain waveforms and $S_h(f)$ is the noise power spectral density of the detector. We employ the zero-detuned high-power advanced LIGO noise curve `ZERO_DET_HIGH_P` given in [4]. The NR waveforms, although very long, cover the entire advanced LIGO frequency band only for $M \geq 100M_\odot$. Thus, to reduce artifacts when considering binaries with $M < 100M_\odot$, we taper both ends of the NR and EOB waveforms using the Planck-taper window function [382] (see Ref. [91] for details). In Fig. 11.10, we show the EOB unfaithfulness when the total mass M varies between $20M_\odot$ and $200M_\odot$. We choose the same direction of GW propagation $\boldsymbol{N}$ as is considered in Fig. 11.9, namely $\theta = \pi/3$ and $\phi = \pi/2$.

For each waveform we estimate the numerical error in the unfaithfulness results of Fig. 11.10 by calculating the unfaithfulness of the EOB waveform with two numerical waveforms: the extrapolated high-resolution waveform shown in Fig. 11.9 and the outermost finite-radius high-resolution waveform. We use the difference between these unfaithfulness results to estimate the extrapolation error. We might estimate the finite resolution errors in the same way by calculating the unfaithfulness of the EOB waveform with the extrapolated high- and medium-resolution numerical waveforms. However, medium resolution simulations for these two cases are not available, but we expect from previous studies that errors due to resolution are smaller than errors due to extrapolation [91].

Since the unfaithfulness of EOB waveforms is below $\sim 2\%$, we expect that

the ineffectualness, which measures the difference between EOB and NR waveforms when minimizing also over the binary parameters $\boldsymbol{\lambda}$, will be below 1% (with a loss of event rates less than 3%). Thus, for those two precessing binary configurations, the EOB waveforms are sufficiently accurate for detection with advanced LIGO detectors.

Although these very encouraging results refer only to two precessing binary configurations, they strongly suggest that the approach we have proposed for modeling precessing compact binaries within the EOB model is bound to succeed. A more comprehensive and careful comparison of the EOB model with a larger number of accurate NR simulations will be carried out in the near future using the entire catalog of simulations in Ref. [67].

11.5 Conclusions

So far, the EOB modeling of GWs emitted from compact binaries has focused primarily on nonprecessing binary configurations [91, 93, 236, 239, 283, 285, 286, 322, 395]. Nonspinning EOB waveforms have been employed in the first searches of GWs from high-mass binary BHs with LIGO and Virgo detectors [352, 353, 387]. Recently, studies carried out within the NRAR collaboration [66] have shown that nonprecessing EOB waveforms originally calibrated to seven NR waveforms [186,210, 403] in Ref. [93] match very well also tens of new NR waveforms produced within the NRAR collaboration. The next, challenging task is to achieve a similar success also for generic, spinning binary configurations. In this paper we have started addressing

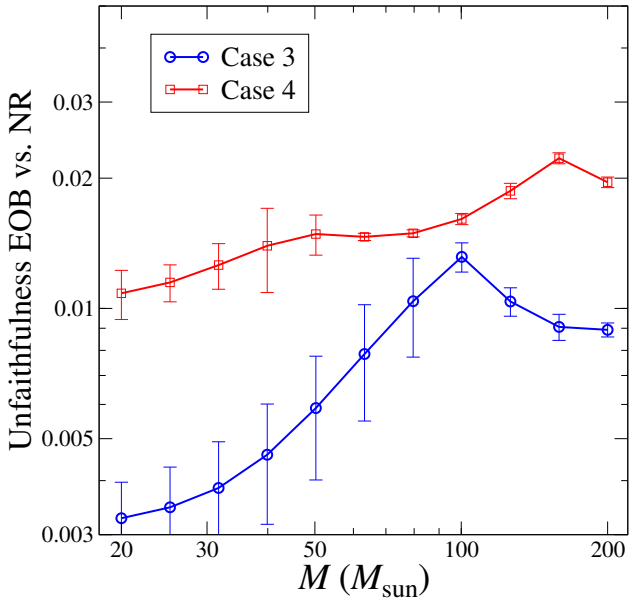

Figure 11.10: Unfaithfulness of the EOB waveforms when compared to NR waveforms as a function of the total binary mass. Shown are cases 3 and 4 of Table 11.1. The error bars are estimates of numerical errors. The direction of GW propagation $\hat{\boldsymbol{N}}$ is specified by the spherical coordinates $\theta = \pi/3$ and $\phi = \pi/2$.

this important problem.

Building on previous work [93,102,166,191–193,239], we have proposed a strategy to generate EOB precessing waveforms. The procedure employs the precessing convention of Ref. [166] that minimizes the precession-induced modulations in the waveform's phase and amplitude, and an inertial frame aligned with the spin of the final BH where the matching between the inspiral-plunge and merger-ringdown EOB waveforms is carried out.

When spins are aligned or antialigned with the orbital angular momentum, the EOB precessing waveforms that we have built reduce to the nonprecessing EOB waveforms calibrated to seven nonprecessing NR waveforms in Ref. [93]. Since the

factorized energy flux is not yet available for precessing spins, we have included in the radiation-reaction force of the EOB dynamics only spin couplings whose projection along the orbital angular momentum is different from zero. This limitation will be relaxed in the future as soon as the radiation-reaction sector of the EOB model is improved. Furthermore, we have limited this first study to the EOB $\ell = 2$ modes.

Without recalibrating the EOB precessing waveforms, we have then compared them to two, long, strongly precessing NR waveforms that were recently produced in Ref. [67]. We have found a remarkable agreement both for the dynamics, that is the spins' components, and the gravitational polarizations. In particular, when using the advanced-LIGO noise spectral density, the mismatches between the EOB and NR waveforms for binary masses 20–200$M_\odot$ are below 2% when maximizing only on the time and phase at coalescence and on the polarization angle. Although those results only refer to two binary configurations, they are very encouraging and suggest that the EOB precessing model developed here is an excellent starting point for building a generic, spinning EOB model for advanced LIGO and Virgo searches. We have also compared the two NR waveforms to PN ST4 waveforms that are largely used in the literature and in LIGO and Virgo software. We have found that the PN waveforms at 3.5PN order agree very well with NR waveforms for several GW cycles, and accumulate a phase difference of ~ 6 rad, starting about 10 GW cycles before merger.

Finally, several analyses were left out in this first study of precessing waveforms. They include (i) a more detailed comparison between spin variables in the numerical simulations and analytical models, (ii) the extension of precessing wave-

forms to modes higher than $\ell = 2$, (iii) a more systematic way of identifying the initial conditions in the numerical and analytical waveforms, and (iv) the inclusion of resolution errors when estimating numerical errors. We defer those important extensions to a future publication where many more NR waveforms will be also analysed.

Chapter 12: **Conclusions and future work**

In this thesis, we presented recent work done at the interface between analytical and numerical relativity that aimed at improving models of the gravitational-wave emission produced by the coalescence of spinning, stellar-mass black-hole binaries. This research was fueled by the approaching era of advanced ground-based gravitational-wave detectors, such as advanced LIGO and Virgo. Binaries of compact objects (black holes and neutron stars) are among the most promising sources accessible to these experiments. Compact binaries can reach an astounding luminosity in gravitational waves, and can be searched for exploiting matched filtering. Indeed, knowing in advance what plausible signals may be buried under the instrumental noise greatly enhances the horizon reach of the detectors to a significant portion of the local Universe, thus increasing the expected detection rate. The necessity of approximate, yet accurate, waveform models stems from two practical considerations: on the one hand, solving the general-relativistic 2-body problem with numerical techniques still has a huge computational cost; on the other hand, large banks of template waveforms will be needed for data analysis; the templates will have to cover the space of physical parameters of the source, in the case of black-hole binaries: masses and spins. Analytical models are orders of magnitude

faster to compute than numerical-relativity simulations, and, at the same time, can be sufficiently accurate for the purpose of detection (*effectual* models) or estimation of the parameters of the source (*faithful* models). Moreover, analytical models help build a physical intuition about the phenomenon of coalescence.

In the Overview we briefly recalled the astrophysical scenarios which may lead to the formation of black-hole binaries: the evolution of stellar binaries and dynamical capture events in dense stellar clusters. Many uncertainties exist, and population synthesis studies predict wide distributions of physical parameters for these binaries. This uncertainty is reflected in the estimated detection rates. Realistically, advanced LIGO should be able to see 20 black-hole binary inspirals per year (with an uncertainty of about two orders of magnitude), reaching out to a distance of about 2 Gpc for a threshold SNR of 8.

The specificity of stellar-mass black hole binaries as sources of gravitational waves for advanced detectors lies in the possibility of accessing the fully relativistic regime of the merger, thanks to the large total mass of these systems ($\sim 5-40M_{\odot}$) that puts them right in the middle of the best sensitivity region of the interferometers, at frequencies around a few hundred Hz.

We also discussed how important spin effects are in the description of black-hole binaries, as they are responsible for phenomena such as: (i) the slower or faster coalescence mainly because of spin-orbit couplings; (ii) precession of the orbital plane, whenever the black-hole spins are not aligned/antialigned with the orbital angular momentum; (iii) increased loudness of the gravitational-wave signal when the spins have large magnitude, which directly affects the horizon distance of the

detectors.

In this thesis, we worked within the effective-one-body (EOB) formalism, wherein the real problem of two coalescing black holes is mapped to the effective problem of a spinning test particle moving in a deformed Kerr spacetime, the deformation parameter being the symmetric mass ratio of the binary. The EOB model resums both the conservative and dissipative post-Newtonian (PN) dynamics, thus extending their validity into the deeply relativistic regime. The inspiral-plunge waveform is directly sourced by the EOB orbital dynamics until the effective particle reaches the light ring. After this point, a superposition of quasinormal modes (QNMs) describes the merger-ringdown signal, which characterizes the relaxation of the remnant black hole to a Kerr geometry.

In the small mass-ratio limit, we used black-hole perturbation theory to compute the gravitational-wave emission of a plunging particle in Kerr spacetime, with the goal of understanding strong-field features of the coalescence that have been exploited to extend comparable-mass EOB models to any mass ratio and spin magnitude. In particular, in Chapter 4 we sourced the time-domain Teukolsky equation with plunging equatorial trajectories whose radiation reaction was computed from the frequency-domain Teukolsky equation for circular orbits. We characterized the main features of the plunge-merger-ringdown of the leading multipolar modes as functions of the Kerr spin of the background: (i) we found a remarkable simplicity and flattening of the modes as the Kerr spin becomes extremal; (ii) we quantitatively studied the QNM mixing, and explained it in terms of a basis effect (i.e., the conversion from spheroidal to spherical harmonics) and an orbital effect (i.e., the

inversion of the plunge for retrograde orbits). In Chapter 5 we computed the gravitational energy flux that is absorbed by the horizon of a Kerr black hole perturbed by an orbiting particle on a circular, equatorial orbit. We also proposed an analytical model of the absorbed flux that resums the PN formulae, thus incorporating two important strong-field features: (i) the zero of the flux for particles orbiting at the frequency of the horizon; (ii) the divergence at the light ring, related to the divergence of the energy-momentum tensor of the perturbing particle.

In the comparable-mass regime, we calibrated a spinning EOB model to state-of-the-art numerical-relativity simulations. The calibrations of the model to nonprecessing simulations were presented in Chapters 7 and 8. The calibrations used the longest and most accurate numerical waveforms that were available at the time. In particular, the model of Chapter 8 used runs with mass ratios from 1 to 8, and spin magnitudes up to 0.98 in the equal-mass limit. Those waveforms were generated by the SXS Collaboration using the SpEC code. The main result of these calibrations was the development of faithful inspiral-merger-ringdown waveforms for nonprecessing stellar-mass black-hole binaries with any mass ratio and spin magnitude. The unfaithfulness was found to be within 1% for the configurations used in the calibration, entailing a negligible loss in detection rate due to modeling error.

We tested the reliability of the calibrated spinning, nonprecessing EOB model of Chapter 7 in two ways. In Chapter 9 we compared the model to new numerical-relativity simulations produced by the NRAR Collaboration, as a way of testing it outside the range of mass ratios and spin magnitudes used in its calibration. In fact, because of the limited availability of long and accurate simulations at the time, the

model was tuned to only 5 nonspinning waveforms up to mass ratio 6, and 2 equal-mass, equal-spin waveforms with spin ± 0.44. We found that the model was effectual (i.e., its ineffectualness was below 3%) for all the nonprecessing black-hole binaries considered, including a nonspinning run with mass ratio 10, and spinning runs with spin magnitudes exceeding 0.5. In Chapter 10 we addressed the question of how stable the calibration of the nonspinning sector is when longer and longer numerical-relativity waveforms are employed. We found that, when the mass ratio is below 8, EOB waveforms calibrated over the 30 cycles before merger are indistinguishable from those calibrated over 60 cycles up to an effective SNR of 110. We also argued that the current calibration of the nonspinning EOB model is sufficiently accurate for advanced-LIGO parameter estimation when the effective SNR is below 20, the mass ratio is below 5, and the total mass is larger than $20M_{\odot}$.

Additional confirmation of the soundness of the EOB formalism in the description of the general-relativistic 2-body dynamics came from the study of the periastron advance in nonspinning black-hole binaries, discussed in Chapter 3. This phenomenon is the generalization of the Mercury-type precession encountered in the test-particle limit to comparable-mass compact objects. We found that the EOB prediction for the periastron advance is in excellent agreement with numerical relativity, even without including information from numerical relativity, in contrast with the PN prediction, that quickly goes outside the numerical error bars toward coalescence.

The calibrated nonprecessing models of Chapters 7 and 8 constitute the starting point and underlying ingredient of the precessing EOB model discussed in Chap-

ter 11. Previous studies based on PN templates had pointed out that the multipolar modes are similar to nonprecessing ones when computed in a specific reference frame (known as "precessing frame") that tracks the precession of the orbital plane of the black-hole binary. Working in the precessing frame has several advantages: (i) amplitude and phase modulations caused by precession are minimized; (ii) a clean mode hierarchy exists; (iii) to a good approximation, one can exploit results obtained for nonprecessing systems. We implemented this idea in the construction of the EOB precessing waveforms by assuming that in the precessing frame the binary emits gravitational-wave modes given by our calibrated nonprecessing models. The validity of this approach was confirmed by comparison with the 2 longest and most accurate numerical simulations of precessing binaries that were available: in both cases, the EOB waveforms were effectual.

All the models developed in this thesis have been or are being implemented into the Algorithm Library of the LIGO Scientific Collaboration, in order to make them available to experimenters. In particular, at the time of writing, the nonprecessing model of Chapter 8 has been chosen by the Compact Binary Coalescence Group of the LIGO Scientific Collaboration for searches of binary black holes with advanced LIGO during the first scientific run of Fall 2015.

The generation of the numerical-relativity simulations that we eventually exploited in our modeling relied on realistic, quasicircular initial conditions. In fact, stellar-mass black-hole binaries will radiate any orbital eccentricity well before entering the sensitivity band of ground-based interferometers. In Chapter 6 we discussed the development of an eccentricity-removal algorithm for the initial conditions of

precessing binaries that is now integral part of the SpEC code, used by the SXS Collaboration.

In the near future, the work presented in this thesis will be completed and extended in several directions. I will compare the precessing EOB model of Chapter 11 to tens of numerical-relativity simulations of the SXS Collaboration with the goal of confirming its reliability over a larger portion of the parameter space. I will extend the EOB model to neutron-star/black-hole binaries by including tidal effects into the inspiral and modeling the post-merger signal, which can significantly differ from that of black-hole binaries. In the test-particle limit, it will be important to generalize our findings to precessing, plunging orbits in Kerr with the goal of extracting strong-field information that can improve the comparable-mass modeling.

Chapter A: Input values for non-quasicircular corrections to EOB merger waveforms in the small mass-ratio limit

In this appendix, we provide useful information about the Teukolsky merger waveforms that can be exploited in the construction of comparable-mass, spinning, nonprecessing EOB models that span the entire physical parameter space, as discussed in Sec. 4.6. We omit spin 0.99 because it is difficult to determine its peak positions $t^{\ell m}_{\rm peak}$, due to the extreme flatness of the mode amplitudes, as shown in Sec. 4.4. We also omit the negative spins for the $(2,1)$ and $(3,2)$ modes since, as discussed in Sec. 4.5.2, QNM mixing has an early onset (around the turning point of the azimuthal motion for $(2,1)$; slightly later than that for $(3,2)$), and affects the peak of the waveform; it is therefore ambiguous where to measure the input values for these cases.

In Fig. A.1 we show how the time delay between the orbital frequency peak $t^{\Omega}_{\rm peak}$ and the Teukolsky amplitude peak $t^{\ell m}_{\rm peak}$ changes with the Kerr spin. As pointed out in Sec. 4.4, the amplitudes tend to peak earlier and earlier as q increases, well before the ISCO when $q > 0.8$. This creates difficulties when applying the non-quasicircular procedure to correct the EOB merger waveforms at $t^{\ell m}_{\rm peak}$, as elucidated

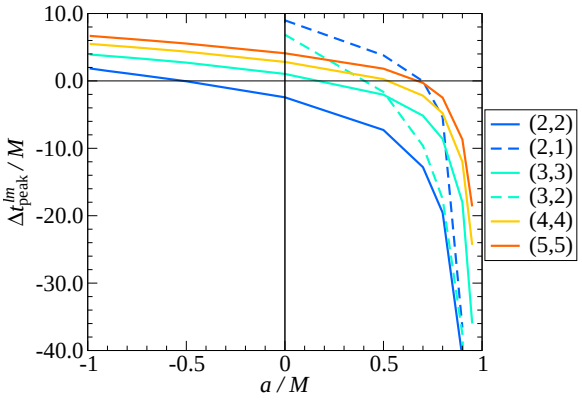

Figure A.1: Time delay between the orbital frequency peak and the Teukolsky amplitude peak, defined as $\Delta t^{\ell m}_{\rm peak} \equiv t^{\ell m}_{\rm peak} - t^{\Omega}_{\rm peak}$. The value of $\Delta t^{22}_{\rm peak}$ for spin 0.95 is $-103M$, and exceeds the range of the plot.

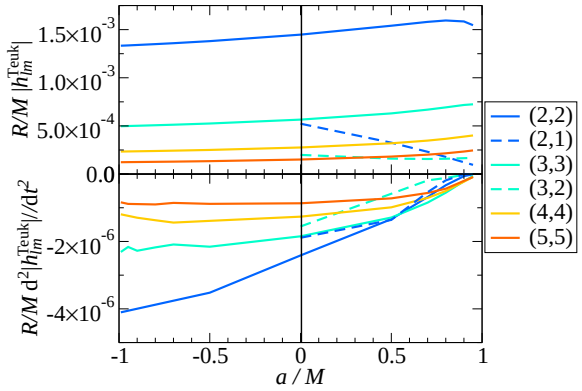

Figure A.2: Amplitude and curvature of the Teukolsky waveforms at their amplitude peak. R is the distance to the source.

in Sec. 4.6. In fact, in the comparable-mass EOB model of Ref. [70], we chose a delay $\Delta t^{22}_{\rm peak}$ which decreases after spin 0.8, thus departing from the blue curve in Fig. A.1.

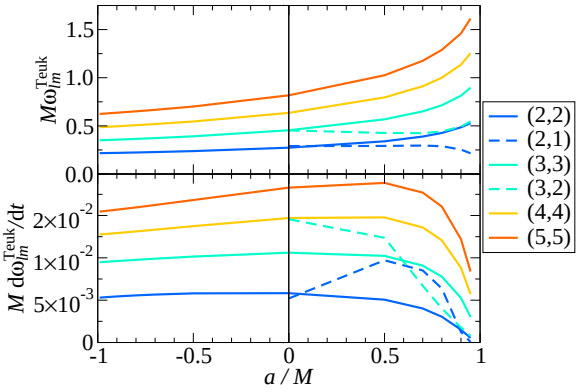

Figure A.3: Frequency and derivative of the frequency of the Teukolsky waveforms at their amplitude peak.

In Figs. A.2 and A.3 we plot the input values computed at the time $t^{\ell m}_{\rm peak}$ when the Teukolsky amplitudes peak. The largest numerical uncertainties are visible on the curvature, but, as it turns out, the EOB waveforms are only mildly sensitive to such input value; in order to get a good modeling, the crucial input values are rather the values of the amplitude and the frequency.

Chapter B: The Teukolsky-equation source term for light-ring orbits

In this appendix, we describe how the divergence in fluxes at the light ring enters through the Teukolsky equation's source term, as well as a simple modification that allows us to factor it from the flux computation. This divergence-free form proved useful for understanding how fluxes behave in the extreme strong field.

We begin with the stress-energy tensor of a body with rest mass μ moving in the Kerr spacetime,

$$T_{\alpha\beta} = \mu \int u_\alpha u_\beta \, \delta^{(4)}[x^\mu - z^\mu(\tau)] \, d\tau \; . \tag{B.1}$$

Here, x^μ is a general spacetime coordinate, and $z^\mu(\tau)$ is the worldline followed by the moving body; $u^\alpha = dz^\alpha/d\tau$, where τ is proper time along the worldline. The delta function is normalized so that

$$\int \sqrt{-g} \, \delta^{(4)} \, d^4x = 1 \; , \tag{B.2}$$

where $g = -\Sigma \sin^2\theta$ is the determinant of the Kerr metric, and $\Sigma = r^2 + q^2 M^2 \cos^2\theta$.

In a typical particle analysis, we integrate Eq. (B.1) immediately to obtain

$$T_{\alpha\beta} = \mu \frac{u_\alpha u_\beta}{\Sigma \sin\theta (dt/d\tau)} \, \delta[r - r(t)] \, \delta[\theta - \theta(t)] \, \delta[\phi - \phi(t)] \; . \tag{B.3}$$

This is well behaved except when $dt/d\tau \to 0$. This occurs at the light ring, and explains why gravitational-wave fluxes diverge as the light ring is approached.

Let us rewrite Eq. (B.1) using $d\lambda = d\tau/\mu$, in anticipation of taking the limit $\mu \to 0$. Using the fact that $dz^\alpha/d\lambda = p^\alpha$, the momentum of the body, we find

$$T_{\alpha\beta} = \frac{1}{\mu}\int p_\alpha p_\beta\, \delta^{(4)}[x^\mu - z^\mu(\lambda)](\mu\, d\lambda) = \int p_\alpha p_\beta\, \delta^{(4)}[x^\mu - z^\mu(\lambda)]\, d\lambda\ . \tag{B.4}$$

This is easily integrated, and we find

$$\begin{aligned} T_{\alpha\beta} &= \frac{p_\alpha p_\beta}{\Sigma \sin\theta\, p^t}\, \delta[r - r(t)]\, \delta[\theta - \theta(t)]\, \delta[\phi - \phi(t)] \\ &= \frac{p_\alpha p_\beta}{\Sigma\, p^t}\, \delta[r - r_{\rm orb}]\, \delta[\theta - \pi/2]\, \delta[\phi - \phi(t)]\ . \end{aligned} \tag{B.5}$$

On the second line, we specialize to a circular orbit of radius $r = r_{\rm orb}$ in the equatorial plane. Equation (B.5) is well behaved as $\mu \to 0$.

The momenta that appear in this stress-energy tensor are determined by the geodesic equations for Kerr orbits [122]

$$\Sigma\, p^t = \frac{(r^2 + q^2M^2)}{\Delta}\left[E(r^2 + q^2M^2) - qML_z\right] + qM(L_z - qME)\ , \tag{B.6}$$

$$\Sigma\, p^\phi = \frac{qM}{\Delta}\left[E(r^2 + q^2M^2) - qML_z\right] + L_z - qME\ , \tag{B.7}$$

$$(\Sigma\, p^r)^2 = \left[E(r^2 + q^2M^2) - qML_z\right]^2 - \Delta\left[\mu^2 r^2 + (L_z - qME)^2\right]\ . \tag{B.8}$$

We have specialized to $\theta = \pi/2$. This allows us to set the Carter constant $Q = 0$ and to neglect p^θ.

Equations (B.6) and (B.7) are proportional to the orbiting body's rest mass μ; Eq. (B.8) is proportional to μ^2. In most Teukolsky solvers, we factor out the overall factors of μ, and thereby express everything on a per-unit-rest-mass basis.

As the light ring is approached, the energy and angular momentum per unit rest mass diverge. In anticipation of this, let us instead divide by the orbital energy E. Defining $\hat{p}^\mu \equiv p^\mu/E$, the stress-energy tensor is written

$$\begin{aligned} T_{\alpha\beta} &= E\,\frac{\hat{p}_\alpha \hat{p}_\beta}{\Sigma \sin\theta\, \hat{p}^t}\,\delta[r-r(t)]\,\delta[\theta-\theta(t)]\,\delta[\phi-\phi(t)] \\ &= E\,\frac{\hat{p}_\alpha \hat{p}_\beta}{\Sigma\, \hat{p}^t}\,\delta[r-r_{\rm orb}]\,\delta[\theta-\pi/2]\,\delta[\phi-\phi(t)]\;, \end{aligned} \tag{B.9}$$

where again the second line is specialized to an equatorial, circular orbit. The momenta appearing here are given by

$$\Sigma\,\hat{p}^t = \frac{(r^2+q^2M^2)}{\Delta}\left[(r^2+q^2M^2)-qMb\right]+qM(b-qM)\;, \tag{B.10}$$

$$\Sigma\,\hat{p}^\phi = \frac{qM}{\Delta}\left[(r^2+q^2M^2)-qMb\right]+b-qM\;, \tag{B.11}$$

$$(\Sigma\,\hat{p}^r)^2 = \left[(r^2+q^2M^2)-qMb\right]^2-\Delta\left[\frac{r^2}{\hat{E}^2}+(b-qM)^2\right]\;. \tag{B.12}$$

We have introduced the orbit's energy per unit rest mass $\hat{E}\equiv E/\mu$ and the orbit's "impact parameter" $b\equiv L_z/E$ [see Eqs. (5.29)–(5.30)]. These expressions work well all the way to the light ring, Eq. (5.15). To implement this form of the source, we follow the recipe outlined in Sec. IV of Ref. [116] [see especially Eqs. (4.32) – (4.34)], but using Eq. (B.9) instead of Eq. (B.3). The code then computes the amplitudes $Z^\star_{\ell m}$ per unit orbital energy rather than per unit rest mass, and hence computes all fluxes per unit orbital energy squared. This factors out the divergence associated with the behavior of the energy per unit mass at the light ring. When this is done, each modal contribution $F^\star_{\ell m}$ is perfectly well behaved at the light ring. The sum of all modes can grow quite large, but only because there are many modes that contribute, not because of the pole at the light ring.

Chapter C: **Expressions for $\tilde{f}^{\rm H}_{\ell m}$**

In this appendix we write the explicit expressions of the $\tilde{f}^{\rm H}_{\ell m}$ polynomials. We find

$$
\begin{aligned}
\tilde{f}^{\rm H}_{22} = 1 + 2v^2 &- \left\{4B_2 + \frac{2q}{\kappa\left(1+3q^2\right)}\left[5 + 4\kappa - q^2\left(2+3q^2\right)\right]\right\}v^3 + \left(\frac{377}{42} - \frac{8}{42}q^2\right)v^4 \\
&- \left\{8B_2 + \frac{q}{1+3q^2}\left[\frac{119}{9} - \frac{25}{3}q^2 + 4\kappa\left(5+3q^2\right)\right]\right\}v^5 + \left\{\frac{547\,402}{11\,025} - \frac{4}{3}\pi^2 - \frac{7\,942}{567}q^2\right. \\
&+ 2q^4 + 8B_2^2 + 8C_2\left(1 + \frac{2}{\kappa}\right) - \frac{856}{105}\left(A_2 + \gamma_E + \log 2 + \log\kappa + 2\log v\right) \\
&- \frac{1}{1+3q^2}\left[\frac{152}{9} - 32qB_2 - 8q\kappa B_2\left(5+3q^2\right)\right] \\
&\left.+ \frac{1}{\left(1+3q^2\right)^2}\left[\frac{224}{9} + 4\kappa\left(5 + 4q^2 + 9q^4 - 18q^6\right)\right]\right\}v^6 \\
&- \left[-\frac{1\,641}{189}q + \frac{73}{189}q^3 + \frac{4\,556q}{63\left(1+3q^2\right)} + \frac{1}{21}\left(377 - 8q^2\right)\left(2B_2 + q\kappa\frac{5+3q^2}{1+3q^2}\right)\right]v^7 \\
&+ \left\{\frac{4\,579\,699}{33\,075} - \frac{8}{3}\pi^2 - \frac{14\,617}{567}q^2 + \frac{529}{126}q^4 - \frac{5\,296}{105}\gamma_E - \frac{1\,712}{105}A_2\right. \\
&+ 16B_2^2 + 16C_2\left(1 + \frac{2}{\kappa}\right) - \frac{100}{9}qB_2 + \frac{1}{1+3q^2}\left[-\frac{712}{27} + 64qB_2 + 16\kappa qB_2\left(5+3q^2\right)\right] \\
&+ \frac{1}{\left(1+3q^2\right)^2}\left[\frac{448}{9} + \kappa\left(40 + \frac{38}{9}q^2 - 28q^4 - 194q^6\right)\right] \\
&\left.- \frac{592}{7}\log 2 - \frac{1\,712}{105}\log\kappa - \frac{2\,336}{35}\log v\right\}v^8 + \mathcal{O}(v^9)\,, \qquad \text{(C.1)}
\end{aligned}
$$

$$\tilde{f}^{\rm H}_{21} = 1 - \frac{2}{3}qv + \frac{7}{6}v^2 + \left\{ -2B_1 + \frac{2q}{4-3q^2}\left[\frac{5}{3} - 2q^2 - \kappa\left(5-3q^2\right)\right]\right\}v^3$$
$$+ \left\{\frac{841}{504} + \frac{4}{3}qB_1 - \frac{1\,165}{378}q^2 + \frac{4}{3\left(4-3q^2\right)}\left[\frac{4}{3} + q^2\kappa\left(5-3q^2\right)\right]\right\}v^4$$
$$+ \left\{\frac{785}{252}q + \frac{13}{14}q^3 - \frac{7}{3}\left[B_1 + \frac{q}{4-3q^2}\left[1+\kappa\left(5-3q^2\right)\right]\right]\right\}v^5$$
$$+ \left\{\frac{303\,727}{19\,600} - \frac{12\,055}{2\,268}q^2 + 2q^4 - \frac{\pi^2}{3} - \frac{214}{105}\left(A_1 + \gamma_E + \log 2 + \log\kappa + 2\log v\right) + 2B_1^2\right.$$
$$+ 2C_1\left(1+\frac{2}{\kappa}\right) - \frac{1}{4-3q^2}\left[\frac{40}{9} - 4qB_1\left(-\frac{5}{3} + 2q^2 + \kappa\left(5-3q^2\right)\right)\right]$$
$$\left. + \frac{16}{3\left(4-3q^2\right)^2}\left[\kappa\left(15 - 52q^2 + 54q^4 - 18q^6\right) - \frac{1}{3}\right]\right\}v^6 + \mathcal{O}(v^7)\,, \tag{C.2}$$

$$\tilde{f}^{\rm H}_{33} = 1 + \frac{7}{2}v^2 - \left\{6B_3 + \frac{q}{\left(1+8q^2\right)\left(4+5q^2\right)}\left[\frac{262}{3} + \frac{628}{3}q^2 - \frac{80}{3}q^4 + 18\kappa\left(5+13q^2\right)\right]\right\}v^3$$
$$+ \left(\frac{1\,549}{120} - \frac{5}{6}q^2\right)v^4 + \mathcal{O}(v^5)\,, \tag{C.3}$$

$$\tilde{f}^{\rm H}_{32} = 1 - \frac{3}{4}qv + \frac{5}{2}v^2 + \mathcal{O}(v^3)\,, \tag{C.4}$$

$$\tilde{f}^{\rm H}_{31} = 1 + \frac{29}{6}v^2 - 2\left\{B_1 + \frac{q}{4-3q^2}\left[\kappa\left(5-3q^2\right) + \frac{1}{9-8q^2}\left(65 - \frac{866}{9}q^2 + \frac{104}{3}q^4\right)\right]\right\}v^3$$
$$+ \left(\frac{1\,195}{72} + \frac{1}{2}q^2\right)v^4 + \mathcal{O}(v^5)\,, \tag{C.5}$$

$$\tilde{f}^{\rm H}_{44} = 1 + \mathcal{O}(v)\,, \tag{C.6}$$

$$\tilde{f}^{\rm H}_{43} = \mathcal{O}(v)\,, \tag{C.7}$$

$$\tilde{f}^{\rm H}_{42} = 1 + \mathcal{O}(v)\,, \tag{C.8}$$

$$\tilde{f}^{\rm H}_{41} = \mathcal{O}(v)\,. \tag{C.9}$$

We have compared the factorized fluxes built using either the $\tilde{\rho}^{\rm H}_{\ell m}$'s or $\tilde{f}^{\rm H}_{\ell m}$'s against the Teukolsky-equation flux and have found that the latter have fractional differences 1 order of magnitude smaller than the former for prograde orbital geometries. For

retrograde orbits, instead, the two factorizations have more similar modeling errors. For this reason we have employed the $\tilde{\rho}^{\rm H}_{\ell m}$ factorization in the paper.

Chapter D: **Fits of the gravitational flux at infinity**

In this appendix we fit the gravitational flux at infinity computed through the Teukolsky equation to further improve the amplitude of the factorized modes, given in Eq. (5.31), and the total factorized flux. The Teukolsky-equation data available to us span frequencies from $v = 0.01$ up to $r = r_{\rm LR} + 0.01M$, and have spins in the range $q \in \{-0.99, -0.95, -0.9, -0.8, -0.7, -0.6, -0.5, -0.4, -0.3, -0.2, -0.1, 0, 0.1, 0.2, 0.3, 0.4, 0.5, 0.6, 0.7, 0.8, 0.9, 0.95, 0.99\}$.

Improving the mode's amplitude $|h_{lm}|$'s (which is equivalent to improving the mode's flux F^{∞}_{lm}) is conducive to the EOB modeling of the merger signal in the small mass-ratio limit for large spins, which we have pursued in Ref. [114]. [Note that the modes in this appendix are spherical-harmonic modes, labeled (l, m).] Earlier efforts in this direction (e.g., see Refs. [118, 119]) were plagued by significant modeling errors in the $|h_{lm}|$'s for spins $q \gtrsim 0.7$. For such systems, the discrepancies between time-domain Teukolsky-equation waveforms and EOB waveforms showed up early on during the adiabatic inspiral, where non-quasi-circular effects are still negligible. This also had the effect of introducing a large error on the total F^{∞}, which depends on the $|h_{lm}|$'s through Eq. (5.26).

We perform the fit by adding to the ρ_{lm}'s of Ref. [101] an additional term

$\rho_{lm}^{\rm amp\,fit}$, which is determined by the fit. We fit the minimal number of unknown higher PN orders beyond the current analytical knowledge of the ρ_{lm}'s, such that the residuals on the individual F_{lm}^{∞} (or, equivalently, on $|h_{lm}|$) are within 5% up to the ISCO. It is worth reminding the reader that Ref. [101] based their factorized model on unpublished Taylor-expanded modes computed in BH perturbation theory by Tagoshi and Fujita. In previous years, Ref. [412] had derived the Taylor-expanded modes needed to compute the 5.5PN energy flux at infinity for the Schwarzschild case, while Ref. [251] had derived the Taylor-expanded modes needed to compute the 4PN energy flux at infinity for a particle in the equatorial plane of a Kerr BH. However, in both instances, the explicit formulas had not been published. Reference [356] independently derived the nonspinning Taylor-expanded multipolar waveforms up to 5.5PN order, and computed a ρ_{lm} factorization which includes some higher PN nonspinning terms as compared to Ref. [101]. Reference [101] itself pointed out [before Eq. (A1)] that their nonspinning ρ_{lm}'s agreed with those of Ref. [356] only up to $\mathcal{O}(v^{11-2(l-2)})$. References [357] and [413] pushed the computation of the energy flux at infinity for Schwarzschild up to 14PN and 22PN order, respectively, but provided only the 6PN term entering the ρ_{22}. Again, for the rest of this appendix we will build upon the analytical results of Ref. [101].

Table I of Ref. [101] lists the PN knowledge of the different modes h_{lm}'s at the time of publication. In particular, given (l, m), from the second line of that table one can read the available PN order beyond the leading term $h_{lm}^{(N,\epsilon)}$ for the Taylor-expanded expression of the mode, with a distinction between nonspinning and spinning terms. It turns out that when $l \leq 5$ the nonspinning sector is known

to a higher or equal PN order than the spinning sector; on the other hand, when $l > 5$ the knowledge of the spinning terms is better than the nonspinning ones.

As already pointed out in Refs. [101, 119, 276, 414], the larger the value of q, the more multipolar modes become comparable with the dominant (2,2) mode: see Fig. 3 of Ref. [119], which shows the mode hierarchy for $q = 0, 0.9$ based on their amplitude $|h_{lm}|$. An analytical explanation for the hierarchy of the modes can also be found using the WKB approximation [242–245]. The multipolar modes we fit are (2,2), (2,1), (3,3), (3,2), (3,1), (4,4), (4,3), (4,2), (5,5), (5,4), (6,6), (7,7), and (8,8).

Note that we perform the fits in the domain of the orbital velocity $v \equiv (M\Omega)^{1/3}$, over the restricted range $0.01 \leq v \leq v_{\rm ISCO}$ (where $v_{\rm ISCO} \equiv (M\Omega_{\rm ISCO})^{1/3} = [(r_{\rm ISCO}/M)^{3/2} + q]^{-1/3}$). The reason for doing so (instead of going up to the final available frequency) is threefold: (i) from the point of view of the waveform, our primary goal is to improve the adiabatic analytical model, and modeling errors in the plunge amplitude can easily be fixed by introducing non-quasi-circular corrections [114]; (ii) from the point of view of the energy flux at infinity, after the ISCO the orbital motion of the binary becomes basically geodetic[1]; (iii) we find it difficult to fit well the post-ISCO data, all the way to the LR without spoiling the low-frequency portion of the fit. As to the spin range covered, we cannot include $q = 0.99$ without affecting in a negative way smaller spins. While computing the fits, we give equal weight to all available spins and fit them all together. This is

[1]The plunge lasts for a time $\mathcal{O}(M)$, in contrast to the inspiral, which lasts for a much longer time $\mathcal{O}(M^2/\mu)$ [62, 231]. Therefore the motion of the plunging particle is well approximated by a geodesic in Kerr spacetime.

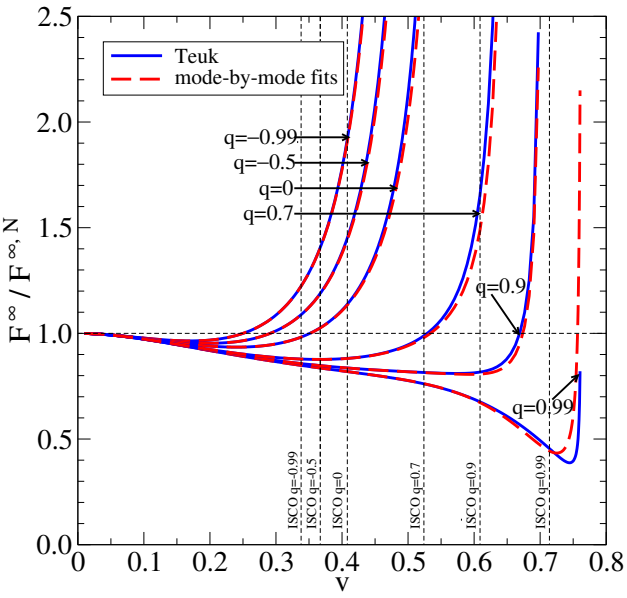

Figure D.1: We plot the total Teukolsky-equation flux at infinity (in solid blue) and the ρ_{lm}-factorized model of Ref. [101], improved with the amplitude fits $\rho_{lm}^{\rm amp\,fit}$ (in dashed red). The curves extend up to $r = r_{\rm LR} + 0.01M$. The fluxes are normalized by the leading quadrupole luminosity at infinity.

achieved by rescaling each range $0.01 \leq v \leq v_{\rm ISCO}$ such that they all have the same measure, and by stitching together all different ranges. We also tried fits in the domain of the orbital frequency $M\Omega$, which amounts to giving more importance to higher frequencies, but this created large relative errors at lower frequencies, where the binary spends the majority of the time, therefore increasing the phase error due to the flux modeling.

Table D.1 lists the fitted functions $\rho_{lm}^{\rm amp\,fit}$. In those expressions we use $\text{eulerlog}_m x \equiv \log\gamma_E + \log 2m + \log\sqrt{x}$ ($\gamma_E \approx 0.577215\ldots$ being Euler's constant).

(l,m)	$\rho_{lm}^{\text{amp fit}}$	Relative error
(2, 2)	$(-20.28 + 12.03\,\text{eulerlog}_2 v^2)\,qv^9$	$\lesssim 0.3\%$
(2, 1)	$(-0.5144 + 3.175\,\text{eulerlog}_1 v^2)\,q^2v^8$	$\lesssim 0.4\%$
(3, 3)	$3.894\,q^2v^8 + (-42.08 + 12.76\,\text{eulerlog}_3 v^2)\,qv^9$	$\lesssim 0.2\%$
(3, 2)	$-0.6932\,qv^7 - 1.558\,q^2v^8$	$\lesssim 1\%$
(3, 1)	$-1.012\,q^2v^8 + (0.8846 - 1.279\,\text{eulerlog}_1 v^2)\,qv^9$	$\lesssim 0.08\%$
(4, 4)	$0.9625\,qv^7 + (-2.069 - 0.7846\,\text{eulerlog}_4 v^2)\,v^8 - 0.2633\,q^2v^8$	$\lesssim 0.2\%$
(4, 3)	$1.424\,q^2v^6 - 2.475\,qv^7$	$\lesssim 0.8\%$
(5, 5)	$(19.51 - 5.623\,\text{eulerlog}_5 v^2)\,v^6 + 0.3443\,q^2v^6$	$\lesssim 1\%$
(6, 6)	$-0.9925\,qv^5 - 0.03416\,q^2v^6 + (19.75 - 5.328\,\text{eulerlog}_6 v^2)\,v^6$	$\lesssim 0.8\%$
(7, 7)	$-1.732\,v^4 + 0.4912\,q^2v^4 - 1.117\,qv^5 + 0.1468\,q^2v^6 + (25.63 - 6.979\,\text{eulerlog}_7 v^2)\,v^6$	$\lesssim 0.2\%$
(8, 8)	$-0.9946\,qv^3 - 0.2949\,v^4 + 0.003748\,q^2v^4 + 2.428\,qv^5$	$\lesssim 1.2\%$

Table D.1: Functions $\rho_{lm}^{\text{amp fit}}$ fitted to individual multipolar modes of the numerical flux at infinity. The coefficients are given with four significant figures. In the last column we show the upper bound on the residual relative error of these fits over the spin and frequency ranges used for the fits, i.e., all spins except $q = 0.99$, and up to the ISCO.

For multipolar modes with $l \leq 4$ the fitting functions contain only spinning terms. But starting from $l = 5$ both nonspinning and spinning terms are fitted. For instance, for the (5,5) mode, both the nonspinning and spinning sectors are known through 2.5PN beyond the leading order, therefore we fit both sectors at 3PN order.

The choice of including logarithmic terms or not is based on the patterns displayed by the currently available expressions for the ρ_{lm}'s: nonspinning (spinning) logarithmic terms show up at 3PN order beyond the leading nonspinning (spinning) term. We also choose the spin dependence for the spinning terms to be either linear of quadratic in q, again based on the patterns present in the ρ_{lm}'s: Spinning terms proportional to odd (even) powers of v are odd (even) in the spin q.

Finally, the (7,7) and (8,8) modes turn out to be quite difficult to fit, due to the limited Taylor-expanded knowledge from BH perturbation theory, and they require as many as 3 PN orders to be fitted within a few percent accuracy, which means a total of six fitting parameters for (7,7) and four fitting parameters for (8,8). In contrast, all other modes with $l \leq 6$ can be accurately fitted using only half or one PN order. We end up fitting a total of 35 coefficients.

The quality of the fits is generally very good on a mode-by-mode basis, with residuals always smaller than $\sim 1.2\%$ for all the values of q (except 0.99), for frequencies up to the ISCO and for all the fitted multipolar modes. In the third column of Table D.1 we list the upper bound for the relative error on the fits of the multipolar modes.

We now turn to the total energy flux at infinity. In Fig. D.1 we show comparisons of $F^{\infty}_{\rm Teuk}$ against the model with the mode-by-mode fits discussed above. When

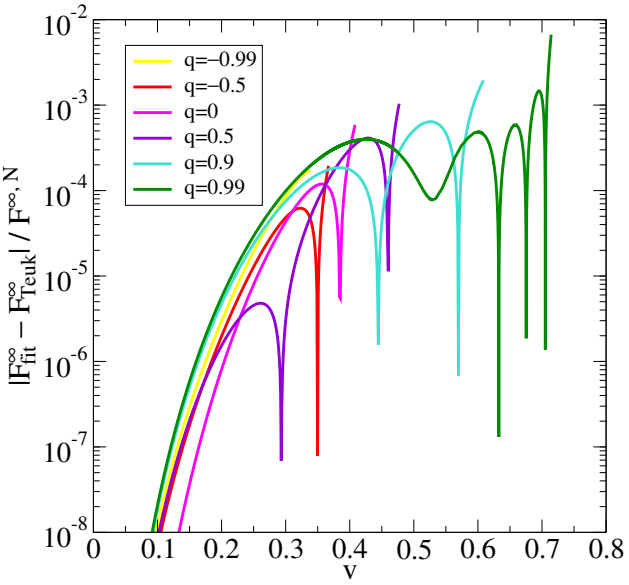

Figure D.2: We show the absolute residual error (normalized by the leading order luminosity at infinity) on the factorized flux at infinity improved with $\rho_{lm}^{\rm amp\,fit} + \rho_{lm}^{\rm tot\,fit}$. All curves extend up to the respective ISCOs.

the spins are negative or small, the factorized model of Ref. [101] actually performs fairly well without any additional fit: For those cases, in fact, the modeling error is less that 1% at the ISCO, as demonstrated by Fig. 5.5. In general, the energy flux diverges at the LR since the energy-momentum tensor of the particle sourcing the GW perturbations diverges there as well. This feature is incorporated in the model through the effective source factor $\hat{S}^{(\epsilon)}_{\rm eff}$, which behaves like $(r - r_{\rm LR})^{-1}$ for $r \sim r_{\rm LR}$ [99–101]. But, when the spin is large and positive, the divergence of the numerical flux is localized in a narrow neighborhood of the LR, while the model without fits starts growing to large values even before the ISCO. For instance, when $q \geq 0.9$, the factorized model differs from the numerical data by more than 100% even before the ISCO, so that an EOB evolution based on such flux would be unre-

liable already in the late inspiral, as already pointed out earlier. When the fits are included, the model agrees with the numerical data to within 0.1% before the ISCO for all the spins up to $q = 0.99$, as shown in Fig. D.1.

As a final refinement, on top of the mode-by-mode fits just discussed, we add eight additional fitting parameters [four in the (2,2) mode, four in the (3,3) mode] and determine them through a global fit on F^{∞} itself, similar to what Refs. [118,415] did. Again we restrict to $0.01 \leq v \leq v_{\rm ISCO}$, but now we include also $q = 0.99$. We can achieve a reduction of the error by about an order of magnitude at the ISCO for all the available spins, as shown in Fig. D.2. These additional terms to be added to $\rho_{lm} + \rho_{lm}^{\rm amp\,fit}$, which we will call $\rho_{lm}^{\rm tot\,fit}$, read

$$\begin{aligned}
\rho_{22}^{\rm tot\,fit} &= (-9.890 + 9.039\,{\rm eulerlog}_2 v^2)\,q^2 v^{10} \\
&+ (-18.84 + 2.486\,{\rm eulerlog}_2 v^2)\,q v^{11}\,, \qquad \text{(D.1)} \\
\rho_{33}^{\rm tot\,fit} &= [73.73 - 36.97\,{\rm eulerlog}_3 v^2 \\
&+ q^2\,(3.955 - 0.7106\,{\rm eulerlog}_3 v^2)]\,v^{10}\,. \qquad \text{(D.2)}
\end{aligned}$$

Chapter E: **Fits of the black-hole absorption gravitational flux**

In this appendix we provide numerical fits to the Teukolsky-equation black-hole absorption fluxes. Our starting point is the $\tilde{\rho}^{\rm H}_{\ell m}$-factorized model developed in this paper. We add to the $\tilde{\rho}^{\rm H}_{\ell m}$'s in Eqs. (F.11)–(F.16) higher-order PN terms $\tilde{\rho}^{\rm H,fit}_{\ell m}$. In particular, we modify only the dominant and leading subdominant modes (2,2), (2,1), and (3,3). We choose the functional form of the $\tilde{\rho}^{\rm H,fit}_{\ell m}$'s based on the lower PN orders, trying to include similar dependences on v and q. We have data for the Teukolsky-equation $F^{\rm H}$ for as many as 22 spins: $q \in \{-0.99, -0.9, -0.8, -0.7, -0.6, -0.5, -0.4, -0.3, -0.2, -0.1, 0, 0.1, 0.2, 0.3, 0.4, 0.5, 0.6, 0.7, 0.8, 0.9, 0.95, 0.99\}$. The fits are done globally on all spins in v–space. The sampled frequency ranges extend from $v = 0.01$ up to $r = r_{\rm LR} + 0.01M$, but we use data only up to $r = (r_{\rm ISCO} + r_{\rm LR} + 0.01M)/2$, since attempts to include the whole available velocity ranges spoil the lower frequency portion of the fits; nonetheless our fits prove very accurate up to the ISCO. To have residual relative errors within a few percent for

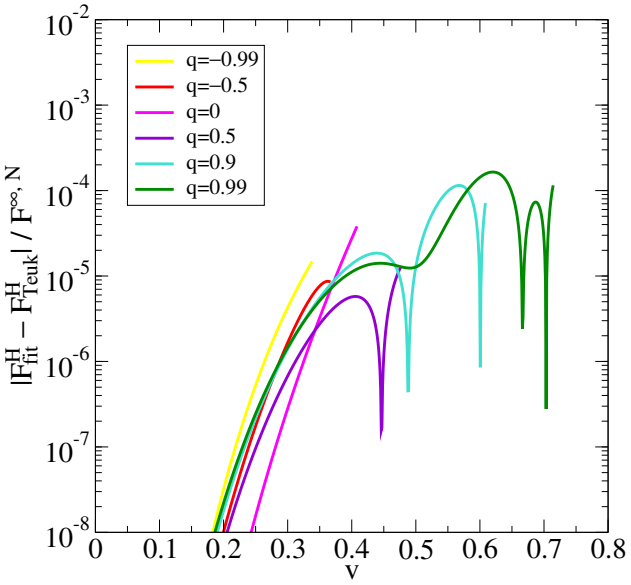

Figure E.1: We show the absolute residual error on the fitted absorption flux, normalized by the leading order luminosity at infinity. All curves extend up to the respective ISCOs.

all the available spins up to the ISCO, we have to use 11 fitting coefficients. We find

$$\begin{aligned}\tilde{\rho}^{\rm H,fit}_{22} &= -(1570 + 118.5\,q + 589.7\,\log v)\,v^9 \\ &+ (1323 + 336.3\,q - 1291\,\log v)\,v^{10}\,, \qquad \text{(E.1)}\\ \tilde{\rho}^{\rm H,fit}_{21} &= (50.25 - 54.95\,q - 40.39\,\log v)\,v^7\,, \qquad \text{(E.2)}\\ \tilde{\rho}^{\rm H,fit}_{33} &= (15.65 - 13.41\,q)\,v^5\,. \qquad \text{(E.3)}\end{aligned}$$

Figure E.1 shows what are the residuals on the fitted ingoing fluxes, normalized by the leading order luminosity at infinity. We plot this quantity, rather than the relative residual errors, because in any realistic setting these fits are going to be added into a radiation reaction term where the flux at infinity is also present. In fact, as discussed before (see Fig. 5.1), $|F^{\rm H}|$ is always much smaller than $|F^{\infty}|$ before

the ISCO, and one is typically interested in an accurate total flux ($F^{\infty} + F^{\mathrm{H}}$); hence our choice of the normalization. It is therefore possible to estimate the modeling error on the total flux by directly adding Fig. D.2 and Fig. E.1.

Chapter F: Expressions of the factorized modes for the spinning EOB model

Using results from Refs. [91,239,285,286], we write here the explicit expressions of the factorized modes employed in Sec. 7.2.2. Even though we calibrated only the (2,2) mode, we will provide expressions for all the modes up to $\ell = 8$, because they enter the computation of the energy flux in Eq. (11.9).

The terms $h^{(N,\epsilon)}_{\ell m}$ in Eq. (11.4) are the Newtonian modes. They read

$$h^{(N,\epsilon)}_{\ell m} = \frac{M\nu}{\mathcal{R}}\, n^{(\epsilon)}_{\ell m}\, c_{\ell+\epsilon}(\nu)\, V^{\ell}_{\Phi}\, Y^{\ell-\epsilon,-m}\left(\frac{\pi}{2},\Phi\right), \tag{F.1}$$

where $\mathcal{R}$ is the distance from the source; the $Y^{\ell m}(\Theta,\Phi)$ are the scalar spherical harmonics; we use $V^{\ell}_{\Phi} = v^{\ell+\epsilon}_{\Phi}$ with

$$v_{\Phi} = r_{\Omega}\hat{\Omega} = \hat{\Omega}\left(\left.\frac{\partial \hat{H}_{\rm real}}{\partial p_{\Phi}}\right|_{p_r=0}\right)^{-2/3}, \tag{F.2}$$

where $p_{\Phi} \equiv |\boldsymbol{r}\times\boldsymbol{p}|$. The functions $n^{(\epsilon)}_{\ell m}$ and $c_{\ell+\epsilon}(\nu)$ in Eq. (F.1) read

$$n^{(0)}_{\ell m} = (i\,m)^{\ell}\frac{8\pi}{(2\ell+1)!!}\sqrt{\frac{(\ell+1)(\ell+2)}{\ell(\ell-1)}}, \tag{F.3}$$

$$n^{(1)}_{\ell m} = -(i\,m)^{\ell}\frac{16\pi i}{(2\ell+1)!!}\sqrt{\frac{(2\ell+1)(\ell+2)(\ell^2-m^2)}{(2\ell-1)(\ell+1)\ell(\ell-1)}}, \tag{F.4}$$

and

$$c_{\ell+\epsilon}(\nu) = \left(\frac{1}{2}-\frac{1}{2}\sqrt{1-4\nu}\right)^{\ell+\epsilon-1} + (-1)^{\ell+\epsilon}\left(\frac{1}{2}+\frac{1}{2}\sqrt{1-4\nu}\right)^{\ell+\epsilon-1}. \tag{F.5}$$

The function $\hat{S}^{(\epsilon)}_{\rm eff}$ in Eq. (11.4) is an effective source term that in the circular-motion limit contains a pole at the EOB light ring. It is given in terms of the EOB dynamics as

$$\hat{S}^{(\epsilon)}_{\rm eff}(r, p_{r^*}, p_\Phi, \mathbf{S}_1, \mathbf{S}_2) = \begin{cases} \hat{H}^{\rm eff}(r, p_{r^*}, p_\Phi, \mathbf{S}_1, \mathbf{S}_2)\,, & \epsilon = 0\,, \\ \hat{L}_{\rm eff} = p_\Phi\, v_\Omega\,, & \epsilon = 1\,, \end{cases} \tag{F.6}$$

where $v_\Omega = \hat{\Omega}^{1/3}$. The factor $T_{\ell m}$ in Eq. (11.4) resums the leading order logarithms of tail effects, it reads

$$T_{\ell m} = \frac{\Gamma(\ell + 1 - 2i\, m\, H_{\rm real}\, \Omega)}{\Gamma(\ell+1)}\, \exp\left[\pi\, m\, \Omega\, H_{\rm real}\right] \exp\left[2i\, m\, \Omega\, H_{\rm real}\, \log(2\, m\, \Omega\, r_0)\right]\,, \tag{F.7}$$

where $r_0 = 2M/\sqrt{e}$ [101].

In what follows we define

$$\delta m \equiv \frac{m_1 - m_2}{M}, \tag{F.8}$$

$$\chi_S \equiv \frac{\chi_1 + \chi_2}{2}, \tag{F.9}$$

$$\chi_A \equiv \frac{\chi_1 - \chi_2}{2}. \tag{F.10}$$

Also we use $\text{eulerlog}_m(v_\Omega^2) \equiv \gamma_E + \log 2 + \log m + 1/2 \log v_\Omega^2$, with γ_E being the Euler constant. We noticed that for even m the $\rho_{\ell m}$'s with spin contributions of Ref. [101] are ill-defined when $\delta m \to 0$. Thus, in this paper, for $m = 1, 3$ and $\ell \leq 4$, we replace the factor $(\rho_{\ell m})^\ell$ in Eq. (11.4) with the nonspinning (NS) limit of $(\rho_{\ell m})^\ell$ plus the spinning (S) part of the $f_{\ell m}$'s of Ref. [101]. More explicitly, the modes we used

read [100, 101]

$$
\begin{aligned}
\rho_{22} = 1 &+ \left(\frac{55\,\nu}{84} - \frac{43}{42}\right) v_\Omega^2 - \frac{2}{3}\left[\chi_S(1-\nu) + \chi_A\,\delta m\right] v_\Omega^3 \\
&+ \left(\frac{19\,583\,\nu^2}{42\,336} - \frac{33\,025\,\nu}{21\,168} - \frac{20\,555}{10\,584}\right) v_\Omega^4 \\
&+ \left(\frac{10\,620\,745\,\nu^3}{39\,118\,464} - \frac{6\,292\,061\,\nu^2}{3\,259\,872} + \frac{41\,\pi^2\,\nu}{192} - \frac{48\,993\,925\,\nu}{9\,779\,616} - \frac{428\,\mathrm{eulerlog}_2(v_\Omega^2)}{105}\right. \\
&+ \left.\frac{1\,556\,919\,113}{122\,245\,200}\right) v_\Omega^6 + \left(\nu\rho_{22}^{(4)} + \frac{9\,202\,\mathrm{eulerlog}_2(v_\Omega^2)}{2\,205} - \frac{387\,216\,563\,023}{160\,190\,110\,080}\right) v_\Omega^8 \\
&+ \left(\frac{439\,877\,\mathrm{eulerlog}_2(v_\Omega^2)}{55\,566} - \frac{16\,094\,530\,514\,677}{533\,967\,033\,600}\right) v_\Omega^{10}\,, \qquad \text{(F.11)}
\end{aligned}
$$

$$
\begin{aligned}
\rho_{21}^{L\,\mathrm{NS}} = 1 &+ \left(\frac{23\,\nu}{84} - \frac{59}{56}\right) v_\Omega^2 + \left(\frac{617\,\nu^2}{4\,704} - \frac{10\,993\,\nu}{14\,112} - \frac{47\,009}{56\,448}\right) v_\Omega^4 \\
&+ \left(\frac{7\,613\,184\,941}{2\,607\,897\,600} - \frac{107\,\mathrm{eulerlog}_1(v_\Omega^2)}{105}\right) v_\Omega^6 \\
&+ \left(\frac{6\,313\,\mathrm{eulerlog}_1(v_\Omega^2)}{5\,880} - \frac{1\,168\,617\,463\,883}{911\,303\,737\,344}\right) v_\Omega^8 \\
&+ \left(\frac{5\,029\,963\,\mathrm{eulerlog}_1(v_\Omega^2)}{5\,927\,040} - \frac{63\,735\,873\,771\,463}{16\,569\,158\,860\,800}\right) v_\Omega^{10}\,, \qquad \text{(F.12)}
\end{aligned}
$$

where $\rho_{22}^{(4)}$ is a nonspinning EOB adjustable parameter, which is determined through the calibration of the nonspinning NR waveforms,

$$\rho_{33}^{\rm NS} = 1 + \left(\frac{2\,\nu}{3} - \frac{7}{6}\right) v_\Omega^2 + \left(\frac{149\,\nu^2}{330} - \frac{1\,861\,\nu}{990} - \frac{6\,719}{3\,960}\right) v_\Omega^4 + \left(\frac{3\,203\,101\,567}{227\,026\,800} - \frac{26\,\mathrm{eulerlog}_3(v_\Omega^2)}{7}\right) v_\Omega^6 + \left(\frac{13\,\mathrm{eulerlog}_3(v_\Omega^2)}{3} - \frac{57\,566\,572\,157}{8\,562\,153\,600}\right) v_\Omega^8 \,, \tag{F.13}$$

$$\rho_{32}^{L} = 1 - \frac{4\nu}{3(3\nu-1)}\chi_S v_\Omega + \frac{320\,\nu^2 - 1\,115\,\nu + 328}{270\,(3\,\nu-1)} v_\Omega^2 + \frac{3\,085\,640\,\nu^4 - 20\,338\,960\,\nu^3 - 4\,725\,605\,\nu^2 + 8\,050\,045\,\nu - 1\,444\,528}{1\,603\,800\,(1-3\,\nu)^2} v_\Omega^4 + \left(\frac{5\,849\,948\,554}{940\,355\,325} - \frac{104\,\mathrm{eulerlog}_2(v_\Omega^2)}{63}\right) v_\Omega^6 + \left(\frac{17\,056\,\mathrm{eulerlog}_2(v_\Omega^2)}{8\,505} - \frac{10\,607\,269\,449\,358}{3\,072\,140\,846\,775}\right) v_\Omega^8 \,, \tag{F.14}$$

$$\rho_{31}^{\rm NS} = 1 - \left(\frac{2\,\nu}{9} + \frac{13}{18}\right) v_\Omega^2 + \left(-\frac{829\,\nu^2}{1\,782} - \frac{1\,685\,\nu}{1\,782} + \frac{101}{7\,128}\right) v_\Omega^4 + \left(\frac{11\,706\,720\,301}{6\,129\,723\,600} - \frac{26\,\mathrm{eulerlog}_1(v_\Omega^2)}{63}\right) v_\Omega^6 + \left(\frac{169\,\mathrm{eulerlog}_1(v_\Omega^2)}{567} + \frac{2\,606\,097\,992\,581}{4\,854\,741\,091\,200}\right) v_\Omega^8 \,, \tag{F.15}$$

$$
\begin{aligned}
\rho_{44} &= 1 + \frac{2\,625\nu^2 - 5\,870\,\nu + 1\,614}{1\,320\,(3\,\nu - 1)} v_\Omega^2 \\
&\quad - \frac{1}{15(1-3\nu)} \left[(42\nu^2 - 41\nu + 10)\chi_S + (10 - 39\nu)\delta m\,\chi_A \right] v_\Omega^3 \\
&\quad + \frac{1\,252\,563\,795\,\nu^4 - 6\,733\,146\,000\,\nu^3 - 313\,857\,376\,\nu^2 + 2\,338\,945\,704\,\nu - 511\,573\,572}{317\,116\,800\,(1-3\,\nu)^2} v_\Omega^4 \\
&\quad + \left(\frac{16\,600\,939\,332\,793}{1\,098\,809\,712\,000} - \frac{12\,568\,\mathrm{eulerlog}_4(v_\Omega^2)}{3\,465} \right) v_\Omega^6 \,, \qquad \text{(F.16)} \\
\rho_{43}^{L\,\mathrm{NS}} &= 1 + \frac{160\,\nu^2 - 547\,\nu + 222}{176\,(2\,\nu - 1)} v_\Omega^2 - \frac{6\,894\,273}{7\,047\,040} v_\Omega^4 \\
&\quad + \left(\frac{1\,664\,224\,207\,351}{195\,343\,948\,800} - \frac{1\,571\,\mathrm{eulerlog}_3(v_\Omega^2)}{770} \right) v_\Omega^6 \,, \qquad \text{(F.17)} \\
\rho_{42} &= 1 + \frac{285\,\nu^2 - 3\,530\,\nu + 1\,146}{1\,320\,(3\,\nu - 1)} v_\Omega^2 \\
&\quad - \frac{1}{15(1-3\nu)} \left[(78\nu^2 - 59\nu + 10)\chi_S + (10 - 21\nu)\delta m\,\chi_A \right] v_\Omega^3 \\
&\quad + \frac{-379\,526\,805\,\nu^4 - 3\,047\,981\,160\,\nu^3 + 1\,204\,388\,696\,\nu^2 + 295\,834\,536\,\nu - 114\,859\,044}{317\,116\,800\,(1-3\,\nu)^2} v_\Omega^4 \\
&\quad + \left(\frac{848\,238\,724\,511}{219\,761\,942\,400} - \frac{3\,142\,\mathrm{eulerlog}_2(v_\Omega^2)}{3\,465} \right) v_\Omega^6 \,, \qquad \text{(F.18)} \\
\rho_{41}^{L\,\mathrm{NS}} &= 1 + \frac{288\,\nu^2 - 1\,385\,\nu + 602}{528\,(2\,\nu - 1)} v_\Omega^2 - \frac{7\,775\,491}{21\,141\,120} v_\Omega^4 \\
&\quad + \left(\frac{1\,227\,423\,222\,031}{1\,758\,095\,539\,200} - \frac{1571\,\mathrm{eulerlog}_1(v_\Omega^2)}{6\,930} \right) v_\Omega^6 \,, \qquad \text{(F.19)}
\end{aligned}
$$

$$\rho_{55} = 1 - \frac{512\,\nu^2 - 1\,298\,\nu + 487}{390\,(2\,\nu - 1)} v_\Omega^2 - \frac{3\,353\,747}{2\,129\,400} v_\Omega^4 \,, \tag{F.20}$$

$$\rho_{54}^L = 1 + \frac{33\,320\,\nu^3 - 127\,610\,\nu^2 + 96\,019\,\nu - 17\,448}{13\,650\,(5\,\nu^2 - 5\,\nu + 1)} v_\Omega^2 - \frac{16\,213\,384}{15\,526\,875} v_\Omega^4 \,, \tag{F.21}$$

$$\rho_{53} = 1 + \frac{176\,\nu^2 - 850\,\nu + 375}{390\,(2\,\nu - 1)} v_\Omega^2 - \frac{410\,833}{709\,800} v_\Omega^4 \,, \tag{F.22}$$

$$\rho_{52}^L = 1 + \frac{21\,980\,\nu^3 - 104\,930\,\nu^2 + 84\,679\,\nu - 15\,828}{13\,650\,(5\,\nu^2 - 5\,\nu + 1)} v_\Omega^2 - \frac{7\,187\,914}{15\,526\,875} v_\Omega^4 \,, \tag{F.23}$$

$$\rho_{51} = 1 + \frac{8\,\nu^2 - 626\,\nu + 319}{390\,(2\,\nu - 1)} v_\Omega^2 - \frac{31\,877}{304\,200} v_\Omega^4 \,, \tag{F.24}$$

$$\rho_{66} = 1 + \frac{273\,\nu^3 - 861\,\nu^2 + 602\,\nu - 106}{84\,(5\,\nu^2 - 5\,\nu + 1)} v_\Omega^2 - \frac{1\,025\,435}{659\,736} v_\Omega^4 \,, \tag{F.25}$$

$$\rho_{65}^L = 1 + \frac{220\,\nu^3 - 910\,\nu^2 + 838\,\nu - 185}{144\,(3\,\nu^2 - 4\,\nu + 1)} v_\Omega^2 \,, \tag{F.26}$$

$$\rho_{64} = 1 + \frac{133\,\nu^3 - 581\,\nu^2 + 462\,\nu - 86}{84\,(5\,\nu^2 - 5\,\nu + 1)} v_\Omega^2 - \frac{476\,887}{659\,736} v_\Omega^4 \,, \tag{F.27}$$

$$\rho_{63}^L = 1 + \frac{156\,\nu^3 - 750\,\nu^2 + 742\,\nu - 169}{144\,(3\,\nu^2 - 4\,\nu + 1)} v_\Omega^2 \,, \tag{F.28}$$

$$\rho_{62} = 1 + \frac{49\,\nu^3 - 413\,\nu^2 + 378\,\nu - 74}{84\,(5\,\nu^2 - 5\,\nu + 1)} v_\Omega^2 - \frac{817\,991}{3\,298\,680} v_\Omega^4 \,, \tag{F.29}$$

$$\rho_{61}^L = 1 + \frac{124\,\nu^3 - 670\,\nu^2 + 694\,\nu - 161}{144\,(3\,\nu^2 - 4\,\nu + 1)} v_\Omega^2 \,, \tag{F.30}$$

$$\rho_{77} = 1 + \frac{1\,380\,\nu^3 - 4\,963\,\nu^2 + 4\,246\,\nu - 906}{714\,(3\,\nu^2 - 4\,\nu + 1)} v_\Omega^2\,, \tag{F.31}$$

$$\rho_{76}^L = 1 + \frac{6\,104\,\nu^4 - 29\,351\,\nu^3 + 37\,828\,\nu^2 - 16\,185\,\nu + 2\,144}{1\,666\,(7\,\nu^3 - 14\,\nu^2 + 7\,\nu - 1)} v_\Omega^2\,, \tag{F.32}$$

$$\rho_{75} = 1 + \frac{804\,\nu^3 - 3\,523\,\nu^2 + 3\,382\,\nu - 762}{714\,(3\,\nu^2 - 4\,\nu + 1)} v_\Omega^2\,, \tag{F.33}$$

$$\rho_{74}^L = 1 + \frac{41\,076\,\nu^4 - 217\,959\,\nu^3 + 298\,872\,\nu^2 - 131\,805\,\nu + 17\,756}{14\,994\,(7\,\nu^3 - 14\,\nu^2 + 7\,\nu - 1)} v_\Omega^2\,, \tag{F.34}$$

$$\rho_{73} = 1 + \frac{420\,\nu^3 - 2\,563\,\nu^2 + 2\,806\,\nu - 666}{714\,(3\,\nu^2 - 4\,\nu + 1)} v_\Omega^2\,, \tag{F.35}$$

$$\rho_{72}^L = 1 + \frac{32\,760\,\nu^4 - 190\,239\,\nu^3 + 273\,924\,\nu^2 - 123\,489\,\nu + 16\,832}{14\,994\,(7\,\nu^3 - 14\,\nu^2 + 7\,\nu - 1)} v_\Omega^2\,, \tag{F.36}$$

$$\rho_{71} = 1 + \frac{228\,\nu^3 - 2\,083\,\nu^2 + 2\,518\,\nu - 618}{714\,(3\,\nu^2 - 4\,\nu + 1)} v_\Omega^2\,, \tag{F.37}$$

$$\rho_{88} = 1 + \frac{3\,482 - 26\,778\,\nu + 64\,659\,\nu^2 - 53\,445\,\nu^3 + 12\,243\,\nu^4}{2\,736(-1 + 7\,\nu - 14\,\nu^2 + 7\,\nu^3)} v_\Omega^2\,, \tag{F.38}$$

$$\rho_{87}^L = 1 + \frac{23\,478 - 154\,099\,\nu + 309\,498\,\nu^2 - 207\,550\,\nu^3 + 38\,920\,\nu^4}{18\,240(-1 + 6\,\nu - 10\,\nu^2 + 4\,\nu^3)} v_\Omega^2\,, \tag{F.39}$$

$$\rho_{86} = 1 + \frac{1\,002 - 7\,498\,\nu + 17\,269\,\nu^2 - 13\,055\,\nu^3 + 2\,653\,\nu^4}{912(-1 + 7\,\nu - 14\,\nu^2 + 7\,\nu^3)} v_\Omega^2\,, \tag{F.40}$$

$$\rho_{85}^L = 1 + \frac{4\,350 - 28\,055\,\nu + 54\,642\,\nu^2 - 34\,598\,\nu^3 + 6\,056\,\nu^4}{3\,648(-1 + 6\,\nu - 10\,\nu^2 + 4\,\nu^3)} v_\Omega^2\,, \tag{F.41}$$

$$\rho_{84} = 1 + \frac{2\,666 - 19\,434\,\nu + 42\,627\,\nu^2 - 28\,965\,\nu^3 + 4\,899\,\nu^4}{2\,736(-1 + 7\,\nu - 14\,\nu^2 + 7\,\nu^3)} v_\Omega^2\,, \tag{F.42}$$

$$\rho_{83}^L = 1 + \frac{20\,598 - 131\,059\,\nu + 249\,018\,\nu^2 - 149\,950\,\nu^3 + 24\,520\,\nu^4}{18\,240(-1 + 6\,\nu - 10\,\nu^2 + 4\,\nu^3)} v_\Omega^2\,, \tag{F.43}$$

$$\rho_{82} = 1 + \frac{2\,462 - 17\,598\,\nu + 37\,119\,\nu^2 - 22\,845\,\nu^3 + 3\,063\,\nu^4}{2\,736(-1 + 7\,\nu - 14\,\nu^2 + 7\,\nu^3)} v_\Omega^2\,, \tag{F.44}$$

$$\rho_{81}^L = 1 + \frac{20\,022 - 126\,451\,\nu + 236\,922\,\nu^2 - 138\,430\,\nu^3 + 21\,640\,\nu^4}{18\,240(-1 + 6\,\nu - 10\,\nu^2 + 4\,\nu^3)} v_\Omega^2\,, \tag{F.45}$$

and

$$f_{21}^{LS} = -\frac{3}{2}\left(\chi_S + \frac{\chi_A}{\delta m}\right) v_\Omega \,, \tag{F.46}$$

$$f_{33}^{S} = -\left[\chi_S\left(2 - \frac{5}{2}\nu\right) + \frac{\chi_A}{\delta m}\left(2 - \frac{19}{2}\nu\right)\right] v_\Omega^3 \,, \tag{F.47}$$

$$f_{31}^{LS} = -\left[\chi_S\left(2 - \frac{11}{2}\nu\right) + \frac{\chi_A}{\delta m}\left(2 - \frac{13}{2}\nu\right)\right] v_\Omega^3 \,, \tag{F.48}$$

$$f_{43}^{LS} = f_{41}^{LS} = -\frac{5\nu}{2(2\nu-1)}\left(\chi_S - \frac{\chi_A}{\delta m}\right) v_\Omega \,. \tag{F.49}$$

Finally, we give the explicit expression of the phase term

$$\delta_{22} = \frac{7}{3}\left(\hat{\Omega}\, H_{\rm real}\right) + \frac{428\pi}{105}\left(\hat{\Omega}\, H_{\rm real}\right)^2 + \left(\frac{1\,712\pi^2}{315} - \frac{2\,203}{81}\right)\left(\hat{\Omega}\, H_{\rm real}\right)^3 - 24\nu\, v_\Omega^5. \tag{F.50}$$

Bibliography

[1] Albert Einstein. On the General Theory of Relativity. *Sitzungsber. Preuss. Akad. Wiss. Berlin (Math. Phys.)*, 1915:778–786, 1915.

[2] Albert Einstein. The Field Equations of Gravitation. *Sitzungsber. Preuss. Akad. Wiss. Berlin (Math. Phys.)*, 1915:844–847, 1915.

[3] Clifford M. Will. The Confrontation between general relativity and experiment. *Living Rev. Rel.*, 9:3, 2006, arXiv: gr-qc/0510072.

[4] David Shoemaker. Advanced LIGO anticipated sensitivity curves, 2010. LIGO Document T0900288-v3.

[5] The Virgo Collaboration. Advanced Virgo Baseline Design, 2010. VIR027A09.

[6] Kentaro Somiya. Detector configuration of KAGRA: The Japanese cryogenic gravitational-wave detector. *Class. Quant. Grav.*, 29:124007, 2012, arXiv: 1111.7185.

[7] Pau Amaro Seoane et al. The Gravitational Universe. 2013, arXiv: 1305.5720.

[8] Jonathan R. Gair, Michele Vallisneri, Shane L. Larson, and John G. Baker. Testing General Relativity with Low-Frequency, Space-Based Gravitational-Wave Detectors. *Living Rev. Rel.*, 16:7, 2013, arXiv: 1212.5575.

[9] North american nanohertz obsevatory for gravitational waves. http://nanograv.org.

[10] European pulsar timing array. http://upta.eu.org.

[11] Parkes pulsar timing array. http://atnf.csro.au/research/pulsar/array/.

[12] Albert Einstein. Approximative Integration of the Field Equations of Gravitation. *Sitzungsber. Preuss. Akad. Wiss. Berlin (Math. Phys.)*, 1916:688–696, 1916.

[13] Albert Einstein. Über gravitationswellen. *Sitzungsber. Preuss. Akad. Wiss. Berlin (Math. Phys.)*, 1918:154–167, 1918.

[14] M Maggiore. *Gravitational Waves - Volume 1*. Oxford University Press, New York, first edition, 2008.

[15] B.S. Sathyaprakash and B.F. Schutz. Physics, Astrophysics and Cosmology with Gravitational Waves. *Living Rev. Rel.*, 12:2, 2009, arXiv: 0903.0338.

[16] Konstantin Postnov and Lev Yungelson. The Evolution of Compact Binary Star Systems. *Living Rev. Rel.*, 17:3, 2014, arXiv: 1403.4754.

[17] Joshua A. Faber and Frederic A. Rasio. Binary Neutron Star Mergers. *Living Rev. Rel.*, 15:8, 2012, arXiv: 1204.3858.

[18] Emanuele Berti, Vitor Cardoso, and Clifford M. Will. On gravitational-wave spectroscopy of massive black holes with the space interferometer LISA. *Phys. Rev. D*, 73:064030, 2006, arXiv: gr-qc/0512160.

[19] Masaru Shibata and Keisuke Taniguchi. Coalescence of Black Hole-Neutron Star Binaries. *Living Rev. Rel.*, 14:6, 2011.

[20] Francois Foucart, M. Brett Deaton, Matthew D. Duez, Lawrence E. Kidder, Ilana MacDonald, et al. Black hole-neutron star mergers at realistic mass ratios: Equation of state and spin orientation effects. *Phys. Rev. D*, 87:084006, 2013, arXiv: 1212.4810.

[21] D.R. Lorimer. Binary and Millisecond Pulsars. *Living Rev. Rel.*, 11:8, 2008, arXiv: 0811.0762.

[22] J.H. Taylor and J.M. Weisberg. A new test of general relativity: Gravitational radiation and the binary pulsar PS R 1913+16. *Astrophys. J.*, 253:908–920, 1982.

[23] Joseph H. Taylor and J.M. Weisberg. Further experimental tests of relativistic gravity using the binary pulsar PSR 1913+16. *Astrophys. J.*, 345:434–450, 1989.

[24] Blent Kiziltan, Athanasios Kottas, Maria De Yoreo, and Stephen E. Thorsett. The Neutron Star Mass Distribution. *Astrophys. J.*, 778:66, 2013, arXiv: 1309.6635.

[25] M. Kramer and N. Wex. The double pulsar system: A unique laboratory for gravity. *Class. Quant. Grav.*, 26:073001, 2009.

[26] Aleksander Sadowski, Krzysztof Belczynski, Tomasz Bulik, Natalia Ivanova, Frederic A. Rasio, et al. The Total Merger Rate of Compact Object Binaries In The Local Universe. *Astrophys. J.*, 2007, arXiv: 0710.0878.

[27] Ryan O'Leary, Richard W. O'Shaughnessy, and Frederic Rasio. Dynamical Interactions and the Black Hole Merger Rate of the Universe. *Phys. Rev. D*, 76:061504, 2007, arXiv: astro-ph/0701887.

[28] Ryan M. O'Leary, Bence Kocsis, and Abraham Loeb. Gravitational waves from scattering of stellar-mass black holes in galactic nuclei. *Mon. Not. Roy. Astron. Soc.*, 395(4):2127–2146, 2009, arXiv: 0807.2638.

[29] M. Coleman Miller and Vanessa M. Lauburg. Mergers of Stellar-Mass Black Holes in Nuclear Star Clusters. *Astrophys. J.*, 692:917–923, 2009, arXiv: 0804.2783.

[30] David Tsang. Shattering Flares During Close Encounters of Neutron Stars. *Astrophys. J.*, 777:103, 2013, arXiv: 1307.3554.

[31] Feryal Ozel, Dimitrios Psaltis, Ramesh Narayan, and Jeffrey E. McClintock. The Black Hole Mass Distribution in the Galaxy. *Astrophys. J.*, 725:1918–1927, 2010, arXiv: 1006.2834.

[32] Laura Kreidberg, Charles D. Bailyn, Will M. Farr, and Vassiliki Kalogera. Mass Measurements of Black Holes in X-Ray Transients: Is There a Mass Gap? *Astrophys. J.*, 757:36, 2012, arXiv: 1205.1805.

[33] Chris L. Fryer, Krzysztof Belczynski, Grzegorz Wiktorowicz, Michal Dominik, Vicky Kalogera, et al. Compact Remnant Mass Function: Dependence on the Explosion Mechanism and Metallicity. *Astrophys. J.*, 749:91, 2012, arXiv: 1110.1726.

[34] Krzysztof Belczynski, Alessandra Buonanno, Matteo Cantiello, Daniel E. Holz, Chris L. Fryer, et al. The Formation and Gravitational-Wave Detection of Massive Stellar Black-Hole Binaries. 2014, arXiv: 1403.0677.

[35] J.M. Miller, C.S. Reynolds, A.C. Fabian, G. Miniutti, and L.C. Gallo. Stellar-mass Black Hole Spin Constraints from Disk Reflection and Continuum Modeling. *Astrophys. J.*, 697:900–912, 2009, arXiv: 0902.2840.

[36] Rebecca Shafee, Jeffrey E. McClintock, Ramesh Narayan, Shane W. Davis, Li-Xin Li, et al. Estimating the spin of stellar-mass black holes via spectral fitting of the x-ray continuum. *Astrophys. J.*, 636:L113–L116, 2006, arXiv: astro-ph/0508302.

[37] Jeffrey E. McClintock, Ramesh Narayan, Shane W. Davis, Lijun Gou, Akshay Kulkarni, et al. Measuring the Spins of Accreting Black Holes. *Class. Quant. Grav.*, 28:114009, 2011, arXiv: 1101.0811.

[38] Davide Gerosa, Richard O'Shaughnessy, Michael Kesden, Emanuele Berti, and Ulrich Sperhake. Capulets and Montagues: distinguishing the rival families of black-hole spin-orbit resonances by their gravitational-wave signatures. 2014, arXiv: 1403.7147.

[39] M.J. Rees. Gravitational waves from galactic centers? *Class. Quant. Grav.*, 14:1411–1415, 1997.

[40] M.C. Begelman, R.D. Blandford, and M.J. Rees. Massive black hole binaries in active galactic nuclei. *Nature*, 287:307–309, 1980.

[41] Pau Amaro-Seoane, Sofiane Aoudia, Stanislav Babak, Pierre Binetruy, Emanuele Berti, et al. Low-frequency gravitational-wave science with eLISA/NGO. *Class. Quant. Grav.*, 29:124016, 2012, arXiv: 1202.0839.

[42] Matthew J. Benacquista. Relativistic Binaries in Globular Clusters. *Living Rev. Rel.*, 9:2, 2006.

[43] B.D. Metzger and E. Berger. What is the Most Promising Electromagnetic Counterpart of a Neutron Star Binary Merger? *Astrophys. J.*, 746:48, 2012, arXiv: 1108.6056.

[44] Leo P. Singer, Larry R. Price, Ben Farr, Alex L. Urban, Chris Pankow, et al. The First Two Years of Electromagnetic Follow-Up with Advanced LIGO and Virgo. 2014, arXiv: 1404.5623.

[45] J. Abadie et al. Predictions for the Rates of Compact Binary Coalescences Observable by Ground-based Gravitational-wave Detectors. *Class. Quant. Grav.*, 27:173001, 2010, arXiv: 1003.2480.

[46] Ravi Kumar Kopparapu, Chad R. Hanna, Vicky Kalogera, Richard W. O'Shaughnessy, Gabriela Gonzalez, et al. Host Galaxies Catalog Used in LIGO Searches for Compact Binary Coalescence Events. *Astrophys. J.*, 675:1459–1467, 2008, arXiv: 0706.1283.

[47] Richard W. O'Shaughnessy, C. Kim, V. Kalogera, and K. Belczynski. Constraining population synthesis models via empirical binary compact object merger and supernovae rates. *Astrophys. J.*, 672:479–488, 2008, arXiv: astro-ph/0610076.

[48] Vassiliki Kalogera, Chung-Lee Kim, D.R. Lorimer, M. Burgay, N. D'Amico, et al. The Cosmic coalescence rates for double neutron star binaries. *Astrophys. J.*, 601:L179–L182, 2004, arXiv: astro-ph/0312101.

[49] Chunglee Kim, Vicky Kalogera, and Duncan R. Lorimer. Effect of PSR J0737-3039 on the DNS Merger Rate and Implications for GW Detection. *New Astron.Rev.*, 2006, arXiv: astro-ph/0608280.

[50] E.S. Phinney. The Rate of neutron star binary mergers in the universe: Minimal predictions for gravity wave detector. *Astrophys. J.*, 380:L17–L21, 1991.

[51] Curt Cutler and Eanna E. Flanagan. Gravitational waves from merging compact binaries: How accurately can one extract the binary's parameters from the inspiral wave form? *Phys. Rev. D*, 49:2658–2697, 1994, arXiv: gr-qc/9402014.

[52] Jessica McIver. Data Quality Studies of Enhanced Interferometric Gravitational Wave Detectors. *Class. Quant. Grav.*, 29:124010, 2012, arXiv: 1204.2497.

[53] J. Aasi et al. The characterization of Virgo data and its impact on gravitational-wave searches. *Class. Quant. Grav.*, 29:155002, 2012, arXiv: 1203.5613.

[54] Bruce Allen, K. Blackburn, P. Brady, J. Creighton, T. Creighton, et al. Observational limit on gravitational waves from binary neutron stars in the galaxy. *Phys. Rev. Lett.*, 83:1498, 1999, arXiv: gr-qc/9903108.

[55] Bruce Allen. A chi**2 time-frequency discriminator for gravitational wave detection. *Phys. Rev. D*, 71:062001, 2005, arXiv: gr-qc/0405045.

[56] Collin Capano, Yi Pan, and Alessandra Buonanno. Impact of Higher Harmonics in Searching for Gravitational Waves from Non-Spinning Binary Black Holes. 2013, arXiv: 1311.1286.

[57] The LSC-Virgo Compact Binary Coalescence Search Group. Search for binary black hole coalescences, 2010. LIGO Document T1400263.

[58] Luc Blanchet. Gravitational Radiation from Post-Newtonian Sources and Inspiralling Compact Binaries. *Living Rev. Rel.*, 17:2, 2014, arXiv: 1310.1528.

[59] K.S. Thorne. Multipole Expansions of Gravitational Radiation. *Rev. Mod. Phys.*, 52:299–339, 1980.

[60] Misao Sasaki and Hideyuki Tagoshi. Analytic black hole perturbation approach to gravitational radiation. *Living Rev. Rel.*, 6:6, 2003, arXiv: gr-qc/0306120.

[61] A. Buonanno and T. Damour. Effective one-body approach to general relativistic two-body dynamics. *Phys. Rev. D*, 59:084006, 1999, arXiv: gr-qc/9811091.

[62] Alessandra Buonanno and Thibault Damour. Transition from inspiral to plunge in binary black hole coalescences. *Phys. Rev. D*, 62:064015, 2000, arXiv: gr-qc/0001013.

[63] Alessandra Buonanno, Gregory B. Cook, and Frans Pretorius. Inspiral, merger and ring-down of equal-mass black-hole binaries. *Phys. Rev. D*, 75:124018, 2007, arXiv: gr-qc/0610122.

[64] Bela Szilagyi. Key Elements of Robustness in Binary Black Hole Evolutions using Spectral Methods. 2014, arXiv: 1405.3693.

[65] Luis Lehner and Frans Pretorius. Numerical Relativity and Astrophysics. 2014, arXiv: 1405.4840.

[66] Ian Hinder, Alessandra Buonanno, Michael Boyle, Zachariah B. Etienne, James Healy, et al. Error-analysis and comparison to analytical models of numerical waveforms produced by the NRAR Collaboration. *Class. Quant. Grav.*, 31:025012, 2014, arXiv: 1307.5307.

[67] Abdul H. Mroué, Mark A. Scheel, Bela Szilagyi, Harald P. Pfeiffer, Michael Boyle, et al. A catalog of 174 binary black-hole simulations for gravitational-wave astronomy. *Phys. Rev. Lett.*, 111:241104, 2013, arXiv: 1304.6077.

[68] L. Pekowsky, R. O'Shaughnessy, J. Healy, and D. Shoemaker. Comparing gravitational waves from nonprecessing and precessing black hole binaries in the corotating frame. *Phys. Rev. D*, 88(2):024040, 2013, arXiv: 1304.3176.

[69] L. Santamaría, F. Ohme, P. Ajith, B. Brügmann, N. Dorband, M. Hannam, S. Husa, P. Mösta, D. Pollney, C. Reisswig, E. L. Robinson, J. Seiler, and B. Krishnan. Matching post-newtonian and numerical relativity waveforms: Systematic errors and a new phenomenological model for non-precessing black hole binaries. *Phys. Rev. D*, 82:064016, 2010.

[70] Andrea Taracchini, Alessandra Buonanno, Yi Pan, Tanja Hinderer, Michael Boyle, et al. Effective-one-body model for black-hole binaries with generic mass ratios and spins. *Phys. Rev. D*, 89:061502, 2014, arXiv: 1311.2544.

[71] Mark Hannam. Modelling gravitational waves from precessing black-hole binaries: Progress, challenges and prospects. 2013, arXiv: 1312.3641.

[72] P. Ajith, M. Hannam, S. Husa, Y. Chen, B. Bruegmann, et al. Inspiral-merger-ringdown waveforms for black-hole binaries with non-precessing spins. *Phys. Rev. Lett.*, 106:241101, 2011, arXiv: 0909.2867.

[73] Mark Hannam, Patricia Schmidt, Alejandro Boh, Leila Haegel, Sascha Husa, et al. Twist and shout: A simple model of complete precessing black-hole-binary gravitational waveforms. 2013, arXiv: 1308.3271.

[74] P. Ajith et al. The NINJA-2 catalog of hybrid post-Newtonian/numerical-relativity waveforms for non-precessing black-hole binaries. *Class. Quant. Grav.*, 29:124001, 2012, arXiv: 1201.5319.

[75] C. Cutler, Eric Poisson, G.J. Sussman, and L.S. Finn. Gravitational radiation from a particle in circular orbit around a black hole. 2: Numerical results for the nonrotating case. *Phys. Rev. D*, 47:1511–1518, 1993.

[76] Eric Poisson. Gravitational radiation from a particle in circular orbit around a black hole. 6. Accuracy of the postNewtonian expansion. *Phys. Rev. D*, 52:5719–5723, 1995, arXiv: gr-qc/9505030.

[77] Alessandra Buonanno, Bala Iyer, Evan Ochsner, Yi Pan, and B.S. Sathyaprakash. Comparison of post-Newtonian templates for compact binary

inspiral signals in gravitational-wave detectors. *Phys. Rev. D*, 80:084043, 2009, arXiv: 0907.0700.

[78] Thibault Damour and Alessandro Nagar. The Effective One Body description of the Two-Body problem. *Fundam. Theor. Phys.*, 162:211–252, 2011, arXiv: 0906.1769.

[79] Thibault Damour. The general relativistic two body problem. 2013, arXiv: 1312.3505.

[80] Frans Pretorius. Evolution of binary black hole spacetimes. *Phys. Rev. Lett.*, 95:121101, 2005, arXiv: gr-qc/0507014.

[81] Manuela Campanelli, C.O. Lousto, P. Marronetti, and Y. Zlochower. Accurate evolutions of orbiting black-hole binaries without excision. *Phys. Rev. Lett.*, 96:111101, 2006, arXiv: gr-qc/0511048.

[82] John G. Baker, Joan Centrella, Dae-Il Choi, Michael Koppitz, and James van Meter. Gravitational wave extraction from an inspiraling configuration of merging black holes. *Phys. Rev. Lett.*, 96:111102, 2006, arXiv: gr-qc/0511103.

[83] E. Brezin, C. Itzykson, and Jean Zinn-Justin. Relativistic balmer formula including recoil effects. *Phys. Rev. D*, 1:2349–2355, 1970.

[84] Piotr Jaranowski and Gerhard Schafer. Towards the 4th post-Newtonian Hamiltonian for two-point-mass systems. *Phys.Rev.*, D86:061503, 2012, arXiv: 1207.5448.

[85] Piotr Jaranowski and Gerhard Schfer. Dimensional regularization of local singularities in the 4th post-Newtonian two-point-mass Hamiltonian. *Phys.Rev.*, D87:081503, 2013, arXiv: 1303.3225.

[86] Thibault Damour, Piotr Jaranowski, and Gerhard Schfer. Nonlocal-in-time action for the fourth post-Newtonian conservative dynamics of two-body systems. *Phys.Rev.*, D89:064058, 2014, arXiv: 1401.4548.

[87] Thibault Damour, Piotr Jaranowski, and Gerhard Schaefer. On the determination of the last stable orbit for circular general relativistic binaries at the third postNewtonian approximation. *Phys. Rev. D*, 62:084011, 2000, arXiv: gr-qc/0005034.

[88] Alexandre Le Tiec, Abdul Mroué, et al. Periastron Advance in Black Hole Binaries. *Phys. Rev. Lett.*, 107:141101, 2011, arXiv: 1106.3278.

[89] A. H. Mroué, H. P. Pfeiffer, L. E. Kidder, and S. A. Teukolsky. Measuring orbital eccentricity and periastron advance in quasi-circular black hole simulations. *Phys. Rev. D*, 82:124016, 2010, arXiv: 1004.4697.

[90] Thibault Damour. Gravitational Self Force in a Schwarzschild Background and the Effective One Body Formalism. *Phys. Rev.*, 81:024017, 2010, arXiv: 0910.5533.

[91] Yi Pan, Alessandra Buonanno, Michael Boyle, Luisa T. Buchman, Lawrence E. Kidder, et al. Inspiral-merger-ringdown multipolar waveforms of nonspinning black-hole binaries using the effective-one-body formalism. *Phys. Rev. D*, 84:124052, 2011, arXiv: 1106.1021.

[92] Tanja Hinderer, Alessandra Buonanno, Abdul H. Mroué, Daniel A. Hemberger, Geoffrey Lovelace, et al. Periastron advance in spinning black hole binaries: comparing effective-one-body and Numerical Relativity. *Phys. Rev. D*, 88:084005, 2013, arXiv: 1309.0544.

[93] Andrea Taracchini, Yi Pan, Alessandra Buonanno, Enrico Barausse, Michael Boyle, et al. Prototype effective-one-body model for nonprecessing spinning inspiral-merger-ringdown waveforms. *Phys. Rev. D*, 86:024011, 2012, arXiv: 1202.0790.

[94] Tullio Regge and John A. Wheeler. Stability of a Schwarzschild singularity. *Phys. Rev.*, 108:1063–1069, 1957.

[95] Frank J. Zerilli. Effective potential for even parity Regge-Wheeler gravitational perturbation equations. *Phys. Rev. Lett.*, 24:737–738, 1970.

[96] F.J. Zerilli. Gravitational field of a particle falling in a schwarzschild geometry analyzed in tensor harmonics. *Phys. Rev. D*, 2:2141–2160, 1970.

[97] Saul A. Teukolsky. Perturbations of a rotating black hole. 1. Fundamental equations for gravitational electromagnetic and neutrino field perturbations. *Astrophys. J.*, 185:635–647, 1973.

[98] Thibault Damour, Bala R. Iyer, and B.S. Sathyaprakash. Improved filters for gravitational waves from inspiralling compact binaries. *Phys. Rev. D*, 57:885–907, 1998, arXiv: gr-qc/9708034.

[99] Thibault Damour and Alessandro Nagar. Faithful effective-one-body waveforms of small-mass-ratio coalescing black-hole binaries. *Phys. Rev. D*, 76:064028, 2007, arXiv: 0705.2519.

[100] Thibault Damour, Bala R. Iyer, and Alessandro Nagar. Improved resummation of post-Newtonian multipolar waveforms from circularized compact binaries. *Phys. Rev. D*, 79:064004, 2009, arXiv: 0811.2069.

[101] Yi Pan, Alessandra Buonanno, Ryuichi Fujita, Etienne Racine, and Hideyuki Tagoshi. Post-Newtonian factorized multipolar waveforms for spinning, non-precessing black-hole binaries. *Phys. Rev. D*, 83:064003, 2011, arXiv: 1006.0431.

[102] Alessandra Buonanno, Yanbei Chen, and Thibault Damour. Transition from inspiral to plunge in precessing binaries of spinning black holes. *Phys. Rev. D*, 74:104005, 2006, arXiv: gr-qc/0508067.

[103] P. C. Peters and J. Mathews. Gravitational radiation from point masses in a keplerian orbit. *Phys. Rev.*, 131(1):435–440, 1963.

[104] Alessandra Buonanno, Gregory B. Cook, and Frans Pretorius. Inspiral, merger, and ring-down of equal-mass black-hole binaries. *Phys. Rev. D*, 75(12):124018, 2007.

[105] `http://www.black-holes.org/SpEC.html`.

[106] Benjamin J. Owen. Search templates for gravitational waves from inspiraling binaries: Choice of template spacing. *Phys. Rev. D*, 53:6749–6761, 1996, arXiv: gr-qc/9511032.

[107] Lee Lindblom, Benjamin J. Owen, and Duncan A. Brown. Model Waveform Accuracy Standards for Gravitational Wave Data Analysis. *Phys. Rev. D*, 78:124020, 2008, arXiv: 0809.3844.

[108] Mark A. Miller. Accuracy requirements for the calculation of gravitational waveforms from coalescing compact binaries in numerical relativity. *Phys. Rev. D*, 71:104016, 2005, arXiv: gr-qc/0502087.

[109] Lee Lindblom. Optimal Calibration Accuracy for Gravitational Wave Detectors. *Phys. Rev.*, 80:042005, 2009, arXiv: 0906.5153.

[110] Lee Lindblom. Use and Abuse of the Model Waveform Accuracy Standards. *Phys. Rev.*, 80:064019, 2009, arXiv: 0907.0457.

[111] Lee Lindblom, John G. Baker, and Benjamin J. Owen. Improved Time-Domain Accuracy Standards for Model Gravitational Waveforms. *Phys. Rev.*, 82:084020, 2010, arXiv: 1008.1803.

[112] Tyson B. Littenberg, John G. Baker, Alessandra Buonanno, and Bernard J. Kelly. Systematic biases in parameter estimation of binary black-hole mergers. *Phys. Rev. D*, 87:104003, 2013, arXiv: 1210.0893.

[113] M. Davis, R. Ruffini, W.H. Press, and R.H. Price. Gravitational radiation from a particle falling radially into a schwarzschild black hole. *Phys.Rev.Lett.*, 27:1466–1469, 1971.

[114] Andrea Taracchini, Alessandra Buonanno, Gaurav Khanna, and Scott A. Hughes. Small mass plunging into a Kerr black hole: Anatomy of the inspiral-merger-ringdown waveforms. 1404.1819, 2014.

[115] S.A. Teukolsky and W.H. Press. Perturbations of a rotating black hole. III - Interaction of the hole with gravitational and electromagnet ic radiation. *Astrophys. J.*, 193:443–461, 1974.

[116] Scott A. Hughes. The Evolution of circular, nonequatorial orbits of Kerr black holes due to gravitational wave emission. *Phys. Rev. D*, 61:084004, 2000, arXiv: gr-qc/9910091.

[117] Steve Drasco and Scott A. Hughes. Gravitational wave snapshots of generic extreme mass ratio inspirals. *Phys. Rev. D*, 73:024027, 2006, arXiv: gr-qc/0509101.

[118] Nicolas Yunes, Alessandra Buonanno, Scott A. Hughes, Yi Pan, Enrico Barausse, et al. Extreme Mass-Ratio Inspirals in the Effective-One-Body Approach: Quasi-Circular, Equatorial Orbits around a Spinning Black Hole. *Phys. Rev. D*, 83:044044, 2011, arXiv: 1009.6013.

[119] Enrico Barausse, Alessandra Buonanno, Scott A. Hughes, Gaurav Khanna, Stephen O'Sullivan, et al. Modeling multipolar gravitational-wave emission from small mass-ratio mergers. *Phys. Rev. D*, 85:024046, 2012, arXiv: 1110.3081.

[120] Andrea Taracchini, Alessandra Buonanno, Scott A. Hughes, and Gaurav Khanna. Modeling the horizon-absorbed gravitational flux for equatorial-circular orbits in Kerr spacetime. *Phys. Rev. D*, 88:044001, 2013, arXiv: 1305.2184.

[121] Wen-Biao Han and Zhoujian Cao. Constructing EOB dynamics with numerical energy flux for intermediate-mass-ratio inspirals. *Phys. Rev. D*, 84:044014, 2011, arXiv: 1108.0995.

[122] James M. Bardeen, William H. Press, and Saul A Teukolsky. Rotating black holes: Locally nonrotating frames, energy extraction, and scalar synchrotron radiation. *Astrophys. J.*, 178:347, 1972.

[123] William Krivan, Pablo Laguna, Philippos Papadopoulos, and Nils Andersson. Dynamics of perturbations of rotating black holes. *Phys. Rev. D*, 56:3395–3404, 1997, arXiv: gr-qc/9702048.

[124] Ernst Nils Dorband, Emanuele Berti, Peter Diener, Erik Schnetter, and Manuel Tiglio. A Numerical study of the quasinormal mode excitation of Kerr black holes. *Phys. Rev. D*, 74:084028, 2006, arXiv: gr-qc/0608091.

[125] Alessandro Nagar, Thibault Damour, and Angelo Tartaglia. Binary black hole merger in the extreme mass ratio limit. *Class. Quant. Grav.*, 24:S109–S124, 2007, arXiv: gr-qc/0612096.

[126] Sebastiano Bernuzzi and Alessandro Nagar. Binary black hole merger in the extreme-mass-ratio limit: a multipolar analysis. *Phys. Rev. D*, 81:084056, 2010, arXiv: 1003.0597.

[127] Emanuele Berti, Vitor Cardoso, and Andrei O. Starinets. Quasinormal modes of black holes and black branes. *Class. Quant. Grav.*, 26:163001, 2009, arXiv: 0905.2975.

[128] Alessandro Nagar and Sarp Akcay. Horizon-absorbed energy flux in circularized, nonspinning black-hole binaries and its effective-one-body representation. *Phys. Rev. D*, 85:044025, 2012, arXiv: 1112.2840.

[129] Curt Cutler, Lee Samuel Finn, Eric Poisson, and Gerald Jay Sussman. Gravitational radiation from a particle in circular orbit around a black hole. II. Numerical results for the nonrotating case. *Phys. Rev. D*, 47(4):1511–1518, 1993.

[130] C. Cutler, D. Kennefick, and Eric Poisson. Gravitational radiation reaction for bound motion around a Schwarzschild black hole. *Phys. Rev. D*, 50:3816–3835, 1994.

[131] Scott A. Hughes. Evolution of circular, nonequatorial orbits of Kerr black holes due to gravitational wave emission. 2. Inspiral trajectories and gravitational wave forms. *Phys. Rev. D*, 64:064004, 2001, arXiv: gr-qc/0104041.

[132] Kostas Glampedakis and Daniel Kennefick. Zoom and whirl: Eccentric equatorial orbits around spinning black holes and their evolution under gravitational radiation reaction. *Phys. Rev. D*, 66:044002, 2002, arXiv: gr-qc/0203086.

[133] R. Penrose. Gravitational collapse: The role of general relativity. *Riv. Nuovo Cim.*, 1:252–276, 1969.

[134] William H. Press and Saul A. Teukolsky. Floating Orbits, Superradiant Scattering and the Black-hole Bomb. *Nature*, 238:211–212, 1972.

[135] Vitor Cardoso and Paolo Pani. Tidal acceleration of black holes and superradiance. 2012, arXiv: 1205.3184.

[136] James B. Hartle. Tidal Friction in Slowly Rotating Black Holes. *Phys. Rev. D*, 8:1010–1024, 1973.

[137] James B. Hartle. Tidal shapes and shifts on rotating black holes. *Phys. Rev. D*, 9:2749–2759, 1974.

[138] Kip S. Thorne, Richard H. Price, and Douglas A. MacDonald. *Black Holes: The Membrane Paradigm*. Yale University Press, New Haven and London, first edition, 1986.

[139] Eric Poisson and Misao Sasaki. Gravitational radiation from a particle in circular orbit around a black hole. 5: Black hole absorption and tail corrections. *Phys. Rev. D*, 51:5753–5767, 1995, arXiv: gr-qc/9412027.

[140] Hideyuki Tagoshi, Shuhei Mano, and Eiichi Takasugi. PostNewtonian expansion of gravitational waves from a particle in circular orbits around a rotating black hole: Effects of black hole absorption. *Prog. Theor. Phys.*, 98:829–850, 1997, arXiv: gr-qc/9711072.

[141] Yasushi Mino, Misao Sasaki, Masaru Shibata, Hideyuki Tagoshi, and Takahiro Tanaka. Black hole perturbation: Chapter 1. *Prog. Theor. Phys. Suppl.*, 128:1–121, 1997, arXiv: gr-qc/9712057.

[142] Marek Artur Abramowicz and Wlodek Kluzniak. A Precise determination of angular momentum in the black hole candidate GRO J1655-40. *Astron. Astrophys.*, 374:L19, 2001, arXiv: astro-ph/0105077.

[143] Tod E. Strohmayer. Discovery of a 450 hz qpo from the microquasar gro j1655-40 with rxte. 2001, arXiv: astro-ph/0104487.

[144] Jeffrey E. McClintock, Rebecca Shafee, Ramesh Narayan, Ronald A. Remillard, Shane W. Davis, et al. The Spin of the Near-Extreme Kerr Black Hole GRS 1915+105. *Astrophys. J.*, 652:518–539, 2006, arXiv: astro-ph/0606076.

[145] Lijun Gou, Jeffrey E. McClintock, Mark J. Reid, Jerome A. Orosz, James F. Steiner, et al. The Extreme Spin of the Black Hole in Cygnus X-1. *Astrophys. J.*, 742:85, 2011, arXiv: 1106.3690.

[146] Andrew C. Fabian and Giovanni Miniutti. The X-ray spectra of accreting Kerr black holes. 2005, arXiv: astro-ph/0507409.

[147] Laura W. Brenneman and Christopher S. Reynolds. Constraining Black Hole Spin Via X-ray Spectroscopy. *Astrophys. J.*, 652:1028–1043, 2006, arXiv: astro-ph/0608502.

[148] L.W. Brenneman, C.S. Reynolds, M.A. Nowak, R.C. Reis, M. Trippe, et al. The Spin of the Supermassive Black Hole in NGC 3783. *Astrophys. J.*, 736:103, 2011, arXiv: 1104.1172.

[149] Christopher S. Reynolds. Measuring Black Hole Spin using X-ray Reflection Spectroscopy. 2013, arXiv: 1302.3260.

[150] B.M. Barker and R.F. O'Connell. Gravitational Two-Body Problem with Arbitrary Masses, Spins, and Quadrupole Moments. *Phys. Rev. D*, 12:329–335, 1975.

[151] B. M. Barker and R. F. O'Connell. The gravitational interaction: Spin, rotation, and quantum effects – a review. *Gen. Relativ. Gravit.*, 11:149–175, 1979.

[152] Lawrence E. Kidder, Clifford M. Will, and Alan G. Wiseman. Spin effects in the inspiral of coalescing compact binaries. *Phys. Rev. D*, 47:4183–4187, 1993, arXiv: gr-qc/9211025.

[153] Lawrence E. Kidder. Coalescing binary systems of compact objects to post-Newtonian 5/2 order. 5. Spin effects. *Phys. Rev. D*, 52:821–847, 1995, arXiv: gr-qc/9506022.

[154] Sylvain Marsat, Alejandro Bohe, Guillaume Faye, and Luc Blanchet. Next-to-next-to-leading order spin-orbit effects in the equations of motion of compact binary systems. *Class. Quant. Grav.*, 30:055007, 2013, arXiv: 1210.4143.

[155] Alejandro Bohe, Sylvain Marsat, Guillaume Faye, and Luc Blanchet. Next-to-next-to-leading order spin-orbit effects in the near-zone metric and precession equations of compact binaries. *Class. Quant. Grav.*, 30:075017, 2013, arXiv: 1212.5520.

[156] Alejandro Boh, Sylvain Marsat, and Luc Blanchet. Next-to-next-to-leading order spinorbit effects in the gravitational wave flux and orbital phasing of compact binaries. *Class. Quant. Grav.*, 30:135009, 2013, arXiv: 1303.7412.

[157] Walter D. Goldberger and Ira Z. Rothstein. An Effective field theory of gravity for extended objects. *Phys. Rev. D*, 73:104029, 2006, arXiv: hep-th/0409156.

[158] Rafael A. Porto. Post-Newtonian corrections to the motion of spinning bodies in NRGR. *Phys. Rev. D*, 73:104031, 2006, arXiv: gr-qc/0511061.

[159] Alessandra Buonanno, Guillaume Faye, and Tanja Hinderer. Spin effects on gravitational waves from inspiraling compact binaries at second post-Newtonian order. *Phys. Rev. D*, 87(4):044009, 2013, arXiv: 1209.6349.

[160] Manuela Campanelli, C.O. Lousto, and Y. Zlochower. Spinning-black-hole binaries: The orbital hang up. *Phys. Rev. D*, 74:041501, 2006, arXiv: gr-qc/0604012.

[161] B.M. Barker and R.F. O'Connell. Derivation of the equations of motion of a gyroscope from the quantum theory of gravitation. *Phys. Rev. D*, 2:1428–1435, 1970.

[162] Daniel A. Hemberger, Geoffrey Lovelace, Thomas J. Loredo, Lawrence E. Kidder, Mark A. Scheel, et al. Final spin and radiated energy in numerical simulations of binary black holes with equal masses and equal, aligned or anti-aligned spins. *Phys. Rev. D*, 88:064014, 2013, arXiv: 1305.5991.

[163] Theocharis A. Apostolatos, Curt Cutler, Gerald J. Sussman, and Kip S. Thorne. Spin induced orbital precession and its modulation of the gravitational wave forms from merging binaries. *Phys. Rev. D*, 49:6274–6297, 1994.

[164] T.A. Apostolatos. Search templates for gravitational waves from precessing, inspiraling binaries. *Phys. Rev. D*, 52:605–620, 1995.

[165] Kip S. Thorne and James B. Hartle. Laws of motion and precession for black holes and other bodies. *Phys. Rev. D*, 31:1815–1837, 1984.

[166] Alessandra Buonanno, Yan-bei Chen, and Michele Vallisneri. Detecting gravitational waves from precessing binaries of spinning compact objects: Adiabatic limit. *Phys. Rev. D*, 67:104025, 2003, arXiv: gr-qc/0211087.

[167] Yi Pan, Alessandra Buonanno, Yan-bei Chen, and Michele Vallisneri. A Physical template family for gravitational waves from precessing binaries of spinning compact objects: Application to single spin binaries. *Phys. Rev. D*, 69:104017, 2004, arXiv: gr-qc/0310034.

[168] B. Abbott et al. Search of S3 LIGO data for gravitational wave signals from spinning black hole and neutron star binary inspirals. *Phys. Rev. D*, 78:042002, 2008, arXiv: 0712.2050.

[169] Chris Van Den Broeck, Duncan A. Brown, Thomas Cokelaer, Ian Harry, Gareth Jones, et al. Template banks to search for compact binaries with spinning components in gravitational wave data. *Phys. Rev. D*, 80:024009, 2009, arXiv: 0904.1715.

[170] Duncan A. Brown, Andrew Lundgren, and R. O'Shaughnessy. Nonspinning searches for spinning binaries in ground-based detector data: Amplitude and mismatch predictions in the constant precession cone approximation. *Phys. Rev. D*, 86:064020, 2012, arXiv: 1203.6060.

[171] P. Ajith, N. Fotopoulos, S. Privitera, A. Neunzert, and A.J. Weinstein. An effectual template bank for the detection of gravitational waves from inspiralling compact binaries with generic spins. *Phys. Rev. D*, 89:084041, 2014, arXiv: 1210.6666.

[172] Stephen Privitera, Satyanarayan R. P. Mohapatra, Parameswaran Ajith, Kipp Cannon, Nickolas Fotopoulos, et al. Improving the sensitivity of a search for coalescing binary black holes with non-precessing spins in gravitational wave data. *Phys. Rev. D*, 89:024003, 2014, arXiv: 1310.5633.

[173] Duncan A. Brown, Ian Harry, Andrew Lundgren, and Alexander H. Nitz. Detecting binary neutron star systems with spin in advanced gravitational-wave detectors. *Phys. Rev. D*, 86:084017, 2012, arXiv: 1207.6406.

[174] I.W. Harry, A.H. Nitz, Duncan A. Brown, A. Lundgren, Evan Ochsner, et al. Investigating the effect of precession on searches for neutron-star-black-hole binaries with Advanced LIGO. *Phys. Rev. D*, 89:024010, 2014, arXiv: 1307.3562.

[175] Mark A. Scheel, Michael Boyle, Tony Chu, Lawrence E. Kidder, Keith D. Matthews, and Harald P. Pfeiffer. High-accuracy waveforms for binary black hole inspiral, merger, and ringdown. *Phys. Rev. D*, 79:024003, 2009, arXiv: 0810.1767.

[176] Alexander H. Nitz, Andrew Lundgren, Duncan A. Brown, Evan Ochsner, Drew Keppel, et al. Accuracy of gravitational waveform models for observing

neutron-star–black-hole binaries in Advanced LIGO. *Phys. Rev. D*, 88:124039, 2013, arXiv: 1307.1757.

[177] Salvatore Vitale, Ryan Lynch, John Veitch, Vivien Raymond, and Riccardo Sturani. Measuring the spin of black holes in binary systems using gravitational waves. 2014, arXiv: 1403.0129.

[178] Jocelyn S. Read, Charalampos Markakis, Masaru Shibata, Koji Uryu, Jolien D.E. Creighton, et al. Measuring the neutron star equation of state with gravitational wave observations. *Phys. Rev. D*, 79:124033, 2009, arXiv: 0901.3258.

[179] Will M. Farr, Niharika Sravan, Andrew Cantrell, Laura Kreidberg, Charles D. Bailyn, et al. The Mass Distribution of Stellar-Mass Black Holes. *Astrophys. J.*, 741:103, 2011, arXiv: 1011.1459.

[180] Stephen Fairhurst. Triangulation of gravitational wave sources with a network of detectors. *New J. Phys.*, 11:123006, 2009, arXiv: 0908.2356.

[181] J. Aasi et al. Prospects for Localization of Gravitational Wave Transients by the Advanced LIGO and Advanced Virgo Observatories. 2013, arXiv: 1304.0670.

[182] Joshua S. Bloom, Daniel E. Holz, Scott A. Hughes, Kristen Menou, Allan Adams, et al. Astro2010 Decadal Survey Whitepaper: Coordinated Science in the Gravitational and Electromagnetic Skies. 2009, arXiv: 0902.1527.

[183] Harald P. Pfeiffer, Gregory B. Cook, and Saul A. Teukolsky. Comparing initial-data sets for binary black holes. *Phys. Rev. D*, 66:024047, 2002.

[184] Sergio Dain, Carlos O Lousto, and Yosef Zlochower. Extra-large remnant recoil velocities and spins from near-extremal-Bowen–York-spin black-hole binaries. *Phys. Rev. D*, 78:024039, 2008, arXiv: 0803.0351v2.

[185] Geoffrey Lovelace, Robert Owen, Harald P. Pfeiffer, and Tony Chu. Binary-black-hole initial data with nearly-extremal spins. *Phys. Rev. D*, 78:084017, 2008.

[186] Tony Chu, Harald P. Pfeiffer, and Mark A. Scheel. High accuracy simulations of black hole binaries: Spins anti-aligned with the orbital angular momentum. *Phys. Rev. D*, 80:124051, 2009, arXiv: 0909.1313.

[187] Alessandra Buonanno, Lawrence E. Kidder, Abdul H. Mroué, Harald P. Pfeiffer, and Andrea Taracchini. Reducing orbital eccentricity of precessing black-hole binaries. *Phys. Rev. D*, 83:104034, 2011, arXiv: 1012.1549.

[188] Thibault Damour. Coalescence of two spinning black holes: an effective one-body approach. *Phys. Rev. D*, 64:124013, 2001, arXiv: gr-qc/0103018.

[189] Thibault Damour, Piotr Jaranowski, and Gerhard Schaefer. Effective one body approach to the dynamics of two spinning black holes with next-to-leading order spin-orbit coupling. *Phys. Rev. D*, 78:024009, 2008, arXiv: 0803.0915.

[190] Brandon Carter. Global structure of the Kerr family of gravitational fields. *Phys. Rev.*, 174:1559–1571, 1968.

[191] Enrico Barausse and Alessandra Buonanno. An Improved effective-one-body Hamiltonian for spinning black-hole binaries. *Phys. Rev. D*, 81:084024, 2010, arXiv: 0912.3517.

[192] Enrico Barausse and Alessandra Buonanno. Extending the effective-one-body Hamiltonian of black-hole binaries to include next-to-next-to-leading spin-orbit couplings. *Phys. Rev. D*, 84:104027, 2011, arXiv: 1107.2904.

[193] Enrico Barausse, Etienne Racine, and Alessandra Buonanno. Hamiltonian of a spinning test-particle in curved spacetime. *Phys. Rev. D*, 80:104025, 2009, arXiv: 0907.4745.

[194] Yi Pan, Alessandra Buonanno, Andrea Taracchini, Lawrence E. Kidder, Abdul H. Mroué, et al. Inspiral-merger-ringdown waveforms of spinning, precessing black-hole binaries in the effective-one-body formalism. *Phys. Rev. D*, 89:084006, 2014, arXiv: 1307.6232.

[195] Leor Barack and Norichika Sago. Gravitational self-force on a particle in eccentric orbit around a Schwarzschild black hole. *Phys. Rev.*, 81:084021, 2010, arXiv: 1002.2386.

[196] Benjamin D. Lackey, Koutarou Kyutoku, Masaru Shibata, Patrick R. Brady, and John L. Friedman. Extracting equation of state parameters from black hole-neutron star mergers: aligned-spin black holes and a preliminary waveform model. *Phys. Rev. D*, 89:043009, 2014, arXiv: 1303.6298.

[197] Michael Pürrer. Frequency domain reduced order models for gravitational waves from aligned-spin black-hole binaries. 2014, arXiv: 1402.4146.

[198] Yi Pan, Alessandra Buonanno, Andrea Taracchini, Michael Boyle, Lawrence E. Kidder, Abdul H. Mroué, Harald P. Pfeiffer, Mark A. Scheel, Béla Szilágyi, and Anil Zenginoglu. Stability of nonspinning effective-one-body model in approximating two-body dynamics and gravitational-wave emission. *Phys. Rev. D*, 89:061501, 2014, arXiv: 1311.2565.

[199] T. Damour, A. Nagar, and M. Trias. Accuracy and effectualness of closed-form, frequency-domain waveforms for nonspinning black hole binaries. *Phys. Rev. D*, 83(2):024006, 2011.

[200] Michael Boyle. Uncertainty in hybrid gravitational waveforms: Optimizing initial orbital frequencies for binary black-hole simulations. *Phys. Rev. D*, 84:064013, 2011.

[201] Frank Ohme, Mark Hannam, and Sascha Husa. Reliability of complete gravitational waveform models for compact binary coalescences. *Phys. Rev. D*, 84:064029, 2011.

[202] Ilana MacDonald, Samaya Nissanke, and Harald P. Pfeiffer. Suitability of post-Newtonian/numerical-relativity hybrid waveforms for gravitational wave detectors. *Class. Quantum Grav.*, 28(13):134002, 2011, arXiv: 1102.5128.

[203] Ilana MacDonald, Abdul H. Mroué, Harald P. Pfeiffer, Michael Boyle, Lawrence E. Kidder, Mark A. Scheel, Béla Szilágyi, and Nicholas W. Taylor. Suitability of hybrid gravitational waveforms for unequal-mass binaries. *Phys. Rev. D*, 87:024009, 2013, arXiv: 1210.3007.

[204] Albert Einstein. Explanation of the Perihelion Motion of Mercury from the General Theory of Relativity. *Sitzungsber. Preuss. Akad. Wiss. Berlin (Math. Phys.)*, 1915:831–839, 1915.

[205] Ingrid H. Stairs. Testing General Relativity with Pulsar Timing. *Living Rev. Rel.*, 6:5, 2003.

[206] Eric Poisson. The Motion of point particles in curved space-time. *Living Rev. Rel.*, 7:6, 2004, arXiv: gr-qc/0306052.

[207] Joan Centrella, John G. Baker, Bernard J. Kelly, and James R. van Meter. Black-hole binaries, gravitational waves, and numerical relativity. *Rev. Mod. Phys.*, 82:3069, 2010, arXiv: 1010.5260.

[208] Carlos O. Lousto, Manuela Campanelli, and Yosef Zlochower. Remnant Masses, Spins and Recoils from the Merger of Generic Black-Hole Binaries. *Class. Quant. Grav.*, 27:114006, 2010, arXiv: 0904.3541.

[209] U. Sperhake, B. Bruegmann, D. Muller, and C.F. Sopuerta. 11-orbit inspiral of a mass ratio 4:1 black-hole binary. *Class. Quant. Grav.*, 28:134004, 2011.

[210] Luisa T. Buchman, Harald P. Pfeiffer, Mark A. Scheel, and Bela Szilagyi. Simulations of non-equal mass black hole binaries with spectral methods. *Phys. Rev. D*, 86:084033, 2012, arXiv: 1206.3015.

[211] Michael Boyle, Duncan A. Brown, Lawrence E. Kidder, Abdul H. Mroué, Harald P. Pfeiffer, Mark A. Scheel, Gergory B. Cook, and Saul A. Teukolsky. High-accuracy comparison of numerical relativity simulations with post-Newtonian expansions. *Phys. Rev. D*, 76:124038, 2007, arXiv: 0710.0158.

[212] T. Damour and Gerhard Schaefer. Higher Order Relativistic Periastron Advances and Binary Pulsars. *Nuovo Cim.*, B101:127, 1988.

[213] H. P. Robertson. Note on the preceding paper: The two body problem in general relativity. *Annals of Mathematics*, 39(1):101–104, 1938.

[214] Thibault Damour, Piotr Jaranowski, and Gerhard Schaefer. Dynamical invariants for general relativistic two-body systems at the third postNewtonian approximation. *Phys. Rev. D*, 62:044024, 2000, arXiv: gr-qc/9912092.

[215] Leor Barack and Norichika Sago. Gravitational self-force correction to the innermost stable circular orbit of a Schwarzschild black hole. *Phys. Rev. Lett.*, 102:191101, 2009, arXiv: 0902.0573.

[216] Leor Barack and Norichika Sago. Beyond the geodesic approximation: conservative effects of the gravitational self-force in eccentric orbits around a Schwarzschild black hole. *Phys. Rev.*, 83:084023, 2011, arXiv: 1101.3331.

[217] Leor Barack, Thibault Damour, and Norichika Sago. Precession effect of the gravitational self-force in a Schwarzschild spacetime and the effective one-body formalism. *Phys. Rev. D*, 82:084036, 2010, arXiv: 1008.0935.

[218] Luc Blanchet. Innermost circular orbit of binary black holes at the third postNewtonian approximation. *Phys. Rev. D*, 65:124009, 2002, arXiv: gr-qc/0112056.

[219] Amos Ori and Kip S. Thorne. The Transition from inspiral to plunge for a compact body in a circular equatorial orbit around a massive, spinning black hole. *Phys. Rev. D*, 62:124022, 2000, arXiv: gr-qc/0003032.

[220] Duncan A. Brown, Hua Fang, Jonathan R. Gair, Chao Li, Geoffrey Lovelace, et al. Prospects for detection of gravitational waves from intermediate-mass-ratio inspirals. *Phys. Rev. Lett.*, 99:201102, 2007, arXiv: gr-qc/0612060.

[221] Alejandra Castro, Alexander Maloney, and Andrew Strominger. Hidden Conformal Symmetry of the Kerr Black Hole. *Phys. Rev. D*, 82:024008, 2010, arXiv: 1004.0996.

[222] Thomas Hartman, Keiju Murata, Tatsuma Nishioka, and Andrew Strominger. CFT Duals for Extreme Black Holes. *JHEP*, 0904:019, 2009, arXiv: 0811.4393.

[223] Achilleas P. Porfyriadis and Andrew Strominger. Gravity Waves from Kerr/CFT. 2014, arXiv: 1401.3746.

[224] Shahar Hadar, Achilleas P. Porfyriadis, and Andrew Strominger. Gravity Waves from Extreme-Mass-Ratio Plunges into Kerr Black Holes. 2014, arXiv: 1403.2797.

[225] Huan Yang, David A. Nichols, Fan Zhang, Aaron Zimmerman, Zhongyang Zhang, et al. Quasinormal-mode spectrum of Kerr black holes and its geometric interpretation. *Phys. Rev. D*, 86:104006, 2012, arXiv: 1207.4253.

[226] Valeria Ferrari and Bahram Mashhoon. New approach to the quasinormal modes of a black hole. *Phys. Rev. D*, 30:295–304, 1984.

[227] Bahram Mashhoon. Stability of charged rotating black holes in the eikonal approximation. *Phys. Rev. D*, 31(2):290–293, 1985.

[228] Sam R. Dolan. The Quasinormal Mode Spectrum of a Kerr Black Hole in the Eikonal Limit. *Phys. Rev. D*, 82:104003, 2010, arXiv: 1007.5097.

[229] Huan Yang, Fan Zhang, Aaron Zimmerman, David A. Nichols, Emanuele Berti, et al. Branching of quasinormal modes for nearly extremal Kerr black holes. *Phys. Rev. D*, 87:041502, 2013, arXiv: 1212.3271.

[230] Huan Yang, Aaron Zimmerman, Anl Zenginolu, Fan Zhang, Emanuele Berti, et al. Quasinormal modes of nearly extremal Kerr spacetimes: spectrum bifurcation and power-law ringdown. *Phys. Rev. D*, 88(4):044047, 2013, arXiv: 1307.8086.

[231] Yasushi Mino and Jeandrew Brink. Gravitational Radiation from Plunging Orbits: Perturbative Study. *Phys. Rev. D*, 78:124015, 2008, arXiv: 0809.2814.

[232] Aaron Zimmerman and Yanbei Chen. New Generic Ringdown Frequencies at the Birth of a Kerr Black Hole. *Phys. Rev. D*, 84:084012, 2011, arXiv: 1106.0782.

[233] Sebastiano Bernuzzi, Alessandro Nagar, and Anil Zenginoglu. Binary black hole coalescence in the extreme-mass-ratio limit: testing and improving the effective-one-body multipolar waveform. *Phys. Rev. D*, 83:064010, 2011, arXiv: 1012.2456.

[234] Sebastiano Bernuzzi, Alessandro Nagar, and Anil Zenginoglu. Binary black hole coalescence in the large-mass-ratio limit: the hyperboloidal layer method and waveforms at null infinity. *Phys. Rev. D*, 84:084026, 2011, arXiv: 1107.5402.

[235] Sebastiano Bernuzzi, Alessandro Nagar, and Anil Zenginoglu. Horizon-absorption effects in coalescing black-hole binaries: An effective-one-body study of the non-spinning case. *Phys. Rev. D*, 86:104038, 2012, arXiv: 1207.0769.

[236] Thibault Damour, Alessandro Nagar, and Sebastiano Bernuzzi. Improved effective-one-body description of coalescing nonspinning black-hole binaries and its numerical-relativity completion. *Phys. Rev. D*, 87(8):084035, 2013, arXiv: 1212.4357.

[237] Thibault Damour and Achamveedu Gopakumar. Gravitational recoil during binary black hole coalescence using the effective one body approach. *Phys. Rev. D*, 73:124006, 2006, arXiv: gr-qc/0602117.

[238] Michael Boyle, Alessandra Buonanno, Lawrence E. Kidder, Abdul H. Mroué, Yi Pan, et al. High-accuracy numerical simulation of black-hole binaries:

Computation of the gravitational-wave energy flux and comparisons with post-Newtonian approximants. *Phys. Rev. D*, 78:104020, 2008, arXiv: 0804.4184.

[239] Yi Pan, Alessandra Buonanno, Luisa T. Buchman, Tony Chu, Lawrence E. Kidder, et al. Effective-one-body waveforms calibrated to numerical relativity simulations: coalescence of non-precessing, spinning, equal-mass black holes. *Phys. Rev. D*, 81:084041, 2010, arXiv: 0912.3466.

[240] Anil Zenginoglu and Gaurav Khanna. Null infinity waveforms from extreme-mass-ratio inspirals in Kerr spacetime. *Phys. Rev. D*, X1:021017, 2011, arXiv: 1108.1816.

[241] Justin McKennon, Gary Forrester, and Gaurav Khanna. High Accuracy Gravitational Waveforms from Black Hole Binary Inspirals Using OpenCL. *Proceedings of XSEDE12*, 2012, arXiv: 1206.0270.

[242] M. Davis, R. Ruffini, J. Tiomno, and F. Zerilli. Can synchrotron gravitational radiation exist? *Phys. Rev. Lett.*, 28:1352–1355, 1972.

[243] R.A. Breuer, R. Ruffini, J. Tiomno, and C.V. Vishveshwara. Vector and tensor radiation from schwarzschild relativistic circular geodesics. *Phys. Rev. D*, 7:1002–1007, 1973.

[244] P.L. Chrzanowski and Charles W. Misner. Geodesic synchrotron radiation in the Kerr geometry by the method of asymptotically factorized Green's functions. *Phys. Rev. D*, 10:1701–1721, 1974.

[245] R. A. Breuer, editor. *Gravitational perturbation theory and synchrotron radiation*, volume 44 of *Lecture Notes in Physics, Berlin Springer Verlag*, 1975.

[246] Emanuele Berti, Vitor Cardoso, Jose A. Gonzalez, Ulrich Sperhake, Mark Hannam, et al. Inspiral, merger and ringdown of unequal mass black hole binaries: A Multipolar analysis. *Phys. Rev. D*, 76:064034, 2007, arXiv: gr-qc/0703053.

[247] Jeremy D. Schnittman, Alessandra Buonanno, James R. van Meter, John G. Baker, William D. Boggs, et al. Anatomy of the binary black hole recoil: A multipolar analysis. *Phys. Rev. D*, 77:044031, 2008, arXiv: 0707.0301.

[248] John G. Baker, William D. Boggs, Joan Centrella, Bernard J. Kelly, Sean T. McWilliams, et al. Mergers of non-spinning black-hole binaries: Gravitational radiation characteristics. *Phys. Rev. D*, 78:044046, 2008, arXiv: 0805.1428.

[249] Bernard J. Kelly, John G. Baker, William D. Boggs, Sean T. McWilliams, and Joan Centrella. Mergers of black-hole binaries with aligned spins: Waveform characteristics. *Phys. Rev. D*, 84:084009, 2011, arXiv: 1107.1181.

[250] Bernard J. Kelly and John G. Baker. Decoding mode mixing in black-hole merger ringdown. *Phys. Rev. D*, 87:084004, 2013, arXiv: 1212.5553.

[251] Hideyuki Tagoshi, Masaru Shibata, Takahiro Tanaka, and Misao Sasaki. Post-Newtonian expansion of gravitational waves from a particle in circular orbits around a rotating black hole: Up to O (v^8) beyond the quadrupole formula. *Phys. Rev. D*, 54:1439–1459, 1996, arXiv: gr-qc/9603028.

[252] Abhay G Shah. Gravitational-wave flux for a particle orbiting a Kerr black hole to 20th post-Newtonian order: a numerical approach. 2014, arXiv: 1403.2697.

[253] Abdul H. Mroué and Harald P. Pfeiffer. Precessing Binary Black Holes Simulations: Quasicircular Initial Data. 2012, arXiv: 1210.2958.

[254] Daniel A. Hemberger, Mark A. Scheel, Lawrence E. Kidder, Bela Szilagyi, Geoffrey Lovelace, et al. Dynamical Excision Boundaries in Spectral Evolutions of Binary Black Hole Spacetimes. *Class. Quant. Grav.*, 30:115001, 2013, arXiv: 1211.6079.

[255] Scott A. Hughes. Gravitational waves from extreme mass ratio inspirals: Challenges in mapping the space-time of massive, compact objects. *Class. Quant. Grav.*, 18:4067–4074, 2001, arXiv: gr-qc/0008058.

[256] Pau Amaro-Seoane, Jonathan R. Gair, Marc Freitag, M. Coleman Miller, Ilya Mandel, et al. Astrophysics, detection and science applications of intermediate- and extreme mass-ratio inspirals. *Class. Quant. Grav.*, 24:R113–R169, 2007, arXiv: astro-ph/0703495.

[257] Leor Barack. Gravitational self force in extreme mass-ratio inspirals. *Class. Quant. Grav.*, 26:213001, 2009, arXiv: 0908.1664.

[258] Eric Poisson, Adam Pound, and Ian Vega. The Motion of point particles in curved spacetime. *Living Rev. Rel.*, 14:7, 2011, arXiv: 1102.0529.

[259] Toshifumi Futamase and Yousuke Itoh. The post-Newtonian approximation for relativistic compact binaries. *Living Rev. Rel.*, 10:2, 2007.

[260] Luc Blanchet. Gravitational radiation from post-Newtonian sources and inspiralling compact binaries. *Living Rev. Rel.*, 9:4, 2006.

[261] Ilya Mandel and Jonathan R. Gair. Can we Detect Intermediate Mass Ratio Inspirals? *Class. Quant. Grav.*, 26:094036, 2009, arXiv: 0811.0138.

[262] Charles W. Misner. Interpretation of gravitational-wave observations. *Phys. Rev. Lett.*, 28:994–997, 1972.

[263] Shahar Hod. Stationary scalar clouds around rotating black holes. *Phys. Rev.*, 86:104026, 2012.

[264] Steven L. Detweiler. Black Holes and Gravitational Waves. I. Circular Orbits About a Rotating Hole. *Astrophys. J.*, 225:687–693, 1978.

[265] Shasvath J. Kapadia, Daniel Kennefick, and Kostas Glampedakis. Do floating orbits in extreme mass ratio binary black holes exist? 2013, arXiv: 1302.1016.

[266] Vitor Cardoso, Sayan Chakrabarti, Paolo Pani, Emanuele Berti, and Leonardo Gualtieri. Floating and sinking: The Imprint of massive scalars around rotating black holes. *Phys. Rev. Lett.*, 107:241101, 2011, arXiv: 1109.6021.

[267] Kashif Alvi. Energy and angular momentum flow into a black hole in a binary. *Phys. Rev. D*, 64:104020, 2001, arXiv: gr-qc/0107080.

[268] Eric Poisson. Absorption of mass and angular momentum by a black hole: Time-domain formalisms for gravitational perturbations, and the small-hole / slow-motion approximation. *Phys. Rev. D*, 70:084044, 2004, arXiv: gr-qc/0407050.

[269] Stephanne Taylor and Eric Poisson. Nonrotating black hole in a post-Newtonian tidal environment. *Phys. Rev. D*, 78:084016, 2008, arXiv: 0806.3052.

[270] Katerina Chatziioannou, Eric Poisson, and Nicolas Yunes. Tidal heating and torquing of a Kerr black hole to next-to-leading order in the tidal coupling. *Phys. Rev. D*, 87(4):044022, 2013, arXiv: 1211.1686.

[271] Ulrich Sperhake, Emanuele Berti, Vitor Cardoso, and Frans Pretorius. Universality, maximum radiation and absorption in high-energy collisions of black holes with spin. 2012, arXiv: 1211.6114.

[272] Ryuichi Fujita and Hideyuki Tagoshi. New numerical methods to evaluate homogeneous solutions of the Teukolsky equation. *Prog. Theor. Phys.*, 112:415–450, 2004, arXiv: gr-qc/0410018.

[273] Ryuichi Fujita and Hideyuki Tagoshi. New Numerical Methods to Evaluate Homogeneous Solutions of the Teukolsky Equation II. Solutions of the Continued Fraction Equation. *Prog. Theor. Phys.*, 113:1165–1182, 2005, arXiv: 0904.3818.

[274] William Throwe and Scott A. Hughes. 2013. In preparation.

[275] Emanuele Berti, Vitor Cardoso, Tanja Hinderer, Madalena Lemos, Frans Pretorius, et al. Semianalytical estimates of scattering thresholds and gravitational radiation in ultrarelativistic black hole encounters. *Phys. Rev. D*, 81:104048, 2010, arXiv: 1003.0812.

[276] Lee Samuel Finn and Kip S. Thorne. Gravitational waves from a compact star in a circular, inspiral orbit, in the equatorial plane of a massive, spinning black hole, as observed by LISA. *Phys. Rev. D*, 62:124021, 2000, arXiv: gr-qc/0007074.

[277] R.A. Breuer, P.L. Chrzanowksi, H.G. Hughes, and Charles W. Misner. Geodesic synchrotron radiation. *Phys. Rev. D*, 8:4309–4319, 1973.

[278] Zhongyang Zhang, Nicolas Yunes, and Emanuele Berti. Accuracy of the post-Newtonian approximation. II. Optimal asymptotic expansion of the energy flux for quasicircular, extreme mass-ratio inspirals into a Kerr black hole. *Phys. Rev. D*, 84:024029, 2011, arXiv: 1103.6041.

[279] S.A. Teukolsky. Rotating black holes - separable wave equations for gravitational and electromagnetic perturbations. *Phys. Rev. Lett.*, 29:1114–1118, 1972.

[280] Mark Hannam. Status of black-hole-binary simulations for gravitational- wave detection. *Class. Quant. Grav.*, 26:114001, 2009.

[281] Ian Hinder. The Current Status of Binary Black Hole Simulations in Numerical Relativity. *Class. Quant. Grav.*, 27:114004, 2010.

[282] Joan Centrella, John G. Baker, Bernard J. Kelly, and James R. van Meter. Black-hole binaries, gravitational waves, and numerical relativity. *Rev. Mod. Phys.*, 82(4):3069, 2010.

[283] Alessandra Buonanno et al. Toward faithful templates for non-spinning binary black holes using the effective-one-body approach. *Phys. Rev. D*, 76:104049, 2007, arXiv: 0706.3732.

[284] P. Ajith, S. Babak, Y. Chen, M. Hewitson, B. Krishnan, J. T. Whelan, B. Brügmann, P. Diener, J. Gonzalez, M. Hannam, S. Husa, M. Koppitz, D. Pollney, L. Rezzolla, L. Santamaría, A. M. Sintes, U. Sperhake, and J. Thornburg. A phenomenological template family for black-hole coalescence waveforms. *Class. Quantum Grav.*, 24(19):S689–S699, 2007.

[285] Thibault Damour and Alessandro Nagar. An Improved analytical description of inspiralling and coalescing black-hole binaries. *Phys. Rev. D*, 79:081503, 2009, arXiv: 0902.0136.

[286] Alessandra Buonanno, Yi Pan, Harald P. Pfeiffer, Mark A. Scheel, Luisa T. Buchman, et al. Effective-one-body waveforms calibrated to numerical relativity simulations: Coalescence of non-spinning, equal-mass black holes. *Phys. Rev. D*, 79:124028, 2009, arXiv: 0902.0790.

[287] B. Aylott et al. Testing gravitational-wave searches with numerical relativity waveforms: Results from the first Numerical INJection Analysis (NINJA) project. *Class. Quantum Grav.*, 26(16):165008, 2009.

[288] P. C. Peters. Gravitational radiation and the motion of two point masses. *Phys. Rev.*, 136(4B):B1224–B1232, 1964.

[289] Konstantin Postnov and Lev Yungelson. The Evolution of Compact Binary Star Systems. *Living Rev. Rel.*, 9:6, 2005, arXiv: astro-ph/0701059.

[290] M.C. Miller and D.P. Hamilton. Four-body effects in globular cluster black hole coalescence. *Astrophys. J.*, 576:894–898, 2002.

[291] L. Wen. On the eccentricity distribution of coalescing black hole binaries driven by the kozai mechanism in globular clusters. *Astrophys. J.*, 598:419–430, 2003.

[292] Luc Blanchet. Gravitational radiation from post-Newtonian sources and inspiralling compact binaries. *Living Rev. Rel.*, 9(4), 2006.

[293] Gregory B. Cook. Three-dimensional initial data for the collision of two black holes II: Quasicircular orbits for equal mass black holes. *Phys. Rev. D*, 50(8):5025–5032, 1994.

[294] Thomas W. Baumgarte. The innermost stable circular orbit of binary black holes. *Phys. Rev. D*, 62:024018, 2000.

[295] Harald P. Pfeiffer, Saul A. Teukolsky, and Gregory B. Cook. Quasicircular orbits for spinning binary black holes. *Phys. Rev. D*, 62(10):104018/1–11, 2000.

[296] Eric Gourgoulhon, Philippe Grandclément, and Silvano Bonazzola. Binary black holes in circular orbits. I. A global spacetime approach. *Phys. Rev. D*, 65:044020, 2002.

[297] Philippe Grandclément, Eric Gourgoulhon, and Silvano Bonazzola. Binary black holes in circular orbits. II. numerical methods and first results. *Phys. Rev. D*, 65:044021, 2002.

[298] Wolfgang Tichy, Bernd Brügmann, and Pablo Laguna. Gauge conditions for binary black hole puncture data based on an approximate helical Killing vector. *Phys. Rev. D*, 68:064008, 2003.

[299] Wolfgang Tichy and Bernd Brügmann. Quasiequilibrium binary black hole sequences for puncture data derived from helical Killing vector conditions. *Phys. Rev. D*, 69:024006, 2004. gr-qc/0307027.

[300] Matthew Caudill, Greg B. Cook, Jason D. Grigsby, and Harald P. Pfeiffer. Circular orbits and spin in black-hole initial data. *Phys. Rev. D*, 74(6):064011, 2006.

[301] Jason D. Grigsby and Gregory B. Cook. Measuring eccentricity in binary black-hole initial data. *Phys. Rev.*, 77:044011, 2008, arXiv: 0706.4286.

[302] Sascha Husa, Mark Hannam, José A. González, Ulrich Sperhake, and Bernd Brügmann. Reducing eccentricity in black-hole binary evolutions with initial parameters from post-Newtonian inspiral. *Phys. Rev. D*, 77:044037, 2008, arXiv: 0706.0904.

[303] Benny Walther, Bernd Bruegmann, and Doreen Mueller. Numerical black hole initial data with low eccentricity based on post-Newtonian orbital parameters. *Phys. Rev.*, 79:124040, 2009, arXiv: 0901.0993.

[304] Harald P. Pfeiffer, Duncan A. Brown, Lawrence E. Kidder, Lee Lindblom, Geoffrey Lovelace, and Mark A. Scheel. Reducing orbital eccentricity in binary black hole simulations. *Class. Quantum Grav.*, 24(12):S59–S81, 2007.

[305] Michael Boyle, Duncan A. Brown, Lawrence E. Kidder, Abdul H. Mroué, Harald P. Pfeiffer, Mark A. Scheel, Gregory B. Cook, and Saul A. Teukolsky. High-accuracy comparison of numerical relativity simulations with post-Newtonian expansions. *Phys. Rev. D*, 76:124038, 2007.

[306] Wolfgang Tichy and Pedro Marronetti. A Simple method to set up low eccentricity initial data for moving puncture simulations. 2010, arXiv: 1010.2936.

[307] Geoffrey Lovelace, Mark. A. Scheel, and Bela Szilagyi. Simulating merging binary black holes with nearly extremal spins. *Phys. Rev. D*, 83:024010, 2011, arXiv: 1010.2777.

[308] Abdul H. Mroué, Harald P. Pfeiffer, Lawrence E. Kidder, and Saul A. Teukolsky. Measuring orbital eccentricity and periastron advance in quasi-circular black hole simulations. *Phys. Rev.*, 82:124016, 2010, arXiv: 1004.4697.

[309] Eric Poisson. Gravitational waves from inspiraling compact binaries: The quadrupole-moment term. *Phys. Rev.*, 57:5287–5290, 1998.

[310] Etienne Racine, Alessandra Buonanno, and Lawrence E. Kidder. Recoil velocity at 2PN order for spinning black hole binaries. *Phys. Rev. D*, 80:044010, 2009.

[311] T. Damour and G. Schäfer. Higher-order relativistic periastron advances and binary pulsars. *Nuovo Cimento Soc. Ital. Fis.*, 101 B(2):127, 1988.

[312] Thibault Damour, Piotr Jaranowski, and Gerhard Schaefer. Hamiltonian of two spinning compact bodies with next-to- leading order gravitational spin-orbit coupling. *Phys. Rev.*, 77:064032, 2008, arXiv: 0711.1048.

[313] Rafael A. Porto. Next to leading order spin-orbit effects in the motion of inspiralling compact binaries. *Class. Quant. Grav.*, 27:205001, 2010, arXiv: 1005.5730.

[314] Delphine L. Perrodin. Subleading Spin-Orbit Correction to the Newtonian Potential in Effective Field Theory Formalism. 2010, arXiv: 1005.0634.

[315] Michele Levi. Next-to-leading order gravitational spin-orbit coupling in an effective field theory approach. *Phys. Rev.*, 82:104004, 2010, arXiv: 1006.4139.

[316] Jan Steinhoff, Steven Hergt, and Gerhard Schaefer. On the next-to-leading order gravitational spin(1)-spin(2) dynamics. *Phys. Rev. D*, 77:081501(R), 2008.

[317] J. Steinhoff, G. Schäfer, and S. Hergt. ADM canonical formalism for gravitating spinning objects. *Phys. Rev. D*, 77:104018, 2008.

[318] J. Steinhoff, S. Hergt, and G. Schäfer. Spin-squared Hamiltonian of next-to-leading order gravitational interaction. *Phys. Rev. D*, 78:101503, 2008.

[319] S. Hergt and G. Schäfer. Higher-order-in-spin interaction Hamiltonians for binary black holes from Poincaré invariance. *Phys. Rev. D*, 78(12):124004, 2008.

[320] Rafael A Porto and Ira Z. Rothstein. Next to Leading Order Spin(1)Spin(1) Effects in the Motion of Inspiralling Compact Binaries. *Phys. Rev. D*, 78:044013, 2008, arXiv: 0804.0260.

[321] Rafael A. Porto and Ira Z. Rothstein. Spin(1)Spin(2) Effects in the Motion of Inspiralling Compact Binaries at Third Order in the Post-Newtonian Expansion. *Phys. Rev. D*, 78:044012, 2008, arXiv: 0802.0720.

[322] Thibault Damour, Alessandro Nagar, Ernst Nils Dorband, Denis Pollney, and Luciano Rezzolla. Faithful Effective-One-Body waveforms of equal-mass coalescing black-hole binaries. *Phys. Rev. D*, 77:084017, 2008, arXiv: 0712.3003.

[323] James W. York. Conformal "thin-sandwich" data for the initial-value problem of general relativity. *Phys. Rev. Lett.*, 82(7):1350–1353, 1999.

[324] Harald P. Pfeiffer and James W. York. Extrinsic curvature and the Einstein constraints. *Phys. Rev. D*, 67(4):044022, 2003.

[325] Gregory B. Cook. Corotating and irrotational binary black holes in quasicircular orbits. *Phys. Rev. D*, 65(8):084003, 2002.

[326] Gregory B. Cook and Harald P. Pfeiffer. Excision boundary conditions for black-hole initial data. *Phys. Rev. D*, 70(10):104016, 2004.

[327] H. P. Pfeiffer, L. E. Kidder, M. A. Scheel, and S. A. Teukolsky. A multidomain spectral method for solving elliptic equations. *Comput. Phys. Commun.*, 152:253–273, 2003.

[328] Lee Lindblom, Mark A. Scheel, Lawrence E. Kidder, Robert Owen, and Oliver Rinne. A new generalized harmonic evolution system. *Class. Quantum Grav.*, 23:S447–S462, 2006.

[329] Helmut Friedrich. On the hyperbolicity of Einstein's and other gauge field equations. *Commun. Math. Phys.*, 100(4):525–543, 1985.

[330] David Garfinkle. Harmonic coordinate method for simulating generic singularities. *Phys. Rev. D*, 65(4):044029, 2002.

[331] Frans Pretorius. Numerical relativity using a generalized harmonic decomposition. *Class. Quantum Grav.*, 22(2):425–451, 2005.

[332] Carsten Gundlach, Jose M. Martin-Garcia, Gioel Calabrese, and Ian Hinder. Constraint damping in the Z4 formulation and harmonic gauge. *Class. Quantum Grav.*, 22:3767–3774, 2005.

[333] Oliver Rinne. Stable radiation-controlling boundary conditions for the generalized harmonic Einstein equations. *Class. Quantum Grav.*, 23:6275–6300, 2006.

[334] Oliver Rinne, Lee Lindblom, and Mark A. Scheel. Testing outer boundary treatments for the Einstein equations. *Class. Quantum Grav.*, 24:4053–4078, 2007.

[335] J. M. Stewart. The Cauchy problem and the initial boundary value problem in numerical relativity. *Class. Quantum Grav.*, 15(9):2865–2889, 1998.

[336] Helmut Friedrich and Gabriel Nagy. The initial boundary value problem for Einstein's vacuum field equation. *Commun. Math. Phys.*, 201(3):619–655, 1999.

[337] James M. Bardeen and Luisa T. Buchman. Numerical tests of evolution systems, gauge conditions, and boundary conditions for 1D colliding gravitational plane waves. *Phys. Rev. D*, 65:064037, 2002.

[338] Béla Szilágyi, Bernd Schmidt, and Jeffrey Winicour. Boundary conditions in linearized harmonic gravity. *Phys. Rev. D*, 65(6):064015, 2002.

[339] Gioel Calabrese, Jorge Pullin, Oscar Reula, Olivier Sarbach, and Manuel Tiglio. Well posed constraint-preserving boundary conditions for the linearized Einstein equations. *Commun. Math. Phys.*, 240:377–395, 2003, arXiv: gr-qc/0209017.

[340] Béla Szilágyi and Jeffrey Winicour. Well-posed initial-boundary evolution in general relativity. *Phys. Rev. D*, 68(4):041501(R), 2003.

[341] Lawrence E. Kidder, Lee Lindblom, Mark A. Scheel, Luisa T. Buchman, and Harald P. Pfeiffer. Boundary conditions for the Einstein evolution system. *Phys. Rev. D*, 71:064020, 2005.

[342] Luisa T. Buchman and Olivier C. A. Sarbach. Towards absorbing outer boundaries in general relativity. *Class. Quantum Grav.*, 23:6709–6744, 2006.

[343] L. T. Buchman and O. C. A. Sarbach. Improved outer boundary conditions for Einstein's field equations. *Class. Quantum Grav.*, 24:S307–S326, 2007.

[344] D. Gottlieb and J. S. Hesthaven. Spectral methods for hyperbolic problems. *J. Comput. Appl. Math.*, 128(1–2):83–131, 2001.

[345] J. S. Hesthaven. Spectral penalty methods. *Appl. Num. Math.*, 33:23–41, 2000.

[346] K. G. Arun, Alessandra Buonanno, Guillaume Faye, and Evan Ochsner. Higher-order spin effects in the amplitude and phase of gravitational waveforms emitted by inspiraling compact binaries: Ready-to-use gravitational waveforms. *Phys. Rev.*, 79:104023, 2009.

[347] Laszlo A. Gergely and Zoltan Keresztes. Gravitational radiation reaction in compact binary systems: Contribution of the quadrupole-monopole interaction. *Phys. Rev.*, 67:024020, 2003.

[348] Etienne Racine. Analysis of spin precession in binary black hole systems including quadrupole-monopole interaction. *Phys. Rev.*, 78:044021, 2008.

[349] B. P. Abbott et al. LIGO: The Laser interferometer gravitational-wave observatory. *Rep. Prog. Phys.*, 72:076901, 2009, arXiv: 0711.3041.

[350] H. Grote. The status of GEO 600. *Class. Quant. Grav.*, 25:114043, 2008.

[351] F. Acernese, M. Alshourbagy, P. Amico, F. Antonucci, S. Aoudia, et al. Virgo status. *Class. Quant. Grav.*, 25:184001, 2008.

[352] J. Abadie et al. Search for gravitational waves from binary black hole inspiral, merger and ringdown. *Phys. Rev. D*, 83:122005, 2011, arXiv: 1102.3781.

[353] J. Abadie et al. Search for Gravitational Waves from Intermediate Mass Binary Black Holes. *Phys. Rev. D*, 85:102004, 2012, arXiv: 1201.5999.

[354] P. Ajith, S. Babak, Y. Chen, M. Hewitson, B. Krishnan, et al. A Template bank for gravitational waveforms from coalescing binary black holes. I. Non-spinning binaries. *Phys. Rev. D*, 77:104017, 2008, arXiv: 0710.2335.

[355] Alessandro Nagar. Effective one body Hamiltonian of two spinning black-holes with next-to-next-to-leading order spin-orbit coupling. *Phys. Rev. D*, 84:084028, 2011, arXiv: 1106.4349.

[356] Ryuichi Fujita and Bala R. Iyer. Spherical harmonic modes of 5.5 post-Newtonian gravitational wave polarisations and associated factorised resummed waveforms for a particle in circular orbit around a Schwarzschild black hole. *Phys. Rev. D*, 82:044051, 2010, arXiv: 1005.2266.

[357] Ryuichi Fujita. Gravitational radiation for extreme mass ratio inspirals to the 14th post-Newtonian order. 2011, arXiv: 1104.5615.

[358] Lawrence E. Kidder. Using full information when computing modes of post-Newtonian waveforms from inspiralling compact binaries in circular orbit. *Phys. Rev. D*, 77:044016, 2008, arXiv: 0710.0614.

[359] Luc Blanchet, Guillaume Faye, Bala R. Iyer, and Siddhartha Sinha. The Third post-Newtonian gravitational wave polarisations and associated spherical harmonic modes for inspiralling compact binaries in quasi-circular orbits. *Class. Quant. Grav.*, 25:165003, 2008, arXiv: 0802.1249.

[360] Luc Blanchet, Alessandra Buonanno, and Guillaume Faye. Tail-induced spin-orbit effect in the gravitational radiation of compact binaries. *Phys. Rev. D*, 84:064041, 2011, arXiv: 1104.5659.

[361] K. G. Arun, Alessandra Buonanno, Guillaume Faye, and Evan Ochsner. Higher-order spin effects in the amplitude and phase of gravitational waveforms emitted by inspiraling compact binaries: Ready-to-use gravitational waveforms. *Phys. Rev. D*, 79:104023, 2009, arXiv: 0810.5336.

[362] Geoffrey Lovelace, Michael Boyle, Mark A. Scheel, and Béla Szilágyi. High-accuracy gravitational waveforms for binary-black-hole mergers with nearly extremal spins. *Class. Quant. Grav.*, 29:045003, 2012, arXiv: 1110.2229.

[363] Thibault Damour, Piotr Jaranowski, and Gerhard Schafer. Poincare invariance in the ADM Hamiltonian approach to the general relativistic two-body problem. *Phys. Rev. D*, 62:021501, 2000, arXiv: gr-qc/0003051. Erratum: *Phys. Rev. D*, 63, 029903(E) (2000).

[364] Rafael A. Porto and Ira Z. Rothstein. The Hyperfine Einstein-Infeld-Hoffmann potential. *Phys. Rev. Lett.*, 97:021101, 2006, arXiv: gr-qc/0604099.

[365] Rafael A. Porto, Andreas Ross, and Ira Z. Rothstein. Spin induced multipole moments for the gravitational wave flux from binary inspirals to third Post-Newtonian order. *JCAP*, 1103:009, 2011, arXiv: 1007.1312.

[366] Michele Levi. Next to Leading Order gravitational Spin1-Spin2 coupling with Kaluza-Klein reduction. *Phys. Rev. D*, 82:064029, 2010, arXiv: 0802.1508.

[367] Michele Levi. Binary dynamics from spin1-spin2 coupling at fourth post-Newtonian order. 2011, arXiv: 1107.4322.

[368] Thibault Damour and Alessandro Nagar. Final spin of a coalescing black-hole binary: An Effective-one-body approach. *Phys. Rev. D*, 76:044003, 2007, arXiv: 0704.3550.

[369] Thibault Damour and Achamveedu Gopakumar. Gravitational recoil during binary black hole coalescence using the effective one body approach. *Phys. Rev. D*, 73(12):124006, 2006.

[370] Emanuele Berti, Vitor Cardoso, and Clifford M. Will. Gravitational-wave spectroscopy of massive black holes with the space interferometer LISA. *Phys. Rev. D*, 73:064030, 2006.

[371] Wolfgang Tichy and Pedro Marronetti. The final mass and spin of black hole mergers. *Phys. Rev. D*, 78:081501, 2008, arXiv: 0807.2985.

[372] Enrico Barausse and Luciano Rezzolla. Predicting the direction of the final spin from the coalescence of two black holes. *Astrophys. J.*, 704:L40–L44, 2009, arXiv: 0904.2577.

[373] Christian Reisswig, Sascha Husa, Luciano Rezzolla, Ernst Nils Dorband, Denis Pollney, et al. Gravitational-wave detectability of equal-mass black-hole binaries with aligned spins. *Phys. Rev. D*, 80:124026, 2009, arXiv: 0907.0462.

[374] Michael Kesden. Can binary mergers produce maximally spinning black holes? *Phys. Rev. D*, 78:084030, 2008, arXiv: 0807.3043.

[375] Richard H. Price and Jorge Pullin. Colliding black holes: The Close limit. *Phys. Rev. Lett.*, 72:3297–3300, 1994, arXiv: gr-qc/9402039.

[376] M. Davis, R. Ruffini, W.H. Press, and R.H. Price. Gravitational radiation from a particle falling radially into a schwarzschild black hole. *Phys. Rev. Lett.*, 27:1466–1469, 1971.

[377] M. Davis, R. Ruffini, and J. Tiomno. Pulses of gravitational radiation of a particle falling radially into a schwarzschild black hole. *Phys. Rev. D*, 5:2932–2935, 1972.

[378] David A. Nichols and Yanbei Chen. A hybrid method for understanding black-hole mergers: head-on case. *Phys. Rev. D*, 82:104020, 2010, arXiv: 1007.2024.

[379] David A. Nichols and Yanbei Chen. Hybrid method for understanding black-hole mergers: Inspiralling case. 2011, arXiv: 1109.0081.

[380] James M. Bardeen, William H. Press, and Saul A Teukolsky. Rotating black holes: Locally nonrotating frames, energy extraction, and scalar synchrotron radiation. *Astrophys. J.*, 178:347, 1972.

[381] Alexandre Le Tiec, Enrico Barausse, and Alessandra Buonanno. Gravitational Self-Force Correction to the Binding Energy of Compact Binary Systems. 2011, arXiv: 1111.5609.

[382] D.J.A. McKechan, C. Robinson, and B.S. Sathyaprakash. A tapering window for time-domain templates and simulated signals in the detection of gravitational waves from coalescing compact binaries. *Class. Quant. Grav.*, 27:084020, 2010, arXiv: 1003.2939.

[383] The numerical relativity and analytical relativity (NRAR) collaboration.

[384] LIGO Scientific Collaboration. LSC Algorithm Library software packages LAL, LALWRAPPER, and LALAPPS.

[385] Alexandre Le Tiec, Luc Blanchet, and Bernard F. Whiting. The First Law of Binary Black Hole Mechanics in General Relativity and Post-Newtonian Theory. 2011, arXiv: 1111.5378.

[386] Enrico Barausse, Alessandra Buonanno, and Alexandre Le Tiec. The complete non-spinning effective-one-body metric at linear order in the mass ratio. 2011, arXiv: 1111.5610.

[387] J. Aasi et al. Search for Gravitational Waves from Binary Black Hole Inspiral, Merger and Ringdown in LIGO-Virgo Data from 2009-2010. *Phys. Rev. D*, 87:022002, 2013, arXiv: 1209.6533.

[388] Donato Bini and Thibault Damour. Analytical determination of the two-body gravitational interaction potential at the fourth post-Newtonian approximation. *Phys. Rev. D*, 87(12):121501, 2013, arXiv: 1305.4884.

[389] Enrico Barausse et al. On the mass radiated by coalescing black-hole binaries. *Astrophys. J.*, 758:63, 2012, arXiv: 1206.3803.

[390] Thibault Damour et al. Energy versus Angular Momentum in Black Hole Binaries. *Phys. Rev. Lett.*, 108:131101, 2012, arXiv: 1110.2938.

[391] Manuela Campanelli et al. The Last orbit of binary black holes. *Phys. Rev. D*, 73:061501, 2006, arXiv: gr-qc/0601091.

[392] Alessandra Buonanno, Bala R. Iyer, Evan Ochsner, Yi Pan, and B. S. Sathyaprakash. Comparison of post-newtonian templates for compact binary inspiral signals in gravitational-wave detectors. *Phys. Rev. D*, 80(8):084043, 2009.

[393] F. Acernese et al. Status of Virgo. *Class. Quant. Grav.*, 25:114045, 2008.

[394] `http://sci.esa.int/lisa`.

[395] Thibault Damour, Alessandro Nagar, Mark Hannam, Sascha Husa, and Bernd Brugmann. Accurate Effective-One-Body waveforms of inspiralling and coalescing black-hole binaries. *Phys. Rev. D*, 78:044039, 2008, arXiv: 0803.3162.

[396] Theocharis A. Apostolatos, Curt Cutler, Gerald J. Sussman, and Kip S. Thorne. Spin-induced orbital precession and its modulation of the gravitational waveforms from merging binaries. *Phys. Rev. D*, 49:6274 – 6297, 1994.

[397] Alessandra Buonanno, Yanbei Chen, Yi Pan, Hideyuki Tagoshi, and Michele Vallisneri. Detecting gravitational waves from precessing binaries of spinning compact objects. II. Search implementation for low-mass binaries. *Phys. Rev. D*, 72:084027, 2005, arXiv: gr-qc/0508064.

[398] Patricia Schmidt, Mark Hannam, and Sascha Husa. Towards models of gravitational waveforms from generic binaries: A simple approximate mapping between precessing and non-precessing inspiral signals. *Phys. Rev. D*, 86:104063, 2012, arXiv: 1207.3088.

[399] Patricia Schmidt, Mark Hamman, Sascha Husa, and P. Ajith. Tracking the precession of compact binaries from their gravitational-wave signal. *Phys. Rev. D*, 84:024046, 2011, arXiv: 1012.2879.

[400] O'Shaughnessy, R. and Vaishnav, B. and Healy, J. and Meeks, Z. and Shoemaker, D. Efficient asymptotic frame selection for binary black hole spacetimes using asymptotic radiation. 2011, arXiv: 1109.5224.

[401] Michael Boyle, Robert Owen, and Harald P. Pfeiffer. A geometric approach to the precession of compact binaries. *Phys. Rev. D*, 84:124011, 2011, arXiv: 1110.2965.

[402] Michael Boyle. Angular velocity of gravitational radiation from precessing binaries and the corotating frame. *Phys. Rev. D*, 87(10):104006, 2013, arXiv: 1302.2919.

[403] M. Scheel, M. Boyle, T. Chu, L. Kidder, K. Matthews and H. Pfeiffer. High-accuracy waveforms for binary black hole inspiral, merger, and ringdown. *Phys. Rev. D*, 79:024003, 2009, arXiv: gr-qc/0810.1767.

[404] J. N. Goldberg, A. J. Macfarlane, E. T. Newman, F. Rohrlich, and E. C. G. Sudarshan. Spin-s spherical harmonics and $\eth$. *Journal of Mathematical Physics*, 8(11):2155–2161, 1967.

[405] Luc Blanchet, Alessandra Buonanno, and Guillaume Faye. Higher-order spin effects in the dynamics of compact binaries. II. Radiation field. *Phys. Rev. D*, 74(10):104034, 2006.

[406] Michael Pürrer, Sascha Husa, and Mark Hannam. An Efficient iterative method to reduce eccentricity in numerical-relativity simulations of compact binary inspiral. *Phys. Rev. D*, 85:124051, 2012, arXiv: 1203.4258.

[407] Michael Pürrer, Mark Hannam, P. Ajith, and Sascha Husa. Testing the validity of the single-spin approximation in inspiral-merger-ringdown waveforms. *Phys. Rev. D*, 88:064007, 2013, arXiv: 1306.2320.

[408] Alessandra Buonanno, Larry Kidder, Yi Pan, and Mark Scheel. *Private Communication*, 2013.

[409] R. O'Shaughnessy, L. London, J. Healy, and D. Shoemaker. Precession during merger 1: Strong polarization changes are observationally accessible features of strong-field gravity during binary black hole merger. *Phys. Rev. D*, 87:044038, 2013, arXiv: 1209.3712.

[410] Evan Ochsner and Richard O'Shaughnessy. Asymptotic frame selection for binary black hole spacetimes II: Post-Newtonian limit. *Phys. Rev. D*, 86:104037, 2012, arXiv: 1205.2287.

[411] Thibault Damour, Bala R. Iyer, and B. S. Sathyaprakash. Improved filters for gravitational waves from inspiraling compact binaries. *Phys. Rev. D*, 57(2):885–907, 1998.

[412] Takahiro Tanaka, Hideyuki Tagoshi, and Misao Sasaki. Gravitational waves by a particle in circular orbits around a Schwarzschild black hole: 5.5 postNewtonian formula. *Prog. Theor. Phys.*, 96:1087–1101, 1996, arXiv: gr-qc/9701050.

[413] Ryuichi Fujita. Gravitational Waves from a Particle in Circular Orbits around a Schwarzschild Black Hole to the 22nd Post-Newtonian Order. *Prog. Theor. Phys.*, 128:971–992, 2012, arXiv: 1211.5535.

[414] Enrico Barausse, Vitor Cardoso, and Gaurav Khanna. Testing the Cosmic Censorship Conjecture with point particles: the effect of radiation reaction and the self-force. *Phys. Rev. D*, 84:104006, 2011, arXiv: 1106.1692.

[415] Jonathan R Gair and Kostas Glampedakis. Improved approximate inspirals of test-bodies into Kerr black holes. *Phys. Rev. D*, 73:064037, 2006, arXiv: gr-qc/0510129.